UNIVERSIDADE FEDERAL DO RIO GRANDE DO SUL

INSTITUTO DE PESQUISAS HIDRÁULICAS

PROGRAMA DE PÓS-GRADUAÇÃO EM RECURSOS HÍDRICOS E SANEAMENTO AMBIENTAL

INUNDAÇÕES EM MÚLTIPLAS ESCALAS NA AMÉRICA DO SUL: DE ÁREAS ÚMIDAS A ÁREAS DE RISCO

Ayan Santos Fleischmann

Orientador: Prof. Walter Collischonn

Coorientador: Prof. Rodrigo Cauduro Dias de Paiva

Coorientador: Dr. Fabrice Papa

Porto Alegre, agosto de 2021.

UNIVERSIDADE FEDERAL DO RIO GRANDE DO SUL

INSTITUTO DE PESQUISAS HIDRÁULICAS

PROGRAMA DE PÓS-GRADUAÇÃO EM RECURSOS HÍDRICOS E SANEAMENTO AMBIENTAL

INUNDAÇÕES EM MÚLTIPLAS ESCALAS NA AMÉRICA DO SUL: DE ÁREAS ÚMIDAS A ÁREAS DE RISCO

Ayan Santos Fleischmann

Tese de Doutorado apresentada ao Programa de Pós Graduação em Recursos Hídricos e Saneamento Ambiental, do Instituto de Pesquisas Hidráulicas, da Universidade Federal do Rio Grande do Sul, como parte dos requisitos para a obtenção do título de Doutor em Recursos Hídricos e Saneamento Ambiental.

Orientador: Prof. Walter Collischonn

Coorientador: Prof. Rodrigo Cauduro Dias de Paiva

Coorientador: Dr. Fabrice Papa

Banca Examinadora:

Dr. David Kaplan (University of Florida)

Dr. Fernando Jaramillo (University of Stockholm)

Dr. Naziano Pantoja Filizola Junior (Universidade Federal do Amazonas)

Dr. David da Motta Marques (Universidade Federal do Rio Grande do Sul)

FEDERAL UNIVERSITY OF RIO GRANDE DO SUL

INSTITUTE OF HYDRAULIC RESEARCH

GRADUATE PROGRAM IN WATER RESOURCES AND ENVIRONMENTAL SANITATION

SOUTH AMERICAN FLOODS ACROSS SCALES: FROM NATURAL WETLANDS TO HUMAN-WATER SYSTEMS

Ayan Santos Fleischmann

A dissertation submitted to the Federal University of Rio Grande do Sul in accordance with the requirements for award of degree of Doctor of Philosophy in the Graduate Program in Water Resources and Environmental Sanitation.

Supervisor: Prof. Walter Collischonn

Co-supervisor: Prof. Rodrigo Cauduro Dias de Paiva

Co-supervisor: Dr. Fabrice Papa

Porto Alegre, August 2021.

CIP - Catalogação na Publicação

Santos Fleischmann, Ayan
Inundações em múltiplas escalas na América do Sul: de áreas úmidas a áreas de risco / Ayan Santos Fleischmann. -- 2021.
453 f.
Orientador: Walter Collischonn.

Coorientador: Rodrigo Cauduro Dias de Paiva.

Tese (Doutorado) -- Universidade Federal do Rio Grande do Sul, Instituto de Pesquisas Hidráulicas, Programa de Pós-Graduação em Recursos Hídricos e Saneamento Ambiental, Porto Alegre, BR-RS, 2021.

1. Inundações. 2. Áreas úmidas. 3. Amazônia. 4. Hidrologia. I. Collischonn, Walter, orient. II. Cauduro Dias de Paiva, Rodrigo, coorient. III. Título.

Elaborada pelo Sistema de Geração Automática de Ficha Catalográfica da UFRGS com os dados fornecidos pelo(a) autor(a).

Na paisagem do rio
difícil é saber
onde começa o rio;
onde a lama
começa do rio;
onde a terra
começa da lama;
onde o homem,
onde a pele
começa da lama;
onde começa o homem
naquele homem.

(João Cabral de Melo Neto, O cão sem plumas)

turvo turvo

a turva

mão do sopro

contra o muro

escuro

menos menos

menos que escuro

menos que mole e duro menos que fosso e muro: menos que furo

escuro

mais que escuro;

claro

(Ferreira Gullar, Poema sujo)

Agradecimentos

Esta tese foi amplamente motivada pela curiosidade, e a vejo como uma interessada jornada pelos rios e áreas úmidas deste continente em que nasci.

Que só pode se desenvolver

com o auxílio luxuoso

e a irrestrita parceria que desenvolvi com inúmeros colegas, amigos e familiares

ao longo de minha vida.

Agradeço especialmente:

Aos meus orientadores e amigos Walter, Rodrigo e Fabrice, por todo ensinamento, motivação e suporte ao longo destes anos;

Aos meus amigos, amigas e colegas do IPH e Engenharia Ambiental (Siqueira, João Paulo, Anderson, Fernando, Hugo, Pedro, Sly, Alice, Léo, Paixão, Veredas, Cléber, Arthur, Aline, Mino, Germano, Otávio, Sofia, Thaís, Rê, Jéssica, Regina, Dani, Beni, Adriana e tantos outros que aqui não menciono por ocasião de brevidade), sem os/as quais esta tese não se desenvolveria;

Aos meus colegas, amigos e amigas de Toulouse (Adrien, Rômulo, Benjamin, Ahmad, Marielle, Stéphane, Sylvain) e da CPRM (Daniel e tantos outros), e das redes "Amazon Dams" (Rafael, Alex, Héctor, Steve, John) e Conexões Amazônicas, que promoveram muitos dos debates que engendraram esta tese;

Aos órgãos financiadores de minha bolsa e variados custeios: CNPq, CAPES, ANA e IRD (França);

Ao IPH e à UFRGS pela infraestrutura cedida, assim como à Université de Toulouse durante o meu período sanduíche, e aos vários professores do PPGRHSA/UFRGS, sempre solícitos e dispostos a cooperação;

À minha família, em especial minha mãe, Nádia, que despertou logo em meu amanhecer o amor pela pesquisa, e a meu pai, Rogério, pelo apoio incondicional;

À Bianca, minha querida companheira que tanto tem despertado em mim

a amazônica alegria que habita em todos nós;

À democracia e aos governos brasileiros, que têm financiado, por anos a fio, os meus estudos e os avanços científicos aqui presentes – um país só pode ser chamado de desenvolvido se faculta a seus jovens o desenvolvimento de seus potenciais. Se tive o privilégio de ter o apoio do estado brasileiro, tantos outros e outras jovens ainda carecem do mesmo.

Aos rios que fluíram por meus caminhos;

À infinda busca pelo desconhecido.

Apresentação geral

Esta tese foi desenvolvida no Programa de Pós-Graduação em Engenharia de Recursos Hídricos e Saneamento Ambiental do Instituto de Pesquisas Hidráulicas (IPH) da Universidade Federal do Rio Grande do Sul (UFRGS) sob a orientação do prof. Walter Collischonn (IPH-UFRGS) e coorientação do Prof. Rodrigo Cauduro Dias de Paiva (IPH-UFRGS) e Dr. Fabrice Papa (IRD/França). A pesquisa foi financiada com bolsa de Doutorado pelo Conselho Nacional de Desenvolvimento Científico e Tecnológico (CNPq – processo 141161/2017-5) no período de Março de 2017 a Maio de 2021, com período de Doutorado Sanduíche na Université de Toulouse (França) financiado com bolsa de estudos concedida pelo CNPq (processo 201148/2019-6), entre Fevereiro e Junho de 2021, o qual foi interrompido pelo avanço da pandemia do Covid-19.

As principais publicações referentes a esta tese estão listadas a seguir:

- **Fleischmann**, A., Paiva, R., Collischonn, W, 2019. Can regional to continental river hydrodynamic models be locally relevant? A cross-scale comparison. Journal of Hydrology X 3, 100027. https://doi.org/10.1016/j.hydroa.2019.100027

- **Fleischmann**, A.S., Paiva, R.C.D., Collischonn, W., Siqueira, V.A., Paris, A., Moreira, D.M., Papa, F., Bitar, A.A., Parrens, M., Aires, F., Garambois, P.A., 2020. Trade-Offs Between 1-D and 2-D Regional River Hydrodynamic Models. Water Resources Research 56, e2019WR026812. https://doi.org/10.1029/2019WR026812

- **Fleischmann**, A.S., Siqueira, V.A., Wongchuig-Correa, S., Collischonn, W., Paiva, R.C.D. de, 2020. The great 1983 floods in South American large rivers: a continental hydrological modelling approach. Hydrological Sciences Journal 65(8), 1358-1373. https://doi.org/10.1080/02626667.2020.1747622

- **Fleischmann**, A.S., Brêda, J.P.F., Passaia, O.A., Wongchuig, S.C., Fan, F.M., Paiva, R.C.D., Marques, G.F., Collischonn, W., 2021. Regional scale hydrodynamic modeling of the river-floodplain-reservoir continuum. Journal of Hydrology 596, 126114. https://doi.org/10.1016/j.jhydrol.2021.126114

- **Fleischmann**, A.S., Fialho Brêda, J.P., Rudorff, C., Dias de Paiva, R.C., Collischonn, W., Papa, F., Ravanello, M.M., 2021. River Flood Modeling and Remote Sensing Across Scales: Lessons from Brazil, in: Schumann, G.J.P. (Ed.), Earth Observation for Flood Applications. Elsevier, 61–103. https://doi.org/10.1016/B978-0-12-819412-6.00004-3

- **Fleischmann**, A.S., Laipelt, L., Papa, F., Ruhoff, A., Paiva, R.C.D., Biudes, M.S., Kayser, R., Prigent, C., Cosio, E., Machado, N.G., Collischonn, W. Patterns and drivers of evapotranspiration in South American wetlands. Em revisão no periódico Nature Communications. Preprint: https://www.researchsquare.com/article/rs-353527/v1

- **Fleischmann**, A., Papa, F., Paiva, R.C.D., Prigent, C., Ovando, A., Paris, A., Calmant, S., Collischonn, W., em preparação. South American wetlands from space: a comparative hydrology approach.

- **Fleischmann**, A., Papa, F., Fassoni-Andrade, A., Melack, J., Wongchuig, S., Paiva, R.C.D., Hamilton, S., Fluet-Chouinard, E., Aires, F., Al Bitar, A., Bonnet, M.P., Coe, M., Ferreira-Ferreira, J., Fontana, R., Hess, L., Jensen, K., McDonald, K., Ovando, A., Park, E., Parrens, M., Pinel, S., Prigent, C., Resende, A., Revel, M., Rosenqvist, A., Rudorff, C., Silva, T., Yamazaki, D., Collischonn, W., em preparação. How much inundation occurs in the Amazon?

- **Fleischmann**, A., Papa, F., Wongchuig, S., Fassoni-Andrade, A., Espinoza, J.C., Paiva, R.C.D., Melack, J.M., Fluet-Chouinard, E., Hamilton, S., Almeida, R., Bonnet, M.P., Castello, L., Alves, L.G., Moreira, D., Yamazaki, D., Revel, M., Collischonn, W., em preparação. A one-fifth increase in the inundation extent over the central Amazon between 1980 and 2020.

Algumas áreas úmidas do nosso continente, registradas durante a elaboração desta tese.

General presentation

This thesis was developed in the Water Resources and Sanitation Graduation Program (PPGRHSA) of the Hydraulic Research Institute (IPH) in the Federal University of Rio Grande do Sul (UFRGS), under the supervision of Prof. Walter Collischonn (IPH-UFRGS) and co-supervision of Prof. Rodrigo Cauduro Dias de Paiva (IPH-UFRGS) and Dr. Fabrice Papa (IRD/France). This research was funded by the Conselho Nacional de Desenvolvimento Científico e Tecnológico (CNPq – grant number 141161/2017-5) between March 2017 and May 2021, with a period abroad in the Université de Toulouse (France) funded by CNPq (grant number 201148/2019-6), between February and June 2021, which was interrupted due to the Covid-19 pandemic.

The main publications related to this thesis are:

- **Fleischmann**, A., Paiva, R., Collischonn, W, 2019. Can regional to continental river hydrodynamic models be locally relevant? A cross-scale comparison. Journal of Hydrology X 3, 100027. https://doi.org/10.1016/j.hydroa.2019.100027

- **Fleischmann**, A.S., Paiva, R.C.D., Collischonn, W., Siqueira, V.A., Paris, A., Moreira, D.M., Papa, F., Bitar, A.A., Parrens, M., Aires, F., Garambois, P.A., 2020. Trade-Offs Between 1-D and 2-D Regional River Hydrodynamic Models. Water Resources Research 56, e2019WR026812. https://doi.org/10.1029/2019WR026812

- **Fleischmann**, A.S., Siqueira, V.A., Wongchuig-Correa, S., Collischonn, W., Paiva, R.C.D. de, 2020. The great 1983 floods in South American large rivers: a continental hydrological modelling approach. Hydrological Sciences Journal 65(8), 1358-1373. https://doi.org/10.1080/02626667.2020.1747622

- **Fleischmann**, A.S., Brêda, J.P.F., Passaia, O.A., Wongchuig, S.C., Fan, F.M., Paiva, R.C.D., Marques, G.F., Collischonn, W., 2021. Regional scale hydrodynamic modeling of the river-floodplain-reservoir continuum. Journal of Hydrology 596, 126114. https://doi.org/10.1016/j.jhydrol.2021.126114

- **Fleischmann**, A.S., Fialho Brêda, J.P., Rudorff, C., Dias de Paiva, R.C., Collischonn, W., Papa, F., Ravanello, M.M., 2021. River Flood Modeling and Remote Sensing Across Scales: Lessons from Brazil, in: Schumann, G.J.P. (Ed.), Earth Observation for Flood Applications. Elsevier, 61–103. https://doi.org/10.1016/B978-0-12-819412-6.00004-3

- **Fleischmann**, A.S., Laipelt, L., Papa, F., Ruhoff, A., Paiva, R.C.D., Biudes, M.S., Kayser, R., Prigent, C., Cosio, E., Machado, N.G., Collischonn, W.

Patterns and drivers of evapotranspiration in South American wetlands. Under review in Nature Communications. Preprint: https://www.researchsquare.com/article/rs-353527/v1

- **Fleischmann**, A., Papa, F., Paiva, R.C.D., Prigent, C., Ovando, A., Paris, A., Calmant, S., Collischonn, W., in preparation. South American wetlands from space: a comparative hydrology approach.

- **Fleischmann**, A., Papa, F., Fassoni-Andrade, A., Melack, J., Wongchuig, S., Paiva, R.C.D., Hamilton, S., Fluet-Chouinard, E., Aires, F., Al Bitar, A., Bonnet, M.P., Coe, M., Ferreira-Ferreira, J., Fontana, R., Hess, L., Jensen, K., McDonald, K., Ovando, A., Park, E., Parrens, M., Pinel, S., Prigent, C., Resende, A., Revel, M., Rosenqvist, A., Rudorff, C., Silva, T., Yamazaki, D., Collischonn, W., in preparation. How much inundation occurs in the Amazon?

- **Fleischmann**, A., Papa, F., Wongchuig, S., Fassoni-Andrade, A., Espinoza, J.C., Paiva, R.C.D., Melack, J.M., Fluet-Chouinard, E., Hamilton, S., Almeida, R., Bonnet, M.P., Castello, L., Alves, L.G., Moreira, D., Yamazaki, D., Revel, M., Collischonn, W., in preparation. A one-fifth increase in the inundation extent over the central Amazon between 1980 and 2020.

Some wetlands of our continent, registered during the elaboration of this thesis.

Resumo

A América do Sul abriga alguns dos maiores sistemas hídricos do planeta, frequentemente associados a grandes planícies de inundação, como o Pantanal e várias áreas da Amazônia. Áreas úmidas (AU's) interfluviais são também encontrados no continente, com características geomorfológicas particulares, e vegetações de savana e gramíneas únicas. As AU's da América do Sul provêm diversos serviços ecossistêmicos, como suporte à biodiversidade, provisão de alimento e atenuação de cheias. Humanos têm se estabelecido ao redor de AU's por milênios, se beneficiando dos recursos providos por elas. Eles se adaptaram ao seu regime de inundação, e adaptaram sua paisagem, definindo o que tem sido chamado de sistemas sociedade-água. Por outro lado, um número crescente de pessoas têm sido negativamente afetado por cheias extremas. Da escala continental à local, esta tese convida o leitor a uma jornada através de importantes AU's da América do Sul e suas particulares dinâmicas de inundação, sob a luz da era dos satélites e dos grandes avanços em modelagem hidrológica-hidrodinâmica das últimas décadas. Este trabalho é baseado na proposta de uma escala continental de pesquisa sobre AU's, e é baseado em uma abordagem de hidrologia comparativa. Inundações são estudadas em múltiplas dimensões, de processos de AU's naturais à questão do perigo para humanos. A primeira parte apresenta uma série de estudos sobre as AU's da bacia amazônica, desde o desenvolvimento de modelos 1D e 2D para simular processos hidrológicos em tipos contrastantes de AU's na bacia do Rio Negro, até a intercomparação de 29 produtos de inundação e avaliação de tendências de inundações de longo prazo para a escala da bacia amazônica. Enquanto a maioria dos estudos de AU's foi conduzida nas várzeas do rio Amazonas, importantes lacunas do conhecimento permanecem para a compreensão da dinâmica hidrológica de áreas interfluviais como Llanos de Moxos e as savanas do rio Negro, onde a inundação é menos previsível e mais rasa. A segunda parte da tese utiliza dados oriundos de satélites relacionados a múltiplas variáveis hidrológicas (níveis d'água, armazenamento total de água, extensão de áreas inundadas, precipitação e evapotranspiração) para estudar a hidrologia de 12 grandes sistemas de AU's do continente. São destacadas as grandes diferenças entre planícies de inundação e AU's interfluviais em termos de amplitude anual de níveis d'água, defasagem entre precipitação e inundação, e dinâmica de evapotranspiração. Por fim, a última parte da tese aborda o componente de perigo de inundação das interações sociedade-água através de avaliações em grande escala da dinâmica de inundação e dos efeitos de infraestruturas construídas (como barragens) na atenuação de cheias. A dinâmica das grandes cheias de 1983, um dos anos mais extremos já registrados no continente, é avaliada com um modelo hidrológico continental. Depois, a capacidade de modelos continentais para simular o *continuum* entre rios, planícies de inundação e reservatórios que existe em grandes bacias hidrográficas é avaliada com estudos de casos para importantes bacias afetadas pela intervenção humana (bacia dos rios Paraná e Itajaí-Açu). Enquanto esta tese avança a compreensão de relevantes processos hidrológicos relacionados a inundações na América do Sul em múltiplas escalas, bem como seus efeitos positivos e negativos nas sociedades humanas e ecossistemas em geral, importantes lacunas do conhecimento persistem e fomentam importantes oportunidades de pesquisa futuras. O lançamento de várias missões satelitais orientadas a hidrologia, e uma cada vez mais crescente capacidade computacional, faz da agenda continental de hidrologia relacionada a AU's e inundações um grande tópico de pesquisa para os próximos anos.

Palavras-chave: planícies de inundação, áreas úmidas interfluviais, Amazônia

Abstract

South America hosts some of the major river systems on Earth, often associated with large floodplains that are inundated every year, such as the Pantanal and many Amazon wetlands. Interfluvial wetland complexes are also found across the continent, with particular geomorphic settings and unique savanna or grassland vegetation. South American wetlands can provide distinctive ecosystem services such as biodiversity supporting, food provision and flood attenuation. On the other hand, humans have settled around wetlands for millennia, benefiting from all resources they provide, and have adapted to its flood regime as well adapted its landscape, defining what has been called human-water systems. Yet, an increasing number of South American people have been negatively affected by extreme floods. Moving from continental to local scales, this thesis invites the readers to a journey across major South American wetland systems and their unique hydrological dynamics, under the light of the satellite era and the breakthrough advances on hydrologic-hydrodynamic modeling in the last decades. This work is founded on the proposition of a continental wetland research agenda, and based on a comparative hydrology approach. Floods are studied through both natural wetland processes and hazard dimensions. The first part presents a set of studies on the Amazon basin wetlands, from the development of 1D and 2D models to simulate hydrological processes in contrasting wetland types in the Negro river basin to the basin-wide intercomparison of 29 inundation products and assessment of long-term inundation trends. While most wetland studies have been conducted over the central Amazon floodplains, major knowledge gaps remain for understanding the hydrological dynamics of interfluvial areas such as the Llanos de Moxos and Negro savannas, where the inundation is less predictable and shallower. The second part of the thesis leverages satellite-based datasets of multiple hydrological variables (water levels, total water storage, inundation extent, precipitation and evapotranspiration) to address the hydrology of 12 large wetland systems in the continent. It shows the major differences among river floodplains and interfluvial wetlands on the water level annual amplitude, time lag between precipitation and inundation, and evapotranspiration dynamics. Finally, the third part addresses the flood hazard component of human-wetland interactions through large-scale assessments of flood hazard dynamics and effects of built infrastructure (dams) on flood attenuation. The dynamics of the great 1983 floods, one of the most extreme years ever recorded in the continent, is assessed with a continental hydrological model. Then, the capabilities of continental models to simulate the river-floodplain-reservoir continuum that exists across large river basins are assessed with case studies for major river basins affected by human intervention (Itajaí-Açu and upper Paraná river basins in Brazil). While this thesis enlightens some relevant hydrological processes regarding South American floods and their positive and negative effects to human societies and ecosystems in general, major knowledge gaps persist and provide great research opportunities for the near future. The launching of many hydrology-oriented satellite missions, and an ever-growing computational capacity, make the continental hydrology agenda related to wetlands and floods a great research topic for the upcoming years.

Key words: inundation, river floodplains, interfluvial wetlands, Amazon

Sobre o idioma de escrita desta tese

Esta tese é redigida principalmente em inglês. A fim de torná-la compreensível para o leitor brasileiro não habituado à leitura em inglês, os capítulos de introdução (1) e conclusão (12) foram também escritos em português, bem como o Capítulo 2 que apresenta um sumário expandido da contribuição científica desta tese. Além disso, uma seção introdutória em português foi adicionada para cada capítulo de revisão bibliográfica (Capítulo 3) e resultados da tese (Capítulos 4-11).

About the writing language in this thesis

This thesis is mainly written in English. However, to address those Portuguese speakers that are not familiar with English, the introduction (Chapter 1) and conclusion (Chapter 2) sections are presented in Portuguese, as well as Chapter 2 which presents a summary of this thesis' scientific contributions. Additionally, an abstract is provided in Portuguese at the beginning of each literature review (Chapter 3) and result section (Chapters 4-11).

Contents

1 Presentation

1.1 Introduction

Wetlands are areas at the interface between aquatic and terrestrial environments, and they can be natural or artificial, permanently or periodically inundated by shallow water, or consist of waterlogged soils (JUNK et al., 2014). Soils, animals and plants are distinct from the surrounding environments and adapt to the local flood pulse regime (JUNK; BAYLEY; SPARKS, 1989; WOODWARD; WUI, 2001). These areas represent extensive parts of river basins, providing diverse ecosystem services as water quality control, nutrient retention/removal/transformation, flood attenuation, provision of animal and vegetal products, and maintenance of biodiversity (ACREMAN; HOLDEN, 2013; COSTANZA et al., 1998; FAN; MIGUEZ-MACHO, 2011; JUNK et al., 2014; MALTBY; ACREMAN, 2015; WHALEN, 2005; WOODWARD; WUI, 2001). In South America, there exist various regions where thousands of square kilometers are seasonally or permanently inundated (Figure 1.1), as the central Amazon floodplains, Llanos de Moxos, Bananal Island and Pantanal (HAMILTON; SIPPEL; MELACK, 2002). Each area presents particular inundation patterns and hydrological processes, as river-floodplain connectivity (TRIGG et al., 2012, 2013), the interaction between soil, evapotranspiration and flooded areas, and the way it is maintained or fed by groundwater (FAN; MIGUEZ-MACHO, 2011; MIGUEZ-MACHO; FAN, 2012). Different hydrologic and hydrodynamic processes then interact throughout the inundation cycle, generating diverse regions where in some cases overbank flow is the main flooding process (e.g., Amazon mainstem floodplains), while in others it is a combination of local rainfall and high water table levels (e.g., Negro savanna wetlands). Given the large dimension of these areas in the regional/continental context, it is fundamental to understand their interaction with the regional climate (TAYLOR; PRIGENT; DADSON, 2018), as well as potential vulnerabilities to environmental alterations (e.g., climate change, dam building, and land use changes), which are still poorly known. In South America, inventories and classification systems of wetlands have been recently proposed at national scales (BENZAQUEN et al., 2017; JUNK et al., 2014; RICAURTE et al., 2012), but there is still a great lack of knowledge on the wetlands hydrologic functioning.

Humans have settled around wetlands, especially along river floodplains (Figure 1.1), for millennia (BLATRIX et al., 2018; DENEVAN, 1996), benefiting from all resources they provide, as well as major facilities such as transportation. They have changed the environment and landscape, such as its land cover, as occurs in current urban centers that occupy periodically flooded areas, and even the river-floodplain dynamics, through building of infrastructure such as dams and levees. However, the proximity to rivers also poses some threats, especially during anomalous high floods, which negatively affect millions of people every year worldwide – and the presence of humans over floodplains has increased in the last decades (MAZZOLENI et al., 2021).

Floodplain societies, often associated with poor and vulnerable communities, have the challenge to adapt to the spatio-temporal variation of the river-wetland hydrological regime, or try to adapt it to their needs, which include the reduction of flood exposure. Wetlands and floodplains must be seen, then, as human-water systems.

Monitoring inundation dynamics is not straightforward, especially for those wetlands located in remote, ungauged areas, for which observation data that are alternative to in situ monitoring are required. Recent advances in remote sensing have been done, and considerably increased our comprehension of the hydrology of wetlands and floods globally (PAPA et al., 2010; RAST; JOHANNESSEN; MAUSER, 2014; SCHUMANN et al., 2009). Products now available include datasets on rivers and wetlands water levels (SANTOS DA SILVA et al., 2010), and surface water extent and storage at high spatial resolutions (AIRES et al., 2017; ALSDORF et al., 2007; CAO et al., 2018; FRAPPART et al., 2005; PRIGENT et al., 2007). Process-based hydrological and hydrodynamic models, that mathematically represent the hydrological cycle processes, are also feasible from local to global scales (BIERKENS et al., 2015; FLEISCHMANN; PAIVA; COLLISCHONN, 2019; PAIVA et al., 2013a; YAMAZAKI et al., 2011), and may be very useful for understanding processes and projecting alterations due, for instance, to climate and land use changes.

In this context, the scientific community has developed in the last decade a research agenda on continental hydrology, addressing the necessity of improving hydrologic-hydrodynamic models at regional (i.e., >10.000 km²) to continental scales (>1.000.000 km²) at high spatial resolution (BATES et al., 2018b; BIERKENS et al., 2015; FLEISCHMANN; PAIVA; COLLISCHONN, 2019; HODGES, 2013; TRIGG et al., 2016; WOOD et al., 2011). Its objectives include the improvement of model representation of the complex wetland water fluxes and the interaction between hydrodynamic (e.g., flooding, backwater, flood attenuation) and hydrological (e.g., evapotranspiration and water infiltration into soil) processes (FLEISCHMANN et al., 2018; HOCH; TRIGG, 2018; NEAL; SCHUMANN; BATES, 2012; PAZ et al., 2011; YAMAZAKI et al., 2014b). These modeling tools have been fostering our comprehension and predictive capacity of wetland hydrology at the continental scale. Overall, continental hydrology research aims at (i) comprehending continental to global processes such as the interaction between land surface and global climate (e.g., for climate change studies), and the export of water and solutes from continents to the oceans; (ii) continentally evaluating water resources for decision-makers such as public managers, NGO's, global agencies (e.g,. World Bank) and other stakeholders; and (iii) developing continental scale products such as maps (e.g., global flood risk maps), alert systems (e.g., for drought and floods) and estimates of variables of interest (e.g., discharge, water level, evapotranspiration) for use in ungauged areas, e.g., developing countries with insufficient monitoring network or under civil conflicts.

In the specific context of wetlands and flood hydrology, their study at continental scale is important for:

- Comprehending processes in different wetlands through comparative hydrology, e.g., by contrasting the hydrological dynamics of different wetland types as river floodplains and interfluvial areas;
- Assessing continental scale, spatio-temporal dynamics of past hydroclimatic events and atmospheric teleconnection patterns affecting different wetlands, in order to understand their relative response to climate change and variability (e.g., response to ENSO);
- Understanding the interaction between wetlands and regional/continental climate, including surface-atmosphere feedbacks and greenhouse gas emissions;
- Developing inventories of wetlands (location, extension, stored volumes, etc.) for management purposes;
- Estimating the vulnerability of wetlands to human threats at continental scale, and the associated impacts on ecosystem services (e.g., threats to water and food security at large scales);
- Understanding the spatio-temporal dynamics of flood hazard at large scales, i.e., larger than the river basin limits, since there are processes that do not occur at the catchment scale alone (e.g. atmospheric moisture transport) and flood losses may reach regions far from the affected catchments through indirect economic effects. This has major implications for flood risk management, assisting local to national and international initiatives.

Then, the following research questions may be enumerated in the context of the hydrology of wetlands and floods in South America, which will be addressed to some extent in this thesis:

- How different are South American wetlands in terms of hydrological behaviors and hydrology-related ecosystem services?
- How do wetlands interact with regional/continental climate, e.g., through evapotranspiration fluxes?
- How do wetlands respond to, and interact with, current and future environmental alterations (e.g., climate change, dam building, land use and cover changes)?
- How do remote sensing datasets, from global to local scales, depict inundation dynamics over multiple wetlands? Do they agree on inundation extent, and how to improve their performance?
- How do continental models represent wetlands and local hydrodynamic processes, and how to improve their performance?
- How humans are affected by, and affect, the normal and anomalous inundation events along wetlands, especially along river floodplains?

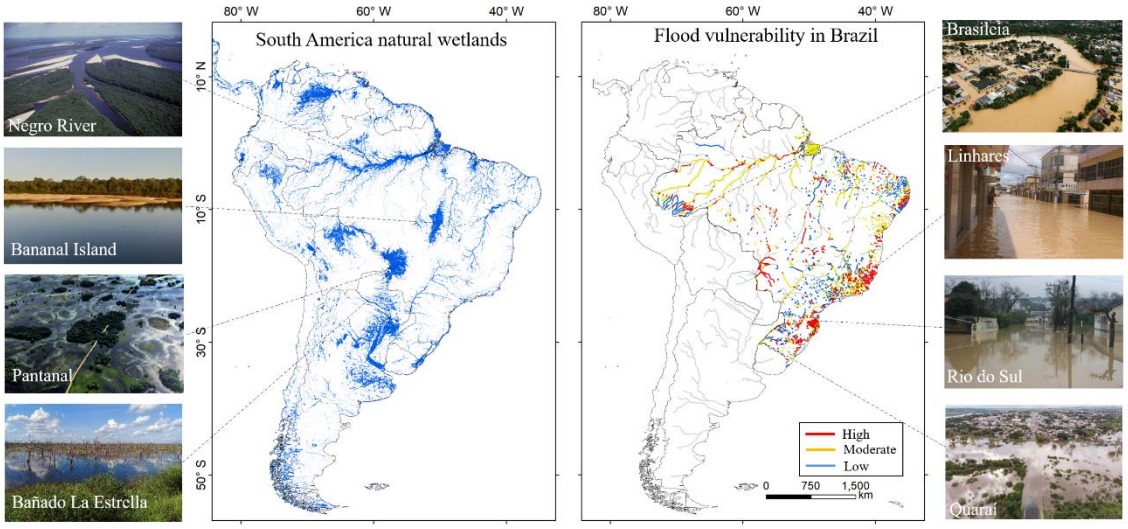

Figure 1.1. The contrasts between natural wetland systems across South America, on the left, and flood vulnerable river reaches in Brazil, on the right, where human societies have been settling for thousands of years. Source: FLEISCHMANN et al. (2021).

1.2 Objectives

The main objective of this thesis is to foster the comprehension of wetland hydrological processes in South America, from a cross-scale perspective and through a comparative hydrology approach. It aims to move forward a continental wetland research agenda that is capable of differentiating major inundation dynamics processes occurring in large South American wetland systems from those occurring in the widespread river floodplains, where millions of people live.

Specific objectives of this thesis are:

- Comprehension of differences among hydrological processes (through variables such as water levels, inundation extent and evapotranspiration) in contrasting wetland types, e.g., river floodplains and interfluvial wetlands, for the large South American wetland systems;
- Synthesis of hydrological processes of the large South American wetlands, especially regarding the dynamics of inundation, precipitation, total water storage, surface water level and evapotranspiration over these areas;
- Development of a 2D regional scale model to simulate coupled hydrologic and hydrodynamic processes over complex wetlands, and comparison of this model with 1D approaches;
- Assessment of current inundation mapping capabilities over distinct wetland types;
- Assessment of previous extreme floods that have affected large-scale domains, such as the 1983 floods in South America and the increased inundation trends over central and northern Amazon basin in the last decades;

- Assessment of how improving continental-scale hydrodynamic models to estimate locally relevant variables and continuous fields of variables such as surface water levels;
- Assessment of how manmade infrastructure, such as dams, affect flood hazard and interact with floodplains to attenuate floods at large scales.

1.3 Thesis organization

This thesis is divided into 13 chapters, which include the introductory chapters 1, 2 and 3, an overview of the studied wetlands and available study tools (Chapter 4), results (Chapters 5 – 12), and a conclusion (Chapter 13).

Results are divided into three main parts, which are subdivided into a few chapters each (Figure 1.2):

- Part I. The Amazon wetlands
  - 5. Modeling different wetlands types
  - 6. How much inundation occurs?
  - 7. What are the inundation trends?
- Part II. South American wetlands: a comparative hydrology approach
  - 8. South American wetlands from space: flood dynamics
  - 9. Patterns and drivers of evapotranspiration in South American wetlands
- Part III. Wetlands as human-water systems: the hazard aspect of inundations
  - 10. Understanding past floods: the year of 1983 in South America
  - 11. On the capability of continental flood models to be locally relevant
  - 12. Modeling the river-floodplain-reservoir continuum in the Paraná basin

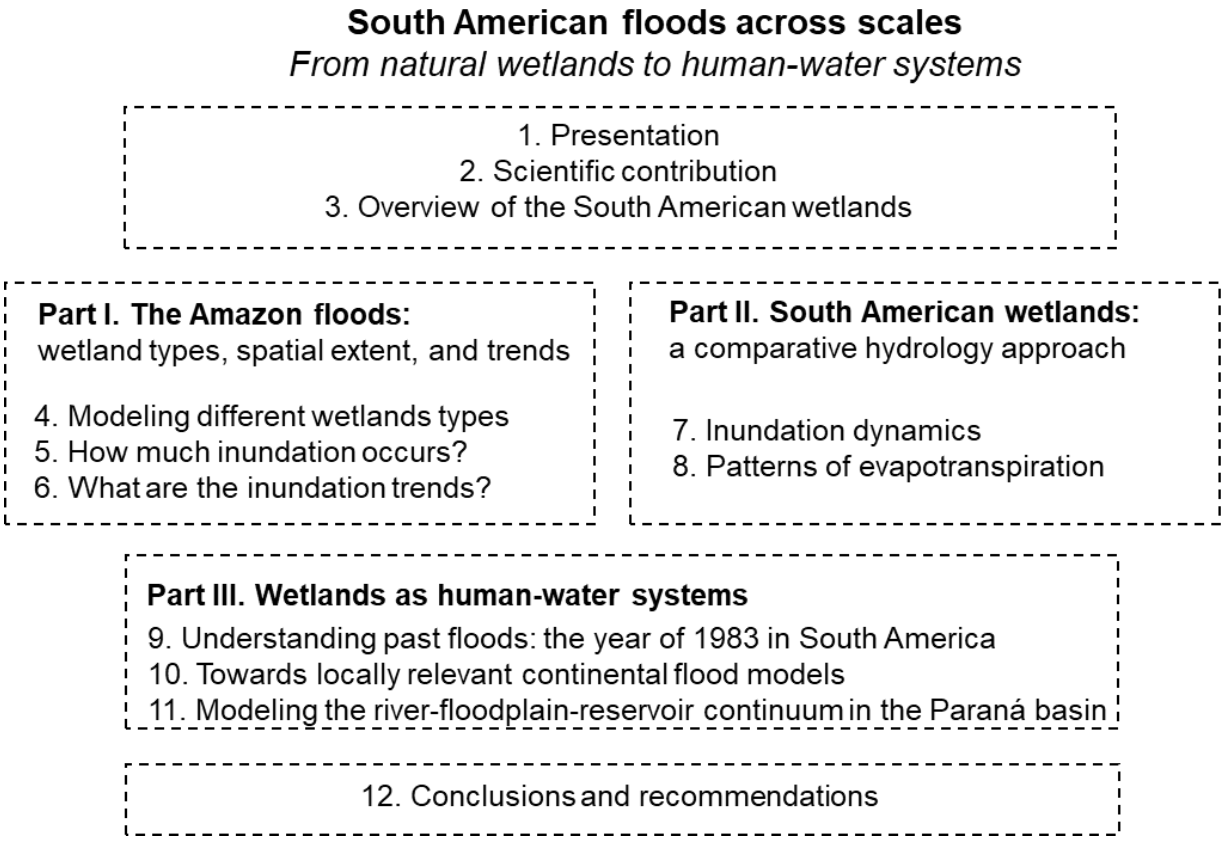

Figure 1.2. Scheme of the thesis structure.

1. Apresentação

1.1 Introdução

Áreas úmidas (AU's) são ambientes na interface entre ambientes aquáticos e terrestres, que podem ser naturais ou artificiais, permanente ou periodicamente inundados por água rasa, ou consistindo de solos encharcados (JUNK et al., 2014). Solos, animais e plantas são distintos dos ambientes ao redor e estão adaptados ao pulso de inundação local (JUNK; BAYLEY; SPARKS, 1989; WOODWARD; WUI, 2001). Estas áreas representam extensas partes de bacias hidrográficas, provendo diversos serviços ecossistêmicos como controle de qualidade da água, transformação e retenção de nutrientes, atenuação de cheias, provisão de produtos animais e vegetais, e manutenção da biodiversidade (ACREMAN; HOLDEN, 2013; COSTANZA et al., 1998; FAN; MIGUEZ-MACHO, 2011; JUNK et al., 2014; MALTBY; ACREMAN, 2015; WHALEN, 2005; WOODWARD; WUI, 2001). Na América do Sul, existem várias regiões onde milhares de quilômetros quadrados são sazonal ou permanentemente inundados (Figura 1.3), como as planícies da Amazônia central, Llanos de Moxos, Ilha do Bananal e Pantanal (HAMILTON; SIPPEL; MELACK, 2002). Cada área apresenta padrões de inundação e processos hidrológicos particulares, como a conectividade rio-área úmida (TRIGG et al., 2012, 2013), a interação entre solo, evapotranspiração e áreas inundadas, e a forma como ela é conectada às águas subterrâneas (FAN; MIGUEZ-MACHO, 2011; MIGUEZ-MACHO; FAN, 2012). Diferentes processos hidrológicos e hidrodinâmicos interagem durante os ciclos de inundação, gerando diversas áreas onde em alguns casos o extravasamento de água dos rios é o principal processo de inundação (e.g., planícies do rio Amazonas), enquanto em outras é uma combinação de chuva local e altos níveis de água subterrânea (e.g., savanas do rio Negro). Dada a grande dimensão destas áreas no contexto regional/continental, é fundamental conhecer a sua interação com o clima regional (TAYLOR; PRIGENT; DADSON, 2018), bem como suas potenciais vulnerabilidades a alterações ambientais (e.g., mudanças climáticas, construção de barragens e mudanças de uso da terra), que ainda são pouco compreendidas. Na América do Sul, sistemas de classificação e inventários de AU's têm sido propostos nos últimos anos (BENZAQUEN et al., 2017; JUNK et al., 2014; RICAURTE et al., 2012), mas ainda existe uma grande lacuna do conhecimento relacionada ao funcionamento hidrológico destas áreas.

Seres humanos têm se estabelecido ao longo de AU's, especialmente em planícies de inundação (Figura 1.1), por milênios (BLATRIX et al., 2018; DENEVAN, 1996), se beneficiando dos recursos providos por elas, bem como facilidades como transporte fluvial. Eles têm alterado o ambiente e a paisagem com obras como barragens e diques, bem como modificado a sua cobertura e uso do solo, como em áreas urbanas que ocupam áreas periodicamente inundadas. No entanto, a proximidade a rios os coloca sob alguns riscos, especialmente durante cheias extremas, as quais negativamente afetam milhões de pessoas todos os anos ao redor do globo (MAZZOLENI et al., 2021). As sociedades que habitam planícies inundáveis, muitas vezes associadas a comunidades socialmente vulneráveis, têm o desafio de se adaptar às variações espaço-temporais do

regime hidrológico destes sistemas rio-área úmida, ou tentar adaptá-los às suas necessidades, as quais incluem a redução da exposição a inundações. AU's e planícies de inundações, assim, devem ser compreendidas como sistemas sociedade-água.

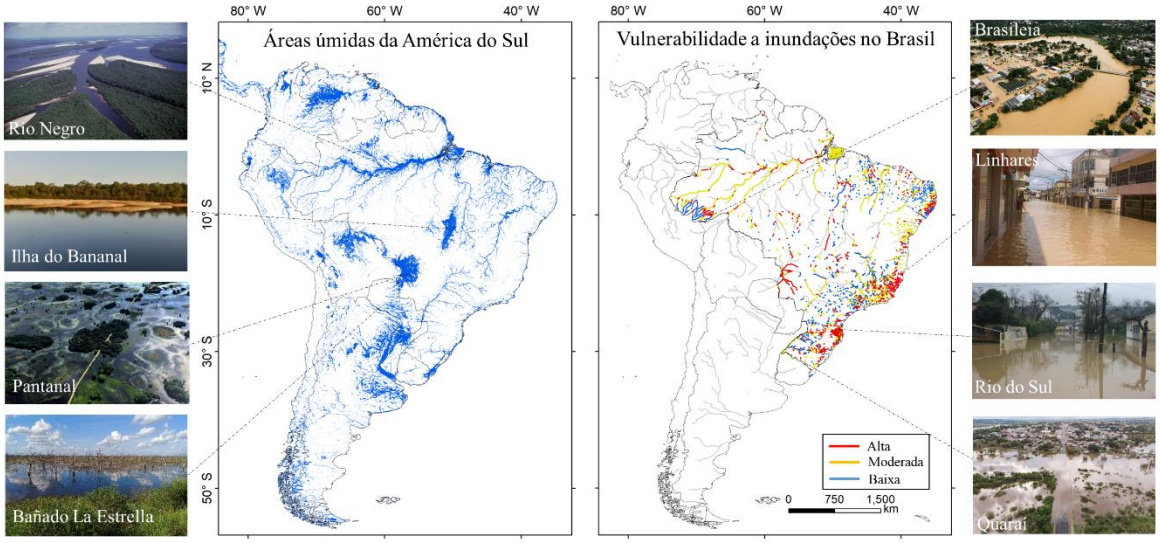

Figura 1.1. Contraste entre áreas úmidas naturais da América do Sul, à esquerda, e trechos de rio vulneráveis a inundações no Brasil, à direita, onde sociedades humanas têm se estabelecido por milhares de anos. Fonte: FLEISCHMANN et al. (2021).

O monitoramento da dinâmica de inundação não é simples, especialmente para aquelas AU's em áreas remotas, para as quais observações alternativas ao monitoramento in-situ são requeridas. Recentes avanços em sensoriamento remoto têm sido feitos e consideravelmente aumentado nossa compreensão da hidrologia de AU's e inundações (PAPA et al., 2010; RAST; JOHANNESSEN; MAUSER, 2014; SCHUMANN et al., 2009). Produtos disponíveis incluem nível d'água em rios e AU's (SANTOS DA SILVA et al., 2010), bem como extensão de áreas inundadas e armazenamento de águas superficiais em altas resoluções (AIRES et al., 2017; ALSDORF et al., 2007; CAO et al., 2018; FRAPPART et al., 2005; PRIGENT et al., 2007). Modelos hidrológicos e hidrodinâmicos baseados em processos, que representam matematicamente processos do ciclo hidrológico, são hoje uma realidade em escalas que vão de local a global (BIERKENS et al., 2015; FLEISCHMANN; PAIVA; COLLISCHONN, 2019; PAIVA et al., 2013a; YAMAZAKI et al., 2011), e são muito úteis para a compreensão de processos e projeções de alterações devidos a mudanças do clima ou do uso da terra.

Neste contexto, a comunidade científica tem desenvolvido na última década a agenda de pesquisa em hidrologia continental, a qual salienta a necessidade de melhorar modelos hidrológico-hidrodinâmicos em escalas regional (i.e., >10.000 km²) a continental (>1.000.000 km²) em altas resoluções espaciais (BATES et al., 2018b;

BIERKENS et al., 2015; FLEISCHMANN; PAIVA; COLLISCHONN, 2019; HODGES, 2013; TRIGG et al., 2016; WOOD et al., 2011). Os seus objetivos incluem a melhoria da representação de processos relacionados aos complexos fluxos de água em AU's e da interação entre processos hidrodinâmicos (e.g., inundação, remanso, atenuação de cheias) e hidrológicos (e.g., evapotranspiração e infiltração de água no solo) (FLEISCHMANN et al., 2018; HOCH; TRIGG, 2018; NEAL; SCHUMANN; BATES, 2012; PAZ et al., 2011; YAMAZAKI et al., 2014b). Estas ferramentas de modelagem têm melhorado nossa compreensão e capacidade preditiva da hidrologia de AU's em escala continental. De modo geral, a pesquisa de hidrologia continental pretende: (i) compreender processos continentais a globais como a interação entre superfície terrestre e clima global (e.g., para estudos de mudanças climáticas), e a exportação de água e solutos dos continentes para os oceanos; (ii) avaliar recursos hídricos para tomadores de decisão em escala nacional/continental, como gestores públicos, ONGs, agência globais (e.g., Banco Mundial), entre outros; e (iii) desenvolver produtos em escala continental, como mapas (e.g., mapas de risco a inundação), sistemas de alerta (e.g., para secas e cheias) e estimativas de variáveis de interesse (e.g., vazões e níveis d'água de rios, evapotranspiração) para uso em regiões mal monitoradas, e.g., países com insuficiente monitoramento hidrológico ou em conflitos civis.

No contexto específico de AU's e inundações, o seu estudo em escala continental é importante para:

- Compreender processos em diferentes AU's com uma abordagem de hidrologia comparativa, através das similaridades e dissimilaridades entre áreas, e.g., contrastando a dinâmica hidrológica de diferentes tipos de AU's como planícies de inundação e áreas interfluviais;
- Avaliar, em escala continental, a dinâmica espaço-temporal de eventos hidroclimáticos passados e padrões de teleconexões que têm afetado diferentes AU's, de modo a compreender suas respostas a mudanças e variações do clima (e.g., respostas a eventos de El Niño);
- Compreender a interação entre AU's e o clima regional/continental, incluindo interações superfície-atmosfera e emissões de gases de efeito estufa;
- Desenvolver inventários de AU's (localização, extensão, volumes de água armazenados, etc.) para fins de manejo integrado sustentável;
- Estimar a vulnerabilidade de AU's a impactos antrópicos em escala continental, e os impactos associados nos serviços ecossistêmicos (e.g., ameaças à segurança hídrica ou alimentar);
- Compreender a dinâmica espaço-temporal de perigo a inundação em grandes escalas, i.e., em áreas maiores que os limites de uma bacia hidrográfica, visto que existem processos que ultrapassam estas fronteiras (e.g., transporte atmosférico de umidade ou transferência de água entre bacias), e inundações podem afetar regiões mutio distantes das bacias diretamente afetadas através de danos econômicos indiretos. Isto tem grandes implicações para gestores de desastres naturais, assistindo iniciativas locais, nacionais e internacionais.

Assim, as seguintes questões científicas podem ser enumeradas, no contexto de hidrologia de AU's e inundações na América do Sul, as quais serão abordadas de alguma forma nesta tese:

- Quão diferentes são as AU's da América do Sul em termos de comportamentos hidrológicos e serviços ecossistêmicos relacionados a hidrologia?
- Como AU's interagem com o clima regional/continental, e.g., através de fluxos de evapotranspiração?
- Como as AU's respondem, e interagem com, as atuais e futuras mudanças ambientais (e.g., mudanças climáticas, construção de barragens, mudanças de uso da terra)?
- Como produtos de sensoriamento remoto, de escalas global a local, descrevem a dinâmica de inundação em múltiplas AU's? Eles concordam em extensão de áreas inundadas, e como melhorar a sua performance?
- Como modelos matemáticos continentais (baseados em processos) representam AU's e processos hidrodinâmicos locais, e como melhorar a sua performance?
- Como seres humanos afetam e são afetados por eventos normais e anômalos de inundações em AU's, especialmente em planícies de inundação?

1.2 Objetivos

O principal objetivo desta tese é promover a compreensão de processos hidrológicos em áreas úmidas (AU's) da América do Sul, com uma perspectiva de múltiplas escalas e uma abordagem de hidrologia comparativa. Pretende avançar a agenda de pesquisas em AU's em escala continental, diferenciando os principais processos de dinâmica de inundação que ocorrem em grandes AU's da América do Sul daqueles ocorrentes nas ubíquas planícies de inundação habitadas por milhões de pessoas.

Objetivos específicos desta tese são:

- Compreender as diferenças entre processos hidrológicos (através de variáveis como níveis d'água, extensão de áreas inundáveis e evapotranspiração) em tipos contrastantes de AU's, e.g., planícies de inundação e áreas interfluviais, para os grandes sistemas de AU's do continente;
- Sintetizar os processos hidrológicos das grandes AU's sul-americanas, especialmente relacionadas à dinâmica de inundação, precipitação, armazenamento de água, níveis d'água e evapotranspiração;
- Desenvolver um modelo 2D de escala regional para simular, de forma acoplada, processos hidrológicos e hidrodinâmicos em complexas AU's, e compará-lo com abordagens de simulação 1D;
- Avaliar as atuais capacidades de mapeamento de inundação (modelagem matemática, sensoriamento remoto) em distintos tipos de AU's;

- Avaliar como cheias passadas afetaram grandes domínios, como as cheias de 1983 na América do Sul e as tendências de aumento de inundações nas regiões norte e central da Amazônia nas últimas décadas;
- Avaliar como melhorar modelos hidrodinâmicos de escala continental para estimar variáveis localmente relevantes, bem como campos contínuos de variáveis como níveis d'água;
- Avaliar como infraestruturas humanas, como barragens, afetam o perigo a inundação e interagem com planícies de inundação para atenuar cheias em grandes escalas.

1.3 Organização da tese

Esta tese está dividida em 13 capítulos, que incluem os capítulos introdutórios 1 e 2, uma breve introdução às AU's estudadas, bem como as principais ferramentas de estudo disponíveis (Capítulo 3), resultados (Capítulos 5 a 12) e conclusões e perspectivas gerais (Capítulo 13).

Os resultados são divididos em três partes principais, que são subdivididas em alguns capítulos cada (Figura 1.2):

- Parte I. Áreas úmidas da Amazônia: tipos, extensão e tendências
  - 5. Modelando diferentes tipos de áreas úmidas
  - 6. Quanta inundação ocorre?
  - 7. Quais são as tendências?
- Parte II. Áreas úmidas da América do Sul: uma abordagem de hidrologia comparativa
  - 8. Dinâmica de inundação
  - 9. Padrões de evapotranspiração
- Parte III. Áreas úmidas como sistemas sociedade-água
  - 10. Cheias passadas: o caso do ano de 1983 na América do Sul
  - 11. Sobre a capacidade de modelos hidrodinâmicos continentais gerarem estimativas localmente relevantes
  - 12. Modelagem integrada de rios, planícies de inundação e reservatórios na bacia do rio Paraná

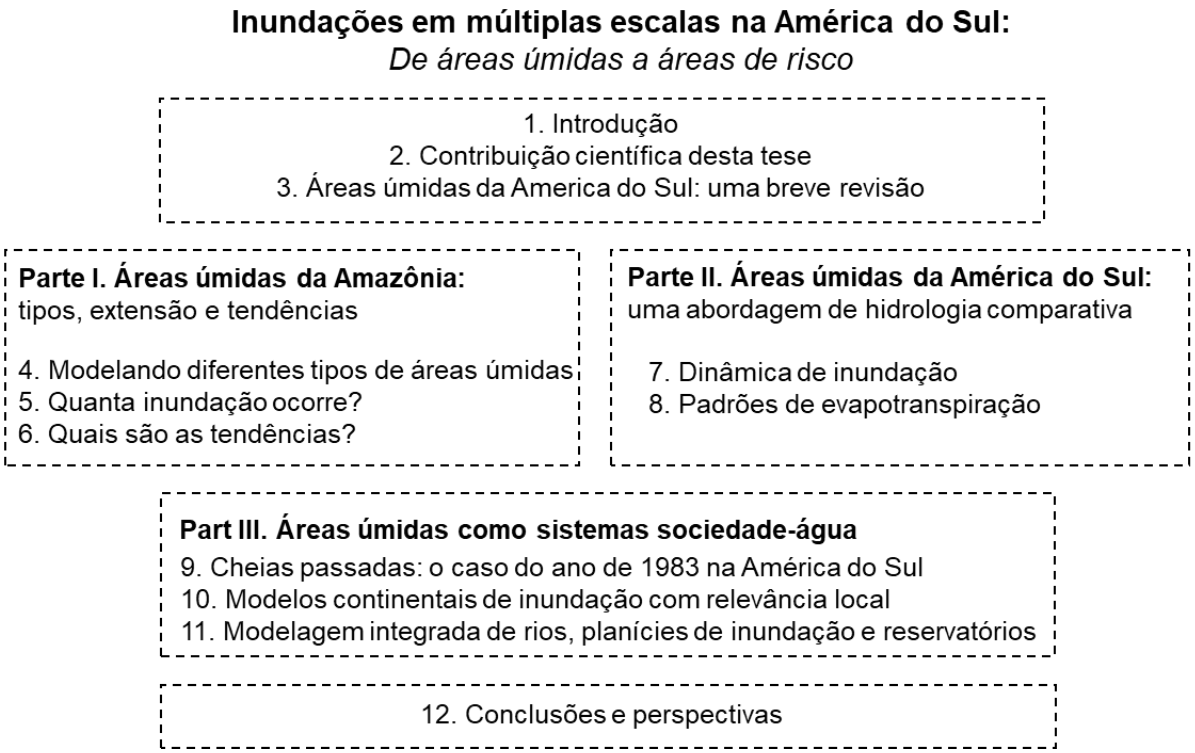

Figura 1.2. Esquema da estrutura da tese.

2 Scientific contribution of this thesis

This chapter provides an extended summary of the thesis. I stress that the work presented here was only possible thanks to the fruitful collaboration with many researchers and institutions during the last four years, for which I'm very grateful.

Wetlands provide major ecosystem services, including food provision, support for biodiversity, and climate and flood regulation. South America hosts some of the major river systems on Earth, often associated with large floodplains that are inundated every year, such as the Pantanal and many Amazon wetlands. Interfluvial wetland complexes are also found across the continent, with particular geomorphic settings and unique savanna or grassland vegetation. While some South American wetlands are still remote and, to some extent, still well-preserved areas (REIS et al., 2018), major human societies have developed for thousands of years along them, and in special along river floodplains, and have altered their landscape, as well as adapted to their seasonal inundation cycles. For instance, in Brazil, natural systems contrast with many river reaches where riparian human settlements and urbanized areas currently face intensifying flood risk (MAZZOLENI et al., 2021; Figure 2.1). This two-way interaction between floodplain hydrological processes and societies, which makes the river-floodplain landscape evolution to respond to both, highlights the need of understanding wetlands as "human-water systems" (DI BALDASSARRE et al., 2018).

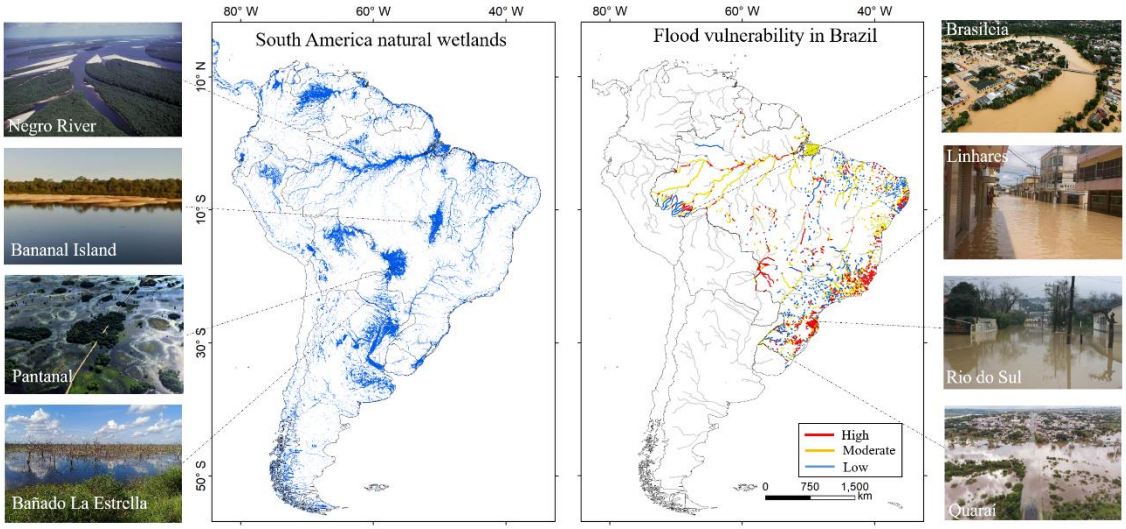

Figure 2.1. The contrasts between natural wetland systems across South America, on the left, and flood vulnerable river reaches in Brazil, on the right, where human societies have settled along rivers for thousands of years. Source: FLEISCHMANN et al. (2021).

This thesis presents a cross-scale investigation of the hydrology of the South American wetlands, and their interaction with human societies, in the context of flood

hazard along river floodplains (Figure 2.2). Here, I invite the readers to travel around the continent floodable areas, starting at the worldly known Amazon wetlands (Part I), then upscaling the analyses to the large South American wetlands, distributed from north to south and involving several climate and vegetation types (Part II), and ending up by addressing major flood prone areas in the continent, where humans have tightly interacted with river floodplain systems and faced an increasing flood risk (Part III).

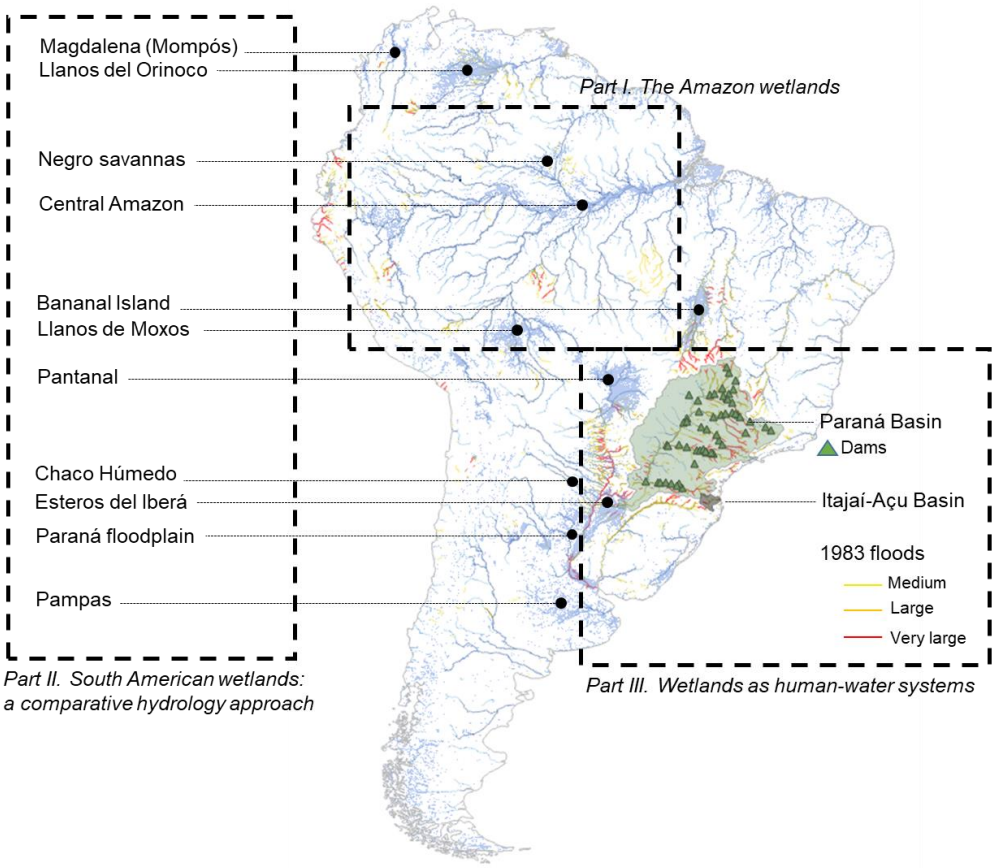

Figure 2.2. Illustrative scheme of the thesis structure, with the main study areas highlighted in the South America map and distributed along the three parts of this thesis. Part I addressed the Amazon River Basin. The location of the wetlands assessed in Part II is shown as black circles. The two river basins studied in Part III are also presented as grey filled polygons (Paraná and Itajaí-Açu), as well as the recurrence (return period) of the 1983 floods, which are addressed in Part III.

My interest on a continental perspective of water resources is aligned with the SAMEWATER research agenda – "South American WATER resources" – that the Large Scale Hydrology research group (www.ufrgs.br/lsh) has been developing in recent years (PAIVA et al., 2017; SIQUEIRA et al., 2020), led by professors Rodrigo Paiva and Walter Collischonn. This agenda was initially motivated by the development of a hydrological-hydrodynamic model for South America (SIQUEIRA et al., 2018), which later promoted other various studies (BRÊDA et al., 2020; FLEISCHMANN et

al., 2020a; PASSAIA et al., 2020), and largely influenced some chapters of this thesis. The fruitful satellite era, with Earth observation data available for multiple hydrological variables as surface water levels, flood extent, water storage, precipitation and evapotranspiration, has allowed the continental-scale assessments performed here. In addition, new computation techniques have benefited from these satellite data, yielding advanced hydrological and hydrodynamic modeling capabilities that allow an unprecedented simulation of wetland processes.

Furthermore, in South America, the development of hydrology research has often followed human water demands, such as studies for densely populated areas and hydropower generation, located far from many wetlands of scientific relevance (DE PAIVA et al., 2020). On the other hand, wetland ecologists and the international environmental research agenda have been extensively studying large natural wetland systems such as the Pantanal and Amazon floodplains. This calls the attention to better connecting water resources engineers with the wetland research community, which very often address similar topics with different tools and interests. Investigating ways to link these two communities is also a motivation for this thesis.

As stated in the thesis' introduction, the continental to global hydrology research agenda has been largely developed in recent years (BIERKENS et al., 2015; WOOD et al., 2011). In this context, we could also devise a continental wetland research agenda, which I assume as the leitmotif of this thesis, and which is addressed through various cross-scale topics. It is firstly addressed through a comparative hydrology approach, which is a basis for understanding patterns based on similarities and dissimilarities, and is performed for different wetland types, as river floodplains and interfluvial wetlands, for the Negro River basin in the Amazon (Chapter 4), for the whole Amazon basin through an intercomparison of 29 inundation datasets, from local to basin scale (Chapter 5), and an assessment of inundation trends across the basin (Chapter 6). A comparative approach is also employed to enlighten inundation (Chapter 7) and evapotranspiration (Chapter 8) patterns over 12 large South American wetland systems, which are representative of multiple climates and floodable vegetation types (grasslands, savannas, forests) of the continent. The investigation of flood hazard due to floodplain inundation is firstly assessed with hydrodynamic models for the continental domain, in the case of the great 1983 floods that devastated a portion of the continent during that strong El Niño year (Chapter 9). Then, from a cross-scale perspective, the capability of estimating locally relevant hydrodynamic variables (flood extent, river water levels and discharges) with continental models is assessed for the Itajaí-Açu River Basin in Southern Brazil, one of the most flood-prone areas in the country (Chapter 10). The thesis finishes by showing that floodplains are more widely distributed across large basins than usually assumed (i.e., they are not located only in downstream flat river reaches), and that their effects on the hydrological regime interact with those of manmade infrastructures such as dams to create a river-floodplain-reservoir continuum (Chapter 11). To address it, a case study is performed in the Paraná River Basin, the basin with the largest total reservoir storage in the continent.

Besides the comprehension of hydrological processes, this thesis also addresses the role of wetlands in providing ecosystem services. These services are generally addressed in most chapters, but they are the specific topic of Chapter 11, about flood attenuation, and Chapter 8, regarding climate regulation through changes in the surface energy balances. Furthermore, the well-functioning of wetland ecosystems depends on the maintenance of the basin-wide hydrological connectivity (REIS et al., 2019a). While this thesis mainly assesses wetland complexes from a regional-scale perspective, lacking more detailed analyses of local-scale wetland hydrological processes, connectivity was addressed in terms of lateral (most chapters that address floodplain lateral inundation), longitudinal (the river-floodplain-reservoir continuum across a river basin drainage network, Chapter 11), and vertical (surface-atmosphere interactions through evapotranspiration, Chapter 8) connectivity components. In particular, Chapter 6 shows the increase in surface water lateral connectivity in the recent decades in the Amazon basin (Figure 2.3).

The next paragraphs provide a broader discussion of each of these chapters.

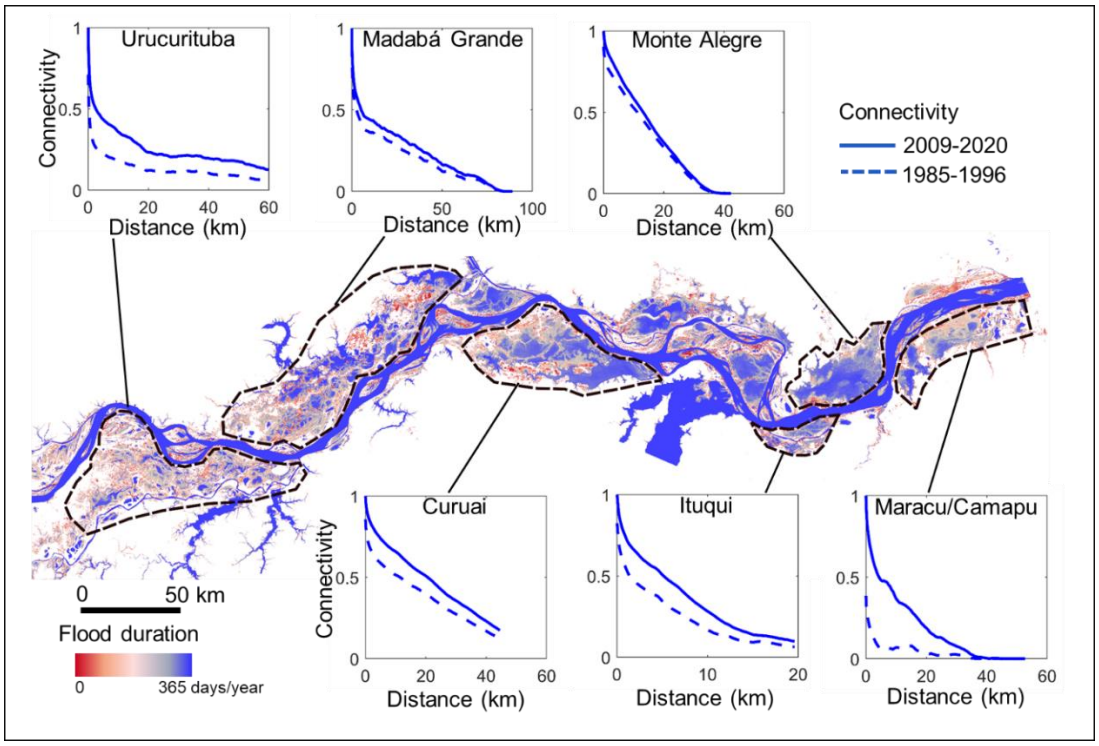

Figure 2.3. The increase in maximum inundation extent over the central Amazon floodplains in the last four decades has also increased the surface water connectivity in many floodplain units of the lower Amazon reaches. This map presents the flood duration for the 2009-2020 decade, and each graph presents, for a given floodplain unit, a connectivity index that is related to the number of pairs of pixels that are connected at a given distance. More details about this analysis are provided in Chapter 6.

The starting point on this thesis is the Amazon basin, which harbors some of the largest wetland systems in the world, with well-adapted human societies and ecosystems. The thesis Part I advances our understanding of Amazonian wetlands in three particular ways (Chapters 4, 5 and 6). Until now, past hydrological and hydrodynamic models have been developed only for the basin-scale or for floodplain areas in the central Amazon. Here we studied and leveraged models and satellite data to investigate the contrasting inundation dynamics between the Negro savannas, a massive interfluvial ecosystem which has adapted to alternating water deficit and excess states, and adjacent river floodplains (Chapter 4). The former have a very different behavior, for being more dependent on local rainfall and having smaller surface water level amplitudes (Figure 2.4a and Figure 2.4b). Different setups of hydrologic-hydrodynamic models were simulated and compared to multiple satellite observations of water levels and inundation extent. A larger difference among 1D and 2D models and satellite-based inundation estimates for the interfluvial areas stresses our limited understanding of their hydrological dynamics. Then, given the large uncertainties that were identified for mapping inundation dynamics across different wetland types, Chapter 5 presents a comprehensive assessment of inundation estimation across the Amazon basin, which was performed through the collection of 29 inundation datasets that span different spatial (12.5 m to 25 km) and temporal (daily to monthly and static) resolutions. While major agreements among the products in terms of inundation spatial distribution are shown to occur along the central Amazon floodplains, especially for the open water areas in the lower reaches, important disagreements persist for interfluvial areas as the Negro, Roraima and Llanos de Moxos savannas, as well as for the Pacaya-Samiria region (Figure 2.4c), for which further developments are needed by the international remote sensing and modeling community. A WebGIS systems was developed and makes it easier to grasp the varied capabilities of each dataset (https://amazon-inundation.herokuapp.com/). Finally, Chapter 6 addresses the long-term trends in the Amazon Basin inundation patterns (Figure 2.4d). Our results used multiple remote sensing and modeling tools to show that the central Amazon floodplains are the major area of inundation changes over the last four decades in the basin. A new hydroclimatic state is operating in the basin since 1998 (BARICHIVICH et al., 2018; ESPINOZA et al., 2019a), which we showed to be translated into a 20% increase in the maximum inundation extent over the Amazon mainstem floodplains. This increase has culminated, in June 2021, in the largest water level ever registered in the 119 years of record in Manaus, in the Amazon-Negro river confluence, which has largely impacted the central Amazon ecosystems and human societies, and perhaps even global greenhouse gas fluxes (BODMER et al., 2018; WILSON et al., 2020).

During this thesis, I also got involved in several studies about the Amazon region, from the improvement of hydrological-hydrodynamic models with remote sensing data (COELHO et al., 2021; FAN et al., 2021; MEYER OLIVEIRA; FLEISCHMANN; PAIVA, 2020) and its use to understand the dynamics of Amazon surface waters (SORRIBAS et al., 2020), to the comprehension of deforestation (LAIPELT et al., 2020, 2021) and development of a review of the “Amazon hydrology from space”

(FASSONI-ANDRADE; FLEISCHMANN; PAPA, 2021). I also shared a first authorship of a study about the climate change projected impacts in hydropower generation for the proposed Amazon dams (ALMEIDA et al., 2021), as well as collaborated in two article about dams' impacts, related to hydropeaking operation (ALMEIDA et al., 2020) and basin-wide planning of allocation of dams, considering environmental impacts (FLECKER et al., under review). The need of better connecting researchers from multiple disciplines that study the Amazon Basin is conspicuous, if we want to better develop the region's vocational capabilities and understand its response to ongoing and future environmental changes. This has motivated me to create and co-lead, together with other colleagues from UFRGS and other institutions, the "Conexões Amazônicas" initiative ("Amazon Connections"), which is now a science communication hub for Amazon research, from the biological to the human and earth system sciences (www.conexoesamazonicas.org).

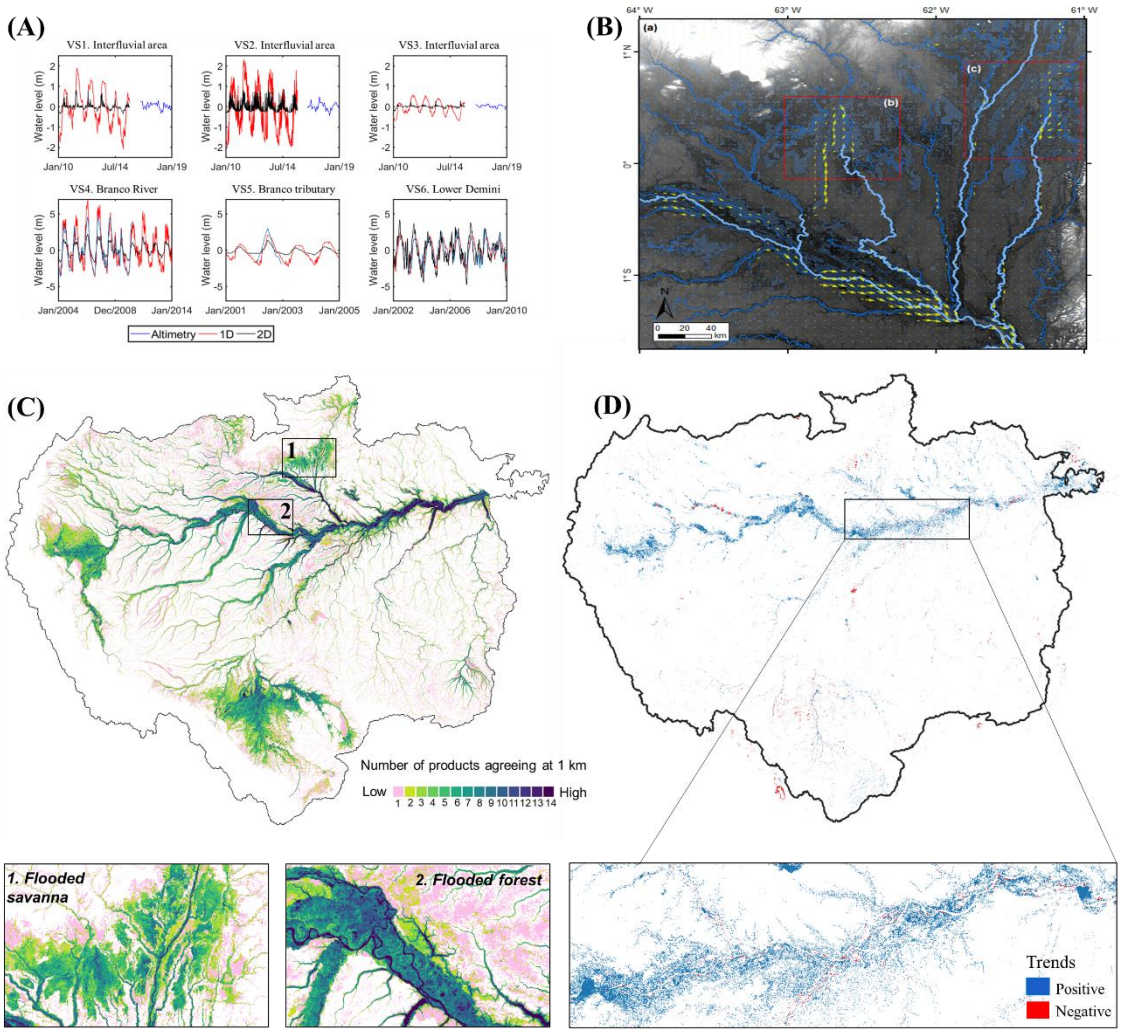

Figure 2.4. The thesis Part I presents a new understanding of the Amazon wetlands inundation dynamics, from differences between river floodplains and interfluvial areas in terms of (a) surface water levels and (b) surface water flow pathways, to a (c) comprehensive assessment of dozens of basin-wide inundation datasets and (d) an analysis of inundation spatial trends for the last four decades.

In order to understand the hydrology of contrasting wetlands types, the upscale of the Amazon basin analyses to the continental domain proved an interesting way forward. This was performed in the context of a comparative hydrology approach, which is the main topic of the thesis Part II and is formed of two main chapters that analyzed 12 large South American wetland complexes (Figure 2.5). The first one, Chapter 7, leverages a set of satellite-based datasets for river and wetlands' water levels (Envisat, SARAL AltiKa, JASON-2/3, Sentinel-3A/B and ICESat missions), total water storage (GRACE mission), inundation extent (GIEMS-2 dataset) and precipitation (MSWEP dataset), and presented an analysis of the data at a monthly time scale for the period 2003-2015. Annual water level amplitude was shown to be much smaller over interfluvial wetlands, e.g., the Negro and Llanos de Moxos floodable savannas (less than 2 m), than along river floodplains, where the levels can vary more than 10 m, e.g., in the Amazon floodplains (Figure 2.6). The time lag between precipitation and inundation was also smaller over interfluvial areas (two or less months), reflecting the longer downstream flood propagation that occurs over river-floodplain systems. In Chapter 8, this analysis was moved to another important component of the hydrological cycle – evapotranspiration (ET). The continental-scale ET mapping has been hindered by the time-consuming process of acquiring and processing satellite data, and was possible in this study thanks to the development of new cloud computation techniques by the ET-Brasil research group led by Prof. Anderson Ruhoff (UFRGS), especially the geeSEBAL tool (https://etbrasil.org/geesebal; LAIPELT et al., 2021). In Chapter 8, major ET differences are found between wetlands and uplands in temperate climates (water-limited environments), while in equatorial ones the difference is smaller (Figure 2.7). In central Amazon, the high forest cover in upstream reaches compensates the higher flood fraction but lower forest cover in the downstream ones, maintaining high evapotranspiration year round. Flood propagation along river floodplains is shown to be a major control of ET dynamics in wetlands associated with a river flood pulse, especially for the Pantanal where the flood wave takes months to propagate across the system (Figure 2.8). Finally, this Part highlights the unique hydrological functioning of South America wetlands, and set forward the importance of performing comparative hydrology studies for wetlands worldwide. In particular, I stress that, for better understanding the hydrology of wetlands, it is necessary that the wetlandscapes are studied as individual units, instead of being lumped together within river basins, which is the most common approach adopted in hydrological analyses. This is especially true for interfluvial wetlands, whilst river floodplains require the understanding of both local and upstream (i.e., the whole river basin) hydrological processes.

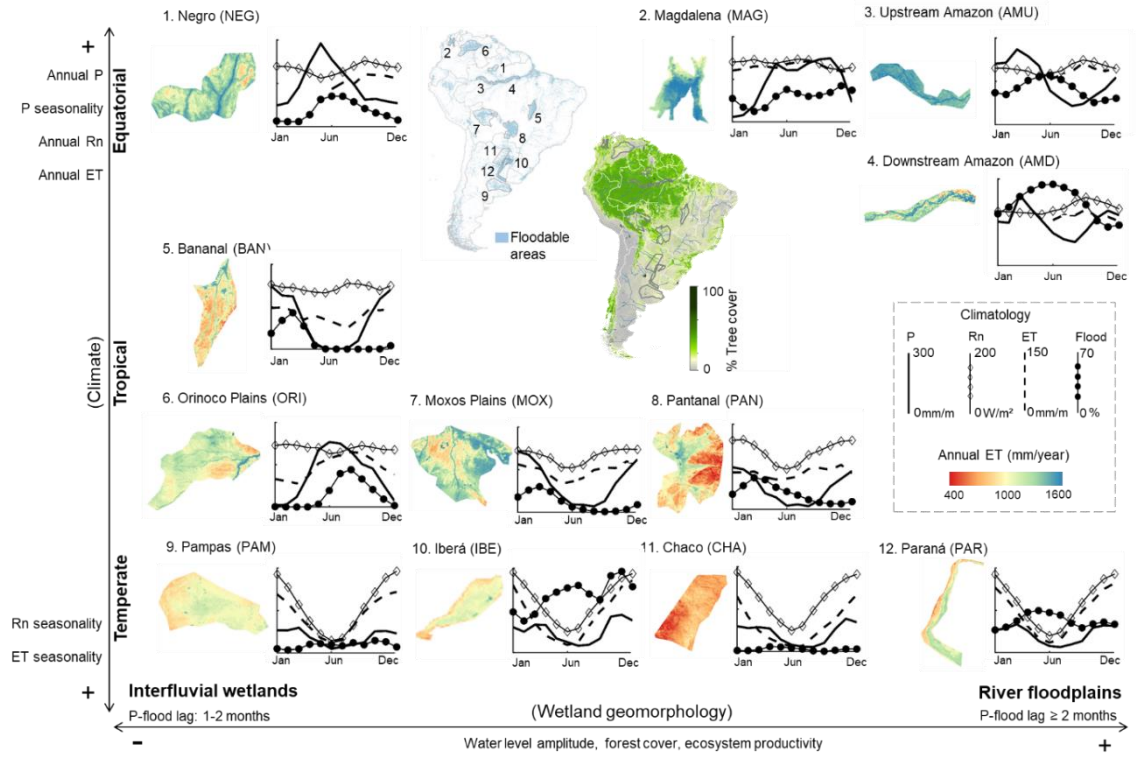

Figure 2.5. The thesis Part II presents a comparative hydrology approach, through which 12 large wetland complexes across South America are compared in terms of inundation dynamics and other hydrological variables as precipitation, surface water level and evapotranspiration. This figure shows the climatology of precipitation (P), net radiation (Rn), evapotranspiration (ET) and flood fraction (FF), and is a reproduction from Chapter 8.

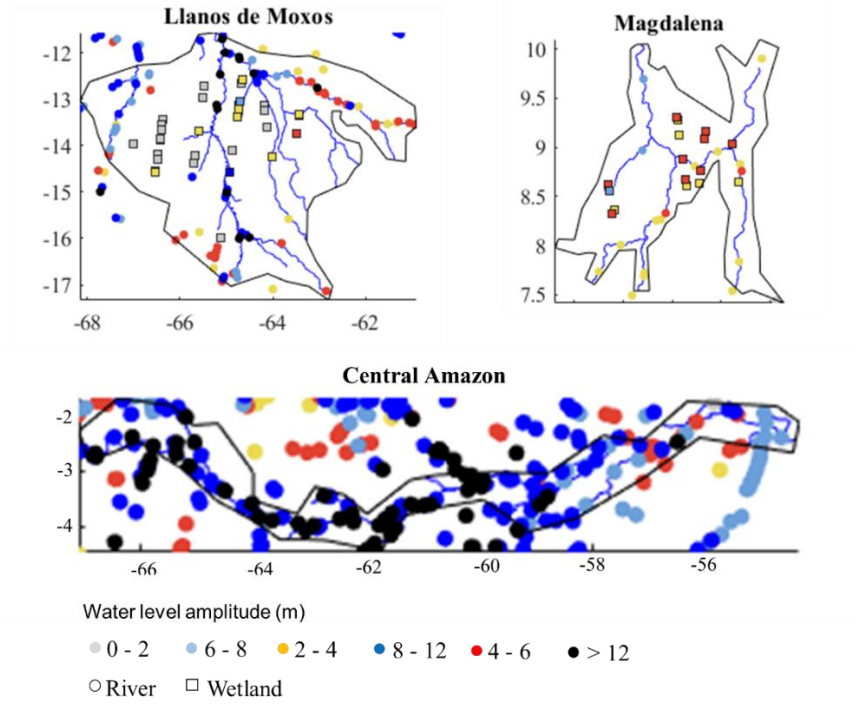

Figure 2.6. Chapter 7 investigates the spatio-temporal Water level amplitude for some selected wetland complexes, for virtual stations in rivers (circles) and wetlands (squares). The data for the 12 analyzed wetlands are provided in Chapter 7.

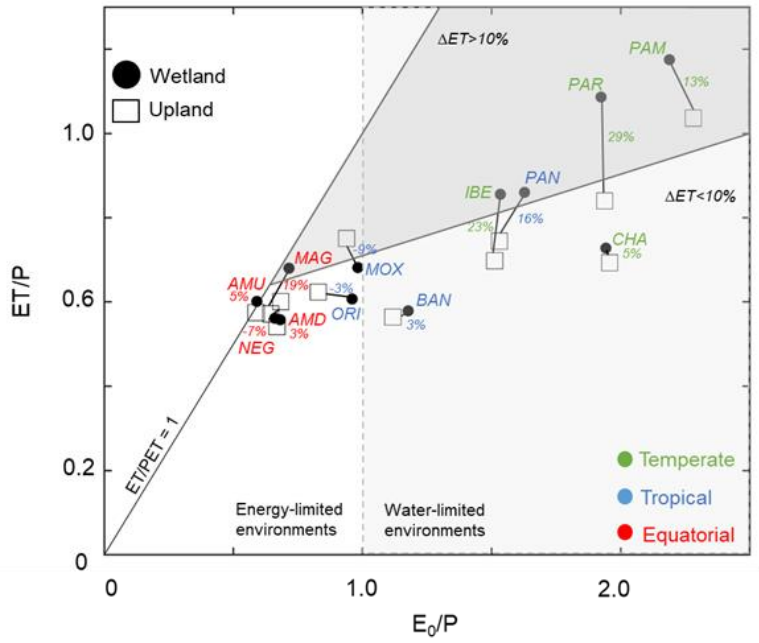

Figure 2.7. Chapter 8 investigates ET differences between wetlands and uplands. This figure shows a Budyko-like framework relating the long-term evaporative index (ET/P) with the aridity index (E0/P), where E0/P > 1 refers to water-limited environments, and E0/P<1 to energy-limited ones. Values are presented for wetlands (black circles) and the adjacent uplands (black squares). Each label refers to one wetland, as presented in Figure 2.5. The wetland-upland long-term differences are shown as numbers between wetland and upland symbols for each wetland, and the dark grey area refers to areas with differences higher than 10%.

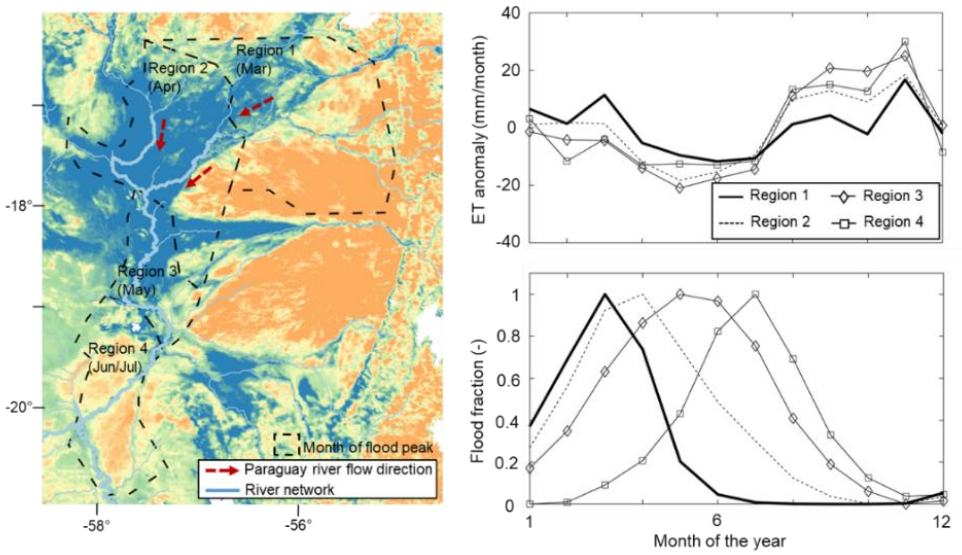

Figure 2.8. Chapter 8 investigates the spatio-temporal dynamics of evapotranspiration (ET) over 12 South American wetlands. Flood propagation affects ET at the seasonal time scale in the Pantanal wetlands. The annual evapotranspiration map is presented in the left figure, together with the location of the four regions of equal month of flood peak (from March to Jun/Jul), while the figures in the right column show the climatology of monthly ET (anomaly values) and flood fraction for the four regions.

Given my water resources engineering background, it was a natural choice to investigate in the thesis Part III how large floods interact with human systems, i.e., the human-water systems. While this topic has been addressed by the socio-hydrology community in recent years, I stress that here my main interest was on understanding the hazard component of flood risk. This Part has three chapters. Chapter 9 investigates the complex spatio-temporal patterns of the El Niño-related 1983 floods in South America, with a special focus on the Brazilian portion, which were one the most devastating flood events ever registered in the continent. There were three main flooding periods (February, June and July), as depicted with peak river discharges based on the continental model by SIQUEIRA et al. (2018), in many South American river basins, such as the Araguaia, Tocantins, São Francisco, Uruguay, La Plata and its tributaries, resulting in high discharge of the Paraguay River for many months. The timing of the events had a southward direction throughout that year, with some of the largest ever recorded river discharges in northern areas such as the upper Araguaia and Tocantins rivers occurring in February 1983, and in July in southern regions as the Uruguay River (Figure 2.9). While the capability of such continental models to estimate peak discharges for extreme events such as 1983 was shown satisfactory, it is still not clear whether they can provide locally relevant estimates of hydrodynamic variables (river discharges and water levels, and inundation extent). This topic was addressed for the Itajaí-Açu River basin, one of the most flood-prone areas in the continent (Chapter 10). To assist interpretation, three main requirements to define estimates from a river hydrodynamic model as locally relevant were defined: the model errors should be equal or smaller (i) than the accuracy requirement for a particular application and location, (ii) than typical local, reach scale models' errors, and (iii) than observation uncertainties. Results showed that it is still a great challenge for continental models to provide locally relevant estimates of absolute water levels and flood extent (Figure 2.10), yet river discharges and anomalies of water levels can be satisfactorily estimated. Some recommendations were then provided for moving towards locally relevant model predictions, e.g., the need for better estimating at-a-station river cross sections, considering the heterogeneity of river channels.

Another important aspect to improve the realism of hydrodynamic models relates to their model structure, i.e., how do they represent relevant processes and with which equations. It is well known that humans alter the river-floodplain systems through the building of infrastructure such as dams, and that large-scale hydrodynamic models must represent them in order to achieve right models for the "right reasons" (KIRCHNER, 2006). Thus, based on a recent development of the MGB model to simulate the hydrodynamics of dams within the drainage network (FLEISCHMANN et al., 2019b), Chapter 11 presents a case study for the upper Paraná River basin (~900,000 km²), the most relevant one in South America in terms of total reservoir storage. The overall aim was to investigate the simulation of what we called the "river-floodplain-reservoir continuum", i.e., the continuous fields of variables such as river water levels and surface water extent that exist across drainage networks. Various ways of representing a set of dam cascades in large-scale models were assessed, in terms of different reservoir

bathymetry and operation schemes, in order to represent them in a simple yet accurate way. The continuum is exemplified in Figure 2.10 for the Iguaçu river mainstem, a major southern tributary of the Paraná. Longitudinal (maximum and minimum) water surface elevation profiles, as well as maximum flooded areas, highlight the connected hydrological-hydraulic processes that occur basin-wide. This is important, for instance, if we want to understand the backwater effects of dams in upstream river reaches, which can be associated with important cities and wetlands. Furthermore, in Chapter 11 it is shown that natural floodplains and reservoirs have a complementary role on flood attenuation in the basin. While floodplains are more important along tributaries' headwaters (e.g., Iguaçu, Paranapanema, Grande and Ivinhema rivers) and in the lower reaches of the Paraná mainstem, reservoir effects are more relevant along medium to lower reaches of tributaries (Figure 2.12). This also shows that floodplains are widespread across the basin, and not located along only downstream, flat reaches, as usually assumed in many large-scale hydrodynamic models, and must be accounted for if we want to move towards locally relevant models.

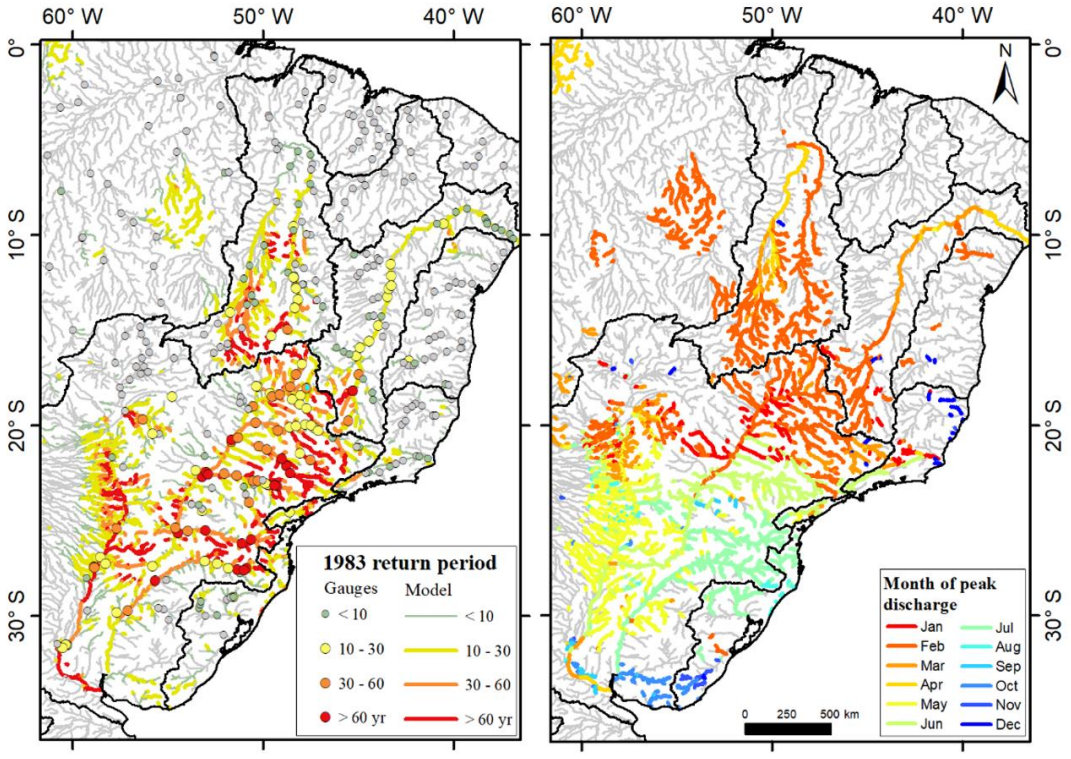

Figure 2.9. Chapter 9 investigates the spatio-temporal dynamics of the great 1983 floods. The left figure show the return period for each river reach (from MGB model simuations), as well for in situ river gauges, while the right figure shows the month of peak discharge based on the MGB model developed by SIQUEIRA et al. (2018).

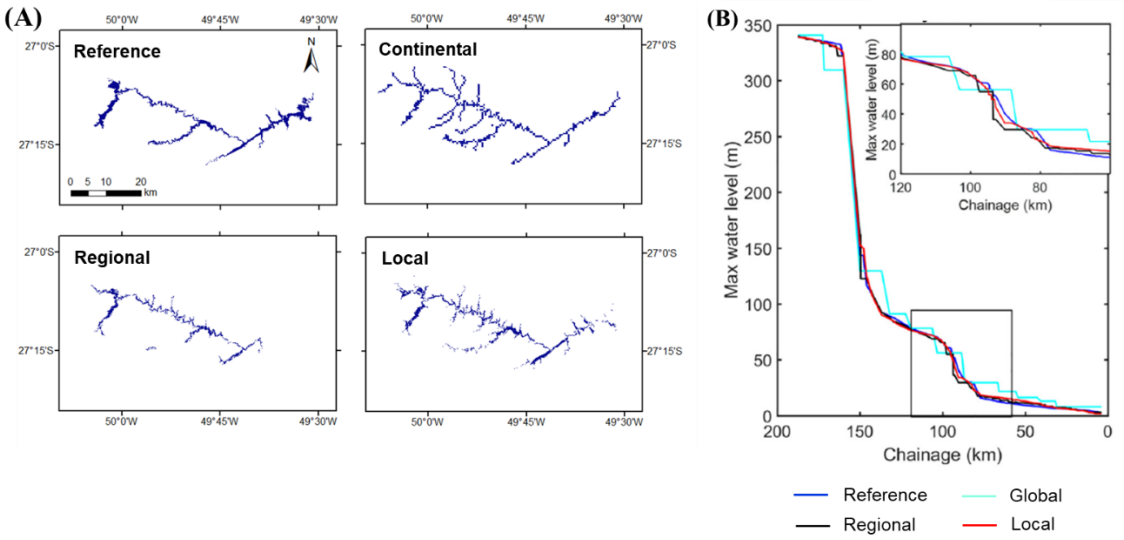

Figure 2.10. Chapter 10 presents the assessment of whether continental-scale hydrodynamic models can provide locally relevant estimates of hydrodynamic variables as (a) flood extent and (b) water levels. This is performed by comparing continental, regional and local-scale models with a local reference, for the flood-prone Itajaí-Açu river basin in south Brazil.

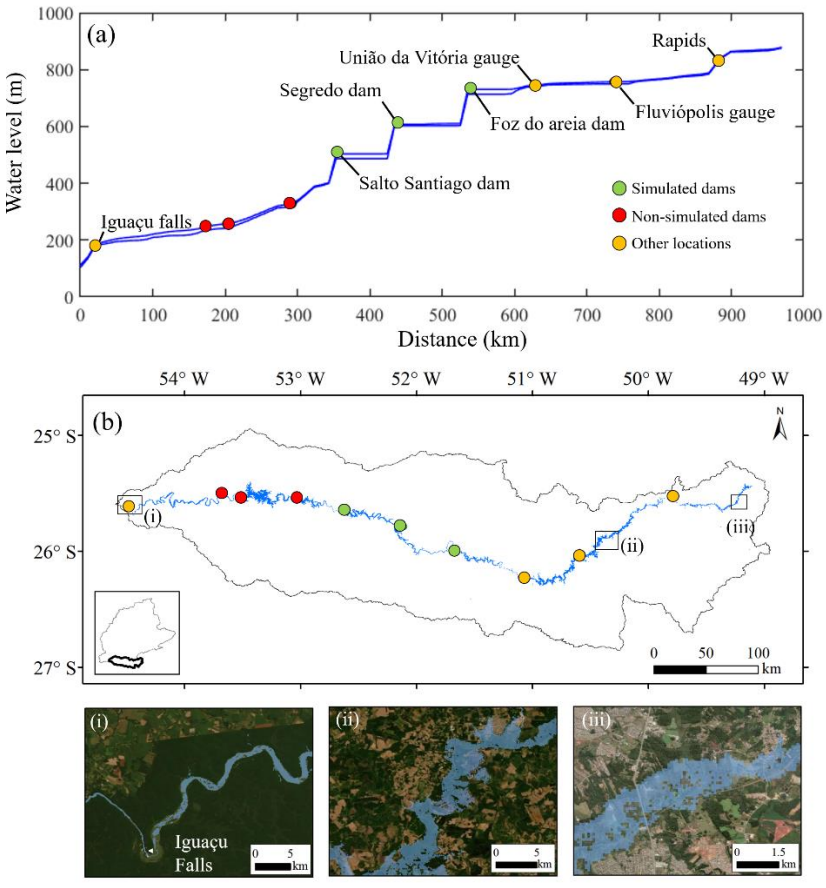

Figure 2.11. Chapter 11 addresses the river-floodplain-reservoir interactions in the Paraná River basin. (a) Longitudinal profiles of maximum and minimum simulated surface water elevation (blue lines) along the Iguaçu river mainstem (a main tributary of Paraná). Distance is measured from the confluence between Iguaçu and Paraná rivers. The three regulation dams simulated are presented as green circles, as well as the run-of-river dams that were not simulated (red) and some locations of interest (yellow). (b) Maximum simulated flood extent for the same reaches from figure a. Details (i), (ii) and (iii) show particular areas together with Google Earth Imagery.

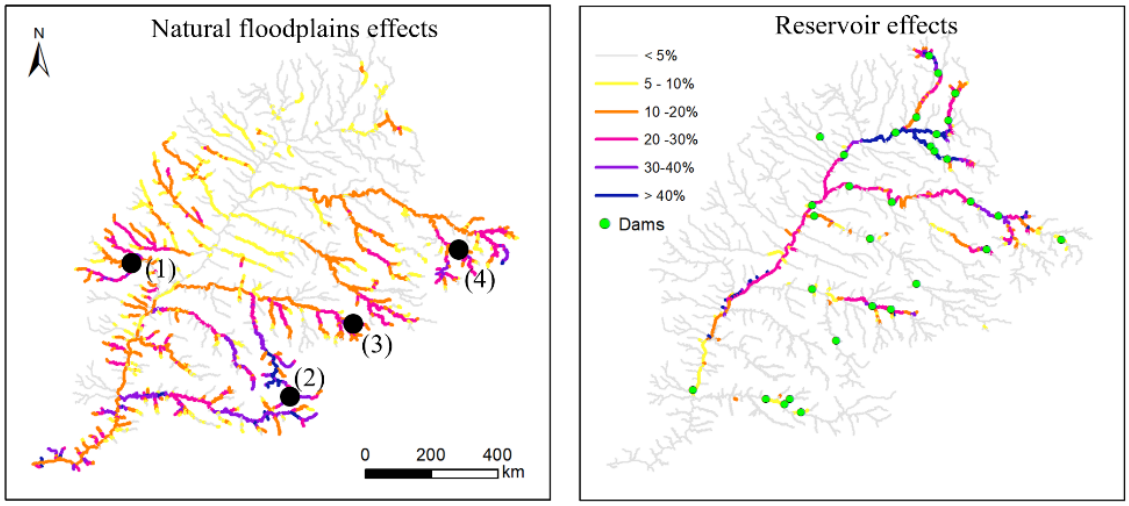

Figure 2.12. Chapter 11 addresses the river-floodplain-reservoir interactions in the Paraná River basin.

The understanding of the wetland systems (ecosystems, human societies, etc.) requires new tools to accurately map long-term changes in the wetland hydrological dynamics. This thesis provides some new bases to improve our methodologies of quantification of inundation and wetland hydrological processes. Regarding process-based modeling tools, new simulation capabilities were developed in order to improve the representation of coupled hydrologic (soil water infiltration, evapotranspiration, runoff generation) and hydrodynamic (downstream flood propagation, floodplain attenuation, dam and backwater effects) processes. Furthermore, it was also shown the capabilities of continental models to depict the spatio-temporal dynamics of regional-scale flood events, as in the case of the 1983 floods. New hydrologic-hydrodynamic modeling capabilities are presented in Chapter 4, for a tightly coupled model in order to simulate contrasting wetland types, and in Chapter 11, for the integrated simulation of the river-floodplain-reservoir continuum that exists in human-altered basins. Regarding satellite-based datasets, state-of-the-art methods were employed to study variables such as water levels, total water storage, inundation extent, precipitation and evapotranspiration. Together with big data and cloud computation analyses, they have largely advanced our understanding of wetlands and inundation processes. In particular, wetland water level has been overlooked by the research community, as well as wetland evapotranspiration. While wetland water levels were extracted here mainly from the ICESat satellite altimetry (https://openaltimetry.org/), new missions as SENTINEL-3A/B and the forthcoming SWOT and NISAR missions are promising for improving the monitoring of this variable. Regarding evapotranspiration, the use of the new geeSEBAL algorithm (available at <https://etbrasil.org/geesebal>; LAIPELT et al., 2021), which integrates the SEBAL land surface temperature-based algorithm (BASTIAANSSEN et al., 1998a) within the Google Earth Engine framework, has allowed an unprecedented monitoring of continental-scale wetland evapotranspiration.

Finally, while this thesis enlightens some relevant hydrological processes regarding South American floods and their positive and negative effects to human societies and ecosystems in general, major knowledge gaps persist and provide great research opportunities for the near future. In particular, the launching of many hydrology-oriented satellite missions, and an ever-growing computational capacity, make the continental hydrology agenda related to wetlands and floods a great research topic for the upcoming years.

2. Contribuição científica desta tese

Este capítulo apresenta um resumo estendido da tese. Reforço que o trabalho aqui apresentado foi possível apenas graças à colaboração frutífera que desenvolvi com inúmeros/as pesquisadores/as ao longo dos últimos quatro anos, aos/às quais sou muito grato.

Áreas úmidas (AU's) prestam importantes serviços ecossistêmicos, incluindo o fornecimento de alimentos, o suporte à biodiversidade e a regulação do clima e de inundações. A América do Sul abriga alguns dos principais sistemas fluviais da Terra, muitas vezes associados a grandes planícies que são inundadas todos os anos, como o Pantanal e muitas AU's da Amazônia. Complexos interfluviais de AU's também são encontrados em todo o continente, com configurações geomorfológicas e vegetações particulares, como savanas ou gramíneas adaptadas ao pulso de inundação. Enquanto algumas AU's da América do Sul ainda são remotas e, em certa medida, ainda bem preservadas (REIS et al., 2018), muitas sociedades humanas desenvolveram-se ao longo delas durante milhares de anos, e em especial ao longo das planícies de inundação, tendo adaptado suas paisagens bem como se adaptado aos seus ciclos sazonais de inundação. Por exemplo, no Brasil, os sistemas naturais contrastam com a grande quantidade de trechos de rios onde as populações ribeirinhas e áreas urbanizadas atualmente enfrentam um crescente risco de inundação (MAZZOLENI et al., 2021; Figura 2.1). Esta interação bidirecional entre os processos hidrológicos de AU's e as sociedades, que faz com que a evolução da paisagem rio-área úmida responda a ambas, realça a necessidade de compreender AU's como "sistemas sociedade-água" (DI BALDASSARRE et al., 2018).

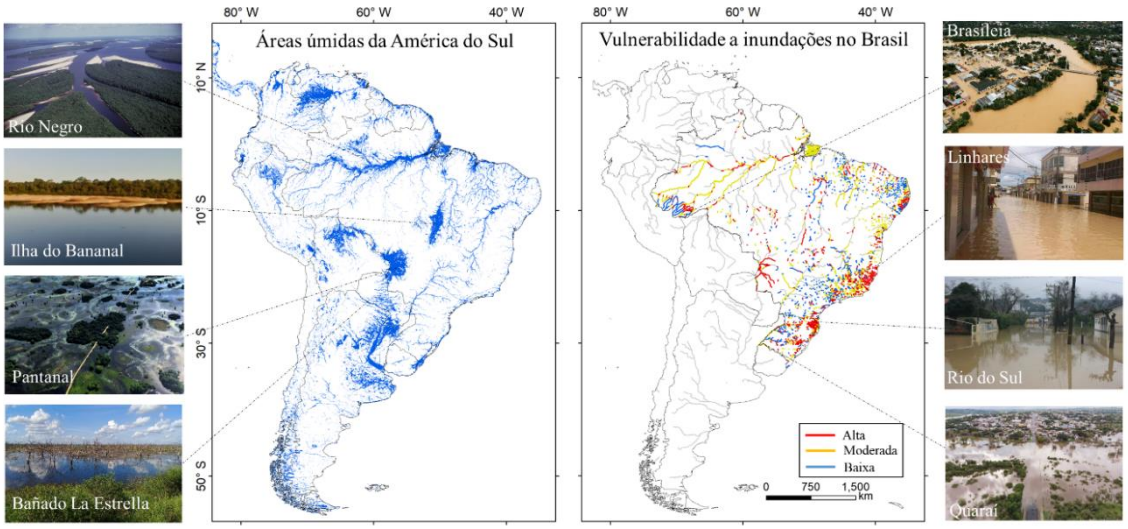

Figura 2.1. Os contrastes entre as AU's naturais em toda a América do Sul, à esquerda, e os trechos de rios vulneráveis às inundações no Brasil, à direita, onde as sociedades humanas se estabeleceram por milhares de anos. Fonte: FLEISCHMANN et al. (2021).

Esta tese apresenta uma investigação em escala cruzada da hidrologia das AU's da América do Sul e sua interação com as sociedades humanas, no contexto de risco de inundação ao longo de planícies de inundação (Figura 2.2). Convido os leitores a viajar pelas áreas inundáveis do continente, partindo inicialmente por análises das AU's da Amazônia (Parte I), seguindo pelas grandes AUs da América do Sul, distribuídas de norte a sul e envolvendo vários tipos de clima e vegetação (Parte II), e acabando por se dirigir a relevantes áreas propensas a risco de inundação no continente, onde os seres humanos interagiram fortemente com sistemas de planícies de inundação (Parte III).

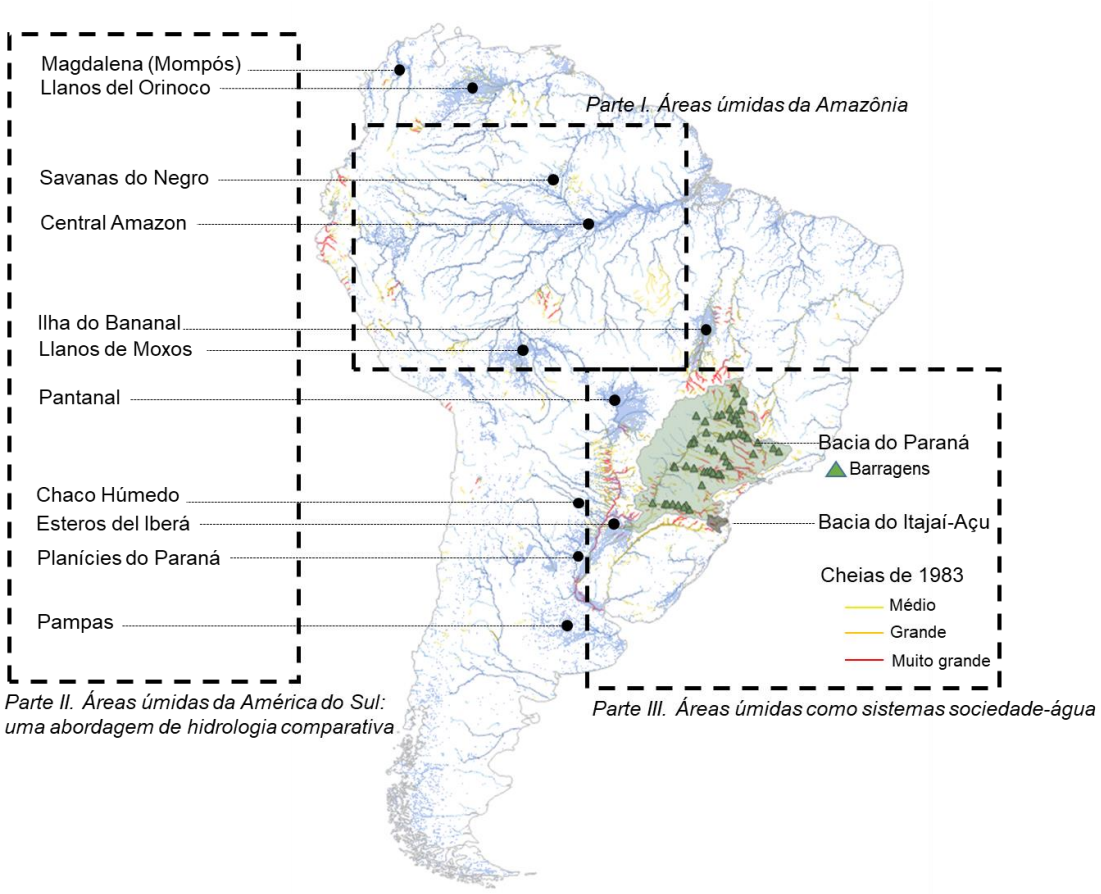

Figura 2.2. Esquema ilustrativo da estrutura da tese, com as principais áreas de estudo destacadas no mapa da América do Sul e distribuídas ao longo das três partes desta tese. A Parte I aborda a bacia do rio Amazonas. A localização das AU's avaliadas na Parte II é apresentada como círculos pretos. As duas bacias hidrográficas estudadas na Parte III são apresentadas como polígonos preenchidos de cinza (Paraná e Itajaí-Açu), bem como a recorrência (período de retorno) das inundações de 1983, que são abordadas no Capítulo 9 da Parte III.

Meu interesse em uma perspectiva continental dos recursos hídricos está alinhado com a agenda de pesquisa SAMEWATER – "South American WATER resources" ou "Recursos Hídricos Sul-Americanos" - que o grupo de pesquisa em Hidrologia de Grande Escala (www.ufrgs.br/hge) vem desenvolvendo nos últimos anos (PAIVA et al.,

2017; SIQUEIRA et al., 2020), liderados pelos professores Rodrigo Paiva e Walter Collischonn. Essa agenda foi inicialmente motivada pelo desenvolvimento de um modelo hidrológico-hidrodinâmico para a América do Sul (SIQUEIRA et al., 2018), que mais tarde promoveu outros diversos estudos (BRÊDA et al., 2020; FLEISCHMANN et al., 2020a; PASSAIA et al., 2020), e influenciou em grande parte alguns Capítulos desta tese. A frutífera era dos satélites, com dados de observação da Terra disponíveis para múltiplas variáveis hidrológicas como níveis de água de superfície, extensão de áreas inundadas, armazenamento de água, precipitação e evapotranspiração, permitiu as avaliações em escala continental aqui realizadas. Além disso, novas técnicas de computação se beneficiaram desses dados de satélite, gerando capacidades avançadas de modelagem hidrológica e hidrodinâmica que permitem uma simulação sem precedentes de processos de AU's.

Além disso, na América do Sul, o desenvolvimento da pesquisa em hidrologia tem acompanhado as demandas hídricas humanas, associadas por exemplo a estudos para áreas densamente povoadas e geração de energia hidrelétrica, que são localizadas longe de muitas AU's de grande relevância ambiental (DE PAIVA et al., 2020). Por outro lado, ecólogos de AU's e a agenda internacional de pesquisas ambientais têm estudado extensivamente grandes sistemas de AU's naturais, como as planícies inundáveis do Pantanal e da Amazônia. Isso destaca a necessidade para uma melhor conexão entre as comunidades de engenharia de recursos hídricos e de pesquisa de AU's, que muitas vezes abordam tópicos semelhantes com diferentes ferramentas e interesses. Investigar formas de vincular essas duas comunidades também é uma motivação para esta tese.

Como mencionado na introdução da tese, a agenda de pesquisa em hidrologia continental a global tem sido amplamente desenvolvida nos últimos anos (BIERKENS et al., 2015; WOOD et al., 2011). Neste contexto, poderíamos igualmente desenvolver uma agenda de investigação sobre as AU's continentais, que assumo ser o fio condutor desta tese, e que é abordada através de vários tópicos em diferentes escalas espaciais e temporais. Uma abordagem de hidrologia comparativa constitui a base desta tese, partindo de semelhanças e diferenças entre distintos sistemas para fomentar a compreensão de processos hidrológicos. Isto é realizado para diferentes tipos de AU's, como planícies de inundação e AU's interfluviais, para a bacia do rio Negro na Amazônia (Capítulo 4), para toda a bacia amazônica, através de uma intercomparação de 29 produtos de inundação, da escala local para a escala da bacia (Capítulo 5), e uma avaliação das tendências de inundação em toda a bacia (Capítulo 6). Uma abordagem comparativa também é empregada para esclarecer os padrões de inundação (Capítulo 7) e evapotranspiração (Capítulo 8) de 12 grandes sistemas de AU's da América do Sul, que são representativos de vários climas e tipos de vegetação inundáveis (gramíneas, savanas, florestas) do continente. A investigação do perigo de inundação, no contexto de desastres naturais, é primeiramente avaliada com modelos hidrodinâmicos para o domínio continental, no caso das grandes inundações de 1983 que devastaram uma porção do continente durante aquele forte ano de El Niño (Capítulo 9). Em seguida, a partir de uma perspectiva de múltiplas escalas ("*cross-scale*"), avalia-se a capacidade de

modelos continentais para estimar variáveis hidrodinâmicas (extensão de áreas inundadas, níveis d'água do rio e vazões) localmente relevantes para a bacia do rio Itajaí-Açu no Sul do Brasil, uma das mais regiões mais afetadas por inundações no país (Capítulo 10). A tese termina mostrando que as planícies de inundação são mais amplamente distribuídas ao longo de grandes bacias do que normalmente assumido (ou seja, elas não estão localizadas apenas nos trechos planos de jusante de grandes rios), e que os seus efeitos sobre o regime hidrológico interagem com os das infraestruturas artificiais, como as barragens, para criar um *continuum* entre rio, planícies inundáveis e reservatórios (Capítulo 11). Para abordar este tema, é realizado um estudo de caso na Bacia do Rio Paraná, que contém o maior volume armazenado em reservatórios no continente.

Além da compreensão de processos hidrológicos, esta tese aborda também o papel das AU's na prestação de serviços ecossistêmicos. Estes serviços são abordados de forma geral na maioria dos Capítulos, mas são o tópico específico do Capítulo 11, sobre atenuação de inundações, e do Capítulo 8, sobre a regulação do clima através de mudanças nos balanços de energia de superfície. Além disso, o bom funcionamento dos ecossistemas das AU's depende da manutenção da conectividade hidrológica ao longo da bacia hidrográfica (REIS et al., 2019a). Enquanto esta tese avalia principalmente complexos de AU's a partir de uma perspectiva de escala regional, sem análises mais detalhadas dos processos hidrológicos de AU's em escala local, a conectividade em AU's foi abordada em termos de seus componentes lateral (a maioria dos Capítulos que abordam inundação lateral de planície de inundação), longitudinal (o *continuum* rio-reservatório-planície de inundação, Capítulo 11) e vertical (interações superfície-atmosfera através de evapotranspiração, Capítulo 8). Em particular, o Capítulo 6 mostra o aumento da conectividade lateral das águas superficiais nas últimas décadas na bacia amazônica (Figura 2.3).

Os próximos parágrafos fornecem uma discussão mais ampla de cada um desses capítulos.

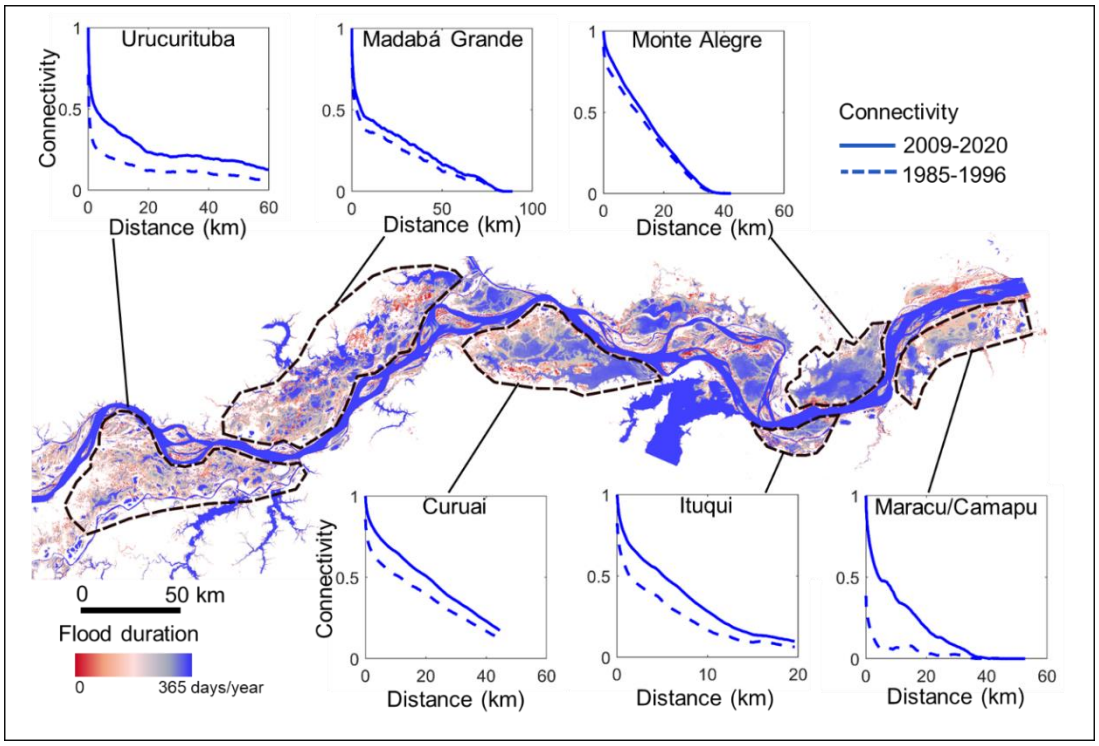

Figura 2.3. O aumento da extensão máxima de inundação sobre as várzeas da Amazônia central nas últimas quatro décadas também aumentou a conectividade de águas superficiais em muitas unidades de várzea, ao longo do baixo Amazonas. Este mapa apresenta a duração da inundação para a década 2009-2020, e cada gráfico apresenta, para uma determinada unidade de planície de inundação, um índice de conectividade que está relacionado com o número de pares de pixels que estão conectados a uma determinada distância. Mais detalhes sobre esta análise são fornecidos no Capítulo 6.

O ponto de partida desta tese é a bacia amazônica, que abriga alguns dos maiores sistemas de AU's do mundo, com sociedades e ecossistemas humanos adaptados ao pulso de inundação sazonal. A Parte I da tese avança nossa compreensão das AU's da Amazônia de três formas particulares (Capítulos 4, 5 e 6). Modelos hidrológicos e hidrodinâmicos anteriores foram desenvolvidos apenas para a escala da bacia ou para áreas de várzea na Amazônia central. Aqui nós estudamos e utilizamos modelos e dados de satélite para investigar a dinâmica de inundação contrastante entre as savanas do rio Negro, um grande ecossistema interfluvial que se adaptou a estados alternados de déficit e excesso de água, e planícies de inundação adjacentes ao longo de rios, os chamados igapós (Capítulo 4). As savanas interfluviais apresentam um comportamento muito diferente das demais AU's da bacia, por serem mais dependentes da precipitação local e possuírem menores amplitudes de nível d'água (Figura 2.4a e Figura 2.4b). Diferentes configurações de modelos hidrológico-hidrodinâmicos foram simuladas e comparadas a múltiplas observações de satélite dos níveis d'água e extensão da inundação. Uma diferença maior entre modelos 1D e 2D e estimativas de inundação baseadas em satélites para as áreas interfluviais enfatiza nossa compreensão limitada de sua dinâmica hidrológica. Em seguida, dadas as grandes incertezas que foram identificadas para mapear a dinâmica de inundação em diferentes tipos de AU's, o Capítulo 5 apresenta

uma avaliação abrangente da estimativa de inundação em toda a bacia amazônica, realizada através da coleta de 29 produtos de inundação que abrangem diferentes resoluções espaciais (12.5 m a 25 km) e temporais (diária a mensal e estática). Enquanto uma grande concordância foi observada entre os produtos, em termos de distribuição espacial da inundação, para as planícies de inundação da Amazônia central, especialmente para as áreas de água aberta ao longo do baixo Amazonas, divergências importantes persistem para áreas interfluviais como o Negro, savanas de Roraima e Llanos de Moxos, bem como para a região de Pacaya-Samiria (Figura 2.4c), para a qual são necessários novos desenvolvimentos pela comunidade internacional de sensoriamento remoto e modelagem. Foi desenvolvido um sistema WebGIS que facilita a compreensão de cada produto analisado (https://amazon-inundation.herokuapp.com/).

Finalmente, o Capítulo 6 aborda as tendências de longo prazo nos padrões de inundação da Bacia Amazônica (Figura 2.4d). Os resultados utilizaram múltiplas ferramentas de sensoriamento remoto e modelagem para mostrar que as várzeas centrais da Amazônia são a principal área de mudanças de inundação nas últimas quatro décadas na bacia. Um novo estado hidroclimático está operando na bacia desde 1998 (BARICHIVICH et al., 2018; ESPINOZA et al., 2019a), que mostramos ser traduzido em um aumento de 20% na extensão máxima de inundação sobre as várzeas do rio Amazonas. Esse aumento culminou, em junho de 2021, no maior nível d'água já registrado nos 119 anos de registro em Manaus, na confluência dos rios Negro e Amazonas, o que tem impactado em grande parte os ecossistemas centrais da Amazônia e as sociedades humanas, e talvez até fluxos globais de gases de efeito estufa (BODMER et al., 2018; WILSON et al., 2020).

Durante esta tese, também me envolvi em vários outros estudos sobre a região amazônica, desde a melhoria de modelos hidrológico-hidrodinâmicos com dados de sensoriamento remoto (COELHO et al., 2021; FAN et al., 2021; MEYER OLIVEIRA; FLEISCHMANN; PAIVA, 2020) e seu uso para entender a dinâmica das águas superficiais da Amazônia (SORRIBAS et al., 2020), até a compreensão de impactos de desmatamento (LAIPELT et al., 2020, 2021) e o desenvolvimento de uma revisão sobre a "hidrologia da Amazônia a partir do espaço" (FASSONI-ANDRADE; FLEISCHMANN; PAPA, 2021). Também compartilhei a primeira autoria de um estudo sobre projeção dos impactos das mudanças climáticas na geração de energia pelas barragens propostas para a Amazônia (ALMEIDA et al., 2021), bem como colaborei em dois artigos sobre os impactos das barragens, relacionados à operação de *hidropeaking* (ALMEIDA et al., 2020) e ao planejamento de alocação de barragens em toda a bacia, considerando impactos ambientais (FLECKER et al., em revisão). A necessidade de melhor conectar pesquisadores de várias disciplinas que estudam a Bacia Amazônica é evidente, se quisermos melhor desenvolver as capacidades vocacionais da região e entender sua resposta às mudanças ambientais atuais e futuras. Isso me motivou a criar e coordenar, junto com outros colegas da UFRGS e outras instituições, a iniciativa "Conexões Amazônicas" (www.conexoesamazonicas.org), que hoje é um fórum de

comunicação científica sobre a pesquisa amazônica, indo desde as ciências biológicas até as ciências humanas e da Terra.

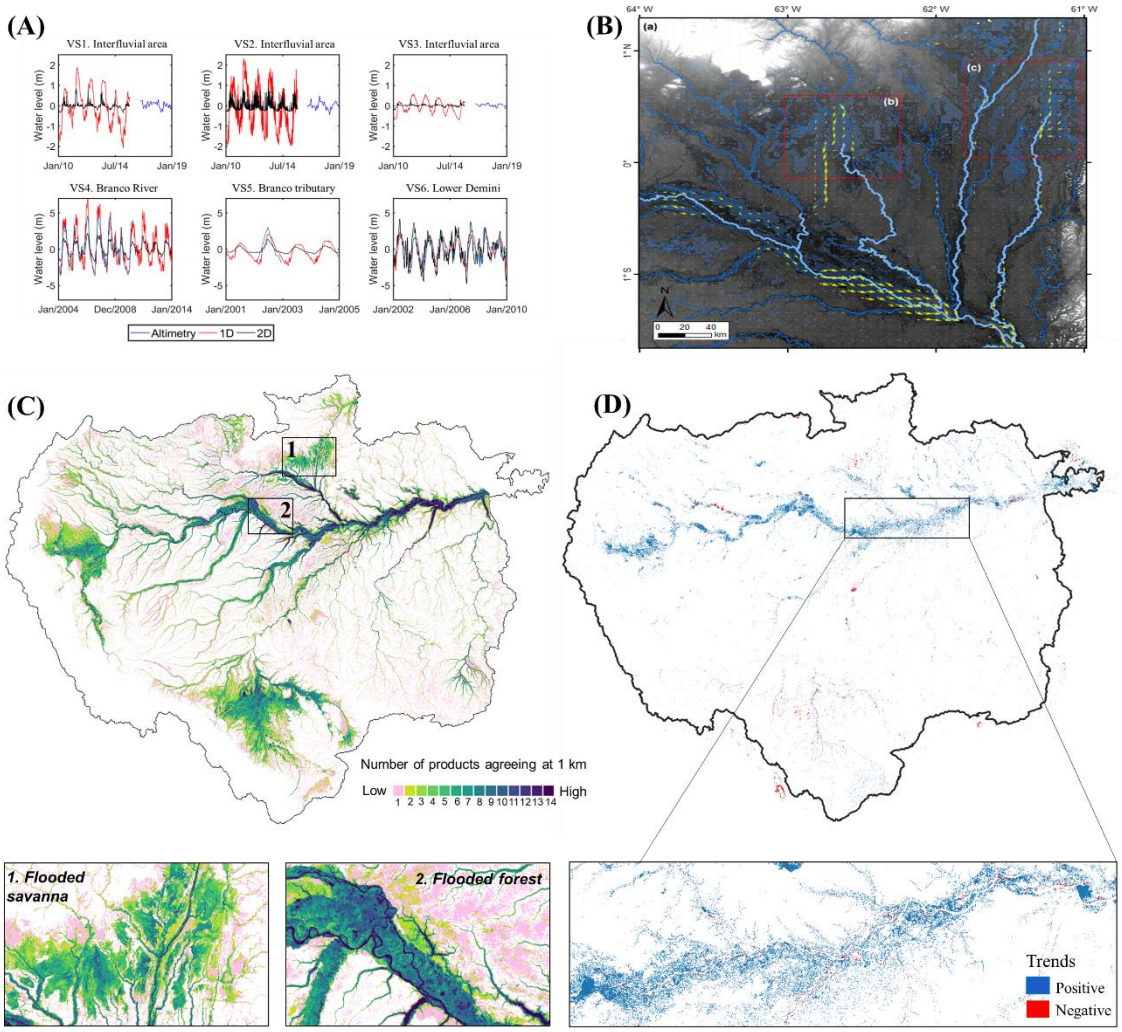

Figura 2.4. A Parte I da tese apresenta uma nova compreensão da dinâmica de inundação das AU's da Amazônia, desde as diferenças entre planícies de inundação e AU's interfluviais em termos de (a) níveis d'água e (b) fluxos superficiais de água, até uma (c) avaliação abrangente de dezenas de produtos de inundação para a bacia e (d) uma análise de tendências espaciais de inundação nas últimas quatro décadas.

Para entender a hidrologia de diversos tipos de AU's, a ampliação de minhas análises, da bacia amazônica para o domínio continental, mostrou-se um caminho interessante. Isso foi realizado no contexto de uma abordagem de hidrologia comparativa, que é o tema principal da Parte II da tese, e é formado por dois capítulos principais que analisaram 12 grandes complexos de AU's da América do Sul (Figura 2.5). O primeiro, Capítulo 7, utiliza um conjunto de dados baseados em satélites para níveis d'água de rios e AU's (missões Envisat, SARAL Altika, JASON-2/3, Sentinel-3A/B e Icesat), armazenamento total de água (missão GRACE), extensão de inundação

(produto GIEMS-2) e precipitação (produto MSWEP) e apresentou uma análise dos dados numa escala temporal mensal para o período 2003-2015. A amplitude anual do nível d'água mostrou-se muito menor sobre as AU's interfluviais, e.g. as savanas alagáveis da bacia do rio Negro e de Llanos de Moxos (menos de dois metros), do que ao longo das planícies de inundação de rios, onde os níveis podem variar mais de 10 m, como por exemplo ao longo do rio Amazonas (Figura 2.6). O intervalo de tempo entre a precipitação e a inundação também foi menor em áreas interfluviais (dois meses ou menos), refletindo a propagação mais lenta da onda de cheia que ocorre em sistemas fluviais. No Capítulo 8, essa análise foi transferida para outro componente importante do ciclo hidrológico, a evapotranspiração (ET). O mapeamento da ET em escala continental tem sido dificultada pelo processo demorado de aquisição e processamento de dados de satélite, e foi possível neste estudo graças ao desenvolvimento de novas técnicas de computação em nuvem pelo grupo de pesquisa ET-Brasil, liderado pelo Prof. Anderson Ruhoff (UFRGS), em especial a ferramenta geeSEBAL (https://etbrasil.org/geesebal; LAIPELT et al., 2021). No Capítulo 8, grandes diferenças de ET são encontradas entre AU's e áreas de terra firme em climas temperados (ambientes limitados por água), enquanto que nas AU's equatoriais a diferença é menor (Figura 2.7). Na Amazônia central, a alta cobertura florestal em trechos de montante compensa a maior fração de inundação e menor cobertura florestal que ocorre em regiões de jusante, mantendo altas taxas de evapotranspiração durante todo o ano. A propagação de inundações ao longo das planícies inundáveis é mostrada como um importante controle da dinâmica de ET em AU's associadas ao pulso de inundação do rio, especialmente para o Pantanal, onde a onda de cheia leva meses para se propagar pelo sistema (Figura 2.8). Por fim, esta parte destaca o funcionamento hidrológico único das AU's da América do Sul, e define a importância da realização de estudos hidrológicos comparativos para as AU's em todo o mundo. Saliento também que, para uma melhor compreensão da hidrologia das AU's, é necessário que estas sejam estudadas como unidades individuais, em vez de serem agrupadas em bacias hidrográficas, que é a abordagem mais comum adotada em análises hidrológicas. Isto é especialmente verdadeiro para as AU's interfluviais, enquanto as planícies de inundação de rios requerem a compreensão dos processos hidrológicos tanto locais como a montante (isto é, toda a bacia hidrográfica).

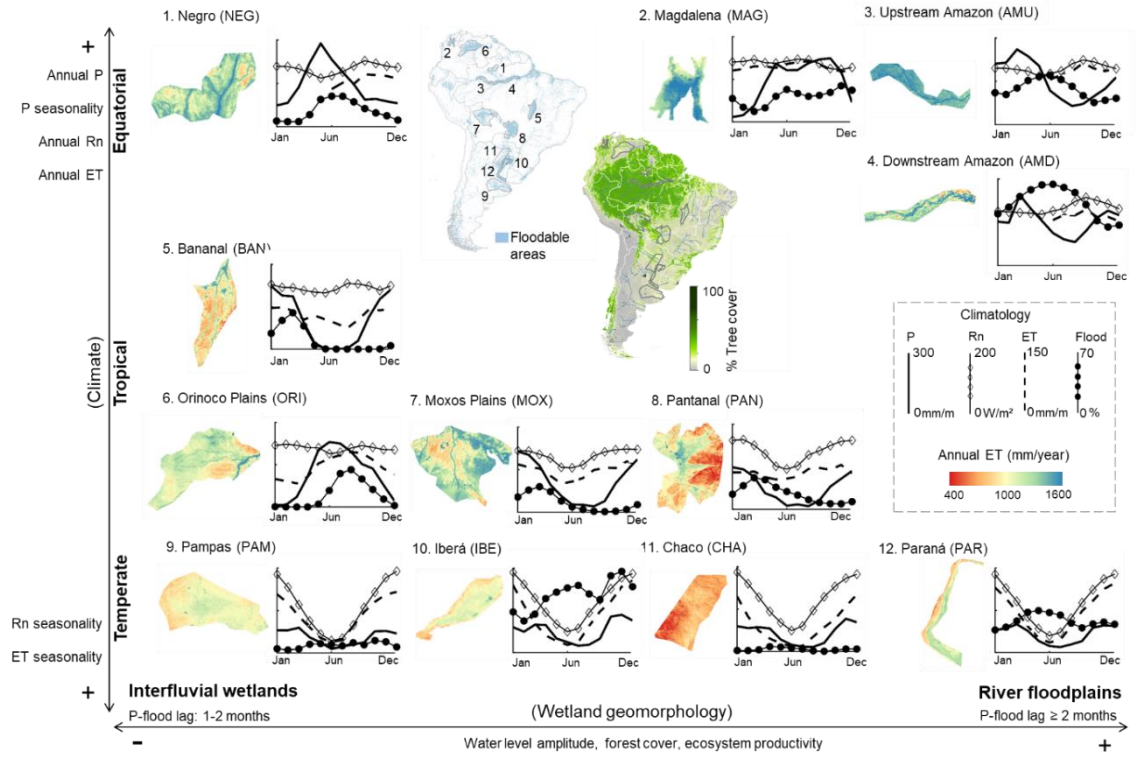

Figura 2.5. A tese Parte II apresenta uma abordagem hidrológica comparativa, através da qual 12 grandes complexos de AU's em toda a América do Sul são comparados em termos de dinâmica de inundação e outras variáveis hidrológicas como precipitação, nível de água superficial e evapotranspiração. Esta figura mostra a climatologia da precipitação (P), radiação líquida (Rn), evapotranspiração (ET) e fração de inundação (FF), e é uma reprodução do Capítulo 8.

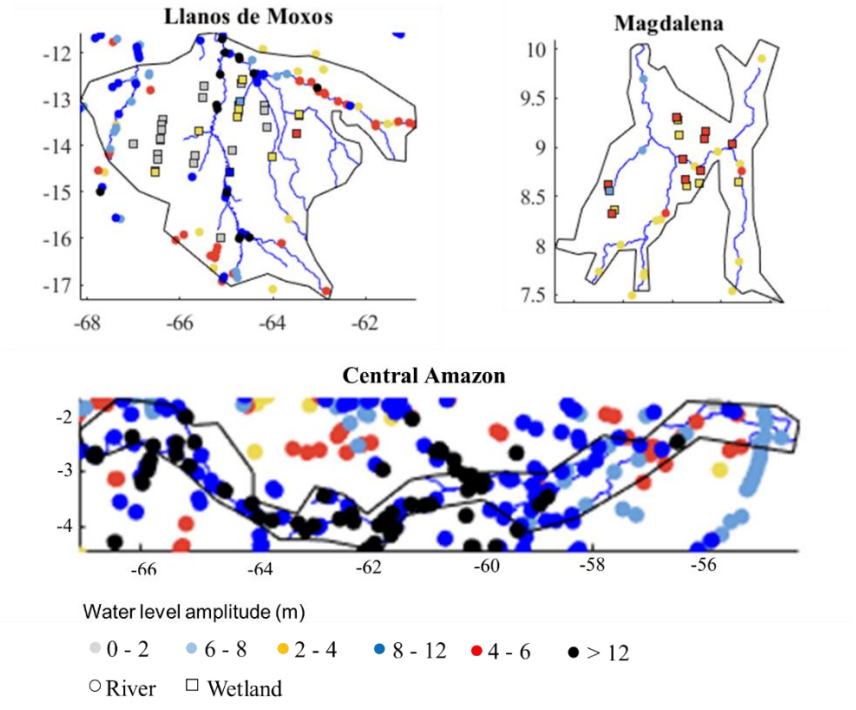

Figura 2.6. O Capítulo 7 investiga a amplitude do nível da água espaço-temporal para alguns complexos de AU's seleccionados, para estações virtuais em rios (círculos) e AU's (praças). Os dados relativos às 12 AU's analisadas são apresentados no Capítulo 7.

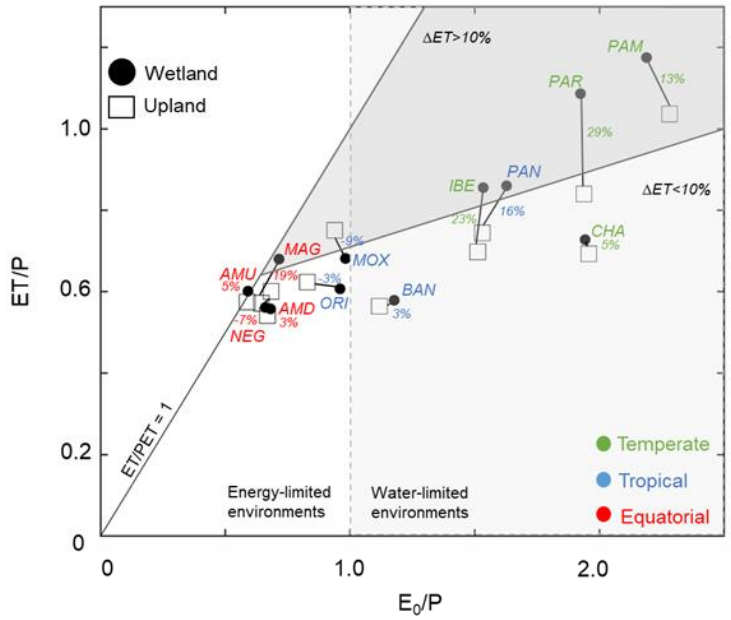

Figura 2.7. O Capítulo 8 investiga as diferenças entre AU's e planaltos. Esta figura mostra uma estrutura semelhante a Budyko relacionando o índice evaporativo de longo prazo (ET/P) com o índice de aridez (E0/P), onde E0/P > 1 refere-se a ambientes limitados por água, e E0/P1 a ambientes limitados por energia. Os valores são apresentados para AU's (círculos negros) e os planaltos adjacentes (quadrados pretos). Cada rótulo refere-se a uma zona húmida, tal como apresentado na figura 2.4. As diferenças a longo prazo entre AU's e planaltos são apresentadas como números entre as AU's e as zonas de montanha para cada zona húmida, e a zona cinzenta escura refere-se a zonas com diferenças superiores a 10%.

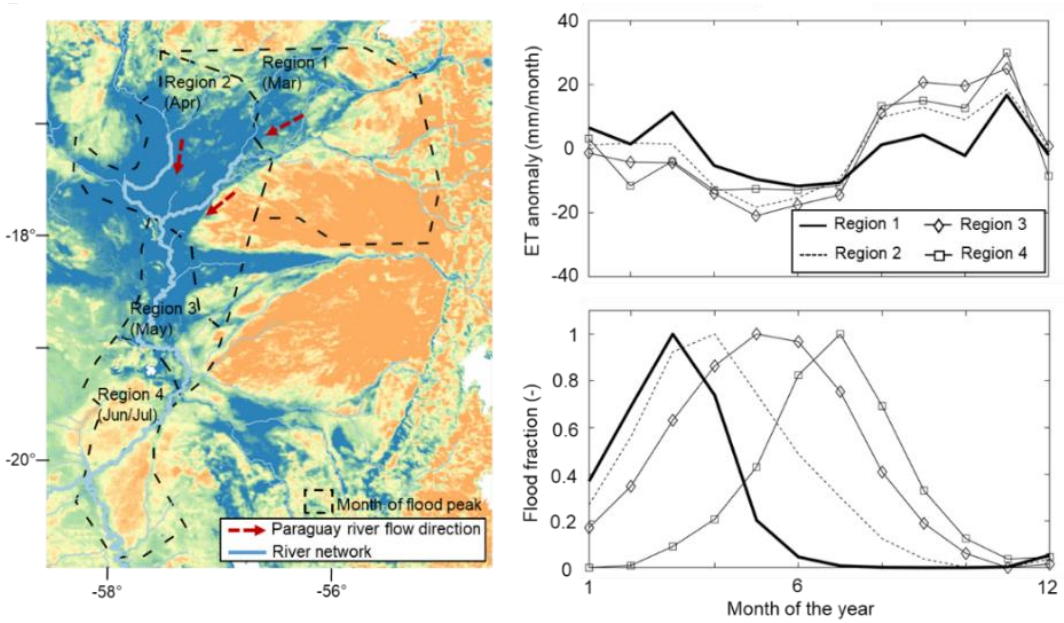

Figura 2.8. O Capítulo 8 investiga a dinâmica espaço-temporal da evapotranspiração (TE) em 12 AU's da América do Sul. (a) A propagação da inundação afeta a ET na escala de tempo sazonal nas AU's do Pantanal. O mapa anual da evapotranspiração é apresentado na figura da esquerda, juntamente com a localização das quatro regiões do mesmo mês de pico de cheia (de março a junho/julho), enquanto as figuras na coluna da direita mostram a climatologia da ET mensal (valores de anomalia) e fração de inundação para as quatro regiões.

Dada a minha formação em engenharia de recursos hídricos, foi uma escolha natural investigar na Parte III da tese como as grandes inundações interagem com os sistemas humanos, isto é, os sistemas sociedade-água. Embora este tema tenha sido abordado pela comunidade de sócio-hidrologia nos últimos anos, saliento que aqui o meu principal interesse foi a compreensão do componente de perigo de inundação. Esta parte tem três capítulos. O Capítulo 9 investiga os complexos padrões espaço-temporais das cheias de 1983 na América do Sul, com um foco especial na porção brasileira, que foi um dos eventos de inundação mais devastadores já registrados no continente. Houve três principais períodos de inundação (fevereiro, junho e julho), conforme os picos de vazão estimados pelo modelo continental de SIQUEIRA et al. (2018), em muitas bacias hidrográficas da América do Sul, como Araguaia, Tocantins, São Francisco, Uruguai, La Plata e seus afluentes, resultando em altas vazões no rio Paraguai por muitos meses. O *timing* dos eventos teve uma direção de norte a sul ao longo desse ano, com algumas das maiores descargas de rios já registradas em áreas do norte, como nas bacias dos rios Araguaia e Tocantins, ocorrendo em fevereiro de 1983, e em julho em regiões do sul como o Rio Uruguai (Figura 2.9). Embora a capacidade destes modelos continentais em estimar as vazões de pico para eventos extremos como o de 1983 tenha se mostrado satisfatória, ainda não está claro se eles podem fornecer estimativas localmente relevantes de variáveis hidrodinâmicas (vazões de rios, níveis d'água e extensão da inundação). Este tópico foi abordado para a bacia do rio Itajaí-Açu, uma das áreas mais propensas a inundações no continente (Capítulo 10). Para auxiliar na interpretação, foram definidos três requisitos principais para definir estimativas de um modelo hidrodinâmico fluvial como localmente relevantes: os erros do modelo devem ser iguais ou menores (i) do que o requisito de acurácia para uma determinada aplicação e localização, (ii) do que os erros obtidos com um típico modelo de escala local/de trecho, e (iii) do que incertezas das observações. Os resultados mostraram que ainda é um grande desafio para os modelos continentais fornecer estimativas localmente relevantes de níveis absolutos d'água e extensão de áreas inundadas (Figura 2.10), enquanto as vazões de rios e anomalias dos níveis d'água podem ser satisfatoriamente estimadas. Algumas recomendações foram então fornecidas para tornar a capacidade preditiva de modelos localmente relevantes, por exemplo, a necessidade de melhor estimar seções transversais de rios, considerando a heterogeneidade dos canais fluviais.

Outro aspecto importante para melhorar o realismo dos modelos hidrodinâmicos relaciona-se à estrutura do modelo, ou seja, como eles representam processos relevantes, e com quais equações. É bem sabido que os seres humanos alteram os sistemas rio-área úmida através da construção de infraestruturas como barragens, e que os modelos hidrodinâmicos em larga escala devem representá-las para desenvolver modelos que sejam corretos pelos "motivos certos" (KIRCHNER, 2006). Assim, com base em um desenvolvimento recente do modelo MGB para a simulação hidrodinâmica de barragens em grande escala (FLEISCHMANN et al., 2019b), o Capítulo 11 apresenta um estudo de caso para a bacia do Alto Rio Paraná (~900.000 km²), a mais relevante na América do Sul em termos de armazenamento total de reservatórios. O objetivo geral foi investigar a simulação do que chamamos de "*continuum* rio-planície de inundação-

reservatório", ou seja, os campos contínuos de variáveis como níveis d'água e águas superficiais que existem ao longo das redes de drenagem. Para tanto, foram avaliadas diferentes formas de representação de múltiplos reservatórios em termos de batimetria e regras de operação, de modo a representá-los de forma simples porém acurada em modelos de grande escala. A Figura 2.11 exemplifica a representação do *continuum* para o rio Iguaçu, um importante afluente do Paraná. Os perfis altimétricos longitudinais (máximo e mínimo) da superfície da água, bem como as máximas áreas inundadas, destacam quão conectados são os processos hidrológicos-hidráulicos que ocorrem em toda a bacia. Isso é importante, por exemplo, se quisermos entender os efeitos de remanso de barragens em trechos de rios a montante, que podem ser associados a cidades e AU's importantes. Além disso, no Capítulo 11 é mostrado que as planícies de inundação e os reservatórios têm um papel complementar na atenuação de cheias na bacia. Enquanto as planícies de inundação são mais importantes ao longo das cabeceiras dos afluentes (por exemplo, rios Iguaçu, Paranapanema, Grande e Ivinhema) e nos trechos inferiores da rede do Paraná, os efeitos dos reservatórios são mais relevantes ao longo dos cursos médio a inferior dos afluentes (Figura 2.12). Isso também mostra que as planícies de inundação estão amplamente distribuídas em toda a bacia, e não localizadas apenas em trechos planos de jusante, como geralmente assumido em muitos modelos hidrodinâmicos de grande escala, e devem ser consideradas se quisermos avançar em direção a modelos localmente relevantes.

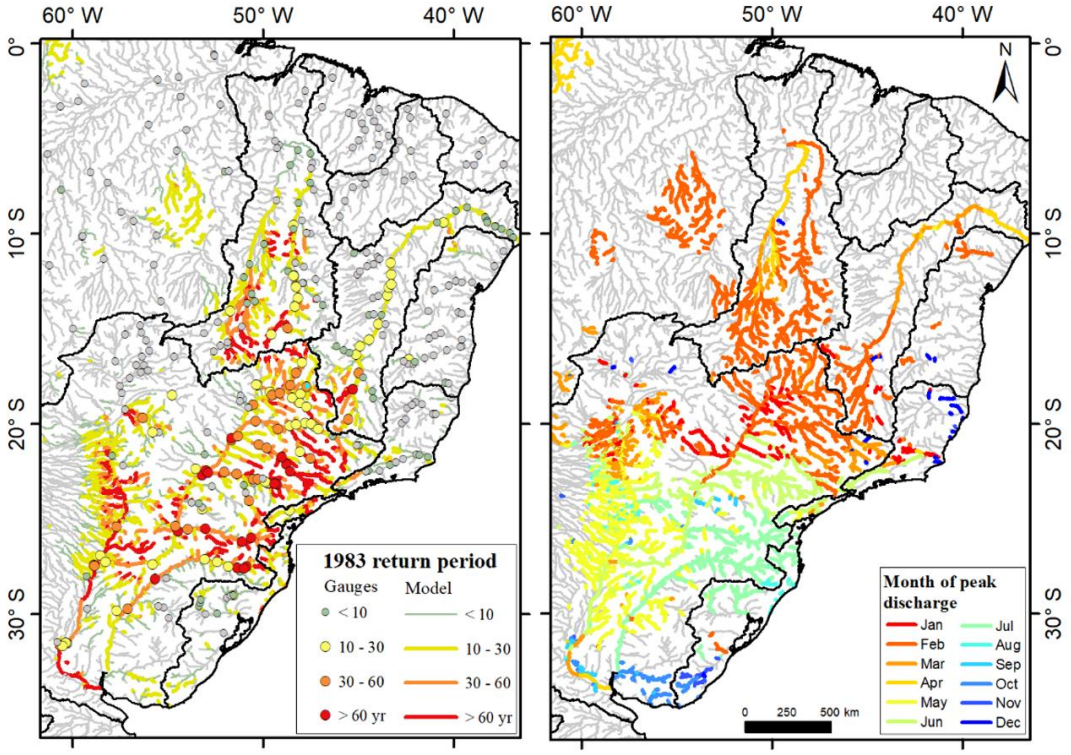

Figura 2.9. O Capítulo 9 investiga a dinâmica espaço-temporal das grandes inundações de 1983. A figura da esquerda mostra o tempo de retorno para cada trecho de rio (simulações do modelo MGB), bem como

para estações in-situ, enquanto a figura da direita mostra o mês em que ocorreu o pico de vazão e cada trecho de rio, de acordo com o modelo MGB desenvolvido por SIQUEIRA et al. (2018).

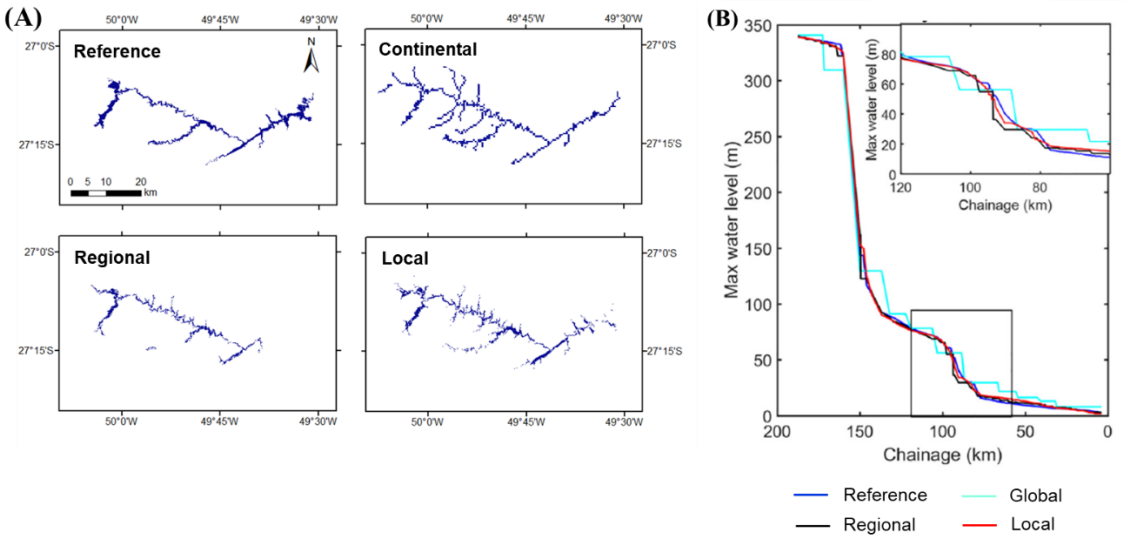

Figura 2.10. O Capítulo 10 avalia se modelos hidrodinâmicos em escala continental podem fornecer estimativas localmente relevantes de variáveis hidrodinâmicas como (a) extensão de inundação e (b) níveis d'água. Isso é realizado através da comparação de modelos de escala continental, regional e local com uma referência local para a bacia hidrográfica do rio Itajaí-Açu.

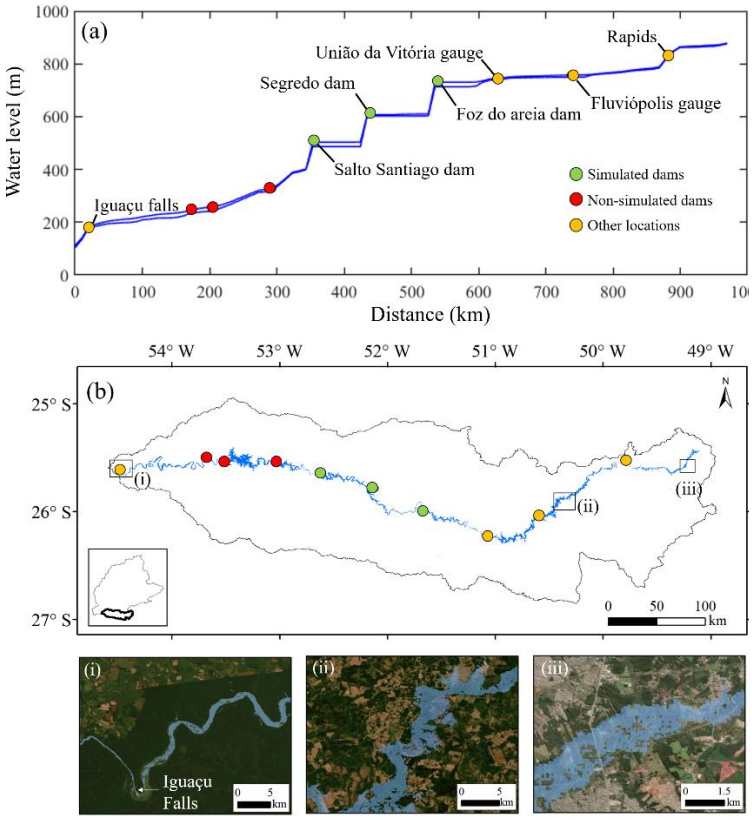

Figura 2.11. O Capítulo 11 aborda as interações rio-reservatório - planície de inundação- na bacia do rio Paraná. (a) Perfis longitudinais de nível d'água máximo e mínimo (linhas azuis) ao longo da rede do rio Iguaçu (principal afluente do Paraná). A distância é medida a partir da confluência entre os rios Iguaçu e Paraná. As três barragens simuladas são apresentadas como círculos verdes, assim como as barragens a fio d'água não simuladas (em vermelho) e alguns locais de interesse (em amarelo). (b) A extensão máxima de inundação simulada para a mesma área da figura a. Detalhes (i), (ii) e (iii) mostram a inundação máxima em algumas áreas, junto com o Google Earth Imagery.

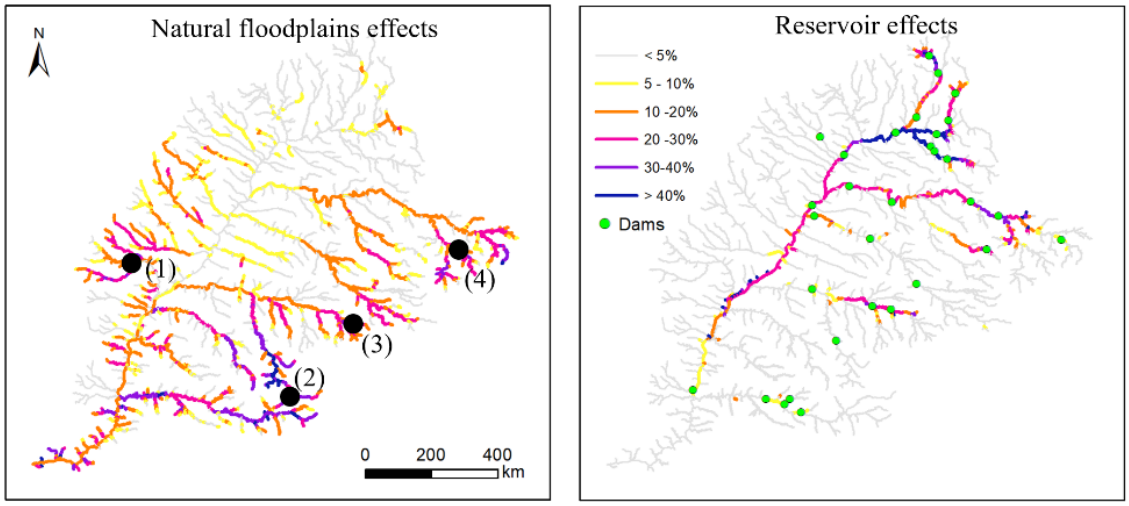

Figura 2.12. O Capítulo 11 aborda as interações rio-planície de inundação-reservatório na bacia do rio Paraná. A figura da esquerda mostra o papel de planícies de inundação em atenuar cheias, e a da direita mostra o papel dos reservatórios.

A compreensão de sistemas de AU's (ecossistemas, sociedades humanas, ambiente físico, etc.) requer novas ferramentas para mapear com acurácia a sua dinâmica hidrológica. Esta tese apresenta algumas metodologias novas para a quantificação de processos hidrológicos de inundação e AU's. Em relação às ferramentas de modelagem baseadas em processos, novas metodologias foram desenvolvidas para melhorar a representação acoplada de hidrologia (infiltração de água do solo, evapotranspiração, geração de escoamento) e hidrodinâmica (propagação de cheias, atenuação de cheias em planícies de inundação, efeitos de barragem e remanso). Além disso, também foi mostrada a capacidade de modelos continentais para descrever a dinâmica espaço-temporal de cheias em grandes escalas, como no caso dos eventos de 1983. Novas capacidades de modelagem hidrológico-hidrodinâmica são apresentadas no Capítulo 4, para um modelo fortemente acoplado ("*fully-coupled*"), a fim de simular tipos distintos de AU's, e no Capítulo 11, para a simulação integrada do *continuum* rio-reservatório-planície de inundação que existe em bacias alteradas pelo homem. Em relação a produtos baseados em satélites, foram empregados métodos que configuram o estado da arte para estudar variáveis como níveis de água, armazenamento total de água, extensão da inundação, precipitação e evapotranspiração. Juntamente com as análises de *big data* e computação em nuvem, eles têm amplamente avançado nossa compreensão de AU's e processos de inundação. Em particular, o nível d'água em AU's tem sido pouco abordado pela comunidade científica, bem como a evapotranspiração das AU's. Embora os níveis d'água de AU's tenham sido extraídos nesta tese principalmente com os dados do satélite ICESat (https://openaltimetry.org/), novas missões como SENTINEL-3A/B e as futuras SWOT e NISAR prometem melhorar o monitoramento desta variável. Em relação à evapotranspiração, o uso do novo algoritmo geeSEBAL (disponível em <https://etbrasil.org/geesebal>; LAIPELT et al., 2021), que integra o algoritmo baseado na temperatura da superfície terrestre SEBAL (BASTIAANSSEN et al., 1998a) dentro

do ambiente do Google Earth Engine, permitiu uma avaliação sem precedentes da evapotranspiração de AU’s em escala continental.

Por fim, embora esta tese esclareça alguns processos hidrológicos relevantes em relação às inundações na América do Sul e seus efeitos positivos e negativos para as sociedades humanas e ecossistemas em geral, grandes lacunas de conhecimento persistem e proporcionam grandes oportunidades de pesquisa para o futuro próximo. Em particular, o lançamento de muitas missões de satélite orientadas para a hidrologia, e uma crescente capacidade computacional, fazem da agenda da hidrologia continental relacionada a AU’s e inundações um grande tópico de pesquisa para os próximos anos.

3 Overview of the South American wetlands and the available study tools

This chapter provides an overview of the South American wetlands, especially those studied in this thesis, their ecosystem services and their interaction with humans, as well as the main study tools available today for studying wetlands (i.e., in situ data, remote sensing and hydrological modeling).

Este capítulo apresenta uma visão geral das áreas úmidas da América do Sul, especialmente aquelas estudadas nesta tese, os serviços ecossistêmicos providos e as suas interações com sociedades humanas, bem como as principais ferramentas de estudo disponíveis para estudar áreas úmidas (i.e., dados in-situ, sensoriamento remoto e modelagem hidrológica). Este capítulo é redigido em inglês.

3.1 Definition and classification of wetlands

Due to the varied types and characteristics of wetlands worldwide, their definition is rarely consensual, which may change according to local/regional understanding, societies and policies. According to MITSCH; GOSSELINK (2007), wetlands' definitions generally include three main components:

- Wetlands are distinguished by the presence of water (surface or within root zone);
- They have unique soil conditions different from adjacent uplands;
- They support biota such as vegetation adapted to the wet conditioning, and are characterized by an absence of flooding-intolerant biota.

One important definition was developed by the Ramsar convention (International Convention on Wetlands, created in 1971 and signed by Brazil in 1993): wetlands are "areas of marsh, fen, peatland or water, whether natural or artificial, permanent or temporary, with water that is static or flowing, fresh, brackish or salt, including areas of marine water, the depth of which at low tide does not exceed six metres" (RAMSAR CONVENTION SECRETARIAT, 2010). This is a broad definition that includes rivers and lakes, although many scientists differ (shallow water) wetlands from deep water systems. Artificial wetlands, as rice paddies and wetlands close to reservoirs, are also considered as wetlands.

More restricted definitions have also been proposed, considering a wetland as a particular system with different characteristics from its neighbor terrestrial and aquatic areas, and stating specific functional aspects (e.g., wetland hydrological and biogeochemical features). In Brazil, the National Institute for Science and Technology in Wetlands (INCT-INAU) recently proposed the following definition (JUNK et al., 2014): "Wetlands are ecosystems at the interface between aquatic and terrestrial environments; they may be continental or coastal, natural or artificial, permanently or periodically inundated by shallow water or consist of waterlogged soils. Their waters may be fresh, or highly or mildly saline. Wetlands are home to specific plant and animal communities adapted to their hydrological dynamics. The extent of a wetland can be determined by the border of the permanently flooded or waterlogged area, or in the case of fluctuating water levels, by the limit of the area influenced during the mean maximum flood. The outer borders of wetlands are indicated by the absence of hydromorphic soils and/or hydrophytes and/or specific woody species that are able to grow in periodically or permanently flooded or waterlogged soils. The definition of a wetland area should include, if present, internal permanently dry areas as these habitats are of fundamental importance to the maintenance of the functional integrity and biodiversity of the respective wetland."

Similarly, KANDUS et al., (2017) presented the following definition from the Argentinian wetlands inventory: wetland is an area where the temporary or permanent presence of surface or subsurface water leads to particular biogeochemical fluxes, which

are different from terrestrial and aquatic environments. Key characteristics are the presence of an adapted biota (usually aquatic plants), and/or hydromorphic soils or substrate. NEIFF et al. (1994) defined wetland systems as complexes composed by aquatic (permanent or not), terrestrial systems and various macrohabitats types, being a macrosystem that acts as functional ecological unit, and which should be the unit for integrated ecological management (similar to the way a watershed is used for integrated water resources management).

Wetlands' names also vary from country to country, and a non-exhaustive list of South American words for inland wetlands include (which may be distinguished by geomorphology, concentration of organic carbon, hydrological functioning, etc.): *área úmida* (the most used translation for wetlands in Portuguese), *pântano, várzea, igapó* (black-water floodplains in Amazon Basin), *ipuca* (in the Araguaia River Basin), *charco, brejo, turfeira, banhado, planície de inundação, veredas* in Brazil, and *humedales* (the most used translation for wetlands in Spanish), *pantanal, llanura inundable, bañado, charcas, pajonales, mallines, esteros, bofedales, vegas, pastizales inundables, bosques fluviales, turbales, turberas* in Spanish speaking countries (KANDUS et al., 2017; NEIFF; IRIONDO; CARIGNAN, 1994). In the first publications on South American wetlands, they were generally called as floodplains (HAMILTON; SIPPEL; MELACK, 2002; JUNK et al., 1993). Here, I understand floodplains as those riparian wetlands that are directly affected by the rivers' flood pulse.

During the last decades, important contributions to the understanding and conservation of wetlands were developed under the Ramsar convention, and initiatives by the Wetlands International, IUCN (International Union for the Conservation of Nature and Natural Resources), and other organizations as The Natural Conservancy (TNC) and Worldwide Fund for Nature (WFF) (JUNK et al., 2013). Countries committed to the Ramsar convention should follow the three following pillars: (i) work toward the wise use of wetlands, (ii) designate suitable wetlands for the list of wetlands of international importance and ensure their effective management, and (iii) cooperate internationally on transboundary wetlands, shared wetland systems and shared species (Ramsar convention, https://www.ramsar.org).

To foster the conservation, management and comprehension of wetlands, classification schemes and wetlands inventories (i.e. defining location, the ecosystem type, flood dynamics, extent and storage, ecosystem services, etc.) are required (DAVIDSON, 2018). Such classifications should take into consideration the links between landscape (geomorphological) setting, water sources (precipitation, surface waters, groundwater) and hydrodynamics (vertical and horizontal water movement), as proposed by BRINSON (1993) in his hydrogeomorphic classification scheme for wetlands. Many recent studies have developed the first South American inventories in Argentina (BENZAQUEN et al., 2017; KANDUS; MINOTTI; MALVÁREZ, 2008; NEIFF, 2001), Brazil (JUNK et al., 2014; MALTCHIK et al., 2018) and Colombia (FLÓREZ et al., 2016; QUINONES et al., 2015; RICAURTE et al., 2012, 2017). Figure

3.1 presents national scale wetland maps developed by these authors. Thus, there is still a need of improving classification of wetlands and inventories (JUNK et al., 2013; KANDUS et al., 2018). Specifically, current research efforts focus much more on ecology than hydrology, and although local, detailed studies are definitely fundamental, a continental/regional scale understanding of these wetlands is also fundamental, which is the focus of this thesis.

The Brazilian INCT-INAU has recently proposed a classification for Brazilian wetlands, which is presented in Figure 3.2 (JUNK et al., 2014), and is interesting for explicitly considering hydrological factors. The first criterion is based on the wetland system (coastal, inland or artificial), and the second on hydrological features (i.e. flood pulse characteristics). Most Brazilian wetlands belong to the "wetlands with fluctuating water level" class, presenting either a high (e.g., large river floodplains as the Amazon one) or a low monomodal and predictable water level amplitude (e.g., Llanos de Moxos and other interfluvial wetlands). The small river floodplains are defined as wetlands with polymodal and unpredictable water level amplitude. The third criterion is based on the concept of macrohabitats, and would be refined together with research advances. This last criterion is particularly complex to be delineated due to difficulties in mapping specific vegetation types with remote sensing techniques.

Colombia
(Ricaurte et al., 2017)

Argentina
(Kandus et al., 2017)

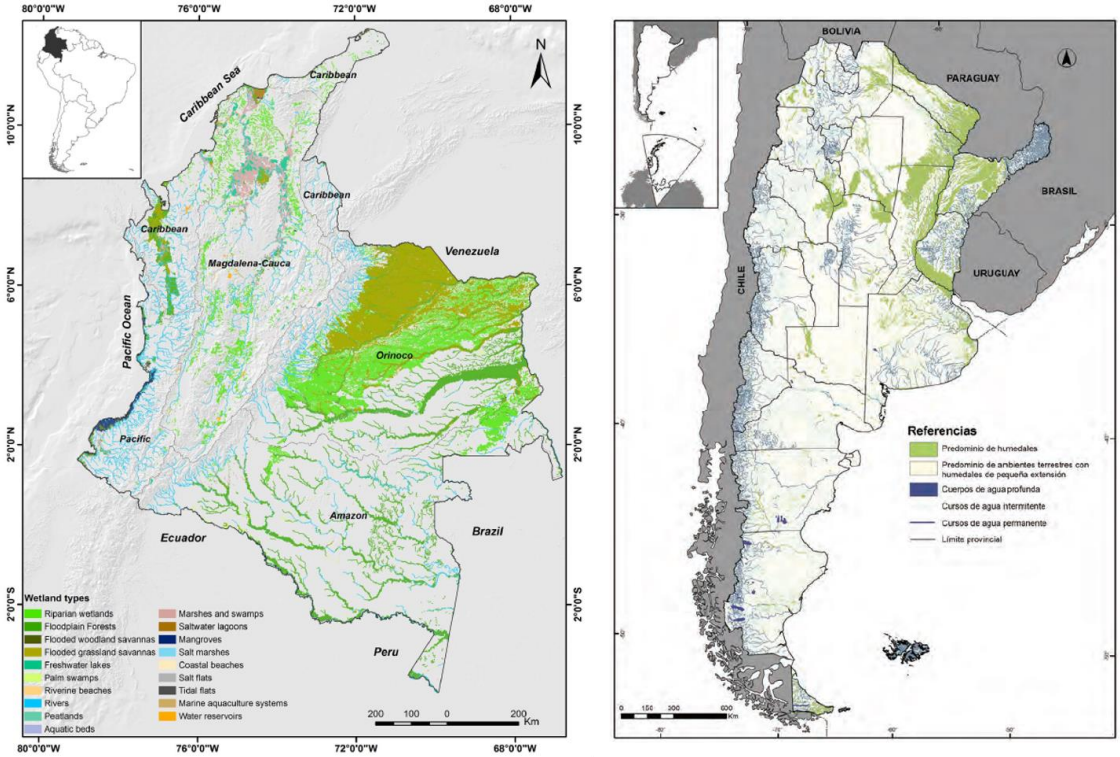

Brazil
(Junk et al., 2014)

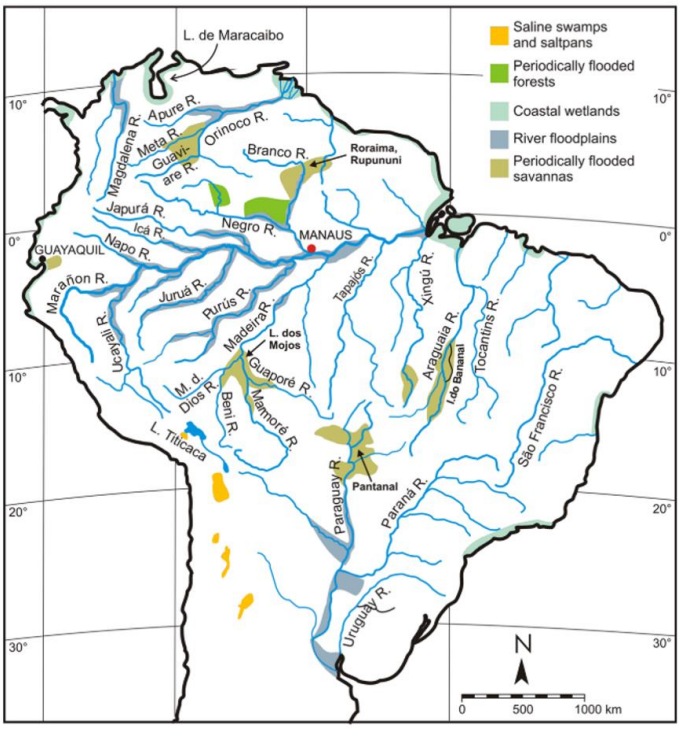

Figure 3.1. National scale wetlands maps for Colombia (RICAURTE et al., 2017), Argentina (KANDUS et al., 2017) and Brazil (JUNK et al., 2014).

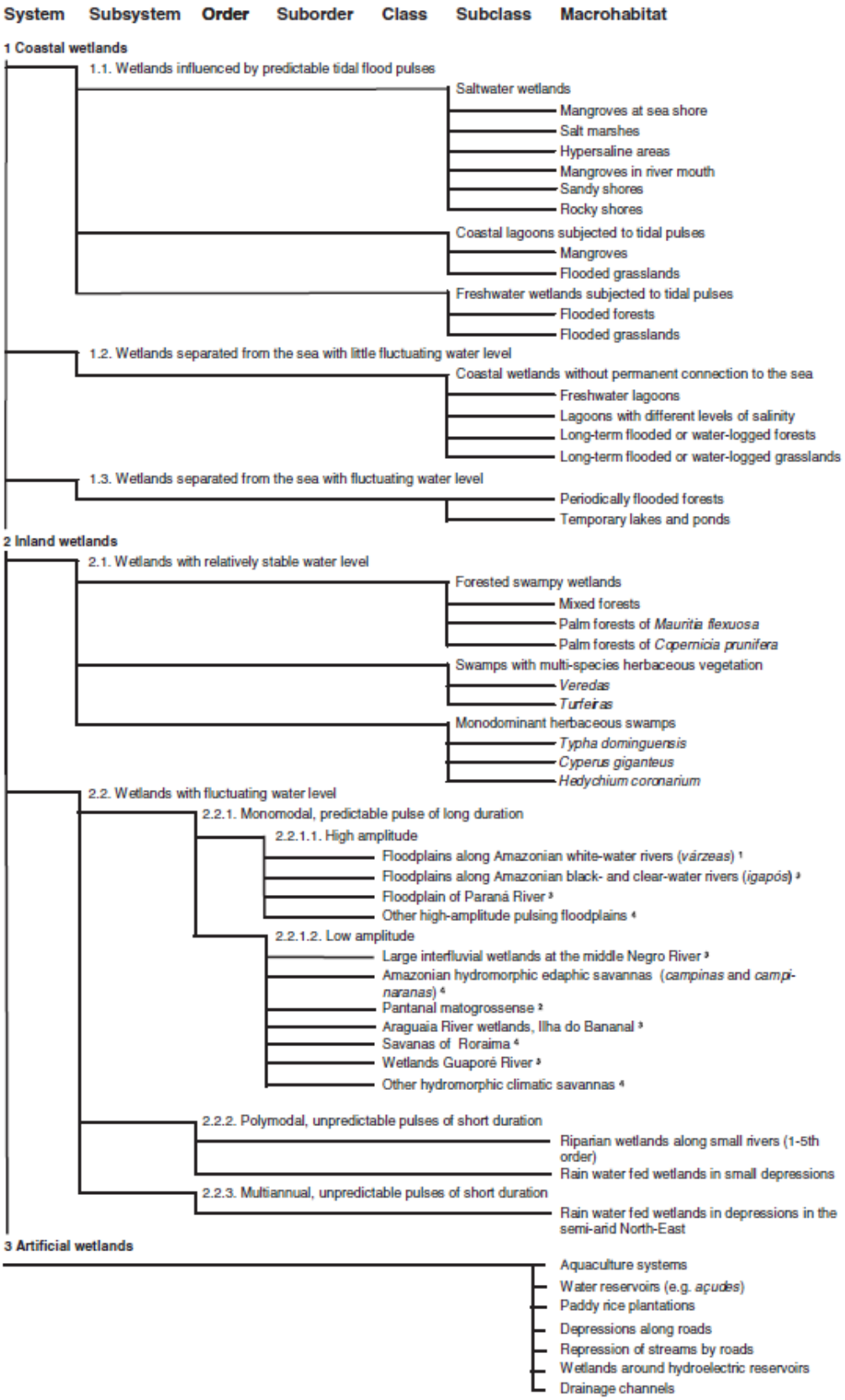

Figure 3.2. Classification of Brazilian wetlands as proposed by JUNK et al. (2014).

3.2 The large South American wetlands

South America has been described as the "fluvial continent" (KANDUS et al., 2018), where the most known wetlands are the riparian ones (i.e. river floodplains) – in turn, the quantity of lakes is relatively small (NEIFF; IRIONDO; CARIGNAN, 1994). The total wetland area is estimated to be higher than the global average, covering about 20% of the continent territory, and about one-fourth of all freshwater inputs into oceans come from the continent (JUNK, 2013). Other wetland extent estimates suggest that they represent 5-12% of the continent area (FLUET-CHOUINARD et al., 2015; REIS et al., 2018). The continent covers a large variety of climate and geological settings, with precipitation rates varying from tens of millimeters per year in the Atacama Desert to more than 5000 mm in the Andes, and altitudes ranging from the continent lowlands to the high Andean mountains (JUNK, 2013). Besides the large river floodplains, which include the vast Amazon, Paraná and Paraguai rivers, other different types of wetlands do exist and are poorly understood, as the interfuvial wetlands in the Negro River Basin and Llanos de Moxos regions. These areas are mainly formed by local rainfall and high water table levels, and consist of thousands of square kilometers seasonally flooded. Some wetlands are associated to large sedimentary basins (e.g., Bananal Island), while others are proposed to have been formed during neotectonic events (e.g., the Negro floodable savannas) (ROSSETTI et al., 2012, 2017a). A recently proposed classification of the Brazilian wetlands (which cover a large portion of South America) by JUNK et al. (2014), based on a previous classification of Amazon lowland wetlands (JUNK et al., 2011), was presented in Figure 3.1 and Figure 3.2, and provides an interesting comprehension of these wetlands hydrological functioning by classifying them in terms of the flood pulse water level amplitude (high for large river floodplains; low for interfluvial wetlands). In a simpler way, the pioneer studies by NEIFF et al. (1994) and JUNK et al. (1993) classified the large South American wetlands into two classes: floodplains (alluvial terrains) and "water-logged wetlands" or "floodplains in poorly drained areas" (i.e., interfluvial wetlands).

Under the Ramsar convention, a total of 104 sites of international importance were selected in the inland South America, as presented in Figure 3.3 (see Table 13.1 in Appendix 13.1 for details). These sites are selected under criteria related to the uniqueness and representativeness of the wetland type within its biogeographic region, and to its importance for biodiversity conservation (e.g., for vulnerable species and ecological communities, waterbirds, fish or other animal species) (Ramsar Convention, https://www.ramsar.org). Most of the large wetlands studied in this thesis have some parts of their areas designated as Ramsar sites (see list below).

The large wetlands of the continent that are studied in this thesis are listed below (see Figure 3.3), with the related Ramsar sites listed in parentheses – only the Pampas and Roraima savannas do not have Ramsar sites associated:

a) **Central Amazon floodplains** (Ramsar sites: “Rio Negro”, “Anavilhanas National Park”, “Mamirauá”, “Rio Juruá”, “Complejo de humedales Lagos de Tarapoto”;
b) **Negro savannas** (“Viruá National Park”);
c) **Roraima savannas**;
d) **Llanos de Moxos** (“Río Yata”, “Guaporé Biological Reserve”, “Río Blanco”, “Río Matos”)
e) **Pacaya-Samiria** (“Reserva Nacional Pacaya-Samiria”, “Complejo de humedales del Abanico del río Pastaza”);
f) **Bananal Island** (“Ilha do Bananal”);
g) **Llanos del Orinoco** (“Complejo de humedales de la Estrella Fluvial Inírida”);
h) **Pantanal** (“Reserva Particular do Patrimonio Natural SESC Pantanal”, “Taiamã Ecological Station”, “Pantanal Matogrossense”, “El Pantanal Boliviano”, “Reserva Particular del Patrimonio Natural Fazenda Rio Negro”, “Río Negro”);
i) **Paraná River floodplains** (“Jaaukanigás”, “Delta del Paraná”);
j) **Esteros del Iberá** (“Lagunas y Esteros del Iberá”);
k) **Magdalena – Depresión Momposina** (“Sistema Delta Estuarino del Rio Magdalena, Ciénaga Grande de Santa Maria”);
l) **Pampas;**
m) **Chaco Húmedo** (“Rio Pilcomayo”, “Tifunque”)**.**

Finally, it must be stressed that while these are the large wetland complexes addressed in this thesis, other floodable areas are also assessed, which were chosen according to criteria such as relevance for flood risk analyses. These additional areas include basin, regional and continental-scale assessments, and were performed for the whole Negro River basin (Chapter 4), Amazon River basin (Chapters 5 and 6), South American rivers (Chapter 9), Itajaí-Açu River basin (Chapter 10) and upper Paraná River basin (Chapter 11).

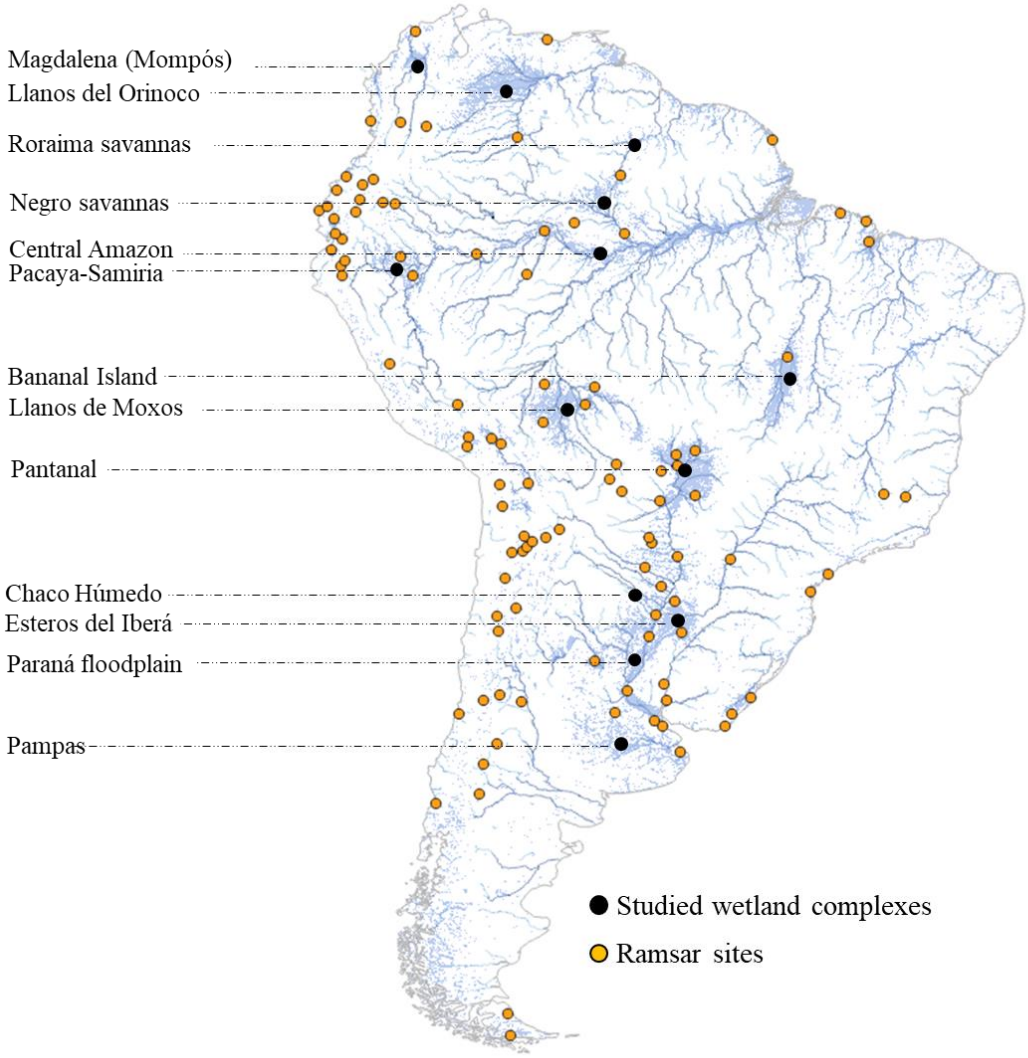

Figure 3.3. Location of the large wetland complexes studied in this thesis, which are named on the left, and the 104 South American Ramsar sites of international importance (continental area only).

3.3 Wetland ecosystem services, society and environmental changes in South America

The role of wetlands on human well-being was investigated within the Millenium Ecosystem Assessment initiative (MEA, 2005). Society directly and indirectly affects ecosystem services, which in turn impacts human well-being and poverty reduction, and so on. Wetlands ecosystem services derive from wetland specific functions, and vary from provisioning food, freshwater, chemical and other products to regulating floods, climate and water quality, promoting cultural aspects as spiritual and recreational activities, and supporting habitats and nutrient cycling (Figure 3.4). Their soils can accumulate huge amounts of carbon, while large methane emissions may occur

in oxygen limited environments, leading wetlands to play a major role in the global methane budget (MELTON et al., 2013; SAUNOIS et al., 2020; ZHANG et al., 2017b). While wetlands are estimated to cover only 0.8% of the Earth surface, they provide habitats for around 10% of the globally known animal species (BALIAN et al., 2008; WWF, 2016).

Regarding hydrology-related services, wetlands may attenuate floods (especially river floodplains, while headwater wetlands may even increase floods; ACREMAN; HOLDEN, (2013)), maintain flow during dry periods, trap sediments, and remove water pollutants (MEA, 2005). From low discharges to high flow periods, floods are fundamental for the maintenance of ecosystems (Figure 3.5). Flood pulses maintain wetland ecosystems productivity and diversity through sediments, nutrient and biological fluxes, and by promoting flood-adapted species. The whole ecosystem adapts to the pulse regime and the wetland characteristics. In the Amazon, flood-tolerant trees develop different adaptation measures to cope with the varying wetland types, e.g., large and heavy seeds in the nutrient-poor Igapós wetlands, which become a local nutrient source, in contrast to smaller seeds in the nutrient-rich Várzeas, being more subjected to seed dispersion through buoyancy or fish transport (WITTMANN; HOUSEHOLDER, 2017). In South America, wetlands harbor a large biodiversity, where more than 3000 (1000) fish species were described in Amazon (Orinoco) river basins (JUNK, 2013), and more than 1000 flood-tolerant tree species in the Amazon River floodplain (WITTMAN et al. (2010) *apud* JUNK, (2013)).

Besides general ecosystem services, local societies are largely adapted to the wetlands flood dynamics. In riparian wetlands, society uses water for domestic use, renewable wetland products, bathing, and other benefits (JUNK, 2013). Many societies have evolved along the Amazon wetlands through the centuries since pre-Columbian periods (BLATRIX et al., 2018; DENEVAN, 1996; JUNK et al., 2013). Today, many indigenous societies and riparian communities live within floodplains and adapt to the flood pulse dynamics, managing the system in a traditional way (JUNK et al., 2013). Flood recession agriculture is performed in many Amazon floodplains, as shown by COOMES et al. (2016) for rice crops in river mud bars near Iquitos (Peru). Fishery production is estimated at 900,000 t/year in the Amazon floodplain (Bayley and Petrere (1989) *apud* JUNK et al., (2013)). In the Lower Paraná River floodplains, "Ganadería de islas" (cattle ranching in islands) is performed by local communities, together with other subsistence activities as hunting, fishing and beekeeping (BÓ; QUINTANA, 2017). With the increasing in ecotourism activities, local people have also changed their traditional subsistence activities towards the tourism related ones, as in the Pantanal and Esteros del Iberá wetlands. Local communities have to adapt to changes in the wetland landscape, which may present sharp multi-year alterations. For example, the Bañado La Estrella in the Argentinian Chaco region has been largely developed since the 1960's due to sediment accumulation in the Pilcomayo River and the associated overbank flows that annually flood huge areas (BROWN et al., 2016). Local traditional communities and new settlers have adapted to hunting and fishing activities in this

newly formed wetland. The recent floods in the Pacaya-Samiria region in the upper Amazon river have altered the activities of local communities, moving from hunting to a more fishing-dependent livelihood (BODMER et al., 2018). On the other hand, urban areas located within river floodplains are under flood risk and may suffer from periodic flooding, as many cities along Orinoco and Magdalena rivers in Colombia, Santa Fe in the Paraná River, or Itajaí and Blumenau cities in the Itajaí River in Brazil (LATRUBESSE; BREA, 2009; RICAURTE et al., 2017; TUCCI; BERTONI, 2003), for which a proper floodplain management is required. In turn, in interfluvial areas and floodable savannas as the Marajó Island and parts of the Pantanal wetlands, flooded grasslands with high productivity are used for livestock grazing (JUNK et al., 2013). Cattle production is adapted to the Pantanal hydrological regime and its lowland native grasslands. In some cases the movement of herds follows a nomadic pattern, looking for recently flooded grasslands, while normal dry periods are benefic for the herds for exposing grassland areas (ARAUJO et al., 2018).

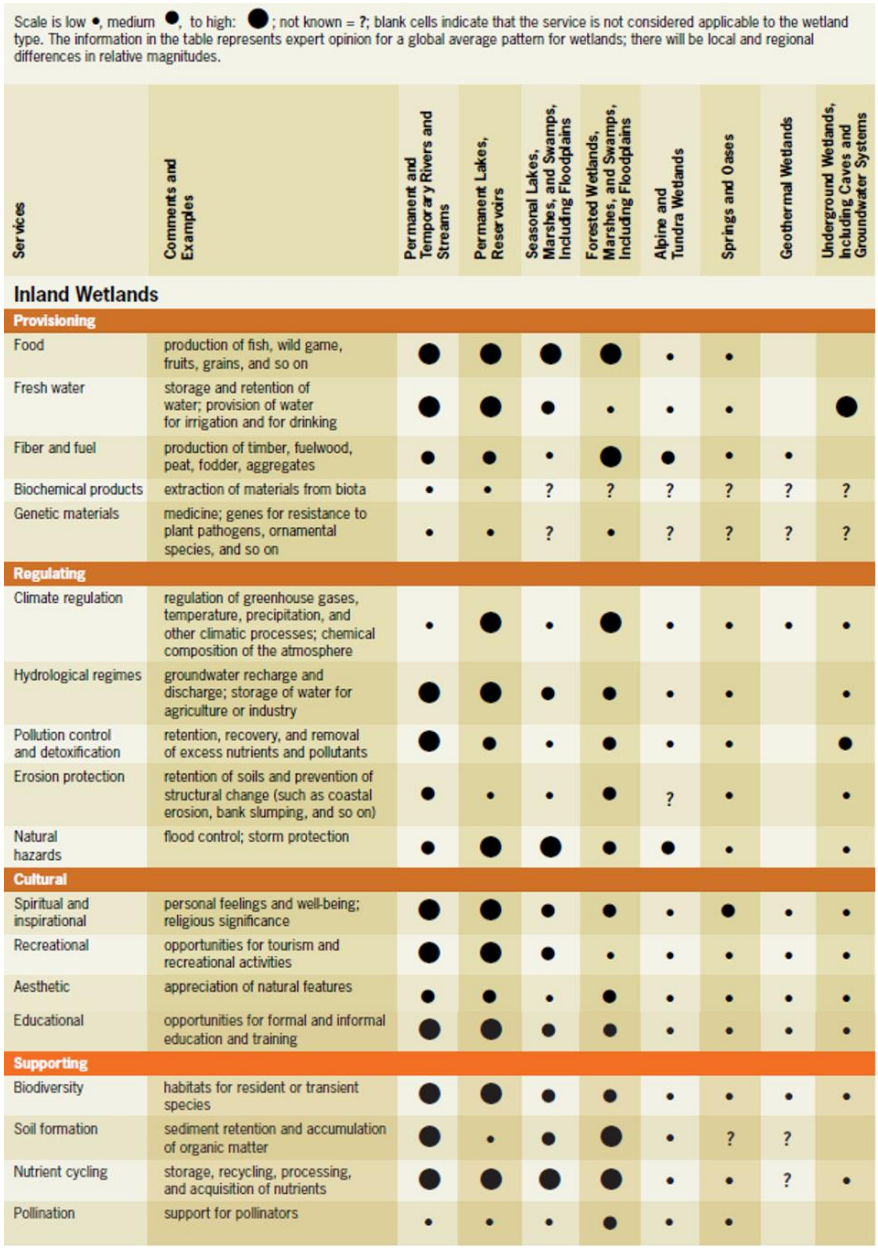

Scale is low •, medium ●, to high: ⬤; not known = ?; blank cells indicate that the service is not considered applicable to the wetland type. The information in the table represents expert opinion for a global average pattern for wetlands; there will be local and regional differences in relative magnitudes.

Services	Comments and Examples	Permanent and Temporary Rivers and Streams	Permanent Lakes, Reservoirs	Seasonal Lakes, Marshes, and Swamps, Including Floodplains	Forested Wetlands, Marshes, and Swamps, Including Floodplains	Alpine and Tundra Wetlands	Springs and Oases	Geothermal Wetlands	Underground Wetlands, Including Caves and Groundwater Systems
Inland Wetlands									
Provisioning									
Food	production of fish, wild game, fruits, grains, and so on	⬤	⬤	⬤	⬤	•	•		
Fresh water	storage and retention of water; provision of water for irrigation and for drinking	⬤	⬤	●	•	•	•		⬤
Fiber and fuel	production of timber, fuelwood, peat, fodder, aggregates	●	●	•	⬤	●	•	•	
Biochemical products	extraction of materials from biota	•	•	?	?	?	?	?	?
Genetic materials	medicine; genes for resistance to plant pathogens, ornamental species, and so on	•	•	?	•	?	?	?	?
Regulating									
Climate regulation	regulation of greenhouse gases, temperature, precipitation, and other climatic processes; chemical composition of the atmosphere	•	⬤	•	⬤	•	•	•	•
Hydrological regimes	groundwater recharge and discharge; storage of water for agriculture or industry	⬤	⬤	●	●	•	•		•
Pollution control and detoxification	retention, recovery, and removal of excess nutrients and pollutants	⬤	●	•	●	•	•		⬤
Erosion protection	retention of soils and prevention of structural change (such as coastal erosion, bank slumping, and so on)	●	•	•	●	?	•		•
Natural hazards	flood control; storm protection	●	⬤	⬤	●	●	•		•
Cultural									
Spiritual and inspirational	personal feelings and well-being; religious significance	⬤	⬤	●	●	•	⬤	•	•
Recreational	opportunities for tourism and recreational activities	⬤	⬤	●	•	•	•	•	•
Aesthetic	appreciation of natural features	●	●	•	●	•	•	•	•
Educational	opportunities for formal and informal education and training	⬤	⬤	●	●	•	•	•	•
Supporting									
Biodiversity	habitats for resident or transient species	⬤	⬤	●	●	•	•	•	•
Soil formation	sediment retention and accumulation of organic matter	⬤	•	●	⬤	•	?	?	
Nutrient cycling	storage, recycling, processing, and acquisition of nutrients	⬤	⬤	⬤	⬤	•	•	?	•
Pollination	support for pollinators	•	•	•	●	•	•		

Figure 3.4. Relative magnitude of ecosystem services derived from different types of wetland ecosystems. Source: MEA (2005).

Flow Component	Ecological Role
Low (base) flows *Normal level:*	provide adequate habitat space for aquatic organisms maintain suitable water temperatures, dissolved oxygen, and other chemical conditions, including salinity maintain water table levels in floodplain and plant soil moisture provide drinking water for terrestrial animals keep fish and amphibian eggs suspended enable passage of fish to feeding and spawning areas support hyporheic organisms (living in saturated sediments)
Low (base) flows *Drought level:*	enable recruitment of certain floodplain plants purge invasive, introduced species from aquatic and riparian communities concentrate prey into limited areas to the benefit of predators
Higher flows (small flood pulses)	shape physical character of river channel, including availability and heterogeneity of different biotopes (such as riffles, pools) and microhabitats restore normal water quality after prolonged low flows, flushing away waste products, pollutants, and proliferations of nuisance algae maintain suitable salinity conditions in estuaries prevent encroachment of riparian vegetation into the channel aerate eggs in spawning gravels, prevent siltation of cobble interstices determine size of river bed substrata (sand, gravel, cobble, boulder)
Large floods	provide fish migration and spawning cues provide new feeding opportunities for fish and waterbirds recharge floodplain water table maintain diversity in floodplain forest types through prolonged inundation (plant species have differing tolerances for flooding) and their natural regeneration processes control distribution and abundance of plants on floodplain trigger new phases of life cycles (such as insects) enable fish to spawn on floodplain, provide nursery area for juvenile fish deposit nutrients on floodplain maintain balance of species in aquatic and riparian communities create sites for recruitment of colonizing plants shape physical character and habitats of river channels and floodplain deposit substrata (gravel, cobble) in spawning areas flush organic materials (food) and woody debris (habitat structures) into channel purge invasive, introduced species from aquatic and riparian communities disburse seeds and fruits of riparian plants drive lateral movement of river channel, forming new habitats (secondary channels, oxbow lakes) provide plant seedlings with prolonged access to soil moisture drive floodplain productivity

Figure 3.5. Hydrological-ecological relationships in wetlands according to flow components (high and low waters). Source: MEA (2005).

Around 18% of South American wetland areas are estimated to be under protected areas (i.e. Ramsar sites or IUCN management categories I-VI) (REIS et al., 2018), and many wetlands are still pristine in the continent. These areas should be managed in terms of a sustainable management strategy (as the "wise use of wetlands" proposed by the Ramsar convention). Their management should be carried out at the basin scale, posing a great challenge for transboundary wetlands, which comprise most of the areas studied in this thesis. One interesting example was presented by the Wetlands International initiative set in 2018 called the "Corredor Azul" Programme (WETLANDS INTERNATIONAL, 2018), which is a 10-years project for sustainable management of the large La Plata basin wetlands: Pantanal, Esteros del Iberá and Paraná Delta (which cover many Ramsar sites). The large scale dimension of the La Plata basin makes its southward flowing large rivers to contribute species from the tropical and subtropical upstream wetlands to the temperate wetlands in the downstream reaches (BRINSON; MALVÁREZ, 2002). The project has an overall goal to preserve the ecosystem integrity and wetlands connectivity in the Paraná-Paraguay system, through varied actions, from the development of new public policies to research production and training of stakeholders. This highlights the importance of continental

scale studies as the performed in this thesis for understanding and monitoring large, transboundary wetlands.

Furthermore, national scale assessments on wetlands' ecosystem services are also required. For example, after the harmful 2010-2011 Colombian floods, initiatives related to understanding national scale ecosystem services were carried out, as the one presented by RICAURTE et al. (2017). A participatory process gathered dozens of wetland experts to define major ecosystem services and drivers of changes on the country's wetlands in the near future (2025). The study suggested that water supply (followed by water regulation and habitat for species) is the main ecosystem service of Colombian wetlands, while mining, followed by agriculture and water infrastructure (e.g., the many dams presented in Magdalena River) is the main driver of changes on the wetlands services. The greatest increase in future is expected for cattle ranching followed by urban development and roads.

Continental scale wetland losses and vulnerabilities need to be better understood as well. The effects of anthropogenic pressure on wetlands depend on the wetland hydrological functioning. Wetlands that are more river dependent will be more affected by upstream dams, while interfluvial wetlands which respond more to rainfall tend to be more sensitive to local climate changes (REIS et al., 2019b). A major concern has been raised on the plans of damming many important river systems as the Amazon (LATRUBESSE et al., 2017a), with implications for flow connectivity, sediment dynamics and other processes. Most proposed dams are being designed for hydropower generation, and many rivers with important wetlands are already dammed in South America, as the Paraná and Magdalena rivers (JUNK et al., 2013). Besides, the effects of rapid, short-term (e.g., at hourly scale) fluctuations in river water levels and discharges due to hydropower releases (hydropeaking) on wetland ecosystems have been increasingly studied (ALMEIDA et al., 2020; BEJARANO; JANSSON; NILSSON, 2018).

In many areas, wetland degradation has been occurring due to beef production and food for domestic animals (i.e. soy beans), associated with the expansion of agriculture and deforestation. Erosion in agricultural lands is associated to increases in sediment loads into wetlands (e.g., in Pantanal wetland; JUNK et al., (2013)). Cattle ranchers own 90% of Pantanal land, and while traditional cattle ranching methods assist preserving the local macrohabitats, a shift to large-scale intensive cattle production may be harmful (JUNK et al., 2018). In Argentina, extensive soy bean production areas are located within wetland environments (ANDELMAN et al., 2018).

Finally, climate change will affect inland wetlands hydrology by altering precipitation and temperature (ERWIN, 2009), and through impacts of sea level changes on river basins' lowlands. Higher CO_2 concentrations, salinity intrusion and more frequent droughts and floods will also affect wetland ecosystems (MOOMAW et al., 2018), which have a great dependence on climate factors (e.g., the large 1983 floods related to ENSO-El Niño; LATRUBESSE; BREA, (2009)). The extent to which climate

change will increase wetland releases of GHGs (CO_2, CH_4, N_2O) through alteration of flood duration and decomposition of wetland soil carbon, for instance, is still unknown. Climate change studies usually couple global or regional climate models predictions with hydrological models to estimate effects on wetlands. However, models still diverge in terms of impacts on large South American wetlands (MONTROULL et al., 2013; SORRIBAS et al., 2016). Recent regional climate change assessments include studies the Esteros del Iberá wetlands (MONTROULL et al., 2013) and the Amazon central floodplains (SORRIBAS et al., 2016). Global assessments suggest that most South American wetlands will face a decreasing water availability under climate change (XI et al., 2020)

3.4 River floodplains and society: the flood hazard component of the human-wetland interaction

While human societies have settled near to rivers for millennia and largely benefited from floodplain soil fertility, water and food provision, an increasing trend of global human exposure to floods has highlighted the hazard component of the human-water interactions along wetlands (BATES et al., 2014; MAZZOLENI et al., 2021). This needs to be better assessed in South America with current capabilities of remote sensing and flood modeling. In Brazil, for instance, substantial understanding of flooding regimes in large natural wetlands, as in the Amazon and Pantanal regions, has been promoted through remote sensing (RS) and river flood modeling (FLEISCHMANN et al., 2021). However, less research attention has been given to the floods with socioeconomic impacts. Around 11 million people were affected by floods between 1970 and 2019 in Brazil (CRED, 2019) and, in general, flood risk has been increasing over the continent (VÖRÖSMARTY et al., 2013) besides other growing water management issues.

Many South American riverside cities are under high flood risk and in need of information to improve management practices. Deriving adequate flood risk information requires accurate hazard mapping for the impact analysis. A flood early warning system is one possible strategy of risk mitigation, as communicating forecasts enables actions to prevent the loss of life and property. Another important benefit of an early warning system is that its development fosters production of risk maps and forecasting tools. Recent developments in South America that can be beneficial to flood mitigation include flood hazard mapping and real-time flood monitoring and forecasting initiatives, from global (e.g., Global Flood Partnership; TRIGG et al. (2016)) to local scales. Figure 3.6 shows two examples of ongoing Alert Systems in Brazil, for the Rio Grande do Sul State and Madeira River Basin. The use of remote sensing-based monitoring can also largely improve flood management in South America, especially if used in combination with river flood models. This includes the provision of surface water extent climatology (AIRES et al., 2018; FLUET-CHOUINARD et al., 2015;

JENSEN; MCDONALD, 2019) and operational mapping products for emergency response. For instance, satellite altimetry water levels have been used in Brazil for operational gap filling and series updating, as well as monitoring of ungauged reaches in transboundary basins (DA SILVA et al., 2014). One example is the Madeira River in the Amazon (Figure 3.6) (SEYLER et al., 2009a), which receives water from Bolivia and Peru, so that the current alert system misses important data monitoring. Near real-time discharge monitoring using altimetry-modeled discharge rating curves as proposed by PARIS et al. (2016) is very promising in such cases.

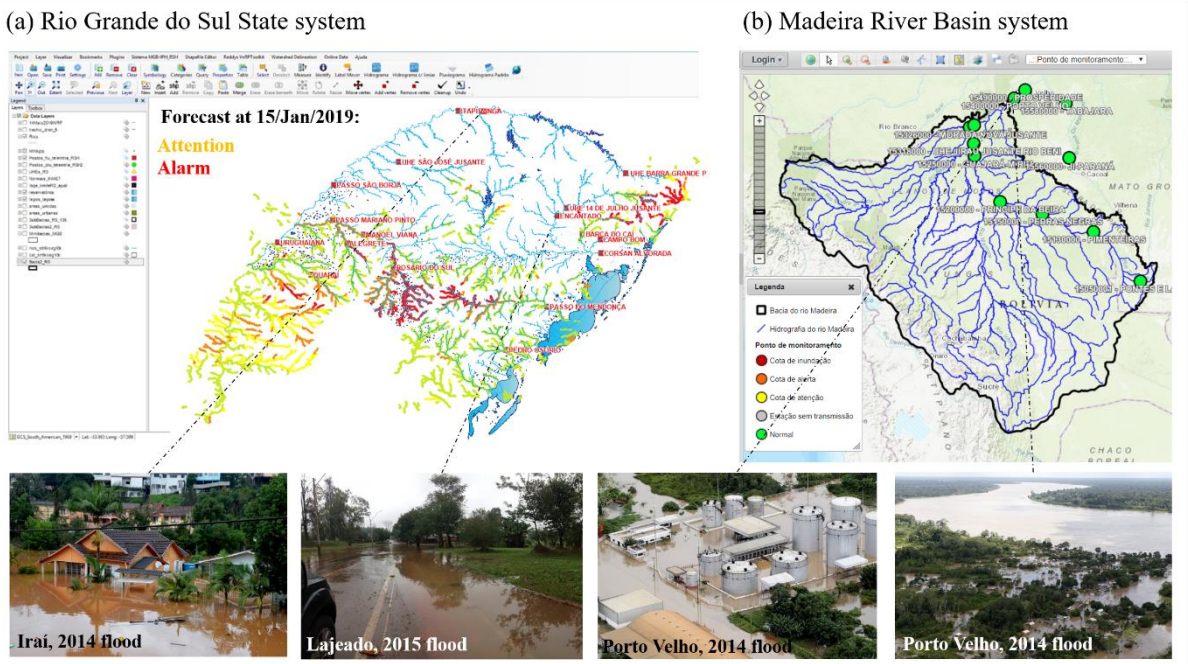

Figure 3.6. Real-time flood monitoring and forecasting systems for (a) the Rio Grande do Sul state and (b) the Madeira River Basin, which is one of the 16 currently available systems from the Geological Survey of Brazil (SACE/CPRM). Source: FLEISCHMANN et al. (2021).

3.5 Available tools to study the hydrology of wetlands and floods

Three main tools to understand wetlands can be defined:

- In situ measurements;
- Mathematical modeling;
- Remote sensing datasets.

In situ data and field campaigns are fundamental to promote a proper understanding of local processes, but the dimension and remoteness of many wetlands makes it a very tough task to be performed. Then, recent technological and computational developments have allowed the creation of many remote sensing-based datasets, which may be used to estimate the most different variables, from hydrodynamic (water levels, discharge, flood extent and storage) to hydrological ones (rainfall, evapotranspiration, local runoff, soil moisture). Additionally, hydrological and hydrodynamic mathematical models have proved very interesting for understanding the functioning of wetlands, especially at regional/continental scales. The integration of all these methods creates new opportunities to tackle the topic of hydrology of the South American wetlands and floods, and will be addressed in the following sections. Especially, given the high uncertainty that exists in most mapping methods, using as many different methods as possible allows one to understand these errors and uncertainties, and to improve these estimates.

3.5.1 Large scale hydrologic-hydrodynamic modeling

Large scale hydrological models are powerful tools to understand alternative scenarios of the area of interest, as the effects of climate and land use and cover changes, to perform hydrological forecasts, to understand processes (e.g., quantifying water balance components or the relative role of wetlands and other processes on flood attenuation), and to estimate variables at ungauged sites. The modeling process involves five main steps, according to BEVEN (2012): (i) the perceptual model, where the main occurring hydrological processes are studied (through the modeler understanding and perception); (ii) the conceptual model, where the equations to be used are chosen; (iii) the procedural model, in which the model code is implemented; (iv) model calibration; and (v) model validation. In the context of wetlands, all these steps are challenging. Particularly, current models have been improving the representation of the main processes that occur in floodable areas, aiming at more physically-based approaches (ANDERSSON et al., 2017; FLEISCHMANN et al., 2018; HOCH et al., 2017a; PAZ et al., 2011; YAMAZAKI et al., 2014b), and considering the recent advances in remote sensing and computational capacity, which allow improvements towards higher

resolution models and better model calibration and validation (e.g. with remote sensing-based water levels and flood extent estimates) (BATES et al., 2018a).

For simulation of wetlands and inundation processes, there has been a growing number of the so-called hydrologic-hydrodynamic models, which typically distinguish between hydrologic (the rainfall-runoff module) and hydrodynamic processes (river/floodplain routing module). While most large scale model applications perform an offline coupling by forcing a hydrodynamic model with outputs from a separate rainfall-runoff model, recent developments have also focused on simulating the coupling processes that exist between them (e.g., infiltration from floodplain water into the adjacent soil) (DA PAZ et al., 2014; FLEISCHMANN et al., 2018; HOCH et al., 2017a). Figure 3.7 presents an example of a process-based model (MGB), which simulates both hydrological (evapotranspiration, precipitation infiltration into soil, surface, subsurface and groundwater flows) and hydrodynamic processes (backwater effects, floodplain storage, flood wave diffusion), and which will be used in this thesis.

A very important aspect of these models refer to the flood propagation method, which varies in complexity from simpler 1D with floodplain storage methods (GETIRANA et al., 2017a; PAIVA et al., 2013a; YAMAZAKI; DE ALMEIDA; BATES, 2013) towards 2D models that represent the complex flow patterns across floodplains (NEAL; SCHUMANN; BATES, 2012; SCHUMANN et al., 2016a; TRIGG et al., 2009; WILSON et al., 2007). Figure 3.8 summarizes the main conceptual frameworks used in hydrodynamic models. For river floodplains, 1D models are often used by adopting either a floodplain storage unit (Figure 3.8a) or an active floodplain (Figure 3.8b), while for more complex wetlands (e.g., the Pantanal with multiple channels, distributaries and floodplain fluxes), simple models representing the wetlands as reservoir units (interconnected or not) with simplified water balance are sometimes used (FERRATI; CANZIANI, 2005). The more sophisticated 2D routing methods (Figure 3.8d) have been recently developed and provide a more physically based approach (NEAL; SCHUMANN; BATES, 2012; PAZ et al., 2010).

Regarding the scale of application, hydrologic-hydrodynamic models vary from reach (i.e. a few to hundreds of kilometers) (TRIGG et al., 2009; WILSON et al., 2007) to regional (NEAL; SCHUMANN; BATES, 2012; PAIVA et al., 2013a; PONTES et al., 2017; SCHUMANN et al., 2016a, 2013) and continental scales (BIERKENS et al., 2015; DOTTORI et al., 2016; HODGES, 2013; SAMPSON et al., 2015; SIQUEIRA et al., 2018; WOOD et al., 2011; YAMAZAKI et al., 2011, 2014b). The recently developed continental scale models present an unprecedented opportunity to study the South American wetlands. Cross-scale (FLEISCHMANN; PAIVA; COLLISCHONN, 2019) and multimodel comparisons (BERNHOFEN et al., 2018; HOCH; TRIGG, 2018; TRIGG et al., 2016) have been performed to evaluate the capacity of these continental models to infer variables at local scales. Particularly, SIQUEIRA et al., (2018) developed an MGB application for the whole continent. Figure 3.9 presents the model domain (i.e. the grey drainage network), the in situ discharge gauges used for model calibration and validation and the model performance for these stations.

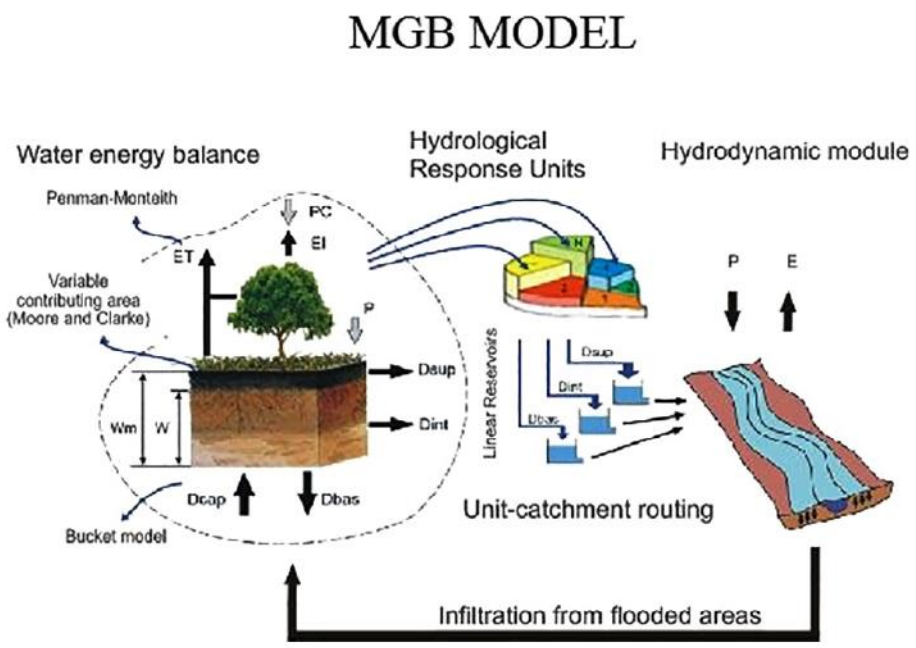

Figure 3.7. MGB model structure, describing the main simulated hydrological processes: evapotranspiration, precipitation infiltration into soil, surface, subsurface and groundwater flows, and flow routing within a unit-catchment and along the river network (i.e. the hydrodynamic module). Source: FLEISCHMANN et al. (2018).

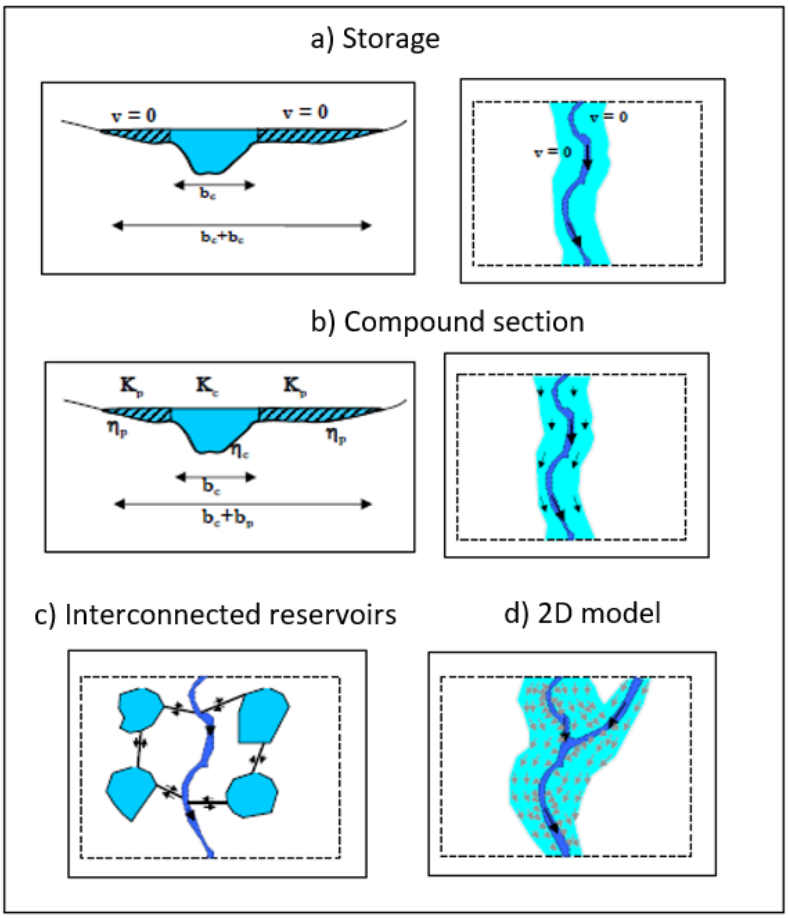

Figure 3.8. The most common types of wetland hydrodynamic simulation: (a) river floodplains considered as storage units or (b) with compound sections; (c) wetlands considered as interconnected reservoirs; and (d) 2D modeling. Source: adapted from PAIVA (2009) and PAZ (2010).

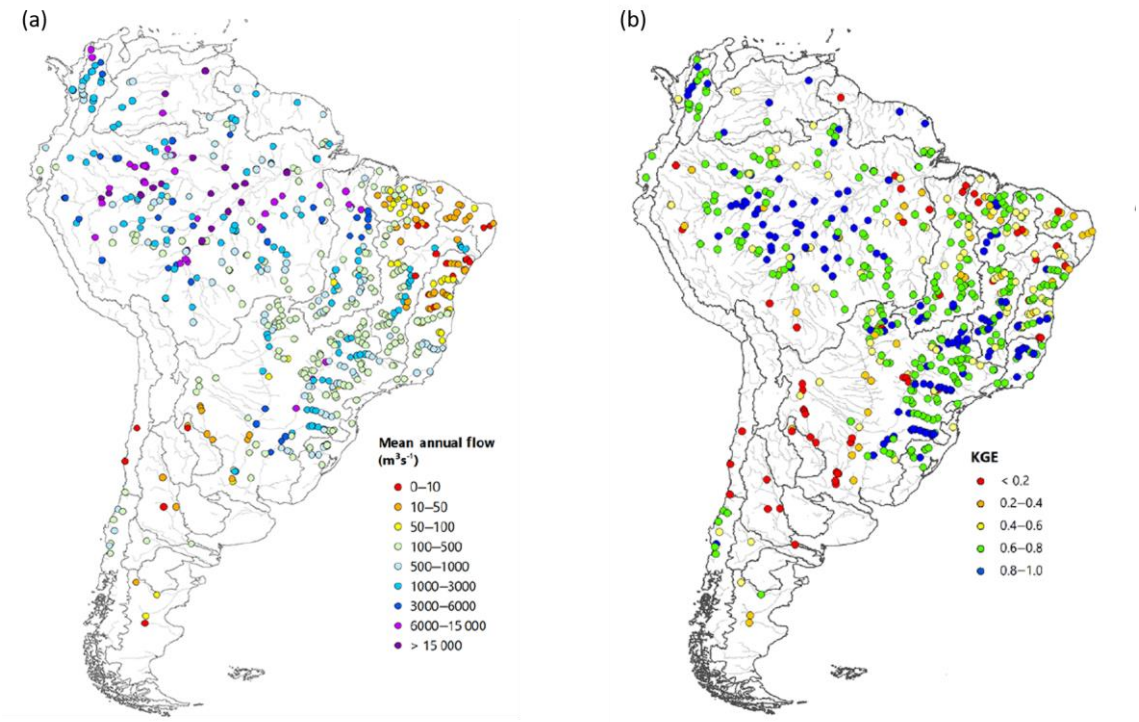

Figure 3.9. Summary of the main discharge gauges used for the MGB South American model setup. (a) Mean annual flow and (b) KGE model performance metric for each gauge. Source: adapted from SIQUEIRA et al. (2018).

3.5.2 Remote sensing

Remote sensing refers to the collection of data about an object from a distance (PIDWIRNY, 2010). The techniques are based on the emitted or reflected energy from targets on land surface, which is measured by sensors on balloons, shuttles or satellites. Recent advances have allowed the creation of a large set of databases useful for mapping wetlands and inundation, and allowing the quantification of hydrological fluxes and processes (ALSDORF et al., 2007; ALSDORF, 2003; RAST; JOHANNESSEN; MAUSER, 2014). There are databases developed from a specific satellite mission, from the combination and processing of many satellite data, or even by a combination of in situ and remote sensing datasets. Remote sensing has a very promising role for fostering water resources management in South America (SHEFFIELD et al., 2018).

According to HU et al. (2017), global scale wetland extent datasets may be derived from remote sensing methods, compilation of datasets, and model simulation. However, current estimates often diverge in their estimates, due to different wetland definitions and particular wetland characteristics that are difficult to measure (e.g., the rapidly changing nature of the wetland landscape, which is a complex mixture of water, soil and vegetation), and to the different adopted classification methods and coarse

resolution, for example (HU; NIU; CHEN, 2017). A review of remote sensing applied to South American wetlands was presented by KANDUS et al., (2018). Their study revealed that although there is a growing research interest on this topic, there is still a lot of developments to be done in terms of inventory and comprehension of wetlands dynamics, while most publications have been carried out for Amazon, Paraná and Pantanal wetlands. A similar conclusion was achieved by the literature review developed by FLEISCHMANN et al. (2021). The following two sections briefly describe remote sensing products and techniques available for studying hydrodynamic and hydrologic variables.

Hydrodynamic variables: flood extent, water level, surface water storage and river discharge

Flood extent. Synthetic Aperture Radar (SAR, an active micro-wave based sensor) have been used to map flooded areas, especially the L-band due to its cloud and vegetation penetration. HESS et al., (2015) developed a wetland map of the whole Amazon Basin from a classification of JERS-1 SAR data for the period 1995-1996. ALOS-PALSAR satellite mission (2006-2011), the JERS-1 successor, had its high resolution data (12.5 to 100 m resolution) recently made available for scientific purposes, and is very promising for detailed mapping of the large South American wetlands, for which many studies of macrohabitats and floodable areas classification have already been carried out (ARNESEN et al., 2013; CAO et al., 2018; CHAPMAN et al., 2015; CORDEIRO; ROSSETTI, 2015; EVANS et al., 2014; FERREIRA-FERREIRA et al., 2015; QUINONES et al., 2015). More recent studies have been using the ALOS-2 PALSAR-2 mission data (JENSEN et al., 2018; ROSENQVIST et al., 2020). Passive micro-wave data have also been used for mapping flooded areas, e.g., HAMILTON; SIPPEL; MELACK, (2002) for South American wetlands, and PRIGENT et al., (2007) and PAPA et al., (2008a) for global wetlands. Finally, optical sensors (e.g., LANDSAT and MODIS) are useful for mapping flood extent (e.g., NDWI indices; GAO, (1996)), with the main drawbacks related to non-canopy penetration and unavailability for periods with cloud cover, during which floods tend to occur. A major dataset developed by PEKEL et al. (2016) globally estimated the surface water fraction at 30 m resolution, by processing and classifying with Google Earth Engine cloud computation technology the long-term LANDSAT archive. Finally, geomorphic approaches based on geomorphological analyses of DEM's and other remote sensing data may also be used to delineate wetlands (NARDI et al., 2019; NARDI; VIVONI; GRIMALDI, 2006). Table 3.1 presents some remote sensing products available for mapping the extension of the large South American wetlands.

Table 3.1. Some available products for mapping flood extent in South America.

Database	Coverage	Methodology	Temporal	Spatial	Reference

			resolution	resolution	
Dual-seasonal Amazon wetlands[1]	Amazon	JERS-1 (SAR)	Static maps (high and low water periods for 1995-1996)	90 m	(HESS et al., 2015)
SWAF[2]	Amazon	SMOS	3 days (2010-today)	25 km	(PARRENS et al., 2017)
GIEMS[3]	Global	Multi-sensors (AVHRR, SSM/I, Scatterometer ERS)	Monthly (1993-2007)	25 km	(PRIGENT et al., 2007)
GIEMS-D3[4]	Global	GIEMS downscalling	Monthly (1993-2007)	90 m	(AIRES et al., 2017)
GIEMS-D15[5]	Global	GIEMS downscalling	Static map	450 m	(FLUET-CHOUINARD et al., 2015)
SWAMPS[6]	Global	Multi-sensors	Daily (1992-2013)	25 km	(SCHROEDER et al., 2015)
GFPLAIN250m[7]	Global	Geomorphic method	Static Static map	250 m	(NARDI et al., 2019)
JRC global surface water extent[8]	Global	LANDSAT	Occurrence, seasonality	90 m	(PEKEL et al., 2016)
GLWD-3[9]	Global	Compilation of many global maps	Static map	1 km	(LEHNER; DÖLL, 2004)
G3WBM[10]	Global	LANDSAT	Static map	90 m	(YAMAZAKI; TRIGG; IKESHIMA, 2015)
Composite Wetlands (CW)[11]	Global	Topographic index and others	Static map	500 m	(TOOTCHI; JOST, 2018)
Dartmouth Flood Observatory (DFO)[12]	Global	Archive of past flood events	1985-hoje	-	(BRAKENRIDGE, 2019)
ESA-CCI Land Cover[13]	Global	Multi-sensors: SPOT vegetation, MERIS products	Annual – 1992-2015	300 m	(HEROLD, M. et al., 2019)

Database sources:

1: https://daac.ornl.gov/LBA/guides/LC07_Amazon_Wetlands.html

2: Contact Ahmad Al Bitar (CESBIO/France)

3, 4, 5: http://www.estellus.fr/index.php?static14/giems-d

6: Contact Ronny Schroeder (University of New Hampshire/United States)

7: https://figshare.com/articles/GFPLAIN250m/6665165/1

8: https://global-surface-water.appspot.com/

9: https://www.worldwildlife.org/publications/global-lakes-and-wetlands-database-lakes-and-wetlands-grid-level-3

10: http://hydro.iis.u-tokyo.ac.jp/~yamadai/G3WBM/

11: https://doi.pangaea.de/10.1594/PANGAEA.892657

12: http://floodobservatory.colorado.edu/

13: https://www.esa-landcover-cci.org/

Water level. The main techniques for measuring water level involve the use of radar altimetry (e.g., Topex-Poseidon, Jason, Envisat missions), for which a nadir satellite signal is vertically emitted to the surface and reflected when it finds the surface, and laser technology (e.g., ICESat mission and airborne LiDAR). Rivers, lakes and wetlands that cross the satellite track can thus be monitored through virtual stations. Temporal resolution of these products vary from ~10 days (Topex-Poseidon and JASON) to ~90 days (ICESat). Additionally, digital elevation models (DEM's; e.g., the SRTM Shuttle Radar Topography Mission, FARR et al., (2007)) based on SAR interferometry can also be useful for estimating water level and longitudinal slope (in the case of SRTM, the collected data refer to February 2000), but it is restricted to non-forested areas. Vegetation removed SRTM DEM's have then been recently developed (O'LOUGHLIN et al., 2016b; YAMAZAKI et al., 2017). SAR interferometry has also been used to estimate temporal water level variation in wetlands (ALSDORF et al., 2007; CAO et al., 2018; JARAMILLO et al., 2018). The future SWOT mission, to be launched in 2021 (BIANCAMARIA; LETTENMAIER; PAVELSKY, 2016) is expected to provide high resolution altimetry swath data for the large world rivers (width larger than 100 m).

Surface water storage. This variable is usually obtained by the combination of flood extent and water level maps or by GRACE terrestrial water storage measurements. The GRACE mission, launched in 2004 (TAPLEY et al., 2004a), provides global terrestrial water storage at a monthly and 100 km resolution, being a breakthrough opportunity for understanding wetland's hydrological dynamics. GRACE-Follow On mission was released in 2018 and is achieves a higher spatial resolution. FRAPPART et al. (2005) presented a pioneer study by combining JERS-1 flood extent maps with Topex-Poseidon satellite altimetry for the Negro River Basin. Later, FRAPPART et al., (2008)

combined GIEMS flood extent maps with the same altimetry database and compared it to GRACE volume variations for the same basin. FRAPPART et al., (2014) studied the Orinoco River basin with a similar methodology, and PAPA et al., (2008) explored global surface water storage with GIEMS, GRACE and hydrological modeling data.

River discharge. Although river discharge cannot be directly estimated from remote sensing techniques, it can be derived from simple Manning-based equations using satellite estimates of water level slope and depth (PAVELSKY; DURAND, 2012; YOON et al., 2016a), through assimilation of remote sensing products into hydrodynamic and hydrologic models (NEAL et al., 2009; PAIVA et al., 2013b; YOON et al., 2012), or through water balance approaches (MOREIRA et al., 2019).

Hydrological variables: precipitation, soil moisture, evapotranspiration

Precipitation. Satellite based precipitation is a fundamental information for studying wetlands and inundation processes. Current techniques involve micro-wave sensors (identifying ice particles within clouds), infra-red (relating precipitation to cloud temperature) and radar (the signal returns when it finds a precipitation mass). TRMM (Tropical Rainfall Measurement Mission, a joint mission between USA and Japan spatial agencies) was the first mission to measure rainfall at a quasi-global coverage, and its main product (TMPA - Multisatellite Precipitation Analyses; HUFFMAN et al., (2007)) combined a set of five different sensors to provide 25 km, 3-hourly precipitation estimates for the period 1998-2015. Its successor mission GPM (Global Precipitation Measurement; SMITH et al., (2007)) has recently released its first results. Other various products are also available, and include CMORPH (JOYCE et al., 2004) and Megha-Tropiques (ROCA et al., 2015).

Soil moisture. The main satellite missions that focus on monitoring worldwide soil moisture are SMOS (Soil Moisture Ocean Salinity; KERR et al., (2001)) and SMAP (Soil Moisture Active and Passive; ENTEKHABI et al., (2010)), which measure soil moisture with a L-band microwave radiometer, map the topsoil moisture (~0-5 cm), and provide daily to 3 days data at 10-25 km spatial resolution.

Evapotranspiration. Actual evapotranspiration can be estimated with energy balance models such as SEBAL and ALEXI, usually based on optical and thermal satellite imagery (ANDERSON et al., 2004; BASTIAANSSEN et al., 1998b), or vegetation-based methods such as the one used by MOD16 product, which estimates Penman-Monteith equation input parameters from MODIS data and vegetation indices (MU et al., 2007).

Part I. The Amazon floods: wetland types, extent and trends

Parte I. Inundações na Amazônia: tipos de áreas úmidas, extensão e tendências

4 Simulating different wetland types in the Amazon: case study in the Negro River Basin

This chapter is presented as a research article, which was published in Water Resources Research:

- Fleischmann, A.S., Paiva, R.C.D., Collischonn, W., Siqueira, V.A., Paris, A., Moreira, D.M., Papa, F., Bitar, A.A., Parrens, M., Aires, F., Garambois, P.A., 2020. Trade-Offs Between 1-D and 2-D Regional River Hydrodynamic Models. Water Resources Research 56, e2019WR026812. https://doi.org/10.1029/2019WR026812

4. Simulando diferentes tipos de áreas úmidas na Amazônia: estudo de caso na bacia do Rio Negro

Nos últimos anos, diversos modelos hidrológico-hidrodinâmicos 1D e 2D em escala regional têm sido desenvolvidos para simular processos de inundação em grande escala. Estes modelos regionais diferem de aplicações de escala local e de trecho em termos de premissas subgrid, parametrização e resolução espacial adotada. Apesar de comparações entre modelos 1D e 2D terem sido realizadas em escalas locais, as diferenças em escala regional foram pouco avaliadas. Além disso, existe uma necessidade de melhorar o acoplamento entre modelos hidrológicos e hidrodinâmicos. Neste estudo, o modelo MGB é aplicado em dimensões 1D e 2D para a bacia do Rio Negro na Amazônia (~700,000 km²), que apresenta contrastantes tipos de áreas úmidas. Simulações contínuas de longo termo foram realizadas e validadas com observações de satélites de múltiplas variáveis hidráulicas. Os resultados indicaram que ambas abordagens são similarmente capazes de estimar vazões e níveis d'água ao longo dos principais rios, especialmente considerando as incertezas dos parâmetros, mas diferem em termos de extensão de áreas inundadas e volume e níveis d'água em áreas úmidas complexas (i.e., áreas interfluviais). No caso destas últimas, o fluxo difuso e os padrões de drenagem foram mais realisticamente representados pelo esquema 2D, assim como a conectividade ao longo da bacia. O modelo 2D gerou mais drenagem de água ao longo da bacia, enquanto o 1D foi mais sensível aos parâmetros hidrodinâmicos para a estimativa de vazões e áreas inundadas, e ambos modelos tiveram uma sensibilidade similar para níveis d'água. Por fim, testes sobre o acoplamento entre processos hidrológicos e hidrodinâmicos sugerem que a sua representação em uma forma online é menos importante para áreas úmidas tropicais que a dimensionalidade adotada no modelo, a qual amplamente afeta a transferência e partição de água ao longo da bacia.

Este capítulo é apresentado na forma de um artigo científico, publicado no periódico Water Resources Research:

- *Fleischmann, A.S., Paiva, R.C.D., Collischonn, W., Siqueira, V.A., Paris, A., Moreira, D.M., Papa, F., Bitar, A.A., Parrens, M., Aires, F., Garambois, P.A., 2020. Trade-Offs Between 1-D and 2-D Regional River Hydrodynamic Models. Water Resources Research 56, e2019WR026812. https://doi.org/10.1029/2019WR026812*

Abstract

Recent years have seen the development of 1D and 2D regional scale hydrological-hydrodynamic models, which differ greatly from reach scale applications in terms of subgrid assumptions, parameterization and applied resolution. Although 1D and 2D comparisons have already been performed at reach and local scales, model differences at regional scale are poorly understood. Moreover, there is a need to improve the coupling between hydrological and hydrodynamic models. It is addressed here by applying the MGB model at 1D and 2D dimensions for the whole ~700,000 km² Negro Basin (Amazon), which presents different wetland types. Long term continuous simulations are performed and validated with multi-satellite observations of hydraulic variables. Results showed that both approaches are similarly able to estimate discharges and water levels along main rivers, especially considering parameter uncertainties, but differ in terms of flood extent and volume and water levels in complex wetlands. In these latter, the diffuse flow and drainage patterns were more realistically represented by the 2D scheme, as well as wetland connectivity across the basin. The 2D model led to higher drainage basin-wide, while the 1D model was more sensitive to hydrodynamic parameters for discharge and flood extent, and had a similar sensitivity for water levels. Finally, tests on the coupling between hydrologic and hydrodynamic processes suggested that their representation in an online way is less important for tropical wetlands than model dimensionality, which largely impacts water transfer and repartition.

Key words: Regional hydrodynamic modeling, wetlands, 1D models, 2D models, MGB model, Amazon Basin

4.1 Introduction

Recent years have seen the development of regional to global scale river hydrodynamic models at increasing resolution, using either the full Saint-Venant equation or its simplifications (diffusive and local inertia), and adopting either 1D or 2D schemes (Bates et al., 2018; Dottori et al., 2016; Falter et al., 2016; Getirana et al., 2017a; Mateo et al., 2017; Paiva et al., 2013; Paiva et al., 2011; Pontes et al., 2017; Sampson et al., 2015; Schumann et al., 2016; Yamazaki et al., 2013; Yamazaki et al., 2014b). These models are important tools for flood risk assessment (Pappenberger et al., 2012; Trigg et al., 2016; Winsemius et al., 2016), flood forecasting (Kauffeldt et al., 2016), climate change studies (HIRABAYASHI et al., 2013; SORRIBAS et al., 2016), and understanding of biogeochemical cycles and hydrological processes (Getirana et al., 2017b; Paiva et al., 2013).

Modeling continental river dynamics faces great challenges such as quantitatively evaluating the implications of upscaling Saint-Venant river models to continental scale,

and estimating river geometry (HODGES, 2013), and its ultimate goal is to provide locally relevant estimates at hyperresolution (Bierkens et al., 2015; Fleischmann et al., 2019; Wood et al., 2011). Intercomparison projects between global models have showed the necessity of improving routing schemes with hydrodynamic modules (ZHAO et al., 2017) and the potentiality of continental 1D models with floodplain modules to represent large scale flooding (Trigg et al., 2016). In this latter, however, a case study in the African continent showed relevant discrepancies between models in large deltas and arid/semi-arid wetlands (Trigg et al., 2016), which frequently present complex 2D hydrodynamic flow patterns.

1D models have often proved satisfactory to represent river processes such as flood wave diffusion, floodplain storage, backwater effects, and river discharges (Paiva et al., 2013; Yamazaki et al., 2011). However, many floodable regions across the globe are subject to a more complex hydrodynamics than what 1D models can address, since a single upstream-downstream connectivity is not able to represent the floodplain flows sub-parallel to the main river channel and the complex diffuse flow, connectivity and multichannel patterns that actually exist (Alsdorf et al., 2007; Altenau et al., 2017; Czuba et al., 2019; Park & Latrubesse, 2017; Pinel et al., 2019; Trigg et al., 2009; Wilson et al., 2007). CaMa-Flood (Yamazaki et al., 2011; Yamazaki et al., 2014b) and MGB (PONTES et al., 2017) are examples of large scale 1D hydrodynamic models that have implemented bifurcation and lateral connection schemes (i.e. connections among multiple neighbor river reaches) to improve the connectivity across floodable areas, trying to move away from a single upstream-downstream flow direction. Indeed, it is generally expected that 2D (or coupled 1D/2D) models should provide a more realistic and coherent framework for representing flood inundation dynamics, in comparison to 1D large scale hydrodynamic models with simple storage floodplain units (Neal et al., 2012; Schumann et al., 2016). However, the extension of these differences were not well explored in the literature. Classically hindered by computational limits, 2D models are now feasible at regional to global scales for both extreme events (Alfieri et al., 2013; Dottori et al., 2016; Sampson et al., 2015; Wing et al., 2017) and continuous simulation (Andreadis et al., 2017; Hoch et al., 2017a; Schumann et al., 2016). The advent of new remote sensing missions dedicated to surface hydrology, such as the Surface Water and Ocean Topography (SWOT), also push towards the development of more detailed hydrodynamic models.

Furthermore, while most large-scale hydrologic-hydrodynamic models perform an offline coupling, by forcing a hydrodynamic model with outputs from a rainfall-runoff model (Biancamaria et al., 2009; Getirana et al., 2017b; Grimaldi et al., 2019; Hoch et al., 2017b; Mejia & Reed, 2011) or with observed discharges (Sampson et al., 2015; Schumann et al., 2016), current efforts are aiming to perform strong (two-way) coupling with feedbacks between the hydrological and hydrodynamic modules. Examples include the applications by Da Paz et al. (2014) in the Pantanal and Fleischmann et al. (2018) in the semi-arid Niger Inner Delta. In the latter case the modeling framework represented both the dynamic evapotranspiration in flooded areas and infiltration from flooded areas

into the unsaturated soil column. The extent to which these coupling strategies may be relevant for tropical wetlands is still unknown.

It remains an open question the extent to which 2D regional scale models are preferable from 1D ones, and for which purposes or variables of interest. If 2D hydrologic-hydrodynamic models at the regional scale are now feasible due to increasing remote sensing datasets and computational power, should we favor it to the detriment of the 1D approach? One important step then is to understand how much detail 1D models miss in comparison to 2D ones with dynamic floodplain fluxes, in terms of changes in relevant hydrodynamic variables or missing hydrodynamic process representation, and to which extent the high uncertainty in 2D model parameterization reduced the benefit of increased dimensionality. Although comparisons between 1D and 2D hydraulic models have already been carried out in the literature for the reach scale and often for urban areas (ALHO; AALTONEN, 2008; CHATTERJEE; FÖRSTER; BRONSTERT, 2008; COOK; MERWADE, 2009; DIMITRIADIS et al., 2016; HORRITT; BATES, 2002), this is not the case for regional scale models, which differ from the reach scale ones in terms of applied resolution, parameterizations and sub-grid assumptions. Such assessments also require intense validation procedures, considering not only water levels and discharges at few observation locations in main rivers, but also basin-wide distributed information of water levels (at-a-station and longitudinal profiles) and flood extent (Fleischmann et al., 2019). Of special interest, regional model validation of the dynamics of wetlands (connected or not to adjacent rivers) need to be better addressed, and this is now possible under the satellite era with multiple remote sensing derived products.

In this context, three main goals are defined for this study. Firstly, to develop and evaluate a 2D hydrologic-hydrodynamic model with a two-way coupling scheme for regional scale applications, where the 2D scheme is applied to the whole basin domain, and not only to flood-prone areas. Secondly, to assess the importance of the 2D scheme in comparison to a 1D one, in terms of processes representation and impacts on important hydrodynamic and hydrological variables such as discharge, water level and flood extent and volume. For this, a thorough model validation is performed with multiple in situ and remote sensing products at the regional scale (flood extent, water levels and water surface slope). Finally, to evaluate the importance of the two-way coupling between hydrology and hydrodynamics in the 2D and 1D approaches. We believe that our discussion will provide new insights on the direction of regional to continental scale modeling, especially for the simulation of basins with complex wetlands.

4.2 Material and methods

4.2.1 MGB model

Model overview

MGB is a semi-distributed rainfall-runoff model developed for large scale basins (Collischonn et al., 2007; Pontes et al., 2017). The basin is divided into unit-catchments using a fixed-length, vector-based discretization (Siqueira et al., 2018), which in turn are divided into Hydrologic Response Units (HRUs) where vertical hydrological processes as canopy interception, evapotranspiration and soil infiltration are considered to model the generation of surface, subsurface and groundwater flows. Each unit-catchment is forced with observed precipitation and climate data, which are interpolated to the corresponding centroid. The calculated flux is routed within three linear reservoirs (surface, subsurface and groundwater). The inertial flood wave routing method (Bates et al., 2010; Neal et al., 2012) is then employed for propagating flows along the drainage network. Evapotranspiration (i.e. soil/vegetation evapotranspiration and open water evaporation) is dynamically computed considering the cell flood fraction at each time step. The 1D hydrodynamic model version considers floodplains as storage units, where the main channel and floodplain have the same water level, and river-floodplain flow exchange is proportional to the floodplain flooded area at a given water level (Paiva et al., 2011). Its potential drawbacks are related to the expected low capabilities of 1D models to represent complex or 2D flow patterns. For more details and equations on both rainfall-runoff modeling and 1D routing approaches, see the Supplementary Material S1 in Siqueira et al. (2018).

2D scheme for surface hydrodynamics

A 2D (or quasi-2D) hydrodynamic propagation method was adapted and implemented into the MGB model framework, enhancing the current version by incorporating fluxes in the two horizontal directions and by separately computing floodplain and channelized flows. Within the 2D scheme, the basin is discretized into a cell grid instead of unit-catchments (Figure 4.1). A subgrid method is applied, where a high-resolution Digital Elevation Model (DEM) is used to derive subgrid information for the coarse resolution cells. A cell is defined as the coarse resolution grid element (i.e., the model calculation unit or model resolution), and a pixel as the high-resolution DEM grid element, following literature (see Figure 2 in Paz et al. (2006) for a clear definition). For a given cell, floodplain flow is calculated for its D4 faces (i.e. orthogonal cell neighbors), while channel flow is computed between a cell and all its D8 neighbors that contain channels. The adopted conceptualization is based on the LISFLOOD-FP subgrid model developed by Neal et al. (2012), while integrating new

features such as the consideration of local runoff generation within each cell in a coupled hydrologic-hydrodynamic strategy, i.e., by allowing feedbacks between flooded areas and the adjacent soils, and by dynamically representing evapotranspiration in the flooded/non-flooded soil surfaces. Also, floodplain topography is derived from a high-resolution DEM, instead of considering a two-stage compound channel. A drainage network is derived from digital elevation model processing and a pre-defined area threshold (i.e., a number of pixels that defines the beginning of drainage) upon a flow accumulation map, following the algorithms proposed by Siqueira et al. (2016), and the channel cross section is considered as rectangular based on bankfull width and depth parameters.

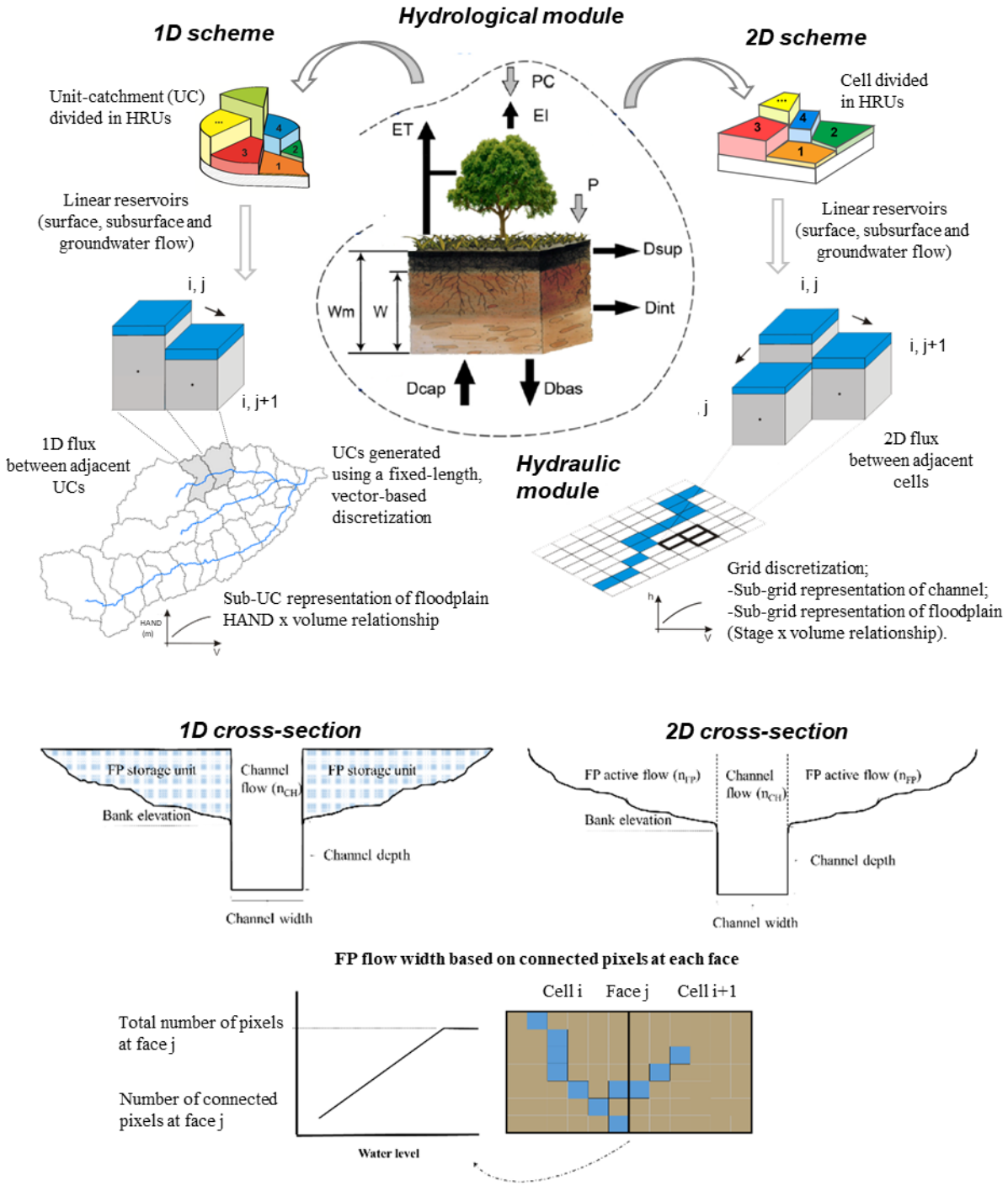

Figure 4.1. General representation of the MGB model for 1D and 2D schemes, with the distinction between hydrological and hydraulic (or hydrodynamic) modules and the coupling between them. The adopted scheme for cross sections for 1D and 2D models are depicted, together with the 2D conceptualization for floodplain (FP) flow depth and width.

At each time step, the i-th cell storage (continuity equation; Equation 1) is updated with the respective flows (see Equation 2 below) and local runoff (hydrological module):

$$\frac{V_i^{t+\Delta t}-V_i^t}{\Delta t} = \sum_{j=1}^{nCh} Q_{ch,j}^{t+\Delta t} - \sum_{j=1}^{nFP} Q_{fp,j}^{t+\Delta t} + Q_{cell,i}^{t+\Delta t} - {E_{f,i}}^t + {P_{f,i}}^t - {Inf_{f,i}}^t \quad (1)$$

where ch stands for channel, fp for floodplain, $cell$ for cell, and f for flooded areas. $V_i^{t+\Delta t}$ is the stored volume in cell i in time $t+\Delta t$, Δt the time step, $Q_{ch,j}^{t+\Delta t}$ the channel flows for each of the nCh channel cell faces, $Q_{fp,j}^{t+\Delta t}$ the floodplain flows for each of the nFP floodplain cell faces, $Q_{cell,i}^{t+\Delta t}$ the local runoff at cell i, ${E_{f,i}}^t$ and ${P_{f,i}}^t$ the evaporation and precipitation over flooded areas, respectively, and ${Inf_{f,i}}^t$ the infiltration from flooded areas into soils. The local runoff is computed by the rainfall-runoff module, which estimates the generated runoff within a given cell at each time step based on vertical hydrological processes (canopy interception, evapotranspiration, soil infiltration) and hillslope routing. The local runoff is affected by the hydraulic model in the adopted online coupling strategy, as described below in "*Online coupling*".

From the updated storage, the cell water level is obtained from the storage-level relationship derived from DEM processing (Paiva et al., 2011; Yamazaki et al., 2011). This relationship is obtained in a preprocessing step by considering the incremental storage for each increment of stage (trapezium integration). Although it is a commonly adopted approach in 1D models, large scale 2D models as LISFLOOD-FP have been considering two-stage channels for each cell, where flow is either confined to the main channel (with pre-defined channel width and bankfull depth) or to the second stage floodplain (with width computed as the whole cell size) (Neal et al., 2012).

The model topology for channel-floodplain interactions is based on pre-defined pair lists of neighbor floodplain and channel cells. For each time step, channel and floodplain fluxes between neighbor cells are decoupled from each other, i.e. the coupling is performed through the mass balance in Equation 1 by accounting for various lateral fluxes on a cell. Then, they are computed separately in an explicit scheme at the connecting face j with the dynamic equation developed by Bates et al. (2010):

$$Q_j^{t+\Delta t} = \frac{Q_j^t - g b_j \Delta t \mathrm{h}_j^t \mathrm{S}_j^t}{1+\frac{g\Delta t\left(\left|Q_j^t\right|\right){n_j}^2}{{b_j}\left(\mathrm{h}_j^t\right)^{7/3}}} \quad (2)$$

where $Q_j^{t+\Delta t}$ is the flow calculated at connection j (floodplain or channel) at time step $t+\Delta t$, g the gravitational acceleration, b the flow width, h the flow depth, S the water surface slope, and n the Manning friction coefficient (for floodplain or channel).

The next paragraphs describe each term of Equation 2.

Flow depth (h in equation 2). For a given cell, flow depth is computed as:

$$h_t = \max(y_i^t, y_{i+1}^t) - \max(z_i^t, z_{i+1}^t) \quad (3)$$

where $y_{i,t}$ is the water surface elevation at cell i and time step t, and z_i^t the floodplain or channel bottom (or bed) elevation. y_i^t is obtained from the DEM derived stage-volume relationship, and z is constant for channels and level-dependent for floodplains flows.

For channelized flow, the bottom elevation z is obtained from the bank elevation (z_{ref}) subtracted by the channel bankfull depth (h_{bf}). z_{ref} is defined as the average of high-resolution DEM pixels located above the drainage network within the cell. The raw (original) DEM is used to estimate z_{ref}, since a hydrologically conditioned DEM (e.g., after correction from pit filling/removal methods) may have unrealistic elevations. The drainage network is obtained from geoprocessing with the IPH-HydroTools package. h_{bf} may be obtained from in situ observations or simplified geomorphic relationships (see next section for the data used in this study). The main channel cross section is assumed to be rectangular.

For floodplain flow, z is calculated within a cell for each time step as the difference between water surface elevation (y) and the average floodplain water depth ($h_{m,FP}$), where $h_{m,FP}$ is computed as the ratio between floodplain volume and floodplain flooded area. This means that the floodplain average bottom elevation for a given cell is level-dependent, i.e., it depends on how much of the floodplain is flooded. The higher is the flood level, the higher will be the average floodplain bed elevation. For each time step, z is assumed the same for all cell faces.

Flow width (b in equation 2). For a given pair of neighbor cells, channel flow width is estimated as the average bankfull width of the two connected cells, which are typically obtained with hydraulic geometry relationships (i.e., simplified relationships using predictive variables as upstream drainage area or average discharge, which are then applied to each river reach) or satellite data (Allen & Pavelsky, 2018; Frasson et al., 2019; Yamazaki et al., 2014a).

Floodplain flow width is computed by counting, for each cell face and for a given water level, the number of pixels that are connected at both faces. When the whole face is connected, the cell size is adopted as the flow width (Figure 4.1).

Water surface slope (S in equation 2). Water surface slope is computed for both channel and floodplain flows as the difference between water levels in neighbor cells divided by a length. The latter is defined as the cell size for orthogonal fluxes (i.e.

between the cell and its orthogonal neighbors) and as the cell diagonal length for fluxes between neighbors in the diagonal direction.

Time step and flow limiter. Time step (Δt) is calculated following the Courant condition with an additional alpha parameter ($\propto$) for ensuring model stability (BATES; HORRITT; FEWTRELL, 2010; YAMAZAKI et al., 2011):

$$\Delta t = \propto \frac{\Delta x}{\sqrt{gh}} \quad (4)$$

where Δx is the cell length. To further enhance stability, a simple flow limiter was adopted to avoid supercritical regime. This was carried out by constraining velocity at each face so that the Froude number does not exceed unity:

$$Q_j^t = \min\left(Q_j^t, bh^{1.5}g^{0.5}\right) \quad (5)$$

This criterion was sufficient to avoid mass balance errors basin-wide, and in practice was only applied for very steep upstream reaches, leading to very small differences in downstream reaches.

Online coupling. Finally, a tight coupling strategy is performed through online coupling between hydrologic and hydraulic modules. For each cell within the basin domain, infiltration from flooded areas into the variably saturated soil column ($Inf_{f,i}$ in equation 1) is considered following the approach by Fleischmann et al. (2018), where the infiltration rate is proportional to the soil dryness. In addition, evapotranspiration is dynamically computed considering the cell flooded fraction at each time step (as defined by Equation 4) as the surface area available for open water evaporation with Penman equation, and evapotranspiration in the remaining non-flooded area with Penman-Monteith equation.

4.2.2 Case study: Negro River Basin, Amazon

Given its large dimensions and the varied wetland types associated to it, the Negro River Basin in the Amazon was considered an interesting case study for evaluating regional scale river hydrodynamic models, especially in terms of their capacity of simulating complex river-wetlands systems. The Negro River (Figure 4.2) has a drainage area of ~700,000 km² and is the second largest tributary of the Amazon River (after the Madeira River). More than 90% of the basin is located within Brazil (LATRUBESSE; STEVAUX, 2015), and its confluence with the Amazon River is located in the city of Manaus. Backwater effects from Amazon mainstem occurs in its downstream 300-400 km reach (MEADE et al., 1991). The main tributary is the Branco

River, which is the main sediments provider for the basin. The Negro River has also two huge fluvial archipelagoes (Mariuá – between Serrinha and Moura stations; and Anavilhanas, downstream of Moura; see Figure 4.2), which are associated to anabranching geomorphological patterns with a multichannel system with stable islands (LATRUBESSE; STEVAUX, 2015). The basin has a seasonal precipitation regime with maximum (minimum) at MJJ (DJF) months, and average annual rainfall around 2000-2200 mm (LATRUBESSE; STEVAUX, 2015). Altitudes range from ~3,000 m highlands in the Pico da Neblina (highest peak in Brazil; 2,995 m) and "tepuis" Precambrian table mountains (e.g., the Monte Roraima) to the lowlands around Manaus city at 92 m.

Wetlands in the basin can be divided into two main groups: river floodplains and interfluvial wetlands, which sum up to 119,600 km² of floodable areas (MELACK; HESS, 2010) and have a floodplain seasonal storage variation ranging from ~170 km³ (FRAPPART et al., 2008) to 331 km³ (Frappart et al., 2005). Floodplains along the Negro River mainstem and its tributaries are locally known as "igapós". They are acid, black-water river systems, and are generally nutrient and sediment-poor, presenting small biodiversity in contrast to the sediment rich, white rivers' floodplains ("várzeas") in the Amazon basin.

Besides river floodplains, the Negro River Basin presents complex and poorly known interfluvial wetlands (Figure 4.2b), which are very different from the well studied Central Amazon wetlands (Belger et al., 2011), and were called the "Septentrional Pantanal" by Santos et al. (1993) given their large extension. They occur in flat terrains associated to low density vegetation, called "campinas" (open, herbaceous vegetation) and "campinaranas" (mixed herbaceous-arboreal formation), and present hydromorphic, Spodosol sandy soils. Most of them have been recently described as formed by neo-tectonic events associated to megafan systems (Rossetti et al, 2012). Flooding in these areas are typically related to high water table levels associated with local rainfall, and is less dependent of flooding from adjacent large rivers. During the dry period, there can occur water deficit and a deep water table (GUIMARÃES; BUENO, 2016). A detailed description of the Viruá megafan, the most well studied interfluvial wetland in the Negro Basin, is presented in Rossetti et al. (2017). In the Roraima Brazilian State in the basin Northeast, wetlands in savanna-like vegetation are also present (the Rupununi wetlands), usually associated to small river floodplains (Hamilton et al., 2002) (Figure 4.2b).

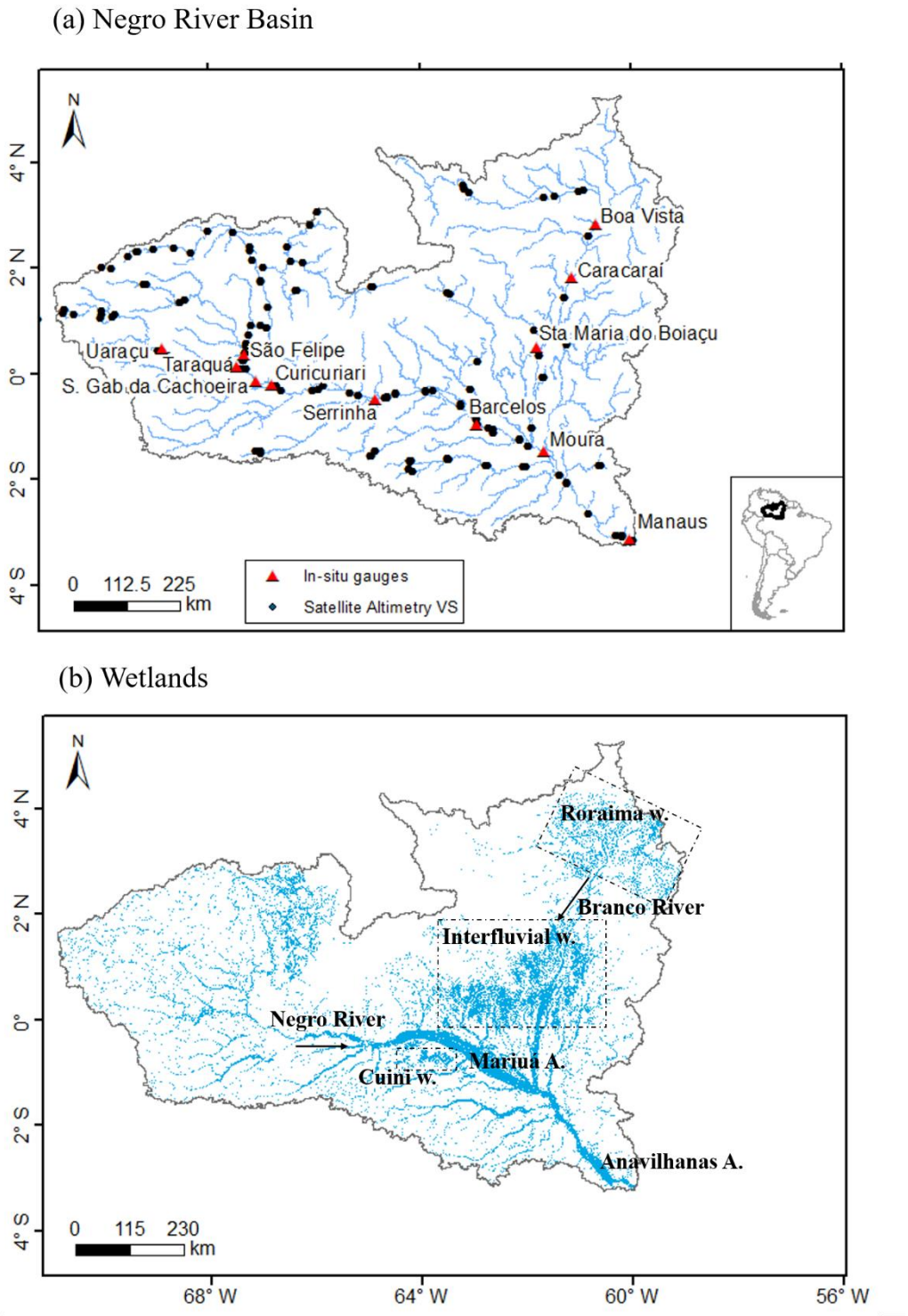

Figure 4.2. (a) Negro River Basin with in situ water level gauges and satellite altimetry virtual stations (VS). (b) Main wetlands in the basin with regions of interest mentioned in the text: Roraima, Interfluvial (in the context of this study only; elsewhere the Roraima and Cuini are also considered interfluvial wetlands) and Cuini wetlands, and Mariuá and Anavilhanas archipelagoes. Arrows indicate the preferential flow direction of Negro and Branco rivers.

4.2.3 Model application in the Negro River Basin

The MGB model was applied to the Negro River Basin with both 1D and 2D schemes. It was run from 1/Jan/1999 to 31/Aug/2015, and was forced with daily TMPA 3B42 precipitation (HUFFMAN et al., 2007) and long term climate averages from CRU database (New et al., 2002) for wind speed, relative humidity, air temperature and sunlight hours variables, which are used for evapotranspiration computation.

The vegetation corrected, high resolution MERIT DEM (YAMAZAKI et al., 2017) was used to estimate floodplain topography at 250 m resolution, and a low-pass filter was used to filter out noise across the floodplain terrain. Channel bank elevation was derived from the average of DEM pixels above river reaches, following the methodology by Siqueira et al. (2018) and using the IPH-HydroTools GIS toolkit (Siqueira et al., 2016). The same bank elevation values were adopted for both 1D and 2D approaches. The stage-area-volume relationships were computed by integrating areas with a level-pool method for the 2D model (i.e. by horizontally computing the flooded pixels below a given water level). For the 1D, it was based on a HAND contour map (Height Above The Nearest Drainage; Rennó et al., 2008), considering the flooded area associated to each height above the bankfull elevation (see a description of this method in Siqueira et al. (2018)).

For the 2D model, it is necessary to identify cells with channels, which were defined to match the same drainage network as the 1D model, in order to ensure model comparability. The only exception was made for wetlands areas, since many interfluvial wetlands have predominantly a diffuse flow pattern without a well-defined drainage pattern. Thus, the high-resolution drainage network developed by Seyler et al. (2009) and based on JERS-1 image classification was combined with the flood extent map by Hess et al. (2015) to infer wetland cells without channels (Figure S1d in Supp Information S1).

Bankfull width (W) was defined with geomorphic relationships with drainage area (A_d), based on an adjustment with in situ surveyed cross sections, while depth values (D) were derived from the regression equation by Paiva et al. (2013), multiplied by a calibration parameter a (assumed constant for the whole basin). Depth values must be calibrated since they have high uncertainties and are difficult to be observed from remote sensing in comparison to other variables as width.

$W = 0.1419{A_d}^{0.7662}$, for the Negro River (6)

$W = 0.2568{A_d}^{0.7057}$, for the Branco River (7)

$D = a1.26{A_d}^{0.20}$, for the whole basin. (8)

The model was manually calibrated considering only two in situ discharge gauges (Serrinha and Caracaraí, see Figure 4.2a) to avoid model over-parameterization, i.e., only two rainfall-runoff parameter sets were calibrated for the whole basin. This is important to yield more physically-based, parsimonious model parameter sets (Siqueira et al., 2018), in the way that a sufficient (yet small) number of parameter sets were adopted to allow a good representation of the physical processes. The rainfall-runoff module parameters and the a multiplier (Equation 8) were also parsimoniously calibrated. Hydrologic Response Units (HRU's) were used to define homogeneous regions for the rainfall-runoff parameters, and were derived from the South America HRU map developed by Fan et al. (2015) and available at <https://www.ufrgs.br/lsh/products/remote-sensing/simplified-hydrological-response-units-map-for-south-america/>.

Figure 4.1 compares the 1D and 2D model configurations. The 2D model was set with ~4 km spatial resolution (a 4.17 km actual resolution was obtained from an upscaling of 3 arcsec resolution by a factor of 4.5), totaling 39.882 units with area 17.4 km², while the 1D model is based on 24.115 unit-catchments (average area ± standard deviation equaling 28.8 ± 11.2 km²) defined as the local drainage area of 10 km river reaches. In both cases, the basin downstream boundary condition was set as the observed in situ water level at Manaus, the Manning coefficient was globally set to 0.035 for channel and 0.1 for floodplains, and the time step alpha parameter for model stability adopted as $\propto$=0.3, leading to time step values around a few minutes. Mass conservation was assessed for all model runs.

The 1D and 2D models were compared in terms of their capacity to represent hydrodynamic variables (discharge, absolute water level, water level anomaly – i.e., water level minus long term average, and flood extent and volume). The coupling scheme between hydrological and hydrodynamic processes was assessed through simulation tests with and without coupling and its impact on the water balance components (evapotranspiration and runoff). The considered scenarios were "default" (i.e., with open water evaporation and without infiltration), "Inf" (with infiltration from floodplain into soil), and "NoETw" (without flooded areas open water evaporation). To compare time series of models and observations and the 1D and 2D model estimates between them, the following performance metrics were calculated: Nash-Sutcliffe coefficient (NSE), Pearson correlation (r), root mean square error (RMSE), relative RMSE (RMSEr - RMSE normalized by the average observation), delay index (DI - time lag in days that leads to maximum cross-correlation between simulation and observation; Paiva et al. (2013)), and bias (relative difference between long term averages). Differences between 1D and 2D models are reported as RMSD and RMSDr (i.e., root mean square deviation). To compare maximum flood extents, the Critical Success Index (CSI) was computed:

$$CSI = 100\,(A \cap B)/(A \cup B) \qquad (9)$$

where A and B are the observed and simulated flood extents for a given area, respectively. CSI ranges from 0 % to 100 %, where 100 % is the optimum value.

4.2.4 Validation datasets

Model outputs were validated against independent flood extent and water level data. Flood extent and surface water estimates from GIEMS-D3 (AIRES et al., 2017), SWAF-HR (PARRENS et al., 2019) and Hess et al., (2015) were used for model validation.

Global Inundation Extent from Multi-Satellites-D3 (GIEMS-D3; Aires et al., 2017) is a unique dataset that provides high-spatial-resolution (~90m) inundation extent globally at a monthly time scale over the 1993–2007 period. It relies on the downscaling of GIEMS dataset (Prigent et al., 2007, Papa et al., 2010), which is based on the data fusion of multiple satellite observations (passive and active microwave, and visible and near-infrared reflectances). This downscaling is performed from the original 25 km resolution to the 90 m resolution through a floodability index model derived from a global topography and hydrology from HydoSHEDS (Lehner et al., 2008). Compared to other global high-resolution datasets based on visible or infrared observations, GIEMS-D3 has the advantage to detect water below the vegetation (Aires et al., 2018). GIEMS is being extended over four decades, to present time; GIEMS-D3 should then become available for this long time record too. For comparison with MGB model, monthly averages were considered for the period from 1999 to 2007.

Surface WAter Fraction-High Resolution (SWAF-HR, Parrens et al., 2019) is a high-resolution (1 km) inundation dataset derived from downscaling of the SWAF product specifically developed for the Amazon Basin. The SWAF product (PARRENS et al., 2017) is derived from the Soil Moisture Ocean Salinity (SMOS; Kerr et al., (2001)) L-band passive microwave brightness temperatures (AL BITAR et al., 2017) with 3-day temporal resolution during the 2010-present period and has the significant advantage to detect water under dense vegetation. The SWAF-HR product was downscaled from its original resolution at 25 km to 1 km by using the Global Surface Water Occurrence from Landsat (Pekel et al., 2016) and the Digital Elevation Model Multi-Error-Removed-Terrain (MERIT DEM; Yamazaki et al., 2017). For comparison with MGB model, monthly averages were considered for the period from 2010 to Aug/2015.

Hess et al., (2015) surface water extent product (called hereafter Hess) is based on classification of Japanese Earth Resources Satellite-1 (JERS-1) Synthetic Aperture Radar (SAR) imagery for the years 1995-1996 (high and low water maps available) and is available at 90 m spatial resolution.

Time series of water level were acquired from 107 satellite altimetry virtual stations and 11 in situ gauges from ANA (Brazilian National Water Agency; available at <www.snirh.gov.br/hidroweb/>). Rivers satellite altimetry water levels time series were obtained from the THEIA/Hydroweb website. Data processing description can be found in Santos da Silva et al. (2010). Time series range from 2002 to 2010 and from 2008 to 2016 for ENVISAT and Jason-2 missions respectively, and the estimated accuracy is around 10-40 cm. To complete the geographical validation, we manually processed three water elevation time series from the recently released Sentinel3-A mission at VSs (Virtual Stations) located in the wetlands (see Figure 4.9c for location of VS1, VS2 and VS3). The manual processing of the land products (SR_2_LAND) from Sentinel3-A SRAL mission was based on a simple filtering of high-resolution observations with a low backscatter coefficient, assuming that the SAR (Synthetic Aperture Radar) mode allows a low echo contamination. More information on S3-A altimetry mission can be found on the dedicated ESA website (available at <https://sentinel.esa.int/web/sentinel/user-guides/sentinel-3-altimetry>). A visual inspection was also performed to ensure that the selected high-resolution measurements come from the considered area. Although there is no overlap between the MGB run (1999 - 2015) and the S3-A data (mid 2016 - today), it is hoped that satellite altimetry provides an interesting insight on water levels fluctuations in the ungauged interfluvial areas. Finally, we used longitudinal profiles of surface water slope derived for 25 km long reaches for the Negro mainstem, the same used by Montazem et al. (2019). These data sets were obtained in two field campaigns with survey ships (25/Sep/2009 during falling limb and 17/Oct/2010 during low flow) and are available for the reach between São Gabriel da Cachoeira location to the confluence with Amazon River. A datum correction was performed to convert the observations into EGM96 datum through field measurements.

4.3 Results

4.3.1 1D vs 2D river discharge

The MGB model rainfall-runoff parameters were calibrated based on discharge data from Caracaraí and Serrinha gauges, which are the most downstream stations along the Branco and Negro rivers (except for Moura station, which is downstream of the Negro-Branco confluence), respectively. The calibrated rainfall-runoff parameters are provided as Supporting Information S1. Figure 4.3 presents simulated and observed discharges for the two gauges, and shows an overall satisfactory agreement between both 1D and 2D observations. Nash–Sutcliffe efficiency coefficient (NSE) values were 0.76 (1D) and 0.66 (2D) at Caracaraí and 0.53 (1D) and 0.53 (2D) at Serrinha. The deviation between 1D and 2D models (RMSEr=22%) is comparable to the errors between the models and observations (26%) in the Negro, but are smaller in the Branco (29% against 41-49%). There is an overall discharge underestimation in the Upper

Negro River which may be related to a biased TMPA precipitation in the region (Getirana et al., 2011). Simulated discharges suggest a higher hydrograph attenuation from river floodplains by the 1D model in both Negro and Branco rivers.

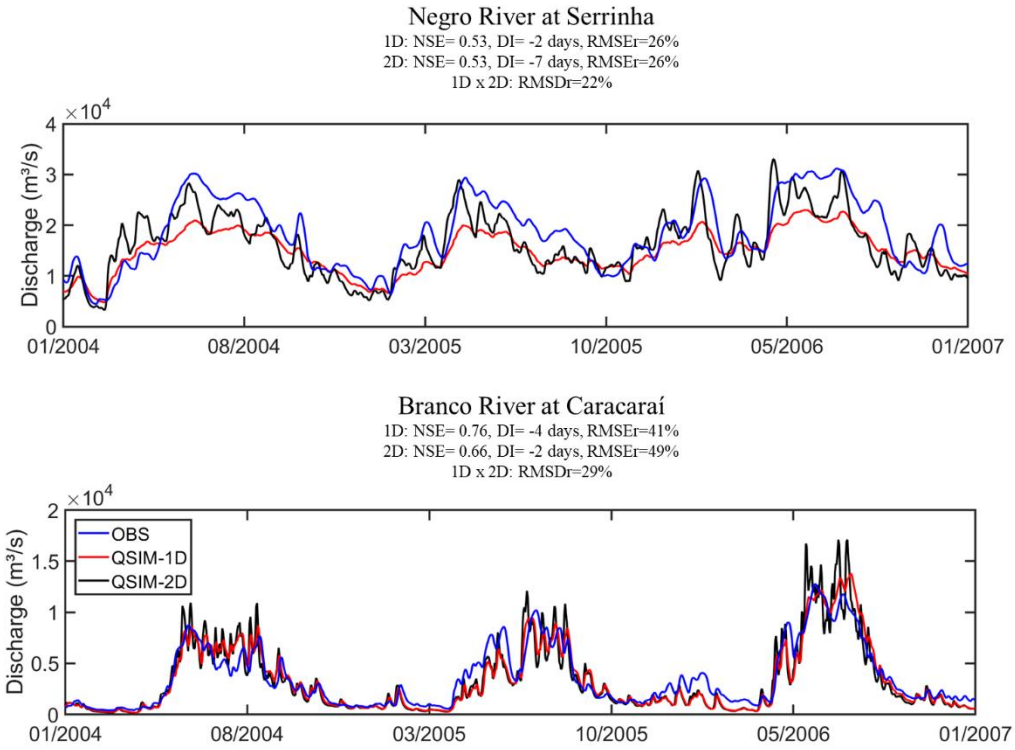

Figure 4.3. Observed and simulated discharges for the 1D and 2D MGB model versions for the in situ gauges Caracaraí and Serrinha.

4.3.2 1D vs 2D river water levels

A spatial analysis of the performance of water level anomalies for all stations is shown in Figure 4.4a. Both 1D and 2D models have similar performance basin-wide. The differences between 1D and 2D water level estimates are presented through a reach by reach analysis in Figure 4.4b. Deviation is relatively small, with most simulated reaches with RMSD<1 m for anomalies. On the other hand, absolute water levels indicate some discrepancies between the model estimates, with RMSD between 2 m and 5 m for most reaches along the Negro River. RMSD values were smaller along upstream reaches and throughout the Branco River, which also presents smaller water level amplitude in comparison to the Negro.

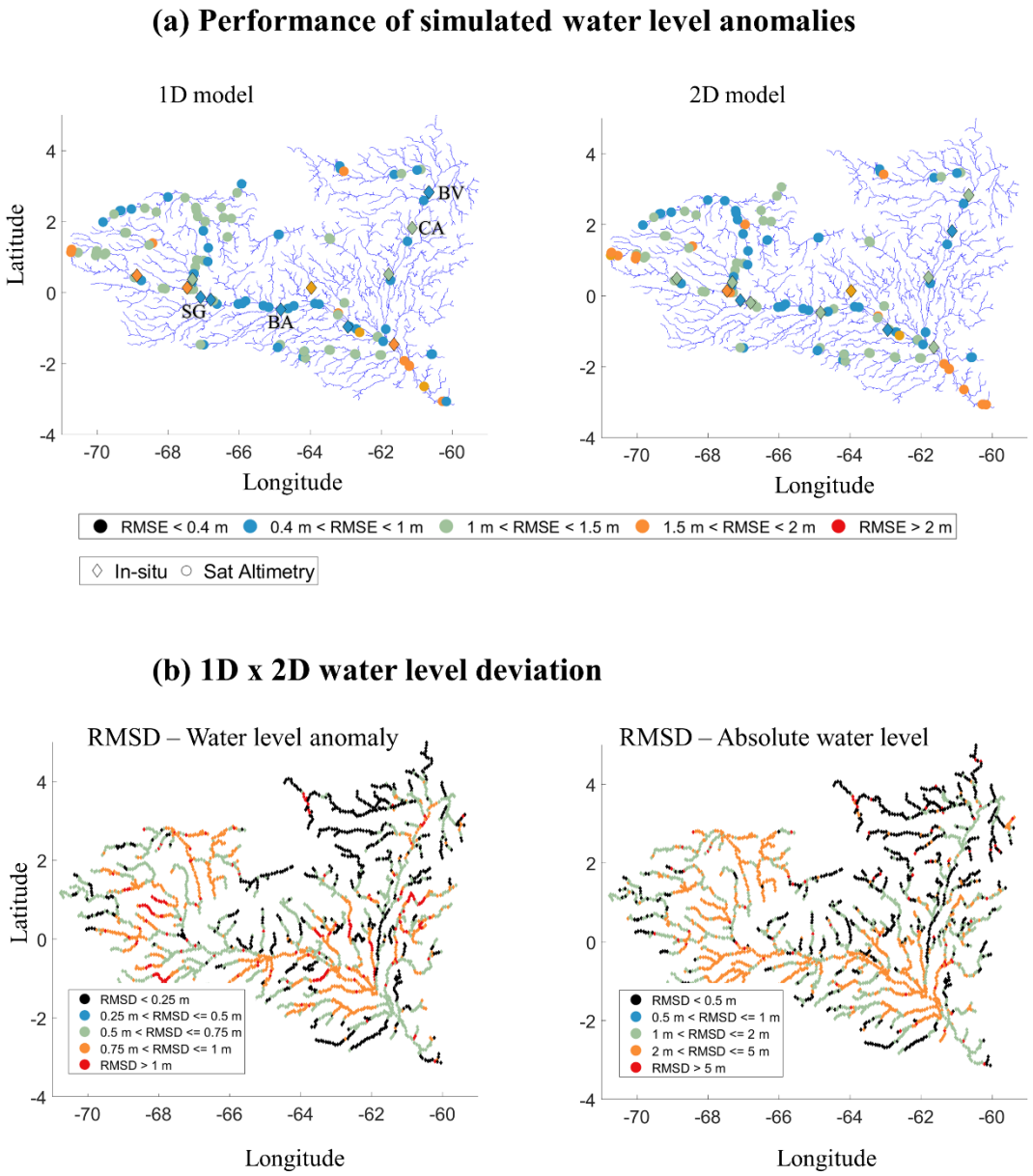

Figure 4.4. (a) Performance (RMSE) of 1D and 2D models for water level anomalies. Locations (see map in Figure 4.2) refer to SG: São Gabriel da Cachoeira; BA: Barcelos; CA: Caracaraí; and BV: Boa Vista. (b) Water level deviation (RMSD) between 1D and 2D models for anomalies and absolute water levels. Values presented only for drainage area>1000km² for figure readability. Please note that the scales have different ranges.

Absolute water level time series along rivers (Figure 4.5) depict the overall coherence between 1D and 2D models in the Branco, where the deviation between them (RMSDr) is smaller than between model and observations. The opposite occurs with the Negro stations, with better agreement among models and observations than among them. The 1D has generally higher water levels in the Negro, what is associated to more floodplain storage as discussed in the next section. Water levels become more

attenuated in the downstream parts of the Negro mainstem, what is also depicted by both models. On the other hand, RMSE values below 2 m as obtained here may be considered satisfactory given all uncertainties related to regional hydrodynamic models in poorly gauged basins as the Negro (e.g., DEM errors, simplified parameter calibration, uncertain model forcing, etc.).

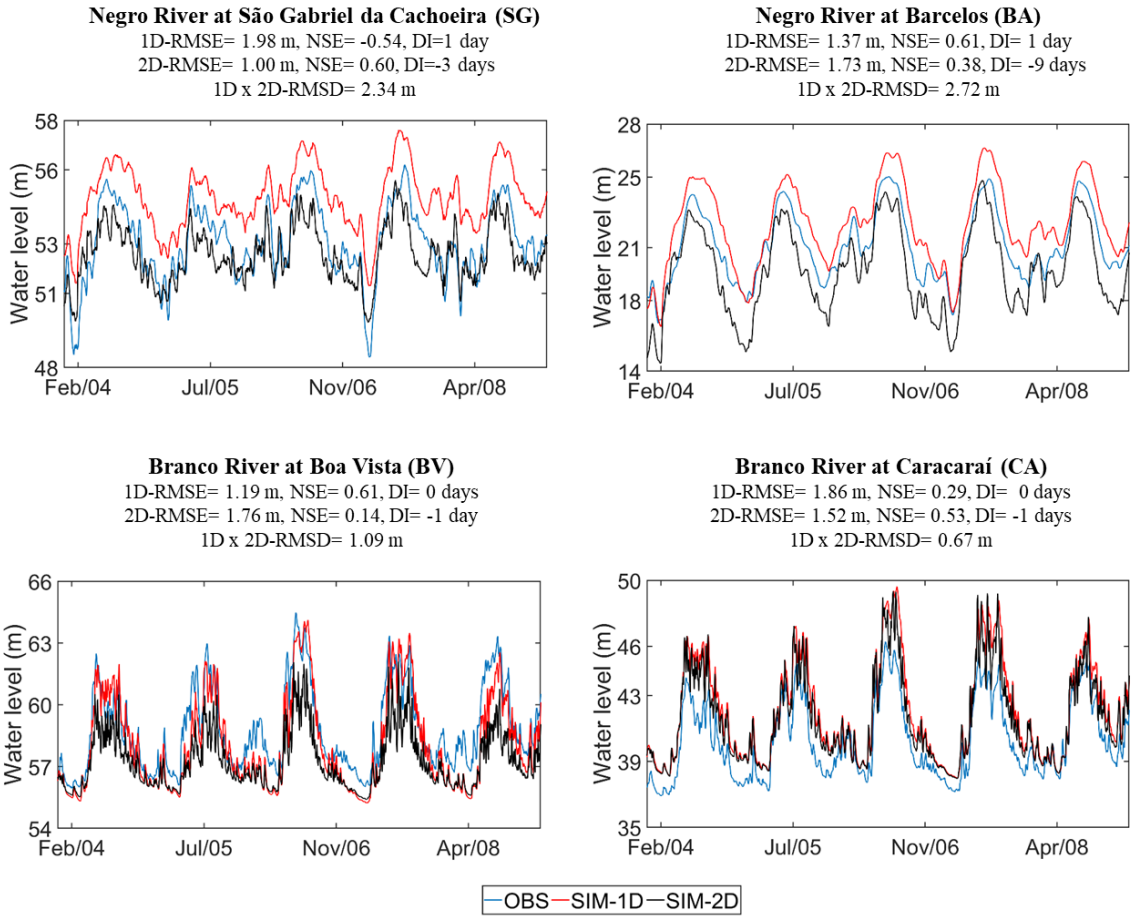

Figure 4.5. Absolute water level time series in Negro River at four locations across the basin (see location in Figure 4a).

The water surface slope is also a very relevant hydrodynamic variable to define flood extent and fluxes. Figure 4.6 shows a comparison between simulated and observed water level slopes obtained in two field campaigns carried out during receding waters, for which RMSE values around 3.3-3.6 cm/km were obtained for both 1D and 2D. These errors are very high if compared with the average slope across the whole assessed profile (3.1 cm/km). Discrepancies between model and observations are higher than between 1D and 2D models (RMSD 1.9-2 cm/km), and errors are higher along the Negro-Branco confluence (chainage between 250 and 400 km) and in the Upper Negro River close to São Gabriel da Cachoeira (chainage larger than 700 km). The observed

slope decreases around Barcelos (450 km; Figure 4.2), maintaining a plateau until Moura, which is located just downstream of the Negro-Branco confluence (chainage 250 km). Downstream of it, slopes sharply decrease to almost 0 cm/km close to the Amazon-Negro confluence at Manaus. While the latter reach is subjected to backwater effects from the Amazon (MEADE et al., 1991), the reach between Barcelos and Moura is associated to the Mariuá fluvial archipelago, which has dozens of stable vegetated islands and is considered the largest in world (MONTERO; LATRUBESSE, 2013). Along the Branco-Negro confluence, just downstream of Mariuá, the Negro River width is largely reduced to around 2 km due to a delta feature, which was formed during Late to Mid Holocene period when the Branco River carried abundant suspended load, being a non-active landform today (LATRUBESSE; FRANZINELLI, 2005). This region acts thus as a hydraulic control for upstream Negro reaches (i.e., creating backwater effects, as discussed by O'Loughlin et al. (2013)).

Some hypotheses could explain the poor 1D and 2D estimates around upstream Negro and Branco-Negro confluence regions. Around the confluence, both models show a sharp decrease in water slope further upstream than it really is (near chainage 400 km). The adopted simple channel parameterization (i.e., regional geomorphic relationships between effective width and depth parameters and drainage area) provides some explanation: important changes on the river width (e.g., around the confluence region) were not represented in the model, so that important hydraulic controls were not represented, what largely affects the simulated slopes (O'Loughlin et al., 2013), and should be addressed in future developments. The adopted coarse grid resolution (4-10 km) also hampers a proper representation of such local scale (yet regionally relevant) features. Along the upstream Negro reaches, there is a somehow constant observed slope value throughout most of the river at around 4 cm/km, while simulation values reach values as high as 15 cm/km in certain reaches. This region is associated to rapids (LATRUBESSE; FRANZINELLI, 2005), and the relatively smaller river widths increase the DEM derived noises in the bed elevation parameter, possibly increasing the variation in simulated slopes. The adopted, simplified subgrid model conceptualization, which defines floodplain flows among cells, also adds some uncertainty to the slope representation. Finally, there are also expected errors in the observed profiles, which were obtained during 10 days boat surveys (given the 900 km survey length) and are also subject to uncertainties related to Geoid model correction and GPS processing.

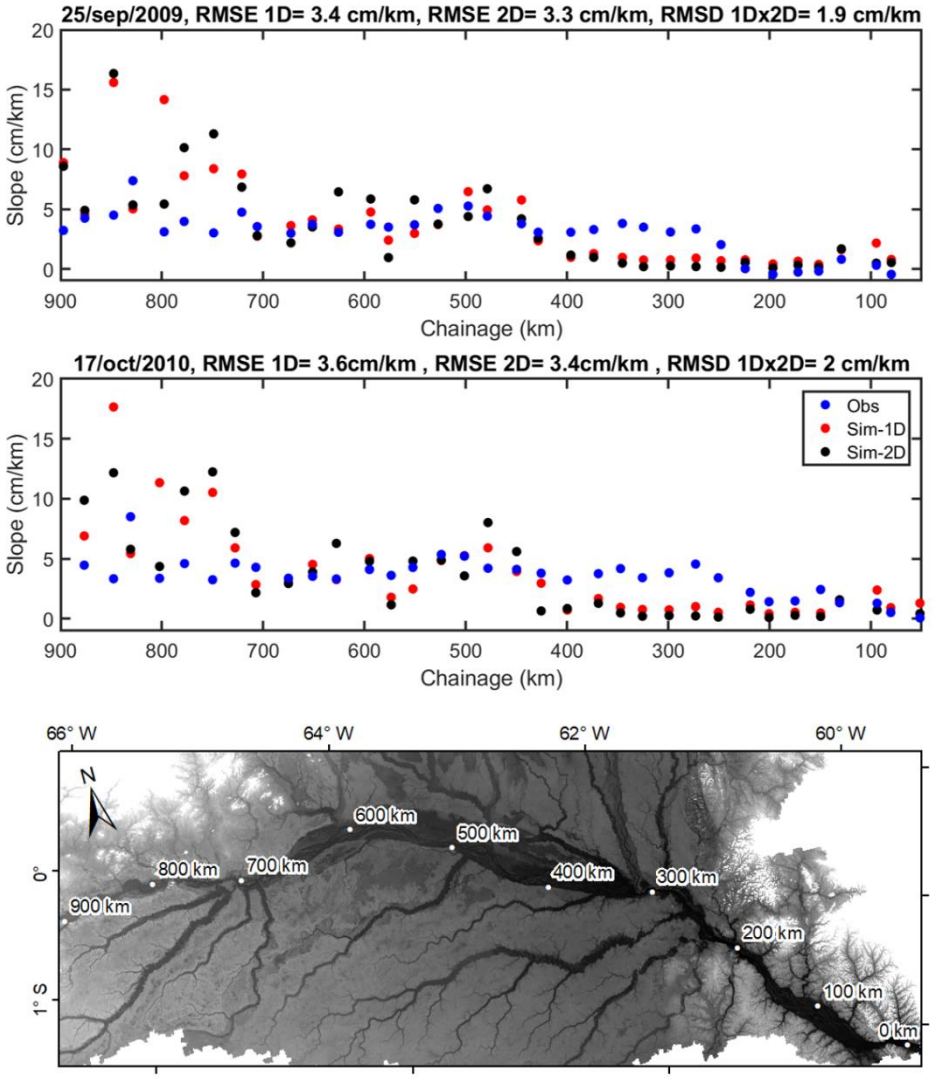

Figure 4.6. Simulated and observed longitudinal water level slope profiles for the Negro mainstem for 25th Sep 2009 and 17th Oct 2010. Chainage is the distance from the basin outlet (at Manaus), as presented in the bottom figure map.

4.3.3 1D vs 2D flood dynamics across wetland types

In this section the differences between 1D and 2D models in representing the complex wetland dynamics in Negro River Basin are assessed. Firstly, maximum flood extent estimates by the models and SWAF-HR, GIEMS-D3 and Hess remote sensing products are compared in Figure 4.7. There is an overall good spatial agreement between all estimates, particularly considering the uncertainties existent in the adopted methods and the different mapping period for each dataset (2000-2015 for MGB, 1995-1996 for Hess, 1993-2007 for GIEMS-D3, and 2010-2016 for SWAF-HR). The CSI

metric (Equation 9) for flood extent spatial assessment (Table 4.1) indicates that all datasets have similar spatial coherence with the modeling outputs, for both interfluvial and mainstem wetlands, while the spatial agreement between 1D and 2D (37% and 76% for interfluvial and mainstem, respectively) was higher than between models and remote sensing datasets. On the other hand, the 2D model shows a poorer performance in comparison to 1D, which in turn was associated to more flooding than the 2D (overall bias between 11% and 18%). It must be noted that the 2D model is dependent on the definition of which 2D wetland cells have river channels – in this study, the intersection between Hess product with the drainage network by Seyler et al (2009) was used (Figure S1d in Supp Information S1). Smaller river floodplains are represented in MGB and Hess, but to a lesser extent in SWAF-HR and GIEMS-D3. This is mainly due to the fact that Hess product comes from truly native high resolution "direct" observations while GIEMS-D3 for instance is downscaled from a low-resolution global product (GIEMS) which is known to have limitations in capturing small water bodies (see Figure 4.7 of Prigent et al 2007 for a comparison between GIEMS and Hess over the Amazon). Wetlands in the southern side of the Negro mainstem (as the Cuini wetland; Belger et al., (2011); Figure 4.2b) are not mapped by SWAF-HR because of radio frequency interference (RFI) and topography effect filtering, while across the basin GIEMS-D3 depicts less smaller size river floodplains than SWAF-HR.

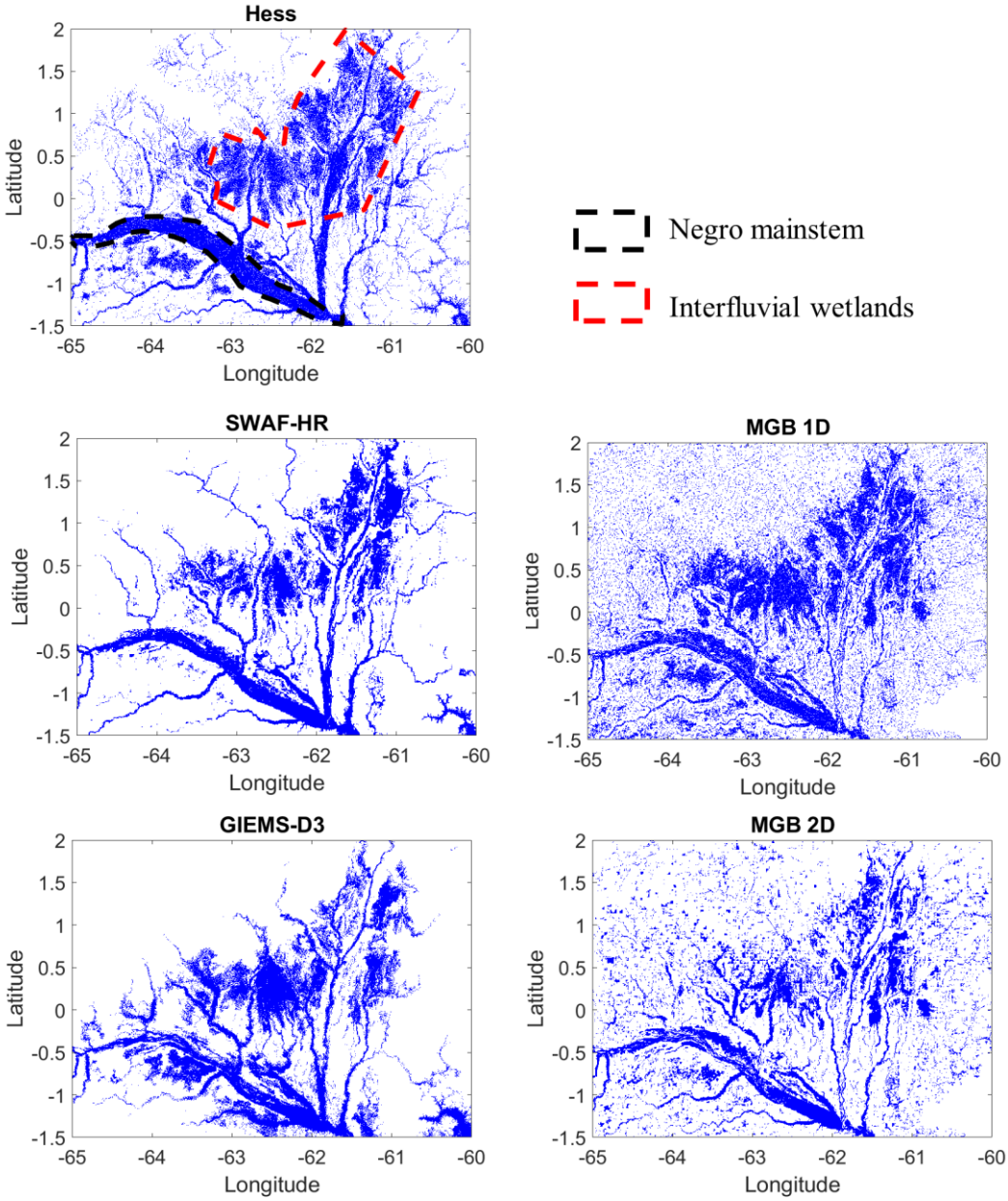

Figure 4.7. Maximum flood extent maps from 1D and 2D MGB model simulations and remote sensing based products (Hess, SWAF-HR and GIEMS-D3) in the central Negro River Basin.

Table 4.1. Performance metrics between simulated and observed flood extent time series (RMSE/RMSD, r and Bias) and maximum extent (CSI), for three remote sensing based products (GIEMS-D3, SWAF-HR and Hess) and two models types (MGB 1D and 2D).

	Interfluvial wetlands						
	1D validation			2D validation			1D x 2D
	GIEMS	SWAF	Hess	GIEMS	SWAF	Hess	
RMSE/D	59%	24%	-	46%	31%	-	27%
r	0.58	0.82	-	0.65	0.87	-	0.89
Bias	55%	2%	-	34%	-5%	-	11%
CSI	43%	44%	44%	25%	24%	23%	37%
	Negro Mainstem						
RMSE/D	27%	14%	-	17%	21%	-	25%
r	0.59	0.79	-	0.74	0.75	-	0.75
Bias	19%	3%	-	-3%	-14%	-	18%
CSI	66%	72%	74%	63%	64%	62%	76%

Flood extent time series for the interfluvial wetlands and the Negro mainstem regions (Figure 4.8 and Table 4.1 for metrics) indicate a higher agreement between MGB and SWAF-HR for the interfluvial wetlands (RMSE 24 to 31%; correlation 0.82 to 0.87; bias -5% to 2%) than between MGB and GIEMS-D3. For the mainstem there is a similar performance in terms of RMSE between MGB 2D and SWAF-HR (21%) and GIEMS-D3 (17%), while MGB 1D is in better agreement with SWAF-HR (14%). The time series show that MGB, GIEMS-D3 and SWAF-HR estimates are contained within the maximum-minimum range of Hess product (green lines), except for dry years in SWAF-HR and most dry periods in GIEMS-D3. Additionally, SWAF-HR indicates that the minimum annual flood extent decreased during the last three years due to an intense drought that affected the region (PARRENS et al., 2019), while MGB represents this effect to a lesser extent. The smallest errors are found between MGB 1D and SWAF-HR in both mainstem and interfluvial areas, and deviations between 1D and 2D models are generally similar to the errors in relation to remote sensing products. Regarding flood extent range, MGB 2D has a smaller amplitude than 1D in the interfluvial areas, and a similar one in the mainstem. In turn, GIEMS-D3 indicates a relatively small amplitude along the Negro mainstem, but a similar range in the interfluvial wetlands.

Simulated flood volume (Figure 4.8b) reveals additional interesting aspects on the wetlands dynamics. The overall behavior of 1D and 2D models is similar to the one obtained for flood extent, i.e. the 1D has more flood volume than the 2D in the interfluvial wetlands and it is similar in the mainstem. However, one must notice the magnitude and flood season length differences between both regions. While in the interfluvial areas flood extent varies between 4600 (5700) km² and 21000 (15000) km² for the 1D (2D) model, it ranges from 2700 (2900) km² to 7810 (7760) km² in the

mainstem. For flood volume, the ranges are 8.6 (6.1) km³ to 43 (29) km³ for interfluvial and 12 (11) km³ to 45 (46) km³ for mainstem. This shows that flood volume magnitudes are similar between both areas, and since the interfluvial areas have a larger total flood extent, water depths are far higher in the mainstem Negro River. Additionally, satellite altimetry virtual stations indicate that water levels have an annual amplitude between 0.3 and 1.0 m in interfluvial wetlands, but may reach up to 8 m in adjacent rivers (Figure 4.9a). It is worth noting that the absolute amplitude of the water surface elevation variation may be slightly underestimated due to the 27-day temporal sampling of the S3-A mission. The 2D model is able to represent the small water level variation in interfluvial areas, while the 1D implementation, which has river channels in all its computational grids, has amplitudes higher than 1 m in all virtual stations. Interestingly, this is in contrast with the Negro mainstem, for which the 2D model had less attenuation and thus a higher amplitude.

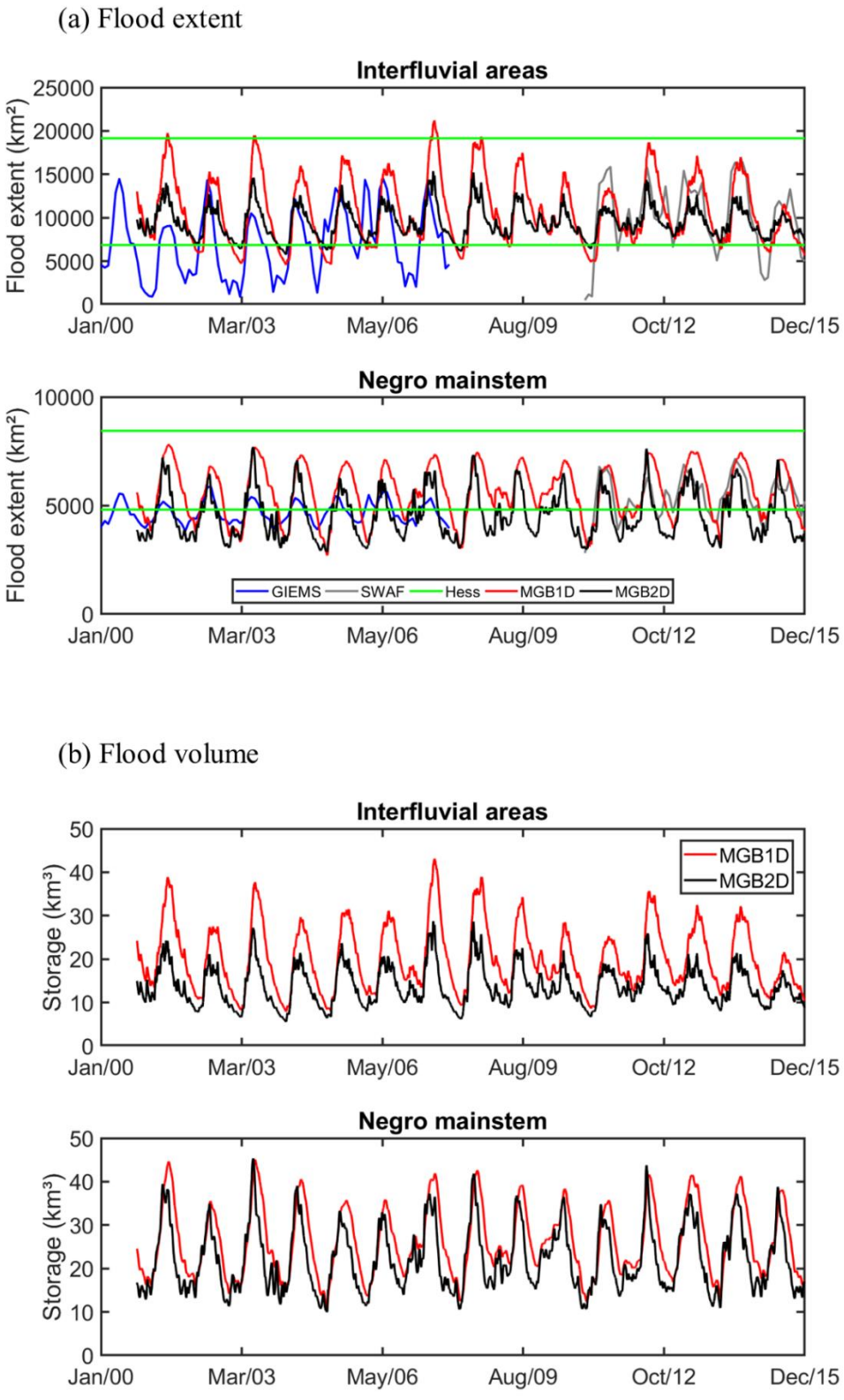

Figure 4.8. Time series of (a) flood extent and (b) volume in the Negro mainstem and interfluvial wetlands.

Simulated transects for the maximum water level (Figure 4.9b) stress the higher connectivity ensured by the 2D model, which has less variation in its water levels in comparison to the 1D one (e.g., along the Negro mainstem between distances 0.5° and 1°). This occurred because of the existing connection among all neighbor 2D cells, in comparison to the single upstream-downstream connectivity in the 1D simulation.

Finally, 2D model outputs were used to estimate floodplain flow directions across the different wetland types for a high water period (Figure 4.10). While the 1D model simulates floodplains as storage units and computes channelized flow along the single upstream-downstream connectivity direction, the 2D model allows floodplain flows among all orthogonal neighbors and channelized flow among all neighbor cells with a pre-defined channel. Figure 4.10 shows how the drainage of interfluvial wetlands (details in Figure 4.10b and Figure 4.10c) occurs with a diffuse pattern, although there are channels that ultimately drain the wetlands, leading to a flow convergence toward them. The 2D flow direction is largely dependent on the terrain elevation, so that the wetland in Figure 4.10b is mainly drained through the Demini River (large downward yellow arrows), but also through other adjacent rivers. The 1D model, however, did not represent correctly this pattern. Since the 1D drainage network was automatically derived with a GIS technique, it can create a wrong stream definition in some regions (especially the flat ones). For the case of the Demini River, it was delineated as if it was a small river flowing northward, so that the main river draining the interfluvial area was the (incorrect) south tributary located in the center of the figure (thick blue line). As a consequence, the smaller drainage capacity of the interfluvial wetlands led to the higher estimated flood volume with the 1D model. This highlights the potential errors that may arise with GIS pre-processing steps, which could be corrected with a DEM processing technique (e.g., burning the DEM with the correct drainage), but which are also avoided when the 2D model is employed. Finally, the highest floodplain flows in the Negro Basin occur along the river mainstem, especially along the Mariuá archipelago near the Negro-Branco confluence.

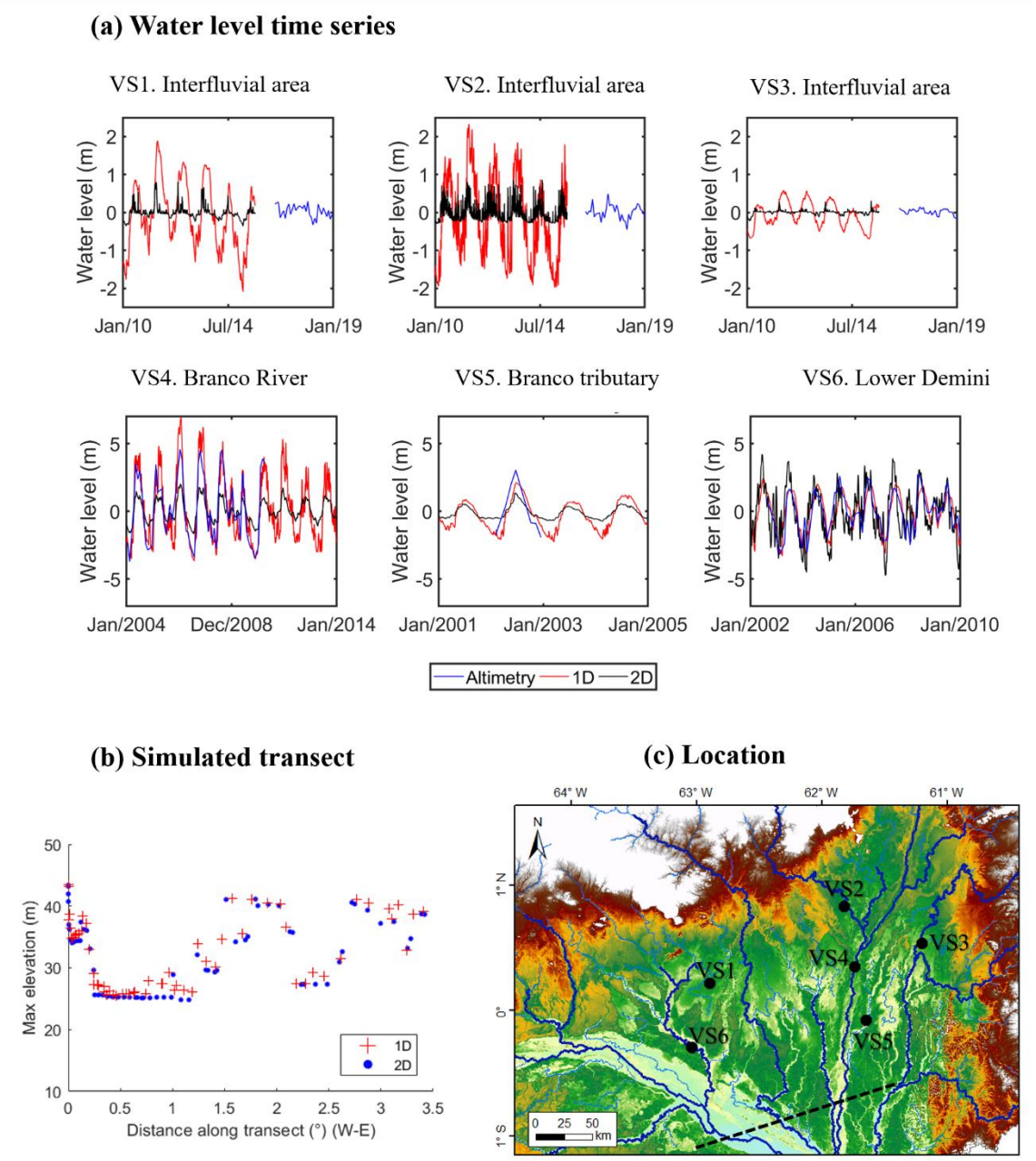

Figure 4.9. (a) Water level anomaly (i.e., water level subtracted by the long term average) time series (simulation and altimetry) for six locations across the Negro basin: three virtual stations located in interfluvial areas (VS1, VS2 and VS3) and three along rivers (VS4, VS5 and VS6). Vertical and horizontal scales are different between the upper and lower figures. (b) Maximum simulated elevation along a transect (dashed black line in figure c) for 1D and 2D models. (c) Location of the virtual stations and transect. Only large rivers are presented in the drainage network for figure readability.

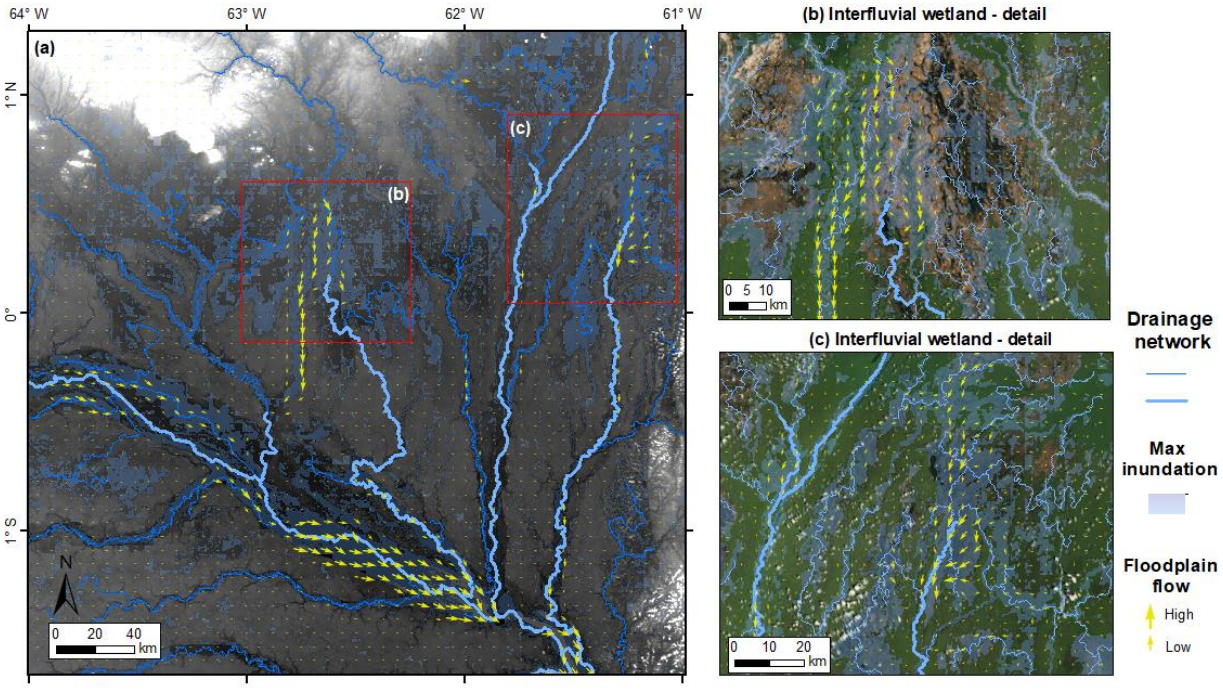

Figure 4.10. Simulated 2D floodplain flow direction and magnitude across interfluvial wetlands and Negro mainstem during high water period (19/June/2003). Source of satellite images on figures b and c: Esri, Digital Globe, GeoEye, Earthstar Geographics, CNES/Airbus DS, USDA, USGS, AeroGRID, IGN, and the GIS User Community (ESRI, 2009).

4.3.4 1D vs 2D model sensitivity to hydrodynamic parameters

To further understand the differences between 1D and 2D models, a local, one-at-a-time sensitivity analysis of model estimates to hydrodynamic parameters is performed by altering the following parameters: channel bankfull depth, width and length, channel and floodplain Manning coefficients, and floodable areas (i.e., the area from the stage-area relationship used to estimate floodplain storage and conveyance) (Figure 4.11). The assessed variables are basin outflow, water level at Moura location and flood extent in interfluvial wetlands. All values were altered from -50% to +50% of its default value, except for floodplain Manning friction which were varied from -50% to +500% (i.e. from 0.05 to 5). The large range of the latter parameter was chosen because of its uncertainties and the interest on analyzing the effect of floodplain storage, since a very high floodplain roughness value would make the 2D model closer to the 1D with storage floodplain unit.

For discharge and flood extent, the 2D model presented a smaller sensitivity than the 1D to all parameters (with the exception of floodplain Manning, which only varied

in the 2D model since the 1D has storage floodplain units). In turn, water levels had similar estimated uncertainties for 1D and 2D.

For the ±50% range, channel width, depth and Manning led to the highest uncertainties in all variables, followed by channel length, and then floodable areas. The 2D model had a small sensitivity to floodplain Manning. The reported sensitivity for the 1D model width, depth and Manning parameters is similar to the values presented by Paiva et al. (2013) and Yamazaki et al. (2011) for 1D hydrodynamic regional models.

For flood extent, the smaller sensitivity of the 2D model occurs due to its higher capacity to drain out flood waters, while altering 1D parameters leads to biases in the estimated flood extent. Results are similar for Negro mainstem flood extent and are not presented here for brevity.

Within the assessed range, with different parameter values both 1D and 2D can yield similar estimates. For instance, a channel Manning value reduction of 50% would lead to an increase in discharge (i.e. the upper bound values of 1D estimates in Figure 4.11) that would make the 1D estimate very close to the 2D one. This shows the higher drainage capacity of the 2D model, since a decrease in 1D Manning is necessary to achieve a similar performance. It is important to stress, on the other hand, the equifinality problem existent in Manning parameterization, what must be taken into account to attain realistic model estimates.

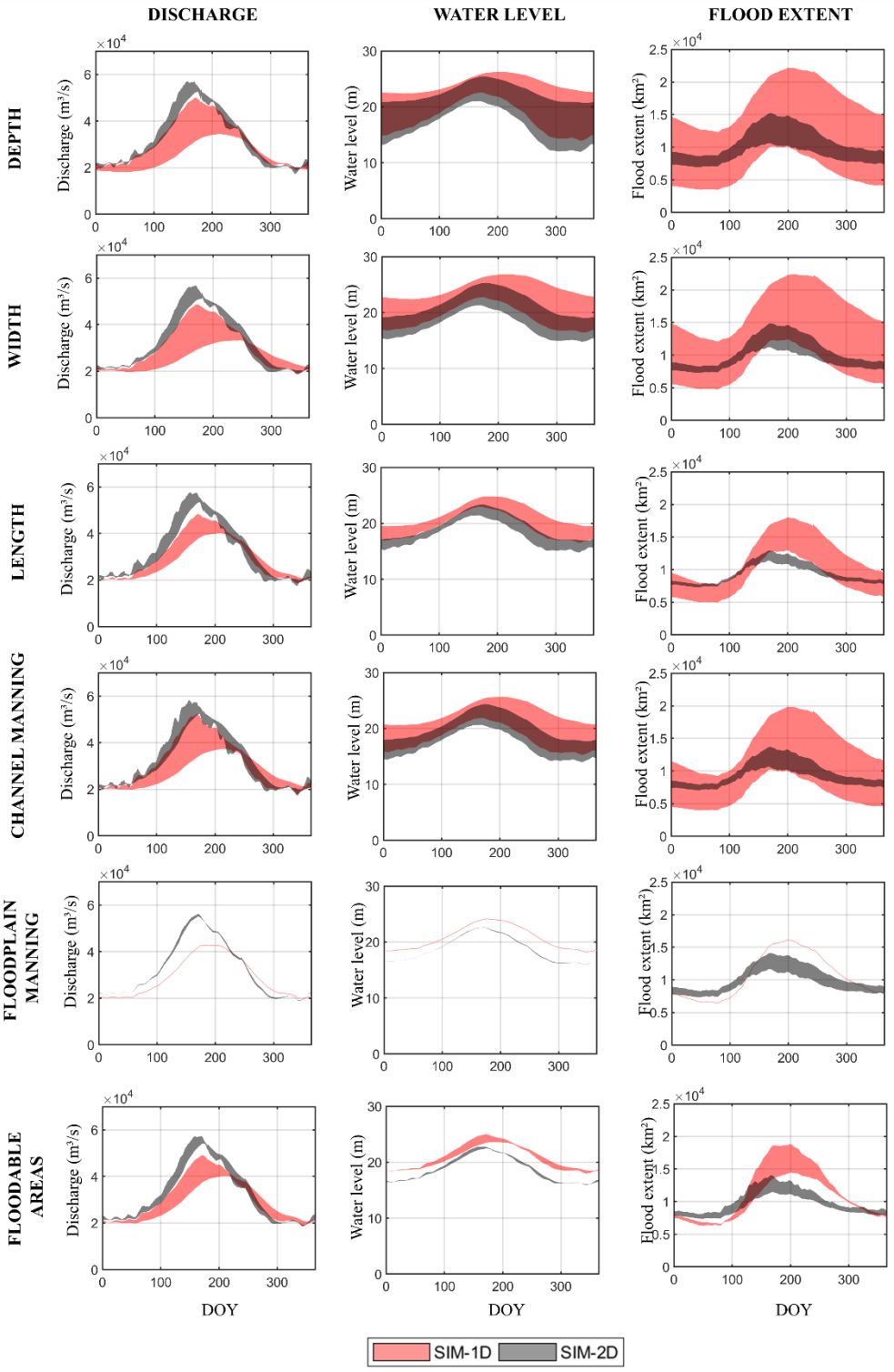

Figure 4.11. Variability of 1D and 2D simulated variables (discharge, water level at Moura location and flood extent of interfluvial wetlands) to alterations in hydrodynamic parameters (values changed from -50% to +50%): channel bankfull depth and width, channel length, channel and floodplain Manning coefficients, and floodable areas (i.e., the area from the stage-area relationship used to estimate floodplain topography

storage). Floodplain Manning is evaluated for the range between -50% and +500% and only for the 2D model, since the 1D adopts storage floodplain units.

4.3.5 On the coupling between hydrological and hydrodynamic processes

The developed 1D and 2D MGB modeling approaches allow a coupling strategy between hydrological and hydrodynamic processes, through (i) infiltration from flooded areas into adjacent unsaturated soils (the default parameter KINF=20 mm/day was adopted for simplicity, see Fleischmann et al., (2018)), and (ii) evapotranspiration computation considering the variable cell flooded fraction. In this section, simulation tests with and without these two mechanisms are analyzed.

Evapotranspiration over the whole basin (Figure 4.12) shows that the 1D model has higher rates than the 2D when open-water evaporation of flooded areas is considered. The scenario without dynamic evapotranspiration (i.e. NoETw, solid lines), i.e. considering evapotranspiration as if the cell had no flooding areas, indicates that the 1D rates would be smaller and similar to the 2D NoETw estimates. These lower ET rates would lead to higher discharges in the Negro River at Serrinha (red solid lines in Figure 4.12), which is already subjected to floodplain effects at this location, and smaller differences in the Branco River at Caracaraí, less subjected to flood storage. Differences among evapotranspiration estimates are smaller in 2D than 1D due to smaller flooded areas, what is also reflected on the simulated discharges. In turn, the effect of infiltration from flooded areas is practically negligible. Different infiltration parameters were tested (a large range between 0 and 40 mm/day as in Fleischmann et al. (2018)) and led to a similar conclusion.

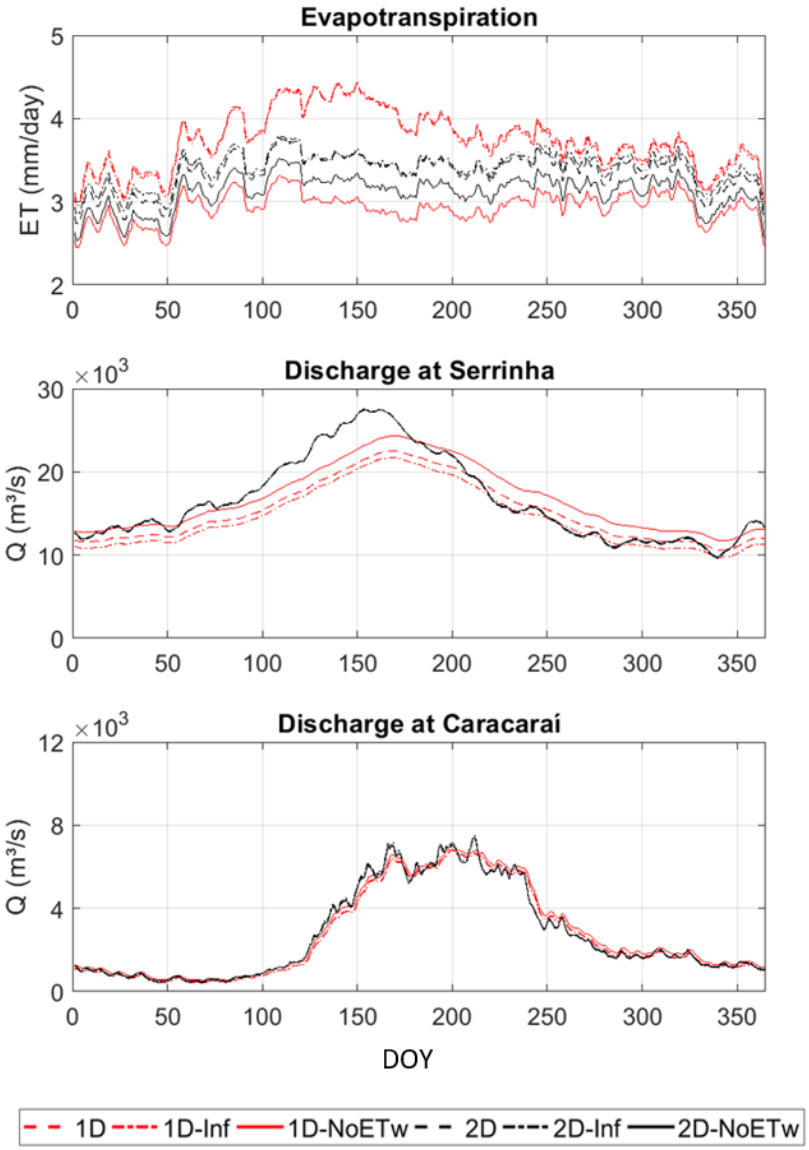

Figure 4.12. Analysis of the coupling between hydrologic and hydrodynamic processes, for simulated evapotranspiration and discharge (Negro River at Serrinha and Branco River at Caracaraí) for the scenarios default (with open water evaporation and without infiltration), "Inf" (with infiltration from floodplain into soil), and "NoETw" (without flooded areas open water evaporation).

4.4 Discussion

4.4.1 1D vs 2D hydrodynamic model estimates: comparison and uncertainties

In this study a comprehensive comparison between 1D and 2D approaches applied at regional scale (~700,000 km²) was performed. A simplified, local sensitivity analysis with one-at-a-time parameter variation (PIANOSI et al., 2016) was performed due to computational constraints, as done by previous studies of regional/continental models (Decharme et al., 2008; Paiva et al., 2013; Yamazaki et al., 2011). This study focused on hydrodynamic modeling only, so that the uncertainty in the rainfall-runoff generation process was not assessed. However, it must be recognized that part of the mismatch between simulation and observation come from uncertainty in the runoff estimates, for which the input precipitation is usually assumed to lead to the highest uncertainties (LIU et al., 2012). This is certainly the case for the Negro basin where rainfall rates are among the highest in the Amazon, and associated to major uncertainties (Getirana et al., 2011). Recent studies have discussed the role of runoff (and other water balance components) uncertainty on regional hydrodynamic models (Bermúdez et al., 2017; David et al., 2019; Grimaldi et al., 2019). Adding to this literature, we have performed tests on the role of an online (two-way) coupling between hydrologic and hydrodynamic processes. Considering a dynamic evapotranspiration and infiltration from floodplains into soils did not lead to major impacts on both 1D and 2D estimates, and model dimensionality and parameterization were more important in defining differences between the models. This is in accordance with Paiva et al. (2013) for an application in the Amazon, where soils are often wet making vegetation ET close to open water evaporation and reducing the coupling relevance. A higher impact of the coupling approach is expected for wetlands as the Pantanal (DA PAZ et al., 2014), Okavango Delta (BAUER; GUMBRICHT; KINZELBACH, 2006) and Niger Inner Delta (Fleischmann et al., 2018). The latter, for instance, is a semi-arid wetland where the interaction between wetlands and regional climate is very relevant (TAYLOR, 2010). The online coupling also requires a proper parameterization of open water evaporation (Penman equation in our case) as well as wetland infiltration capacity, which is complicated in large ungauged wetlands. This, however, suggests that more research should be performed to better understand how feedbacks occur between wetlands and the adjacent soils and atmosphere, e.g., by using micrometeorological and eddy-covariance flux towers across wetland systems (BORMA et al., 2009).

Both 1D and 2D MGB models were capable to estimate satisfactory discharges and water levels along major rivers. Major differences occurred between 1D and 2D models for flood extent and volume estimates. The 2D model generally led to less flooding (lower flood extent and flood volume and less attenuated discharges), due mainly to an enhanced drainage capacity through floodplain and channel cells. Changes in parameter values mainly altered the flood extent during high water periods, while low water values remained similar. In turn, the 1D led to far more flooding than the 2D (i.e.,

it totally filled the interfluvial depressions), and it was also more sensitive to hydrodynamic parameters.

Regional scale models differ from the reach scale ones through coarser resolution and typical subgrid approach. The decoupled formulation presented here has been called 1.5D or quasi-2D, and usually do not represent momentum transfers at confluences, while proper 2D models should be able to account for local scale processes as recirculation zones and mixing layers, and more localized head losses (CHEN et al., 2018), associated for example to local scale floodplain obstacles and channel bends. In this study a 4 km spatial resolution was adopted, which is in accordance with current regional models for continuous simulation (O'Loughlin et al., 2020). Increasing resolution will not necessarily improve model performance (Bernhofen et al., 2018; Dottori et al., 2013), and at different scales different processes will be represented, and diverse parameter values are likely to be required. Mateo et al. (2017) evaluated the bifurcation scheme of 1D CaMa-Flood (Yamazaki, et al., 2014b), which was developed to better represent complex wetlands with 2D flow patterns. They concluded that this implementation led to flow connectivity and maintained flow capacity within river floodplains at different model resolutions. The CaMA-Flood 1D model with single upstream-downstream connectivity had restrictive flow directions, and when a fine resolution was applied, excessive backflow occurred in lateral tributaries, while the bifurcation scheme did not lead to it. These results are in accordance with the ones obtained in this study. Besides, this study showed that the 2D model was less sensitive to hydraulic parameters than the 1D. This suggests that, even with relatively similar outputs, the former could be preferred to be adopted, especially considering the uncertainties inherent to large scale model parameterization. Smaller variability in 2D predictions in relation to 1D was also found elsewhere (COOK; MERWADE, 2009).

More attention should be paid for uncertainties on regional model structure. For example, a few studies have addressed the definition of subgrid flow parameters. Although subgrid methods are used in all scales (CASULLI; STELLING, 2011), e.g., porosity parameters in urban flood models to simulate building effects on storage and conveyance (Dottori & Todini, 2013; Sanders et al., 2008), particular settings are adopted for regional models. In this study, 2D channel flow was allowed between all neighbors (D8), while others have adopted a D4 direction (Neal et al., 2012). Upscale of flow directions algorithms (PAZ; COLLISCHONN; LOPES DA SILVEIRA, 2006) could be adopted to estimate channel flow with a single upstream-downstream connectivity, especially where wetland diffuse flow does not occur. 2D floodplain flow width was defined based on the connected pixels at each cell face, while other models adopt different strategies for it, e.g., flooded area divided by cell length (Getirana et al., 2017a). The effect of not properly considering channel length within a cell must also be addressed (PAZ; COLLISCHONN, 2007). In this study, the vector-based 1D model yielded less uncertain river lengths for major rivers in comparison to the 2D one with flow slope based on the cell size.

4.4.2 On the capability of 1D and 2D models to simulate different wetland types

For comparisons between hydrodynamic models, it is fundamental to consider wetlands with contrasting hydraulics (BERNHOFEN et al., 2018). The Negro River Basin is an interesting case study for understanding the capability of regional hydrodynamic models to represent processes at varying wetland types. While river floodplains typically have high water level variation and volume derived from both local and upstream catchments, interfluvial wetlands are more dependent on local runoff and rainfall (JUNK et al., 2011; REIS et al., 2019b), and present smaller water level amplitudes. The way that 1D and 2D models represent these divergent flows defines the overall capacity of each one to simulate flood dynamics. Furthermore, the diverse wetlands may have different sensitivity to extreme events. For instance, a recent drought has caused a large decrease in the Negro interfluvial wetlands flood extent (see the decrease in SWAF-HR estimates during the last three years in Figure 4.8a), while the floods along the mainstem, which respond to a much larger upstream drainage area, seemed to be less impacted. The hydrological regime in interfluvial wetlands may also be less impacted by human alterations in the mainstem than in river floodplains, given the smaller surface connectivity between mainstem and interfluvial areas. However, this hypothesis must be further assessed, including possible wetland-groundwater interactions, and especially considering the current scenario in the Branco River basin, where a large dam is planned to be built in the next years (LATRUBESSE et al., 2017a).

Our results show that 1D and 2D models respond differently for each wetland type. While 1D and 2D models had similar performance for flood extent and volume, discharges and water levels in the Negro mainstem, the main difference related to the interfluvial wetlands. 1D models are developed for river floodplains, and they are expected to be sufficient for large scale in-channel river hydrodynamics only (Schumann et al., 2013). They have typically adopted floodplains as storage units, although exceptions do exist (Getirana et al., 2017a).

Along the interfluvial wetlands, no channel dominates the flow pattern, so that the consideration of channels in the 1D model led to high and erroneous water level amplitude (Figure 4.9). The 2D was able to reproduce the small amplitude (<1 m) which is characteristic of rain-fed wetlands. An interesting future validation for such poorly gauged wetlands relates to fusing model estimates with remote sensing, swath-based water level estimates (Alsdorf et al., 2007; Cao et al., 2018; Kim et al., 2017), and assessing the assumption of a horizontal water level in the models' cells. In our modeling framework, following the current state-of-the-art regional scale models, water level was assumed horizontal within a model unit (~4 to 10 km). Although a high resolution 2D model (e.g., 90 m) may correctly represent the heterogeneous water surface elevation reported in floodplains (Alsdorf, 2003), this is certainly not the case of coarse resolution 1D and 2D models.

The 1D model could not represent the drainage that occurs along the interfluvial wetlands, so that water storage was erroneously large. With the 1D model, the wetland behaved as a laterally constrained floodplain (in the sense of Hunter et al. (2007)). The 2D regional model also enhanced connectivity (especially for large wetlands), as showed for the Negro mainstem, which is in accordance with recent regional hydrodynamic model studies (Altenau et al., 2017; Bernhofen et al., 2018; Fleischmann et al., 2018; Mateo et al., 2017; Neal et al., 2012). This study outcomes are relevant for the modeling of other basins such as the Congo (Revel et al., 2019; Tshimanga & Hughes, 2014), which presents complex hydraulic controls (O'Loughlin et al., 2013) and interfluvial wetlands (Jung et al., 2010; Kim et al., 2017; Yuan et al., 2017) along the large Cuvette Centrale that are still poorly understood.

Water storage is a fundamental variable to understand global biogeochemical cycles and wetland water balance, and to foster water resources and flood risk management related to climate variability (Frappart et al., 2014, 2012, 2005; Papa et al., 2013; Schumann et al., 2016; Yuan et al., 2017). In the case of the Negro Basin, flood storage is generally smaller in interfluvial wetlands due to smaller water depths than river floodplains. Both 1D and 2D models agreed on it, although 1D seemed to overestimate floods in the former. The structure of 1D models is designed for river floodplains, and complex wetlands with diffuse patterns and many outflow drainage channels may lead to overestimation of flood storage. On the other hand, the 2D model applied here suggested that flood storage was too small, and a better parameterization could perhaps be achieved, e.g., by refining the definition of cells without channel flows (Figure S1d in Supp Information S1).

Finally, discrepancies between flood extent estimated by models and remote sensing highlight the importance of better understanding and considering the uncertainties inherent to each classification method. Part of the disagreement is related to the fact that the remote sensing products are not fully consistent among themselves. Also, datasets driven by passive microwave observations (GIEMS-D3 and SWAF-HR, typically of ~25km spatial resolution before being downscaled) have difficulties to retrieve very small wetlands due to the inherent low resolution of original data (PARRENS et al., 2019; PRIGENT et al., 2007), while the models and SAR based products can better achieve this. Small allocation errors or noise can slightly change the results, even if the overall pattern is satisfactory. The better agreement between model and SWAF-HR may be explained by the fact that the latter uses an improved DEM (MERIT) in comparison to GIEMS-D3. Since MGB also uses MERIT as auxiliary information, what might reinforce the agreement with SWAF-HR. Furthermore, SWAF-HR was developed specifically for the Amazon (as is Hess product), so that it is expected to have a better performance than global products as GIEMS-D3. Comparison and validation of flood extent is not trivial because of the lack of in situ data. The conclusions here should be considered with care as the remote sensing datasets do not all cover the same time period and one of them was used for model calibration (i.e. Hess map to define 2D cells without channels).

4.4.3 Towards better estimates with 1D and 2D regional hydrologic-hydrodynamic models

The choice between 1D or 2D physically-based models to realistically simulate river-wetland processes depends on the scale and variables of interest, and the intended application with its required accuracy (e.g., environmental impact assessment, flood hazard studies, biogeochemical and sediments estimates, etc.). Data availability is also a fundamental element of decision, since good DEM's are required for accurate, locally relevant 2D flood modeling, but seem to be less important for 1D models that aggregate floodplain storage within coarse units (FLEISCHMANN; PAIVA; COLLISCHONN, 2019). Our results showed that the type of wetlands being simulated is also relevant: a river floodplain can be satisfactorily represented by both 1D and 2D approaches for variables as discharges, water levels and flood extent, but interfluvial wetlands, which are less connected to the main river systems, would require a 2D approach, given the nature of the diffuse flow pattern. Besides, given that the 2D scheme was less sensitive to most hydraulic parameters than the 1D one, it could be chosen preferably. The higher 2D computational cost is also relevant, since it computes flows across all neighbor cells, and not only along upstream-downstream direction as in the 1D case. When fast models are required, and especially for estimating discharges, simplifications of model equations (e.g., Muskingum-Cunge routing) may be implemented for the whole basin or for only part of it, for which kinematic routings are usually sufficient (David et al., 2015; Follum et al., 2017; Getirana et al., 2017a; Paiva et al., 2013). An optimum setup is likely related to a 1D-2D coupling strategy (Andreadis et al., 2017; Hoch et al., 2017b; Hodges, 2013), e.g., the hybrid model systems used to represent river-lake modeling systems (Dargahi & Setegn, 2011; Li et al., 2014; Lopes et al., 2018; Munar et al., 2018; Tanaka et al., 2018; Zhang et al., 2017), and adaptive model meshes are also promising (Hoch, et al., 2017a). In the case of the Negro basin, a 1D river-floodplain simulation could be performed for most of the basin, and a 2D mainly for the interfluvial wetlands and the large floodplains around Negro mainstem (in the case that other output variables than discharge are required). A mixed 1D/2D model capability has already been developed for simulating regional areas at coarse scale, including LISFLOOD-FP subgrid model to deal with subgrid floodplain channels (Neal et al., 2012; Schumann et al., 2016), the MGB lateral connections scheme (FLEISCHMANN et al., 2018; PONTES et al., 2017), the CaMa-Flood bifurcation scheme (Ikeuchi et al., 2015; Mateo et al., 2017; Yamazaki et al., 2014), and the SIRIPLAN model for the Pantanal wetlands (PAZ et al., 2011). In all these approaches, however, the subgrid parameterization poses important challenges as discussed previously, e.g., definition of floodplain flow among neighbor cells. We finally stress that model intercomparison projects are paramount to guide the selection of model dimensionality, including different model structures and case studies, and that new frameworks to compare large scale hydraulic models are required, especially when considering models at different spatial resolutions and with different model structures (e.g., subgrid parameterization) (Hoch & Trigg, 2018).

Regarding simulated processes, the MGB model is focused on surface water dynamics modeling, while soil and groundwater processes are simulated with simpler strategies. The rainfall-runoff module represents a bucket, single soil layer model, and a multi-layer scheme could improve wetlands subjected to dry periods as the interfluvial wetlands. Moving towards integrated surface-groundwater hydrosystems at regional/continental scales is fundamental (Frappart et al., 2019), e.g., with lateral groundwater fluxes and stream-aquifer interactions (FLIPO et al., 2014; MIGUEZ-MACHO; FAN, 2012). Although MGB simplistically simulates the different water table level conditions in the simplified bucket approach within a given model cell, more studies should be performed to understand the extent to which groundwater level interacts with the interfluvial wetlands to maintain their flood levels. On the other hand, earth system models should also include hydrodynamic routings in their frameworks (ZHAO et al., 2017). Finally, this study analyzed a coupled hydrologic-hydrodynamic model with calibrated rainfall-runoff parameters. It has been showed even for the continental scale that it is now feasible to satisfactorily calibrate rainfall-runoff parameters to force hydrodynamic models (Siqueira et al., 2018), and it should be pursued by current hydrologic-hydrodynamic models in order to ultimately provide the necessary flow peak estimates (Grimaldi et al., 2019).

Finally, effective parameters in large scale models should be estimated by aiming at reach scale estimates with more local relevance (Fleischmann et al., 2019), and considering meaningful hydraulic information (Garambois & Monnier, 2015), by for example understanding the river hydraulic visibility and considering remote sensing datasets and location of hydraulic controls for drainage segmentation (Frasson et al., 2017; Garambois et al., 2017; Montazem et al., 2019). Previous regional scale studies have adopted simplified empirical hydraulic geometry relationships for estimating channel width and depth (Beighley et al., 2009; Coe et al., 2008; Decharme et al., 2008, 2012; Häfliger et al., 2015; Luo et al., 2017; Neal et al., 2012; Paiva et al., 2013; Siqueira et al., 2018; Yamazaki et al., 2012), but distributed parameter values are required, especially for channel cross sections (Fleischmann et al., 2019; Grimaldi et al.,2018; Neal et al., 2015; Tuozzolo et al., 2019). There are now ways of estimating cross sections from remote sensing data (Domeneghetti, 2016; Garambois & Monnier, 2015; Grimaldi et al., 2018), especially in the context of the forthcoming SWOT mission (Biancamaria et al., 2016).

4.5 Conclusions

This study presents a comparison between 1D and 2D regional scale, fully coupled hydrologic-hydrodynamic models for an entire large river basin with extensive wetlands, and its relevance relies on the fact that most previous evaluations of hydraulic model dimensionalities were performed for local/reach scales only. Conclusions of this study are:

- Both 1D and 2D models can provide similar discharge, water levels and flood extent and volume for large rivers, especially considering parameter uncertainty;
- Regional 1D and 2D hydrodynamic models do not provide similar results for complex interfluvial wetlands, where the accurate representation of the diffuse flow pattern and local drainage processes and distributaries is fundamental. In this case 2D models are preferable;
- The 2D model generally led to more connectivity among cells, and thus facilitated water drainage throughout the basin;
- Model calibration of 1D or 2D models can lead to similar discharge and water surface elevation results; however, effective parameter values (e.g., bankfull width and depth and Manning roughness) may be out of the realistic parameter ranges expected at local scales. In this study, the adopted parameter values were parsimoniously kept within realistic ranges;
- A sensitivity test indicated that the 1D model has an overall larger sensitivity to hydrodynamic parameters for discharge and flood extent, but not for water levels;
- The coupling between hydrologic and hydrodynamic processes is less important than differences in hydrodynamic model dimensionality and parameter uncertainty in the case study (Negro basin, a major tributary of the Amazon).

Such comparison studies are fundamental to foster better understanding of current regional scale models, and to provide important insights for guiding future model developments, especially in the context of future remote sensing observations capabilities and improved computational capacity. Especially, given SWOT and other high resolution remote sensing data that are arising for estimating hydrodynamic parameters, there is a great opportunity to improve regional scale models towards hyperresolution and more detailed process representation.

5 How much inundation occurs in the Amazon?

This chapter is presented as a research article, to be submitted to the Remote Sensing of Environment journal.

- Fleischmann, A., Papa, F., Fassoni-Andrade, A., Melack, J., Wongchuig, S., Paiva, R.C.D., Hamilton, S., Fluet-Chouinard, E., Aires, F., Al Bitar, A., Bonnet, M.P., Coe, M., Ferreira-Ferreira, J., Fontana, R., Hess, L., Jensen, K., McDonald, K., Ovando, A., Park, E., Parrens, M., Pinel, S., Prigent, C., Resende, A., Revel, M., Rosenqvist, A., Rudorff, C., Silva, T., Yamazaki, D., Collischonn, W., in preparation. How much inundation occurs in the Amazon?

5. Qual a extensão de áreas inundadas nas áreas úmidas da Amazônia?

A bacia do rio Amazonas abriga alguns dos maiores complexos de áreas úmidas do planeta. Milhares de pessoas e variados ecossistemas estão adaptados à sua dinâmica sazonal de inundação, e importantes processos biogeoquímicos ocorrem ali. A estimativa de variações de inundação, em múltiplas escalas espaciais e temporais é, portanto, fundamental para a compreensão da hidrologia, ecologia, biogeoquímica, economia e gestão de desastres naturais da bacia. Nas décadas recentes, mais de 50 produtos de inundação em variadas escalas espaciais foram geradas para a região. No entanto, grandes diferenças existem entre estas estimativas, e uma avaliação compreensiva destas se faz necessária. Assim, este estudo apresenta uma intercomparação de 29 produtos de inundação para a bacia amazônica considerando produtos baseados em sensoriamento remoto, modelagem hidrológica e combinações destas, que são subdivididos em 18 produtos de escala de bacia e 11 de escala local/subregional. As resoluções espaciais variam de 12.5 m a 25 km, e as temporais de estáticas a mensais, cobrindo até algumas décadas de extensão temporal. A inundação máxima de longo período ao longo da bacia (áreas baixas com altitude inferior a 500 m) é estimada em 599,700 ± 81,800 km² se considerar apenas os produtos baseados em radar de abertura sintética (SAR), e 490,300 ± 204,800 km² considerando todos os 18 produtos. No entanto, mesmo os produtos SAR de maior resolução espacial subestimaram os valores máximos estimados localmente, sugerindo uma subestimativa de ~10% ao longo da bacia. A inundação mínima apresentou uma discrepância maior: 112,392 ± 79,265 km² com todos os produtos, e 139,300± 127,800 km² com aqueles baseados em SAR. As diferenças existem devido à variabilidade interanual, data de aquisição dos produtos, diferenças nos algoritmos, resolução espacial e inconsistências relacionadas ao processamento de dados. A área total de planícies de inundação médias a grandes (> 1,000 km² de área de drenagem) foi de 323,700 km² (valor mediano), excedendo a inundação estimada para áreas úmidas interfluviais e pequenas planícies. A melhor concordância foi observada para áreas de água aberta, como na várzea do baixo rio Amazonas, enquanto uma concordância intermediária foi obtida em planícies de inundação florestadas ao longo de rios (como as planícies do alto e médio rio Amazonas). Uma importante discordância foi obtida para as áreas interfluviais (Llanos de Moxos, Pacaya-Samiria, Negro e Roraima), onde a inundação tende a ser mais variável no tempo. Enquanto dados de SAR têm maior resolução espacial e acurácia, séries de longo termo são hoje disponíveis com produtos baseados em micro-ondas passiva e modelagem hidrológica. Os últimos apresentam uma satisfatória performance principalmente em planícies de inundação. Terminamos por identificar as principais lacunas do conhecimento relacionadas ao mapeamento de inundações na Amazônia, considerando múltiplas observações e as futuras missões de satélites orientadas a hidrologia, e recomendando futuros desenvolvimentos para as estimativas de inundação na maior bacia hidrográfica do planeta. Uma aplicação WebSIG

(https://amazon-inundation.herokuapp.com/) foi desenvolvida para permitir uma fácil visualização dos produtos aqui avaliados.

Este capítulo é apresentado na forma de um artigo científico, a ser submetido para o periódico Remote Sensing of Environment:

- *Fleischmann, A., Papa, F., Fassoni-Andrade, A., Melack, J., Wongchuig, S., Paiva, R.C.D., Hamilton, S., Fluet-Chouinard, E., Aires, F., Al Bitar, A., Bonnet, M.P., Coe, M., Ferreira-Ferreira, J., Fontana, R., Hess, L., Jensen, K., McDonald, K., Ovando, A., Park, E., Parrens, M., Pinel, S., Prigent, C., Resende, A., Revel, M., Rosenqvist, A., Rudorff, C., Silva, T., Yamazaki, D., Collischonn, W., em preparação. How much inundation occurs in the Amazon?*

Abstract

The Amazon River basin harbors some of the largest wetland complexes on Earth, on which thousands of people rely for their livelihoods, contrasting ecosystems are adapted to its seasonal inundation dynamics, and major biogeochemical processes occur. Estimation of inundation variations, at diverse spatial and temporal scales, is thus fundamental to the hydrology, ecology, economy, disaster management and biogeochemistry of the basin. In recent decades, more than 50 inundation datasets at various spatial scales have been generated for this region. However, major differences exist among the multiple estimates, and a comprehensive assessment of them is lacking. To address this question, we present an intercomparison of 29 inundation datasets for the Amazon basin considering remote sensing-based products, hydrological models and products based on a combination of sources, which are further divided into 18 basin-scale and 11 local/subregional-scale datasets. Spatial and temporal resolutions range from 12.5 m to 25 km, and from static to monthly interval, covering up to a few decades. The long-term maximum inundation across the entire basin (lowland areas with elevation < 500 m) is estimated as 599,700 ± 81,800 km² if considering only the synthetic aperture radar (SAR)-based products, and 490,300 ± 204,800 km² if considering the 18 basin-scale datasets. However, even the highest resolution SAR-based product underestimated the local maximum values, suggesting basin-wide underestimation of ~10%. The long-term minimum inundation extent showed greater disagreement; 112,392 ± 79,265 km² was obtained for all products, and 139,300± 127,800 km² for SAR-based products. Differences arise from interannual variability, date of acquisition, algorithm differences, spatial resolution, or inconsistencies regarding data processing. The median total inundation area of medium to large river floodplains (> 1,000 km² of drainage area) was 323,700 km², exceeding the estimated inundation in smaller floodplains and interfluvial wetlands. The best spatial agreement was observed for open water areas such as along the lower mainstem rivers, whereas intermediate agreement was found along major vegetated floodplains fringing larger rivers (e.g., Amazon mainstem floodplain). A striking disagreement exists among interfluvial wetlands (Llanos de Moxos, Pacaya-Samiria, Negro, Roraima), where inundation tends to be more variable in time. While SAR data have higher spatial resolution and accuracy, long-term time series are available with passive microwave-based products or hydrological models. The latter tend to perform satisfactorily mainly over river floodplains. We finish by identifying the major knowledge gaps regarding inundation mapping in the Amazon, considering multiple applications and the forthcoming hydrology-oriented satellite missions, and by providing recommendations for future developments of inundation estimates for the largest river basin in the world. A WebGIS application (https://amazon-inundation.herokuapp.com/) was developed to provide user-friendly visualization of the inundation datasets.

Key words: flooding, surface water extent, floodplains, interfluvial wetlands

5.1 Introduction

Aquatic ecosystems cover extensive areas of the Amazon basin, and are associated with temporally and spatially dynamic habitats such as floodable forests, savannas and grasslands, and large and small rivers and lakes (HESS et al., 2015; JUNK et al., 2011; MELACK; COE, 2021; REIS et al., 2019b). These systems, hereafter called wetlands, are adapted to the flood pulse and play key roles in regional and global biogeochemical cycles, especially the carbon cycle (ABRIL et al., 2014; GUILHEN et al., 2020; MELACK et al., 2004; PANGALA et al., 2017), and regulate the riverine transport of dissolved and particulate material, including sediment and organic matter (ARMIJOS et al., 2020; FASSONI-ANDRADE; PAIVA, 2019; MELACK; FORSBERG, 2001; WARD et al., 2017). Human settlements along Amazonian wetlands have existed for thousands of years (BLATRIX et al., 2018; DENEVAN, 1996), and have benefited from various ecosystem services including food provision from native plants and animals as well as crops and livestock (COOMES et al., 2010, 2016; JARDIM et al., 2020). Much of the wetland area is considered floodplain because it is subject to seasonal or sporadic flooding by river overflow or local rainfall, and the spatiotemporal patterns of inundation (i.e., the flood pulse). Water sources and geomorphology interact to determine the structure and function of these biodiverse ecosystems (JUNK et al., 2011; LATRUBESSE, 2012). In addition, large interfluvial wetlands occur, which contrast with floodplains by being flooded mainly by local rainfall and runoff and with shallow water (BELGER; FORSBERG; MELACK, 2011; JUNK et al., 2011).

Today, 34 million people live in the Amazon basin (Agudelo et al., 2020), of which a large portion live near rivers. Many urban centers are facing intensified flood risk (e.g., Porto Velho, Rio Branco, Iquitos, Cruzeiro do Sul; (LANGILL; ABIZAID, 2020)) as a consequence of changes in the regional climate (BARICHIVICH et al., 2018; ESPINOZA et al., 2019a) and insufficient flood risk management (ANDRADE et al., 2017; MANSUR et al., 2016). Rural livelihoods (e.g., agriculture, fisheries) and sanitation (e.g., waterborne diseases) are affected by floods, especially large ones (COOMES et al., 2016; LANGILL; ABIZAID, 2020; ROSINGER, 2018). The Amazon basin is thus in transition due to anthropogenic pressure and climate variability (BARICHIVICH et al., 2018; DAVIDSON et al., 2012; LATRUBESSE et al., 2017b), which calls for a better understanding of its water resources and inundation regime. This observation was reinforced in 2021, with the highest recorded river level over the last 119 years at Manaus, in the central basin.

The extent of land subject to inundation (also called flood or surface water extent) is a core variable to understand wetland processes, and is of interest for multiple scientific disciplines including ecology (Silva et al., 2013), surface-atmosphere energy interactions (SANTOS et al., 2019; TAYLOR; PRIGENT; DADSON, 2018), carbon cycle and greenhouse gas emissions (GUILHEN et al., 2020; MELACK et al., 2004; RICHEY et al., 2002), and natural hazard management (Restrepo et al., 2020; Trigg et

al., 2016). The Amazon basin has been a focus for remote sensing developments in hydrology (FASSONI-ANDRADE; FLEISCHMANN; PAPA, 2021), and especially for inundation estimation, given its global environmental relevance, relatively pristine landscape, and technical challenges posed by persistent cloud cover and dense vegetation (Table 5.1, with the datasets addressed in this study, and Table 5.2, with additional ones). Optical remote sensing systems such as Landsat are of limited value in many Amazonian wetlands, where inundation tends to be obscured by persistent cloud cover and/or vegetation canopies. Large-scale wetland inundation mapping was firstly pioneered in the Amazon through analysis of nine years of SMMR passive microwave observations, which provided all-weather capability and sensitivity to inundation even when overlain with some vegetative cover (HAMILTON; SIPPEL; MELACK, 2002; SIPPEL et al., 1998). Meanwhile, research showed how the all-weather capability and superior spatial resolution of synthetic aperture radar (SAR) systems, particularly L-band SAR that penetrates forest canopies and can reveal underlying water through the "double bounce" effect, was promising for mapping inundation in the Amazon (Hess et al., 2003). In particular, the high-resolution, dual-season classification of JERS-1 L-band SAR data for the entire, lowland Amazon basin by Hess et al. (2015), validated with airborne videography images, has been used as a benchmark for the inundation extent of Amazonian wetlands. It is worth noting, however, that the JERS-1 data were mosaics of images acquired over about a month approximating the time of higher and lower water in the central Amazon mainstem. Hence, these mosaics do not include the highest and lowest inundation in other parts of the basin, which can have different seasonal patterns of inundation and drainage (HAMILTON; SIPPEL; MELACK, 2002; REIS et al., 2019b). Since these initial studies, remote sensing researchers seeking to map and characterize inundation have employed various combinations of SAR and passive microwave data (AIRES; PAPA; PRIGENT, 2013; JENSEN; MCDONALD, 2019; PAPA et al., 2010; PARRENS et al., 2017, 2019; PRIGENT et al., 2007; SCHROEDER et al., 2015).

Besides basin-scale maps that typically represent the seasons of maximum and minimum inundation (CHAPMAN et al., 2015; HESS et al., 2015; ROSENQVIST et al., 2020), many research communities (e.g., ecology, biogeochemistry, risk management) would benefit from inundation products of higher spatial and temporal resolution. Currently, dynamic products are mainly based on satellite passive microwave observations of coarse spatial resolution (GIEMS, SWAMPS, SWAF, WAD2M products - Table 5.1), which more recently have been downscaled using other datasets (AIRES et al., 2017; AIRES; PAPA; PRIGENT, 2013; PARRENS et al., 2019). Basin-scale, dynamic inundation estimates based on the ALOS satellite are limited given its low temporal resolution (repeat cycle of 46 days). Some studies have analyzed time series of ALOS-PALSAR data (ARNESEN et al., 2013; FERREIRA-FERREIRA et al., 2015) and ALOS-2 PALSAR-2 data (JENSEN et al., 2018) for subsets of Amazon wetlands. However, with a few exceptions for local scale datasets (ARNESEN et al., 2013; FERREIRA-FERREIRA et al., 2015; HESS et al., 2003; JENSEN et al., 2018; RESENDE et al., 2019), validation of these estimates has seldom been

performed, given the remoteness of much of the Amazon basin and the forest cover, which hampers airborne monitoring of below-canopy surface waters.

As an alternative approach, process-based river discharge and flooding models have been developed and assessed from basin to local scales in the major floodplain rivers of the Amazon. Local scale hydraulic models with coarse (TRIGG et al., 2009; WILSON et al., 2007) and detailed input data (JI et al., 2019; PINEL et al., 2019; RUDORFF; MELACK; BATES, 2014) have estimated inundation dynamics for wetland areas mainly in the floodplains fringing the Amazon mainstem. More recently, large-scale hydrologic-hydraulic models have been applied to the Negro savanna wetlands, which lie on interfluvial terraces between the Negro and tributary rivers (FLEISCHMANN et al., 2020b). At the large scale, the advent of new computational and modeling capabilities has allowed development of basin-scale hydrologic and hydraulic (or hydrodynamic) models (BEIGHLEY et al., 2009; COE; COSTA; HOWARD, 2008; GETIRANA et al., 2012, 2017a; HOCH et al., 2017a; LUO et al., 2017; MIGUEZ-MACHO; FAN, 2012; PAIVA et al., 2013a; YAMAZAKI et al., 2011), which have been compared to satellite-based water levels and inundation datasets.

Several inundation datasets for the Amazon basin have been developed recently (Tables 5.1 and 5.2), partially because of data availability from the ALOS-PALSAR mission and its successor ALOS-2 PALSAR-2. Differences among multiple datasets, however, have been noted (AIRES et al., 2018; FLEISCHMANN et al., 2020b; PARRENS et al., 2019; PHAM-DUC et al., 2017; ROSENQVIST et al., 2020), and a comprehensive assessment of inundation estimates for the Amazon is lacking. Meanwhile, major ongoing environmental changes in the basin underscore the need for a better understanding of Amazon hydrology (FASSONI-ANDRADE; FLEISCHMANN; PAPA, 2021). Better understanding starts with the straightforward yet fundamental question “How much inundation occurs in the Amazon?”. Although this question does not have a simple answer, quantifying its uncertainty through the evaluation of existing inundation datasets is a necessary first step. The need to compare different hydrological datasets for the Amazon has been recently highlighted in the context of river discharge (TOWNER et al., 2019), precipitation (WONGCHUIG CORREA et al., 2017; ZUBIETA et al., 2019) and evapotranspiration (PACA et al., 2019; WU et al., 2020a). To assess the state of understanding of inundation patterns in the Amazon wetlands, we address the following questions: 1) How much land is subject to seasonal inundation across the basin, and what are uncertainties in the estimates? 2) Which areas are in particular disagreement, and thus deserve further attention? 3) How do basin-scale estimates with coarser resolution and less calibrated classification methods differ from the local-scale ones or large scales ones with independent validation? 4) How do the various inundation estimation approaches (optical imagery, SAR, passive microwave, hydrologic models) differ in terms of inundation mapping, and for different wetland types (e.g., floodplains and interfluvial areas)? In order to answer these questions, we gathered an unprecedented collection of 29 inundation

datasets for the Amazon basin spanning a wide range of spatial (12.5 m–25 km) and temporal (static, dual-season, monthly, daily) scales, and from basin to local coverage (Table 5.1). In the context of forthcoming hydrological observations by satellite missions such as SWOT and NISAR, this study is timely, identifying data gaps that limit understanding of the water resources of the largest basin in the world.

Table 5.1. List of 29 studies that mapped inundation in the Amazon, from basin to local scales, and which were analyzed here based on data availability and relevance for this intercomparison study. *** The presented hydrologic models' time resolutions are the values assessed or provided by the models, which may be able to provide higher time resolution if necessary, since many of them actually compute flood maps at daily or sub-daily time steps and report time-integrated results. The column "Type of inundation captured" has three classes: "All", meaning both open water and vegetated wetlands, "Open water", and "Wetland only (no open water)".

	Reference	Product name / Type	Spatial. res.	Temporal resolution	Time period	Region	Type of inundation captured
1	Aires et al., 2017	Multi-satellite / GIEMS-D3	90 m	Monthly	1993-2007	Basin	All
2	Arnesen et al., 2013	ALOS-PALSAR	90 m	Irregular	2006-2010	Curuai	All
3	Bonnet et al., 2017	Hydrological model	180 m	Monthly	2006-2019	Janauacá	All
4	Chapman et al., 2015	ALOS-PALSAR / SAR	90 m	Monthly	2006-2011	Basin	All
5	Coe et al., 2008	THMB / Hydrological model	5-min	Monhtly	1961-2010	Basin	All
6	Bontemps et al., 2013	ESA-CCI / mainly MERIS	300 m	annual	1992-2015	Basin	All
7	Ferreira-Ferreira et al., 2015	ALOS-PALSAR / SAR	12.5 m	Flood frequency	2007-2010	Mamirauá	All
8	Fluet-Chouinard et al., 2015	GIEMS-D15 / Multi-satellite	500 m	Monthly climatology	1993-2004	Basin	All
9	Gumbricht et al., 2017	CIFOR / Hydrological model + topographic index	232 m	Static (max inundation)	1950-2000	Basin	All
10	Hess et al., 2015	JERS-1 / SAR	90 m	Static (high and low water)	1995-1996	Basin	All
11	Jensen et al., 2018	ALOS-2 PALSAR-2 / SAR	50 m	Irregular	2014-2018	Pacaya-Samiria	All
12	Jensen and Mcdonald, 2019	Multi-satellite/SWAMPS	25 km	Monthly	1992-2020	Basin	All
13	Lehner and Döll, 2004	GLWD (data collection)	1 km	Static	1992-2004	Basin	All
14	Ovando et al., 2016	MODIS	500 m	8 days	2001-2014	Llanos de Moxos	Open water
15	Ovando et al., 2016	ALOS-PALSAR / SAR	100 m	Irregular	2006-2010	Llanos de Moxos	All
16	Park and Latrubesse, 2019	MODIS	230 m	Monthly climatology	2000-2015	Amazon River downstream of Manaus	Open water
17	Parrens et al., 2019	SWAF-HR / Passive microwave	1 km	Monthly	2010-2020	Basin	All
18	Pekel et al., 2016	GSWO / Landsat	30 m	Monthly (cloud cover may occur)	1984-2019	Basin	Open water

19	Pickens et al., 2020	Landsat	30 m	Annual/monthly climatology	1999-2018	Basin	Open water
20	Pinel et al., 2019	ALOS-PALSAR	30 m	Irregular	2007-2011	Janauacá	All
21	Pinel et al., 2019	TELEMAC-2D	30 m	Monthly	2006-2015	Janauacá	All
22	Prigent et al., 2020	Multi-satellite/GIEMS-2	25 km	Monthly	1992-2015	Basin	All
23	Resende et al., 2019	ALOS-PALSAR	25 m	Static (max inundation)	2006-2011	Uatumã	All
24	Rosenqvist et al., 2020	ALOS-2 PALSAR-2 / SAR	50 m	Max/min annual inundation	2014-2017	Basin	All
25	Rudorff et al., 2014	LISFLOOD-FP / Hydraulic model	90 m	Monthly	1994-2015	Curuai	All
26	Siqueira et al., 2018	MGB / Hydrological-hydraulic model	500 m	Monthly	1980-2015	Basin	All
27	Yamazaki et al., 2011	CaMa-Flood / Hydraulic model	500 m	Monthly	1980-2014	Basin	All
28	Yamazaki et al., 2015	G3WBM / Landsat	30 m	Static (open water areas)	1990-2010	Basin	Open water
29	Zhang et al., 2020	WAD2M	25 km	Monthly	2000-2018	Basin	Wetland only (no open water)

Table 5.2. List of additional studies that mapped inundation in the Amazon.

	Reference	Product name / Type	Spatial. resolution	Temporal resolution	Time period	Region	Type of inundation captured
1	Aires et al. (2013)	GIEMS + downscaling with SAR	500 m	Monthly	1993 - 2007	Central Amazon	All
2	Belger et al. (2011)	Radarsat-1 / C-band SAR	25 m	Irregular	2004 - 2005	Cuini and Itu (Negro basin)	All
3	Bonnet et al. (2008)	Hydrological model	90 m	Daily	1997 - 2003	Curuai	All
4	Canisius et al., 2019)	Radarsat-2 / C-band SAR	2.5 m	Irregular	2014 - 2016	Lower Amazon River	All
5	Fleischmann et al. (2020)	MGB / Hydrological-hydraulic model	4 km	Daily	1999 - 2015	Negro River basin	All
6	Frappart et al. (2005)	JERS-1 / L-band SAR	90 m	Static (high and low water)	1995 - 1996	Negro River basin	All
7	Langerwisch et al. (2013)	LPJmL / Hydrological model	0.5 degrees	Monthly	1961 - 1990	Basin	All
8	Lesack and Melack (1995)	In situ data	-	-	-	Lake Calado	All
9	Li et al. (2020)	Landsat (Mapbiomas)	30 m	Annual	1985 - 2019	Madeira River close to Santo Antônio and Jirau dams	All
10	Meyer Oliveira et al. (2020)	ALOS-PALSAR / L-band SAR	100 m	Irregular	2006 - 2010	Purus River basin	All
11	Paiva et al. (2013)	MGB / Hydrological-hydraulic model	500 m	Daily	1998 - 2010	Basin	All
12	Rodriguez-Alvarez et al. (2019)	CYGNSS / GNSS-R	500 m - 7 km	Daily	2017 - 2018	Pacaya-Samiria	All
13	Rosenqvist et al.	JERS-1 / L-band SAR	90 m	Irregular	1995 -	Jaú River basin	All

	(2002)				1996		
14	Silva et al. (2013)	Radarsat-1 / C-band SAR	25 m	Irregular	2003 - 2005	Amazon River (Juruti - Monte alegre)	All
15	Souza et al. (2019)	Landsat	30 m	Annual	1985 - 2017	Brazilian Amazon	Open water
16	Trigg et al. (2009)	LISFLOOD-FP and HEC-RAS / Hydraulic models	180 m / irregular	Daily	1995 - 1997	Solimões River (Itapeua - Manaus)	All
17	Wilson et al. (2007)	LISFLOOD-FP / Hydraulic model	270 m	Daily	1995 - 1997	Solimões River (Itapeua - Manaus)	All

5.2 Methodology

5.2.1 Study area

The Amazon basin spans around 6 million km² in nine South American countries (Figure 5.1; Latrubesse et al. (2017)). The Amazon lowlands were adopted by many inundation products and our comparisons, considering an altitude lower than 500 m, given some limitations in estimating flooding in mountainous terrain (HESS et al., 2015). The total area of lowlands assessed here is 5.11 x 10^6 km². The basin was delimited until the city of Gurupá, ~390 km from the ocean, and does not include the Tocantins-Araguaia basin and parts of the Amazon estuary or Marajó Island.

Inundation estimates were compared for 11 wetland complexes in the Amazon basin to understand how estimates may vary in accuracy among different wetland types: Curuai floodplain lake (ARNESEN et al., 2013; RUDORFF; MELACK; BATES, 2014), Janauacá floodplain lake (BONNET et al., 2017; PINEL et al., 2019), Uatumã River floodplain (RESENDE et al., 2019), Mamirauá Reserve (FERREIRA-FERREIRA et al., 2015), Pacaya-Samiria wetlands (JENSEN et al., 2018), Llanos de Moxos wetlands (OVANDO et al., 2016), lower Amazon floodplain (PARK; LATRUBESSE, 2019), Amazon mainstem floodplain (from Iquitos to Gurupá), Purus floodplain, Roraima savannas, and Negro savannas (Figure 5.1). Curuai is representative of the shallow lakes in the lower Amazon floodplain, it is separated from the river by narrow levees (RUDORFF; MELACK; BATES, 2014), and has a high suspended sediment concentration. Janauacá is typical of the middle Amazon River floodplain, and is composed of a ria lake (i.e., a blocked valley lake with black-water; Latrubesse (2012)) and "várzea" environments (white-water floodplains) in its northern part (Pinel et al., 2019). Uatumã River is an Amazon tributary with black-water floodplain ("igapó"), and includes Balbina hydroelectric reservoir, inaugurated in 1987, which affects the river's hydrological regime (SCHÖNGART et al., 2021). The Uatumã floodplain reach assessed here is the 300-km reach between Balbina dam and the confluence with the Amazon River. The Mamirauá Sustainable Development Reserve is located in the confluence between Solimões and Japurá rivers, and is characterized by a mosaic of chavascal, herbaceous, and low and high várzea vegetation (FERREIRA-FERREIRA et al., 2015). The Purus River is a major tributary, and its floodplain was chosen because of its large floodplain to river width ratio. Pacaya-Samiria wetlands are composed of

flooded forests, palm swamps and peatlands in the upper Solimões River (DRAPER et al., 2014; LÄHTEENOJA et al., 2012). The Llanos de Moxos floodable savannas occupy the interfluvial areas among Beni, Mamoré and Madre de Dios rivers in the upper Madeira basin (HAMILTON; SIPPEL; MELACK, 2004). The Negro savannas, locally known as "campinas" and "campinaranas", depending on the vegetation density, have been related to regional depressions due to neotectonic events and were called the "Septentrional Pantanal" given their large area (ROSSETTI et al., 2017a, 2017b; SANTOS; NELSON; GIOVANNINI, 1993). The Roraima savannas extend from the Roraima State in Brazil to the Rupununi savannas in Guyana, and comprise mainly smaller river floodplains interspersed with poorly drained interfluvial savannas subject to flooding by local rainfall in the upper Branco River basin (HAMILTON; SIPPEL; MELACK, 2002); here we only considered the Roraima savannas within the Amazon basin.

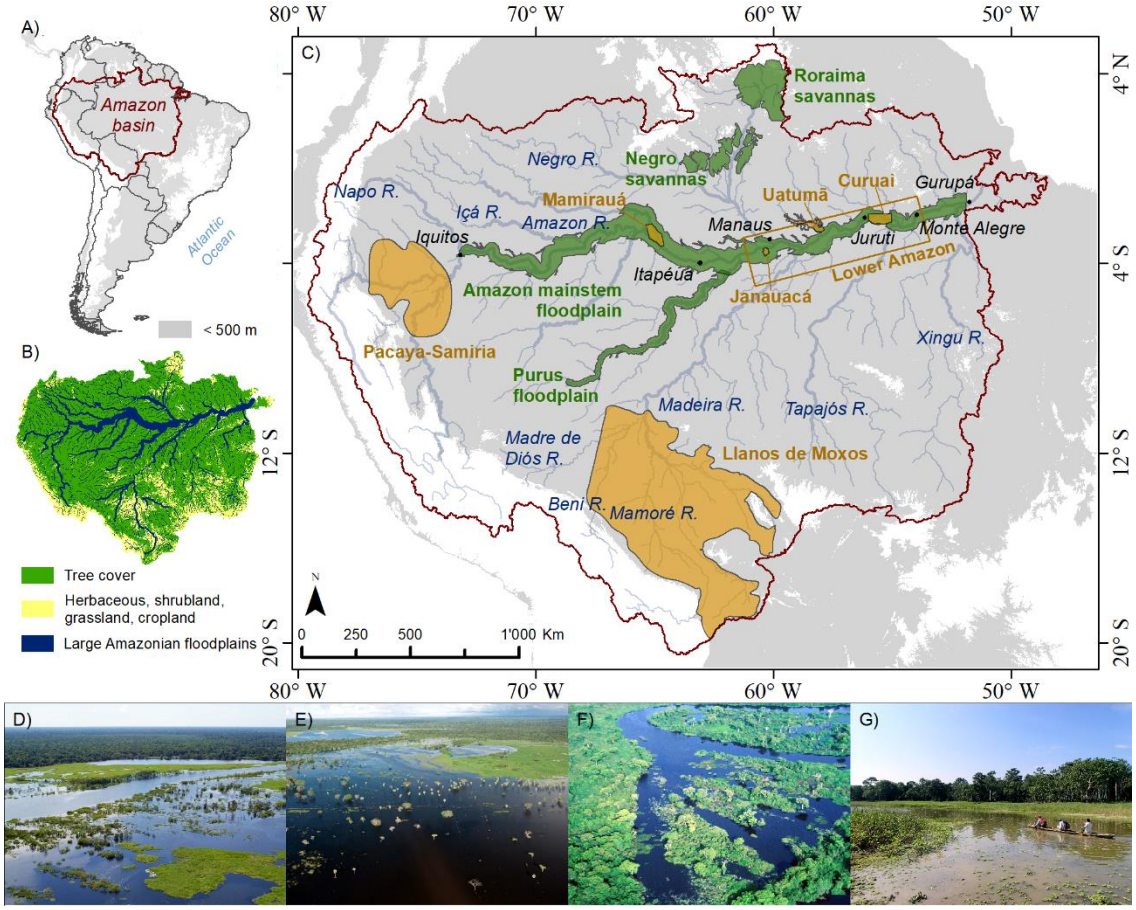

Figure 5.1 (a) Amazon basin location in South America. (b) Land cover based on a 2010 map from the European Space Agency Climate Change Initiative (ESA-CCI) (BONTEMPS et al., 2013), showing the distribution of forest and savanna across the basin, as well as large floodplains (see methodology Section 5.2.3). (c) Basin distribution of major wetland systems showing locations of interest for this study. Elevations lower than 500 m are shown in grey. The orange polygons refer to the areas

for which a local dataset was available for this study (Figure 5.4), and the green ones for wetland areas of interest that do not have products specifically designed for these subregions, yet basin-scale datasets cover them. Photos depicting different wetland complexes are presented in D-G for Mamirauá (courtesy by João Paulo Borges Pedro), Llanos de Moxos (courtesy by Luiz Claudio Marigo), Cabaliana floodplain lake close to Manacapuru (courtesy by Stephen Hamilton), and Pacaya-Samiria (courtesy by Katherine Jensen) regions, respectively.

5.2.2 Datasets

Twenty-nine inundation datasets, including multiple data sources, spatial and temporal resolutions, and scales, from local to regional and global products, were assembled (Table 5.1). The proliferation of inundation datasets in recent years is evident by the number of products published in the last 5 years: 18 out of the 29 inundation datasets had their original publication since 2016, and 27 of them since 2011. While additional products do exist (Table 5.2), these were chosen due to data availability and representativeness of the selected datasets.

Based on spatial and temporal resolution, the basin-scale datasets are divided into dynamic hydrological models (CaMa-Flood, MGB, THMB), dynamic coarse-scale (GIEMS-2, SWAMPS, WAD2M), dynamic fine-scale (GIEMS-D3 and SWAF-HR), annual fine-scale (GSWO and GLAD), dual-season fine-scale (Rosenqvist, Hess, Chapman), and static fine-scale (ESA-CCI, G3WBM, CIFOR, GIEMS-D15 and GLWD). Thus, there are eight dynamic products and 11 static or dual-season basin-scale products. In Figure 5.2, long-term flood frequency maps are provided for the dynamic products, and maximum flood extent for the static/dual-season ones.

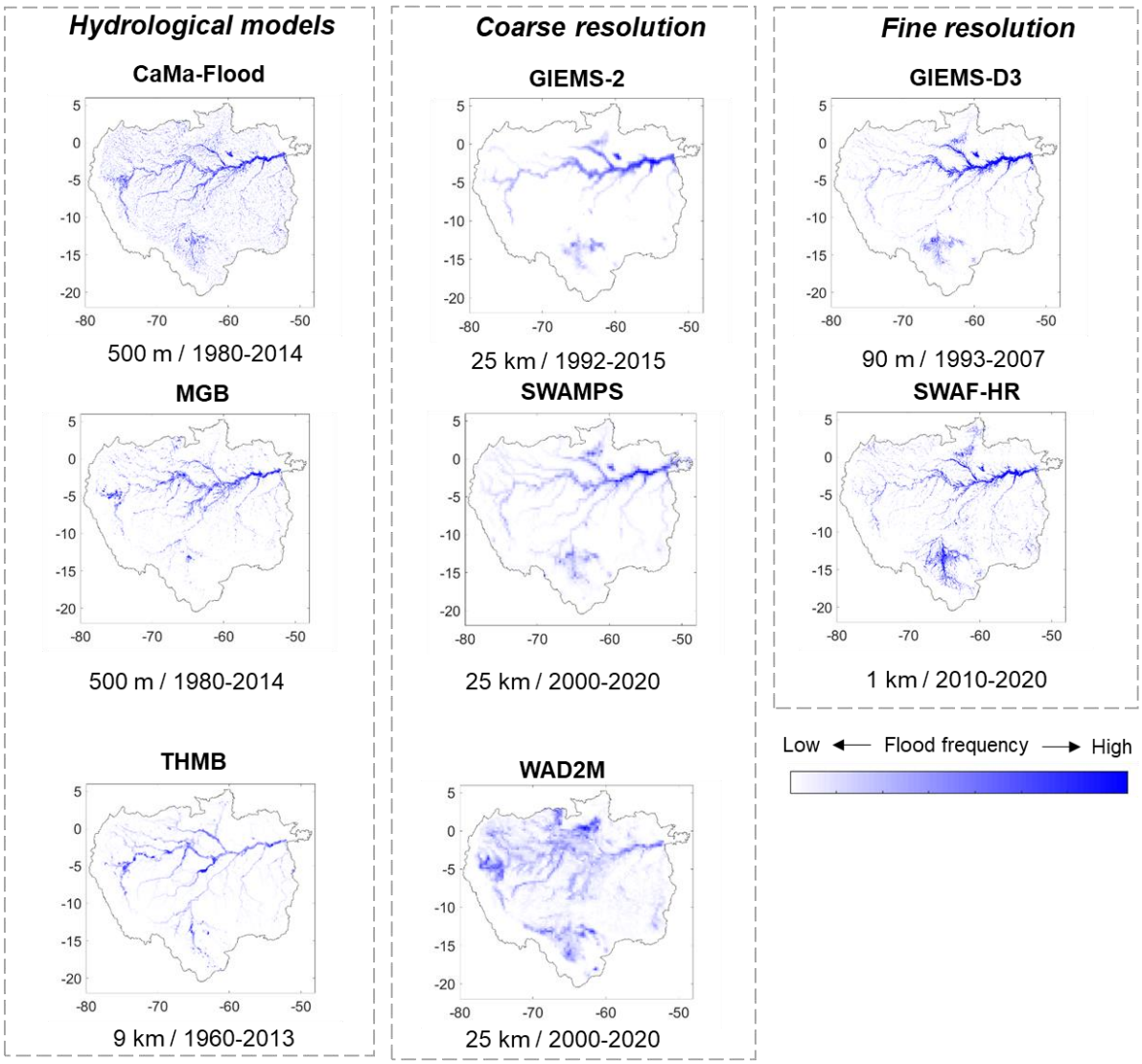

Figure 5.2. Basin-scale, dynamic inundation products used in this study. Long-term flood frequency maps are provided for each dataset. Regional products developed especially for the Amazon basin are noted with a red dot.

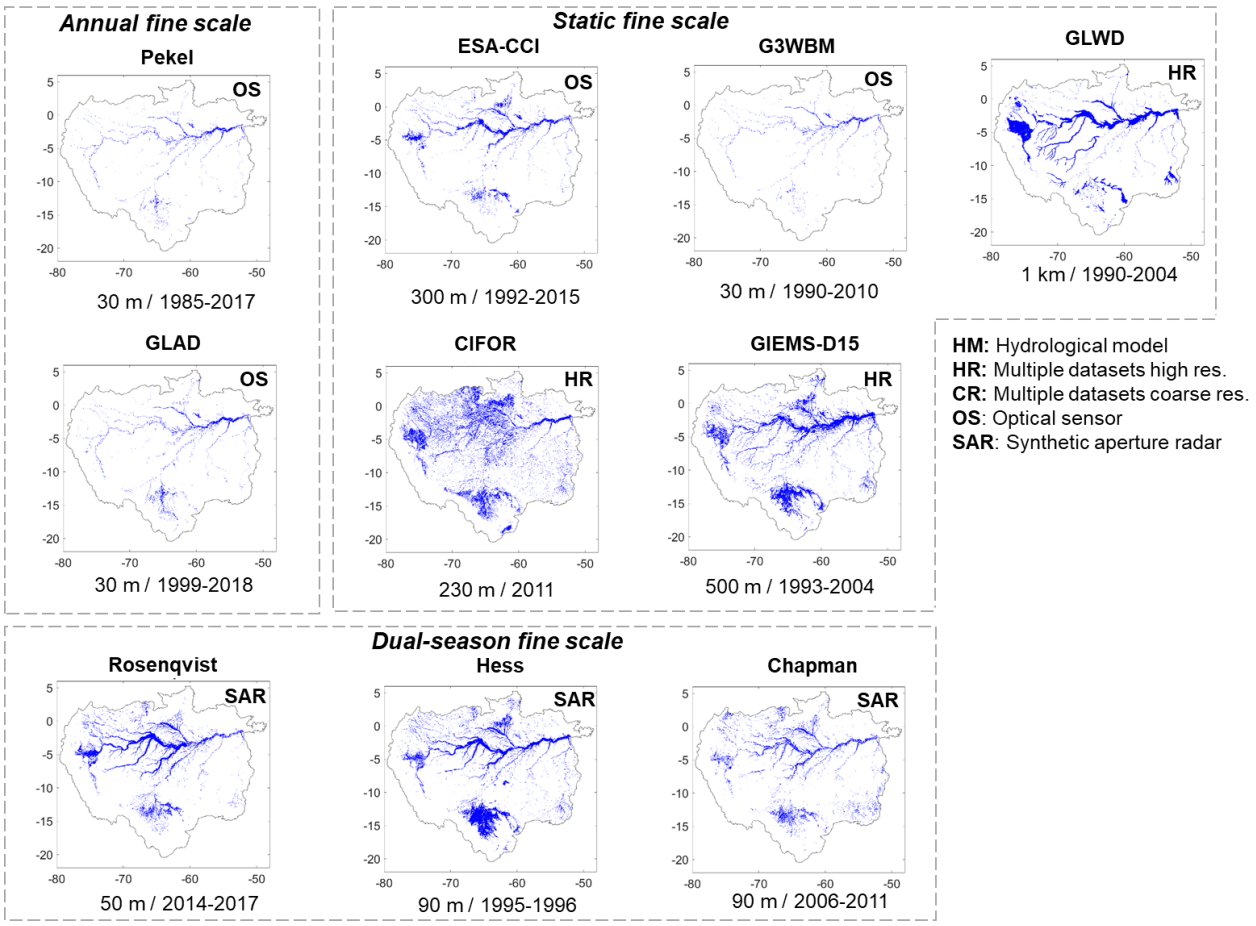

Figure 5.3. Basin-scale, static or dual-season inundation products used in this study. Regional products developed especially for the Amazon basin are noted with a red dot.

Passive microwave (PM) data are the basis of SWAF-HR, GIEMS family (GIEMS-D15, GIEMS-D3, GIEMS-2), and SWAMPS, and they use additional data (i.e., optical imagery and microwave scatterometry) to complement the PM signal. SWAF-HR is based on the SWAF SMOS-derived flood fraction. Three basin-scale products are based mainly on SAR data from JERS-1 (Hess et al., 2003, 2015), and its successor missions ALOS-PALSAR (CHAPMAN et al., 2015) and ALOS-2 PALSAR-2 (ROSENQVIST et al., 2020).

Three of the optical-based products are based on Landsat data: GSWO (PEKEL et al., 2016), G3WBM (YAMAZAKI; TRIGG; IKESHIMA, 2015) and GLAD (PICKENS et al., 2020). Although GSWO and GLAD are capable of providing monthly estimates for the Landsat archive (1984-today), given the inability of optical data to estimate flooding under cloud cover or vegetated waters only annual maximum and minimum values are used. For GLAD and GSWO, we consider a threshold of occurrence of surface water of 95% to estimate the minimum inundation (i.e., for the permanently inundated areas; Aires et al. (2018)); otherwise, only a few isolated open water areas would be considered for the minimum extent.

The European Space Agency Climate Change Initiative (ESA-CCI) product is based mainly on surface reflectance from MERIS, the Advanced Very High Resolution Radiometer (AVHRR) and PROBA-V data and Global Water Body from the Envisat Advanced Synthetic Aperture Radar (ASAR) (BONTEMPS et al., 2013). Since the wetland pixels in this product hardly varied throughout the years of observations, we choose to use only the 2010 product as the ESA-CCI estimate for wetland maximum inundation.

Another set of products is based on the fusion of multiple global datasets: GLWD, GIEMS-D15 and WAD2M. GLWD (LEHNER; DÖLL, 2004) is one of the first globally consistent databases of wetlands, which was based on a collection of wetland estimates from diverse institutions worldwide. GIEMS-D15 combines GLWD, the Hydrosheds drainage network, and Global Land Cover 2000. WAD2M is based on SWAMPS and CIFOR within its merging framework. WAD2M is the only product to not include open water (removal based on GSWO) due to its goal of estimating wetland methane emissions. The SWAF-HR (PARRENS et al., 2019) and GIEMS-D3 (AIRES et al., 2017) products use additional data and methodologies to downscale the original passive microwave-based SWAF (PARRENS et al., 2017) and GIEMS (PAPA et al., 2010; PRIGENT et al., 2007) products from 25 km to 1 km and 90 m, respectively. While the GIEMS-D3 has a different inundation magnitude than the original GIEMS product, SWAF-HR has the same magnitude as the original one.

Among hydrological models we use one of the following modeling types: 1) a process-based hydrologic model that has any kind of flood routing able to represent inundation processes (i.e., from a simple kinematic wave model coupled to an inundation method to more complex flow routing methods); or 2) a hydraulic (or hydrodynamic) model that considers the shallow water equations (or its simplifications) at any dimension (1D, 2D or 3D). For our analysis, we adopted one basin-scale hydrologic model (THMB; Coe et al. (2008)), a basin-scale hydrologic-hydrodynamic model (MGB, Siqueira et al. (2018)) and a global-scale one (CaMa-Flood, Yamazaki et al. (2011), in the Earth2Observe version available at <http://www.earth2observe.eu/>). Although other hydrologic models have been applied to the Amazon basin (Tables 5.1 and 5.2), the models were selected as representative of global to local models, for having been well validated and applied over the Amazon basin, and for representing state-of-the-art Amazonian hydrologic modeling. All basin-scale models represent one-dimensional flows only (i.e., they are 1D models, and floodplains are represented as storage units without active flow), and thus do not represent 2D horizontal flows that occur in wetlands (ALSDORF et al., 2007; FLEISCHMANN et al., 2020b). A detailed comparison of model capabilities and structure uncertainties is out of our scope. Each hydrologic model has a different temporal resolution, depending on its numerical stability and forcing data, e.g., MGB model runs at a timestep shorter than 1 minute, but is usually assessed at daily resolution given the daily precipitation data used as forcing. To make the models comparable to the remote sensing dynamic products, their estimates were averaged to yield monthly values.

The products available for local or regional scales are presented in Figure 5.4. ALOS-2 PALSAR-2 data were used for the Pacaya-Samiria region (JENSEN et al., 2018), and the ScanSAR mode of ALOS/PALSAR for the following local products: Curuai floodplain lake (ARNESEN et al., 2013), Mamirauá Reserve (FERREIRA-FERREIRA et al., 2015), Uatumã River floodplain (RESENDE et al., 2019), and Janauacá floodplain lake (PINEL et al., 2019). MODIS optical data were used for the Llanos de Moxos savannas in the upper Madeira River basin (OVANDO et al., 2016) and the lower Amazon floodplain (PARK; LATRUBESSE, 2019). Two local scale 2D hydraulic models (LISFLOOD-FP for Curuai lake, Rudorff et al. (2014), and TELEMAC-2D for Janauacá lake, Pinel et al. (2019)), and one local-scale hydrologic model (for Janauacá lake; Bonnet et al. (2017)) were considered; together, these are representative of the state-of-the-art of hydrological modeling in Amazonian wetlands.

The products were provided in a variety of formats (i.e., raster and polygon shapefiles) and projections (mainly projected UTM and geographic coordinate system with WGS84 datum), and were converted to the WGS84 geographic coordinate system to compute areas, with the exception of one product that was provided at the Equal-Area Scalable Earth (EASE) Grid (SWAMPS), and which was used in its original format to estimate flooded areas. Hydrologic model outputs were provided as either binary inundation maps or as flood depth raster files, which were then converted into binary maps by assuming depth > 0 m as inundated pixels.

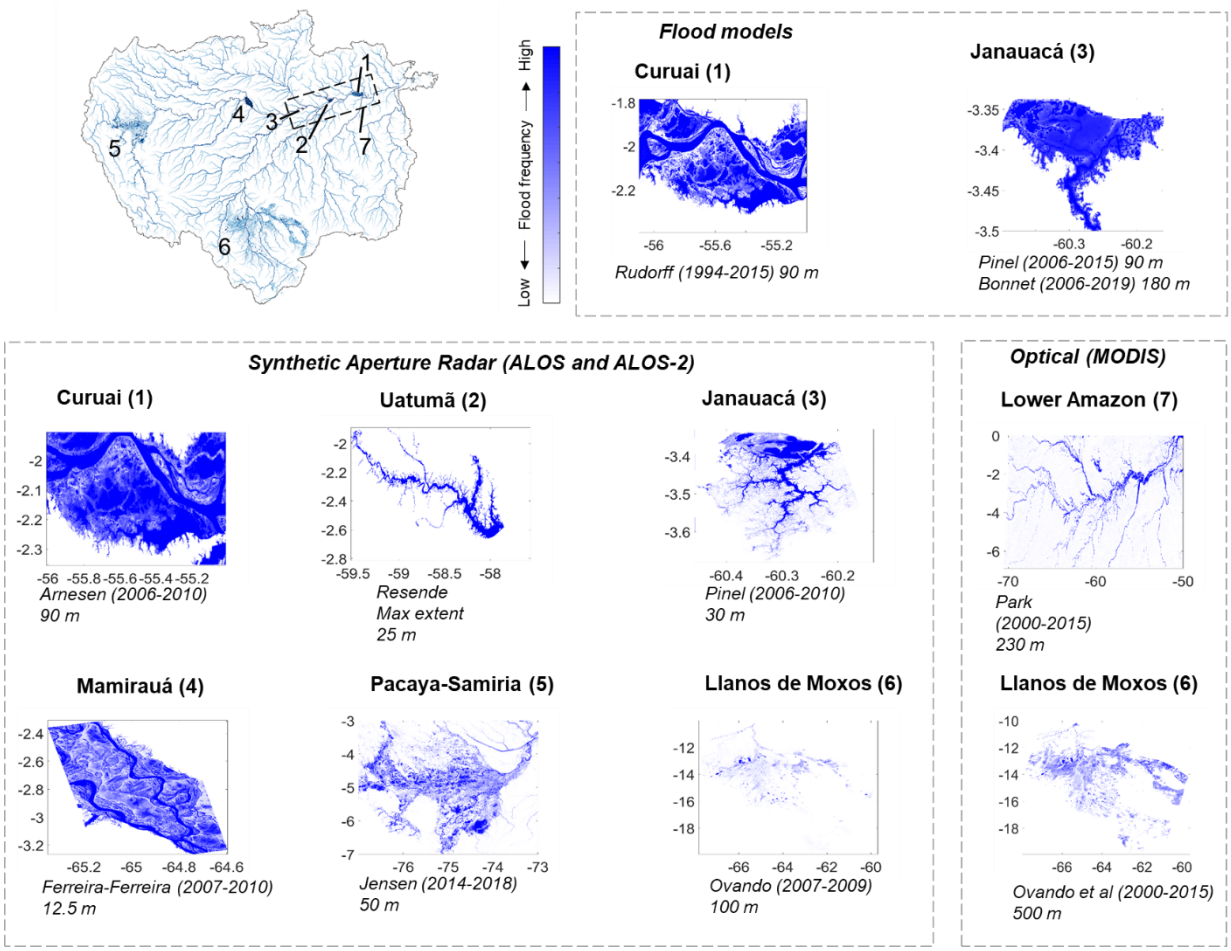

Figure 5.4. Local-scale inundation products used in this study. Long-term flood frequency maps are provided for all products except for the Uatumã one, which is a static product, and thus the maximum extent is shown in that case.

5.2.3 Comparison framework

The comparison framework involved the following analyses, considering the entire basin and 11 wetland subregions (seven areas with available local inundation estimates and four additional areas):

- Annual maximum and minimum inundation estimates for each basin-scale product (Section 5.3.1);
- Basin-wide, long-term maximum and minimum inundation estimates for each basin-scale product, as well as inundation amplitude based on the maximum to minimum inundation ratio (Section 5.3.1);
- Local-scale, long-term maximum and minimum inundation estimates for each of the 18 basin-scale and 11 local-scale products (Section 5.3.2);
- Comparison between basin-scale and local products with temporal (nRMSD and Pearson correlation) and spatial (Fit metric) assessment (Section 5.3.2);

- Assessment of basin-wide agreement among the 18 basin-scale products at 1 km, for both long-term maximum and minimum inundation maps (Section 5.3.3);
- Estimation of long-term maximum inundation for two classes of wetlands for the entire basin: (i) medium to large river floodplains and (ii) interfluvial wetlands and small floodplains (Section 5.3.4).

The long-term maximum and minimum inundation extent were estimated by computing the area of all pixels that were inundated at least once in the whole time series available for each dataset. This was performed for all products and analyzed in terms of absolute values as well as amplitude, computed as the difference between maximum and minimum inundation extent divided by the minimum inundation, in order to obtain an estimate of how many times the minimum extent is increased during the maximum inundation.

The agreement of all basin-scale, high-resolution products (i.e., all products except for THMB, GIEMS-2, SWAMPS and WAD2M, which have a coarse resolution between 9 and 25 km) was assessed for long-term maximum and minimum inundation at 1 km resolution, which is the resolution of SWAF-HR, the coarsest resolution among the high-resolution products. For each 1 km pixel, the total number of products agreeing that it was inundated (either for maximum or minimum extent) was computed, following Trigg et al. (2016). Given the size of the Amazon basin, a 1 km resolution was considered adequate for the analysis. The analysis was done by degrading all products to 1 km, by considering that a 1 km pixel is flooded if, for a given product, it had more than 50% of inundation. This value has been adopted by other studies (HAMILTON; SIPPEL; MELACK, 2002). A sensitivity test was performed for the 25% threshold and led to similar conclusions basin-wide (Figure S1).

The basin-scale products and four additional products were compared to the following seven local products, which were assumed as local references, although they are not free of uncertainties: Curuai (ARNESEN et al., 2013), Uatumã (RESENDE et al., 2019), Janauacá (PINEL et al., 2019), Mamirauá (FERREIRA-FERREIRA et al., 2015), Pacaya-Samiria (JENSEN et al., 2018), Llanos de Moxos MODIS (OVANDO et al., 2016) and lower Amazon (PARK; LATRUBESSE, 2019). The four additional local products are: Curuai LISFLOOD-FP model (RUDORFF; MELACK; BATES, 2014), Janauacá hydrological model (BONNET et al., 2017), Januacá TELEMAC-2D model (PINEL et al., 2019), and Llanos de Moxos ALOS-PALSAR (OVANDO et al., 2016).

To assess the representation of the local inundation dynamics, the basin-scale and four additional local products were compared to the local references at monthly time scale, considering the total inundated area per wetland area (i.e., the whole Curuai Lake domain, the whole Uatumã floodplain, and so forth). The polygons of each wetland area, used to extract the information from the basin-scale datasets, were delineated as a buffer around the maximum inundated area, according to each locally derived product. For the four areas without local products (Amazon mainstem and Purus floodplains, and

Roraima and Negro savannas), the polygons were created considering the maximum lateral extent in accordance to MERIT Digital Elevation Model (Yamazaki et al., 2017) and ESA-CCI land cover for savannas. The time series were compared with the Pearson linear correlation (R) and the normalized root mean square deviation (nRMSD), computed as the RMSD between a given inundation map and the reference map (i.e., the local wetlands) divided by the reference long-term average inundation. The term 'deviation' was preferred over 'error' to stress the uncertainties inherent to all products, for both basin and local scales, although the local ones are considered as a reference for having a more dedicated product development for that particular area, and being validated with in situ surveys in some cases.

The products' ability to estimate the local spatial patterns at maximum inundation was assessed with the Fit metric (BATES; DE ROO, 2000), which has been successfully applied to compare inundation datasets to local references (BERNHOFEN et al., 2018), and is computed as:

$$Fit = 100\% * \frac{A \cap B}{A \cup B} (1)$$

Where A and B are the reference (e.g., the local map) and the basin-scale maximum inundation maps.

In order to differentiate medium to large river floodplains from interfluvial wetlands and small floodplains, an estimation of the total flooded area of the former was computed, considering river reaches with upstream drainage area larger than 1,000 km², and a buffer mask around the river reaches (mask presented in Figure 5.1). The buffer was defined based on the Hydrosheds drainage network (LEHNER; GRILL, 2013), segmented into 15 km-long reaches by Siqueira et al. (2018). The buffer was proportional to the local reach drainage area and further manually adjusted to include the maximum floodplain lateral extent, as estimated from a visual inspection of the MERIT DEM (YAMAZAKI et al., 2017) and the three basin-scale SAR-based products (Hess, Chapman and Rosenqvist datasets). Buffer values varied from 4 km in upper reaches to 150 km on the Amazon mainstem close to the Mamirauá Reserve. The estimation of floodplain total inundated area is relevant in order to differentiate the Amazonian floodplains from non-floodplain wetlands (here referred to as interfluvial wetlands).

Finally, in order to assess the current capabilities of basin-wide mapping of inundation dynamics at high spatial and temporal resolution, a further assessment of the four high-resolution dynamic products (GIEMS-D3, CaMa-Flood, SWAF-HR and MGB) at their native resolutions was performed by computing their long-term flood frequency for the basin scale.

5.3 Results and Discussion

5.3.1 How much inundation is estimated to occur in the Amazon basin?

We analyzed the annual maximum and minimum inundation estimates for the entire basin scale (Figure 5.5), as well as the long-term maxima and minima (Figure 5.6 and Table 5.2). The annual values vary widely. Annual values for the 18 basin-scale products are plotted together, though some products provide only long-term average estimates (e.g., GLWD, Chapman, G3WBM). SAR estimates, especially those based on L-band sensors and when validated, are usually assumed the most accurate given their high spatial resolution and capability of mapping flooded areas under trees and in all seasons. Basin-wide, SAR-based estimates range from maximum annual inundation of 424,600 km² (Rosenqvist) to 633,500 km² (Hess), and minima from 53,900 km² (Rosenqvist) to 284,200 km² (Hess). By using long-term maximum inundation (i.e., all pixels that were inundated at least once in the full available series), instead of annual maxima, the SAR-based estimates range from 506,400 km² (Chapman) to 659,100 km² (Rosenqvist) for the entire basin (Table 5.4). The minima vary from 42,400 km² (Rosenqvist) to 284,200 km² (Hess). This highlights the large differences that exist, especially for the minima, usually referred to as "low-water period". Chapman's product, based on the 2006-2011 ALOS-PALSAR archive, has a smaller total maximum inundation area than the other two SAR datasets, as well as a smaller estimate for minimum inundation in relation to Hess' estimate. Differences among the three products may occur due to acquisition dates, interannual inundation variability, algorithm differences, spatial resolution, or inconsistencies regarding the data processing, e.g., Chapman provides long-term maxima and minima while Hess and Rosenqvist provide annual values. For minimum inundation, the interannual variability seems to be a minor factor, since Hess' dataset was derived for a below-average water level condition in central Amazon (HESS et al., 2003), lower than that of the acquisition date by Rosenqvist, although relatively higher than Chapman's one (see Fig. 8 in Rosenqvist et al., 2020). Thus, the larger minimum inundation extent by Hess et al. (2015) seems to be more related to algorithm differences (Figure S2). For the maximum water level, the Hess' period was associated to an average year condition, below the levels in Chapman and Rosenqvist, and this may explain the relatively higher long-term maximum inundation by Rosenqvist, while Chapman's smaller values are likely due to algorithm differences. Hess' estimate is based on JERS-1 data mostly from June (HESS et al., 2015), what could have missed some of the inundation in the western basin as in the Pacaya-Samiria region and may explain to some extent the larger value by Rosenqvist (see next section). Spatial resolution is also an important factor: Rosenqvist's resolution is 50 m, and is capable to represent smaller floodplains than the other two (Figure S3), as will be discussed in the next section.

The coarse-scale products and hydrologic models generally estimate smaller annual inundation areas in relation to the SAR datasets, with the exception of SWAF-HR, WAD2M and CaMa-Flood that yield similar annual maximum inundation. This results from low sensitivity of the passive microwave signal, used in most coarse-scale

datasets, to reveal small fractional flooded areas within the grid cells, flooding under particularly dense vegetation, and flooding of short duration (i.e., less than one month of consecutive inundation) (HAMILTON; SIPPEL; MELACK, 2002). Given the long-term data availability from dynamic, coarse-scale datasets, their long-term estimates are closer to the SAR ones, varying from 450,800 km² (THMB) to 630,900 km² (SWAF-HR), when compared to the annual scale analysis. Therefore, no clear relationship between long-term minimum or maximum inundation and the spatial resolution of the products is observed (Figure 5.6), which could be expected if analyzing the annual values (Figure 5.5).

As expected, the optical-based products (GSWO, G3WBM, GLAD) cannot map flooded vegetation and thus lead to much smaller, unrealistically low inundation area estimates at the basin-wide scale (AIRES et al., 2018). Similarly, the ESA-CCI product, based on land cover classification of optical imagery with the addition of SAR inputs for delineation of wetland areas, yields low basin-wide inundation areas, although relatively higher than the purely optical-based estimates. In turn, the multisatellite-based CIFOR provides an unrealistically large estimate of maximum inundation area (872,700 km²), which may be due to overestimation of soil moisture by the topographic index used. This method is sensitive to rainfall overestimation, what may have occurred in 2011, the year for which CIFOR was developed (GUMBRICHT et al., 2017). While the product does represent well the spatial extent of peatlands across the Pacaya-Samiria region (GUMBRICHT et al., 2017), its estimation of widespread inundation across the basin has limitations to represent the large Amazonian river floodplains, especially the forested ones, which are classified as “swamps (including bogs)” by this dataset together with large patches of interfluvial areas (Figure S4).

By computing average and standard deviation estimates for each type of data, for the long-term maximum inundation, we obtain the following values: 138,200 ± 45,300 km² (average ± S.D.) for optical, 533,500 ± 217,800 km² for combination of multiple products at high resolution, and 579,100 ± 108,900 km² for those at coarse resolution, 599,700 ± 81,800 km² for SAR, and 542,800 ± 80,600 km² for hydrological models. If we assume that the ensemble of products could be a proxy of inundation uncertainty in the Amazon basin, and neglecting the optical and land cover-based data (G3WBM, GLAD, GSWO and ESA-CCI) and CIFOR products, given their lower capability to map wetlands as discussed above, 13 products are left, yielding an estimation for the long-term maximum inundation of 559,300 ± 81,100 km². This value is around 40,000 km² lower than the mean estimated inundation area from the three SAR products: 599,700 ± 81,800 km². The figure considering all 18 products is 490,300 ± 204,800 km².

None of the products are capable of mapping small, narrow floodplains or riparian zones, for which only simple calculations are currently available (JUNK et al., 1993). For instance, a wetland mask developed by Hess et al. (2015) in order to assist their SAR classification technique yielded a basin-wide estimation of 840,000 km². This

estimate is much larger than the long-term maximum area obtained with SAR data (659,100 km² with Rosenqvist's product). In Section 5.3.2, it will be shown that almost all products tend to underestimate the maximum inundation, when compared to specific local/subregional products. The two SAR-based products with highest accuracy underestimate inundation by 9% (Rosenqvist) and 13% (Hess) in these comparisons. If this holds true for the whole basin, the basin-scale maximum inundation would be around 10% higher. For the long-term minimum inundation area, the relative variance among available estimates is higher than for the long-term maximum extent —125,900 ± 77,600 km² for the 12 basin-scale products that provide an estimate for the low-water period, and 139,300 ± 127,800 km² for the three SAR-based datasets.

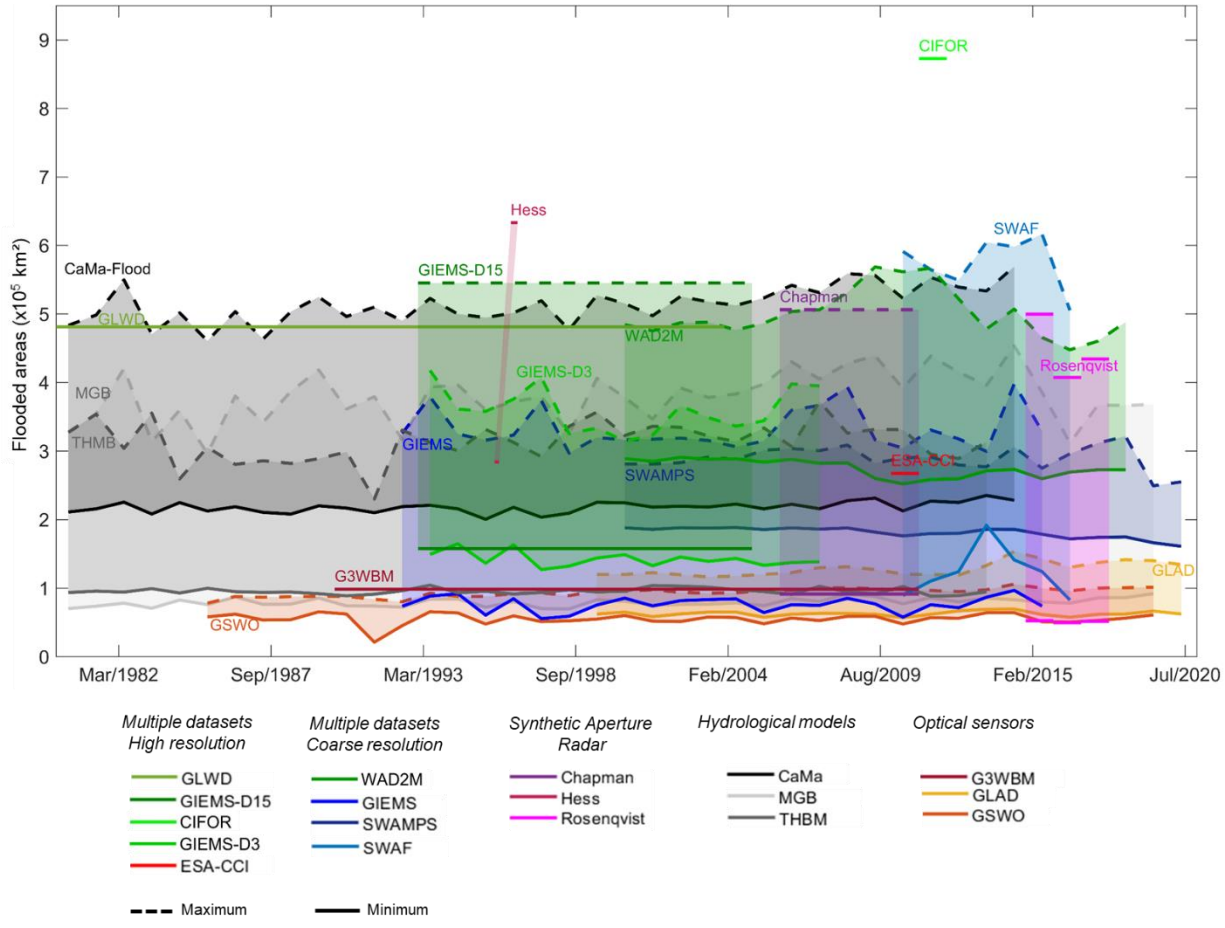

Figure 5.5. (a) Annual minimum and maximum flooded areas for the Amazon basin (< 500 m) for 18 basin-scale products.

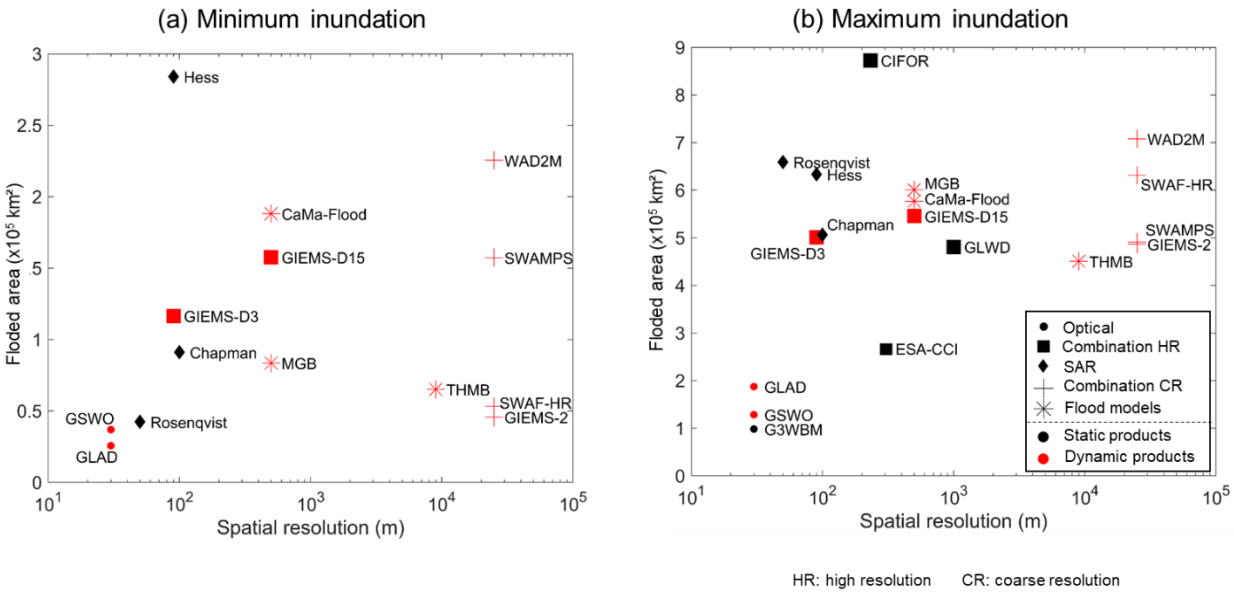

Figure 5.6. Summary of long-term (a) minimum and (b) maximum inundation for the 18 basin-scale products, which are categorized into five types (optical data; combination of datasets at high resolution; combination of datasets at low resolution; synthetic aperture radar; and hydrological models). The dynamic products' estimates are not directly comparable to the static ones; thus, each is colored differently:red (dynamic) and black (static).

Table 5.2. Basin-wide, long-term minimum and maximum inundation estimates for the 18 basin-scale products.

Product	Minimum	Maximum
G3WBM	-	98,500
ESA-CCI	-	267,400
GLAD	25,700	187,600
GSWO	37,000	128,500
GLWD	-	481,200
CIFOR	-	872,700
GIEMS-D15	157,700	545,400
GIEMS-D3	116,600	500,700
WAD2M	225,500	707,900
Chapman	91,200	506,400
Hess	284,200	633,500
Rosenqvist	42,400	659,100
GIEMS-2	45,800	486,600
SWAMPS	157,400	491,100
SWAF-HR	53,200	630,900
CaMa-Flood	188,100	576,700

MGB	83,600	600,900
THMB	65,200	450,800

5.3.2 How much inundation is estimated to occur at local scales?

Inundation estimates for the 18 basin datasets were compared with the estimates for 11 individual wetland complexes (Tables 5.3, 5.4 and 5.5). The subregional products are considered as a local reference, given the in situ validation performed for most of them, use of a region-specific classification and often a higher spatial resolution (12.5 m for some based on ALOS-PALSAR imagery). However, these products are not uncertainty-free, and that different degrees of validation exercises were performed for each dataset, with some being extensively validated with airborne videography (HESS et al., 2003) or local surveys (ARNESEN et al., 2013; FERREIRA-FERREIRA et al., 2015; JENSEN et al., 2018; RESENDE et al., 2019). The assessment of the other products was performed with comparison with other datasets (PINEL et al., 2019), as well as through visual inspection by the developers, especially for those covering a large domain, as the Llanos de Moxos (OVANDO et al., 2016) and lower Amazon (PARK; LATRUBESSE, 2019) subregional datasets.

The comparison of the long-term maximum and minimum observed inundation over the available time periods indicates differences between basin-scale products, subsampled for the subregions, and the local references. Overall, the local products had a larger maximum inundation extent; on average, the underestimation by the basin-scale datasets varied from 49% for the Pacaya-Samiria region to 5% for the lower Amazon. Only three products overestimated the locally estimated maximum extent of inundation: GIEMS-D3, GIEMS-D15 and GLWD. The three basin-scale SAR products (Hess, Chapman and Rosenqvist) underestimated the maximum extent in the regions represented by all local products, with the exception of Rosenqvist for Janauacá Lake, and Hess for the Llanos de Moxos region. This is likely related to the higher resolution of many of the individual products (e.g., 12.5 m resolution for the Uatumã ALOS-PALSAR classification by Resende et al., 2019), as well as fine tuning that may occur with dedicated products for a particular region.

Regarding the maximum inundation extent, the Janauacá case provides a representative example to understand the differences among multiple SAR products: these estimated total inundated area as 209 km², 184 km² and 446 km² for Hess, Chapman and Rosenqvist, respectively, in contrast to 404 km² with the local ALOS-PALSAR-based data (12.5 m resolution; Pinel et al., 2019). Part of these differences occur because of interannual variability, but other factors such as spatial resolution and algorithm differences seem to be relevant. Rosenqvist led to a more consistent estimation of the inundation spatial extent in terms of maximum inundation (Table 5.5) and Fit metric (Table 5.3), that can be a consequence of its higher spatial resolution (50 m) in contrast to the other two (90 m; Figure S3). Overall, Rosenqvist provided a larger

inundation extent in comparison to the other two for all areas along the Amazon mainstem floodplain, except for the Curuai floodplain and the savanna wetlands, and also the smallest differences (-9% ± 13%; average ± S.D.). Hess estimated the largest inundation values in the savanna wetlands (Llanos de Moxos, Roraima and Negro). However, Hess' values are larger than the subregional estimate for Llanos de Moxos (+39%), while the other two SAR estimates are lower (-26% and -41% for Chapman and Rosenqvist, respectively).

By comparing Hess and Rosenqvist patterns for the inundation spatial pattern, the former had a better average Fit metric (0.64 versus 0.58), which mainly reflects the better performance of Hess for the Llanos de Moxos, while Rosenqvist outperformed the former in the Pacaya-Samiria interfluvial area. This may be partially explained by the fact that the flood wave had already passed the Peruvian wetlands when the high-water analyses were performed by Hess. Furthermore, Hess suggests much more inundation during the low-water period for the Amazon mainstem floodplains (54,500 km²), mainly for the upstream forested reaches, and for the whole basin in general (284,200 km²) than recent estimates with ALOS (28,500 and 91,200 km²) and ALOS-2 data (19,500 and 42,400 km²). Supplementary Figure S2 shows low-water maps that depict the different estimations for the Amazon mainstem floodplain for Rosenqvist and Hess datasets. An assessment with the local products along the Amazon floodplain suggests that Hess overestimates the minimum extent for Curuai, Mamirauá and lower Amazon, and is accurate for the Janauacá floodplain lake. Rosenqvist generally underestimates the minimum inundation. For instance, for the Mamirauá dataset, the minimum extent (i.e., permanently flooded areas) sums up to 715 km², which is increased to 1545 km² if considering all pixels flooded for more than 295 days per year. For this area, the SAR estimates are 1756 km² (Hess), 866 km² (Chapman) and 422 km² (Rosenqvist). Overall, this suggests that the true value of minimum inundation across the central Amazon floodplains is somewhere between the Hess and Rosenqvist's estimates.

Large discrepancies are observed for the floodable savanna areas of Roraima and Negro. The Roraima wetlands are small river floodplains interspersed with open savannas subject to flooding, which can be identified by optical data. In addition, the typical timing of high and low water in the Roraima region coincides approximately with the JERS-1 dual-season mosaics that were designed to reflect the seasonality of the central Amazon River floodplain (Hamilton et al. 2002). For these reasons, the Hess product seems to satisfactorily represent most of the Roraima floodplains, but misses some small-scale riparian forests, given its 90 m spatial resolution and snapshot coverage that likely missed flooding events on smaller, flashier rivers (Figure S5). Thus, the maximum inundation is likely higher than Hess' estimate (8,900 km²), which in turn is larger than the other SAR products (1,900 - 4,100 km²). The only dataset to estimate a higher value is the coarse SWAF-HR product (18,100 km²), which is similar to the value previously estimated by Hamilton et al. (2002) (16,500 km²), also with coarse data (SMMR passive microwave), though a part of the discrepancy may be due to

interannual variability. More studies are necessary for this area. Similarly, the inundation estimates in the Negro interfluvial savannas are subject to large uncertainty, with the long-term maximum inundation varying between 95 (GLWD) and 20,700 km² (CIFOR), considering all basins-scale datasets. The SAR-based products estimate it between 5,900 and 15,800 km². In turn, for the Pacaya-Samiria interfluvial area, which is associated to a large complex of forested wetlands, peatlands and palm swamps, the discrepancies are smaller than for the savanna interfluvial regions, although still considerable. The SAR, basin-scale estimates range between 24,000 (Chapman) and 56,200 km² (Rosenqvist), with the local reference yielding 57,900 km². The good agreement between Rosenqvist and the local reference product was already reported by Rosenqvist et al. (2020).

Overall, four products had the best overall representation of spatial patterns (average Fit between 0.64 and 0.67 for all areas): Hess, GLWD and the two hydrodynamic models (MGB and CaMa-Flood). While hydrologic models as MGB, CaMa-Flood and THMB have a satisfactory agreement basin wide, they are unable to represent wetlands not primarily inundated by rivers (FLEISCHMANN et al., 2020b; ZHOU; PRIGENT; YAMAZAKI, 2021). For example, the Llanos de Moxos inundation is underestimated by both CaMa-Flood and MGB with low Fit metric values (0.19-0.28). This is expected for interfluvial wetlands such as the Llanos de Moxos and Roraima savannas, where much of the flooding is caused by poor drainage of local rainfall, as opposed to riverine overflow onto adjacent floodplains. The four alternative local products assessed here - three hydrological models (one for Curuai and two for Janauacá) and one classification of ALOS-PALSAR data for the Llanos de Moxos area - were generally better or similar to some of the best-performing basin-scale products, as could be expected given their fine tuning for the specific areas, which often includes local topography surveys.

The inability of optical data for detecting water under forest canopies is well known. Although the use of optical data can be used to map flooding in some open savanna wetlands (e.g., Llanos de Moxos; Ovando et al., 2016) and open water areas (e.g., lower Amazon mainstem), the Landsat-based products (GLAD, GSWO, G3WBM) had generally a low Fit value for the Llanos de Moxos, possibly due to cloud cover and reliance on open water areas to indicate inundation as in the GSWO algorithm. Persistent cloud cover has been shown to hamper the usage of optical data in the Amazon (ASNER, 2001).

Some of the products based on multiple datasets were the ones that most overestimated the local wetland inundation area, especially GIEMS-D15, GIEMS-D3 and GLWD. Furthermore, as mentioned earlier, the CIFOR product was originally designed for peatland mapping in the tropics, and generally overestimates inundation, suggesting a widespread distribution of wetlands, i.e., along interfluvial terraces across the whole basin. For the local floodplain areas, however, it generally underestimated inundation, and also had a poor estimation of spatial patterns of inundation (low Fit

metric). WAD2M was the one that mostly underestimated the maximum inundation, which is understandable given its removal of open water areas; however, its main constituents (CIFOR and SWAMPS) also underestimate inundated area compared to the local results. This does not mean, however, that WAD2M underestimates basin-wide inundation, since it tends to scatter floodable area around the basin as does the CIFOR product.

By comparing the different wetland complexes, the long-term maximum inundation extent over the Amazon River floodplains (from Iquitos to Gurupá) is similar to that of the Llanos de Moxos region: 106,800 ± 25,800 km² and 113,500 ± 53,400 km², respectively, considering the three SAR-based products, and 94,100 ± 32,500 km² and 85,300 ± 52,400 km² considering all 18 basin-scale datasets. Besides these two areas, the third largest Amazon wetland region is Pacaya-Samiria, with 29,700 ± 20,600 km² (all products) and 40,000 ± 4,200 km² (SAR). Finally, to investigate the products' depiction of inundation dynamics, we assessed the correlation among the dynamic products and the local wetland time series of flooding, considering the total inundation in each local area. Overall, all products agreed well (average Pearson correlation larger than 0.63 for the four local wetlands with available time series), showing a similar depiction of the inundation seasonality. However, their ability to monitor high-resolution flood frequency is limited, as will be further discussed in the Perspectives section. A visual comparison of the time series (Figure S6) shows agreement on seasonal timing of flooding and drainage, but disagreement in the extent of inundation. In particular, two datasets have a small overall annual amplitude (SWAMPS and WAD2M).

Inundation amplitude was assessed by comparing the long-term maximum and minimum values for the whole basin and for different regions based on basin-scale products (Figure 5.7). At the basin-wide scale, the maximum inundation area varies from 2.2 to 15.5 times the minimum inundation area, reflecting the large differences discussed above. Among the three SAR datasets, amplitude variation differed considerably: 2.2 (Hess), 5.6 (Chapman) and 15.5 (Rosenqvist). The largest amplitudes were estimated for the seasonally flooded savannas (Llanos de Moxos, Roraima and Negro). In particular, the Negro has a large disagreement among the products, with amplitude varying between 2 and 6000. Both GIEMS-2 and SWAF-HR coarse-resolution datasets estimated the Roraima minimum extent as zero, as GIEMS-2 also did for the Negro savannas. These savanna regions have been called hyperseasonal savannas (BATALHA et al., 2005; DALMAGRO et al., 2016b) by plant ecologists who observed that the vegetation is adapted to both soil water excess and deficit throughout the year. The coarse-scale, mainly passive microwave-based products estimated very large amplitude values (5,000 to infinitum) because of their inability to measure small isolated flooded areas during the season of low flows or rainfall. Furthermore, for this analysis we considered the long-term minimum estimate, which has also contributed to this conclusion. An alternative would be to consider a percentile of the time series instead (e.g., 95%).

Table 5.3. Comparison metrics (R and nRMSD for time series, and Fit for the spatial analysis of maximum observed inundation area) for all products against the local reference products for individual wetlands: Curuai (Arnesen et al., 2013), Uatumã (Resende et al., 2019), Janauacá (Pinel et al., 2019), Mamirauá (Ferreira-Ferreira et al., 2015), Pacaya-Samiria (Jensen et al., 2020), Llanos de Moxos (Ovando et al., 2016) and Lower Amazon (Park et al., 2019). Four additional local products were compared to the local ones mentioned above: Curuai LISFLOOD-FP model (Rudorff et al., 2014), Janauacá hydrological model (Bonnet et al., 2017), Janauacá TELEMAC-2D model (Pinel et al., 2019), and Llanos de Moxos ALOS-PALSAR (Ovando et al., 2016). The Fit metric was applied by converting all maps to 1 km, considering a pixel with inundation fraction higher than 50% as inundated.

	Product	-	Curuai			Uatumã	Janauacá			Mamirauá	Pacaya-Samiria			Llanos de Moxos			Lower Amazon
	-	Period	2006-2010			2006-2011	2007-2011			2007-2010	2014-2018			2001-2014			2000-2020
			R	nRMSD	Fit	Fit	R	nRMSD	Fit	Fit	R	nRMSD	Fit	R	nRMSD	Fit	Fit
Other local products	Curuai-Model	1994-2015	0.82	12%	0.86	-	-	-	-	-	-	-	-	-	-	-	-
	Janauacá-Bonnet	2006-2019	-	-	-	-	0.75	25%	0.49	-	-	-	-	-	-	-	-
	Janauacá-Pinel	2006-2015	-	-	-	-	0.57	17%	0.82	-	-	-	-	-	-	-	-
	Llanos de Moxos - ALOS	2006-2010	-	-	-	-	-	-	-	-	-	-	-	0.52	99%	0.33	-
Optical sensors	G3WBM	1990-2010	-	-	0.64	0.29	-	-	0.19	0.14	-	-	0.03	-	-	0.04	0.59
	ESA-CCI	1992-2015	-	-	0.76	0.40	-	-	0.40	0.70	-	-	0.36	-	-	0.14	0.69
	GLAD	1999-2018	-	-	0.84	0.39	-	-	0.30	0.20	-	-	0.04	-	-	0.16	0.78
	GSWO	1984-2019	-	-	0.75	0.31	-	-	0.21	0.17	-	-	0.04	-	-	0.09	0.68
Multiple datasets	GLWD	1992-2004	-	-	0.88	0.45	-	-	0.79	0.93	-	-	0.63	-	-	0.08	0.51
	CIFOR	2011	-	-	0.91	0.39	-	-	0.24	0.33	-	-	0.55	-	-	0.30	0.69
	GIEMS-D15	1993-2004	-	-	0.92	0.58	-	-	0.68	0.59	-	-	0.51	-	-	0.38	0.46
	GIEMS-D3	1993-2007	-	-	0.92	0.61	-	-	0.80	0.81	-	-	0.14	-	-	0.44	0.45
	WAD2M	2000-2018	0.9	82%	-	-	0.79	63%	-	-	0.46	2%	-	0.9	123%	-	-
SAR	Chapman	2006-2011	-	-	0.65	0.27	-	-	0.22	0.68	-	-	0.28	-	-	0.24	0.50
	Hess	1995-1996	-	-	0.96	0.47	-	-	0.28	0.98	-	-	0.48	-	-	0.47	0.69
	Rosenqvist	2014-2018	-	-	0.59	0.34	-	-	0.59	0.98	-	-	0.64	-	-	0.19	0.48
Passive Microwave	GIEMS-2	1992-2015	0.96	21%	-	-	0.78	157%	-	-	0.88	68%	-	0.91	85%	-	-
	SWAMPS	2000-2020	0.91	2%	-	-	0.8	38%	-	-	0.52	74%	-	0.92	171%	-	-
	SWAF-HR	2010-2019	-	-	0.95	0.64	-	-	0.63	0.71	0.66	73%	0.22	0.75	213%	0.39	0.57
Hydrological models	CaMa-Flood	1980-2014	0.80	11%	0.97	0.73	0.68	111%	0.88	0.83	-	-	0.49	0.82	218%	0.28	0.58
	MGB	1980-2014	0.83	7%	0.96	0.58	0.64	293%	0.82	0.93	-	-	0.52	0.91	26%	0.19	0.52
	THMB	1961-2013	0.72	62%	-	-	0.73	73%	-	-	-	-	-	0.54	7%	-	-

Table 5.4. Long-term minimum inundation areas for the 11 local wetland areas, for the local products (up to three local products per area) and the 18 basin-scale products. The flooded area values for the local products are presented for (in this order): Curuai ALOS (Arnesen et al., 2013) and model (Rudorff et al., 2014); Janauacá ALOS (Pinel et al,. 2019), hydrologic model (Bonnet et al., 2017) and TELEMAC-2D model (Pinel et al., 2019); Mamirauá ALOS (Ferreira-Ferreira et al., 2015); Pacaya-Samiria ALOS-2 (Jensen et al., 2020); Llanos de Moxos MODIS (Ovando et al., 2016) and ALOS (Ovando et al., 2016); and lower Amazon MODIS (Park et al., 2019). Average, standard deviation (S.D.) and coefficient of variation (CV) are presented for each area in the last row.

		Product	Curuai	Uatumã	Janauacá	Mamirauá	Pacaya-Samiria	Llanos de Moxos	Lower Amazon	Amazon mainstem	Purus	Roraima savannas	Negro savannas
	1	Local	1690, 1278	-	108, 38, 18	715	3824	1014, 3962	17797				
Optical sensors	2	G3WBM	-	-	-	-	-	-	-	-	-	-	-
	3	ESA-CCI	-	-	-	-	-	-	-	-	-	-	-
	4	GLAD	474	77	8	288	514	1513	6243	9857	335	13	20
	5	GSWO	736	345	10	314	401	2934	11908	16428	735	117	2
Multiple datasets	6	GLWD	-	-	-	-	-	-	-	-	-	-	-
	7	CIFOR	-	-	-	-	-	-	-	-	-	-	-
	8	GIEMS-D15	3942	1265	116	1077	3409	15074	44277	59066	3401	2966	2622
	9	GIEMS-D3	2712	861	151	1115	2731	8375	33253	44853	2696	383	146
	10	WAD2M	403	97	97	633	20421	31713	14728	29932	4240	258	10443
SAR	11	Chapman	1894	385	68	866	6775	10090	18413	28539	2951	1025	2843
	12	Hess	2770	584	106	1756	32107	56337	28981	54493	7061	1217	6084
	13	Rosenqvist	1514	313	49	422	1077	4566	13413	19512	575	60	5
Passive Microwave	14	GIEMS-2	995	263	183	1117	1578	500	19717	26807	349	0	0
	15	SWAMPS	2840	479	197	790	4433	24622	38345	53256	3492	309	6375
	16	SWAF-HR	1502	544	69	469	215	8304	20944	30242	784	0	3
Hydrological	17	CaMa-Flood	2741	861	184	1135	8269	17776	31569	45848	4128	1001	672
	18	MGB	3005	212	0	587	6101	4508	21333	32073	1769	226	35
	19	THMB	487	38	1	266	5349	7172	6708	18099	5596	383	195
		Average	1858	452	89	774	6670	13820	22131	33500	2722	568	2103
		S.D.	1148	350	71	430	8978	15190	11637	15551	2094	801	3285
		CV	0.62	0.77	0.80	0.56	1.35	1.10	0.53	0.46	0.77	1.41	1.56

Table 5.5. Long-term maximum inundation areas for the 11 local wetland areas, for the local products (up to three local products per area) and the 18 basin-scale products. The flooded area values for the local products are presented for (in this order): Curuai - ALOS (Arnesen et al., 2013) and model (Rudorff et al., 2014); Janauacá - ALOS (Pinel et al,. 2019), hydrologic model (Bonnet et al., 2017) and TELEMAC-2D model (Pinel et al., 2019); Mamirauá - ALOS (Ferreira-Ferreira et al., 2015); Pacaya-Samiria - ALOS-2 (Jensen et al., 2020); Llanos de Moxos - MODIS (Ovando et al., 2016) and ALOS (Ovando et al., 2016); and Lower Amazon - MODIS (Park et al., 2019). Average, standard deviation (S.D.) and coefficient of variation (CV) are presented for each area in the last row.

		Product	Curuai	Uatumã	Janauacá	Mamirauá	Pacaya-Samiria	Llanos de Moxos	Lower Amazon	Amazon mainstem	Purus	Roraima savannas	Negro savannas
		Local	4162, 3720	1471	404, 336, 176	4476	57913	125422, 133470	56722	-	-	-	-
Optical sensors	1	G3WBM	2732	628	135	795	2694	9564	27451	37718	2351	352	1238
	2	ESA-CCI	3236	855	260	3045	28727	39795	37475	84803	8883	510	12623
	3	GLAD	3479	832	204	1141	4196	38897	36930	53121	3903	3495	3885
	4	GSWO	3163	675	150	962	3637	19240	31191	44731	2982	1442	1880
Multiple datasets	5	GLWD	4275	2267	535	4259	79124	40661	67746	140921	14840	1048	95
	6	CIFOR	3796	994	177	1714	52590	116201	43509	86301	10844	3728	20712
	7	GIEMS-D15	4635	2681	416	2444	44536	117979	86123	127150	11186	8129	14854
	8	GIEMS-D3	4643	2732	505	3569	11562	150285	92908	127552	9045	12355	15123
	9	WAD2M	681	243	166	888	42635	102780	29276	49261	6698	3173	15450
SAR	10	Chapman	2796	934	184	2694	24001	73710	39677	77632	12499	4077	5935
	11	Hess	3996	1045	209	3985	39741	174198	52156	115822	15155	8950	15758
	12	Rosenqvist	3055	1238	446	4362	56160	92693	55262	126806	20738	1867	9935

Passive Microwa	13	GIEMS-2	3080	984	623	3344	23344	156176	79871	116379	7208	7173	12237
	14	SWAMPS	3359	722	280	1131	9929	88753	58626	72468	5618	4970	8819
	15	SWAF-HR	4439	2199	388	3205	16900	159712	69539	110468	10785	18146	15375
Hydrolo gical	16	CaMa-Flood	4246	1613	534	3208	34096	80725	63963	118577	20947	3454	6560
	17	MGB	4098	1549	474	3750	33344	21757	61997	115047	20394	240	3224
	18	THMB	2883	554	164	2840	27748	52693	39193	89658	19733	4307	3640
		Average	3477	1264	325	2630	29720	85323	54050	94134	11323	4856	9297
		S.D.	949	748	163	1226	20591	52387	19956	32503	6185	4666	6201
		CV	0.27	0.59	0.50	0.47	0.69	0.61	0.37	0.35	0.55	0.96	0.67

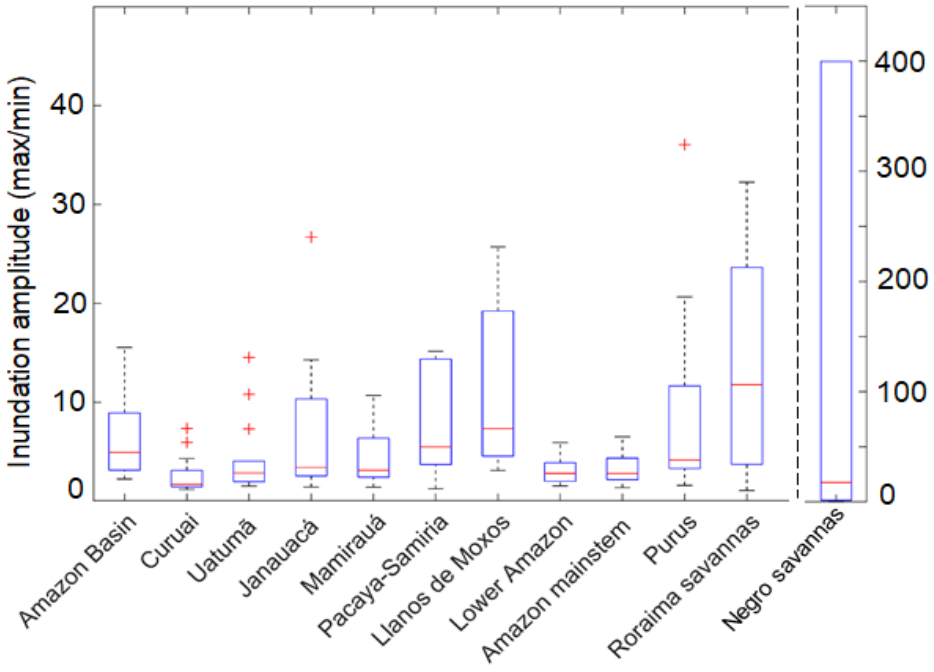

Figure 5.7. Inundation amplitude for the entire Amazon basin (< 500 m) and for specific regions, as estimated by the ensemble of 18 basin-scale products (i.e., each boxplot reflects 18 values). Amplitude is computed as the ratio between maximum and minimum inundation, e.g., a value of 10 means that the maximum inundation is 10 times larger than the minimum value. The Negro savannas have a much higher amplitude, and thus a specific y-axis range (secondary axis on the right) is used here, and three outliers were not added: 1010 (GSWO), 1960 (Rosenqvist) and 5960 (SWAF-HR).

5.3.3 Do the products agree on the spatial distribution of inundation?

Agreement maps of the high resolution products (< 1 km) were developed for both long-term maximum and minimum inundation areas, based on the number of products that agree that a given 1 km pixel is subject to inundation (Figures 5.8 and 5.9 and their categorization for specific regions areas in Figure 5.10). Overall, 26% of the Amazon lowlands area (5,960,200 km² according to the adopted 500 m mask) has been estimated as subject to inundation by at least one product (bottom left panel, Figure

5.8). Based on the agreement between two datasets, this value decreases to 948,300 km², which is larger than the value estimated when four products agree (553,200 km²). This latter estimate is more similar to the average maximum inundation as estimated by the ensemble of datasets (559,300 km²) and the three SAR-based ones (599,700 km²). Furthermore, there is a lower agreement for the minimum inundation than for the maximum inundation among individual regions (Figure 5.10).

For specific regions, a high degree of agreement for open water areas is evident for the lower Amazon reaches, followed by the forested floodplains, especially along the Amazon mainstem, Purus and Negro rivers. The generally higher accuracies over central Amazon floodplains may also be related to the dedication that many product developers have devoted to it, in contrast to other regions. Furthermore, the floodplain maximum extent can be somewhat delineated with terrain elevation data (i.e., DEMs) with algorithms such as HAND (RENNÓ et al., 2008); this could also help explain the relatively small disagreement for the floodplains fringing the largest rivers. In such cases, the use of newly developed vegetation bias-removed DEMs is welcome (O'LOUGHLIN et al., 2016b; YAMAZAKI et al., 2017). The best agreement (for both maximum and minimum inundation extent) occurred for the Curuai floodplain along the lower Amazon mainstem, with 37% of its area being estimated as flooded by all 14 products for the maximum inundation (Figure 5.8a). An agreement among all 14 products occurred, in part (i.e., more than 10% of the wetland area), for the central Amazon floodplains (Curuai, Uatumã, Janauacá and lower Amazon) because of their relatively large fractions of open water areas.

In the interfluvial wetlands (Negro and Roraima savannas, Pacaya-Samiria and Llanos de Moxos), the inundation patterns are less dependent on riverine overflow and more dependent on local rainfall, making them less predictable (HESS et al., 2003). The largest disagreement for both maximum and minimum inundation area occurs for these regions, e.g., 65–78% of their areas was estimated as flooded by only one model for the minimum inundation (Figure 5.9b). The Llanos de Moxos is conspicuous as a region of particular disagreement, perhaps because flooding is mainly shallow and in vegetated areas (mainly savannas/grasslands), and is highly variable from year to year. Similar disagreement occurred in other interfluvial wetlands as the Negro and Roraima savannas, and would be expected elsewhere in savanna floodplains of South America (e.g., Pantanal, Llanos de Orinoco and Bananal Island; Hamilton et al., 2002). The poor agreement over interfluvial areas, however, may also reflect, to some extent, the longer history of study of Amazon mainstem floodplains, for which there are river gage records that reflect floodplain water levels and inundation, while more remote areas such as the Negro savannas and Pacaya-Samiria regions have received much less attention. The challenges in estimating inundation over interfluvial areas also occur for the SAR-based products, which disagreed over these regions (see Section 5.3.5 and discussion in Rosenqvist et al., 2020).

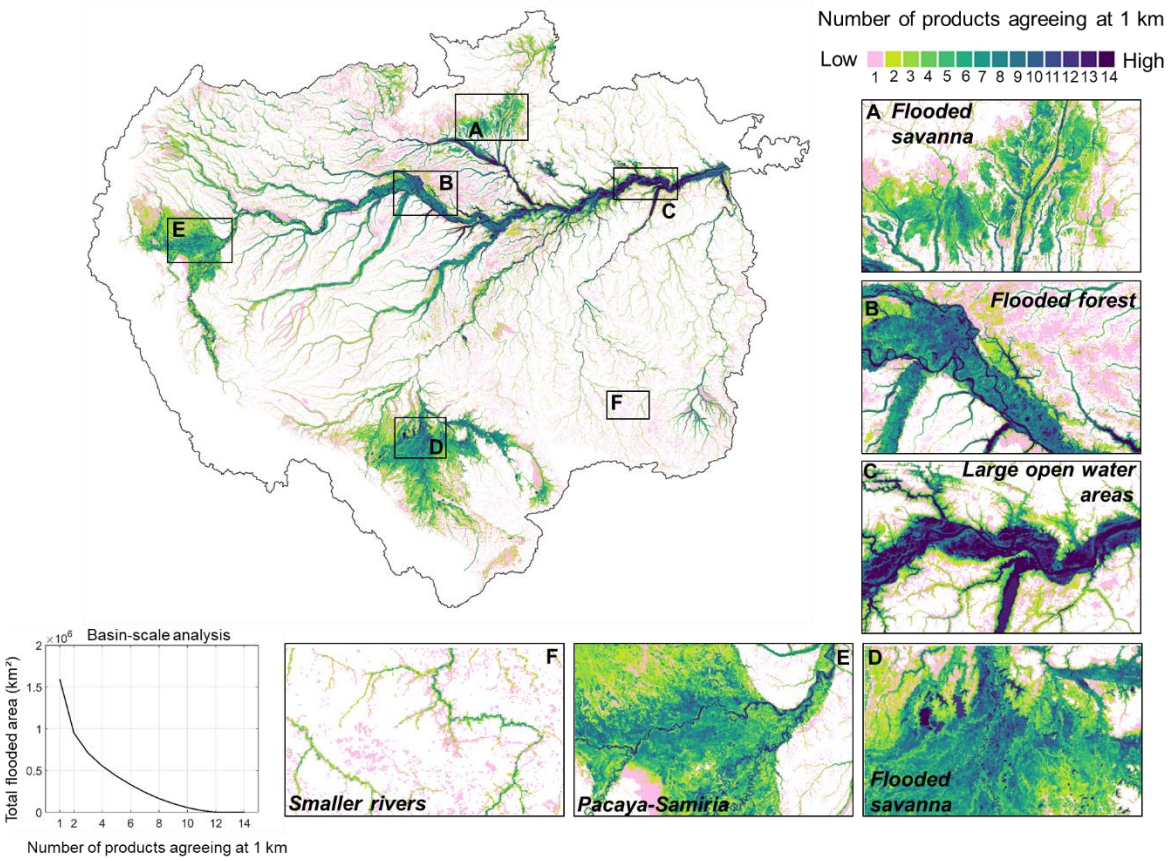

Figure 5.8. Agreement for maximum flood extent among 14 basin-scale products at high resolution (≤1 km): G3WBM, ESA-CCI, GLAD, GSWO, GLWD, Gumbricht, GIEMS-D15, GIEMS-D3, Chapman, Hess, Rosenqvist, SWAF-HR, CaMa-Flood, MGB. For a given pixel of a product with resolution higher than 1 km, more than 50% of flooding at the maximum inundation extent is classified as flooded.

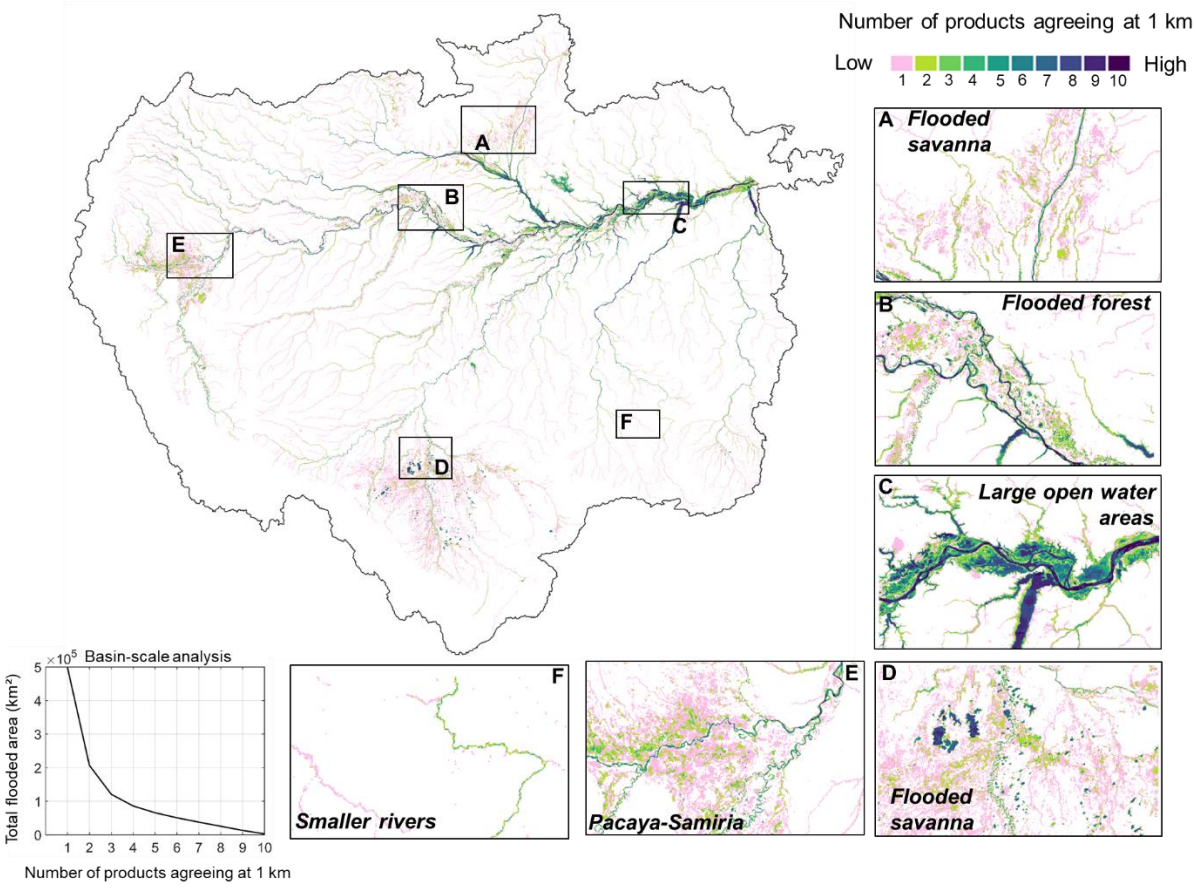

Figure 5.9. Agreement of minimum flood extent at 1 km resolution. 10 basin-scale products at high resolution (<= 1 km) are compared in this analysis at 1 km: GIEMS-D15, Chapman, Hess, Rosenqvist, SWAF-HR, CaMa-Flood, MGB, GIEMS-D3, GSWO, GLAD. For a given pixel of a product with resolution higher than 1 km, more than 50% of flooding for the minimum inundation extent is classified as flooded.

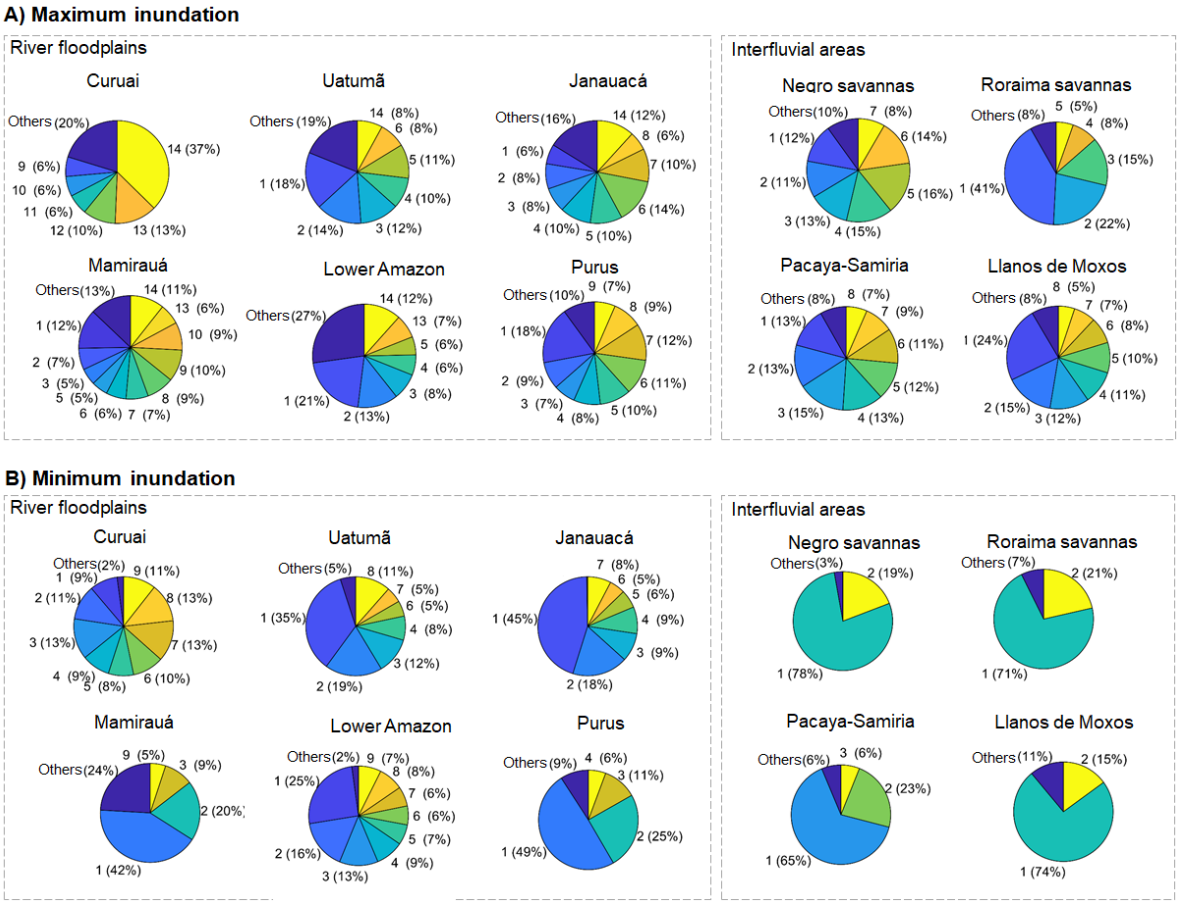

Figure 5.10. Degree of agreement for (a) maximum and (b) minimum inundation area for 10 local wetland regions, based on the 1 km agreement map (Fig. 7. The percentage values indicate the fraction of each area where a given number of products agreed that it was flooded, e.g., 14 models agreed on 37% of the Curuai area to be flooded. The class "others" refers to all classes that had less than 5% of pixels.

5.3.4 Quantifying the inundation extent of different wetland types

Amazon wetlands include a myriad of contrasting systems. The classification system proposed by Junk et al. (2011) differentiated Amazonian wetlands according to amplitude and range of water level change. Wetlands varied from the forested swamps with stable water levels to river floodplains with oscillating water levels, to interfluvial areas, more affected by local rainfall and runoff and thus having local amplitude reflecting the wet season (FLEISCHMANN et al., 2020b; JUNK et al., 2011; OVANDO et al., 2018).

A simpler, yet hydrologically meaningful classification is the categorization into river floodplains and interfluvial wetlands adopted here, since the former have typically a greater hydrological connection to the main river, and thus are subject to a different control of inundation area by river levels (REIS et al., 2019b). We performed a

quantitative analysis of inundation area in these two main hydrological classes. All pixels considered flooded by at least two products, based on the 1 km agreement map for maximum inundation extent (Figure 5.8), is presented in Figure 5.11. Overall, the medium to large river floodplains (upstream drainage area > 1000 km²) have a larger inundation extent than small floodplains and interfluvial areas. An average total area subject to inundation of 317,800 ± 84,400 km² (average ± S.D.; median equal to 323,700 km²) was obtained, not including the optical and land cover products (G3WBM, GLAD, GSWO and ESA-CCI). A larger area for large floodplains was estimated by all products except for CIFOR, SWAMPS and WAD2M (which is partially based on SWAMPS and CIFOR). Two datasets estimated a similar value between the two classes (Chapman and GIEMS-2), which may be related to an overestimation of basin-scale isolated flooded patches.

Large floodplains fringing the main rivers including the Amazon, Negro and Purus are relatively well studied. However, large river-connected wetlands are also present in reaches of the upper Napo and Içá rivers in northwest Amazon basin, and upper Xingu in the southeastern portion (see location in Figure 5.1). These upper reaches are subject to more sporadic, flashy river hydrological regimes (HAMILTON et al., 2007), which make their inundation area difficult to map with current products because of the relatively low temporal resolution. In our analysis, the non-floodplain areas include mainly the large interfluvial areas (black rectangles in Figure 5.11), small river floodplains that are difficult to be mapped by the currently available products, and some reservoirs, such as Balbina reservoir on the Uatumã River. Regarding open water areas, Melack (2016) reported values ranging from 64,800 km² (MELACK; HESS, 2010) to 72,000 km² (SRTM) and 92,000 km² (HANSEN et al., 2013) for the Amazon basin (< 500 m). The three Landsat-based products assessed here, which are mainly capable to detect open water areas, estimate 98,500 km² (G3WBM), 128,500 km (GSWO) and 187,600 km² (GLAD).

While mapping large floodplains is interesting for a regional-scale analysis, as performed here, considerable heterogeneity of aquatic ecosystems occurs (e.g., grasslands, floating macrophytes, swamp palms, various savanna vegetation types) with differing degrees of combination of local (endogenous) and exogenous hydrological processes (BOURREL; PHILLIPS; MOREAU, 2009; OVANDO et al., 2018). The heterogeneity of surface-groundwater interactions also can contribute to inundation variations, e.g., a hydrological continuum that leads to groundwater-fed, permanently flooded wetlands in distal parts of river floodplains, and high, sporadic flooding in areas closer to the river (Hamilton et al., 2007). Therefore, there is a need to better understand the different degrees of river-wetland connectivity (PARK, 2020; PARK; LATRUBESSE, 2017b), which depends on the ratio of local runoff to mainstem inflow for floodplain lake systems (BONNET et al., 2008; BOURGOIN et al., 2007; LESACK; MELACK, 1995; PINEL et al., 2019; RUDORFF; DUNNE; MELACK, 2018; RUDORFF; MELACK; BATES, 2014).

Furthermore, while the central Amazon floodplains have been widely studied, other wetland complexes deserve more studies, as the Negro savannas, and the Roraima savanna, which were assessed by one only study (HAMILTON; SIPPEL; MELACK, 2002). The inundation mapping of the Pacaya-Samiria region in upper Amazon has received scientific attention recently (JENSEN et al., 2018; RODRIGUEZ-ALVAREZ et al., 2019), partially because of the region's role as a carbon sink via formation of peat (DRAPER et al., 2014; LÄHTEENOJA et al., 2012).

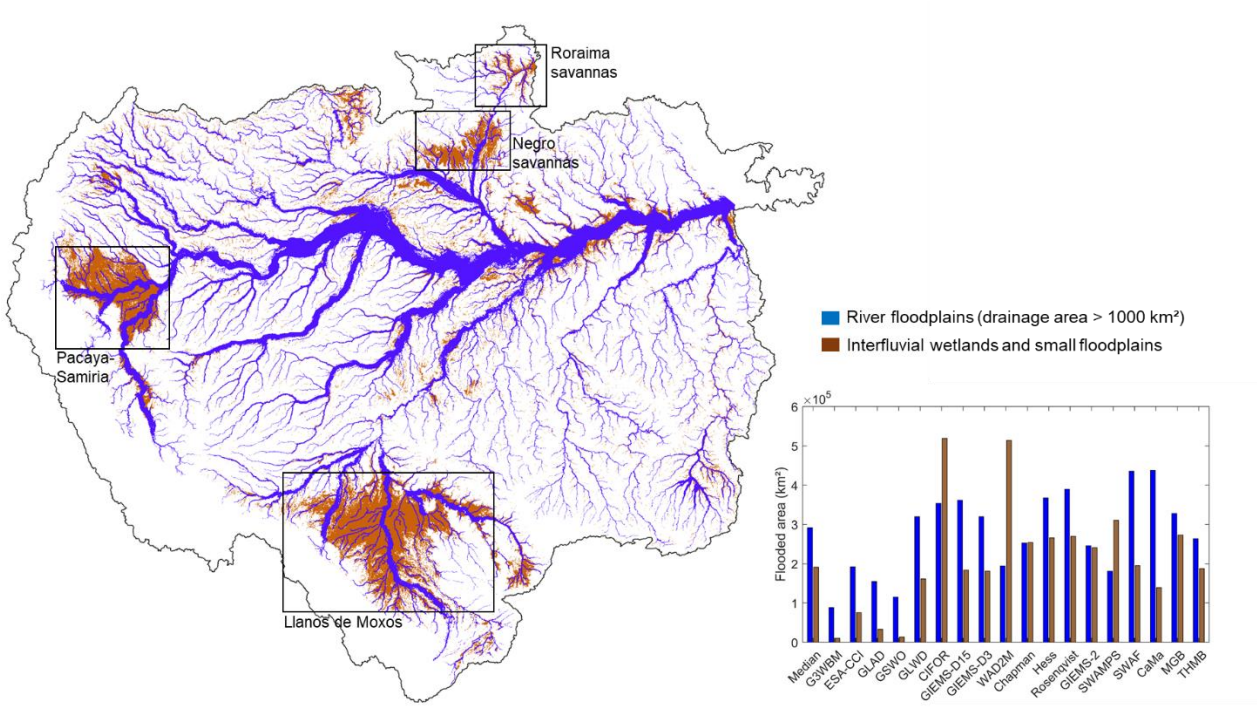

Figure 5.11. Quantification of maximum inundated areas over river floodplains with drainage area larger than 1,000 km², and interfluvial wetlands and small floodplains (area<1,000 km²) within the Amazon basin. The maximum inundation map refers to all 1 km pixels with at least two products agreeing (i.e., a reclassification of Fig. 5), in order to avoid overestimation caused by pixels with one only product classifying them as subject to inundation. The four large areas of interfluvial wetlands are highlighted (Pacaya-Samiria, Llanos de Moxos, Negro and Roraima savannas).

5.3.5 Limitations in comparing the inundation area products

Some of the differences in large-scale inundation mapping evident in our study occur because different products map temporal inundation in different ways. Figure 5.12 shows the agreement maps for maximum inundation for four classes of products, considering the 14 basin-scale high-resolution datasets. Those based on multiple datasets (GLWD, CIFOR, GIEMS-D3, GIEMS-D15, SWAF-HR) have the best

agreement for the Llanos de Moxos area, and to a smaller degree, for Pacaya-Samiria, Negro and Roraima regions. The SAR datasets have less overall agreement (Figure 5.12c), while the optical data are mainly limited to open water areas in the Amazon mainstem floodplain (Figure 5.12b). The 1D hydrological models cannot represent interfluvial wetlands where flooding is not controlled by river level and discharge (Figure 5.12d).

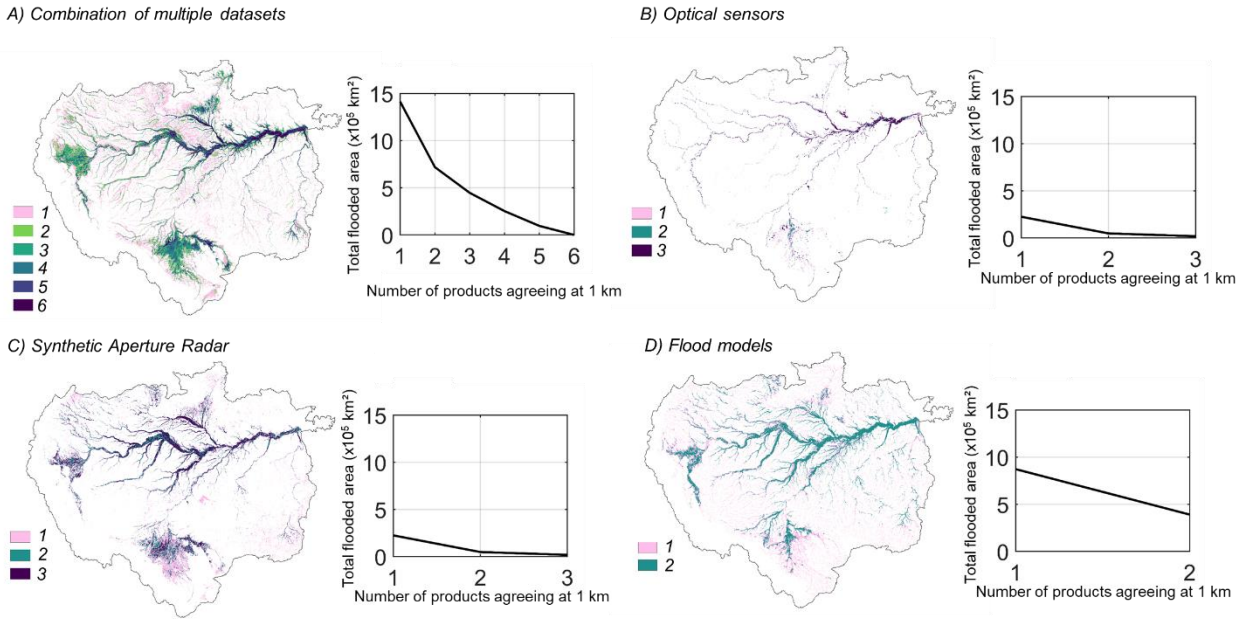

Figure 5.12. Amazon basin (< 500 m elevation) agreement maps at 1 km resolution, for maximum inundation and for each type of product, considering only the high-resolution products (≥1 km spatial resolution): (a) six datasets based on multiple sensor systems (GLWD, CIFOR, GIEMS-D3, GIEMS-D15, SWAF-HR, ESA-CCI), (b) three datasets based on optical sensors (G3WBM, GLAD, GSWO), (c) three datasets based on synthetic aperture radar (Hess, Chapman, Rosenqvist), and (d) two hydrological models (MGB and CaMa-Flood). The right column graphs present the total inundation area in the Amazon basin for a given number of products agreeing, e.g., the area of the basin where the two hydrological models (Fig. d) agree to be flooded is 390,903 km².

The different methodologies used to produce each dataset complicate their intercomparison (ROSENQVIST et al., 2020). Here we used long-term dynamic inundation datasets (e.g., GIEMS or hydrologic models), short-term dual-season products (e.g., Rosenqvist, based on four years), and products derived for a particular year (e.g., Hess product). Other datasets use alternative approaches to derive long-term maximum inundation area, such as GIEMS-D15, which generated estimates by fusing 3-year moving-window maximum values with the GLWD dataset. Thus, a comparison of all these datasets must be performed with caution. For instance, the comparison of

dual-season products with dynamic datasets at a monthly basis can yield erroneous conclusions, although it has been a common practice to compare multiple studies. Some datasets also consider a "high-water assumption" (FERREIRA-FERREIRA et al., 2015; HESS et al., 2003), whereby the high-water maps do not have any non-flooded pixel that is estimated as flooded for the low-water map.

Furthermore, each dataset was developed for different periods (Table 1), and thus interannual variability account for some of the differences among them. To address this, we performed the annual analysis (Figure 5.5), which suggests that although there is some degree of interannual changes, the long-term inundation estimate is fairly stable for each product, i.e., a given product's variability is generally not larger than the differences in comparison with the other estimates. However, the Amazon hydrological cycle has been changing (BARICHIVICH et al., 2018; GLOOR et al., 2013), and a recent increase in recorded floods over central Amazon suggests a new hydroclimatic state (ESPINOZA et al., 2019a) that deserves more studies. Some wetlands have also been subject to deforestation, and so the detectability of inundation by remote sensing may also increase over time, e.g., major deforestation has occurred along the lower Amazon floodplain (RENÓ et al., 2011). Similarly, widespread burning has been suggested to convert floodplain forest into savanna (FLORES; HOLMGREN, 2021), and in a way that these wetlands seem particularly vulnerable to fire in comparison to uplands, due to a drier microclimate, a more open canopy, and higher availability of organic matter during anomalously dry years (DE RESENDE et al., 2014; FLORES et al., 2017). However, analyzing long-term change in inundation patterns is beyond the scope of this study, and thus we assumed stationarity to estimate the long-term maximum and minimum inundation extents.

Although we used the local wetland products as references, they are not free of uncertainties. New, locally derived inundation datasets would be helpful for calibration and validation, especially in the less studied floodplain regions. Some of the local products assessed here have been validated with in situ data (aerial videography, UAV, local survey) (ARNESEN et al., 2013; FERREIRA-FERREIRA et al., 2015; HESS et al., 2003; JENSEN et al., 2018; RESENDE et al., 2019).

Hydrologic models currently available at the Amazon basin scale are one-dimensional, and thus are capable of simulating flooding mainly along river floodplains, as corroborated by various validation exercises in the Amazon that have relied on the Hess, GIEMS and SWAF-HR datasets for validation (FLEISCHMANN et al., 2020b; LUO et al., 2017; PAIVA et al., 2013a; ZHOU; PRIGENT; YAMAZAKI, 2021). Furthermore, given that a 500 m elevation mask (Amazon lowlands) has been used for some SAR products (HESS et al., 2015), and the difficulty of some radar and passive microwave products to detect inundation in high elevations due to slope and snow effects, for instance (PARRENS et al., 2017), we have also adopted the 500 m mask here to improve the comparability among the datasets. Some products, especially the hydrological models (MGB, CaMa-Flood and THMB), do estimate inundation in higher

elevation parts of the basin, although in this case uncertainties may also be large given errors in precipitation (low density of in situ gauges and high rainfall spatial heterogeneity) and thus runoff fields over mountainous areas, as well as the tendency for river flows to vary over short time scales (ESPINOZA VILLAR et al., 2009a; ZUBIETA et al., 2015). Besides, the availability of in situ river discharges for model calibration and validation is also low in the Andean and highland portions of the western Amazon (FENG et al., 2020; WONGCHUIG et al., 2019; ZUBIETA et al., 2017).

Our analyses were performed at 1 km resolution and at regional scales, which avoids geolocation problems that are common if performing analyses at higher resolutions (e.g., 30 or 90 m). Small disagreements among our estimates and the values presented in the original publication may arise from the use of the WGS84 datum with a geographical coordinate system for all datasets (except for SWAMPS which was provided in the EASE-Grid format). Also, the coarse-resolution products, especially GIEMS-2 and SWAMPS with 25 km spatial resolution, can be difficult to compare with local wetland products (e.g., Curuai and Janauacá), since only a few 25-km pixels may be located within the wetland boundaries.

The quantification of inundation over larger river floodplains (Figure 5.11) is also subject to uncertainties. The maximum floodplain lateral extent was estimated based on an automatic buffer procedure around the Hydrosheds drainage network, further manually edited by considering the three SAR-based, basin-scale products and the MERIT DEM-based topography. Although it does capture the basin-wide geomorphological differences along major floodplains, some uncertainties remain regarding the true lateral extent for areas where floodplain savannas are present, and areas of widespread flooding such as the Pacaya-Samiria and Llanos de Moxos regions. For these areas in particular, we assumed buffer values similar to adjacent upstream and downstream floodplains (e.g. the Amazon River downstream of Pacaya-Samiria region), which is reasonable but should undergo future scrutiny, mainly with local ground-based surveys.

Another important challenge is to find a common definition of wetlands among products. Here we focused on inundation extent, however some products (e.g., CIFOR) are associated with potential peatland locations instead of inundated area, although there should be a general correspondence between peat formation and flooding. Some products based on SAR or passive microwave may also be sensitive to saturated soil without standing water above it, and thus the observed inundation can have some ambiguity. Hydrologic models provide simulated surface water extent, and we have considered inundation those pixels with water depth greater than zero. Hydrologic models have uncertainties related to model structure (e.g., are the represented processes adequate to simulate inundation?), input data (e.g., precipitation and radiation forcing) and parameterization (e.g., soil water capacity and river channel width and depth). Remote sensing-based datasets have uncertainties related to spatial and temporal scale

(e.g., coarse-scale products not capable of detecting small patches), and detection uncertainty (e.g., dense vegetation canopies can obscure passive microwave emission from underlying surfaces). Thus, a comparative framework provides an opportunity to highlight and stress the uncertainties and limitations of each dataset.

5.4 Perspectives

Considerable advances have been achieved in the last decades in the mapping of inundation extent across the Amazon basin. Here, we have presented an analysis of 29 inundation datasets for the basin, covering multiple scales, spatial and temporal resolutions, and data sources. We showed that large discrepancies persist, and this is especially true at local-scales. In order to advance understanding of how much inundation occurs in the Amazon, it is paramount to understand the cross-scale expectations and requirements of different inundation-interested disciplines (ecology, biogeochemistry, natural disasters, social sciences, etc.), from local to basin-scale estimates.

What are the best data sources for inundation mapping in the Amazon River basin available today? At basin scale, the ALOS-2 PALSAR-2 Rosenqvist's product is now available at 50 m, and shows a good overall agreement with the 90 m Hess one over the large river floodplains, while the latter seems more accurate for interfluvial savannas (e.g,. Negro and Roraima ones). Detection of inundation by L-band SAR has a sound theoretical and empirical basis that has been validated for the Amazon (Hess et al., 2003). Optical products with resolution higher than 30 m are available, but detection of inundation is restricted to non-vegetated wetlands and clear-sky periods, as in the lower Amazon floodplains. ALOS-PALSAR at 12.5 m resolution and Sentinel SAR at 10 m resolution (with C-band and less vegetation penetration) can be applied to specific regions. Time series of these products can estimate seasonal variations in inundation, but are limited by the length of the acquisitions. Weekly to monthly, spatially coarser data (25 km) are available from passive microwave-based datasets as GIEMS, SWAF and SWAMPS. Downscaling techniques have improved their spatial resolution to 90 m (GIEMS-D3) and 1 km (SWAF-HR). Hydrological models (e.g., CaMa-Flood and MGB) are capable of accurately estimating inundation over river floodplains, and at temporal resolution depending on the input rainfall data (e.g., hourly to daily). However, they are still limited over interfluvial wetlands which have less connection with rivers, unless they are upgraded for simulating 2D inundation processes and complex floodplain channels (FLEISCHMANN et al., 2020b; YAMAZAKI et al., 2014b).

Regarding future developments by remote sensing and modeling communities, there is a need by end users for the development of inundation datasets at high spatial (e.g., < 30 m) and temporal (e.g., weekly) resolutions. At the Amazon basin scale, high-resolution, long-term flood frequency can be estimated by four of the products analyzed

here (GIEMS-D3, SWAF-HR, MGB and CaMa-Flood), with spatial resolution ranging from 90 m to 1 km. The discrepancies, however, are clearly large (Figure 5.13). The average of the basin-scale flood frequency based on the four products shows a higher agreement for areas with high flood frequency along the lower Amazon (Figure 5.13a). These are associated with many floodplain lakes and open water areas, and have the lower uncertainty across the basin (Figure 5.13b). There is generally a smaller variation along Amazon floodplains (except for their fringes) than in interfluvial areas, especially in the Negro and Roraima savannas (Figure 5.13b). A detail for the Mamirauá Sustainable Reserve in the Amazon mainstem floodplain (Figure 5.13c) reinforces the challenges for mapping local spatio-temporal inundation dynamics. The northern part of the Mamirauá reserve has shorter flood frequency in all products, while three products (SWAF-HR, GIEMS-D3, CaMa-Flood) estimate that large portions of it are actually never flooded. Furthermore, a dynamic characterization of the changing floodplain landscape is still lacking at both local and regional scales, e.g., considering migrating meanders and development of multiple floodplain lakes and superficially disconnected areas (e.g., oxbow lakes, meander cutoffs).

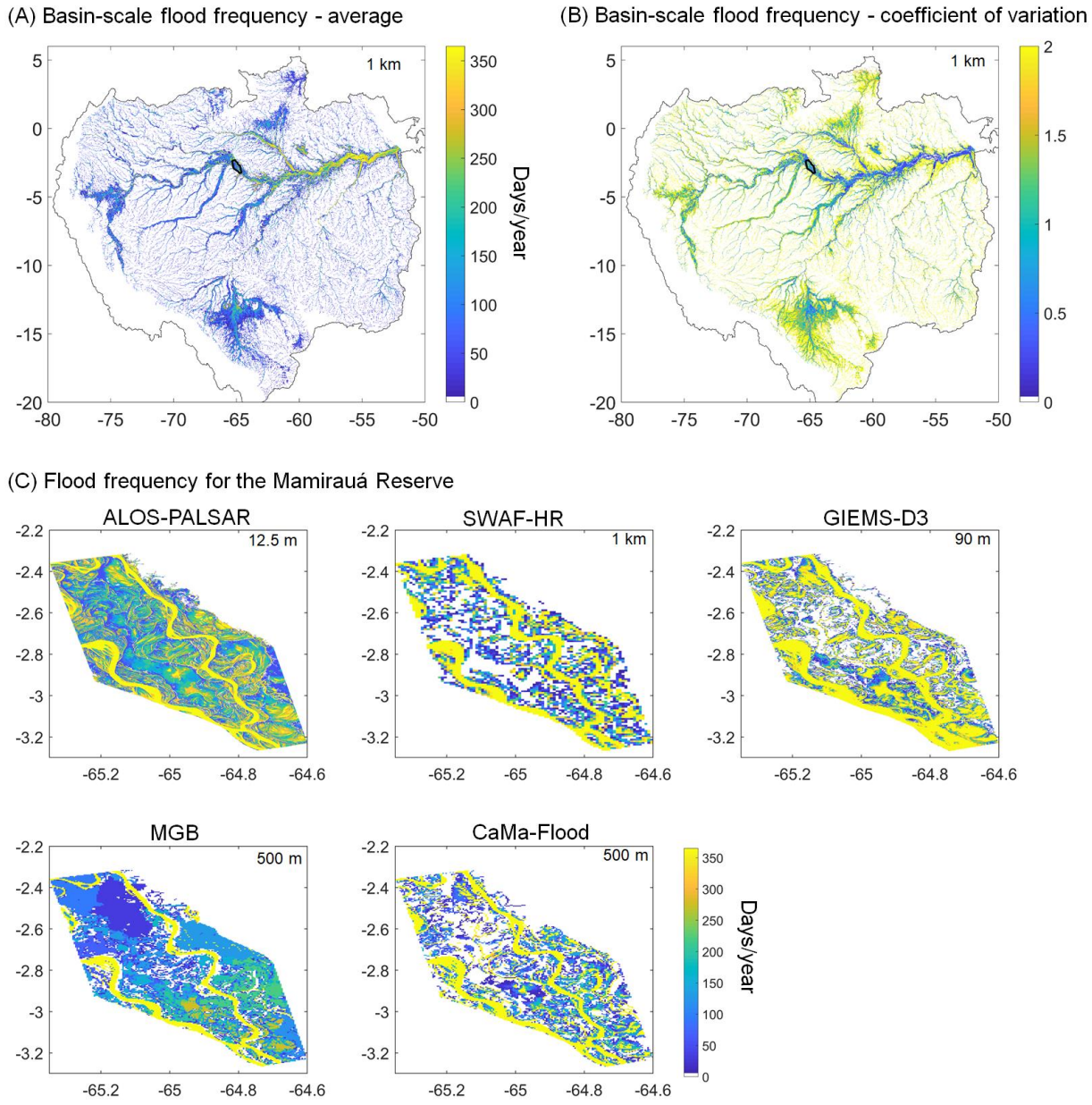

Figure 5.13. Analysis of flood frequency for (a) basin-wide average and (b) coefficient of variation of the long-term flood frequency estimated from four high-resolution dynamic products (GIEMS-D3, SWAF-HR, CaMa-Flood and MGB). (c) The four basin-scale products are compared to the local product (Ferreira-Ferreira et al., 2015) for the Mamirauá Sustainable Reserve in central Amazon (location shown in figure a).

The divergent estimates of Amazon inundation extent have major implications for the quantification of the role of wetlands on global biogeochemical cycles. Different products have been used to quantify the role of Amazon wetlands in the carbon cycle (GUILHEN et al., 2020; MELACK et al., 2004; RICHEY et al., 2002; SAUNOIS et al., 2020). An intercomparison assessment of global models forced with different inundation datasets for the Amazon could provide some insights on their sensitivity to

the estimated inundation. This would be particularly important for methane models, given the region relevance of global methane emissions from natural wetlands. Furthermore, for a proper estimation of methane and carbon dioxide fluxes, dynamic inundation estimates are necessary; this study shows that most coarse-scale dynamic datasets captures well the seasonality of annual flooding at the large scale (but not at the detailed scales), yet the inundation magnitude is still associated with large errors (Fig. S6).

The understanding of the ecology of Amazon freshwaters has improved over last decades thanks toadvances in remote sensing-based mapping of inundation. Hydrological variables of interest in relation to wildlife (ALVARENGA et al., 2018; BODMER et al., 2018) and vegetation distribution (HESS et al., 2003, 2015) include hydroperiod, floodplain water depth (ARANTES et al., 2013; FASSONI-ANDRADE et al., 2020), and (lateral) surface water connectivity (CASTELLO, 2008; DUPONCHELLE et al., 2021; REIS et al., 2019b, 2019a), and should be better constrained by future datasets. In addition, many wetland ecosystem studies are performed at the tree stand level (e.g., floristic inventories), given the large spatial heterogeneity of wetland vegetation, and thus require high spatial resolution inundation estimates to perform meaningful spatial analyses. Furthermore, besides a simple interfluvial/floodplain categorization of wetlands as performed here (Section 5.3.4), which is reasonable from a hydrologic perspective, improving our understanding of the ecology of Amazon freshwater systems requires an accurate mapping of habitats and their diverse vegetation types (e.g., grasslands, particular monodominant tree species, macrophytes). For instance, floodplain forest cover has been positively correlated to fishery yields (ARANTES et al., 2018) and fish abundance (LOBÓN-CERVIÁ et al., 2015). While this wetland habitat mapping already been done by some initiatives at the basin (HESS et al., 2003, 2015) and subregional scale (FERREIRA-FERREIRA et al., 2015; SILVA; MELACK; NOVO, 2013), there is a need for higher resolution, dynamic datasets.

From a hydrologic perspective, the categorization into floodplains and interfluvial wetlands is relevant for understanding basin-wide hydrological regime (REIS et al., 2019b), since floodplains are directly affected by alterations in river hydrologic regime, while the interfluvial ones are less connected to it. For instance, contrasting wetland types will be differently affected by the existent and proposed dams along the Amazon basin. While current dams have already altered the floodplain flood pulse at some parts of the basin (FORSBERG et al., 2017; RESENDE et al., 2019), the proposed ones have the potential to disrupt the Amazon hydrological regime (ALMEIDA et al., 2019; LATRUBESSE et al., 2017a). While in the Brazilian Amazon there is a policy trend to avoid regulation reservoirs, with most recent dams being run-of-river plants for which effects on hydrological regime are restricted to sub-weekly hydropeaking effects (ALMEIDA et al., 2020), this is not the case of many dams proposed for Ecuador, Peru and Bolivia (FORSBERG et al., 2017). However, even run-of-river dams can affect sediment dynamics and, consequently, downstream floodplain

hydrological dynamics to a still unknown extent. The use of high-resolution SAR data and ALOS and ALOS-2 for mapping tree mortality due to dams in floodplain areas is also possible (RESENDE et al., 2019). This is consistent for floodplains, but the effects are more unclear for areas as the Negro and Roraima savanna, more dependent on local rainfall. Thus, a better understanding of river-wetland connectivity, in combination with water level variation (JARAMILLO et al., 2018; PARK, 2020), is paramount, together with a more thorough comprehension of surface-groundwater interactions. These interactions are still poorly characterized, especially considering the complex feedbacks in many riparian wetlands as in the upper Madeira (HAMILTON et al., 2007).

Finally, regarding flood monitoring in the context of natural disaster management, current alert systems in the basin are restricted to river discharge and water level monitoring (e.g., Brazilian's Geological Survey SACE system; <http://sace.cprm.gov.br/amazonas/#>). The currently available, basin-scale inundation datasets are unable to map flood hazard at the detailed resolution required for a proper flood management, especially for the urban areas. However, assessments of inundation extent for particular areas have been performed with locally developed hydraulic models, as for the Madeira 2014 floods (FLEISCHMANN et al., 2021; SANTOS et al., 2017), based on local surveys of river bathymetry with LiDAR, for instance. In June 2021, the central Amazon River had its largest ever recorded flood (119 years at Manaus), which, if added to the other extreme floods in the last decade, is indicative of the new hydroclimatic state that the Amazon is experiencing since 1998 (BARICHIVICH et al., 2018; ESPINOZA et al., 2019a). This requires that the newly available inundation mapping capabilities, from both remote sensing and hydrological modeling, be developed to assist local to regional risk disaster-related stakeholders. Additional missing data for flood management relates to accurate mapping of rural populations which are affected by extreme floods and droughts.

5.5 Recommendations

To make progress on the quantification of the extent of the Amazon surface waters, especially given its changing regime under current and projected environmental change, we need to better assess the currently available inundation data. Performing optimal data fusion approaches is one way forward, considering the uncertainties in each product in a smart integration framework, as there are some promising mathematical ways to combine all this in an optimal way (PELLET et al., 2021). Regarding the currently available inundation products, downscaling techniques applied for all products could enhance estimates at local scales, and also be useful for further dataset merging techniques. Bias correction of different datasets could be achieved by considering the errors of each product, as estimated here for various wetland complexes across the basin. Recent studies have performed inundation bias correction using the Hess' product, for instance (AIRES; PAPA; PRIGENT, 2013; SORRIBAS et al., 2016). The combination and integration of multiple inundation products seems the best

approach (GUMBRICHT et al., 2017; HU; NIU; CHEN, 2017). For instance, optical data from Landsat may be suitable for monitoring long-term changes on downstream Amazon and floodable savannas, but are limited for flooded forests, and are incapable of monitoring monthly changes in surface water given cloud cover limitations. In turn, current hydrological models have limitations for non-floodplain wetland systems, while for river floodplains they are likely to be a suitable tool, especially for large river floodplains (e.g., the MGB model version used here is available only for upstream drainage areas higher than 1000 km²). Data fusion including new types of datasets (e.g., GNSS-R with SAR) is also welcome (JENSEN et al., 2018).

There is a need for the development of basin-wide 2D hydrological models, especially for large wetland complexes as the Llanos de Moxos and Pacaya-Samiria, to better represent inundation dynamics (FLEISCHMANN et al., 2020b). 2D models have been applied mainly to some local-scale areas in the Amazon mainstem floodplain (PINEL et al., 2019; RUDORFF; MELACK; BATES, 2014; TRIGG et al., 2009; WILSON et al., 2007) while, for other large, poorly gauged regions as the Congo Cuvette Centrale and the Niger Inner Delta, recent studies have shown the satisfactory performance of regional-scale 2D models (NEAL; SCHUMANN; BATES, 2012; O'LOUGHLIN et al., 2020). Future satellite missions will provide opportunities for improved inundation mapping in the Amazon, especially the polarimetric and interferometric L-band SAR data from the NASA/ISRO mission (NISAR) and the Ka-band Radar Interferometer (KaRIn) swath observations from the forthcoming SWOT mission (BIANCAMARIA; LETTENMAIER; PAVELSKY, 2016).

There is a need for a proper usage of the currently available inundation datasets by multiple local and regional stakeholders (e.g., local water authorities, national water agencies), as well as research communities not close to remote sensing groups. This will only be achieved through a two-way interaction with these actors and development of easy-to-access visualization platforms (i.e., investment on hydroinformatics and WebGIS systems, as the one developed for this study - https://amazon-inundation.herokuapp.com/), as well as training of regional/local user communities. The interaction with local users would also bring important feedback on the large-scale datasets as well, perhaps through citizen science initiatives that are ongoing in the Amazon (https://www.amazoniacienciaciudadana.org/).

Comprehensive comparison exercises of multiple inundation products, as presented here, are scarce in the literature, and we urge the scientific community to tackle such approaches in order to foster our understanding of inundation dynamics worldwide. The Earth System modeling community has been using such intercomparison projects to improve understanding of global water cycle, as done for the Amazon Basin river discharges recently with global hydrological models (TOWNER et al., 2019). However, initiatives for inundation extent are scarce - a few examples include a continental-scale assessment of flood model hazard maps in Africa (TRIGG et al., 2016) and regional assessment of inundation in floodplains of Nigeria

and Mozambique (BERNHOFEN et al., 2018), both based on global hydrological models. In order to achieve comparable products, data standardization and interoperability could be promoted in the Earth observation community that deals with surface water extent. In this study, each product was made available in a different format (shapefile or raster at NetCDF, binary, ASCII text, GeoTIFF) and projection (mainly projected UTM and geographic coordinate system with WGS84 datum), what can make the comparison among multiple products exhaustive.

New inundation techniques with Global Navigation Satellite System-Reflectometry (GNSS-R) as the Cyclone GNSS (CYGNSS) constellation of GNSS-R satellites using signal-to-noise ratio can improve the current mapping inundation capabilities for Amazon vegetated wetlands (JENSEN et al., 2018; RODRIGUEZ-ALVAREZ et al., 2019). More studies with the ALOS-2 PALSAR-2 data are promising, in order to achieve dynamic inundation estimates, as well as ongoing assessments of the accuracy of the now available high temporal resolution inundation products (e.g., SWAF-HR with 3-day availability). Regarding the need for new products, consistent and updated validation products of Amazon inundation are required, which could be derived from airborne, satellite, or UAV-based LiDAR surveys along multiple wetlands, in particular for overlooked wetlands as the Negro and Roraima savannas. This is especially important for the minimum inundation extent, which was associated to large uncertainty by the multiple datasets.

Collection of new in situ data in representative calibration/validation sites across the Amazon River basin is also imperative, including river and floodplain geomorphology and bathymetry (FASSONI-ANDRADE et al., 2021) and continuous recording of water levels using sensors (for both rivers and wetlands), which could be achieved through coordinated data collection among multiple Amazonian countries and institutions. Such information is fundamental to better understand the capabilities and limitations of remote sensing systems as well as to develop and improve hydrological models (BIERKENS et al., 2015; FLEISCHMANN; PAIVA; COLLISCHONN, 2019; WOOD et al., 2011). The CAMELS family (CHAGAS et al., 2020) of hydrometeorological data for multiple countries could provide a basis for such data sharing frameworks.

Finally, regarding inundation-related variables that need to be better addressed by the scientific community, we stress that inundation anomalies are still poorly understood by the lack of local truth inundation estimates for extreme floods and droughts - validation of extreme years has been usually performed with river water level data (in situ or from satellite altimetry) (SILVA et al., 2018; WONGCHUIG et al., 2019). Pioneer works have focused on the integration of only one inundation dataset (FRAPPART et al., 2005) to other hydrological variables such as total water storage and precipitation. Future works should address which products and methodologies are the most suitable for mapping extreme events. Besides hydrological models, long-term inundation records based on satellite data are still in their infancy, with recent 20 - 24

years long products made available (JENSEN; MCDONALD, 2019; PRIGENT; JIMENEZ; BOUSQUET, 2020), but for which abilities to depict long-term trends are still to be assessed. In order to provide a better estimation of inundation (or the analogous flood extent or surface water extent), we propose that it becomes an essential water variable (EWVs; Lawford (2014)) recognized by the international remote sensing community, in order to improve the monitoring of long-term trends and changes in this fundamental variable, especially in the context of a changing Amazon hydrological regime. Besides inundation extent, flood storage (FRAPPART et al., 2005; PAPA et al., 2008a; SCHUMANN et al., 2016a) and water velocity (PINEL et al., 2019) are necessary hydraulic variables to properly address multiple environmental studies (e.g., flood monitoring, flood attenuation by floodplains, fish floodplain habitats) that are still poorly addressed in the Amazon. It is also necessary to improve wetland habitat mapping across the Amazon basin towards more dynamic products, moving forward from a simplistic river floodplain / interfluvial wetlands classification as performed in this study, which would largely improve the ecological understanding of the Amazon diverse freshwater systems.

6 A one-fifth increase in the inundation extent over the central Amazon between 1980 and 2020

This chapter is presented as a research article:

- Fleischmann, A., Papa, F., Wongchuig, S., Fassoni-Andrade, A., Espinoza, J.C., Paiva, R.C.D., Melack, J.M., Fluet-Chouinard, E., Hamilton, S., Almeida, R., Bonnet, M.P., Castello, L., Alves, L.G., Moreira, D., Yamazaki, D., Revel, M., Collischonn, W., in preparation. A one-fifth increase in the inundation extent over the central Amazon between 1980 and 2020.

6. Um aumento de 20% na extensão máxima de áreas inundadas na Amazônia central entre 1980 e 2020

As planície de inundação do rio Amazonas são componentes importantes dos ciclos globais de água e carbono, representando uma grande fração das emissões globais de metano por áreas úmidas, além de abrigar uma grande biodiversidade e múltiplas sociedades humanas. A região tem enfrentado um novo regime hidroclimático desde a década de1990, caracterizada por um aumento da precipitação na parte norte da bacia. Isto se traduziu em uma série de eventos de inundações sem precedentes a partir de 2009, culminando em Junho de 2021 no maior nível já registrado nos 119 anos de registro em Manaus. Apesar disso, o aumento associado na extensão de áreas inundadas e suas potenciais consequências ainda não foram estimadas. Neste estudo, utilizamos dados de satélites e modelos de inundação para mostrar que a inundação máxima anual ao longo das planícies do rio Amazonas aumentaram em 20% desde a década de 1980, com uma quebra na série em 1998. Isto resultou em um aumento da conectividade das águas superficiais, e uma maior duração da inundação em 70% da planície a jusante de Manaus, com um aumento de 14% na área inundada por mais de 180 dias por ano. A intensificação do regime hidrológico da maior bacia hidrográfica do mundo tem importantes implicações para emissões de gases de efeito estufa, ecossistemas aquáticos e gestão de risco de inundação ao longo da bacia, e salienta a urgente necessidade de adaptação por parte das populações vulneráveis que vivem ao longo de muitos rios amazônicos.

Este capítulo é apresentado na forma de um artigo científico:

- *Fleischmann, A., Papa, F., Wongchuig, S., Fassoni-Andrade, A., Espinoza, J.C., Paiva, R.C.D., Melack, J.M., Fluet-Chouinard, E., Hamilton, S., Almeida, R., Bonnet, M.P., Castello, L., Alves, L.G., Moreira, D., Yamazaki, D., Revel, M., Collischonn, W., in preparation. A one-fifth increase in the inundation extent over the central Amazon between 1980 and 2020.*

Abstract

The Amazon River floodplains are a key component of the global water and carbon cycles, accounting for a large fraction of global wetland methane fluxes, besides harboring a great biodiversity and multiple human societies. The region has been facing a novel hydroclimate regime since late 1990s, characterized by an increase of precipitation in the northern portions of the basin, that has translated into a series of record-breaking flood events in central Amazon since 2009, culminating in the largest ever recorded water level in June 2021 over the 119 years of record. Yet the associated increase in inundation extent and its potential consequences have not been measured. Here we leverage state-of-the-art satellite data and flood models to show that the maximum annual inundation extent along the central Amazon floodplains has increased by 20% since the 1980s, with a major break after 1998. This results in an increased surface water connectivity in floodplain lakes, and a longer annual flood duration in 70% of the floodplain areas downstream of Manaus, with an increase of 14% in the area flooded for more than 180 days per year. The rapidly intensifying hydrological regime of the largest river basin in the world has significant implications for greenhouse gas emissions, aquatic ecosystems, and flood risk management across the basin, and presents an urgent need for adaptation of vulnerable populations living along many Amazon rivers.

6.1 Main

Every year, the flood pulse in Amazon wetlands dictates the rhythm of human societies and ecosystems along the largest river system on Earth (JUNK; BAYLEY; SPARKS, 1989; RAMALHO et al., 2021; SCHOR; AZENHA, 2017; TOMASELLA et al., 2013). This annual flooding regime impacts regional climate (SANTOS et al., 2019), and global carbon cycles through carbon dioxide (ABRIL et al., 2014; RICHEY et al., 2002) and methane emissions (MELACK et al., 2004; PANGALA et al., 2017). Changes in maximum floods can induce large ecosystem changes and be harmful to humans, affecting water and food security across the basin (LANGILL; ABIZAID, 2020; SHERMAN et al., 2016). Today, approximately 34 million people live in the Amazon Basin (RUIZ AGUDELO et al., 2020), from which a large portion lives close to its rivers and is vulnerable to changes in the Amazon flood pulse (DOLMAN et al., 2018; SCHOR; AZENHA; BARTOLI, 2018).

The Amazon freshwater systems have been changing (CASTELLO et al., 2013; DAVIDSON et al., 2012) through both climate cycles and effects of human pressure, in particular the construction of new dams (ALMEIDA et al., 2019; ARIAS et al., 2020; LATRUBESSE et al., 2017a; RESENDE et al., 2019) and deforestation in both uplands (ARIAS et al., 2020; COSTA; BOTTA; CARDILLE, 2003) and floodplains (RENÓ et al., 2011). This has resulted in an intensification of floods in the Amazon since the late 1990s (BARICHIVICH et al., 2018; ESPINOZA VILLAR et al., 2009b; GLOOR et al.,

2013), associated with an increasing of precipitation over the northern part of the basin (north of 5˚S; DA MOTTA PACA et al., 2020; ESPINOZA et al., 2019; FUNATSU et al., 2021; HAGHTALAB et al., 2020). The major role of sea surface temperature (SST) on the Amazon rainfall and hydrological regime is well known (FRIEDMAN et al., 2021; MARENGO; ESPINOZA, 2016; SCHÖNGART; JUNK, 2007; YOON; ZENG, 2010), and the recent increase in floods has been related to a strengthening of the Walker and Hadley circulations, associated in turn to a strong tropical Atlantic warming and tropical Pacific cooling (Arias et al., 2015; Espinoza et al., 2016; Barichivich et al 2018; Wang et al., 2018; Espinoza et al., 2019a; Friedman et al 2021). This trend contrasts with drier conditions observed in the Southern Amazon, as in the Llanos de Moxos wetlands (ESPINOZA et al., 2019b; MOLINA-CARPIO et al., 2017).

Over the northern Amazon basin, the average rainfall during March-April-May (MAM) has increased steeply since the year 1998, marking a clear breakpoint in the trend (ESPINOZA et al., 2019a), suggesting that a new hydroclimatic state has been operating since then in the Amazon. This has translated into an increase in river water levels and discharges of the northern tributaries (ESPINOZA VILLAR et al., 2009b; HEERSPINK et al., 2020). For instance, seven out of the ten highest water levels from the 119-years record in Manaus (Negro-Amazon confluence) have occurred since 2009 (Figure 6.1). This has culminated with the largest ever recorded water level in June 2021, which affected more than half million people in the Amazonas State in Brazil (~10% of the state population; MDR, 2021), a region already among the most affected by the COVID-19 pandemic worldwide (DE CASTRO; LOPES; BRONDIZIO, 2020). The intensification of flooding in the Amazon has directly affected local wildlife, biodiversity and human communities living along the Amazon floodplains, which need to adapt their activities to these climate-induced changes (BODMER et al., 2018; ENDO; PERES; HAUGAASEN, 2016).

While the new hydroclimatic state of the northwestern/central Amazon regions has been analyzed from a meteorological perspective (BARICHIVICH et al., 2018; ESPINOZA et al., 2019a; WANG et al., 2018), its impact on the Amazon inundation patterns has been limited to analyses of river discharges and water levels from a few in situ river gauges, which are only a proxy of inundation. An effective understanding of these changes on Amazon inundation patterns, in order to promote the societies' disaster resilience and a proper understanding of large-scale effects in ecological and geochemical fluxes, requires the spatialization of the inundation extent (HESS et al., 2015).

Here, for the first time, we quantify the long-term changes in inundation extent across the Amazon basin over the last 40 years, and evaluate the implications of continued changes over the next decades. Trends are assessed both spatially and for the central Amazon as a whole. Given the major significant trends are concentrated along the Amazon River floodplain and lower reaches of tributaries affected by backwater effects (MEADE et al., 1991), we give particular focus to the Amazon mainstem. We firstly show the trends in major hydrological variables as precipitation, river water

levels and total water storage, based on in situ and satellite-based datasets. Then, we leverage two state-of-the-art hydrological-hydrodynamic models and one long-term surface water dataset from satellite imagery (GSWO; PEKEL et al. (2016)) to investigate the annual changes of inundation extent along the central Amazon floodplains (see Methods). These hydrodynamic models have been extensively validated over the basin (PAIVA et al., 2013a; SIQUEIRA et al., 2018; YAMAZAKI et al., 2012) and allow the evaluation of the basin's wide geographic patterns.

6.2 Methods

6.2.1 Dynamic inundation from hydrological models

Monthly inundation estimates were obtained from two state-of-the-art hydrological-hydrodynamic models - MGB (SIQUEIRA et al., 2018) and CaMa-Flood (YAMAZAKI et al., 2011). MGB has been used to investigate Amazon hydrological processes for several years (PAIVA et al., 2013; SORRIBAS et al., 2016, 2020, FORSBERG et al., 2017; FLEISCHMANN et al., 2020). It is a rainfall-runoff model coupled to a physically-based hydrodynamic routine developed to represent the river-floodplain interactions in large basins (PONTES et al., 2016). The version used here was developed by Siqueira et al. (2018) for the entire South America, and was validated against extensive in situ and satellite data across the continent. It is forced with daily MSWEP v 1.1 rainfall (BECK et al 2017), and provides daily inundation extent at 500 m resolution for the period 1980-2014. CaMa-Flood is a global hydrodynamic model (YAMAZAKI et al 2011) which uses equations similar to MGB in order to simulate river-floodplain processes (YAMAZAKI et al., 2013; BATES et al., 2010). The model is forced with HTESSEL model runoff fields from the eartH2Observe platform (http://www.earth2observe.eu; Dutra et al., 2017), providing daily estimates of inundation extent over the period 1980-2014. In addition to inundation extent, we also assess the flood storage estimates with both models, given their satisfactory capability to estimate both inundation and water depth across the basin (YAMAZAKI et al., 2011; PAIVA et al., 2013; SIQUEIRA et al., 2018). The long-term maximum inundation over the Amazon mainstem floodplain, between the cities of Iquitos and Gurupá, are 118,500 km² and 115,000 km² for CaMa-Flood and MGB, respectively, which are very close to the estimation by Hess et al. (2015) of 115,800 km², which product is widely considered as the benchmark for Amazon wetland mapping

6.2.2 Open water remotely-sensed data

Long-term remote sensing estimates of inundation are very scarce. Here we use the Global Surface Water Occurrence product (GSWO; PEKEL et al 2016; available at <https://global-surface-water.appspot.com/download>) to assess high-resolution (30 m) trends. This dataset is based on data classification of the entire archive of the Landsat 5 Thematic Mapper (TM), the Landsat 7 Enhanced Thematic Mapper-plus (ETM+) and the Landsat 8 Operational Land Imager (OLI) orthorectified images, covering the period 1985-2020. Currently, optical images are the only ones available for measuring surface water across the last four decades. Given its inability to measure flooded vegetation (AIRES et al., 2018), it is only capable of monitoring open water areas or areas with sparse vegetation. Its applicability for the Amazon region is restricted to areas with extensive floodplain lakes or open vegetation as grasslands. Thus, the Lower Amazon river reaches, mainly downstream of the Negro-Amazon River confluence, are especially relevant for the usage of GSWO, given their extensive fractions of open water areas, also associated to large deforested areas (RENÓ et al., 2011). Upstream from it, flooded forests are ubiquitous, although floodplains lakes bordered with non-forest vegetation are also present and are used here to monitor long-term inundation extent changes. Besides being in agreement with the other inundation datasets and the increasing trend for water levels across the Amazon River (Fig. 6.3), the ability of GSWO to represent open water inundation changes is validated here by correlating it with the in situ water levels in the Amazon River at Óbidos gauge (Fig S8), which shows the very high agreement between in situ water levels and inundation dynamics ($R = 0.81$, $P<0.001$).

6.2.3 Passive microwave inundation extent data

Firstly, the linear model developed by Hamilton et al. (2002) is employed, which is based on passive microwave data from SMMR and in situ data from the Manaus river gauge. Although the linear model was developed for a water level range shorter than the one assessed here, it is used as an additional source of inundation extent. Secondly, we investigate inundation patterns with the new GIEMS-2 product (PRIGENT et al., 2020), which is an extension of the original GIEMS dataset (PRIGENT et al., 2007, PAPA et al. 2010), from 1993-2007 to the 1992-2015 period, and provides monthly inundation at 25 km spatial resolution with global coverage. It is based on a combination of passive and active microwave data from Special Sensor Microwave/Imager (SSM/I) and Earth Remote-Sensing Satellite (ERS), respectively, with ancillary data as NDVI from AVHRR. While the coarse GIEMS-2 product does not provide long-term inundation since the 1980's, it is used here to further validate our estimations of inundation trends over central Amazon.

6.2.4 Ancillary data

Precipitation data from CHIRPS (FUNK et al., 2015) at 0.01° spatial resolution were used to assess long-term trends across the basin, given its high accuracy for the Amazon basin (WONGCHUIG et al., 2017; HAGHTALAB et al. 2020; PACA et al., 2020; FUNATSU et al., 2021). Total water storage data from GRACE (April 2002-June 2017) and GRACE-FO (January 2018-today) missions (LANDERER et al., 2020; TAPLEY et al., 2004b), based on the JPL RL06M Mascon solution, were used to understand the impact of extremely wet years on the central Amazon storage. Given its short-term data availability (2003-today) and coarse resolution (300 km), no long-term trend analysis was performed, but it was used instead to infer large-scale patterns of water storage. In situ river water levels were obtained from the Brazilian National Water Agency (ANA; available at <http://www.snirh.gov.br/hidroweb/>) for all gauges in the Brazilian Amazon basin, in addition to in situ data from the Peruvian SENAMHI's for the Tamshiyacu gauge in the Amazon River, which is located close to the city of Iquitos (https://www.senamhi.gob.pe/?p=pronostico-meteorologico).

6.2.5 Trend analysis

Maximum and minimum annual inundation trends were obtained from MGB (1980-2014), CaMa-Flood (1980-2014) and GSWO datasets (1984-2020). Statistical changes (or breaks) in the series were evaluated using the Pettitt method (PETTITT, 1979), and spatial trends were mapped with the Mann Kendall tau (KENDALL; GIBBONS, 1975) at the products resolution (500 m for MGB and CaMa-Flood and 30 m for GSWO). The annual maximum inundation extent was averaged for the decades 1985-1996 and 2009-2020 for three floodplain areas: (1) the whole Amazon River floodplain between the cities of Iquitos and Gurupá, and two subsets of it, one for the area upstream from the city of Manaus, and another for the area downstream of it. Given the unsuitability of GSWO to be used for forested floodplains, only MGB and CaMa-Flood were used to estimate the long-term changes in inundation extent in the floodplains upstream from Manaus, and the three datasets were used for estimating the changes in the downstream ones. This was defined given the large differences between the two floodplains areas, with the one downstream of Manaus associated with large open water and low vegetation areas, in contrast with the upstream reaches with extensive floodplain forests. The two decades were chosen for being representative of 12 years of recent (2009-2020) and earlier (1985-1996) inundation dynamics, given the first year of GSWO availability (1985). The year of 2021 was not considered since it is not available in the GSWO dataset. Finally, besides inundation, we also assess flood storage trends with both MGB and CaMa-Flood models, following the same

methodology adopted for the assessment of inundation extent. As flood storage we understand all surface water accumulated in the river-floodplain system.

6.2.6 Surface water connectivity

Surface water connectivity and flood duration changes were computed over the 1985-1996 and 2009-2020 decades with the GSWO dataset, for the lower Amazon floodplain between Manaus and Prainha cities, which is representative of the floodplain systems with large lakes of the lower Amazon. To estimate surface water connectivity changes, we used the methodology presented by TRIGG et al. (2013). This analysis estimates, for a given floodplain area, the degree of connectivity across a given direction, measured as the number of pixel pairs connected by a given distance. The direction adopted for each analyzed area refers to the longest dimension of the floodplain unit, e.g., West-East for Madabá Grande Lake (Figure 6.3b). For the flood duration changes, long-term flood duration maps (i.e., estimation of how many days per year a given pixel was, on average, inundated) were computed for the decades 1985-1996 and 2009-2020, and subtracted from each other.

6.3 Results and discussion

6.3.1 The recent intensification of Amazon floods

A precipitation increase is observed over the northern Amazon (north of 5°S) since the 1980s, with a break in the series in 1998, as well as over the upper Purus and Juruá rivers, and parts of southern Peru (Figure 6.1a and Figure S1). In particular, rainfall increased 17% during MAM between 1981 and 2017 over the northern Amazon due to enhanced moisture flux from the tropical North Atlantic Ocean (ESPINOZA et al., 2019a). These changes are in agreement with Wang et al (2017), who analyzed several rainfall datasets, and with Funatsu et al. (2021), where an increase in deep convective clouds has been detected in Amazonia since the beginning of the 2000s. At the basin scale, this has led to positive, significant trends for both annual maximum water levels and water level amplitudes over the Amazon river mainstem, along the Negro and Purus rivers, as well as in tributaries subject to backwater effects from the mainstem (Figure 6.1a and Figure S2). Annual minimum water levels along the central Amazon did not increase (Figure S2). At Óbidos, where the largest increase is observed, the average maximum water level has risen by 87 cm (13% of the mean annual amplitude of ~6.90m, computed for the period 2009-2021) between 1985-1996 and 2009-2021 decades. Increases of maximum water level in other areas of the basin, as in the Ji-Paraná river, are related to deforestation (RODRIGUEZ; TOMASELLA;

LINHARES, 2010). Additionally, the total water storage (TWS) measured by the GRACE and GRACE-FO missions along the central Amazon floodplains peaks in the years of the great floods. While TWS change for particular events for the Amazon have previously been shown (CHEN; WILSON; TAPLEY, 2010), here we extend the TWS analysis to the whole 2003-2021 period, confirming the large role of inundation on the region's water storage. In agreement with the rainfall diminution in the extreme south of the Amazon basin, a negative trend of minimum annual discharge has been documented in the upper Madeira River (ESPINOZA et al., 2019b; MOLINA-CARPIO et al., 2017).

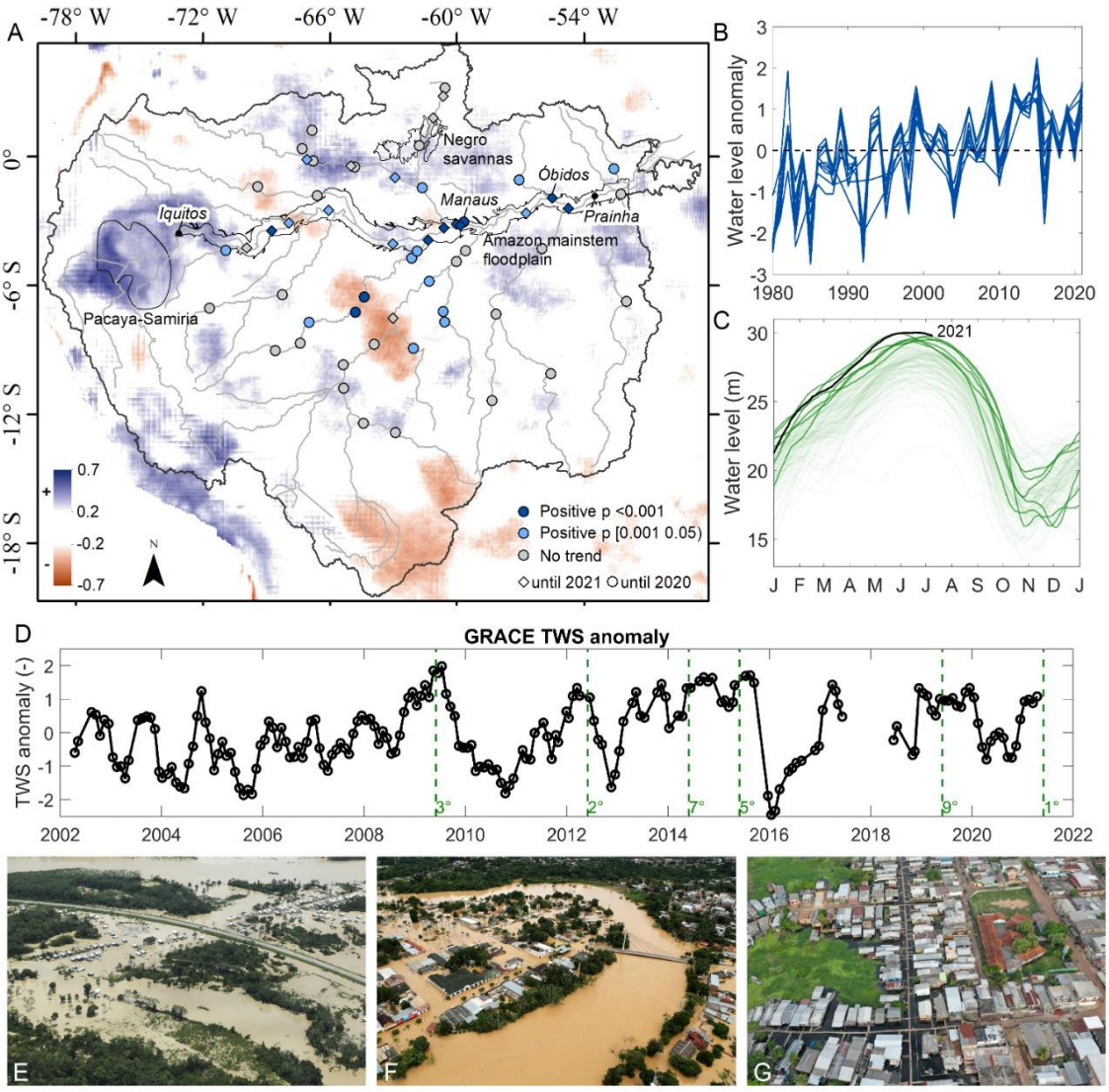

Figure 6.1. The recent intensification of Amazon floods. (a) Trends in precipitation and annual maximum water levels from 58 in situ gauges. Precipitation colors refer to the Mann-Kendall tau-value, where larger values are depicted as blue and are associated with more positive and significant trends. Water level gauges are colored according to their long-term linear trend P-values. (b) Anomalies of the annual maximum water levels for 12 gauges along the Amazon mainstem for the period 1980-2021; the individual series are presented in Figure S3. (c) Annual time-series of water levels for

each of the 119 years of record in the Manaus gauge time series. The years with the seven extreme floods observed since 2009 are highlighted in dark green. These floods are also shown in Figure d as vertical dashed lines for the month of maximum water level. (d) Monthly series of total water storage anomalies for the Amazon main channel and floodplain between the cities of Iquitos and Gurupá. The rank of the annual maximum water levels in the 119-years record is noted. Before 2009, the other extreme years were 1953 (4th largest), 1976 (6th), 1989 (9th) and 1922 (10th). Photos in (e-g) show the extreme recent floods in the (E) Madeira river at Porto Velho, (F) Acre river at Brasiléia, and (G) Amazon river at Manacapuru.

6.3.2 The flood propagation over Amazon floodplains

Over the Amazon River basin, positive and significant increases in inundation extent for the 1980-2020 period are present over the floodplains along the Amazon mainstem and a few tributaries subject to backwater effects according to the two flood models and GSWO (Figure 6.2a). This is a direct effect of the propagation of the increased precipitation in the upper Amazon and Negro basins downstream to the central Amazon. In the basin, a few decreasing inundation trends over 1980-2020 occur mainly in the upper Madeira Basin, corroborated by precipitation analyses over the region (ESPINOZA et al., 2019a, 2019b) and discharge evolution (MOLINA-CARPIO et al., 2017). Over the Amazon river floodplains between Iquitos and Gurupá cities, a 21% increase is observed in the maximum inundation extent, moving from 95,000 to 105,000 km² of inundated areas between the 1980s and 2010 decades, based on the two flood models. A similar 18% increase is estimated with the inundation rating curve developed by Hamilton et al. (2002) (Figure S8b).

The increasing inundation trends are also revealed with the global surface water extent dataset (GSWO) based on Landsat data (PEKEL et al., 2016), which unlike the hydrodynamic models, is independent from rainfall trend. Since optical data are not capable of monitoring flooded forests, the GSWO positive trends are restricted to open water and non-forest floodplain areas, which are rare upstream from the Amazon-Japurá confluence, but widespread downstream of Manaus (Figures 6.2c and S4). In the large mainstem floodplains, the presence of permanent lakes results in an annual increase of inundation (7%-13%) downstream of Manaus smaller than in upstream reaches (25%-32%). Annual minimum inundation extent has not changed over the same period. As a result, the inundation amplitude has significantly increased (Figure S5).

The series of inundation maxima and amplitude from the two flood models exhibit the same break point observed for precipitation in 1998 (ESPINOZA et al., 2019a). The time-series show a smaller slope after 1998, and the continuous increase led to a maximum flood extent from 98,000 km² for the period 1980-1998 to 110,000 km² for the period 1999-2020. Furthermore, while the 2015 El Niño drought led to anomalously low maximum water levels at Óbidos, the impact on inundation extent was

not as high given the surface water accumulation from the previous extremely wet years. The increase in maximum inundation extent and water levels also translates into increased surface water storage (Figure S6), confirming the previously mentioned trends in TWS (Figure 6.1d).

Flood duration across the Amazon floodplain was substantially altered (Figure 6.3a): an increase was observed in 70% of the area between the cities of Manaus and Prainha between the decades of 1986-1995 and 2009-2020, with an increase of 13.7% in the area subject to inundation for more than 180 days per year (Figure S7a). Additionally, 20% of the area had 50 more days of flooding per year on average, and 12% had 100 more days of flooding per year between the two decades (Figure S7b). Areas with decreased flood duration are associated with floodplain sedimentary processes and sediment inputs into lakes, as represented by the linear development of a crevasse with delta formation (Lewin et al., 2017) in the detail of Figure 6.3a, with increased flood duration over the newly formed connection channel between the mainstem and the lake, and decreased duration over the deposition area in the lake. The exchange of sediment between floodplain lakes and the river channel has intensified due to recent floods, with increasing sediment inflow and storage being reported for the Curuai lake (RUDORFF; DUNNE; MELACK, 2018) and increased load at the Amazon river mouth (ANTHONY et al., 2021).

Furthermore, the lateral (within wetland) connectivity (see Methods) has increased over multiple floodplain units (Figure 6.3b). The largest effect was observed in the Maracu and Camapu lakes in the downstream reaches, with the connectivity increasing significantly, e.g., for short distances as 1 km, the number of connected areas (pixels) increased 3.5 times; this number increased to 5.3 times for 10 km, and to 6.0 for 20 km. In the Curuai lake, an increase between 1.2 and 1.4 is observed for all distances smaller than 45 km. These steady increases for different distances are associated to the Curuai lake morphology, where the inundation extent impact was mainly related to its shore expansion. For the Maracu and Camapu lakes, the increased flood extent led to the connection between previously unconnected floodplain areas (Figure 6.3b).

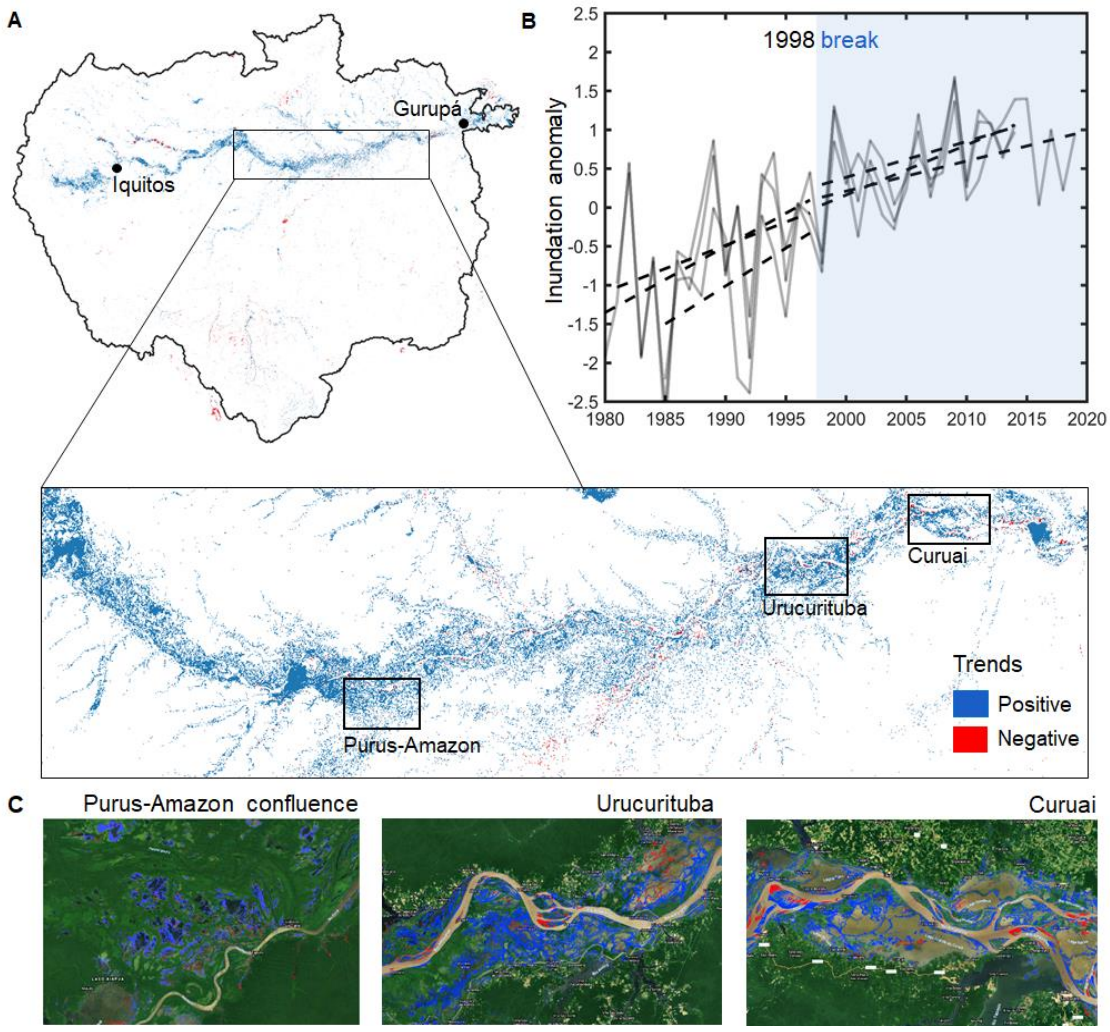

Figure 6.2. Large-scale increase of inundation extent over the Amazon river floodplain. (A) Spatial assessment of inundation trends over the Amazon basin according to two flood models and GSWO, showing areas with positive and negative trends over 1985-2020. (B) Anomalies of maximum inundation extent for the whole Amazon mainstem floodplain region, between the cities of Iquitos and Gurupá, depicting trends before and after the 1998 break in the series, based on the two flood models and GSWO. (C) Detailed spatial trends on four floodplain regions (location in figure A) based on the GSWO optical imagery classification.

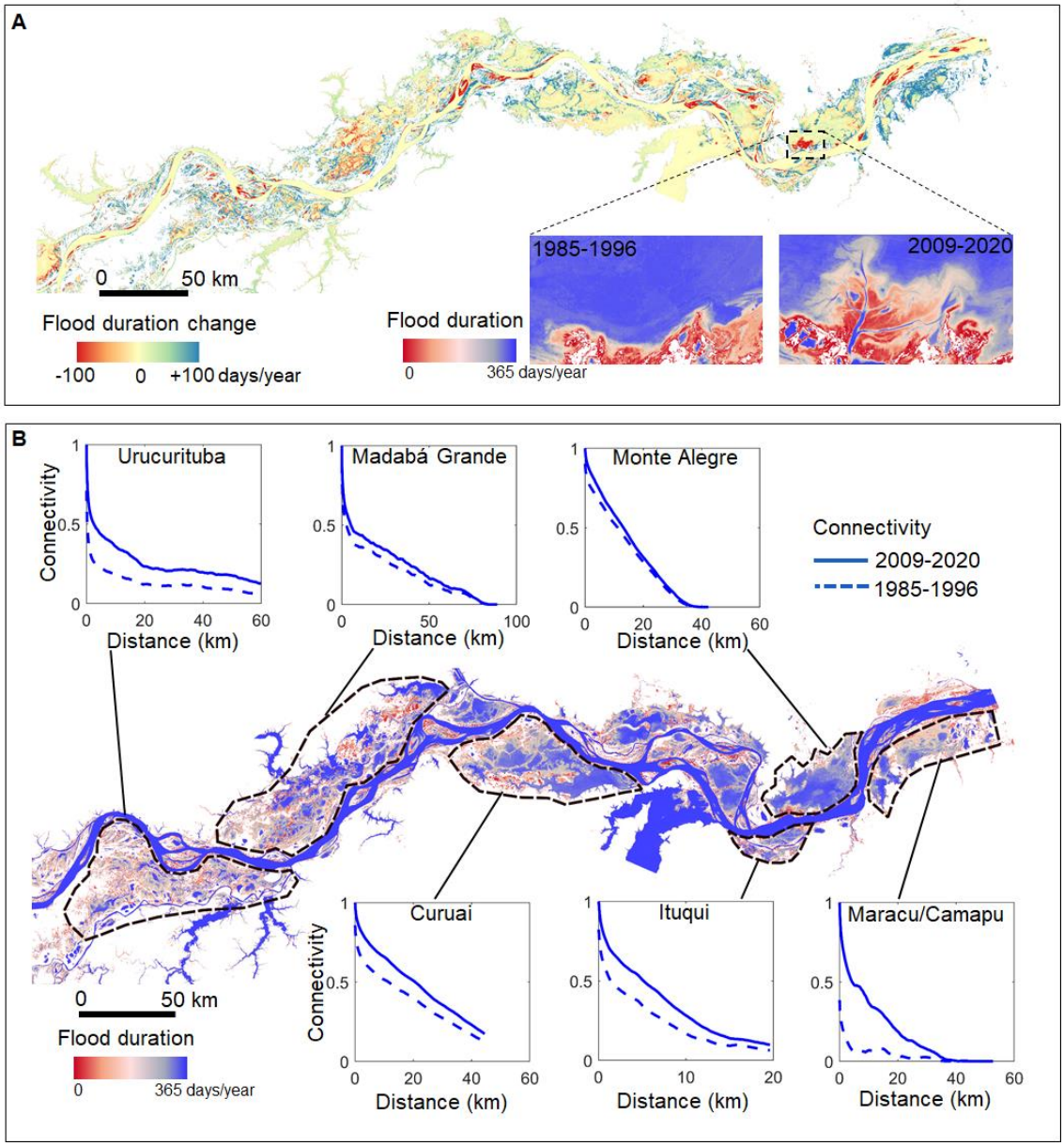

Figure 6.3. Large increase of Amazon surface water connectivity and floodplain lake areas in the last decades. (A) Change in flood duration between 1985-1996 and 2009-2020 decades. Areas where flood duration has decreased are associated with floodplain sedimentary processes, as shown in the detail for a crevasse formation in the Lago Grande de Monte Alegre. (B). The lateral surface water connectivity increased in multiple Amazon floodplain regions in the last decade, in contrast to 1985-1996. The background map shows the averaged 2009-2020 annual flood duration. In some locations, such as the Maracu and Camapu lakes, short distance connectivity has more than doubled.

6.3.3 Amazon river floodplains: a new inundation regime?

The 20% increase in maximum inundation extent over the Amazon river floodplains, overlaps with a number of human-driven changes in the basin. The most important drivers of change the basin include: construction of hydropower dams in the Upper Amazon, as well as on the Madeira and Tapajós tributaries, deforestation for agriculture in the lower Amazon, development of waterways in the Upper Amazon river, including the Andes-Amazon transition zone (e.g., continuous river dredging in the Amazon Waterway Project to connect Marañón, Ucayali and Huallaga rivers), and increasing urbanization and population in riparian cities where most people in the Brazilian Amazonia and the Loreto department (Peru) reside (SCHOR; AZENHA; BARTOLI, 2018; SZLAFSZTEIN, 2015) (Fig. 6.4a). A synergistic effect of ongoing changes may occur, such as along the deforested areas in the lower Amazon (RENÓ et al., 2011) which surround areas with increased inundation (Figure 6.4c).

While climate projections for the middle and end of the XXIst century suggest increased inundation in the Amazon reaches upstream from the Amazon-Purus confluence (BRÊDA et al., 2020; SORRIBAS et al., 2016; ZULKAFLI et al., 2016), the propagation of these effects to downstream Amazon reaches based on model projections remains uncertain, especially considering the projected decreases of precipitation and river discharges over Southern Amazon tributaries (BOISIER et al., 2015; BRÊDA et al., 2020). The +20% change of maximum inundation extent we describe over 1980-2020 is similar to the +18% projection for the end of the century for the Peruvian Amazon (Figure 6.4b), but larger than the +3.6% projection for the central Amazon (SORRIBAS et al., 2016). Furthermore, CMIP5 climate models project more frequent extreme El Niño events under 1.5°C and 2°C, but little to no change of La Niña extremes (WANG et al., 2017a).

The effects of the proposed dams (Figure 6.4d) on the Amazon river inundation regime depend on the future dam operation schemes. Today, most dams operate as run-of-river, and the regulation of seasonal flow regime at the basin scale remains relatively small aside from a few tributaries such as the Uatumã river (SCHÖNGART et al., 2021) (Schöngart et al., 2021), and from sub-daily hydrological variation due to hydropeaking operation (Almeida et al., 2020). However, while the proposed Brazilian dams will likely operate as run-of-the-river plants given environmental regulations, dams in the upper Amazon reaches of Peru, Bolivia and Ecuador will likely be storage dams (FORSBERG et al., 2017). Storage dams pose great threats to the Amazon river flood pulse in regions such as the Pacaya-Samiria region, in the Marañón-Ucayali confluence (ANDERSON et al., 2018).

The Amazon's hydrology is not stationary, and thus it is not straightforward to define whether it is facing a new inundation regime due to a combination of oceanic circulation changes and global warming. The ongoing phase of the Pacific Decadal Oscillation, with a current Pacific SST decrease, seems to be reverting towards an El

Niño-like Ocean state (BARICHIVICH et al., 2018; CHA; MOON; SONG, 2018; FRIEDMAN et al., 2021), while tropical Atlantic SST increase is likely to continue in next decades due to global warming and Atlantic Multidecadal Oscillation (BARICHIVICH et al., 2018).

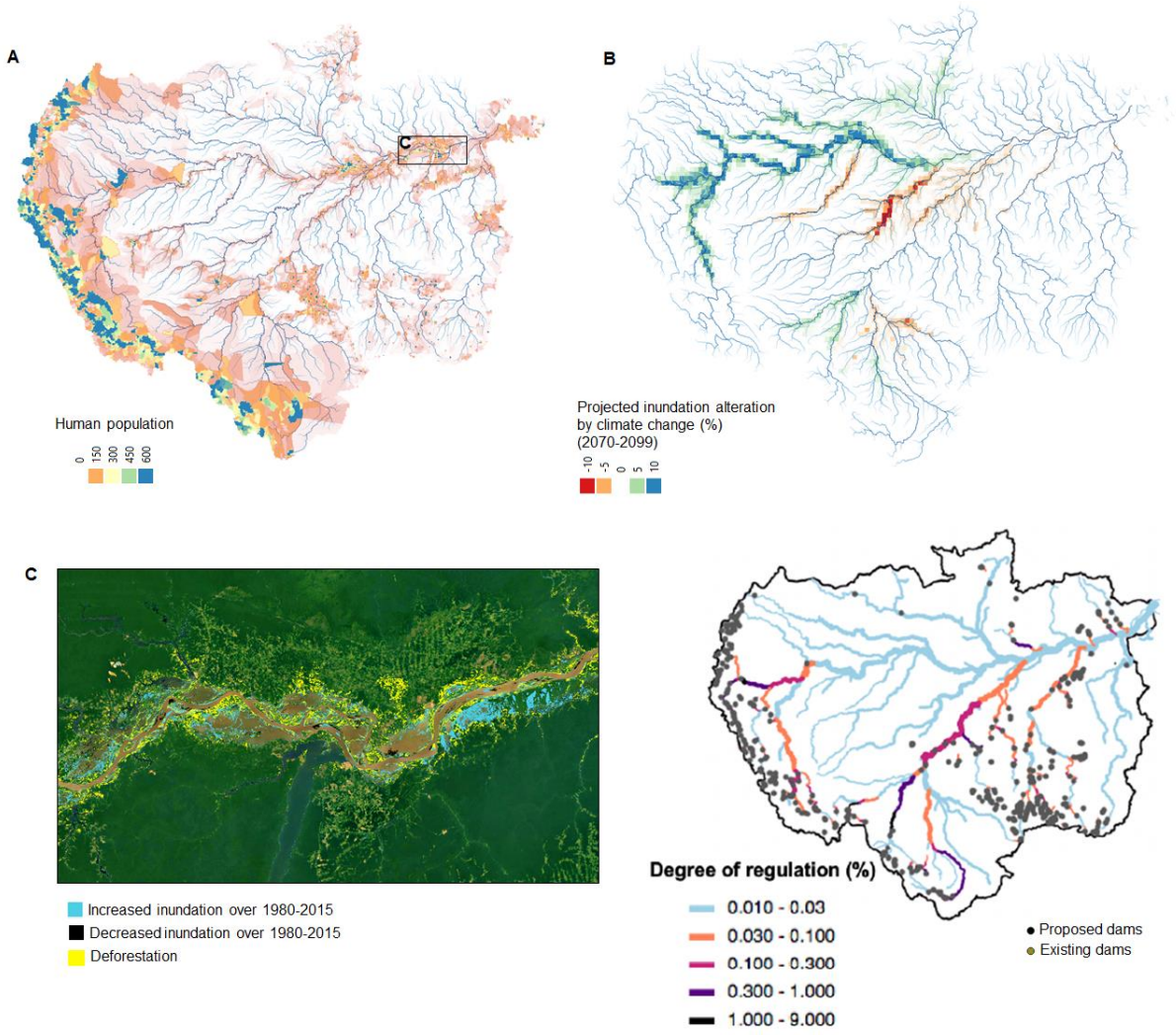

Figure. 6.4. Amazon floodplains under climate and human-driven changes. (A) Human population (GPW, 2010). (B) Projected alteration of maximum inundation extent by climate change (SORRIBAS et al., 2016). (C) Deforestation (RENÓ et al., 2011) and maximum inundation extent trends (this study) over the lower Amazon floodplain. (D) Degree of regulation index, showing the potential hydrological alteration by current and proposed dams.

6.3.4 Environmental implications

The substantial change in inundation extent along the largest river basin on Earth raises large adaptation challenges for both human societies and ecosystems, and climate change mitigation strategies. The effects of climate change on wetland ecosystems are uncertain (BARROS; ALBERNAZ, 2014). While recent studies have focused on potential effects of future climate change-induced droughts in the Amazon (HURD et al., 2016; SZLAFSZTEIN, 2014), projected for the Southern tributaries, we stress the impacts of extreme floods on Amazon freshwater systems, which may persist in the forthcoming years along with a warming climate.

The increased flood duration and lateral hydrological connectivity along floodplains may increase habitat availability for that fish with lateral migration (ARANTES et al., 2013; CASTELLO, 2008; DUPONCHELLE et al., 2021) or for those that migrate to upper reaches seeking deep waters for spawning (FENG et al., 2020). Areas of flooded forest are a predictor of fishery catches for some species (CASTELLO; ISAAC; THAPA, 2015; GOULDING et al., 2019; LOBÓN-CERVIÁ et al., 2015). However, the persistence of higher flood duration may lead vegetation to move towards more flood-tolerant species as grasslands or macrophytes, and less diverse forest communities (BARROS; ALBERNAZ, 2014; GLOOR et al., 2015; SILVA; MELACK; NOVO, 2013). The impact of increased sediment loads and enhanced erosion processes could further alter the distribution of habitats, possibly impairing fish recruitment and survival (CASTELLO et al., 2018). Increase in river discharge is particularly related to higher coarse sediment flux across the Amazon, while fine sediments are more related to changes in precipitation (ARMIJOS et al., 2020). While fisheries tend to be positively affected two to three years after great floods, vegetation changes may occur much slower. An additional threat to floodplains may come from fires in dry periods, especially for the black-water “igapós” which are particularly vulnerable to conversion to savanna-like vegetation (FLORES et al., 2017; FLORES; HOLMGREN, 2021).

Wetlands are the largest natural source of CH4 (BOUSQUET et al., 2006; ZHANG et al., 2017b), and the Amazon wetlands may contribute up to ~30% of the global annual CH4 wetland flux (WILSON et al., 2020). The changing flooding regime could potentially alter the contribution of CO2 and CH4 emissions to the atmosphere. Floods have been reported to increase CO2 outgassing in the Madeira floodplain (ALMEIDA et al., 2017). While changes in global CH4 emissions are still poorly understood (SCHAEFER et al., 2016), there is a renewed increase of methane concentration since 2007 (ROSENTRETER et al., 2021), and a recent increase in CH4 emission from East Amazonia in 2010-2018 has been associated with the recent large floods (WILSON et al., 2020). Yet climate change effects on Amazon wetlands CH4 contribution are still uncertain (ZHANG et al., 2017), particularly because of the unknown impact of changing hydrology on the distribution of wetland and methanogenesis conditions.

6.3.5 Adaptation to increased flooding

While regular floods are generally beneficial to local human societies, extreme floods can lead to severe impacts, especially for vulnerable populations along rivers (ANDRADE et al., 2017; CHACÓN-MONTALVÁN et al., 2021; PINHO; MARENGO; SMITH, 2015). Adaptation of these populations to environmental changes requires developing a broad portfolio of diversified livelihoods throughout the annual hydrological cycle (OVIEDO et al., 2016). A characterization of the new Amazon hydroclimatic state, in terms of flood duration, magnitude and timing, is paramount in order to understand how "bad can be the floods" for these societies (LANGILL; ABIZAID, 2020). Urbanization in the Amazon is unique, and there are major ongoing changes in the relationship between *ribeirinhos* and urban areas in the rural centers, due for instance to increased *ribeirinhos*' incomes by Brazilian government welfare programs as *Bolsa família* (MARU et al., 2014; SCHOR; AZENHA; BARTOLI, 2018). During extreme floods, houses can stay flooded for three months, waterborne diseases (e.g., diarrhea, hepatitis A and B, ringworm and malaria) sharply increase (WOLFARTH-COUTO; FILIZOLA; DURIEUX, 2020), and even birth outcomes are affected (CHACÓN-MONTALVÁN et al., 2021). Rural settlements often have very low sanitation infrastructure and during high floods require localized water treatment plants to be distributed. Other impacts of flooding include: increased drowning by children, proximity to dangerous animals such as snakes (LANGILL & ABIZAID, 2020), intense fluvial traffic and generation of waves close to houses, shortage of timber for building pathways within and among houses ("*marombas*"), and many civil infrastructure. For instance, some hospitals need rebuilding every few years because of the recurrent floods, as in the city of Anamã, the "Amazon Venice", which was entirely flooded in 2021. Migration from flooded zones have also been reported in many regions of the Amazon, as either seasonal (during the high-water season) or permanent relocation (ALMUDI, 2019; IGARAPÉ, 2018; SHERMAN et al., 2016). The Brazilian Amazonas State is the most affected by natural disaster-induced migrations in Brazil, with 840,000 people (20% of the state) estimated to have migrated between 2000 and 2018 due to disasters (IGARAPÉ, 2018). However, even larger difficulties of settling in urbanized areas have made many people return to flood prone riverine areas (SHERMAN et al., 2016; ALMUDI, 2019).

Food security is threatened in the Amazon. Floodplain crops cannot cope with prolonged floods (LANGILL & ABIZAID, 2020), and agriculture (both plants and livestock) is impaired by unpredicted floods, as "repiquetes" or early floods (COOMES et al., 2016; LANGILL; ABIZAID, 2020; LIST; COOMES, 2017; PINHO; MARENGO; SMITH, 2015), which are related to rainfall anomalies over northwestern Amazon (FIGUEROA et al., 2020). In the recent extreme floods, indigenous people have been losing crops to inundation and becoming unable to burn the land ahead of cropping due to excess of wet-days, resulting in tons of manioc lost (ISA, 2021). Loss

of upland tree species not adapted to flooding has also been reported, as the managed Brazil nuts stands during the 2014 Madeira flood (HERRAIZ; GRAÇA; FEARNSIDE, 2017), while some communities are no longer capable of growing upland tree species such as avocado in the Mamirauá reserve (Castello, *pers. comm.*). On the other hand, if the rural communities are prepared to deal with the increasing floods, they can reap some benefits (SHERMAN et al., 2016). Floods facilitate timber extraction during high water periods (SHERMAN et al., 2016; TOMASELLA et al., 2013) and rice growing due to increased soil fertility. The difficulties in fishing during the extreme flood (OVIEDO et al., 2016) may change into an increase in fish yield in the aftermath (BODMER et al., 2018, LANGILL & ABIZAID, 2020). Adaptation may include changing activities from hunting to fishing as happened with the Cocama indigenous community in the Pacaya-Samiria National Reserve in the Peruvian Amazon (BODMER et al., 2018), raising another set of questions relating to food and nutritional security (HEILPERN et al., 2021).

A number of adaptation actions can be taken to cope with the recurrent extreme floods, which include: improving flood risk mapping in remote and urban areas by scientists and risk managers, strengthening of civil defense, social programs for disaster preparedness and post-event response, and early warning systems by the government (Marengo et al., 2013; Pinho et al., 2015). Current alert systems have been performing satisfactory forecasts along the Peruvian (SENAMHI; https://www.senamhi.gob.pe/?dp=loreto&p=pronostico-caudales) and Brazilian Amazon river reaches (SACE CPRM; http://sace.cprm.gov.br/amazonas/#). An effective relationship has been established between CPRM and local civil defense, as well as with national-scale media. Yet the communication to remote rural communities remains challenging (ANDRADE et al., 2017). Local communities can enact strategies such as pre-event food saving, increase of mutual support (ALMUDI, 2019), and agriculture adaptation towards water-resilient structures (e.g., floating planting beds) and new crop types, perhaps moving temporarily to the usually less fertile uplands. The hardship from floods may promote innovative solutions in the communities by making them active participants of the adaptation process (MARU et al., 2014; ALMUDI, 2019), but there is a need for implementing a cross-scale set of programs for risk management. The national and pan-Amazon policies of natural disasters will require continued investment in prevention, not only on post-event mitigation (SZLAFSZTEIN, 2015). The current situation is already alarming and must draw the attention of governments from local to national and international scale, even if future projections in inundation extent are uncertain.

Flood-risk research must skew towards the most vulnerable people (HINO; NANCE, 2020), in order to assist them to improve their resilience (MARU et al., 2014; HINO & NANCE, 2020), with a high risk of turning traditional people into environmental refugees. The ongoing changes largely impair the ancestral knowledge practices of indigenous communities across the Amazon, which have adapted to the annual hydrological regime (CABALZAR, 2016). In the upper Negro Basin, for

instance, one of the locations in South America with the largest indigenous diversities, there are major ongoing difficulties, which are summed to the COVID-19 pandemic situation. Basin-wide water, human and ecological resources management must be promoted (CASTELLO et al., 2013).

Part II. South American wetlands: a comparative hydrology approach

Part II. Áreas úmidas da América do sul: uma abordagem de hidrologia comparativa

7 South American wetlands from space: flooding patterns and trends

This chapter is presented as a research article:

- Fleischmann, A., Papa, F., Paiva, R.C.D., Prigent, C., Ovando, A., Paris, A., Calmant, S., Collischonn, W., in preparation. South American wetlands from space: a comparative hydrology approach.

7. Áreas úmidas da América do Sul vistas do espaço: padrões e tendências de inundação

A América do Sul abriga alguns dos maiores rios da Terra, e grandes complexões de áreas úmidas como o Pantanal e as da bacia amazônica, cobrindo 5-12% do território do continente. No entanto, o funcionamento hidrológico de muitas destas áreas permanece pouco descrito e conhecido, e mudanças ambientais em curso urgem para uma melhor compreensão destes sistemas. Nesta pesquisa, utilizamos produtos de sensoriamento remoto para estudar 12 grande regiões de áreas úmidas da América do Sul, englobando variados tipos de clima e vegetação, numa perspectiva de hidrologia comparativa. Estimativas de precipitação (MSWEP), extensão de áreas inundadas (GIEMS-2), armazenamento total de água (GRACE), e níveis d'água em rios e áreas úmidas (ENVISAT, ICESat, SARAL, TOPEX-POSEIDON, JASON-2, SENTINEL-3/A/B, totalizando 888 estações virtuais) são utilizados para compreender a dinâmica hidrológica destas áreas. Áreas úmidas associadas a planícies de inundação (e.g., Magdalena, Pantanal, Amazonas e Paraná) têm uma propagação de cheias mais lenta associada aos processos de transporte em rios, e apresentam uma maior amplitude anual de níveis. Por outro lado, áreas interfluviais (e.g., Llanos de Orinoco, Llanos de Moxos, Bananal) são mais dependentes do escoamento gerado localmente, e têm um atraso menor entre os picos de precipitação e inundação, assim como de amplitude dos níveis. Enquanto a maioria das regiões têm um pulso de inundação anual regular, a região dos Pampas na Argentina se destaca por ter um padrão bastante errático, com anos com muitas cheias seguidos de anos com muitas secas. Os resultados aqui obtidos destacam o funcionamento hidrológico único que ocorre nas áreas úmidas da América do Sul, e salientam a importância de estudos de hidrologia comparativa para promover a compreensão de áreas úmidas ao redor do globo.

Este capítulo é apresentado na forma de um artigo científico:

- *Fleischmann, A., Papa, F., Paiva, R.C.D., Prigent, C., Ovando, A., Paris, A., Calmant, S., Collischonn, W., em preparação. South American wetlands from space: a comparative hydrology approach.*

Abstract

South America hosts some of the largest rivers on Earth, and major wetland complexes as the Pantanal and Amazon ones, which account for 5-12% of the continent territory. However, the hydrologic functioning of many of these wetlands remain poorly described and understood, and ongoing environmental changes urge for a better comprehension of these systems. Here we use state-of-the-art remote sensing datasets to apply a comparative hydrology approach to 12 wetlandscapes in South America, from temperate to tropical and equatorial ones. Estimates of precipitation (MSWEP), surface water extent (GIEMS-2), total water storage (GRACE), and river and wetlands' water levels (ENVISAT, ICESat, SARAL, TOPEX-POSEIDON, JASON-2, SENTINEL-3/A/B, totaling 888 virtual stations) are combined to understand their flood dynamics. Wetlands associated to river floodplains (e.g., Magdalena, Pantanal, and Amazon and Paraná mainstems) have a slower flood propagation associated to river routing and feature a higher annual water level amplitude, while the interfluvial ones (e.g., Llanos de Orinoco, Llanos de Moxos, Bananal) are more dependent on local runoff and have a smaller delay between precipitation and flood peak as well as water level amplitude. While most wetlands have a regular annual flood pulse, the Pampas in Argentina stand out as having a very erratic pattern with flood-rich years followed by drought-rich ones. Our findings highlight the unique hydrological functioning of South America wetlands, and set forward the importance of performing comparative hydrology studies for wetlands worldwide.

7.1 Introduction

Wetlands cover ~14 % of South America (FLUET-CHOUINARD et al., 2015), providing multiple ecosystem services related to food provision, and flood and climate regulation, and have a major role in the global carbon cycle (PANGALA et al., 2017; PARKER et al., 2018). Recent efforts have proposed classification schemes for Brazilian (JUNK et al., 2014), Colombian (RICAURTE et al., 2019) and Argentinian wetlands (KANDUS et al., 2017), which largely builds upon climate and hydrology variables to differentiate wetland types. Each wetland ecosystem is adapted to its flood pulse regime (JUNK; BAYLEY; SPARKS, 1989), which varies from relatively stable water levels, as in palm forests with *Mauritia flexuosa* trees in the Peruvian interfluvial wetlands, to monomodal predictable, as in central Amazon river floodplains, and polymodal unpredictable regimes, as in headwater wetland systems (JUNK et al., 2014; RICAURTE et al., 2019). The water level amplitude is also a fundamental descriptor of the system dynamics, ranging from small annual variations (tens of centimeters) to values exceeding 10 m along the Amazon river floodplain. Regarding the river-wetland surface connectivity, wetlands can be further categorized into river floodplains and interfluvial areas (rain-fed, with most water contribution from local runoff), although a

whole continuum exists among them (BOURREL; PHILLIPS; MOREAU, 2009; HAMILTON et al., 2007).

The recent development of satellite data has brought unprecedented capabilities to comprehend the hydrology of wetlands (GALLANT, 2015; KANDUS et al., 2018; PENATTI et al., 2015), providing powerful tools to monitor freshwater systems in South America (CARABAJAL; BOY, 2020), including precipitation , river and wetland water levels (PARK, 2020), total water storage (FRAPPART et al., 2019; PAPA et al., 2008b), surface water extent (HESS et al., 2015; PARRENS et al., 2017; PRIGENT et al., 2007) and evapotranspiration (FISHER et al., 2017; LAIPELT et al., 2020). In this context, there are great opportunities to understand the hydrology of the large South American wetlands from space, within a comparative hydrology approach (DA ROCHA et al., 2009; PAPA et al., 2008a; SUTCLIFFE; PARKS, 1989). This allows us to understand hydrological processes by looking at the similarities and dissimilarities among wetlands, from both regional scale and among-wetlands perspectives. Addressing wetlands from a continental perspective is also relevant since there are major surface-atmosphere interactions that may affect the regional climate (TAYLOR; PRIGENT; DADSON, 2018), as well as teleconnection patterns (e.g., due to ENSO) that may lead to correlated inundation anomalies in distant wetlandscapes. Also, national to regional scale socio-political decisions and changes (dam building, agriculture development) can affect distant wetlands, and wetland inventories are usually performed at national scales, requiring consistent hydrological datasets to characterize their dynamics. Many wetlands are also connected through drainage networks, as the multiple wetlands in the La Plata basin (e.g., Pantanal, Iberá, Paraná floodplains), and through continental routes of migratory wildlife (DE TARSO ZUQUIM ANTAS, 1994).

Recent studies suggest a decline in global wetland area (DARRAH et al., 2019; DAVIDSON, 2018), and major ongoing environmental changes have been threatening South American wetlands and their ability to provide ecosystem services, including climate change (both natural and human-induced components), building of dams, land cover changes and water pollution (ANGARITA et al., 2018; JUNK, 2013; LATRUBESSE et al., 2017b; PATIÑO, 2016; RENÓ; NOVO, 2019; SIMONIT; CATTANEO; PERRINGS, 2005; XI et al., 2020). This reinforces the necessity of understanding the wetlands functioning in order to predict their future changes.

Here we leverage satellite-based estimation of river and wetland water levels, surface water extent, precipitation and total water storage across 12 wetlandscapes in South America. We address how different wetland types (i.e., river floodplain and interfluvial areas) differ in terms of hydrological variables, how hydrological signals correlate among multiple wetlands, and how ongoing and future environmental changes may differently affect each wetland type.

7.2 Methods

Twelve major wetland complexes in South America were selected as study areas, which are evenly distributed along climate types (equatorial, tropical and temperate) (Figure 7.1). They are associated with various vegetation types, from grasslands and savannas (e.g., Llanos del Orinoco and Bananal Island) to forests (e.g., Amazon floodplain), and geomorphic settings, from alluvial plains, such as the Paraná and Amazon rivers, to huge sedimentary basins as the Bananal Island (VALENTE; LATRUBESSE; FERREIRA, 2013) and depressions associated with neotectonic events as the Negro savannas (ROSSETTI et al., 2017a). The Amazon river floodplain is analyzed as two separate areas (upper and lower), which are delineated as the upstream and downstream areas of the city of Manaus, respectively, given the differences that exist between the upper (more flooded forests) and lower (more open water and lower vegetation and larger deforestation; RENÓ; NOVO, 2019) areas.

The following satellite-based datasets are used:

- Precipitation (PREC) from MSWEP v.2.2 (BECK et al., 2017) at 10 km resolution, available for the period 1979-2017;
- Total water storage (TWS) from the GRACE mission (TAPLEY et al., 2004a) at 300 km spatial resolution, for the period 2003-2016, which encompasses the sum of all water storage components (i.e., surface water, soil moisture, groundwater, snow, etc.);
- Surface water extent (SWE) from GIEMS-2 at 25 km resolution (PRIGENT; JIMENEZ; BOUSQUET, 2020), available for the period 1992-2015;
- River water levels for 693 virtual stations distributed along the 12 wetlands, from the missions Envisat, SARAL AltiKa, JASON-2/3, Sentinel-3A/B, and available from the Hydroweb platform (http://hydroweb.theia-land.fr/);
- Over the Llanos de Moxos region, we also use time series from Envisat and SARAL AltiKa altimeters for both river and wetland targets - which were developed exclusively by OVANDO et al. (2018);
- Wetland water levels for 195 virtual stations distributed along the 12 wetlands were obtained in the OpenAltimetry portal (https://openaltimetry.org/) for the ICESat mission.

PREC, TWS and SWE were spatially averaged over each wetland area on a monthly timescale. The period 2003-2015 was adopted as it represents the period for which all datasets are overlapping. The data were analyzed through linear Pearson correlation among PREC, TWS and SWE for each of the 12 wetlands, looking for the time lag (in months) that produces the highest correlation between TWS and SWE and PREC. The month of climatological maximum PREC and SWE were also estimated at a pixel level to investigate the flood propagation across the wetland.

For each wetland, the variation of SWE was analyzed in terms of long-term mean, maximum and minimum values, as well as variation related to mean (difference

between max and min, divided by the mean) and elasticity (max/min ratio). A cross-correlation analysis was performed for SWE anomalies (i.e., deseasonalized values, obtained by subtracting, from each month, the long-term average for that month) among all 12 wetlands. This was performed to understand teleconnections in the wetlands, and to which extent some wetlands share similar anomalous SWE due to regional meteorological processes.

Finally, regarding river and wetland water levels, and given the low temporal resolution of ICESat data (91 days), which were the main ones used for estimating wetland water levels, the water level analysis was performed for annual water level amplitude only, which is a relevant variable to differentiate wetland types (JUNK et al., 2014).

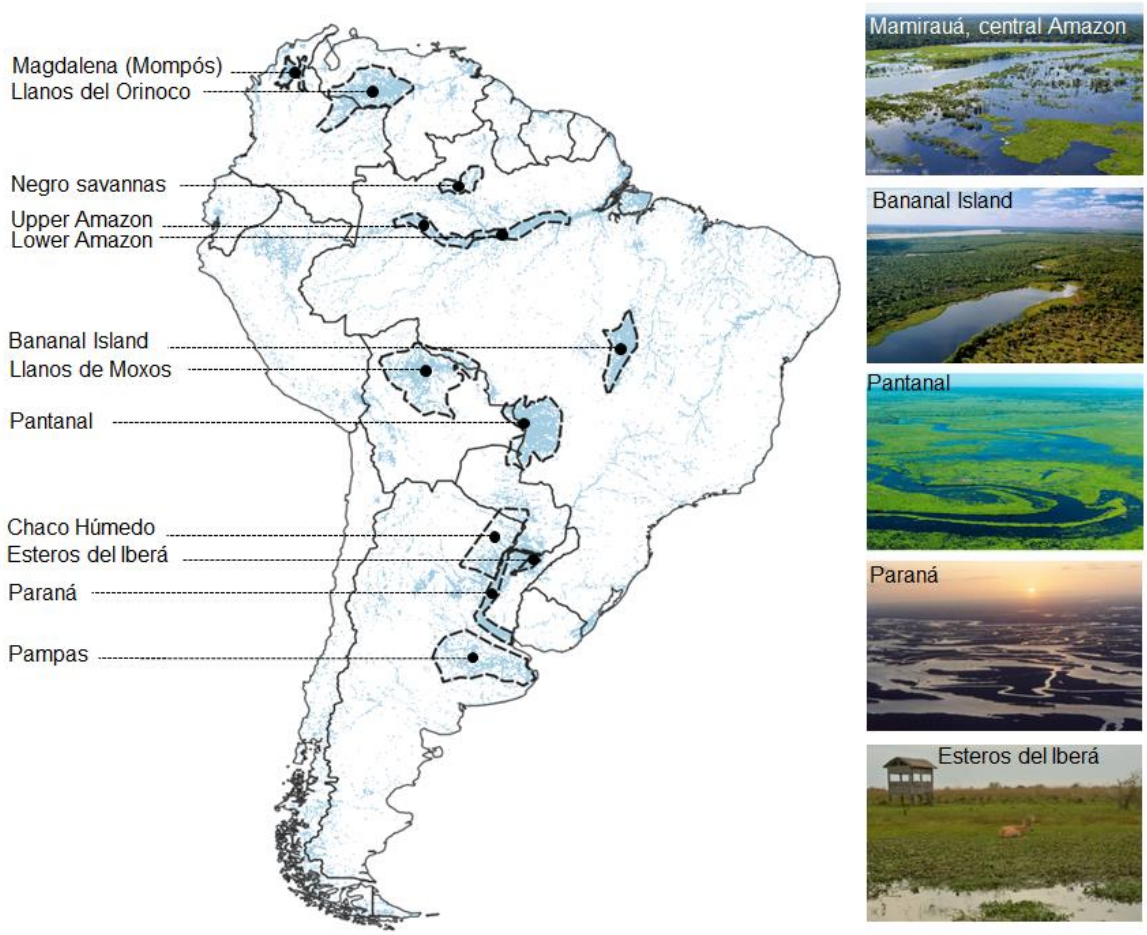

Figure 7.1. Location of the 12 wetland areas in South America. Background inundation map from the GIEMS-D15 product (Fluet-Chouinard et al., 2015).

7.3 Results and discussion

7.3.1 Inundation dynamics

Figure 7.2 provides an overall understanding of the 12 wetlands inundation seasonal patterns and their relation with precipitation. Interfluvial areas have a small lag between precipitation and inundation, of two or less months (Table 7.1), which is expected given that they are mostly rain-fed. The interfluvial savannas (Llanos de Moxos, Negro, Llanos del Orinoco, Bananal Island and parts of Pantanal) are located in the tropical and equatorial/tropical transition (Negro savannas), and have been called "hyperseasonal savannas" (BATALHA et al., 2005) because their vegetation faces alternating water-excess and water-deficit areas throughout the year. Their inundation annual amplitude shows clearly this dynamic, with most of the largest amplitude values among the 12 studied areas (Table 7.2). Two of these areas, Llanos de Moxos and Pantanal, are estimated as having the largest maximum inundation extent in the continent, with 111,400 and 101,000 km², respectively, followed by the Llanos del Orinoco (90,100 km²) (Table 7.2). It must be stressed that if the Amazon mainstem floodplain was considered as one only wetland unit, between the cities of Iquitos and Gurupá, this would present the lasted maximum inundation, as estimated with GIEMS-2, with 116,400 km² (see Table 5.5 in Chapter 5). The Pampas region is very particular for its very erratic inundation pattern, with flood-rich periods followed by flood-poor ones. The last major flood-rich period occurred in 2000-2003 (Fig S1; KUPPEL et al. (2015)); thus, no climatological pattern can be defined for this wetland.

In turn, river floodplains have a lag of two or more months between precipitation and inundation, with a lag of three to four months for the Paraná, Amazon and Pantanal areas. The Pantanal has the longest flood delay in South America, due to geomorphic controls as major channel constrictions (GONÇALVES; MERCANTE; SANTOS, 2011). While precipitation peaks at January along most of the region, inundation peaks at March in the upper parts, and the flood propagation makes the most downstream peaks to occur in July (Figure 7.3 and Figure 7.4). The Llanos de Moxos region shows a downstream delay in inundation peak which coincides with the downstream delay in precipitation peaks (from January to March in downstream regions), while the most downstream portions peaking in April also suffer delay from floodplain attenuation.

In turn, among TWS, SWE and PREC variables, the highest correlations are obtained between SWE and TWS (Table 7.1; see seasonality in Figure 7.5). This suggests the large role of surface water storage in the total storage along these areas. Furthermore, the largest values are observed for the equatorial wetlands and the Pantanal ($R>0.87$). It must be noticed, however, that for the Pantanal the assessed wetland areas should be further divided into subregions according to the inundation

flood propagation, in order to understand the role of SWE on TWS across the multiple areas (PENATTI et al., 2015).

Regarding climate teleconnections (Table 7.3), three pairs of wetlands share similar SWE anomalies (R > 0.6): Negro savannas and Magdalena (both in the Northern Hemisphere), upper and lower Amazon (connected through drainage network), and Pantanal and Llanos de Moxos (which have in common a similar tropical climate with close variability). Other areas with high correlation (R > 0.3) are Magdalena and Llanos del Orinoco (both in the Northern Hemisphere), Paraná and Pantanal (connected through drainage network), and many combinations of the temperate wetlands (Iberá, Chaco, Paraná and Pampas). Interestingly, the Pampas and Iberá have a high correlation, even though the erratic flood pattern in the former.

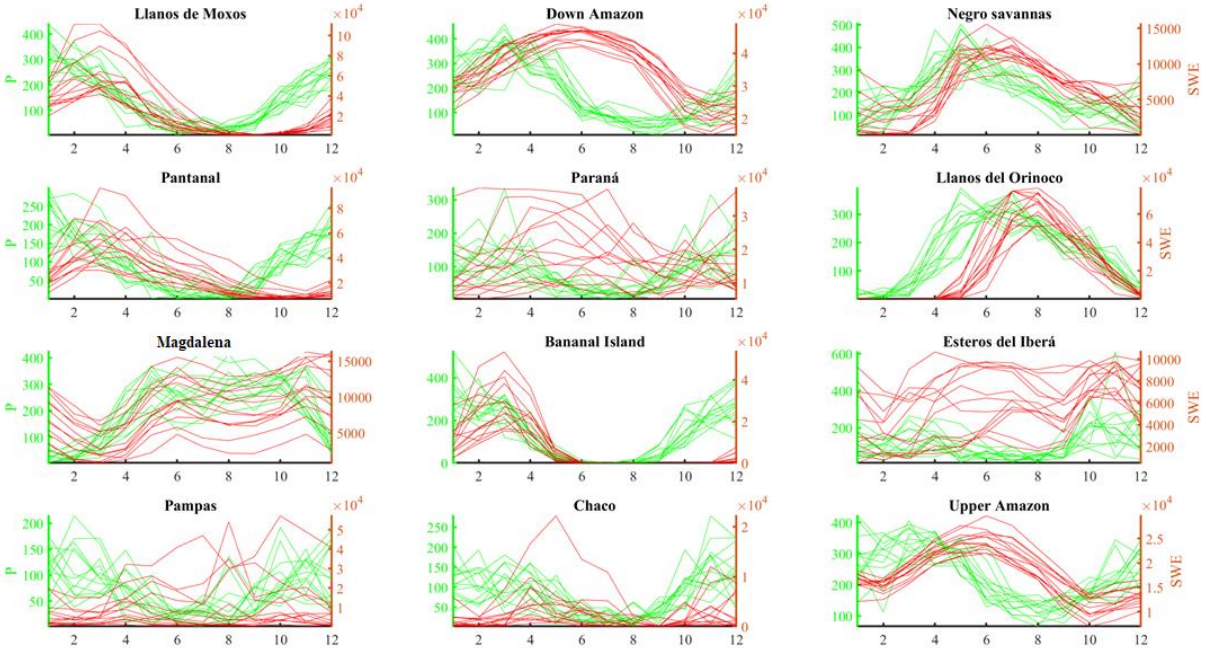

Figure 7.2. Seasonal variation of precipitation (green) and surface water extent (red) for the 12 wetland complexes, for the period 2003-2015. Each line refers to one year.

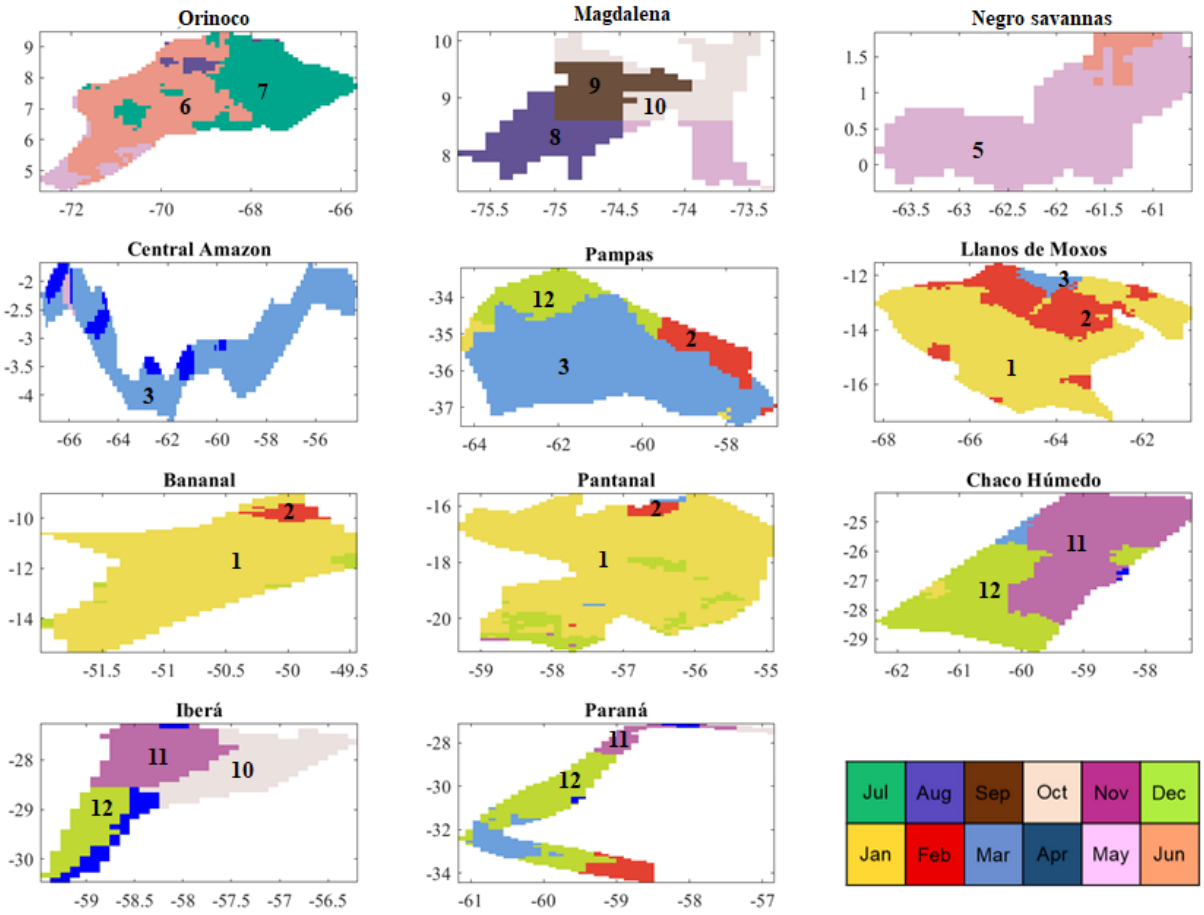

Figure 7.3. Month of precipitation climatological peak for each of the 12 analyzed wetlands. The main months are labeled with the respective numbers for each region. The two Amazon floodplain areas (upstream and downstream) were plotted together for visualization purposes.

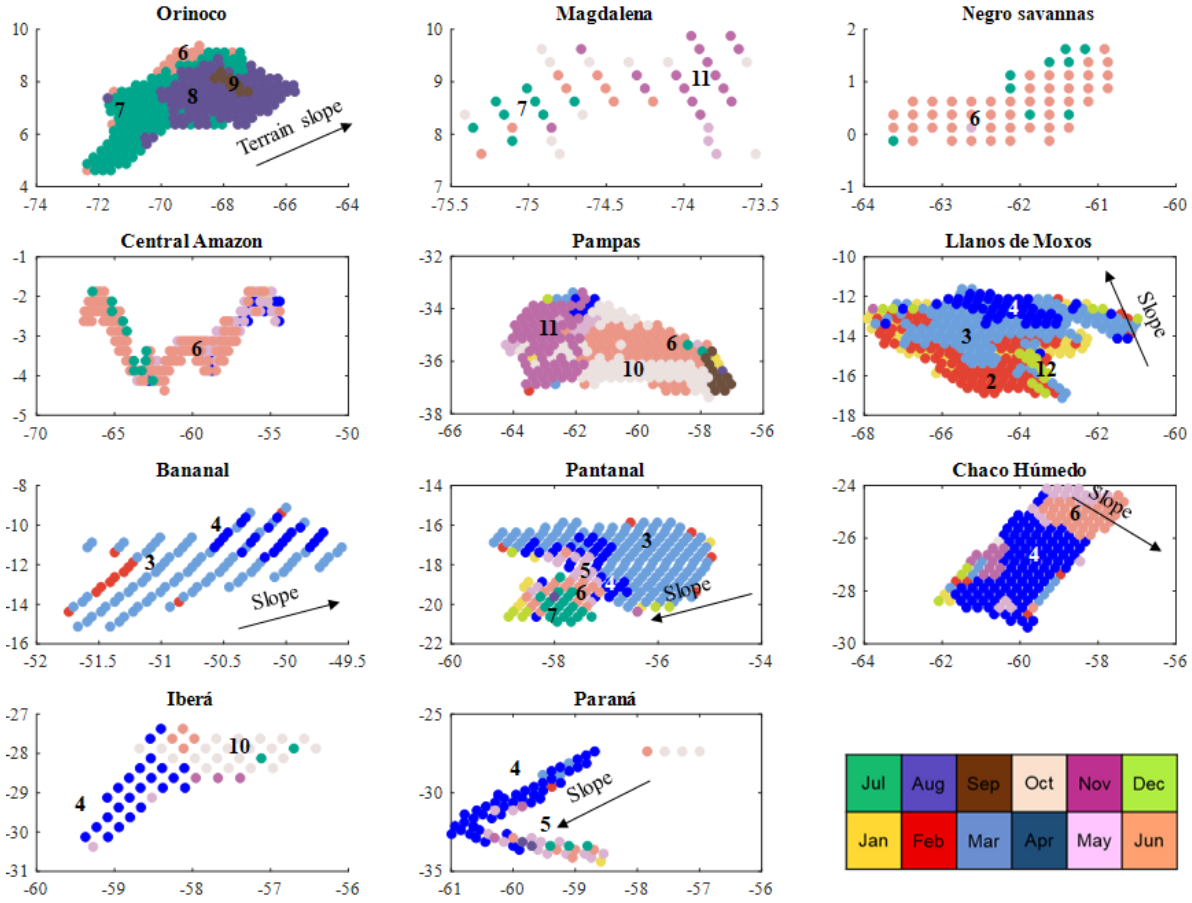

Figure 7.4. Month of surface water extent climatological peak for each of the 12 analyzed wetlands. The main months are labeled with the respective numbers for each region. The arrows indicate the main terrain slope for some wetlands where this pattern is clear. The two Amazon floodplain areas (upstream and downstream) were plotted together for visualization purposes.

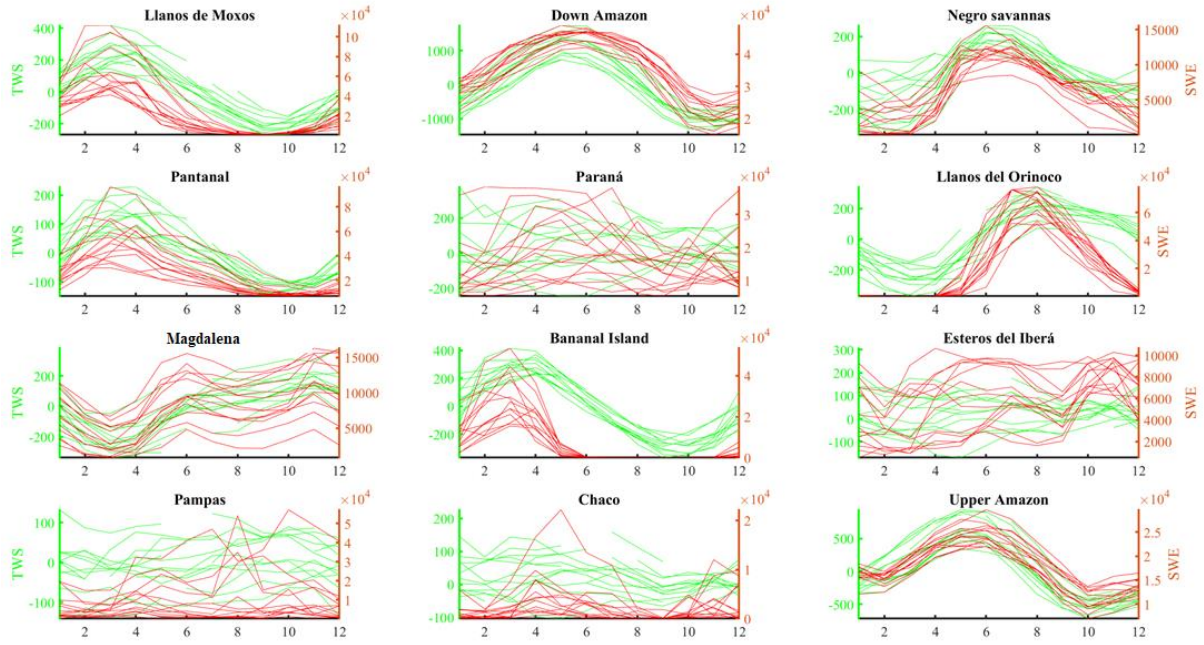

Figure 7.5. Seasonal variation of total water storage (green) and surface water extent (red) for the 12 wetland complexes, for the period 2003-2015. Each line refers to one year.

Table 7.1. Correlation among SWE, PREC and TWS for absolute values. “Int” refers to interfluvial wetlands, “Fp” to floodplains, and “Int/Fp” to systems with a mixed type. For the correlations between P and TWS, and P and SWE, the correlation is provided for the highest correlation with the respective time lag (in months) in parentheses.

			P x TWS	P x SWE	SWE x TWS
Latitude N→S Equatorial	*Int/Fp*	Magdalena	0.71 (2)	0.50 (2)	0.87
	Int	Negro	0.67 (1)	0.70 (1)	0.93
	Fp	Up Amazon	0.70 (2)	0.68 (3)	0.94
	Fp	Down Amazon	0.82 (2)	0.77 (3)	0.93
Latitude N→S Tropical	*Int*	Orinoco	0.86 (2)	0.85 (1)	0.82
	Int	Bananal	0.84 (2)	0.68 (2)	0.76
	Int/Fp	Moxos	0.83 (3)	0.77 (2)	0.88
	Int/Fp	Pantanal	0.80 (3)	0.71 (3)	0.93
Latitude N→S Temperate	*Int/Fp*	Chaco	0.14 (3)	0.17 (1)	0.43
	Int	Iberá	-0.03 (2)	-0.04 (0)	0.74
	Fp	Paraná	-0.03 (0)	0.07 (4)	0.54
	Int	Pampas	-0.06 (0)	0.02 (4)	0.61

Table 7.2. Assessment of SWE for the 12 wetlands: long-term mean, minimum (min) and maximum (max) values, as well as variation related to mean (difference between max and min, divided by mean) and elasticity (max/min ratio). “Int” refers to interfluvial wetlands, “Fp” to floodplains, and “Int/Fp” to systems with a mixed type.

			Mean	Min	Max	Variation related to mean	Elasticity (max/min)
Latitude N–S	Equatorial	Int/Fp	Magdalena	7120	620	16310	2.2	26.3
		Int	Negro	5900	0	15600	2.6	>500.0
		Fp	Up Amazon	17980	6990	29650	1.3	4.2
		Fp	Down Amazon	34860	14780	48930	1.0	3.3
Latitude N–S	Tropical	Int	Orinoco	21560	30	90130	4.2	>500.0
		Int	Bananal	7700	0	53340	6.9	>500.0
		Int/Fp	Moxos	24660	1120	111360	4.5	99.4
		Int/Fp	Pantanal	29490	6550	101030	3.2	15.4
Latitude N–S	Temperate	Int/Fp	Chaco	3090	0	35710	11.6	>500.0
		Int	Iberá	6380	510	10850	1.6	21.3
		Fp	Paraná	18900	5260	48580	2.3	9.2
		Int	Pampas	12070	140	85200	7.0	>500.0

Table 7.3. Categorization of flood anomaly correlation among wetlands, for those pairs with correlation higher than 0.18, which defines a P-value equal to 0.001. Colors highlight the pairs of wetlands where both belong to the same climate type (equatorial in red, tropical in blue, and temperate in green). *Both wetlands are located in the Northern Hemisphere. **Both wetlands are connected through a drainage network.

Very high (R > 0.6)	High (R > 0.3)	Moderate (R > 0.18)
NEG+MAG*	MAG+ORI*	ORI+MAG*
AMU+AMD**	PAR+PAN**	NEG+AMD**
PAN+MOX	IBE+CHA	NEG+ORI*
	IBE+PAR**	IBE+AMU
	CHA+PAR**	PAM+AMU
	IBE+PAM	BAN+MOX
		BAN+PAN
		MOX+CHA
		MOX+PAR
		MOX+CHA
		CHA+PAM
		PAR+PAM

7.3.2 Water level annual amplitude

The water level annual amplitude varies largely across South American rivers and wetlands (Figure 7.6), and its analysis shows the much smaller values obtained for the interfluvial areas, less connected to rivers, than over river floodplains. In the assessed systems, the largest variation for rivers occurs in the central Amazon, with amplitudes that can reach values larger than 10 m. Regarding wetlands, interfluvial areas as the Negro savannas have the smaller amplitudes (less than two meters). Wetlands with abundant lakes, as the Iberá, also have small amplitudes. The wetlands along floodplain systems, as the Magdalena Mompós depression and the central Pantanal region, have amplitudes close to the main river variation, between 2 and 4 m. In mixed river floodplains/interfluvial wetland systems as the Llanos de Moxos, high amplitude is found along floodplains (larger than 4 m), and low along the interfluvial savanna areas (less than 2 m). The same pattern is observed over the Negro floodable savannas, corroborating earlier findings of low water level amplitude in these areas (FLEISCHMANN et al., 2020b).

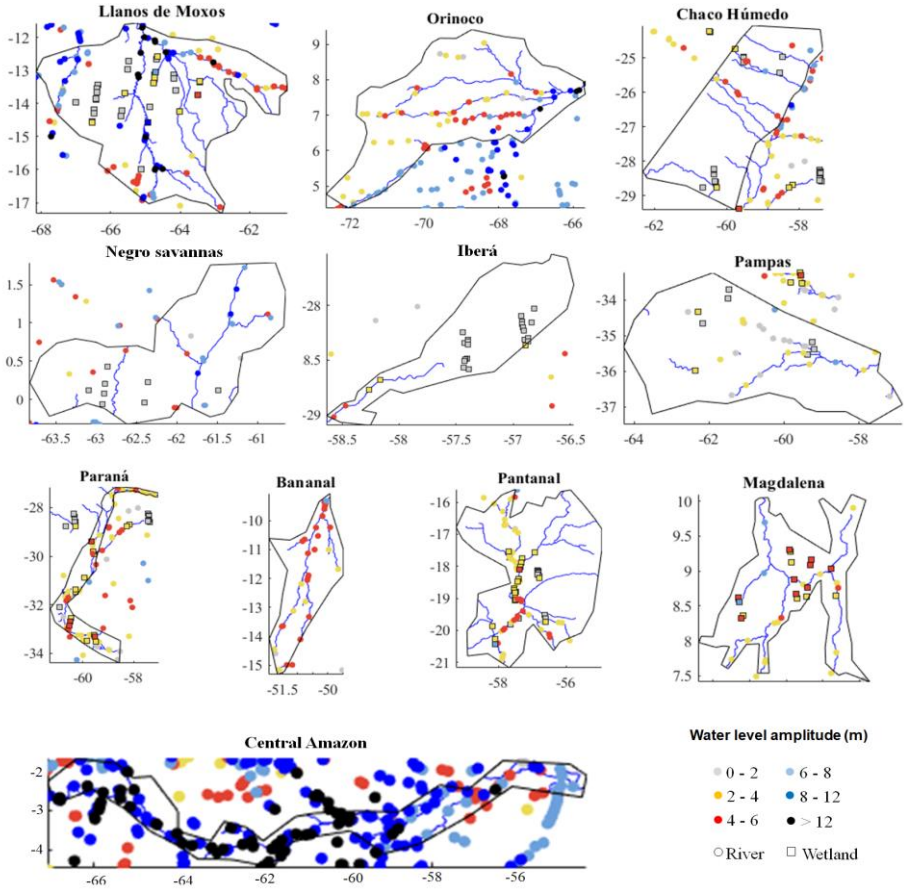

Figure 7.6. Water level amplitude for the 12 wetland complexes, for virtual stations in rivers (circles) and wetlands (squares). The two Amazon floodplain areas (upstream and downstream) were plotted together for visualization purposes.

7.3.3 South American wetlands under a changing environment

The large South American wetlands are mostly located in relatively remote areas, with an overall small population, and many of them are associated with protected areas as Ramsar sites, with most protected areas (both indigenous and conservation areas) located in the Amazon region (Reis et al., 2018; Figure 7.7). However, there are major ongoing environmental changes that threaten their ability in providing ecosystem services, and the differentiation between natural variability, climate change and direct human impacts can improve our prediction capability of future changes (RODELL et al., 2018; VISHWAKARMA et al., 2021).

Different wetland types face environmental changes through different ways. While interfluvial wetlands are mainly subject to local climate and land cover changes, river floodplains also depend on discharge, sediment and nutrient alteration from the upstream basin, that can occur through upstream reservoir regulation. Today, major human pressure through land use change (typically agricultural use) occurs, for the wetlands assessed here, mainly in the Pampas, Chaco, Llanos del Orinoco, Esteros del Iberá, Magdalena and lower Amazon floodplain wetlands (RENÓ et al., 2011; RICAURTE et al., 2017). Some wetlands are close to human-altered land covers, such as the Bananal Island in the Amazon-Cerrado ecotone.

Large wetland systems currently affected by dams are the Magdalena (ANGARITA et al., 2018) and upper Paraná river (AGOSTINHO; PELICICE; GOMES, 2008). While a few dams exist today in the upper Paraguay basin surrounding the Pantanal wetlands, dozens of small ones are proposed and threaten the wetland system, especially with hydropeaking operation (i.e., sub-daily flow regime alteration; FIGUEIREDO et al. (2021)) and alteration in sediment and nutrients (FANTIN-CRUZ et al., 2020; OLIVEIRA et al., 2020). In the Amazon basin, while a few storage reservoirs exist and largely disrupt the hydrological regime and downstream ecosystems, as the Balbina and Tucuruí dams (FORSBERG et al., 2017; RESENDE et al., 2019), multiple run-of-the-river plants have been built in the last decade and affect downstream floodplains through hydropeaking operation (ALMEIDA et al., 2020). Additional large storage reservoirs are planned for the Andean Amazonian portions and threatens especially the Llanos de Moxos and the upper Amazon river floodplains (ALMEIDA et al., 2019; ANDERSON et al., 2018; LATRUBESSE et al., 2017b). Interfluvial wetlands tend to be less dependent upon the main river hydrological regime (REIS et al., 2019b), but may be connected to it through groundwater fluxes. Thus, the impacts of upstream dams must be carefully studied. For instance, a proposed large run-of-the-river dam in the Branco river, which connectivity with the Negro floodable savannas is still poorly understood, has been proposed to be built soon (FILIZOLA et al., 2020), and its potential impacts must be further studied.

The effect of climate change on the wetlands hydrologic regime is better understood if differentiating interfluvial areas and river floodplains types of wetlands.

While the former are more affected by local rainfall and temperature projections, which in turn affect local river tributaries, floodplains may also be affected by changes in upstream areas, sometimes thousands of kilometers upstream. Overall, climate change projections have suggested a decrease in water availability for wetlands worldwide (XI et al., 2020). When looking at the median of 25 CMIP5 (Coupled Model Intercomparison Project – phase 5) general circulation models' runs coupled to a continental hydrological model for South America (BRÊDA et al., 2020), the model projections agree with that of XI et al. (2020). Decreases are projected, under the RCP8.5 scenario (the most severe one with no control policies of greenhouse gas emissions) for the end of the XXIst century, and for both average river discharges and precipitation, for the Magdalena, Llanos del Orinoco, Negro savannas, Llanos de Moxos, Pantanal, Bananal Island, Chaco and Lower Amazon wetlands. Increases are only projected for the Pampas and Esteros del Iberá (both river discharges and precipitation; MONTROULL et al. (2013)), and Paraná (precipitation only). There is no agreement for the upper Amazon, yet other studies have projected an increase in upper Amazon river flows and maximum inundation (SORRIBAS et al., 2016). These trends are in agreement with some recent climate trends, such as the ongoing droughts in Pantanal and central Brazil in general (Marengo et al., 2021). In central Amazon, however, there has been rather an increase in floods (FLEISCHMANN et al., Chapter 6 of this thesis).

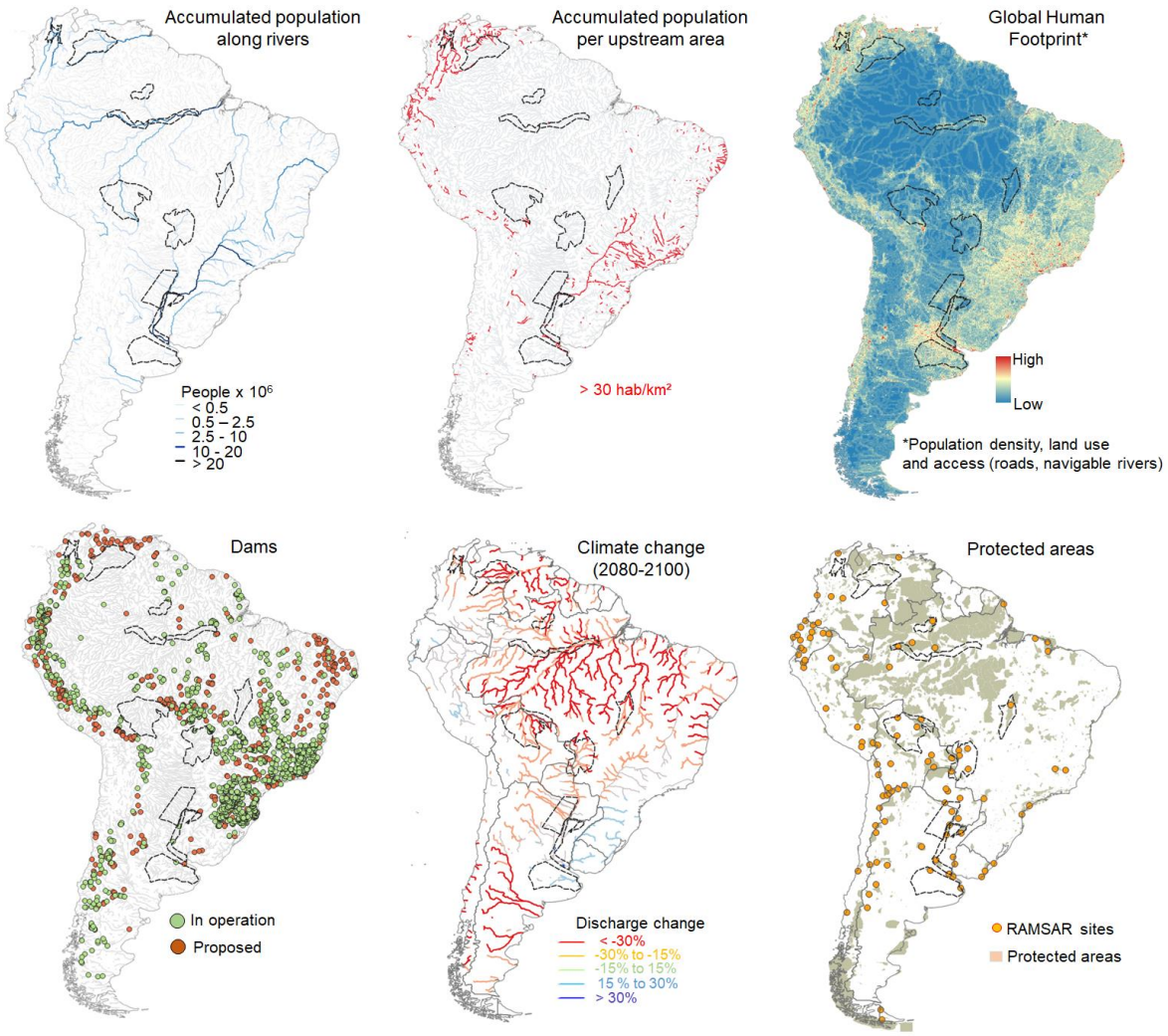

Figure 7.7. Ongoing and projected human threats and environmental changes over South America, in the context of the 12 wetland complexes assessed in this study (black polygons). Source of data: population from Gridded Population of the World (GPW) v4 (https://sedac.ciesin.columbia.edu/data/collection/gpw-v4); Global Human Footprint (Geographic), v2 (1995–2004) ((WCS; CIESIN, 2005); available at https://sedac.ciesin.columbia.edu/data/set/wildareas-v2-human-footprint-geographic); dams in operation from Global Reservoir and Dam Database (GRanD) v1.3 (LEHNER et al. (2011); available at http://globaldamwatch.org/grand/); proposed dams from Future Hydropower Reservoirs and Dams Database (FHReD; ZARFL et al. (2014); available at http://globaldamwatch.org/fhred/); dams in operation and proposed for the Amazon are derived from the data collected by ALMEIDA et al. (2019); climate change discharge projections from South American Climate Change Impacts on water resources dataset (SACCI; BRÊDA et al., 2020; available at https://www.ufrgs.br/lsh/products/climate-change-in-south-america/); protected areas from (UNEP-WCMC; IUCN, (2021); available at www.protectedplanet.net); Ramsar sites from the Ramsar convention (available at https://rsis.ramsar.org/).

7.4 Conclusion and perspectives

This chapter presented a comparative hydrology assessment of 12 large South American wetland complexes, by analyzing the relations among precipitation, total water storage and surface water extent, as well as water level variation across the various regions. We leveraged multiple datasets which reinforce that the satellite era is largely enlightening the hydrology of South American wetlands. We showed the differences between wetland types, with a specific distinction between river floodplains and interfluvial wetlands. While this is a simplistic categorization, from a hydrological perspective, it is interesting. These two classes have contrasting interaction with river drainage networks and contrasting water level amplitude. Other ways to differentiate wetland types from space may involve the use of InSAR to assess connectivity (JARAMILLO et al., 2018). Furthermore, while we used almost 900 satellite altimetry virtual stations over rivers and wetlands, they were mainly located on rivers. Ongoing efforts are increasing the number over wetland targets. New data from ongoing missions as GRACE-FO and soil moisture from SMOS and SMAP, surface water extent from new real-time products as GIEMS, SWAF and SWAMPS are promising for addressing South American wetlands. Analysis of long-term inundation trends over wetlands is also an interesting way forward, for instance considering the major intensification of floods and droughts over the Amazon (MARENGO; ESPINOZA, 2016) and the alternation between flood-rich and flood-period over the Pampas wetlands (KUPPEL et al., 2015). This is now possible thanks to the long-term inundation dataset recently developed (JENSEN; MCDONALD, 2019; PRIGENT; JIMENEZ; BOUSQUET, 2020). The understanding of the hydrology of wetlands is paramount if we want to estimate their future alteration under environmental changes, and their monitoring from space has been proving extremely fruitful.

8 Patterns and drivers of evapotranspiration in South American wetlands

This chapter is presented as a research article, under review in Nature Communications:

- Fleischmann, A. S., Laipelt, L., Papa, F., Ruhoff, A., Paiva, R., Biudes, M., Kayser, R., Prigent, C., Cosio, E., Machado, N., Collischonn, W., under review in Nature Communications. Patterns and drivers of evapotranspiration in South American wetlands.

8. Padrões e fatores determinantes da evapotranspiração em áreas úmidas da América do Sul

Evapotranspiração (ET) é um processo-chave que conecta os balanços energéticos da superfície e da atmosfera. No entanto, os padrões e fatores determinantes desta variável em áreas úmidas são ainda pouco conhecidos. Neste capítulo a dinâmica de ET em 12 áreas úmidas da América do Sul é investigada, revelando importantes diferenças entre climas temperado, tropical e equatorial. Enquanto a radiação líquida de energia é um fator dominante da sazonalidade de ET na maioria dos ambientes, a inundação também tem um papel importante em áreas úmidas tropicais e equatoriais, especialmente para atender à demanda evaporativa. Além disso, importantes perdas de água e diferenças entre áreas úmidas e áreas de terra firme ocorrem em ambientes temperados, que são limitados pela disponibilidade de água, e em áreas com grandes extensões inundadas como o Pantanal, onde a lenta propagação da cheia anual tem um importante papel na dinâmica de ET. Por fim, florestas ripárias geram as maiores taxas de ET em todos ambientes exceto na Amazônia central, onde florestas de terra firme sustentam altas taxas ao longo de todo o ano. Estes resultados destacam o funcionamento único e serviços ecossistêmicos providos por áreas úmidas em escala continental.

Este capítulo é apresentado na forma de um artigo científico, em revisão no periódico Nature Communications:

- *Fleischmann, A. S., Laipelt, L., Papa, F., Ruhoff, A., Paiva, R., Biudes, M., Kayser, R., Prigent, C., Cosio, E., Machado, N., Collischonn, W. Patterns and drivers of evapotranspiration in South American wetlands. Em revisão no periódico Nature Communications.*

Abstract

Evapotranspiration (ET) is a key process linking surface and atmospheric energy budgets, yet its drivers and patterns across wetlandscapes are poorly understood worldwide. Here we assess the ET dynamics in 12 wetlands complexes across South America, revealing major differences under temperate, tropical, and equatorial climates. While net radiation is a dominant driver of ET seasonality in most environments, flooding also contributes strongly to ET in tropical and equatorial wetlands, especially in meeting the evaporative demand. Moreover, significant water losses through wetlands and ET differences between wetlands and uplands occur in temperate, water-limited environments and in highly flooded areas such as the Pantanal, where slow river flood propagation drives the ET dynamics. Finally, floodplain forests produce the greatest ET in all environments except the central Amazon, where upland forests sustain high rates year round. Our findings highlight the unique hydrological functioning and ecosystem services provided by wetlands on a continental scale.

8.1 Introduction

Wetlands support diverse and complex ecosystems worldwide, offering important environmental and societal benefits. They play a critical role in providing freshwater and food, regulating climate, mitigating floods, sequestering carbon, and supporting biodiversity (BRINSON; MALVÁREZ, 2002; WITTMANN et al., 2015). Approximately 5%–12% of South America is covered by wetlands (FLUET-CHOUINARD et al., 2015; REIS et al., 2018), including the massive wetland systems of the Amazon and the Pantanal (HAMILTON; SIPPEL; MELACK, 2002; JUNK, 2013; NEIFF; IRIONDO; CARIGNAN, 1994) (Figure 8.1), which encompass a great variety of climates from equatorial to tropical and temperate. Although South American wetlands remain mainly natural systems and nearly 20% of them are protected today (REIS et al., 2018), recent anthropogenic pressures, such as deforestation, fires, waterway development, climate change, and dam building, have highlighted the need for a better comprehension of ecosystem services and sustainable management of these areas (JUNK, 2013; LIBONATI et al., 2020; NUNES DA CUNHA; JUNK, 2004; RICAURTE et al., 2017).

While South America is known as the “fluvial continent” for its large rivers and floodplains, interfluvial wetland complexes are also found across it, and these interfluvial complexes are associated with particular geomorphic settings and savanna or grassland vegetation (BRINSON; MALVÁREZ, 2002; JUNK, 2013). Interfluvial areas include tropical, hyperseasonal ecosystems, where savanna vegetation has adapted to cope with a soil that ranges from completely dry to fully saturated (BATALHA et al., 2005; DALMAGRO et al., 2016b; HAMILTON; SIPPEL; MELACK, 2002), which poses many survival challenges for plants given typical shallow roots in waterlogged

soils (FAN et al., 2017; SALIS et al., 2014). Apart from the central Amazon and some monodominant forests in interfluvial areas with flood-adapted tree species (e.g., *Vochysia divergens* in the Pantanal (NUNES DA CUNHA; JUNK, 2004) and palm species, such as *Mauritia flexuosa,* in the tropical and equatorial wetlands), the forests of the large South American wetlands are generally located along rivers. In the highly dynamic river floodplains, the floristic composition is driven by sedimentation processes and the channel-upland flooding gradient (SCHIETTI et al., 2014); thus, grasses dominate the most floodable areas, while trees flourish in the less floodable areas - in the cases of the Paraná and Amazon rivers, they remain under water less than 210–270 days per year (MARCHETTI et al., 2013; WITTMANN, F., SCHÖNGART, J., BRITO, J. M., OLIVEIRA-WITTMANN, A., PAROLIN, P., PIEDADE, M. T. F., & GUILLAUMET, 2010).

Evapotranspiration (ET), a key flux linking surface and atmospheric energy budgets, is also the main consumer of incoming energy and water in wetlands. At the regional landscape level (i.e., the wetlandscape (THORSLUND et al., 2017)), the existence of large wet surfaces has the potential to affect the partition of available energy into sensible and latent heat, influencing not only local temperature and water quality but also the regional atmospheric boundary layer (PAL; LEE; CLARK, 2020), the vertical transport of heat and water vapor in the atmosphere, and local-to-regional atmospheric circulation (BIUDES et al., 2015; HOUSPANOSSIAN et al., 2018; TAYLOR; PRIGENT; DADSON, 2018). The river or wetland breeze effect, observed, for instance, in the central Amazon (PAIVA et al., 2011; SANTOS et al., 2019), has been suggested to suppress precipitation over flooded areas and initiate convection over wetland edges (PRIGENT et al., 2011; TAYLOR; PRIGENT; DADSON, 2018). However, the role of wetland systems on regional to continental atmospheric circulation remains poorly understood, and efforts to develop a global theory of wetland ET dynamics involving the co-evolution between climate, soil, flooding mechanisms, and vegetation is imperative (SÁNCHEZ-CARRILLO et al., 2004). A proper consideration of wetland hydrological processes within land surface models simulating regional to global climate similarly requires improved physical representations and parameterizations (SCHRAPFFER et al., 2020), especially to assess future - and, as yet, uncertain - climate change impacts on wetland hydrology (XI et al., 2020). Such efforts are necessary to complement the recent inventories of wetlands developed in South America and to advance toward a continental-scale quantification of wetland ecosystem services (JUNK et al., 2014; KANDUS et al., 2017; RICAURTE et al., 2019).

To date, few studies have been performed on the ET of South American wetlands, and the few studies that do exist have focused on individual wetlands and local scales, especially parts of the Amazonian and Pantanal wetlands (BIUDES et al., 2015; BORMA et al., 2009; PENATTI et al., 2015; TEIXEIRA et al., 2015), which hampers comparisons. A comparative hydrology approach involving multiple wetlands, as well as the wetland and its adjacent uplands (MACKAY et al., 2007), arises as a promising framework to understand ET in wetlandscapes across multiple climates and biomes. In

doing so, the framework has the potential to facilitate a consistent understanding of the role of various environmental drivers (e.g., precipitation, flooding, available energy, and vapor pressure deficit) and to enable predictions regarding these areas' responses to ongoing environmental changes (FISHER et al., 2009). Such comparative hydrology can be undertaken based on remote sensing techniques, which are powerful tools for wetland ET monitoring. This is especially true for diagnostic models that are based on the land surface temperature (LST), which can be coupled with cloud computation frameworks, thus providing long-term and consistent ET spatial patterns (VAN DIJK et al., 2018; YILMAZ et al., 2014). While cloud computation has engendered groundbreaking advances in wetland hydrology by enhancing the understanding of flooding processes in large areas (PEKEL et al., 2016), here we go further by analyzing the spatio-temporal dynamics of ET in 12 large wetland complexes in South America. We employ a Google Earth Engine algorithm based on the Surface Energy Balance Algorithm for Land (SEBAL) (BASTIAANSSEN et al., 1998b) model and Moderate Resolution Imaging Spectroradiometer (MODIS) imagery to generate monthly ET estimates, which are jointly analyzed with a state-of-the-art inundation dataset (PRIGENT; JIMENEZ; BOUSQUET, 2020) for the period of 2000–2015. Our results facilitate efforts to unravel the interplay between available energy and flooding dynamics in driving wetland ET dynamics across various biomes and geomorphic settings on the continent.

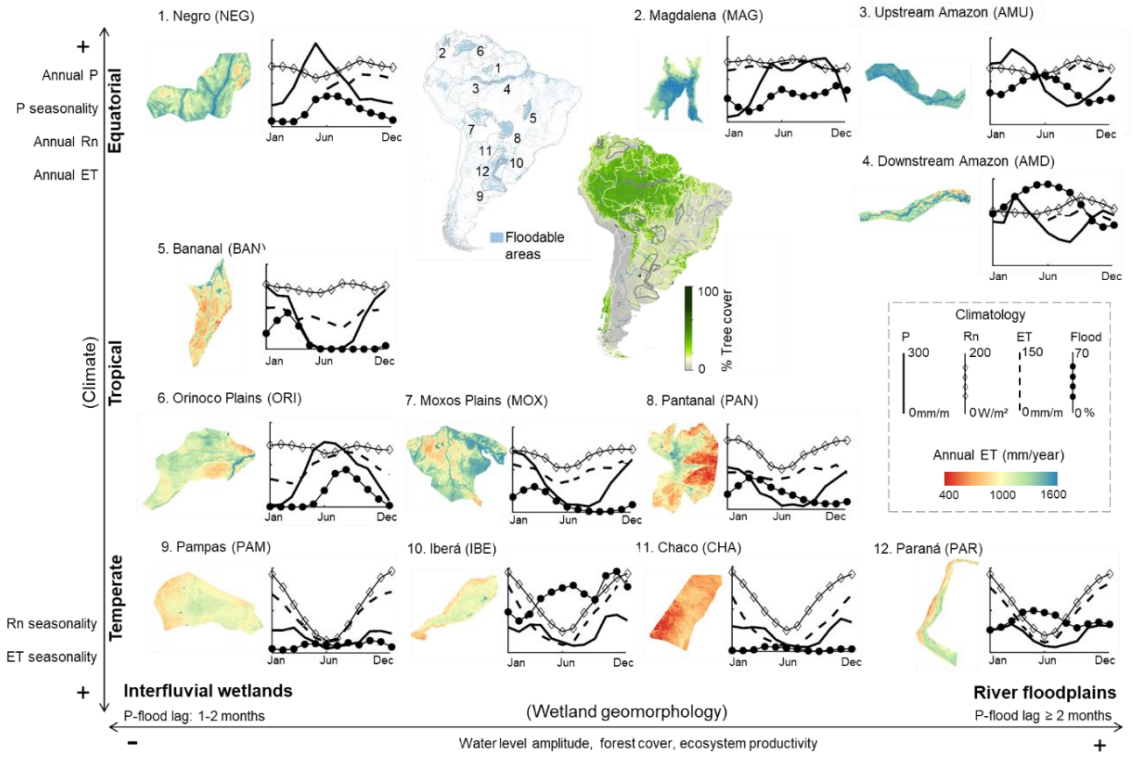

Figure 8.1. Evapotranspiration patterns across South American wetland complexes. Long-term average ET maps are presented together with climatology of precipitation

(P), evapotranspiration (ET), net radiation (Rn) and flood fraction (Flood). The location of the wetlands in South America are presented together with the continent tree cover map. The wetlands are organized following gradients of climate (from temperate to equatorial) and wetland geomorphology (from interfluvial wetlands to river floodplains, which are more coupled to adjacent rivers). All Y-axes have the same scale, with values provided in the dashed box in the right. Tree cover from MOD44B Version 6 Vegetation Continuous Fields product for 2010, available at <https://lpdaac.usgs.gov/products/mod44bv006/>.

8.2 Methods

8.2.1 Remote sensing-based evapotranspiration

We implemented the Surface Energy Balance Algorithm for Land (SEBAL) model (BASTIAANSSEN et al., 1998b) within Google Earth Engine (GEE) cloud computation environment, and a detailed explanation is provided in Supplementary Note 1. Overall, SEBAL estimates instantaneous evapotranspiration as the residual of the surface energy balance (Equation 1), using remote sensing and meteorological data (wind speed, specific humidity, surface air temperature, incoming shortwave radiation and atmospheric pressure) as input. The main model premise is that the near-surface vertical air temperature difference is linearly related to the surface temperature (BASTIAANSSEN et al., 1998b), and that there are two extreme conditions that characterize the energy partitioning between sensible and latent heat. At the hot extreme condition, the latent heat is assumed as zero so that all available energy ($R_n - G$) becomes sensible heat. Conversely, at the cold extreme condition all available energy becomes latent heat. To be consistent with the monthly inundation product (see ancillary data section below), we computed monthly evapotranspiration based on 8-day estimates.

$$LE = R_n - G - H \quad (1)$$

where LE is the latent heat flux ($W.m^{-2}$), R_n the net radiation ($W.m^{-2}$), G the soil heat flux ($W.m^{-2}$), and H the sensible heat flux (W.m-2).

Net radiation is computed as:

$$Rn = (1 - \alpha)Rs_{down} + Rl_{down} - Rl_{up} - (1 - \varepsilon_0)\, Rl_{down} \quad (2)$$

where α is the broad-band surface albedo, Rs_{down} the incoming short-wave radiation ($W.m^{-2}$), Rl_{down} the incoming long-wave radiation ($W\, m^{-2}$), and Rl_{up} the outgoing long-wave radiation ($W\, m^{-2}$).

Rs_{down}, Rl_{down} and Rl_{up} were estimated following (ALLEN; TASUMI; TREZZA, 2007).

Soil heat flux (G) is computed with the following equation, calibrated with remote sensing data and ground measurements at the flux towers.

$$G = R_n(T_s - 273.15)(0.015\alpha)(1 - 0.8\,(NDVI)^{1/3}) \quad (3)$$

where T_s is the land surface temperature (K), and α is the broad-band surface albedo.

The following equation is used to estimate the sensible heat flux (H):

$$H = \rho_{air} Cp \frac{dT}{r_{ah}} \quad (4)$$

where ρ_{air} is the air density ($kg.m^{-3}$), Cp the specific heat of air at constant pressure ($J.kg^{-1}K^{-1}$) and r_{ah} the aerodynamic resistance (s m-1) between two near-surface heights, $z1$ and $z2$, where $z1$ = 0.1 and $z2$ = 2 m above the zero-plane displacement height. dT is the temperature gradient and represents a linear function of T_s, as proposed by (BASTIAANSSEN et al., 1998b):

$$dT = aT_s + b \quad (5)$$

where a and b are internally calibrated.

Since both H and r_{ah} are unknown, SEBAL adopts an iterative process. For the first iterative process, r_{ah} is estimated assuming neutral stability:

$$r_{ah} = \frac{\ln(z2/z1)}{u_* k} \quad (6)$$

where $z1$ and $z2$ are the heights above the zero-plane displacement of the vegetation where dT are defined, u_* the friction velocity ($m.s^{-1}$) and k the von Karman's constant (0.41).

To select the hot and cold endmember pixels, we used a simplified version adapted from the automated methodology from the METRIC model based on the Calibration using Inverse Modeling at Extreme Conditions (CIMEC) process(ALLEN et al., 2013). The CIMEC process considers a population of candidate members based on quantiles of remote sensing estimations of Ts and NDVI to select the hot (dry) and cold (wet) pixels.

The 8-day evapotranspiration (ET_{8-day}) is computed with the following steps. Firstly, the 8-day evaporative fraction (Λ) is calculated as:

$$\Lambda = \frac{LE}{R_n - G} \quad (7)$$

Then, ET_{8-day} is calculated considering Λ constant during the period of eight days. The 8-day net radiation (Rn_{8-day}) was obtained by averaging the daily values.

$$ET_{8-day} = 0.0864\ \Lambda \frac{Rn_{8-day}}{\lambda} \quad (8)$$

The monthly evapotranspiration is finally computed as the average of all 8-day values within a given month.

8.2.2 SEBAL input data and application for South American wetlands

SEBAL input data were based on the following products available in Google Earth Engine (GEE ID's are provided):

- Surface Reflectance - MOD09A1.006 Terra Surface Reflectance 8-Day Global 500m. GEE ID = MODIS/006/MOD09A1;
- Land Surface Temperature and Emissivity - MOD11A1.006 Terra Land Surface Temperature and Emissivity 8-Day Global 1km. GEE ID = MODIS/006/MOD11A2;
- NDVI and EVI - MOD13A1.006 Terra Vegetation Indices 16-Day Global 500m. GEE ID = MODIS/006/MOD13A1 (linearly interpolated to 8 days);
- LAI - MCD15A3H.006 MODIS Leaf Area Index/FPAR 4-Day Global 500m. GEE ID = MODIS/006/MCD15A3H. For images between 2000-2002, a monthly average from 2003-2005 was used, given the unavailability of MODIS LAI data (linearly interpolated to 8 days);
- Meteorological input (wind speed, specific humidity, surface air temperature and incoming shortwave radiation): GLDAS 2.1(RODELL et al., 2004); GEE ID = NASA/GLDAS/V021/NOAH/G025/T3H;
- Digital Elevation Model (DEM) from SRTM9; GEE ID = USGS/SRTMGL1_003.

The criteria for the selection of endmember (hot and cold) pixels were based on a simplified method based on the CIMEC algorithm (ALLEN et al., 2013). For each wetland, a MODIS image of 1 x 106 km² centered on the wetland was used to select the endmembers for calibration. MODIS data quality masks were used for each image, in addition to elevation masks (values lower than 600 m were assessed for all wetlands). For the central Amazon (i.e., Amazon Upstream, Amazon Downstream and Negro interfluvial wetlands), the images from January to May were not considered given the persistent cloud cover in the region, which largely decreased data quality. Since we used MODIS 8-day (surface reflectance and LST) averages to estimate ET, we computed the 8-day average of the evaporative fraction (Λ) and Rn to estimate the 8-day ET. To compute monthly ET, we averaged the 8-day estimates in monthly time steps. The main

SEBAL model output was monthly ET maps at 1 km spatial resolution for the period 2000-2015.

While the SEBAL methodology was already satisfactorily applied to individual wetlands worldwide, it was further validated here with 10 in situ monitoring sites located within or close to the assessed wetlands. The validation yielded a satisfactory accuracy of the ET seasonality across the continent, with a RMSE ranging between 0.4 and 1.2 mm.d-1 (Figs. S9 and S10), considering the 8-day average ET. Supplementary Note 2 presents more details on the model validation.

8.2.3 Ancillary data

The developed ET dataset is conjointly analyzed with other state-of-the-art ancillary data at monthly time scale: GIEMS-2 monthly inundation at 25 km spatial resolution (PRIGENT; JIMENEZ; BOUSQUET, 2020), MSWEP precipitation (BECK et al., 2017), GLDAS 2.1 (RODELL et al., 2004) reanalysis data for Rn, VPD and Ws, and MODIS LAI. Evaporative demand (E0) was computed with the FAO reference evapotranspiration equation, which was chosen for explicitly considering atmospheric variables as VPD and Ws into the evaporative demand, allowing a consistent comparison among different locations.

8.2.4 Experimental design

Each wetland polygon (Figure 8.1) was defined as the GIEMS-2 maximum flood extent around the wetland location. The 25 km inundation fraction pixels were classified into two classes of floodability (50% most floodable, and 50% least flooded pixels), which defined the most floodable and least floodable areas depicted in the boxplots of Figure S3. To avoid uncertain flood estimates in pixels with low flood fraction values, the analyses presented in Figures 1-3 were performed for the set of the most flooded pixels. In addition, for each wetland the adjacent upland was identified as the non-flooded pixels within a 100 km buffer around the wetland polygon, randomly selected to have the same number of pixels as the most flooded pixels. The 2000-2015 period was adopted for being common to GIEMS-2, MSWEP and MODIS datasets. Linear correlations were performed among the estimated monthly ET, ET anomaly (normalized by monthly averages) and E0 and environmental variables to understand the drivers of ET processes (Figure 8.3). The long term difference between wetland and adjacent upland ET was computed based on the long term (i.e., 2000-2015) average ET for each set of most flooded and upland pixels (Figure 8.2).

8.3 Results

8.3.1 Long-term patterns of wetland evapotranspiration across climates

The long-term patterns of ET in South American wetlands follow a climate gradient (Figure 8.1). The combination of high precipitation and available energy (assessed here as net radiation; Rn) in equatorial wetlands (Figure 8.2a and 2b) produces the highest annual ET rates (1296–1542 mm/year), and these areas also exhibit the greatest leaf area index (LAI) values (Figure 8.2c). Meanwhile, the lowest annual ET rates occur in the temperate wetlands (743–1128 mm/year). Because of persistent cloud cover in the Amazon, ET was not estimated for the months of January to May; however, the available period is representative of the flood maximum and minimum stages, enabling us to understand the seasonal dynamics of ET in this region, while the small ET amplitude in Amazon enables us to estimate its annual rate. While annual Rn is relatively similar between equatorial and tropical wetlands, the higher water availability (precipitation) leads to higher ET in the former. In turn, the fraction of available energy that is converted into ET depends on surface water availability, i.e., the extent to which incoming waters accumulate on the terrain surface. Our regional-scale analysis indicates that the higher the wetland flood fraction, the higher the evaporative fraction, independent of climate type (Figure 8.2d). Examining regional flood fraction values that exceed 0.3, however, reveals that the evaporative fraction reaches a plateau around 0.7–0.8. The fraction of precipitation that becomes evapotranspiration (ET/P) ranges from 0.5–0.7 in equatorial and most tropical wetlands to greater than 0.8 in temperate ones, with the highest values in the Pampas and Paraná floodplains (Figure 8.2e). In the Pampas, relatively little runoff is routed out of the wetland through a consolidated river drainage network, and almost all precipitation turns into ET. An ET/P ratio greater than unity for the Pampas suggests a memory effect within the system that is associated with groundwater storage (KUPPEL et al., 2015). Meanwhile, the Paraná floodplain receives water from the upstream basin, and total water inflow exceeds precipitation.

Comparing ET in wetlands and adjacent uplands at the regional scale, we uncover greater differences among temperate wetlands, which are located within water-limited environments (E0/P > 1, where E0 stands for atmospheric evaporative demand, indicated here by the reference ET), with values reaching 29%, 23%, 13%, and 5% for the Paraná, Iberá, Pampas, and Chaco wetlands, respectively (Figure 8.2e). For instance, for the case of Paraná river, this means that the floodplain inundation due to waters coming from upstream may increase the annual average latent heat flux by around 20 W/m², and reduce sensible heat flux by the same amount. This is equivalent to an annual evapotranspiration increase of around 250 mm/year in relation to uplands (see values for other wetlands in Supplementary Fig. S1). The increased surface water availability in these areas enables them to meet the evaporative demand, i.e., higher ET/E0 values in wetlands than uplands. In contrast, the ET/E0 rate is close to unity (i.e., points close to

the 1:1 line in Figure 8.2e) for both uplands and wetlands in the equatorial regions. The high flood fraction in large portions of the equatorial Magdalena Mompós depression and the tropical Pantanal wetlands (Fig. S2) produces significant wetland-upland differences (19% and 16%, respectively). Flooding in these areas stems from a combination of geomorphological processes (i.e., depressions associated with sedimentary basins) and large river inflows (the Magdalena and Paraguay rivers, respectively) within a mostly non-forest vegetation landscape. In contrast, the equatorial wetland forest in the central Amazon exhibits only small differences (3% to 5%) because the large upland forest ("terra-firme") maintains high ET rates throughout the year. Furthermore, trees in the Amazonian wetlands are less diverse and smaller and include a larger proportion of deciduous species than those in the adjacent uplands; therefore, wetland trees are expected to exhibit lower annual transpiration rates than upland ones (HAASE, 1999; HAUGAASEN; PERES, 2005; WITTMANN, F., SCHÖNGART, J., BRITO, J. M., OLIVEIRA-WITTMANN, A., PAROLIN, P., PIEDADE, M. T. F., & GUILLAUMET, 2010). The small wetland-upland ET difference (3–5%) is due to open water evaporation, and this effect may be further enhanced by reduced precipitation in the Amazonian floodplains compared to the uplands (-5% (PAIVA et al., 2011)), which increases energy availability in the floodplains because of decreased cloud cover. On the other hand, most tropical hyperseasonal savannas (Orinoco, Negro, Moxos, and parts of the Bananal and Pantanal) are surrounded by upland forests. In this case, while the flooded savannas exhibit higher ET rates than do the adjacent non-flooded savannas, the surrounding forests maintain high ET rates year-round and therefore exhibit annual ETs that exceed those of the flooded savannas (Fig. S3).

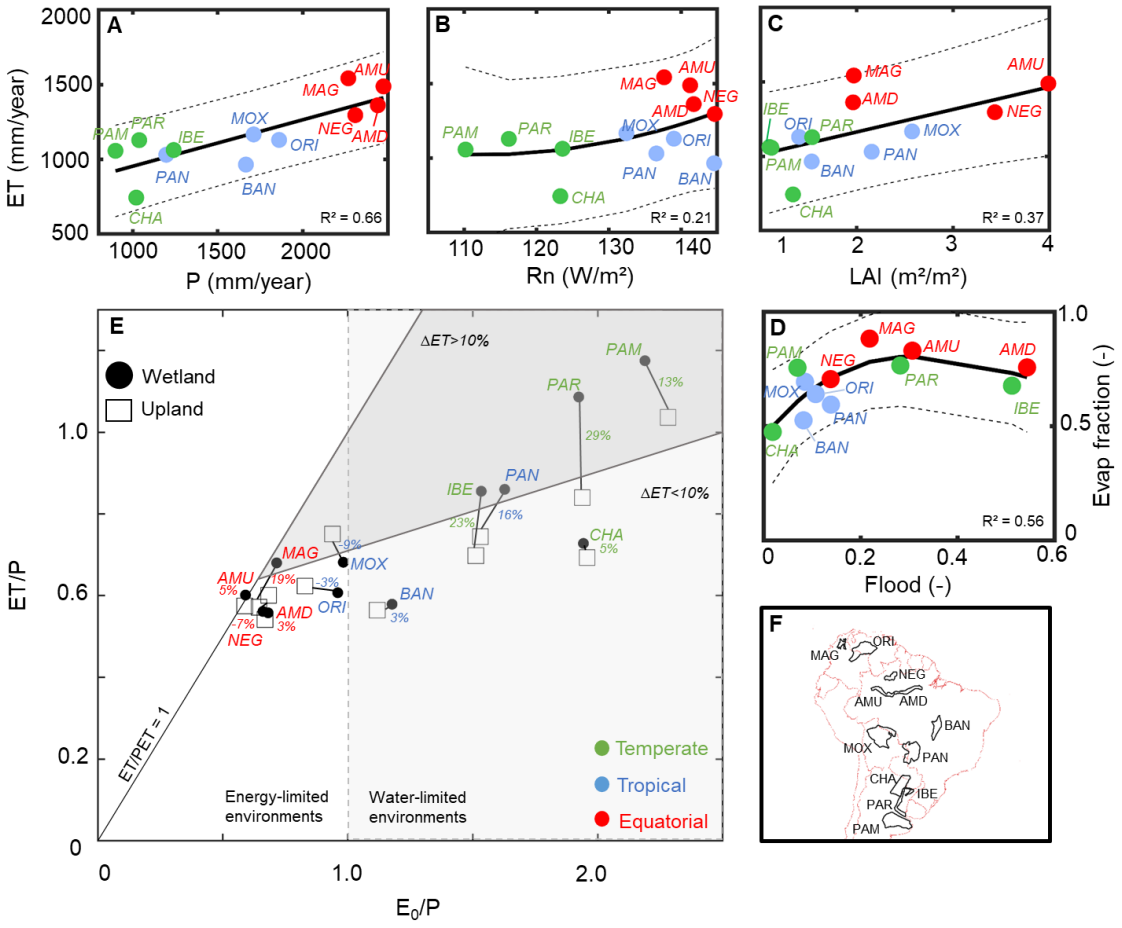

Figure 8.2. Relationships between long-term mean evapotranspiration and environmental drivers in South American wetlands. Relationships between long-term mean evapotranspiration and annual average (a) precipitation (P), (b) net radiation (Rn) and (c) leaf area index (LAI), and (d) between evaporative and flood fractions. Polynomial fits are presented together with the 95% confidence interval. (e) Budyko-like framework relating the long-term evaporative index (ET/P) with the aridity index (E0/P), where E0/P > 1 refers to water-limited environments, and E0/P<1 to energy-limited ones. Values are presented for wetlands (black circles) and the adjacent uplands (black squares) (see the Methods section for definition of the areas). The wetland-upland long-term differences are shown as numbers between wetland and upland symbols for each wetland, and the dark grey area refers to areas with differences higher than 10%. Each wetland area refers to its floodable areas and not to its whole catchment, as in the original Budyko framework, so that evaporative index values higher than unity may indicate incoming water from out of the analyzed area. (f) Location of the 12 wetland complexes.

8.3.2 Seasonal patterns of wetland evapotranspiration and its environmental drivers

We investigate the role of environmental drivers on ET dynamics by correlating monthly ET estimates with six main drivers: flooding, precipitation, LAI, Rn, vapor pressure deficit (VPD), and wind speed (Ws; Figure 8.3a; see detailed correlation matrices and scatterplots in Figs. S4 and S5). While precipitation is identified as the main driver of annual ET magnitude in all wetlands (Figure 8.2), the available energy (Rn) is the main driver of ET seasonality for equatorial (high water availability throughout the year) and temperate wetlands (high Rn seasonality). In temperate climates, the wet season is in phase with Rn, producing the highest ET rates in the austral summer (Figure 8.1). In turn, the tropical wetlands face a dry season water deficit; thus, water availability (measured via both flooding and precipitation variables) complements Rn as a major ET driver.

Wetland LST exhibits strong variation across the continent (Figure 8.3b). While it is mainly driven by flooding in equatorial wetlands (a strong correlation between flood fraction and LST), a different pattern occurs in the temperate wetlands, where the strong Rn seasonality is responsible for the large LST amplitude (Fig. S4). Meanwhile, the tropical wetlands exhibit an intermediate pattern, with both Rn and flooding moderately correlated with LST. These differences have major implications for ET dynamics.

While, in average years, ET seasonality follows strong Rn variation, years with anomalous flooding lead to anomalously high ET in many South American wetlands (see the correlation for ET anomaly in Figure 8.3). This is the case of the Argentine Pampas, which is characterized by an erratic interannual flooding pattern, with alternately flood-rich (2000–2004 and 2011–2015) and flood-poor periods (2005–2010). While the highest ET rates occurred in the flood years (Figure 8.4a), high ET values persisted some years after the main flooding period (2000–2004), indicating memory effects on groundwater storage in the Pampas (KUPPEL et al., 2015).

A strong correlation between flood fraction and ET/E0 for many wetlands (Figure 8.3) also corroborates the finding of our long-term scale analysis, i.e. that the flooding process generally enables the water supply to meet the evaporative demand. In the areas downstream of the Amazon and the Magdalena and the hyperseasonal savanna wetlands (Fig. S6), the highest ET/E0 values occur during the flood peak. In the temperate wetlands, however, ET/E0 is mainly driven by Rn. While the temperate wetlands exhibit the greatest annual amplitude and the highest monthly rates (e.g., 170 mm/month in December in Iberá; Figure 8.1), confirming the hypothesis that grassland wetlands have ET rates as high as forested ones in some months (SANCHES et al., 2011), the equatorial wetlands exhibit nearly constant ET rates (from 100 to 130 mm/month in the central Amazon). Heavy cloud cover in the equatorial Amazon wetlands prevents available energy rates from increasing, especially during the wet season. Months with more significant flooding are associated with the smallest wetland-

upland differences between hyperseasonal savanna wetlands and the surrounding upland forests (Negro, Orinoco, Moxos, and Bananal). However, the differences increase during the dry season, with the forests exhibiting higher ET (Figs. S1 and S7). During the wet season, the differences between the flooded savannas and non-flooded forests likewise decrease. Conversely, in the central Amazon, greater flooding produces a greater difference.

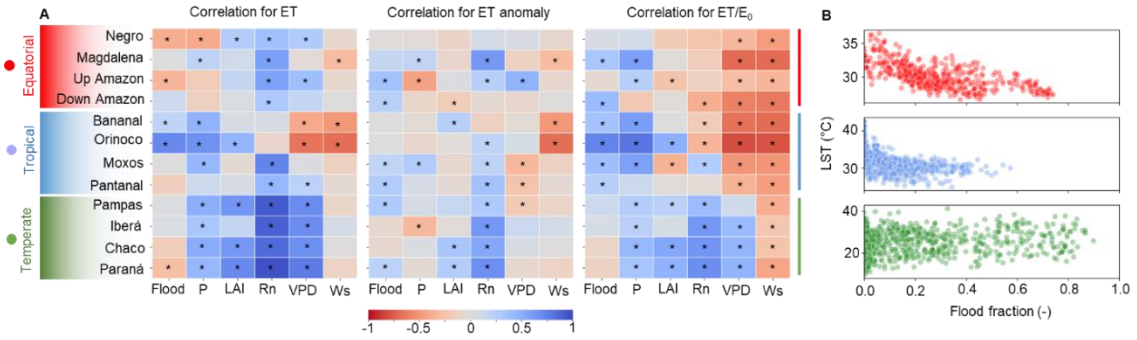

Figure 8.3. Relationships between monthly evapotranspiration and environmental drivers in South American wetlands. (a) The assessed evaporation-related variables are evapotranspiration (ET), ET anomalies (i.e., seasonal effects are removed), and actual evapotranspiration / evaporative demand ratio (ET/E0). The assessed environmental variables are land surface temperature (LST), flood fraction (Flood), precipitation (P), leaf area index (LAI), net radiation (Rn), vapor pressure deficit (VPD) and wind speed (Ws). The table colors refer to Pearson correlation values. (b) Relationship between monthly LST and flood fraction. The colors refer to climate type (temperate, tropical and equatorial). *Significant correlations with P<0.01.

8.3.3 The role of flood propagation on floodplain evapotranspiration

In terms of flooding mechanisms, inland wetlands can be classified into 1) interfluvial wetlands, which are associated with local runoff and vertical hydrological processes (endogenous processes), 2) river floodplains, where flooding is related to the overbank transfer of waters from upstream areas (exogenous processes), and 3) a combination of both (BOURREL; PHILLIPS; MOREAU, 2009; JUNK, 2013). The flood wave propagation along river floodplains produces a delay of many months between maximum precipitation and flooding at the farthest downstream reaches of the Paraná (two months), the Amazonian (three months), and the Pantanal (six months) wetlands. These delays derive from a combination of vertical soil wetting, which can produce a delay of up to two months, as seen in the interfluvial wetlands in Figure 8.1, and flood wave translation, which can lead to longer delays depending on river

hydrodynamics. We demonstrate that flood propagation largely affects the ET dynamics in the Pantanal, which experiences more than 100,000 km² of flooding annually (HAMILTON; SIPPEL; MELACK, 2002). While precipitation peaks in January across the entire region, the month of maximum flooding varies from March in the upstream reaches to July in the downstream ones (Figure 8.4b). ET climatological behavior is driven by the complementary role of flooding and evaporative demand, which reaches its maximum between August and November in the entire region, according to VPD and Ws patterns (Fig. S8). Consequently, the upstream regions that experience their flood peak in March (i.e., Region 1 in Figure 8.4b) exhibit ET peaks in both March and November. Conversely, the downstream regions, where evaporative demand and surface water availability due to floodplain inundation are in phase, reach their annual ET peak between August and November. The higher ET rates in the downstream regions are likely associated with open water evaporation. Meanwhile, the Pantanal's unique geomorphology causes longer delays in its flood wave translation compared to the other two large floodplains addressed here (the Amazon and the Paraná). However, the effects of flood propagation on ET dynamics are also evident in these wetlands, where anomalous ET rates are strongly correlated with periods of anomalous flooding (Figure 8.3).

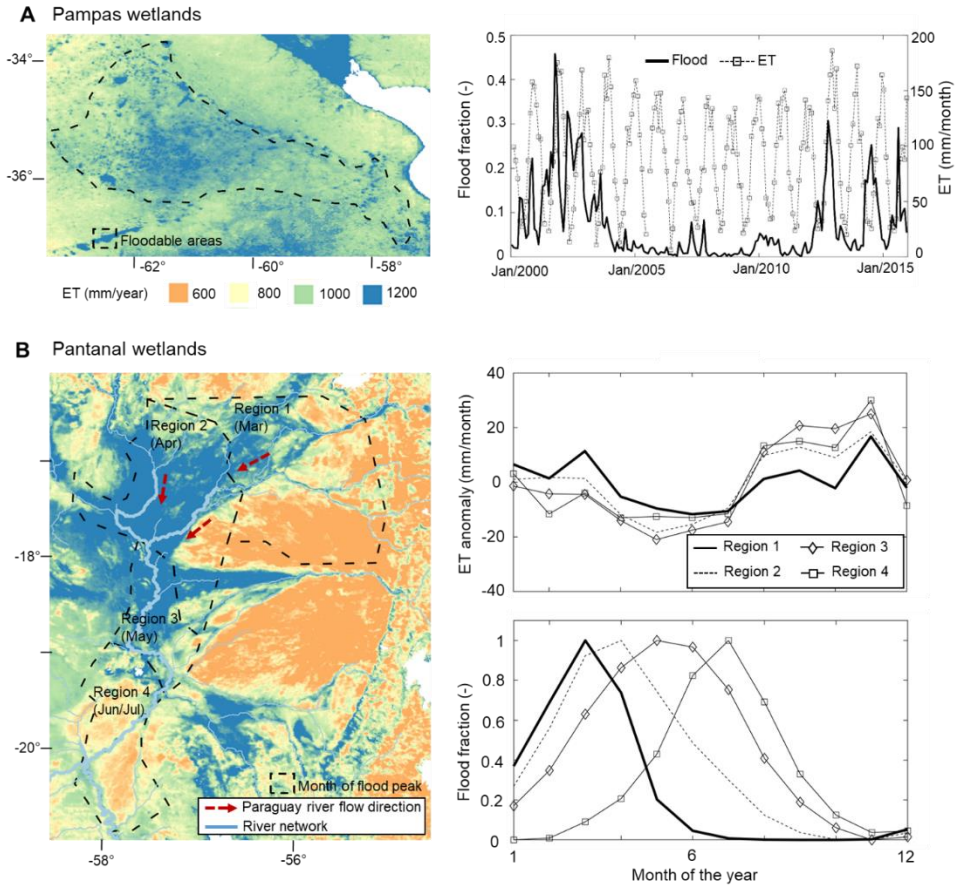

Figure 8.4. The role of flooding on evapotranspiration spatial pattern. (a) The interannual variation of floods in the Pampas wetlands in Argentina relates to evapotranspiration patterns. The left figure presents the annual evapotranspiration map, with the floodable areas highlighted, and the right figure shows 15 years of flood fraction and absolute monthly evapotranspiration. (b) Flood propagation affects ET at the seasonal time scale in the Pantanal wetlands. The annual evapotranspiration map is presented in the left figure, together with the location of the four regions of equal month of flood peak (from March to Jun/Jul), while the figures in the right column show the climatology of monthly ET (anomaly values) and flood fraction for the four regions.

8.3.4 Evapotranspiration of floodplain forests across biomes

The partition of wetland ET into vegetation transpiration and open water and soil evaporation is difficult to disentangle. Open water evaporation tends to increase with surface water availability and can potentially offset plant transpiration, which may, in turn, be reduced by flooding due to anoxic or hypoxic conditions, an increase of toxic compounds, or a decrease in the availability of nutrients (AROCA; PORCEL; RUIZ-LOZANO, 2012; DALMAGRO et al., 2016a; SCHÖNGART et al., 2002). These effects can induce stomatal closure, while flood adaptation measures, such as

adventitious roots and aerenchyma, can, in contrast, increase stomatal conductance during flood peaks (HERRERA, 2013; PAROLIN, 2009). The total canopy conductance depends on stomata opening and total leaf area; therefore, the various adaptation strategies plants use to cope with alternating cycles of flooding and drying ultimately determine transpiration seasonality.

Here we compare ET processes in five floodplain forests across South America, using the MODIS Enhanced Vegetation Index (EVI; see Methods) as a proxy of stomatal activity and forest dormancy under flooding conditions (FONSECA et al., 2019; HESS et al., 2009; IVORY et al., 2019). Although the EVI signal may be affected by the inundation itself, its use here is reasonable given the high tree cover in the assessed floodplains. Both water excess and a water deficit can hinder wetland forest activity across South America, depending on plant adaptation and local-scale factors, including the soil's water retention capacity. The highest ET rates occur during the wet season (or dry-wet transition in the Amazon, which corresponds to the floodplain leaf shedding period (HAUGAASEN; PERES, 2005)) in all floodplains, while the flood peak leads to reduced vegetation activity or forest dormancy (low EVI) in all but the Paraná floodplain (Figure 8.5). The phenological seasonality of the Paraná forests is predominantly driven by flooding, which occurs during the dry season (austral winter) due to the flood wave translation along the upstream river network, and its associated nutrient-rich sediments (MARCHETTI et al., 2013). In the Paraná, the lowest EVI occurs during periods of receding waters, which correspond with periods of minimum energy availability, and EVI levels remain low until the onset of the wet season. In the Bananal forest, we observe that ET is not water-limited; in the adjacent floodable savannas, however, ET exhibits the opposite characteristic and decreases in the dry season (see the BAN flux tower in Fig. S9). A small—and, indeed, below the annual average—ET peak, which may be associated with soil evaporation,(BORMA et al., 2009; FONSECA et al., 2019) occurs in the month of maximum flooding in the Bananal and Pantanal floodplains. ET decreases in the Orinoco floodplains during flooding; in contrast, the large-scale flooded savanna experiences its maximum ET during the flood period (Figure 8.1), which suggests the greater importance of direct surface evaporation in this region associated with limited vegetation activity in riparian forests during flooding. Finally, the assessed Pantanal floodplain is a Vochysia divergens monodominant forest, which is not water-limited during the dry season due to plant adaptation strategies and exhibits a relatively high soil moisture content throughout the entire year (DALMAGRO et al., 2016a; SANCHES et al., 2011). In this case, the reduced vegetation activity observed during the dry season may be related more strongly to a reduction in available energy.

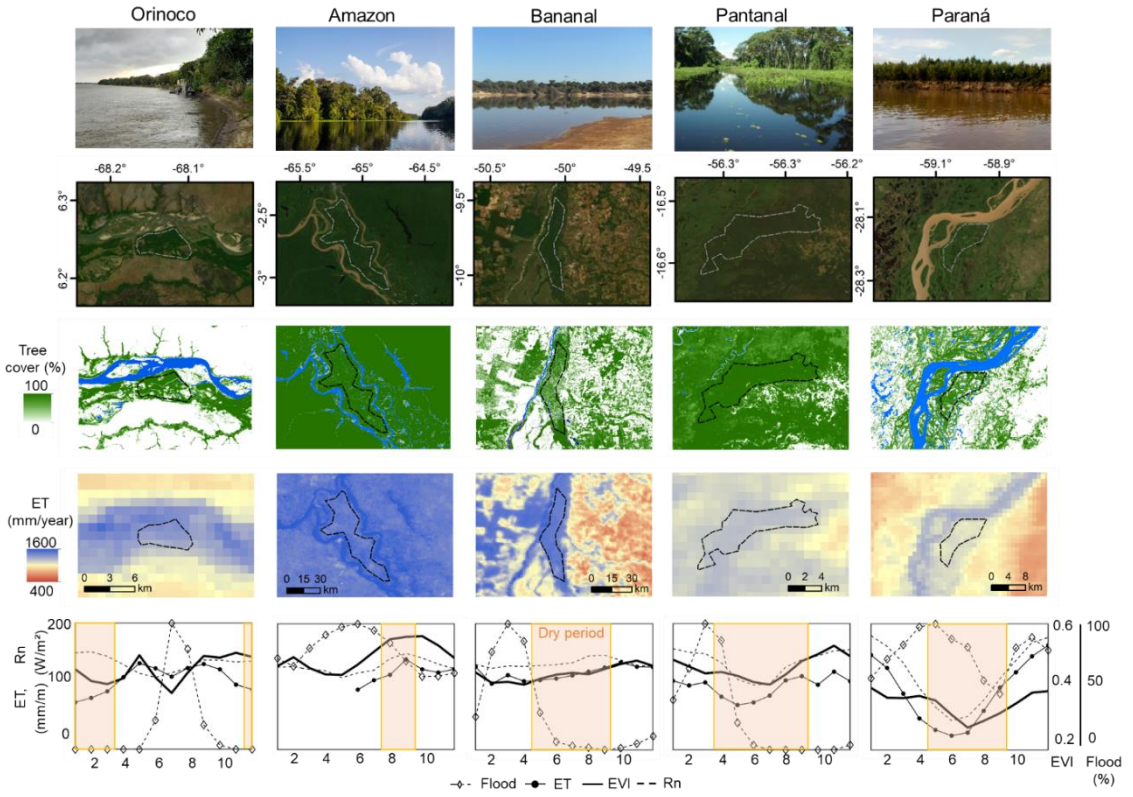

Figure 8.5. Evapotranspiration patterns and drivers in floodplain forests across South America. The figures present true color RGB composition (second row), tree cover fraction (third row), and annual ET map (fourth row). In the fifth row, climatology of evapotranspiration, flood fraction and EVI variables are presented for the polygons in the map of the fourth row, and the dry period is defined according to precipitation regime. Dry period in the bottom figure is defined as months with precipitation smaller than 100 mm/month. Source of satellite images on second row: Source Esri, Digital Globe, GeoEye, Earthstar Geographics, CNES/Airbus DS, USDA, USGS, AeroGRID, IGN, and the GIS User Community.

8.3.5 Contrasting mechanisms in the central Amazon

In the central Amazon, the maximum wetland ET occurs at the transition between the dry and wet periods, which corresponds with maximum VPD, Ws and E0 values. This pattern is similar to the ET pattern that occurs in the Amazon uplands (DA ROCHA et al., 2009), where ET is energy-limited and strongly correlated with Rn, the highest values of which occur in the dry-wet period transition when cloud cover is limited. In addition, as discussed in the previous section, forest transpiration in flooded areas tends to be limited by flooding, which peaks during the dry season because of the river flood propagation process. In contrast, the ET/E0 ratio peaks during maximum

flooding in the most floodable, downstream reaches (Fig. S6), highlighting the role of open water evaporation. On a large scale, two compensating effects interact to determine the actual annual ET in the central Amazonian wetlands (Figure 8.6). First, more dense tree cover occurs in the upper reaches (roughly upstream from the city of Manaus; Figure 8.6d), whereas the downstream reaches—with their lower tree height and a large proportion of native herbaceous plants—are associated with lower precipitation rates, a longer dry season, smaller flood depths, less nutrient availability (ALBERNAZ et al., 2012), and the conversion of forestlands to agricultural areas and pastures (RENÓ et al., 2011). Second, the downstream reaches feature more lakes and experience flooding for a lengthier period of the year, and both of these characteristics increase ET. The combination of these two opposing effects produces the highest annual ET rates in the upstream reaches, which exhibit greater tree cover, while a decreasing ET trend is observed in the downstream direction, with an exception (i.e., an increase) only in the furthest downstream parts with the largest flood fraction. The downstream Amazon surpasses the upstream region only during the high flood period (June and July) because of open water evaporation (Fig. S1).

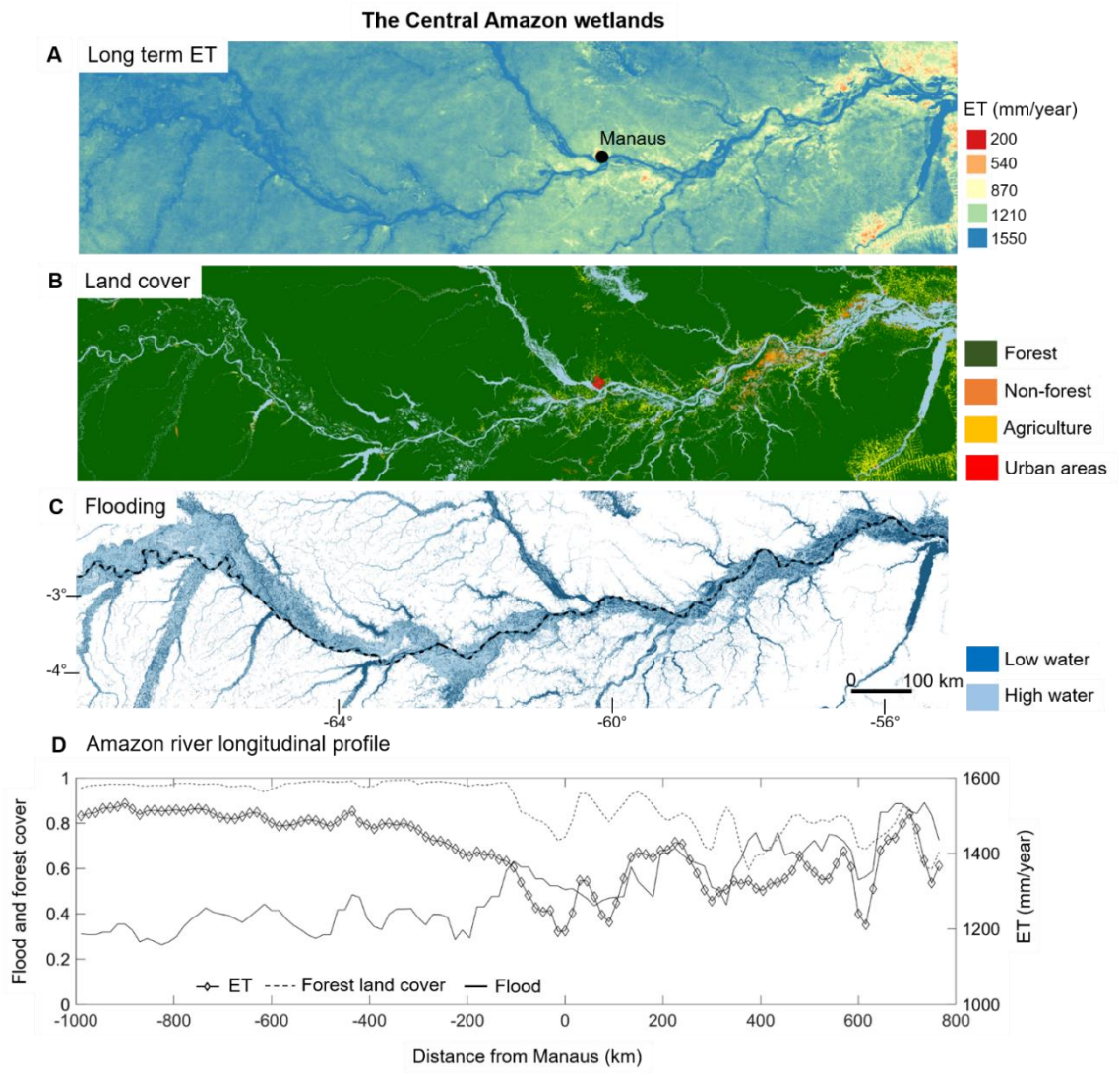

Figure 8.6. Spatial patterns of evapotranspiration across forest and non-forest areas in wetland environments. (a) Long term evapotranspiration (2000-2015) across different land covers in the central Amazon wetlands. The lower reaches are associated to larger cover of non-forest vegetation (savanna and grasslands) and higher flood fraction. (b) Land cover. Note that forest refers to both flooded and non-flooded areas. (c) Flooding. (d) River longitudinal profile showing ET and fraction of forest and flood cover. Forest land cover data for the year 2009 from the Project MapBiomas - Collection 4.1 of Brazilian Land Cover & Use Map Series, accessed on 1st Dec 2021 through the link <https://plataforma.mapbiomas.org/>. High and low water maps from the Wetland Extent, Vegetation, and Inundation high-resolution map for the Lowland Amazon Basin (<https://daac.ornl.gov/LBA/guides/LC07_Amazon_Wetlands.html >).

8.4 Discussion

Utilizing a comparative hydrology approach, our study provides new insights on wetland ET processes on a continental scale. The interplay between climate, landscape geomorphology, soil, and vegetation drives ET patterns in South American wetlands. We confirm that wetlands largely affect the regional energy balance in temperate to tropical areas (VAN DIJK et al., 2018), and thus have a major role on climate regulation. Wetlands act as a major source of water loss in South American basins by moving 13%–29% more water to the atmosphere than do the uplands adjacent to the Paraná, Iberá, Magdalena, Pantanal and Pampas wetlands. While differences between the wetlands and uplands of the central Amazon are not quite as distinct, an exception among equatorial wetlands occurs for the Magdalena Mompós depression in the transition between equatorial and tropical climates, which is associated with one of the most flooded environments in South America (i.e., a geomorphological factor) and is surrounded by non-forest vegetation with relatively low ET rates. Our results also highlight the role of flood translation in the ET dynamics of river floodplains, especially for the Pantanal, the largest continuous wetland in the world, and they corroborate recent findings that flood dynamics drive the seasonality of the wetland vegetation activity (IVORY et al., 2019). While the strong seasonal variation of available energy (Rn) drives the overall magnitude of ET in temperate wetlands, seasonal ET variation in tropical and equatorial wetlands is more susceptible to variability in surface water availability and vegetation phenology. In turn, the flood pulse generally enables wetland systems to meet the evaporative demand while depressing vegetation activity in all assessed floodplain forests, except for the Paraná River, where input of nutrient-rich sediments during flooding may increase vegetation activity. Although maximum ET occurs during the wet season in all floodplains, it does not coincide with maximum flooding, which hampers transpiration. These conclusions have implications for the development of earth system models, which can improve their predictive capabilities regarding surface-atmosphere interactions under future environmental changes by accurately representing wetland flooding dynamics and their impacts on wetland vegetation. For instance, the increased latent heat observed in our study has been shown to decrease precipitation rates in wetlands worldwide (TAYLOR; PRIGENT; DADSON, 2018). However, a proper understanding of such mechanisms, especially under the dense cloud cover of equatorial environments, requires further study. Although the implemented ET algorithm is limited in depicting local-scale patterns due to the misrepresentation of microtopography features, soil heterogeneity (WU; SHUKLA; SHRESTHA, 2016), and dynamics of open water and macrophyte cover over flooded areas (MOHAMED et al., 2012; SÁNCHEZ-CARRILLO et al., 2004), the regional scale of our analysis and its validation with in situ data (Supplementary Note 2) support the suitability of the model adopted for this study. Given the close relation between LST and surface water availability within the landscape, ET algorithms based on LST are considered more appropriate for estimating wetland ET than other remote sensing methods that depend upon vegetation indices and land cover maps (VAN DIJK

et al., 2018; YILMAZ et al., 2014). Compared to other LST-based methods, moreover, the algorithm exhibits low sensitivity to meteorological input data (LAIPELT et al., 2020). As they advance toward local-scale analyses, future studies should aim to fine-tune the ET calculation for each case by developing strategies of parameterization individually for each wetland.

Across South America, tropical and temperate wetlands face alternating cycles characterized by a range of soil conditions—from fully saturated to completely dry. Consequently, flooded savannas surrounded by forests generally exhibit similar ET rates during flooding but the similarity diminishes during the dry season. This finding has important implications for understanding the potential impacts of environmental changes since these ecosystems have evolved based on feedback between the vegetation and the physical environment. For instance, the flood-adapted savanna vegetation in the Negro interfluvial wetlands is hypothesized to have colonized a neotectonic-induced depression, which was filled by white sand and became subject to periodic flooding (ROSSETTI et al., 2017a). If this hypothesis holds, changes in wetland flooding dynamics would largely affect the regional vegetation distribution and thus its energy partition. In such hyperseasonal savannas, groundwater appears to play a minor role, given the usual dry season water deficit (BORMA et al., 2009), while the opposite seems true in temperate grasslands such as the Pampas, as demonstrated by our analysis (Figure 8.4b) and estimates by the NASA's Gravity Recovery and Climate Experiment (GRACE) mission for the system's slow water storage depletion (KUPPEL et al., 2015).

Because a two-way feedback system operates between wetland vegetation and physical flooding mechanisms, ET losses may serve as regulatory feedback. This hypothesis has been suggested for the Pampas (KUPPEL et al., 2015) and the Pantanal wetlands in South America. In the latter, the system's self-maintenance has been proposed to occur through tree expansion (especially Vochysia divergens) during extremely wet years (NUNES DA CUNHA; JUNK, 2004); these trees invade pastures (NUNES DA CUNHA; JUNK, 2004), exhibit higher growth and transpiration rates, and use water less efficiently than do non-dominant trees (DALMAGRO et al., 2016a; SANCHES et al., 2011). Our study demonstrates that these "super-dominant" tree species indeed alter the energy partition in the Northern Pantanal (forest in Figure 8.5) towards higher water losses through ET; however, the long-term distribution of such species should be assessed in future research to better evaluate the ET regulation hypothesis. In the highly dynamic reaches of the Amazon basin, after floodplain disturbances caused by bank erosion, some pioneer trees colonize the river banks and can exhibit higher ET rates than non-pioneer trees (PAROLIN; WALDHOFF; PIEDADE, 2010). In addition, the importance of regional-scale vegetation-atmosphere feedback in the Amazonian upland forests has been suggested because forest's maintenance require high precipitation rates, while the forests' ET is also responsible for downwind precipitation. In such cases, forest loss could further reduce precipitation and thereby accelerate the loss of additional forestlands (ZEMP et al., 2017) while also reducing precipitation in downwind wetlands, such as the Pantanal (BERGIER et al.,

2018). However, the impact of deforestation may be offset by the development of secondary forests in the Amazon, which have been shown to exhibit higher ET rates than primary forests (VON RANDOW et al., 2020).

The vulnerability of wetlands to environmental changes must be better understood to ensure the sustainable provision of ecosystem services. For instance, agriculture expansion poses significant challenges for wetland conservation across South America (JUNK, 2013), and understanding the impacts of these changes on wetland ET remains challenging. While forest loss in upstream areas can increase water availability in wetlands located downstream (WOODWARD et al., 2014), the removal of trees may increase the availability of open water as well as encourage the colonization of new trees with higher ET rates. Fires pose a particular threat to floodplains, and this has recently been debated in the Amazon black-water floodplains, which, during the dry season, may be more vulnerable to fires than are uplands due to the former's lower LAI, more open canopy, and lower relative humidity (DE RESENDE et al., 2014; FLORES et al., 2017; SAN JOSÉ et al., 2001). In 2020, a large-scale drought affected the Pantanal, triggering the most impactful fires ever reported. These fires destroyed a large portion of the biome (LIBONATI et al., 2020), and their impact on vegetation will affect the wetland ET for years to come. Flood pulse alterations caused by dams in large river-floodplain systems (e.g., the Paraná, the Amazon, the Magdalena, and the Pantanal) also hold the potential to modify regional wetland ET dynamics and their associated vegetation, while interfluvial wetlands are less connected to rivers and thus less vulnerable. Finally, the potential effects of climate change on wetland ET and vegetation must be addressed. Although floodplain forests generally have deep roots (BIUDES et al., 2015), uncertainties remain regarding their ability to cope with the precipitation reductions (by some estimates, up to 20%) and concomitant decreases in water availability that are projected to afflict all equatorial and tropical South American wetlands by the end of the century (BRÊDA et al., 2020; XI et al., 2020). Such decreases could lead equatorial wetlands to face a tropical climate regime, which would likely decrease ET. In turn, future research should assess the ability of savanna vegetation, which tends to have superficial roots, to cope with such challenges in hyperseasonal wetlands. Recent studies have suggested that severe droughts may affect floodplain tree photosynthesis and growth to a greater extent than do anomalous floods (HAASE, 1999; PAROLIN; WALDHOFF; PIEDADE, 2010). As research continues, the complex interplay between climate change—with a likely increase of VPD and CO2 concentrations (YUAN et al., 2019)—and regional differences in available energy and water availability will ultimately define the fate of South American wetlands.

Part III. Wetlands as human-water systems

Parte III. Áreas úmidas como sistemas sociedade-água

9 The great 1983 floods in South American large rivers: a continental hydrological modelling approach

This chapter is presented as a research article, which was published in Hydrological Sciences Journal:

- Fleischmann, A.S., Siqueira, V.A., Wongchuig-Correa, S., Collischonn, W., Paiva, R.C.D. de, 2020. The great 1983 floods in South American large rivers: a continental hydrological modelling approach. Hydrological Sciences Journal 65(8), 1358-1373. https://doi.org/10.1080/02626667.2020.1747622

9. As cheias de 1983 nos grandes rios da América do Sul: uma abordagem de modelagem hidrológica continental

Este estudo apresenta uma análise espaço-temporal das grandes cheias de 1983 que afetaram os rios Sul-Americanos, através de dados hidrometeorológicos e estimativas de um modelo hidrológico-hidrodinâmico de escala continental. O extremo ano de 1983 teve três principais períodos de cheias (Fevereiro, Junho e Julho) em bacias como Araguaia, Tocantins, São Francisco, Uruguai, La Plata e seus tributários, fazendo por exemplo que o rio Paraguai mantivesse vazões com altos períodos de retorno durante muitos meses. Curvas profundidade-área-duração de precipitação indicaram que os eventos de 3 dias nas regiões do norte estiveram entre os 15 maiores eventos entre 1980 e 2015 apenas para algumas regiões especificas, enquanto nas áreas do sul os eventos registrados foram os mais extremos neste período para durações maiores (precipitação ≥ 7 dias). A análise do volume total de água exportado para os oceanos indicou que os rio que drenam para o Atlântico Sul atingiram uma anomalia positiva de 3.7 em 1983, seguido pelos anos de 1998 (1.9) e 1992 (1.1), todos relacionados a anos de El Niño.

Este capítulo é apresentado na forma de um artigo científico, publicado no periódico Hydrological Sciences Journal:

- *Fleischmann, A.S., Siqueira, V.A., Wongchuig-Correa, S., Collischonn, W., Paiva, R.C.D. de, 2020. The great 1983 floods in South American large rivers: a continental hydrological modelling approach. Hydrological Sciences Journal 65(8), 1358-1373. https://doi.org/10.1080/02626667.2020.1747622*

Abstract

This study provides a spatiotemporal analysis of the great 1983 floods in South American rivers using hydrometeorological data and outputs from a continental-scale hydrologic-hydrodynamic model. The extreme year of 1983 led to three main flooding periods (February, June and July) in basins like the Araguaia, Tocantins, São Francisco, Uruguay, La Plata and its tributaries, causing the Paraguay river to be with high return periods during many months. Depth-Area-Duration curves showed that 3-day precipitation events in northern regions were among the largest 15 events between 1980–2015 but only for specific locations, whereas in southern areas events were the most extreme ones in the same period for larger durations (≥ 7-day precipitation). Modelled total export of water volume to the oceans indicated that rivers draining to the South Atlantic reached an anomaly of 3.7 during 1983, followed by 1998 (1.9) and 1992 (1.1), all of them corresponding to El Niño years.

9.1 Introduction

The field of regional process hydrology ($10^4 – 10^6$ km²) has drawn the attention of the hydrologic community (SIVAPALAN, 2018). In the context of floods, there are processes that do not occur at the catchment scale only (e.g., atmospheric moisture transport), and flood losses may reach regions far from the affected catchments through indirect economic effects (DURÁN-QUESADA; REBOITA; GIMENO, 2012; GIMENO et al., 2016; JONGMAN et al., 2014; KOKS et al., 2019; VOROGUSHYN et al., 2018). Data-intensive methods have allowed studies from regional to continental scales, addressing how the frequency of floods has changed in the last years, whether they are clustered in flood-rich periods, and what are the associated flood generation mechanisms (BARTIKO et al., 2019; BERGHUIJS et al., 2017; BLÖSCHL et al., 2015, 2017, 2019; GUDMUNDSSON et al., 2019; MARENGO; TOMASELLA; UVO, 1998; MERZ; NGUYEN; VOROGUSHYN, 2016; MERZ; BLÖSCHL, 2003; SCHMOCKER-FACKEL; NAEF, 2010; SHARMA; WASKO; LETTENMAIER, 2018; ZHANG et al., 2018). Characterization methods of regional scale floods have also been proposed, e.g., by defining metrics of timing, seasonality and correlation among floods and attributes as climatology, geomorphology and topography in areas as the Europe and United States (BERGHUIJS et al., 2016; HALL; BLÖSCHL, 2018; SAHARIA et al., 2017), while the role of climate change and alterations as land use on changing flood patterns is a major challenge at such scales (ALFIERI et al., 2018b; ARHEIMER; LINDSTRÖM, 2015; CHAGAS; CHAFFE, 2018; KUNDZEWICZ et al., 2014; ROGGER et al., 2017; VEIJALAINEN et al., 2010), especially considering the interactions between society and river systems in the context of socio-hydrology (PANDE; SIVAPALAN, 2017; VIGLIONE et al., 2014). Furthermore, regional flood risk estimation (and flood frequency in general) requires appropriated methods, moving away from the assemblage of local scale maps, and taking into consideration the spatial

dependence of meteorological and catchment processes (FALTER et al., 2015; VOROGUSHYN et al., 2018). For instance, a homogeneous return period applied to a whole region (e.g., 100 years) will lead to an overestimated flood damage, with a much higher return period (THIEKEN; APEL; MERZ, 2015). National and continental scale stakeholders (governments, NGO's, (re-) insurance companies, etc.) are major beneficiaries of such studies, using this information to foster water resources management and allocation of investments.

Understanding and characterizing past hydrological extremes as floods is also paramount to improve our capacity to cope with similar disasters through better design of structural (e.g., dams and levees) and non-structural measures (e.g., flood risk mapping and forecasting). This may be carried out at regional scales through characterization of spatial-temporal dynamics of hydrological/hydrodynamic variables as discharges, water levels, flood extent and volume, and soil water content, and correlation with precipitation fields (KHANAL et al., 2019). Thorough descriptions of the most important historical floods at national scales have been carried out (KUNDZEWICZ; PIŃSKWAR; BRAKENRIDGE, 2013; MACDONALD; SANGSTER, 2017; RETSÖ, 2015; WETTER, 2017), as well as assessments of particular extreme events as the 2013 European floods (BLÖSCHL et al., 2013; BRÁZDIL; KOTYZA; DOBROVOLNÝ, 2006; KUNDZEWICZ; SZAMALEK; KOWALCZAK, 1999; SCHRÖTER et al., 2015).

While observations of past rivers floods rely on historical (i.e., focused on pre-instrumental events with the use of documentary evidence), palaeo-information (i.e., geophysical archives), and instrumental data from the systematic era (BRÁZDIL; KUNDZEWICZ, 2006; BRÁZDIL; KUNDZEWICZ; BENITO, 2006), the monitoring and understanding of floods have been recently improved with remote sensing and mathematical modeling techniques (BATES et al., 2014; BRAKENRIDGE, 2019). New initiatives aim at near real-time operations and flood disaster response (ALFIERI et al., 2018a; SCHUMANN et al., 2016b, 2018), and regional hydrological-hydrodynamic models have been improved with recent computational advances and new global datasets, fostering our understanding of flooding processes, flood risk and socio-economic impacts (ALFIERI et al., 2014, 2016; BATES et al., 2018b; BERNHOFEN et al., 2018; DOTTORI et al., 2016; FALTER et al., 2015; FLEISCHMANN; PAIVA; COLLISCHONN, 2019; NEAL; SCHUMANN; BATES, 2012; SAMPSON et al., 2015; SCHUMANN et al., 2016a; SIQUEIRA et al., 2018; TRIGG et al., 2016; WINSEMIUS et al., 2013).There is then a great opportunity to improve our understanding of past extreme events (e.g., spatial-temporal extension, interannual variability) by using regional scale hydrological models and long term precipitation products (e.g., reanalysis datasets) (ANDREADIS et al., 2017b; GRÜNDEMANN; WERNER; VELDKAMP, 2018; WONGCHUIG CORREA et al., 2017; WONGCHUIG et al., 2019).

Regarding regional scale flood mechanisms, the relationship between floods and ENSO (El Niño-Southern Oscillation) periods has been studied for areas all over the world (NOBRE et al., 2017; RÄSÄNEN; KUMMU, 2013; WARD et al., 2014), and in

South America in special (ARTEAGA; TUTASI; JIMÉNEZ, 2006; BAYER et al., 2014; BERRI; GHIETTO; GARCÍA, 2002; CAMILLONI; BARROS, 2003, 2000; DEPETRIS et al., 1996; DEPETRIS; KEMPE, 1990; PASQUINI; DEPETRIS, 2010; PRIETO, 2007; TARRAS-WAHLBERG; CAUDWELL; LANE, 2006; WAYLEN; CAVIEDES, 1986), for which ENSO based methods have been developed to estimate flood risk (KHALIL et al., 2007; SILVA; NAGHETTINI; PORTELA, 2016). During the strong El Niño 1982-1983 period, major floods occurred in regions worldwide, as in Spain (BARREDO; SAURÍ; LLASAT, 2012) and Mississippi and Chao-Phraya rivers (KOMORI et al., 2012; READ; ROBINSON, 1985), while in South America major events were registered in the Southeast of the continent, as in the La Plata river system (CAMILLONI; BARROS, 2000; LATRUBESSE; BREA, 2009; PENNING-ROWSELL, 1996), Northern Peru and Ecuador (BAYER et al., 2014), and major basins in central Brazil. The floods met unprepared societies (CAVIEDES, 1985) in the continent, leading to great damages and losses: estimates include US$ 83 million in the Upper Iguaçu River (TUCCI et al., 2003), U$ 1.1 billion in Itajaí-Açu basin (Frank, 2003) and U$ 1.5 – 2.0 billion in Argentina (CAPUTO et al., 1985; VON LANY et al., 2000). Numbers of displaced people were more than 40,000 in the city of Resistencia in the Chaco region (BARRETO, 1993), 300,000 to 350,000 in Argentina as a whole (BELLO et al., 2018; CAPUTO et al., 1985), 85,000 in Paraguay (OFDA, 1983), and 151,069 in the Itajaí-Açu river valley (FRANK, 2003). 27,652 people were estimated to be affected by the floods in the Uruguay River Basin (TUCCI; CLARKE, 1998), and 75,000 in the Upper Tietê (TUCCI et al., 2003). Effects on diseases (HEDERRA, 1987), ecosystems (GARCIA et al., 2004; GLYNN, 1988) and sediments were also reported (DEPETRIS; KEMPE, 1990).

Although being the most severe recorded floods in many large basins along the continent, a thorough description of the spatial-temporal dynamics of the 1983 floods is lacking in the literature, and especially from a regional view, what may bring important information for ungauged basins and large scale stakeholders. Past hydrological studies addressed the 1983 flood magnitude and impacts mainly for specific river basins and by looking at a few gauges, and also in terms of hydrometeorological patterns, especially for the La Plata River Basin (CAMILLONI; BARROS, 2000; DEPETRIS et al., 1996; ISLA; TOLDO JUNIOR, 2013; PENNING-ROWSELL, 1996). In this context, and considering the new methodologies recently made available for understanding floods at regional scales, this study has two main objectives. First, to provide a regional analysis of the floods in the year of 1983 across South America, with a focus on the quantification of maximum discharges with the use of hundreds of discharge and precipitation gauges and large scale modeling. Secondly, to evaluate the potentiality of a continental hydrological-hydrodynamic model (the MGB model applied to the whole South America domain, called hereafter MGB-SA; Siqueira *et al.*, (2018)) to depict the dynamics of the floods. For this, the MGB-SA model accuracy is validated in terms of representation of absolute peak discharges, what is typically not performed for continental models.

This paper is organized as follows: MGB-SA is detailed in the Methodology section. Results are presented firstly for the observed precipitation during the year of 1983. Discharges are evaluated in terms of the in situ gauges where the 1983 floods were the largest recorded, followed by an analysis of the capacity of MGB-SA to estimate hydrographs, peak discharges and return periods. The many events that occurred in the year were further investigated with continental scale maps of the date of peak discharge and return periods for different months' maximum discharges. Finally, the export of water volume from the continent to the oceans was evaluated, in order to understand how anomalous the 1983 flood volumes have been.

9.2 Methodology

9.2.1 South America MGB model

The MGB model (COLLISCHONN et al., 2007; PONTES et al., 2017) ("*Modelo de Grandes Bacias*") is a conceptual, semi-distributed hydrological model that has been widely applied in large tropical basins. For this study, we used the continental-scale hydrodynamic model version from Siqueira et al., (2018) (MGB-SA) that was developed to perform an integrated, multi-basin simulation over the whole South America domain. It uses a fixed-length, vector-based discretization to divide basins into unit-catchments with equal river flow distances ($\Delta x = 15$ km), and each river has an associated floodplain profile computed using the Height Above Nearest Drainage (HAND) approach (RENNÓ et al., 2008). Unit-catchments are further divided into Hydrological Response Units (HRUs) categorized based on soil type and land use, and for each HRU the water and energy budget are calculated through the soil-vegetation system. Surface, subsurface and groundwater flows generated from water balance are propagated to the main channel of the unit catchment using linear reservoirs, while flow routing in river networks is computed using the local explicit inertial approximation of Saint-Venant equations (PONTES et al., 2017).

The model was manually calibrated for the period of 1990–2010 using hundreds of gauges stations (> 10,000 km²) from several hydrological institutions, and was validated using products from multiple sources, including remote sensing data (e.g., terrestrial water storage, evapotranspiration and water levels). For additional details about MGB-SA the reader is referred to SIQUEIRA et al., (2018).

9.3 Datasets

9.3.1 Precipitation and climate data

The MGB-SA originally uses the Multi-Source Weighted Ensemble Precipitation (MSWEP) v1.1 (BECK et al., 2017) as the rainfall forcing. This is a 0.25º resolution, global-scale product that optimally combines satellite, reanalysis and in situ observations, being available from 1979 to 2015 in sub-daily (3h) or daily accumulated rainfall fields. Here we merged the daily precipitation grids from XAVIER; KING; SCANLON, (2016) to the MSWEP one, keeping the latter only for areas outside the Brazilian territory. The precipitation data from XAVIER; KING; SCANLON, (2016) whose updated version v2.1 (XAVIER; KING; SCANLON, 2017) spans 1980–2015 and has the same resolution of MSWEP (0.25º), but uses a large dataset of rain gauges from ANA (Brazilian National Water Agency), DAEE-SP (Department of Water and Electric Energy) and SUDENE (Superintendence of Northeast Development) interpolated to the grid center points using the inverse and angular distance weighting methods. For the merging procedure we adopted the 1980–2015 period according to the availability of both datasets.

Additionally, precipitation data from 1821 in situ gauges from ANA, the National Water Institute of Argentina (INA) and the Direction of Meteorology and Hydrology of Paraguay (DMH) located around the region affected by the 1983 floods were evaluated to investigate maximum precipitation rates at point scale.

The Depth-Area-Duration (DAD) curves were plotted to synthesize the extreme precipitation events at various spatial and temporal scales. The traditional WMO method was applied to obtain DAD curves from point rainfall data (WMO, 1969). Here an automated method to identify extreme events based on DAD curves was performed by using the final merged gridded rainfall product described above. This method is based on the concept that starting at the core (i.e., a pixel in a rainfall grid) the average rainfall depth gradually decreases as the area of coverage is expanded.

Meteorological variables were kept the same as in the original MGB-SA. These are derived from the CRU Global Climate v.2 (NEW et al., 2002), a dataset that provides long term monthly means (period of 1961-1990) of relative humidity, wind speed, sunlight hours and surface air temperature for all land areas at 10’ resolution.

9.3.2 Streamflow data

Daily streamflow records were acquired from ANA and INA, as well as from the Brazilian National Electricity System Operator (ONS) that provides reservoir naturalized flows without the regulation effect of dams. Data refer to gauges with more than 10,000 km² of upstream area that were previously collected by Siqueira et al. (2018), spanning the 1980-2010 period. Only gauges with more than 20 years of available data (297 gauges from ANA, 23 gauges from INA and 94 from ONS) were used to compute the return periods in Section 9.4.2. In addition, a longer period was

analyzed for particular gauges of interest, and the corresponding period was presented in parenthesis for each station.

9.4 Results and discussion

9.4.1 Spatial-temporal dynamics of precipitation in 1983

Precipitation in the 1983 year was evaluated with the daily MSWEP+Xavier database. In order to investigate the spatial-temporal evolution of the precipitation extreme events in 1983, Figure 9.1 and Figure 9.2 present precipitation maps of the largest observed events considering the mean rainfall (at the whole continent) in each month of the year (January-August, since after August no major event was registered) for durations of 3 and 7 days. As an example, the presented July event was responsible for the largest recorded discharges in the Uruguay river (see next section).

By looking at in situ gauges (not shown here for brevity), throughout the year, 41.9% (7%) of the 1821 analyzed stations had a maximum daily precipitation > 100 (150) mm. In turn, 20% of the gauges had 3-days precipitation >200 mm, and 2% had 7-days precipitation >500 mm. Maximum observed values at gauges with duration of 3 days, for months from January to August, were: 241.9 mm (Jan), 271.8 mm (Feb), 175.6 mm (Mar), 205 mm (Apr), 249.8 mm (May), 218.1 mm (Jun), 390.2 mm (Jul), 164 mm (Aug). For duration of 7 days, these values were: 297 mm (Jan), 388.3 mm (Feb), 364.7 mm (Mar), 352.8 mm (Apr), 503.4 mm (May), 425 mm (Jun), 618.8 mm (Jul), 204.1 mm (Aug). The largest volumes were observed in July for both durations, and February was the month with the second or third largest value. For comparison, long term annual precipitation ranges from 900 mm in the northeast of the northern region (see next pararagraph) to 2200 mm in some high altitudes along the studied area.

To further understand how extreme the 1983 events were, the largest 15 events in the 1980-2015 period for each accumulated area are plotted in Figure 9.3 (DAD curves) for the two regions displayed in Figure 9.4. These regions were observed to have different climatological patterns, with the northern one having higher precipitation rates in the beginning of the year, and the southern one a more even precipitation throughout the year (FLEISCHMANN et al., 2019a; PASCALE et al., 2015). Results are presented for durations of 3 and 7 days, and the 1983 and non-1983 rainfall events are differed to address how extreme was the 1983 year. The 1983 northern events were observed to be among the largest 15 events only for the duration of three days and for small areas, i.e., in this region the 1983 rainfall events were not the most extreme in the records, although they were indeed very high at specific locations. A duration of 14 days was also analyzed and did not present 1983 events. As will be discussed in section 9.4.4, there may have occurred in this year a combination of high rainfall rates associated with a high antecedent water storage to generate the large observed floods. On the other

hand, events in the southern region were the most extreme for the period 1980-2015, and their importance increased for larger durations (7 days or larger, not shown here for brevity). Although there were some events larger than the 1983 ones, this year was also particular due to the large number of extreme events registered.

This analysis highlights the extreme precipitation events that occurred along the 1982-1983 El Niño period, which led to major floods at many South American rivers in 1983. The next sections address the observed and simulated effects on river discharges.

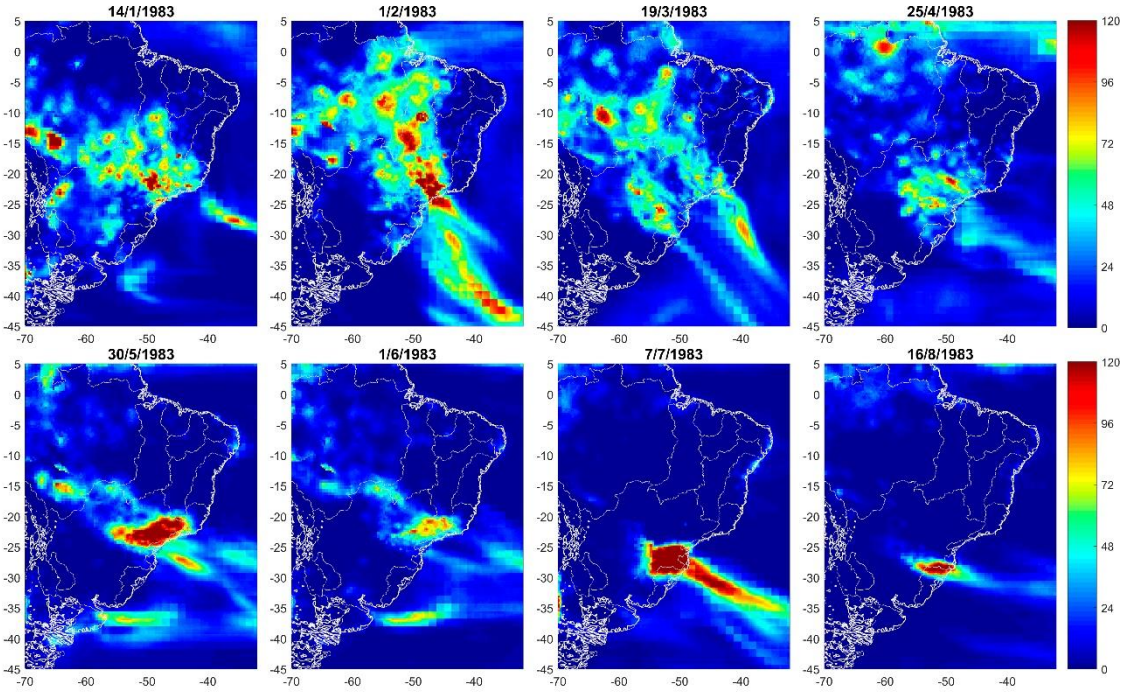

Figure 9.1. Precipitation maps of the largest event at each month of 1983 (January-August) with duration of 3 days. Titles refer to the date on which the 3-days event was centered. Grey polygons are the major river basins in South America.

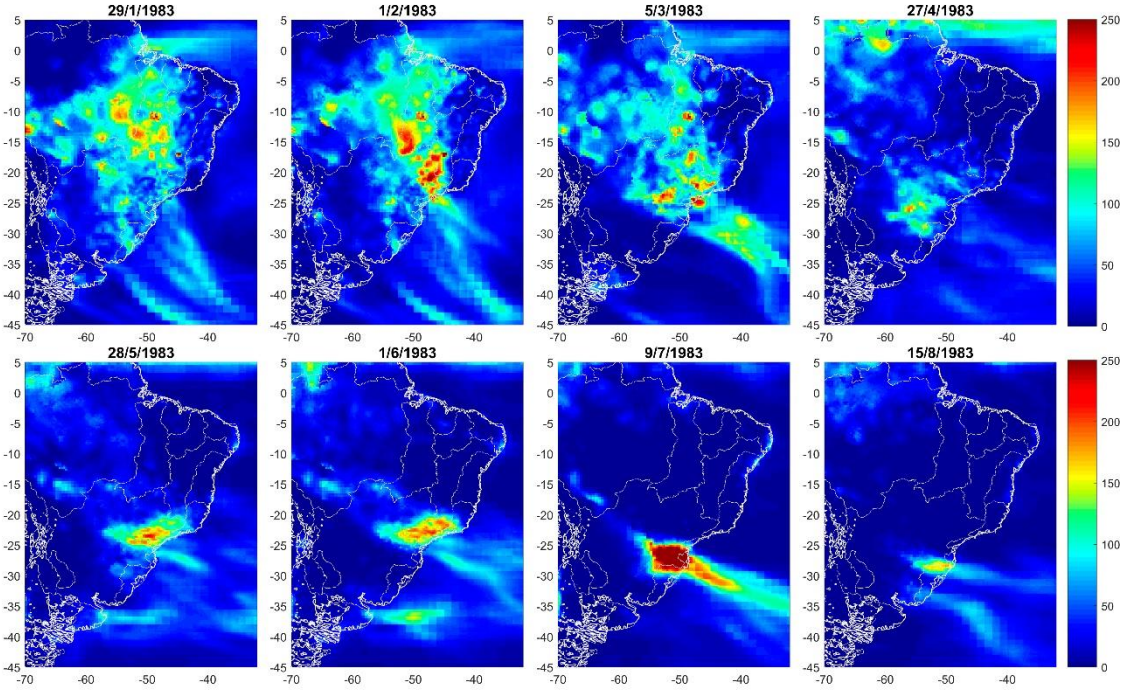

Figure 9.2. Precipitation maps of the largest event at each month of 1983 (January-August) with duration of 7 days. Titles refer to the date on which the 7-days event was centered. Grey polygons are the major river basins in South America.

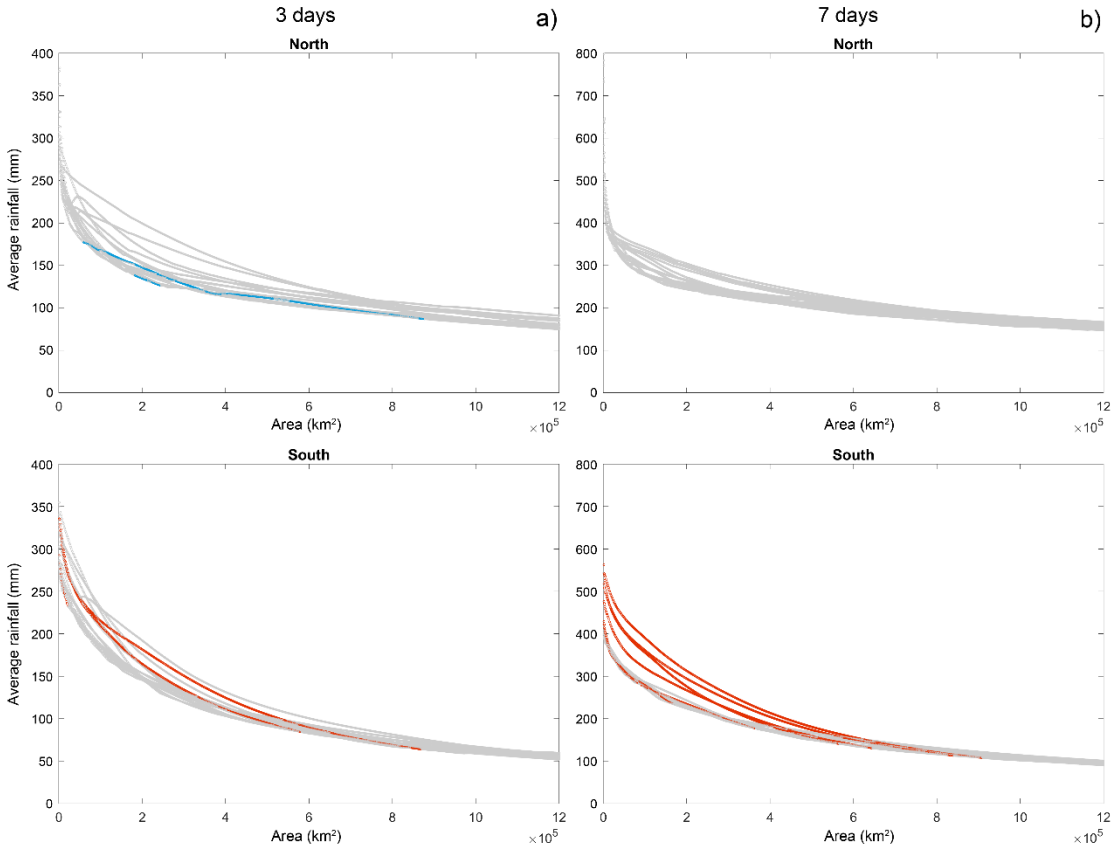

Figure 9.3. Depth-Area- Duration (DAD) curves of the 15 largest events for each accumulated area with duration of 3 (a) and 7 (b) days. Grey lines are the events for non-1983 years during the period 1980-2015, and blue (red) lines those related to the 1983 events in the Northern (Southern) region.

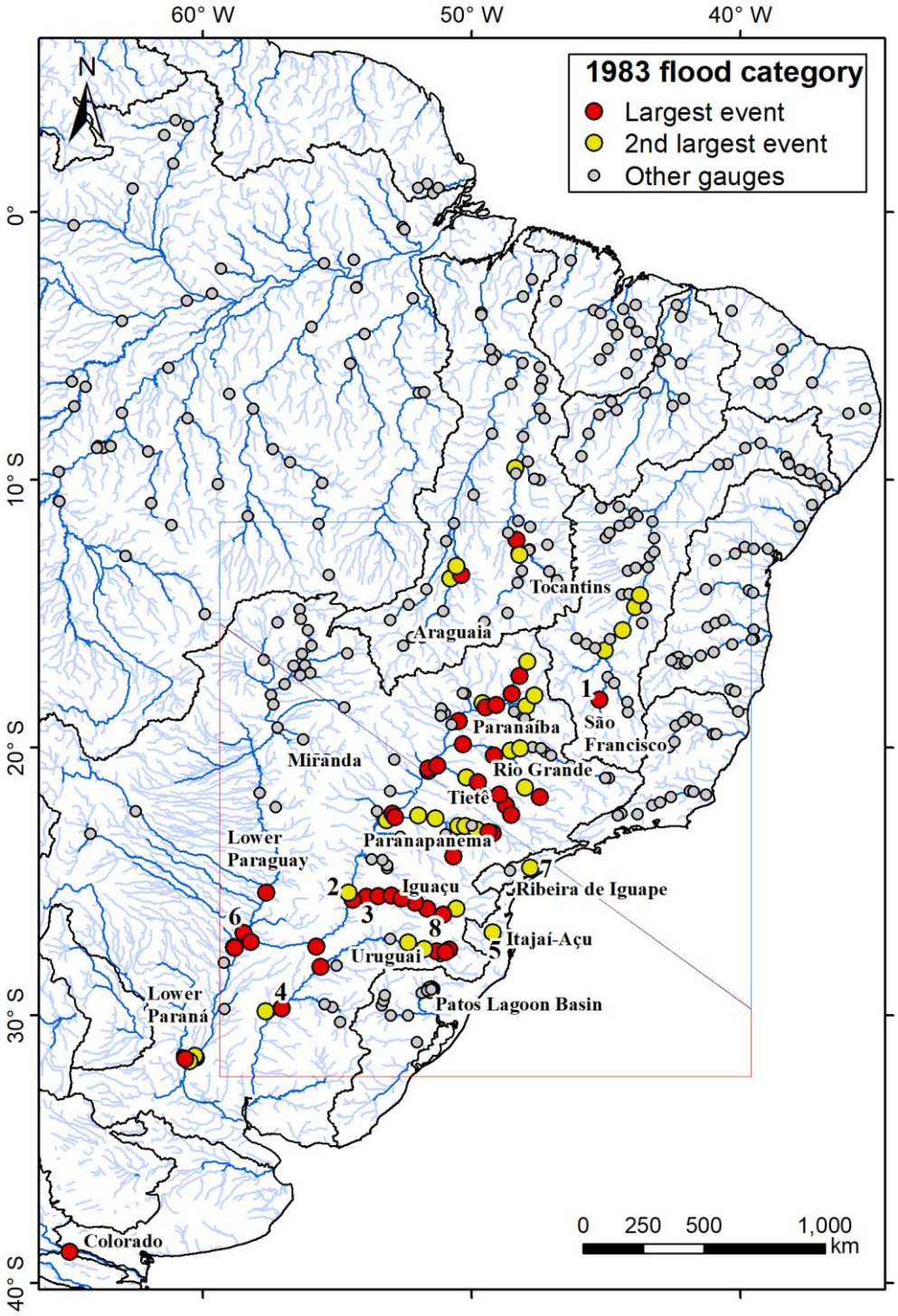

Figure 9.4. Streamflow gauges where the 1983 flood was the largest (red dots) or the second largest (yellow dots) recorded event in the 1980-2010 period. Only gauges with more than 20 complete years of observations (including 1983) were considered in the analysis. Black polygons are the major river basins in South America, and the blue (red) polygons refer to the Northern (Southern) regions used to estimate the DAD curves. Text labels refer to main rivers discussed in the text, and numbered labels to the following gauges: (1) Três Marias in São Francisco River; (2) Itaipu in Paraná River; (3) Salto Caxias in Iguaçu River; (4) Uruguaiana in Uruguay river; (5) Indaial in Itajaí-

Açu River; (6) Puerto Bermejo in Paraguay River; and (7) Registro in Ribeira de Iguape River.

9.4.2 River discharges at specific sites

Across the continent, the 1983 flood was the largest recorded in many gauges in the analyzed period 1980-2010 (Figure 9.4). This was observed in most of the gauges in Paraná, Lower Paraguay and Uruguay rivers, and in a few gauges in the Araguaia, Tocantins and São Francisco basins.

A satisfactory model performance was obtained for the magnitude of the 1983 events, as depicted by observed and simulated hydrographs at six different locations across the continent (Figure 9.5) and a comparison between peak flows for the gauges where an extreme flood occurred in 1983 (defined as gauges with at least a 2-yr return period for this event) (Figure 9.6). For all analyzed gauges, a mean absolute percentage error (MAPE) value of 34% may be considered satisfactory, compared for example to errors in rating curve extrapolation for high flows, which may be as high as 40% (DI BALDASSARRE; MONTANARI, 2009; LANG et al., 2010). It is usually difficult for continental/global hydrological models to have good accuracy on daily simulated discharges due to the coarse resolution of input data, limitations in depicted processes and simplified calibration (Siqueira *et al.*, 2018). An erroneous flow attenuation was simulated in the São Francisco River at Três Marias dam (Figure 9.5), because the reservoir lake existent in the Bare Earth DEM (O'LOUGHLIN et al., 2016b) adopted in the continental model acted as an artificial floodplain (i.e., a very flat area) and led to overestimated attenuation. In addition, the Paraguay river (Figure 9.5 at the bottom) is one of the most challenging rivers to simulate in South America since it is highly affected by both horizontal and vertical water fluxes in the Pantanal Wetland (DA PAZ et al., 2014).

In the next paragraphs we provide here a short description of the records in some sites of interest (see Figure 9.4 for the location of all sites mentioned in the next paragraphs). União da Vitória in the Iguaçu River faced its largest recorded maximum flow (observed peak discharge: 5,072 m^3/s at 18/Jul/1983; drainage area: 24,200 km^2; available period: 1930-2014) (STEFFEN; GOMES, 2018). In the time series of Ribeira de Iguape river at Registro the second largest peak discharge and the largest flood volume were recorded (observed peak discharge: 2,473 m^3/s at 14/Jun/1983; drainage area: 20,900 km^2; available period: 1953-2017) – the largest peak occurred in the 1997 El Niño year, as in the Paraná river at Itaipu dam. Naturalized flow at the dam indicated that the peak (naturalized flow: 40,057 m^3/s at 14/Jun/1983; drainage area: 820,000 km^2; available period: 1931-2010) was the second largest in the records (the highest peak was in 1997; see Figure 9.5), but the event was associated to the largest recorded volume, considering the year total runoff (i.e., a hydrological year starting at September). Interestingly, the 1983 flood had two main bulks (the first with peaks in 18-Feb-1983

and 08-Mar-1983 and the second one in 14-Jun-1983). The first one was related to the Upper Paraná, and the second to lateral inflows between Porto Primavera dam and Itaipu (i.e., Paranapanema, Ivaí and Piquiri rivers). The largest recorded events were registered in the Paraná river at Corrientes (peaks of 60,215 m³/s at 18/Jul/1983, for which an important contribution came from Medium Paraná tributaries as the Iguaçu river (CAMILLONI; BARROS, 2000), and 60,092 m³/s at 23/Jun/1983; drainage area: 2,140,000 km²; available period: 1904-2018) and Uruguay river at Uruguaiana (observed peak discharge: 32,076 m³/s at 19/Jul/1983; drainage area: 190,000 km²; available period: 1942-2019). In the Paraguay river at Asunción, the 1983 flood was reported as the second largest in the 1904-1998 series (1905 flood was the largest) (BARROS et al., 2004), and at Puerto Bermejo the peak was 10,574 m³/s at 02/Jun/1983.

In central Brazil, the floods reached the upper parts of Araguaia, Tocantins and São Francisco basins. 1983 was the second to third largest recorded flood in the period 1980-2010 in many gauges in the Upper Araguaia. In the São Francisco river, the largest recorded flood event occurred in 1979 for the medium and lower parts reaches, but in its Upper sub-basins (e.g., upstream from Três Marias reservoir), 1983 was the largest recorded.

In the Itajaí-Açu River, although the 1983 flood was the most impactful flood in the XX century in the basin, the 1984 one was the largest recorded according to discharge in Indaial gauge (Figure 9.5), and the same was observed in water levels at Blumenau (FRANK, 2003). This may have occurred because the peak discharge (or maximum water level) is not the only relevant variable for determining flood damages. The 1983 event at Indaial (observed peak discharge: 4,772 m³/s at 09/Jul/1983; drainage area: 9,850 km²; available period: 1929-2014) had a larger duration (discharges remained 15 (7) days above 1,000 m³/s during the 1983 (1984) event) and volume. Furthermore, the population may have become more resilient to extreme events after the great 1983 flood.

In the Patos Lagoon Basin, although the 1983 flood was intense, the extreme 1941 flood (also an El Niño year) was far larger, with the largest recorded water level in the Guaíba Lake at Porto Alegre city, for example (GUIMARÃES, 2009; ISLA; TOLDO JUNIOR, 2013). Moving southward, the Colorado river at Pichi Mahuída located in the northern limit of Argentinian Patagonia experienced the largest peak discharge registered in the 1980-2010 period (776 m³/s at 08/Jan/1983). At that time, the 1983 flood reactivated the connection between the Colorado and Desaguadero-Curacó river systems (left tributary that drains most of the arid central Andes from 30ºS to 37ºS), as the streamflow of Desaguadero river has been progressively reduced over time due to anthropogenic impacts (ISLA; TOLDO JUNIOR, 2013).

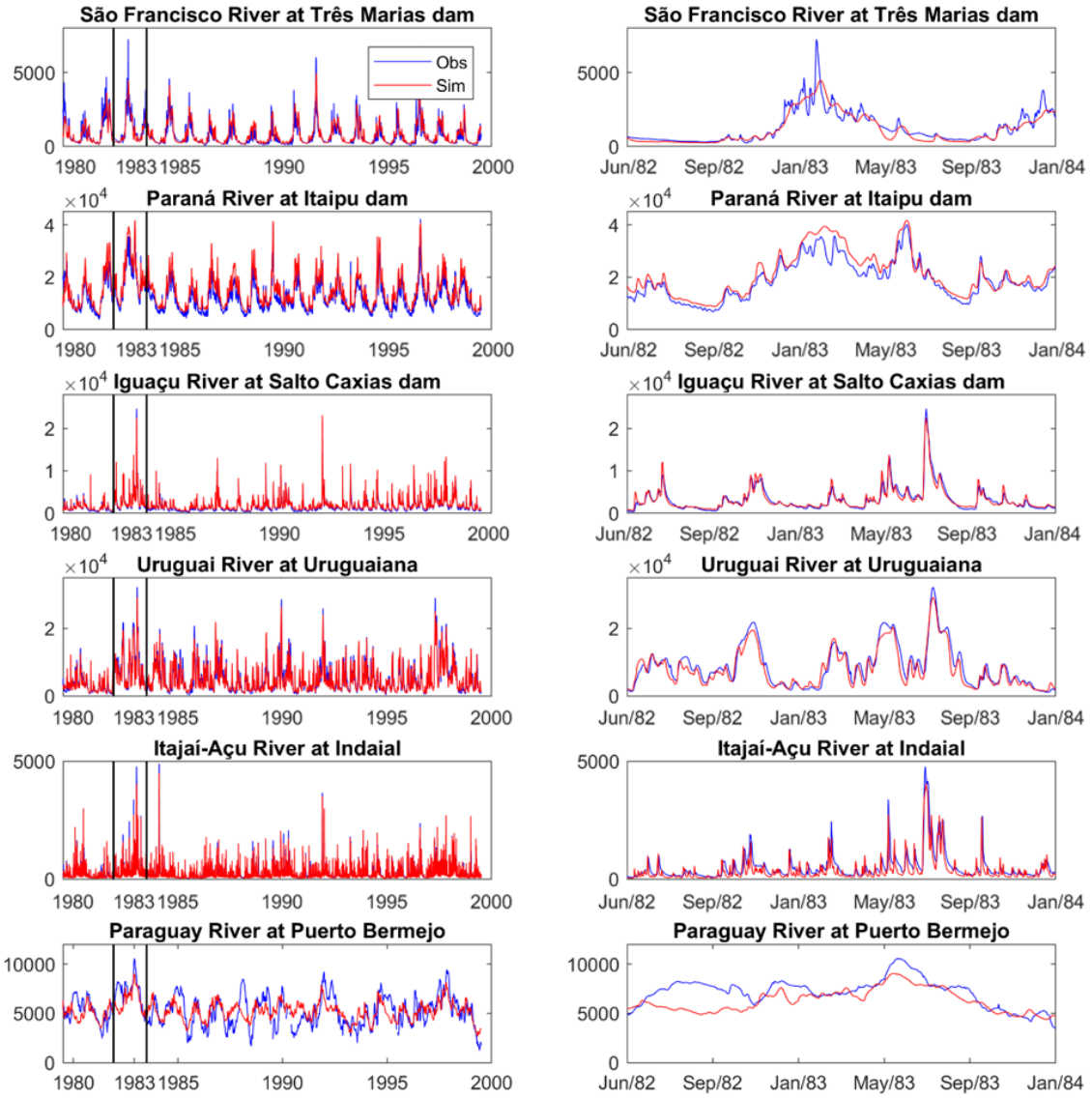

Figure 9.5. Simulated and observed hydrographs at six locations across South American rivers for the period 1980-2000 (left columns; the 1983 year is highlighted with a black box) and the 1983 year (right column). Drainage areas: 50,600 km² (Três Marias dam); 820,000 km² (Itaipu dam); 58,000 km² (Salto Caxias dam); 190,000 km² (Uruguaiana); 9,850 km² (Indaial); and 1,135,000 km² (Puerto Bermejo). For the dams, naturalized flows are plotted as observations.

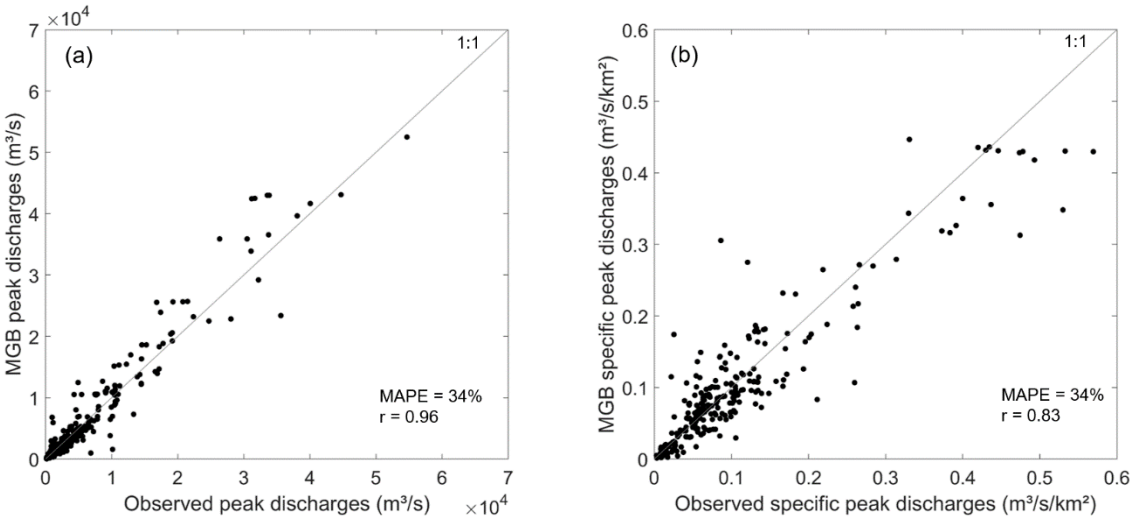

Figure 9.6. Comparison between observed and simulated peak discharges, considering (a) absolute and (b) specific values (i.e., peak discharge divided by upstream drainage area). Results are plotted for gauges with more than 2 years return period for the 1983 event. MAPE: mean absolute percentage error.

9.4.3 Spatial-temporal dynamics of river discharges in 1983

The continental hydrological model allows a regional view of the spatial-temporal dynamics of the 1983 floods in terms of maximum estimated return period (Gumbel distribution applied to the 1980-2015 period) and month of peak flow for each river reach (Figure 9.7). The floods can be further understood by looking at the monthly variation of peak discharges or return periods (Figure 9.8; an animated GIF file with the time evolution of return periods is provided as Supplementary Material).

There is a general agreement between return period values from simulation and observations. The largest return periods (>60 years) were estimated in specific areas, as the Upper São Francisco close to the Três Marias dam, and the upper portions of Tietê, Paranapanema, Iguaçu and Uruguay rivers. In turn, overestimation of return periods occurred in the Upper Araguaia, with values generally higher than in observations, although high annual discharges were observed in this region (Figure 9.4). Although the largest return period values should be considered with caution given the relatively short period of analysis and the consideration of stationary series, assessing model based return periods is interesting since its computation is related to the model climatology. From the 276 gauges with return period > 2 years, 24 (9%) had values > 60 years with a maximum value of 209 years. In turn, from the 5,242 15-km river reaches of MGB-SA that had return period > 2 years, 117 reaches (2%) had values > 60 years with a maximum value of 540 years, and 15 reaches had values > 150 years.

The particular time evolution of the extreme 1983 year led to three main flooding periods (Figure 9.7 and Figure 9.8). In February, major floods occurred in central Brazil (Upper Araguaia, Tocantins and São Francisco basins), in the Upper Paraná basin (Paranaíba, Rio Grande and Tietê rivers), and also in the Miranda and Negro rivers in the Upper Paraguay Basin (latitudes roughly between 23°S and 15°N). By June, the Paranapanema, parts of the Tietê basin and the Paraná at Itaipu dam had their largest peak discharges Bain (latitudes between 25°S and 22°S). By July, another event led to major floods in the Iguaçu, Itajaí-Açu and Uruguay basins (latitudes between 30°S and 25°S).

A particular hydrological behavior is observed in the Paraguay River, with a slow annual flood dynamics due to extensive floodplains and the Pantanal wetlands. Most of the precipitation fell in the Lower Paraguay river, but some isolated events occurred in the Miranda river in the upper basin. The annual flood along the river is a very slow one, so that return periods remained high during many months across this basin (see Figure 9.8 and the hydrograph at Puerto Bermejo in Figure 9.5).

Regarding reservoirs at the regional scale, besides Três Marias and Itaipu dams (Figure 9.5), other reservoirs along the basin faced the large 1983 floods, and the year was defined as an important extreme discharge reference for hydraulic design in Brazil. For instance, the operation of Foz do Areia reservoir was adjusted since then to ensure flood protection at União da Vitória city, located upstream from the dam (TUCCI; BERTONI, 2003). At that period, many large dams in Brazil were in their final building stages or starting operation: Itaipu (inauguration year: 1982) and Ilha Solteira (1978) in the Paraná river, Foz do Areia in the Iguaçu river (1980), São Simão (1978), Emborcação (1982) and Itumbiara (1981) in the Paranaíba River, Água Vermelha (1978) in the Rio Grande river, and Sobradinho (1982) in the São Francisco River. Then, the 1983 flood raised from one side a public debate about the role of dams on altering floods, and on the other side the attention of energy agencies and companies on the possibility of occurrence of other similar extreme events. In Itaipu, spillway discharges reached 40,000 m³/s (roughly 2/3 of the spillway capacity) and the event volume was 88% of the probable maximum flood (PMF), fostering new studies of the dam PMF (SZPILMAN et al., 1992).

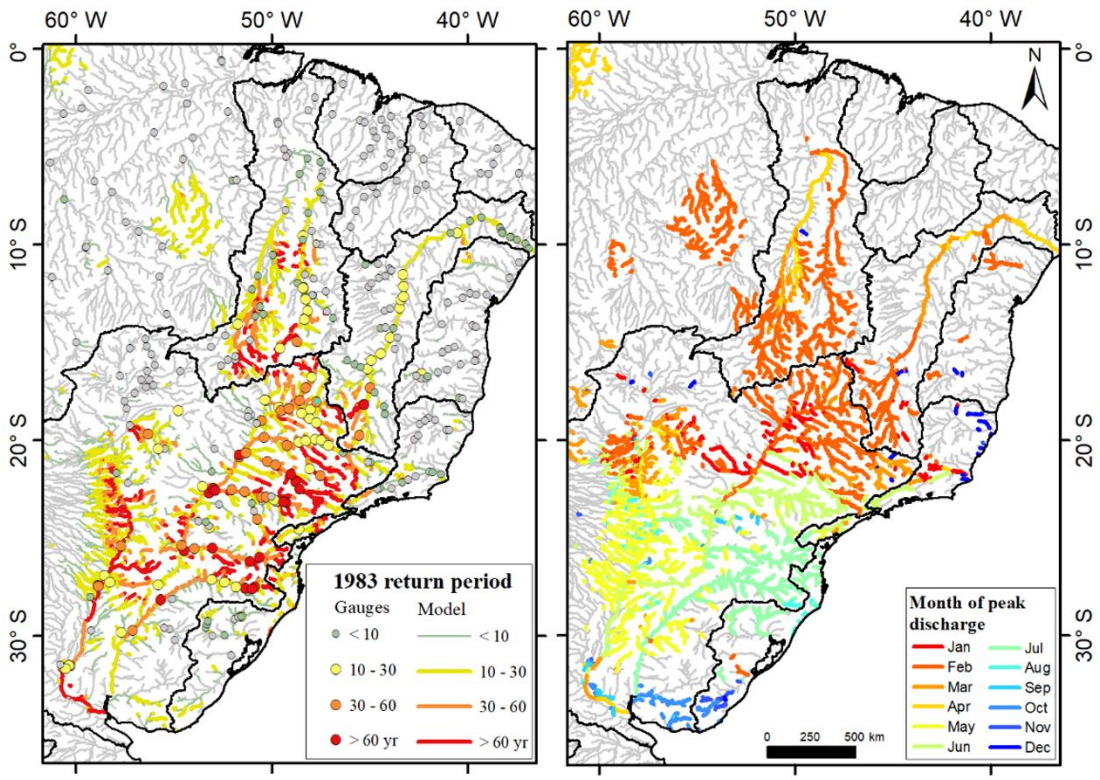

Figure 9.7. Spatial and temporal distribution of the 1983 floods in terms of (a) return period of the peak discharges estimated from in situ gauges (minimum of 20 years of data in the period 1980-2015) and MGB-SA simulation (period 1980-2015) and (b) month when the peak discharge occurred, based on the MGB-SA simulation.

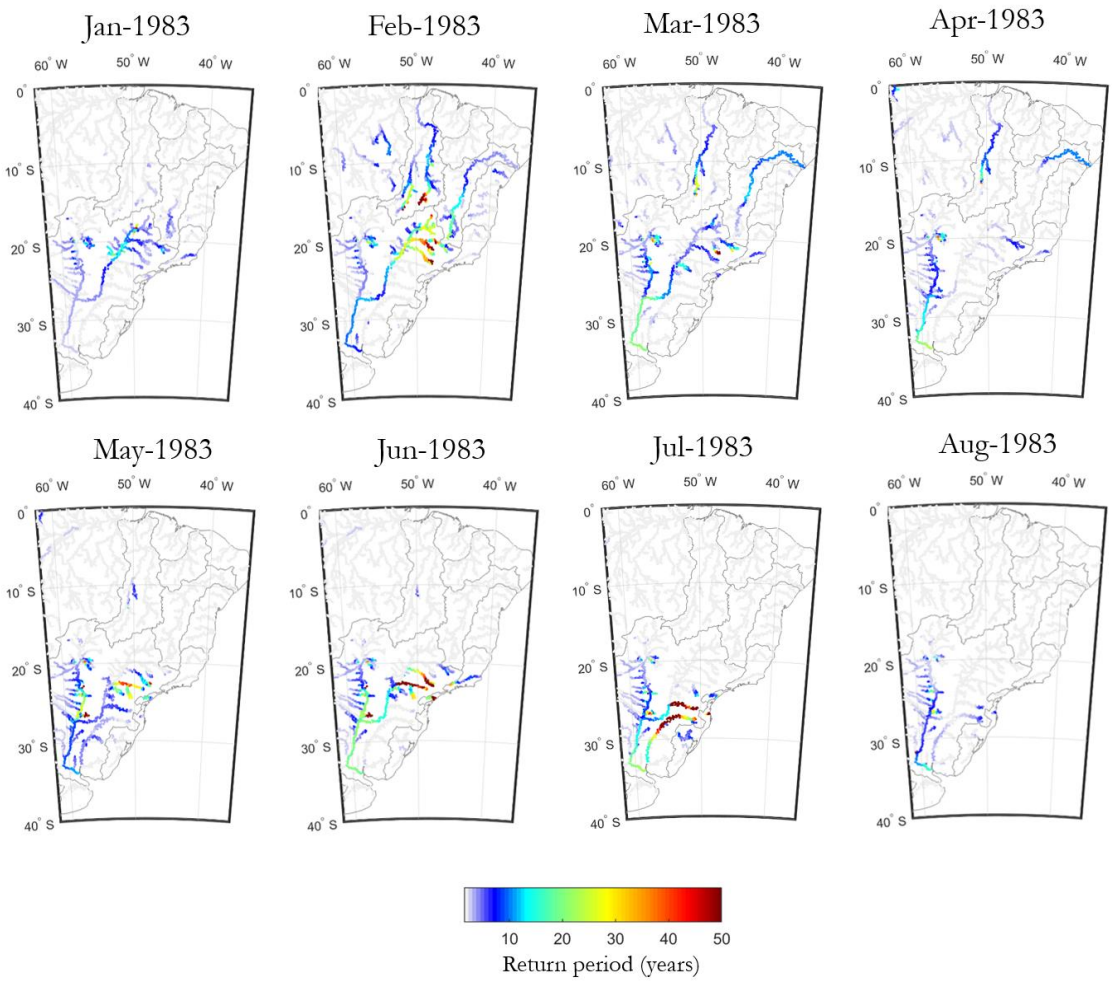

Figure 9.8. MGB-SA estimates of the return period of peak discharges (in years) for each month of 1983 (January to August).

9.4.4 Water storage in the continent and water export to the oceans

In order to further evaluate the magnitude of the 1983 events, we computed the MGB-SA based total terrestrial water storage in the continent for the regions North and South (Figure 9.9; see Figure 9.4 for location of the regions), and the total annual export of water volume for different sets of rivers across the continent (Figure 9.10). The capacity of the model in representing total water storage was assessed by Siqueira et al. (2018). Results indicate that the 1982-1983 El Niño period led to wet conditions at the two analyzed regions, while the South America as a whole did not show it. This occurred because the storage in the Amazon basin is responsible for a large portion of the continental storage, and this region faced a drought during these years (MARENGO; ESPINOZA, 2016). The analysis further shows that at the beginning of 1983 the affected region (especially the Southern region) was already wet, so that the extreme 1983 precipitation rates led to even larger floods. However, the role of the antecedent water storage on increasing the 1983 floods should be more carefully analyzed in future

studies, considering long term TWS (e.g., Humphrey & Gudmundsson, (2019)) and soil moisture data from multiple sources, what is beyond the scope of this study. The maximum storage in the South region occurred later than the Northern region, in accordance with the period of peak flows (Figure 9.7).

When summing the outflow of all rivers draining to South Atlantic located between São Francisco and La Plata river outlets (including these two rivers), and evaluating its standardized anomaly, 1983 is highlighted as the most extreme year in the continent from 1980-2015 with a value of 3.7 (Figure 9.10). The second largest export occurred in the 1998 (anomaly of 1.9), followed by 1992, all three being El Niño years. In turn, when looking at the whole South America, a different situation is found, since the large volumes in the Amazon Basin are preponderant in the total export to oceans from South American rivers (here we also include rivers that drain to the Pacific). In this case, the year with largest water export in South America would be 2011 (1.5), and the driest 1992 (-2.5). The increasing trend of water export in the Amazon basin is in accordance to recent literature (BARTIKO et al., 2019; GLOOR et al., 2013). The smallest exports from the Amazon in the 1980-2015 period were estimated to occur in 1992, followed by 1983 and 1998, all of them strong El Niño years. This is in agreement with observed discharges at Óbidos in the Lower Amazon. The great drought of 1926 in the Amazon was also an El Niño year, while La Niña years are typically associated to years with floods in the basin – although not all Amazon droughts are related to these phenomena (MARENGO; ESPINOZA, 2016). Interestingly, the 1992 year is usually not recognized as an extreme drought year in the Amazon (with the exception of sites as the Upper Negro River). Indeed, the minimum discharges were not the lowest in the record (as observed at Manacaparu or Óbidos gauges along the Solimões and Amazon rivers, respectively), but a dry wet season led to a very dry year in terms of volume. This was also noticed in terms of rainfall amount in the western part of the Amazon (ESPINOZA et al., 2011). This analysis of water export may be useful to understand interannual changes on ocean circulation patterns and the dynamics of nutrient export (BOUWMAN et al., 2005; COLES et al., 2013; MASSON; DELECLUSE, 2001; PIOLA et al., 2005).

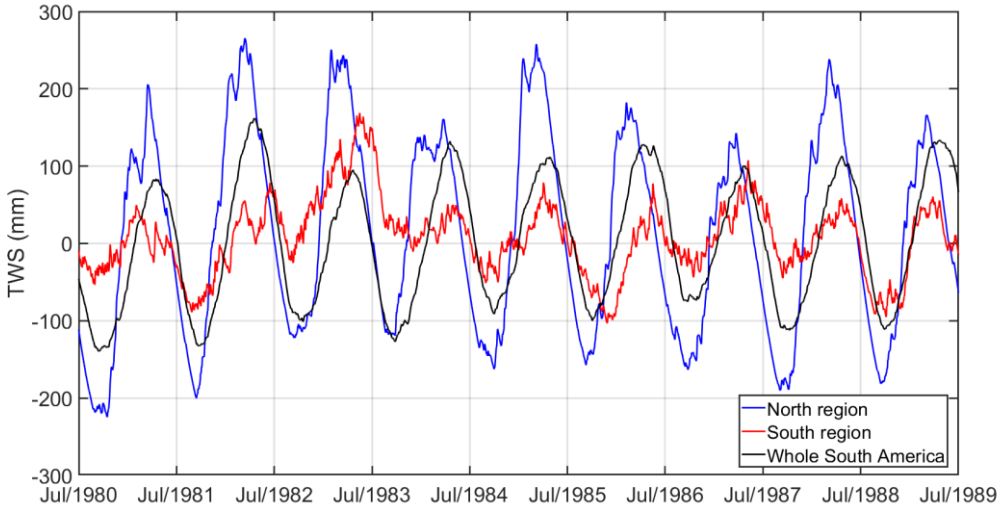

Figure 9.9. Daily anomalies of the total terrestrial water storage during the period 1980-1990 in the whole South America (black), and in the Northern (blue) and Southern (red) regions depicted in Figure 9.4, which were the most affected by the 1983 floods.

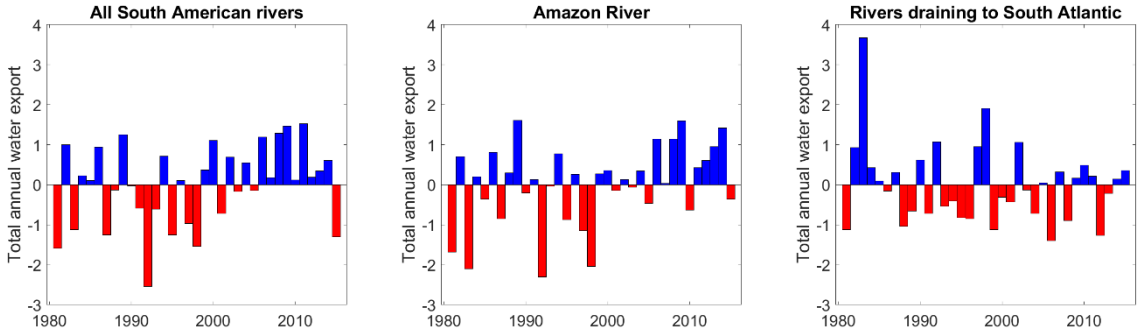

Figure 9.10. Anomaly of the total annual simulated water export (i.e., annual outflow volume) to the oceans from (a) all South American rivers, (b) the Amazon river, and (c) rivers draining to South Atlantic (i.e., rivers between São Francisco and La Plata river outlets, including them).

9.5 Discussions and limitations

There is an urge to understand floods from a regional perspective. This is in accordance with the continental hydrology agenda, which aims to provide locally relevant and distributed estimates of hydrological and hydrodynamic variables with hyperresolution models (BIERKENS et al., 2015; FLEISCHMANN; PAIVA; COLLISCHONN, 2019; LIN et al., 2019; WARD et al., 2015; WOOD et al., 2011). Coupled hydrological-hydrodynamic models with calibrated rainfall-runoff parameters

(SIQUEIRA et al., 2018) provide a unique opportunity for understanding past floods, with a more accurate estimate of flood wave propagation and thus river discharges and water levels.

Continental scale studies of past floods are very rare in South America, especially in comparison to other regions as Europe and United States. Although the 1983 year was a very extreme one, other years also faced floods at different parts of the continent, and other studies could be carried out to understand their pattern in a similar way to this study. For instance, assessing the major 2014 floods that affected rivers as far as the Madeira in the Amazon (ESPINOZA et al., 2014) and the Iguaçu in the Paraná. Other global hydrological models could also be included in such analyses (e.g., Alfieri *et al.*, (2019), Schellekens *et al.*, (2017)), as the multi-model comparison studies performed by Siqueira et al (2018) and Towner *et al.* (2019). Although in this study we focused on discharges (and particularly on peak discharges), other relevant variables as water levels, flood extent and volume could be evaluated with the continental model, as well as other flood indicators (STEFFEN; GOMES, 2018). Simulated discharges in large scale models are generally more accurate than water levels (FLEISCHMANN; PAIVA; COLLISCHONN, 2019), and they could be used to force local hydrodynamic models at reach scales. The management of natural systems subject to floods may also benefit from regional scale distributed estimates, what could for instance assist country-wide inventories of wetlands (JUNK et al., 2014; KANDUS et al., 2017; RICAURTE et al., 2017; SCOTT; JONES, 2012), or the evaluation of the impact of extreme floods on the dynamics of floodplain ecosystems (JUNK; BAYLEY; SPARKS, 1989).

Different flood patterns emerge by looking at different basins at regional scale, making the linkage to atmospheric processes clearer. The spatial-temporal dynamics of the 1983 floods along the whole year is impressive. The strong El Niño period (1982-1983) led to floods occurring in different months of the year, and maximum observed flows in July 1983 occurred in basins close to others where peaks occurred in February 1983. The extension to which such continent scale events occurred in other extreme years is an interesting future research question. Furthermore, there are major challenges related to the dependence of hydrological events at very broad scales, and to associated engineering tasks as defining the maximum probable precipitation of a large basin. Although integrated basin water management typically focuses at the basin scale, continental scale models as presented here are a powerful tool to evaluate regional scale impacts, for instance, for national water planners.

Even though there are uncertainties in the model estimates, evaluating return periods avoids assessing absolute magnitudes, since it is a relative measure using the model climatology. However, return periods were estimated in this study considering discharge stationarity, and changes in the basin hydrological regime has certainly occurred and preclude a more thorough interpretation of absolute values. For example, the La Plata basin has undergone a large increase in discharges since the 1970's due to a combination of land use alteration and changing precipitation, although the complete causes are still not clear (COLLISCHONN; TUCCI; CLARKE, 2001; DOYLE;

BARROS, 2011; FLEISCHMANN et al., 2019a; GARCÍA; VARGAS, 1998; KREPPER; GARCÍA; JONES, 2008; LEE et al., 2018). Additionally, other time series properties should be assessed when estimating flood frequencies, as the role of oscillation periods (as El Niño) and the time correlation between annual maxima due to flood clustering in time (JAIN; LALL, 2001; MERZ; NGUYEN; VOROGUSHYN, 2016). Under a climate change, more extreme El Niño periods are also expected to occur (CAI et al., 2014; TANG; LI; SUN, 2016).

Uncertainties in hydrological modeling arise from model structure, parameterization, input and validation data. Extreme floods can be used as a stress case to assess the model structure and possible ways of improvement. In the case of the 1983 floods, it was evident that not performing a terrain correction along reservoir lakes may lead to erroneous flood attenuation (e.g., simulation at Três Marias dam, Figure 9.5). It could be further corrected, for example, by adopting a rectangular cross section along the model unit-catchments within the reservoir. The effect of reservoirs on flow regulation was not considered in this model, although for very large events as the 1983 one they are likely to have small effects (CAMILLONI; BARROS, 2000). This is corroborated by the fact that MGB-SA simulates naturalized flows (i.e., no effects of dams or water abstraction), and even then it had a satisfactory performance for both observed (ANA and INA gauges) and naturalized (ONS gauges) peak flows. There were availability of naturalized (unregulated) flow data for the dams, but this was not the case for actual reservoir inflows and outflows. That would allow a thorough assessment of the effect of dams on the event attenuation. An exception of dam regulation during 1983 may have occurred in the São Francisco River, where its most downstream reaches were estimated to face 10-30 years return period values, but observations did not yield high peak discharges. This may be associated to the Sobradinho dam attenuation, which started operating in 1979.

In the case of snow-fed rivers, the Colorado river in Argentina had its largest flood in 1983 in the 1980-2010 period (Figure 9.4), but this flood was not represented by the model and more studies should be carried out to understand the model inaccuracy. MGB-SA currently does not have a snow module.

Finally, MGB-SA was developed for modeling large scale basins in the continent, and its performance for medium to small basins was not yet performed in detail. It was evaluated against gauges with upstream drainage area larger than 10,000 km² only (Siqueira *et al.*, 2018). Then, floods in smaller scales were not considered in this study, as the events occurred in 1983 in Northern Peru and Ecuador.

Regarding observation uncertainties, it must be noticed the high precipitation errors that may occur. During extreme events, rainfall measurement is very difficult, and a heterogeneous pattern in mountainous areas may hamper even more its estimation. The evaluated observed discharges are subject to important errors due to rating curve extrapolation, since discharges are rarely measured during extreme events. This error may be as high as 40% (DI BALDASSARRE; LAIO; MONTANARI, 2012;

DOMENEGHETTI; CASTELLARIN; BRATH, 2012). To take into consideration uncertainties in both modeling and observations, data assimilation techniques now provide a great opportunity to improve the comprehension of past floods, and are recommended here for future studies (e.g., Wongchuig *et al.*, 2019).

9.6 Conclusion

This study presented a regional scale evaluation of the 1983 floods that occurred in large South American rivers. This year was associated to a strong El Niño event, and was particular in the sense that many extreme floods occurred in different months and across a vast region of the continent. The study was carried out by using gridded and in situ precipitation data, in situ discharges, and a continental hydrological-hydrodynamic model. Simulated maximum daily discharges were validated with the in situ data. The model outputs were then used to estimate peak discharges, return periods and month of maximum discharges across the continent in a distributed way, providing a continental hydrological reanalysis.

Although high precipitation rates occurred all along the year, three main periods were observed, in February, June and July, which affected large river systems as the Paraguay, Paraná, Uruguay, Araguaia, São Francisco, Itajaí-Açu, Ribeira de Iguape and Tocantins (the relatively smaller river basins in Peru and Ecuador were not considered in the analysis). In many gauges, the largest recorded flood occurred in this year. An analysis of the simulated total terrestrial water storage showed that by the beginning of 1983 an overall wet condition was already existent in the affected region, increasing the extension of the floods. The role of the antecedent water storage on the increasing of floods should be further addressed in future studies.

The total water export from the continental rivers to the oceans was then assessed with the model, and showed that the largest export in the analyzed period (1980-2015) was estimated to occur in 1983 when analyzing the rivers draining to the South Atlantic Ocean (defined as the rivers between São Francisco and La Plata river outlets), with a standardized anomaly of 3.7. Interestingly, the other two largest exports were in 1998 and 1992, which were also El Niño years. On the other hand, when looking at the whole South America, given the role of the Amazon river in the continental water export, and which faced a drought in this year, the export in 1983 was actually a below-average one.

Finally, we stress the potentiality of such continental models to foster our understanding of floods at regional and national scales, what could be further improved through data assimilation methods to take into consideration uncertainties in modeling and observations.

10 Can regional to continental river hydrodynamic models be locally relevant?

This chapter is presented as a research article, which was published in Journal of Hydrology X:

- Fleischmann, A., Paiva, R., Collischonn, W, 2019. Can regional to continental river hydrodynamic models be locally relevant? A cross-scale comparison. Journal of Hydrology X 3, 100027.

10. Quão localmente relevantes podem ser modelos hidrodinâmicos de rios em escala regional a continental?

Modelos hidrodinâmicos de rios em escala regional a global são uma realidade, e têm sido amplamente desenvolvidos nos anos recentes graças ao aumento em capacidade computacional, dados de sensoriamento remoto e novas metodologias de modelagem. É fundamental compreender o quanto estes modelos conseguem gerar estimativas localmente relevantes de variáveis como áreas inundadas e vazão e nível d'água dos rios. Este tópico é abordado aqui através da simulação, em três diferentes escalas espaciais (global, regional e local), do modelo hidrológico-hidrodinâmico de grande escala MGB, baseadas em diferentes dados de topografia, parametrização de seções transversais e comprimentos de trechos. Estas versões do modelo são comparadas a uma aplicação detalhada do modelo HEC-RAS, preparado com mais de 620 seções levantadas in-situ na bacia do rio Itajaí-Açu no Brasil. Todos os modelos são forçados com os mesmos parâmetros do módulo chuva-vazão, de modo que os efeitos das incertezas dos dados de vazão que forçam os modelos não foram consideradas. Para facilitar a interpretação, três principais requerimentos para definir se a estimativa de um modelo hidrodinâmico é localmente relevante foram propostos: os erros do modelo deveriam ser iguais ou menores que (i) o requerimento de acurácia para uma determinada aplicação e localidade, que (ii) erros típicos de modelos de escala local, e que (iii) a incerteza das observações. Os resultados indicaram que as versões regional e local do MGB (e, em menor grau, a versão global) poderiam estimar vazões e anomalias de níveis localmente relevantes para várias partes da bacia. Para valores de nível absolutos, todas versões falharam em gerar RMSE menor que 0.4 m ao longo da bacia, embora a versão local do MGB gerou um RMSE médio de 2.1 m, em comparação aos valores de 4.4 m (regional) e 26.1 m (global). Para extensão de áreas inundáveis, todas versões geraram estimativas insatisfatórias com o valor médio da métrica F inferior a 65%. Por fim, diferente versões do modelo MGB regional foram rodadas para investigar o papel de diferentes fatores na melhoria das estimativas do modelo. De modo geral, um trecho de rio mais grosseiro (15 km) é incapaz de capturar a dinâmica de inundação e variações de níveis d'água ao longo da bacia, enquanto trechos menores (1 km) melhoram as estimativas de vazões, nível d'água e extensão de áreas inundadas. Um modelo digital de elevação (MDE) gerado localmente não proporcionou melhorias significativas se comparadas ao MDE global. Por sua vez, os menores erros de nível d'água seriam obtidos com o uso de informações in-situ de seções transversais em modelos regionais. Os resultados deste estudo são encorajadores para o futuro do desenvolvimento de modelos hidrodinâmicos regionais a globais, considerando as novas técnicas e desenvolvimentos de sensoriamento remot, e o aumento gradual de nossa capacidade computacional, capazes de melhorar as estimativas de seções transversais e discretização dos modelos.

Este capítulo é apresentado na forma de um artigo científico, publicado no periódico Journal of Hydrology X:

- *Fleischmann, A., Paiva, R., Collischonn, W, 2019. Can regional to continental river hydrodynamic models be locally relevant? A cross-scale comparison. Journal of Hydrology X 3, 100027.*

Abstract

Regional to global river hydrodynamic models are now a reality, and have largely improved in the recent years due to increasing computation power, remote sensing datasets and new modeling methods. It is fundamental then to understand to which extent these models can provide locally relevant estimates of variables as discharge and water levels. It is addressed here by setting up three different versions of the large scale MGB hydrologic-hydrodynamic model with increasing spatial scale (global, regional and local), based on different topography datasets, cross section parameterization and reach lengths. These model versions are then compared to a detailed HEC-RAS model, set up with more than 620 locally surveyed cross sections in the Itajaí-Açu basin in Brazil. All models are run with calibrated rainfall-runoff parameters, so that effects of non-calibrated runoff fields or uncertain forcing data are not taken into consideration. To assist interpretation, three main requirements to define estimates from a river hydrodynamic model as locally relevant are defined: the model errors should be equal or smaller (i) than the accuracy requirement for a particular application and location, (ii) than typical local, reach scale models' errors, and (iii) than observation uncertainties. Results then indicate that the regional and local MGB versions (and to a lesser extent, the global one) could estimate locally relevant discharges and water level anomalies for many parts of the basin. For absolute water levels, all models failed to provide RMSE smaller than 0.4 m basin-wide, although the local MGB model yields an average 2.1 m RMSE, in comparison to 4.4 m (regional) and 26.1 m (global). For flood extent, all model versions generally yielded unsatisfactory results with average Fit metric values smaller than 65%. Lastly, different setups of the regional MGB model were run to investigate the role of different factors in improving model estimates. Results showed that a coarse reach length (15 km) is unable to capture flood dynamics and water level variations in the basin, while a smaller 1 km long reach improves discharges, water level and flood extent. A locally derived DEM did not lead to significant improvements in relation to a global DEM. In turn, the smallest water level errors would be attained by using information from the in situ cross sections in the regional models. This study's outcomes are encouraging for the future development of regional to global hydrodynamic models, with new remote sensing techniques and higher computational power improving cross section estimation and model discretization.

10.1 Introduction

Large scale river hydrodynamic models are powerful tools for water resources studies related, for example, to flood risk assessment and flood forecasting, and have been recognized as fundamental to yield satisfactory discharge, water level and flood extent model estimates (Dottori et al., 2016; Hirabayashi et al., 2013; Paiva et al., 2013; Sampson et al., 2015; Schumann et al., 2013; Trigg et al., 2016; Yamazaki et al., 2011; Zhao et al., 2017). Improvements in computational power, remote sensing datasets and

modeling frameworks have allowed the development of several regional hydrodynamic models in the last years moving toward hyperresolution spatial resolution, i.e. 100 m-1 km (BATES et al., 2018a; BIERKENS et al., 2015; HODGES, 2013; WOOD et al., 2011). Today, application scales range from thousands to millions of square kilometers (Fleischmann et al., 2018; Lai et al., 2013; Miguez-Macho and Fan, 2012; Paiva et al., 2013) and extend to continents (SCHUMANN et al., 2016a; SIQUEIRA et al., 2018; TRIGG et al., 2016; WING et al., 2017) and even to the whole globe (DOTTORI et al., 2016; SAMPSON et al., 2015; YAMAZAKI; DE ALMEIDA; BATES, 2013; ZHAO et al., 2017). These models have also been coupled to hydrologic ones with both online and offline strategies (e.g., Fleischmann et al., 2018; Hoch et al., 2017; Siqueira et al., 2018; Zhao et al., 2017), allowing a better comprehension of regional water resources. However, the scale to which these large scale hydrodynamic estimates can be locally used is still unknown. At the opposite side, local (i.e., reach scale) hydrodynamic models with consolidated 1D or 2D numerical schemes have widespread use in practical hydrologic engineering, such as the HEC-RAS model (USACE, 2010). These models are employed to perform flood forecasting and understand flood risk and flood management structures at detailed scales (e.g., urban domain or dam break studies) (ADAMS; CHEN; DYMOND, 2018; DE MOEL et al., 2015; HEINE; PINTER, 2012).

The scale of a model application depends on its intended use. Continental to global hydrodynamic models typically employ non-calibrated parameters and more general approaches (e.g., global databases of river bankfull width and depth; Andreadis et al., 2013), aiming at estimating global hydrological fluxes under a changing planet (HIRABAYASHI et al., 2013) and at developing flood forecasting and hazard products (DOTTORI et al., 2016; SAMPSON et al., 2015). They have high relevance for ungauged countries, global development agencies and flood (re)insurance companies (DE MOEL et al., 2015; SMITH et al., 2018; WARD et al., 2018), as well as for global assessments of biogeochemical cycles, climate, food security, energy and loss of biodiversity (BIERKENS, 2015; DÖLL et al., 2016). However, these models usually present difficulties to properly reproduce streamflows (ARCHFIELD et al., 2015; SIQUEIRA et al., 2018) and other variables that are locally relevant, since they are often forced with non-calibrated runoff fields or applied with non-locally adjusted hydrodynamic parameters. Model improvements in this direction involve the inclusion of human induced changes and water uses in global hydrologic models (DÖLL; FIEDLER; ZHANG, 2009) and better hydrodynamic model parameterization (YAMAZAKI et al., 2014b) and calibration (SIQUEIRA et al., 2018).

In turn, regional models may present a higher degree of adjustments. This may include higher resolution datasets (e.g., digital elevation models), simplified cross section geometries (e.g., rectangular shape) derived for the basin scale using both in situ (Paiva et al., 2013) and remote sensing estimates (NEAL; SCHUMANN; BATES, 2012), representation of more complex and realistic cross section shape (GRIMALDI et al., 2018; NEAL et al., 2015), or even section improvements with varying Manning roughness (LUO et al., 2017). There is also a possibility of modeling flow bifurcations

and complex drainage network patterns which tend to be simplified in global models, with both 1D or 2D hydrodynamic approaches (Altenau et al., 2017; Fleischmann et al., 2018; Pontes et al., 2017). Regional models may also benefit from local expert knowledge to improve models (ANDERSSON et al., 2017; KRUEGER et al., 2012; SIQUEIRA et al., 2018), and they may have a relevant role in national to basin scale water resources management.

On the other hand, local hydrodynamic models have a much higher degree of customization, since their applications (e.g., development of detailed flood hazard maps) usually require a precise estimate of variables such as water level, water velocity, floodplain water storage and extent, discharge, water slope and peak travel time. Such approaches typically use locally surveyed cross sections and represent detailed river engineering structures (e.g., bridges and levees; Fewtrell et al., 2011; Heine and Pinter, 2012). In many cases worldwide, high-resolution and high-accuracy data sets are available for river reaches under flood risk (GRIMALDI et al., 2018), providing more locally relevant estimates.

A cross-scale comparison is therefore needed. The recent developments of regional to global hydrodynamic models mentioned above naturally invoke the question on whether and to which extent those models can approach local, detailed hydrodynamic models, and what is the appropriate model complexity (ALTENAU et al., 2017). To which extent can we use regional to continental models to map and estimate local flood hazard? To which degree can we trust discharge and water level estimates from coarse resolution models? While the effects of errors in input data and parameterization on hydrodynamic models outputs have been somehow studied in recent literature for both local and regional and for 1D and 2D models (Altenau et al., 2017; Cook and Merwade, 2009; Dimitriadis et al., 2016; Fewtrell et al., 2011; Hoch et al., 2017; Horritt and Bates, 2002; Jung and Merwade, 2015; Liu and Merwade, 2018; Mateo et al., 2017; Mejia and Reed, 2011; Neal et al., 2015; Paiva et al., 2013; Pappenberger et al., 2005; Savage et al., 2016; Savage et al., 2016; Tayefi et al., 2007), the trade-offs between each model approach (global x regional x local) are still not understood. This comprehension is fundamental for the development and understanding of current regional to continental and global models (Mateo et al., 2017; Paiva et al., 2013; Siqueira et al., 2018; Yamazaki et al., 2013), so that they ultimately move toward more locally relevant hydrodynamic estimates (DE MOEL et al., 2015).

In this context, this paper presents, to the knowledge of the authors, a first cross-scale comparison between global, regional and local 1D hydrodynamic modeling strategies. A local HEC-RAS model application (USACE, 2010) set up with more than 850 km of simulated river reaches and over 600 in situ cross sections is compared with different local, regional and global applications based on the large scale MGB model (Pontes et al., 2017). Multiple tests are performed to address different levels of customization in hydrodynamic modeling, varying cross section shape, floodplain topography and length computations.

10.2 Methods

10.2.1 Methodology overview and experimental design

This study is divided in two main parts, (i) a cross-scale hydrodynamic model intercomparison, and (ii) an analysis of the drivers of the differences in model performance.

In the first part, three different model configurations are set up based on the MGB hydrologic-hydrodynamic model with increasing scale modeling approaches – called henceforth global, regional and local MGB models. These three configurations are compared to a locally based HEC-RAS hydrodynamic model for the Itajaí-Açu river basin in Southern Brazil, for which there was availability of 620 in situ surveyed cross sections and a locally developed Digital Elevation Model (DEM). The goal of this part is to assess how locally relevant are the different model configurations, considering the locally developed HEC-RAS model as a reference benchmark, as assumed in many practical hydraulic engineering studies. The compared hydrodynamic models are forced with the same calibrated rainfall-runoff parameters, so that uncertainties related to hydrological inputs (e.g., simulated runoff fields) were not considered.

The three MGB model configurations are based on typically adopted approaches for the respective scales, as summarized by Table 10.1. Three main factors were defined to differ hydrodynamic modeling approaches at the different scales: (i) spatial discretization (given by river reach length); (ii) adopted DEM to estimate floodplain topography and channel bank elevations; and (iii) cross section geometry. Reach length refers to the equal distance segments in which the drainage network is divided, and ultimately affects the length and number of computational units in the simulated domain and the estimated bank elevation, which is computed from the average pixel elevations above the reach (see Siqueira et al., 2018 Supplementary Material for description of the method). The adopted DEM is used to define floodplain topography and the reach bank elevation. In turn, the MGB cross section geometry is set as a rectangular cross section (as typically adopted in regional to global models), and thus channel bankfull depth and width values are required as model parameters.

The global model version uses a global database of cross section geometry (Andreadis et al., 2013), SRTM DEM at 500 m spatial resolution and a reach length of 15 km. This is analogous to the MGB continental application by Siqueira et al. (2018). The regional model adopts a basin scale derived geomorphic relationship between cross section bankfull width and depth and drainage area, 30 m SRTM DEM and a reach length of 5 km. Finally, in the local model the 620 cross sections parameters (estimated bankfull width, bankfull depth and bank elevation) are directly inserted into the respective model reaches where they are located, while for those reaches without surveyed cross sections the basin scale geomorphic relationship is used. A locally developed DEM (hereforth called SDS, see DEM description in “2.3 Datasets section”)

at 30 m is used together with 1 km long reaches. The HEC-RAS model was defined as the local truth, and was developed by directly including the 620 cross sections within the model domain, which covered the most important river reaches across the Itajaí-Açu basin.

The second part of the study aims at understanding which factors drive the differences found among the three models configurations. Then, the regional MGB model is set as a reference, and different configurations are evaluated alone by varying reach length, DEM and cross section geometry.

For all tests, the different MGB model configurations were run with the same rainfall-runoff model parameters, and the HEC-RAS model was forced with MGB model discharges derived from the regional model version. The models were run for the extreme 1983 flood in the Itajaí-Açu river basin, and the predicted discharge, water level, water level anomaly and flood extent were analyzed.

Table 10.1. Summary of the three MGB model configurations compared with the detailed HEC-RAS model. XS: river cross sections; wbf: bankfull width; dbf: bankfull depth; ybank: bank elevation.

	Reach length	Floodplain topography	XS geometry
Global model	15 km	SRTM-500 m	- w_{bf} and d_{bf} from global database - y_{bank} from SRTM-500 m
Regional model	5 km	SRTM-30 m	- w_{bf} and d_{bf} from regional relationship - y_{bank} from SRTM-30 m
Local model	1 km	SDS-30 m	- Local XS insertion (w_{bf}, d_{bf} and y_{bank} values) - For unit-catchments without XS: w_{bf} and d_{bf} from regional relationship and y_{bank} from SDS-30 m
HEC-RAS model	Variable (20 to 500 m)	XS + SDS-10 m	- 620 local XS's

10.2.2 Study area

The Itajaí-Açu River Basin in Southern Brazil (Figure 10.1) was used as a case study due to its contrasting floodplain geomorphology types and its size, being of a suitable spatial scale for regional scale evaluation (drainage area of ~15,000 km²), and with a large range of slopes and channel width and depths (Figure 10.3). A large

number of surveyed river cross sections are available together with a locally developed, high-quality DEM. The Itajaí-Açu river is formed by three main tributaries, the Itajaí do Oeste, Itajaí do Norte and Itajaí do Sul rivers. There are relevant floodplains throughout the whole basin varying from laterally constrained floodplains (with terraces crops as rice) to non-constrained ones (in its most downstream reaches). In some reaches, river rapids and waterfalls occur and define local hydraulic controls downstream of reaches with river-floodplain interactions, such as downstream of Rio do Sul city (Figure 10.1a).

The basin has a long history of damaging floods, and today more than 1.5 million people live within it, with most cities located around river floodplains. The highest recorded flood in 1983 (which is used for simulations in this study) affected over 90 cities throughout the basin, and around 200,000 people were displaced, leading to an estimated impairment of R$ 1.1 billion (Brazilian currency) (CEPED/UFSC, 2015; FRANK, 2003). To cope with such disasters, three large flood control dams are located in the river three main tributaries. Recent flood events have also pushed new efforts to improve basin-wide flood control, including the proposal of new levees and flood control dams, making the basin a relevant case study for improving our comprehension of hydrodynamic modeling estimates.

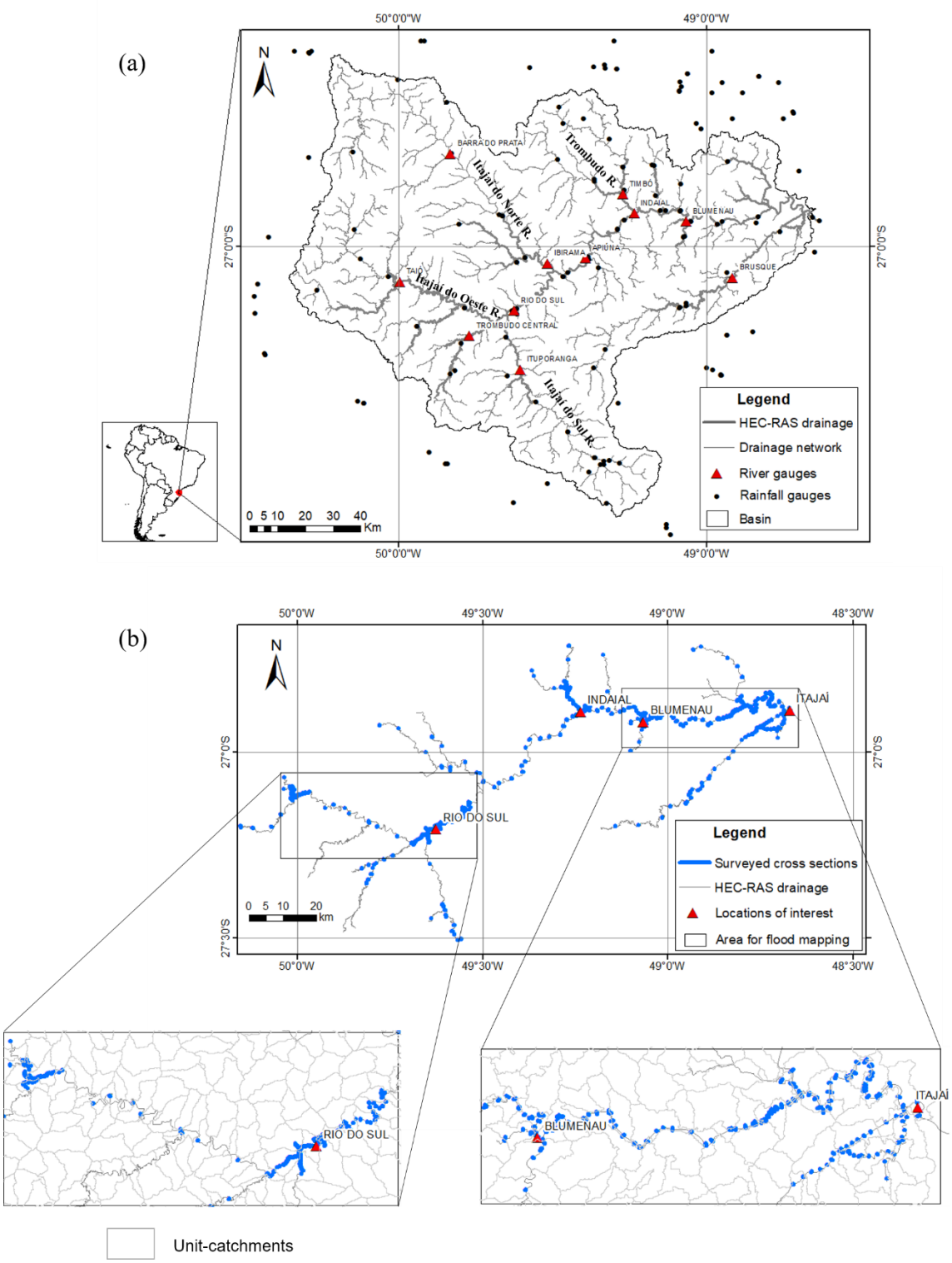

Figure 10.1. a) The Itajaí-Açu River Basin, its main tributaries (Itajaí do Sul, Itajaí do Oeste, Itajaí do Norte and Trombudo rivers), precipitation and discharge gauges used for rainfall-runoff model calibration, and locations of interest for this study. (b) Location of the 620 locally surveyed cross sections that were used to set up the HEC-RAS model. The two black boxes indicate the regions used to analyze maximum flood extent, and *F* metric values are derived for each unit-catchment within it (grey polygons in the bottom figures).

10.2.3 Datasets

Three different DEM's were used for the global, regional and local MGB model configurations and the HEC-RAS setup (Table 1). The global and regional ones use the Shuttle Radar Topography Mission (SRTM) DEM (Farr et al., 2007; available at < http://srtm.csi.cgiar.org) at 500 m and 30 m spatial resolutions, respectively. The local MGB and HEC-RAS models used a DEM (SDS DEM) developed for the whole Santa Catarina State in Brazil by the States's Secretary of Sustainable Economic Development (SDS, 2013; available at < http://sigsc.sds.sc.gov.br/>). The DEM has a 1 m spatial resolution and an estimated vertical accuracy of 0.39 m. To allow data management, it was upscaled to 10 m for HEC-RAS, and to 30 m for the MGB local model version to be comparable with SRTM spatial resolution. All DEM's were converted to Brazilian SIRGAS2000-MAPGEO2015 geoid model (IBGE, 2015) because SDS DEM and in situ cross sections were referenced to it. Differences between MAPGEO2015 and EGM96 (SRTM's datum) data in the region ranged from around -0.6 to +0.6 m.

Figure 10.2 presents HAND (Height Above Nearest Drainage; Rennó et al., 2008) terrain maps derived from the SRTM 500 m, SRTM 30 m and SDS 30 m for the locations of Rio do Sul and Itajaí cities (see Figure 10.1 for location). These maps highlight the extensive floodplains occurring along these areas as well as the large differences between the DEM's. It is noticeable the better description of terrain elements such as roads and urban areas in the SDS DEM in comparison to SRTM 30 m, which features a pronounced speckle noise.

A total of 620 locally surveyed river cross sections were used, which are displayed in Figure 10.1b. A post-processing was performed to complement all sections that did not cover the full lateral extent of the river floodplains with the SDS DEM at 10 m spatial resolution.

Channel bankfull width and depth values were required for the MGB runs, which adopts a rectangular cross section for simulation. For the global model configuration, the global database developed by Andreadis et al., (2013) was used (Figure 10.3), which was based on regressions between these variables and average annual discharge. The regional model used a basin scale (i.e. regional) regression between these variables and drainage area, based on the 620 locally surveyed cross sections and by adjusting a rectangular cross section to each section (i.e. bankfull depth estimated by dividing wetted area by bankfull width). Examples of the adjusted rectangular cross sections are presented in Figure 10.4. Finally, the local model used average cross sections values for the model river reaches where the sections were located, while for the basin areas without cross sections the regional regression was adopted. Figure 10.3 presents the estimates with 95% confidence intervals for global and basin scale regressions, which show that the global estimates include the local based ones within the 95% interval for bankfull width, but underestimate bankfull depth values.

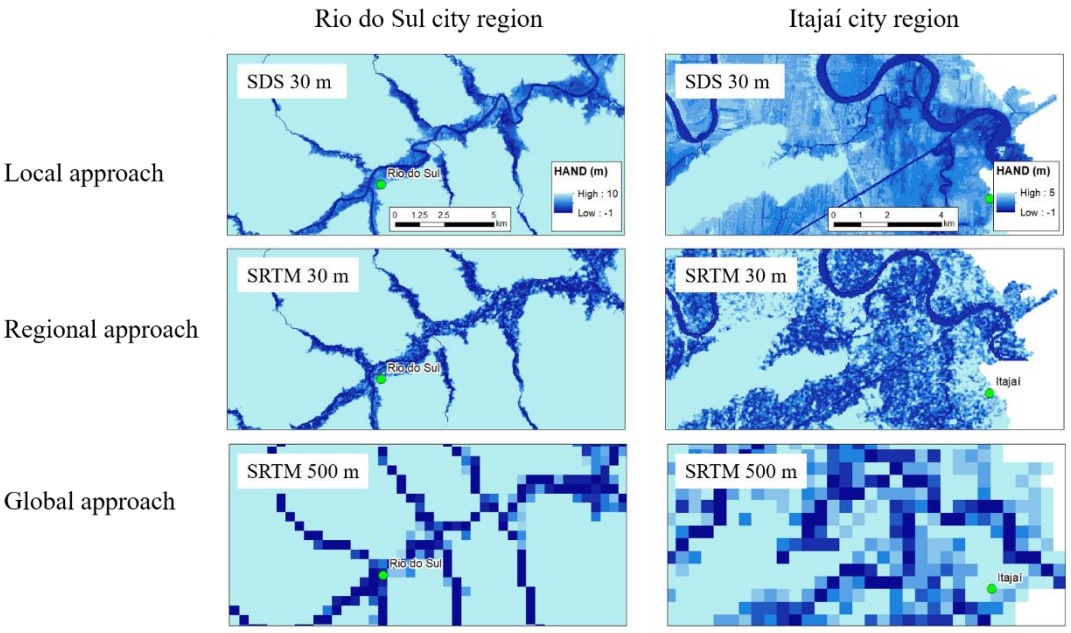

Figure 10.2 HAND (Height Above Nearest Drainage) maps derived from the SDS 30 m, SRTM 30 m and SRTM 500 m DEM's for the locations of Rio do Sul and Itajaí cities (see Figure 10.1 for location), highlighting the differences between local and global approaches used in this study.

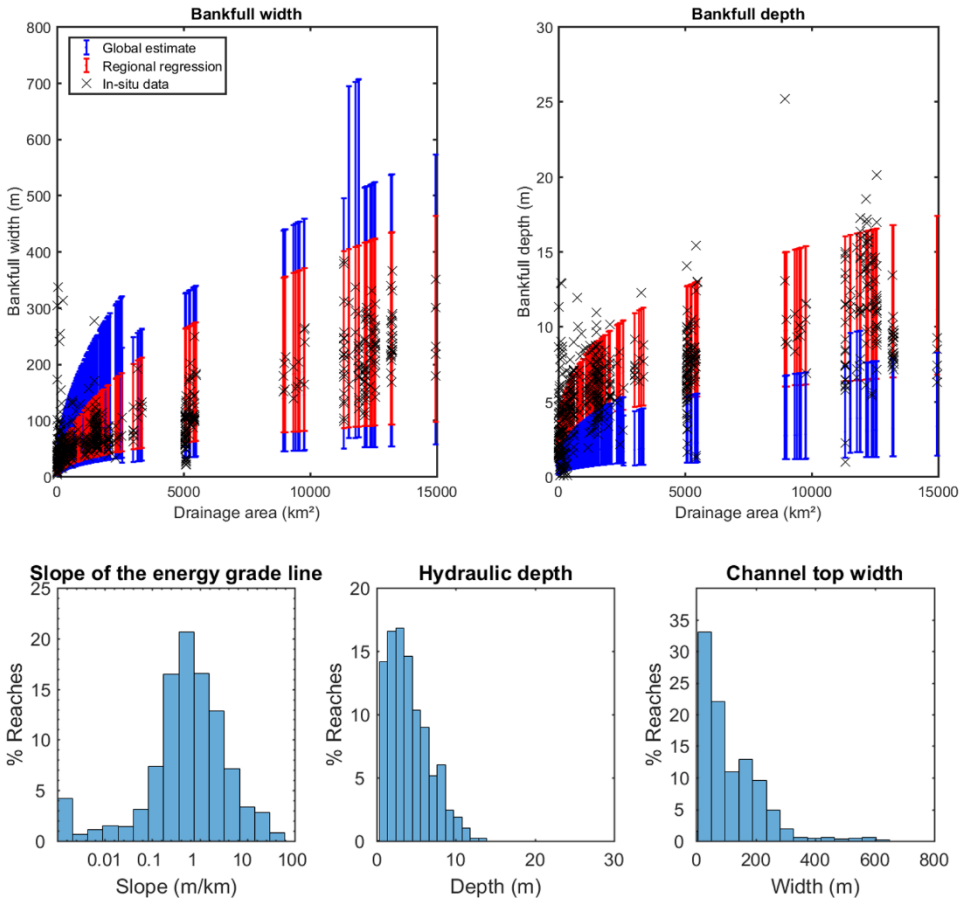

Figure 10.3. Relationship between drainage area and bankfull width and depth values from global and regional estimates and in situ surveyed cross sections. Bottom histograms present slope of the energy grade line, hydraulic depth and channel top width values for

10.2.4 MGB hydrologic-hydrodynamic model

The MGB model (Collischonn et al., 2007; Pontes et al., 2017) is a semi-distributed hydrologic-hydrodynamic model developed for large scale basins. The basin is divided into unit-catchments that are further split into hydrologic response units (HRU's), for which vertical hydrological processes are computed (evapotranspiration, soil infiltration, and surface, subsurface and groundwater flow generation). Runoff generated within each unit-catchment is routed along the drainage network with the local inertial approximation of Saint-Venant equations proposed by Bates et al., (2010). In this section the hydrodynamic module is focused, and the reader is referred to Pontes et al. (2017) and Siqueira et al. (2018) for a more detailed explanation of rainfall-runoff model conceptualization and parameters.

In the current version of the model (Siqueira et al., 2018 Supp Material), unit-catchments are defined as the local drainage area of river segments. For this, the

drainage network is segmented into constant length reaches (which varied from 1 km to 15 km in the performed tests). Then, for the model configurations based on the 30 m spatial resolution DEM's, the 1 km based model led to 4444 unit-catchments, while the 5 km (15 km) one had 1118 (614) units. For the 500 m DEM model run, the drainage network slightly differed from the 30 m one, so that the number of unit-catchments changed to 573 for 5 km and 945 for 15 km long reaches.

One rectangular cross section is defined for each unit-catchment reach, with bank elevation, channel bankfull width and depth, and Manning's coefficient as main parameters. Hydraulic geometry theory (LEOPOLD; MADDOCK, 1953) is used to estimate bankfull width and depth based on simple geomorphic relationships, e.g., by relating these values to local drainage area. In this study this strategy was adopted by using different relationships of cross section geometry with drainage area, based on global or regional estimates (see section 2.3 Datasets for details). For each unit-catchment, average bankfull elevation was estimated from a linear regression of all DEM pixels above the unit-catchment river pixels. Floodplain topography (i.e. level-area relationships for each unit-catchment) was extracted with a HAND (RENNÓ et al., 2008) based algorithm. These pre-processing steps are described in Siqueira et al. (2018) Supplementary Material.

The explicit inertial numerical scheme (BATES; HORRITT; FEWTRELL, 2010) is run at a time step defined by Courant-Friedrichs-Lewy condition with a stability alpha parameter, set to 0.2 in this application. Downstream boundary condition in the basin outlet to Atlantic Ocean was set as a zero elevation, to be consistent with the HEC-RAS application. MGB model rainfall-runoff parameters were adjusted with observed discharges and are not presented here for brevity.

For the tests performed in this study, the July 1983 flood event was selected due to its extreme nature, and the simulated discharges at hourly time step during the event (simulation period from 1st June 1982 to 1st August 1983 to include spin-up period) were used to force the HEC-RAS model.

10.2.5 Detailed hydraulic model

The 1D HEC-RAS hydrodynamic model (USACE, 2010) outputs were adopted as a proxy of locally relevant variables due to the software's widespread use in hydraulic engineering applications. The software solves the full Saint-Venant equations with a Preissmann four-point implicit scheme. A model application including 620 in situ surveyed cross sections was set up, covering 863 km of river reaches in the Itajaí-Açu River Basin and including all the main basin tributaries (Figure 10.1b). A post-processing was performed to complement the sections to the whole floodplain area with the SDS 10 m for those sections that did not cover the whole floodplain. In river reaches with low cross section density the sections were linearly interpolated to improve

numerical representation. Figure 10.4 presents three cross sections located in different parts of the Itajaí-Açu mainstem as an example. The adjusted rectangular cross sections used to derive the regional scale geomorphic relationship are also displayed.

As boundary conditions, HEC-RAS was forced with MGB regional model simulated discharges as contributing upstream hydrographs for upstream sections, as contributing lateral inflow for the tributaries not represented in HEC-RAS, and as local runoff generated for the MGB unit-catchments located within each cross section. At the downstream boundary condition, sea level was adopted at elevation zero. Manning's roughness coefficient was set as 0.035 for channel and 0.1 for floodplains basin-wide, following general river hydrodynamic applications (CHOW, 1959; USACE, 2016).

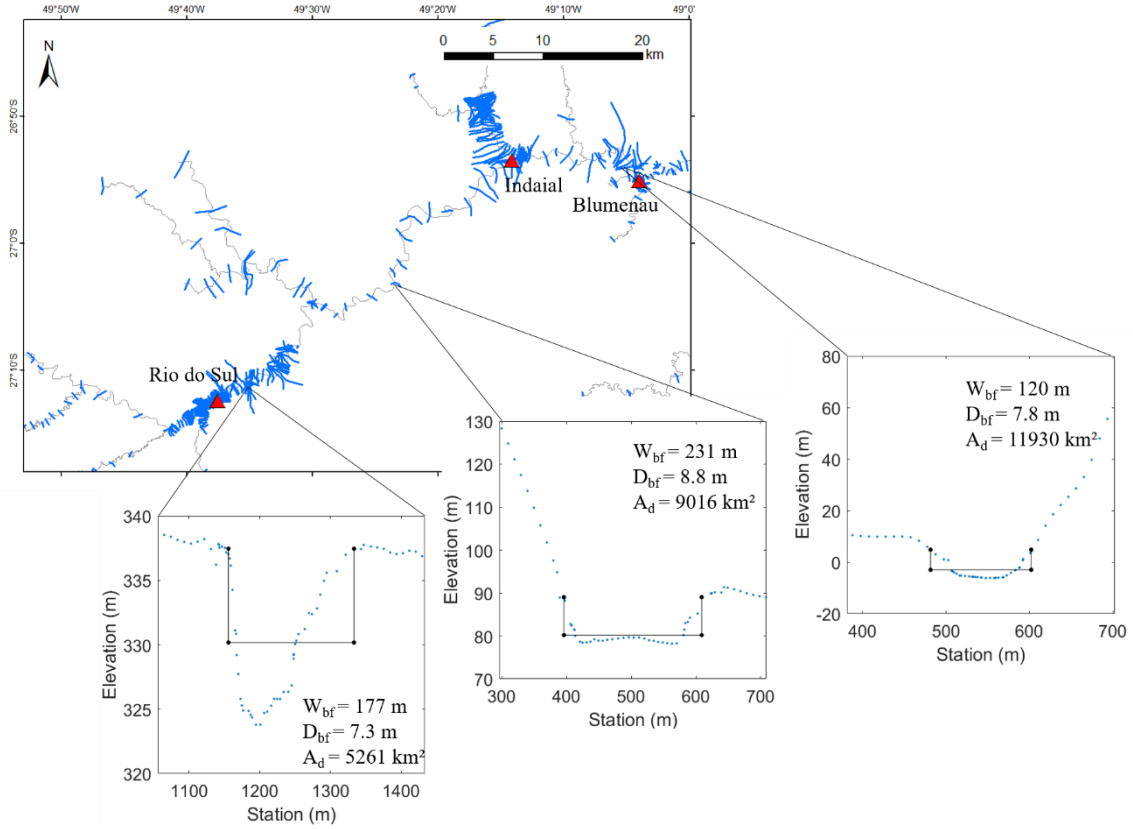

Figure 10.4. Cross sections along the Itajaí-Açu mainstem and detail of three sections located in two floodable areas (Rio do Sul, upstream section, and Blumenau, downstream section) and in a reach with rapids (intermediate section, between Rio do Sul and Blumenau). Cross sections are plotted with the respective adjusted rectangular cross section. W_{bf}: bankfull width; D_{bf}: bankfull depth; A_d: drainage area at the section location.

10.2.6 Performance metrics

Four main hydrodynamic variables were evaluated in this study: discharge, water level (i.e. absolute water level), water level anomaly (i.e. hourly level subtracted from long term average level) and maximum flood extent. For the first three ones, the global, regional and local MGB model versions were compared to HEC-RAS at each river cross section with the metrics Nash-Sutcliffe efficiency (NSE; it ranges from -∞ to 1, where 1 is the optimum value) for discharge and root mean square error (RMSE; it ranges from 0 to +∞, where 0 is the optimum value) for water levels. The 620 cross sections enabled then a basin scale comparison of the models.

Different runs of the regional model are performed in section 10.3 by changing reach length, DEM and cross sections. To evaluate the difference between mean values, and to create a performance ranking for each factor, a paired Student's T test was performed between each pair of boxplots at a 95% significance level, following the method for two samples with different variances described by Naghettini (2017).

Maximum flood extent was evaluated with the Fit metric F (Bates and De Roo, 2000; sometimes referred to as Critical Success Index) (Equation (1)):

$$F = 100\ \% * (A \cap B)/A \cup B \quad (1)$$

Where A and B are the observed (i.e. HEC-RAS) and simulated (i.e., MGB global, regional and local model configurations) flood extents for a given area. F ranges from 0 % to 100 %, where 100 % is the optimum value. The metric was computed for each unit-catchment with maximum flood fraction higher than 10 % in the HEC-RAS simulation located within two main floodable areas (Rio do Sul and Itajaí city locations; Figure 10.1b). In order to compare models with different spatial resolution (global - 500 m; regional and local - 30 m; HEC-RAS - 10 m), all flood maps were resampled to 10 m with a nearest neighbor algorithm.

10.3 Results

10.3.1 Cross-scale comparison

Simulated maximum water level longitudinal profiles for two rivers (Itajaí-Açu mainstem and Trombudo, see Figure 10.1 for location) with high cross section density are presented in Figure 10.5. Results are displayed for HEC-RAS and the global, regional and local MGB model configurations. The global one is very limited to estimate absolute water level in comparison to the regional and local ones. Its coarse resolution (15 km) is also evident, in contrast to 5 km (1 km) for regional (local) models. A detail with a zoom in the Itajaí-Açu middle reaches (60–120 km) is also

provided, and further stresses the differences between the local (with local insertion of cross sections) and regional models and the closer results between local and HEC-RAS estimates.

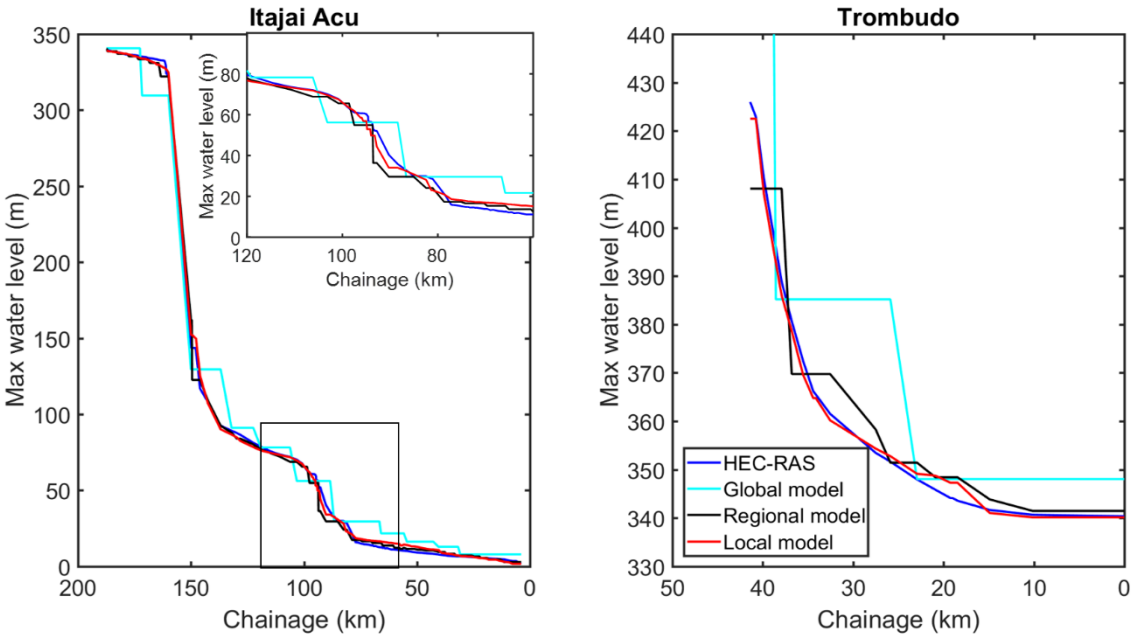

Figure 10.5. Longitudinal profile of maximum water level for HEC-RAS and MGB global, regional and local model simulations, for rivers Itajaí-Açu and Trombudo. The upper box in Itajaí-Açu figure is a detail of the 60-120 km chainage reach showed in the black rectangle.

Figure 10.6 shows discharge, water level and water level anomaly time series at Rio do Sul, Indaial and Blumenau cities along Itajaí-Açu mainstem (see Figure 10.1 for location). Peak discharge delay and reduction by the global model are associated with exaggerated floodplain attenuation, while local and regional ones are much closer to HEC-RAS. For example, peak discharge differences are 2 % and 12 % for local and global models for Rio do Sul, and 3 % and 20 % for Blumenau locations.

The global setup overestimates absolute water level in the three locations, indicating that its coarse resolution and reach length may hamper its use for precise local water level estimation. It is interesting to note how satisfactory were the regional and local simulations in Rio do Sul, especially considering the rapids and hydraulic controls existent downstream of it, which are represented in HEC-RAS but not in MGB. On the other hand, in terms of water level anomaly in Indaial, all models are relatively satisfactory, while in Rio do Sul and Blumenau the amplitude is smaller in the global model due to excessive floodplain.

The performance for discharge (NSE metric), water level (RMSE) and water level anomaly (RMSE) variables is summarized in the boxplots of Figure 10.7, which plot for each model configuration the performance of all 620 cross sections. Average and standard deviation (including all outliers values) of the metrics are displayed below each model name. The local model outperforms the regional one only on the absolute water level estimates, while the differences to global estimates are significantly high and suggest that the latter's water levels are unsatisfactory for local scale usage, as observed in Figure 10.6 with water level time series. For this variable, the local model also leads to less dispersion on its estimates. For discharge and water level anomaly estimation, both regional and local models provide similar results.

Boxplots related to flood extent F metric are presented in Figure 10.7 for all unit-catchments and separately for Itajaí and Rio do Sul locations, which present different floodplain geomorphologies. In Rio do Sul, the floodplain features a highly constrained lateral extent, following the description by Hunter et al. (2007), which could be understood as similar to a two-stage compound channel. In turn, the lower Itajaí-Açu around Itajaí city has a more unconstrained lateral extent, where a binary flood extent map would be more difficult to estimate. All model versions have similar performance in Itajaí with F averages between 36 % and 43 %, while the local MGB outperforms the others in Rio do Sul with 52 % against 39 % and 34 % F values. The regional model has a larger interquartile range than the others in both areas.

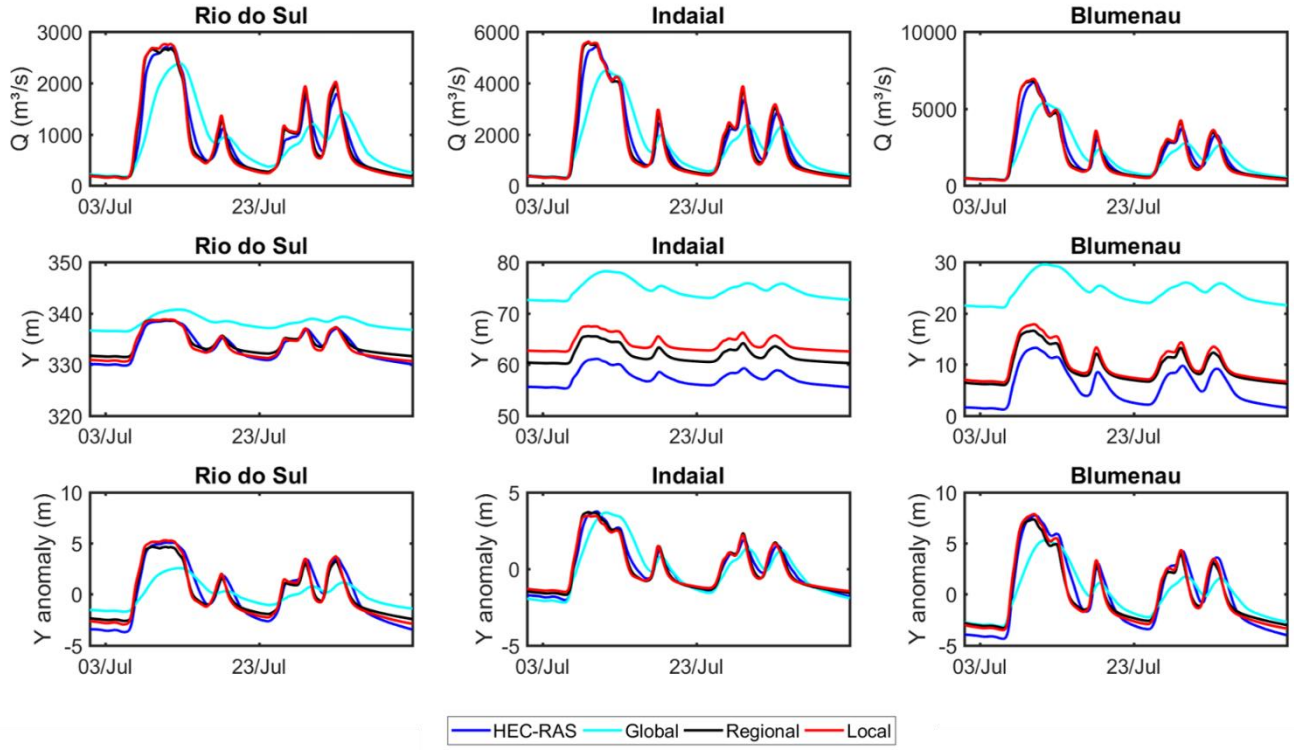

Figure 10.6. Discharge, water level and water level anomaly time series for the locations of Rio do Sul, Indaial and Blumenau in the Itajaí-Açu river. Results are presented for HEC-RAS and MGB global, regional and local models.

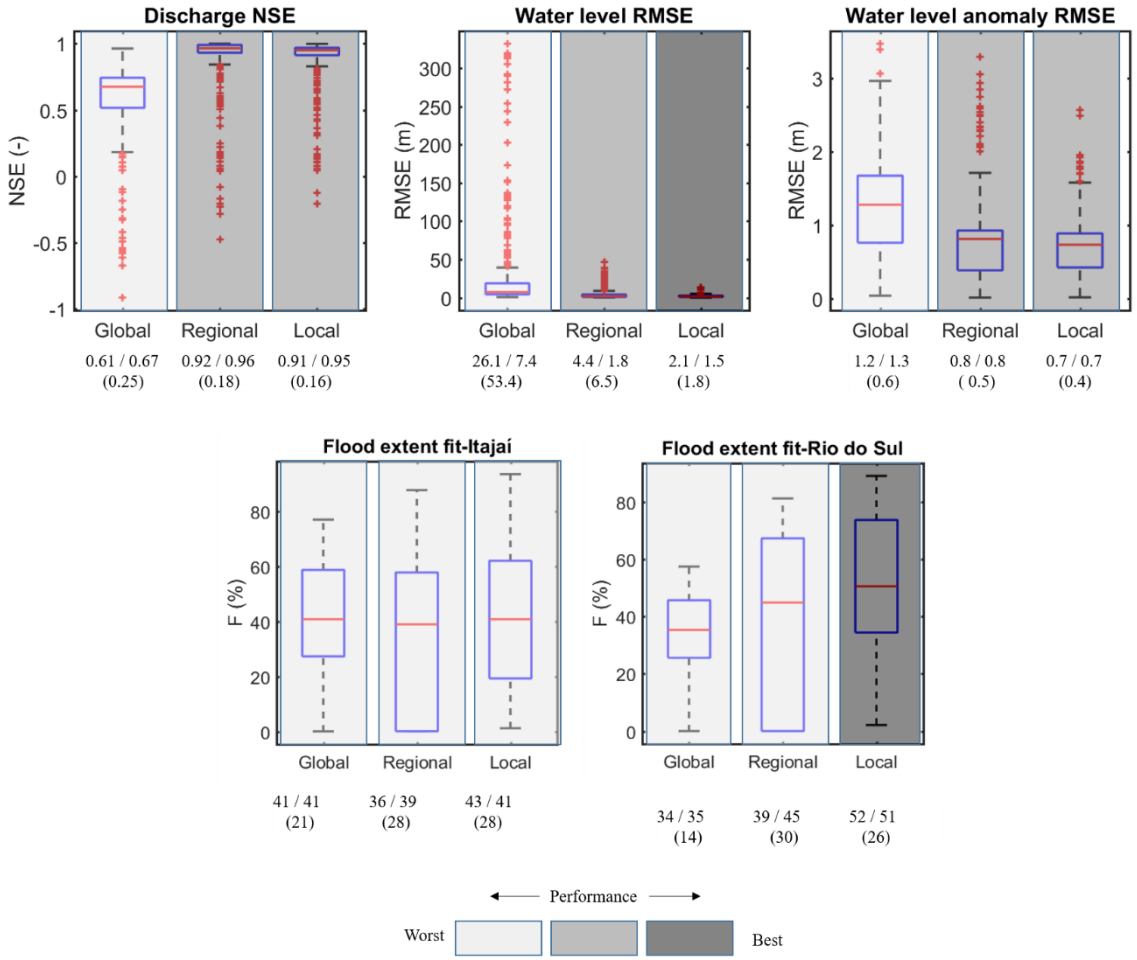

Figure 10.7. Boxplots of global, regional and local MGB models performance for discharge (Nash-Stucliffe – NSE), water level (RMSE) and water level anomaly (RMSE) for the 620 surveyed cross sections' locations. Flood extent *F* metric is derived for all unit-catchments with maximum flood fraction higher than 10 % in the HEC-RAS simulation within Itajaí and Rio do Sul locations (Figure 10.1b). Bottom numbers indicate average/median and standard deviation (in parenthesis) for each series. Shaded boxes represent a performance ranking based on paired Student-T test with $P < 0.05$. Light grey indicate the poorest, middle grey the intermediate and dark grey the best performance among the three configurations.

To further understand the spatial differences between the models, the performance of discharge, water level and water level anomaly variables for each cross section is presented in the Figure 10.8 maps. The colors represent different performance classes, ranging from blue (satisfactory) to red (unsatisfactory), and allows interpretation of where each model could provide a locally relevant estimate, which are defined here as a class with discharge NSE>0.9 or water level RMSE < 0.4 m (see discussion in Section 10.4.1). Firstly, it is clear that the global model performs poorly for both discharge and water level variables, while for water level anomaly the three model configurations are reasonable. Major areas of poor global discharge estimation are the upstream headwaters and the lower Itajaí-Açu, which are coincident with steep reaches and areas

subjected to major flooding, respectively. Also, most cross sections present discharge NSE > 0.9 and water level anomaly RMSE < 0.4 m for regional and local models, indicating that for these two variables there would be a satisfactory confidence in the predictions in many points. Only a few isolated locations present discharge estimates with NSE < 0.6 (red points), in many cases due to bifurcation channels which were represented in the HEC-RAS model. In turn, for absolute water level, only in a few isolated cross sections does the local model perform well (RMSE < 0.4 m), stressing its general difficulty of accurately estimating levels. Along the Itajaí-Açu mainstem, reaches at chainage 100-150 km (see water level longitudinal profile in Figure 10.5) present the worst absolute water level estimations (red to orange cross sections), what can be explained by the steep channels that occur in this part. In the lower Itajaí-Açu, near its mouth (i.e. reaches subjected to backwater effects by the downstream boundary condition), the model provided satisfactory estimates of water level anomaly (RMSE < 0.4 m) and relatively good absolute water level (RMSE < 1 m).

Maximum flood extent maps are presented in Figure 10.9 for the locations of Rio do Sul and Itajaí cities (Figure 10.1b). F values are presented for the whole area extent, and represent how accurate are the MGB runs in comparison to HEC-RAS. For Rio do Sul, the local MGB model (F = 45 %) performed better than both regional (F = 35 %) and global (F = 26 %) ones, in accordance with Figure 10.7 boxplots. In Itajaí city, all model versions had similar performance ranging from 38 % (regional) to 42 % (global) and 44 % (local). Flooded areas in Itajaí were also much larger than Rio do Sul ones. The relatively low values (less than 50 %) suggest a difficulty in all MGB model configurations to estimate this variable, what could be improved by calibrating channel depth, for example. The next section will address the relative effects of cross section geometry, DEM and reach length on these results.

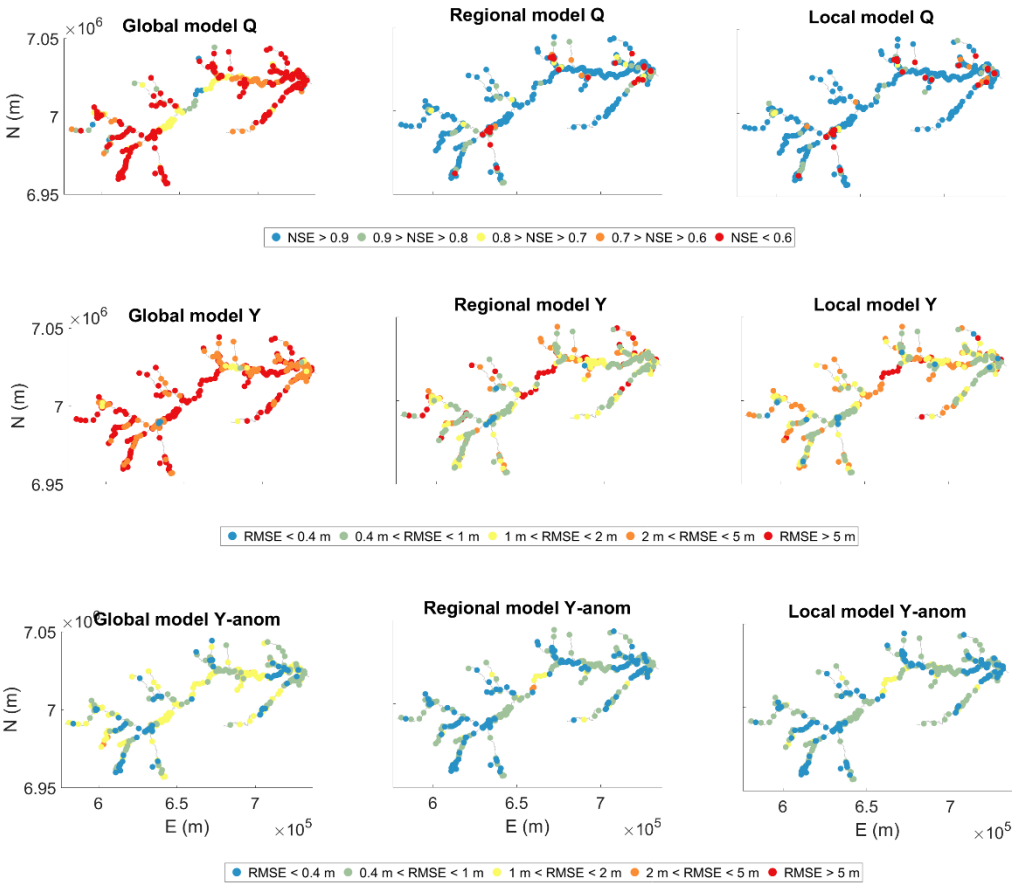

Figure 10.8. Maps of global, regional and local MGB models performance for discharge (Nash-Stucliffe – NSE), water level (RMSE) and water level anomaly (RMSE), for the location of the 620 surveyed cross sections throughout the Itajaí-Açu basin.

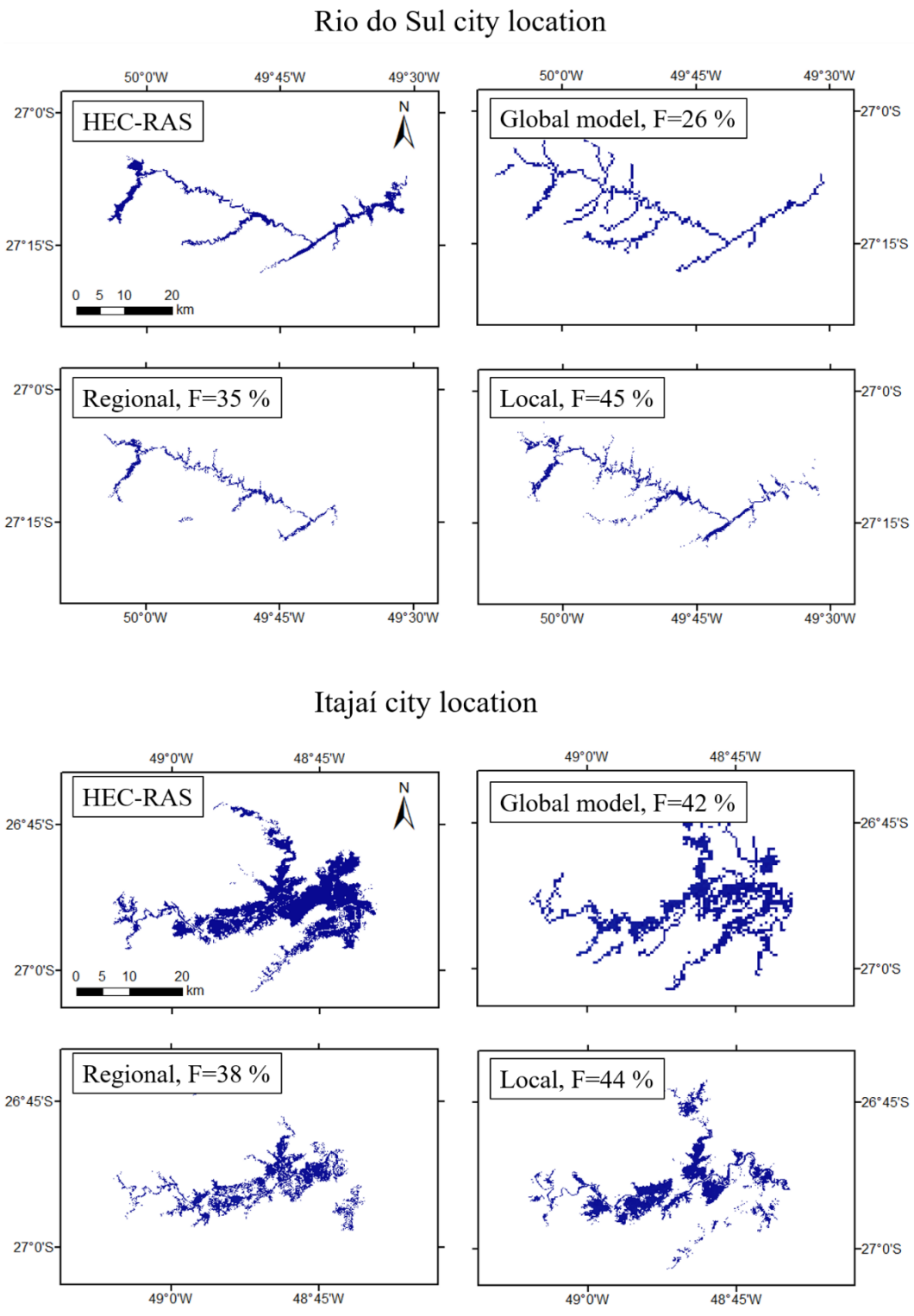

Figure 10.9. Maximum flood extent maps for HEC-RAS and global, regional and local MGB models' outputs for the locations of Rio do Sul and Itajaí city (black boxes in Figure 10.1b). *F* metric is presented for the extent of the whole area.

10.3.2 On the drivers of cross-scale differences

In order to understand the differences between global, regional and local model runs from the previous section, here a set of simulations is performed by considering the regional MGB model as a reference and by changing its main components (i.e. reach length, DEM and cross section geometry). Figure 10.10 summarizes the results for discharge, water level (absolute and anomaly) and flood extent by presenting boxplots for each model configuration, considering the MGB model performance in relation to HEC-RAS simulations for the ensembles of cross sections (discharge and water level) and unit-catchments (flood extent; Itajaí and Rio do Sul regions are plotted together in this analysis, in contrast to the previous 10.3.1 section). Discharge results indicate a model improvement by using 1 km long reaches in comparison to 5 and 15 km, while for DEM and cross sections the regional and local configurations are similar (i.e. SRTM 30 and SDS 30, and regional and local geometries, respectively), and perform better than the global one. Differences between SRTM and SDS at 30 m do not seem to be relevant in terms of stored volume in the river-floodplains system, even considering the higher speckle noise in SRTM (HAND maps in Figure 10.2). In the global application, both DEM (SRTM 500 m) and global geometry (with smaller bankfull depths) led to higher flooding and thus discharge underestimation and smaller NSE.

For water level, the 1km long reach and the local geometry configurations (i.e. the local approaches) improved model estimates, while regional DEM (SRTM 30 m) performed better than the local one (SDS 30 m). The 15 km length seems to be inadequate to represent the flood dynamics in the Itajaí-Açu river basin, especially if considered some steep reaches with relevant changes in river bed elevation. Moving from 15 km to 5 km lengths water level RMSE would be improved from 15.8 m to 4.4 m. The smallest water level RMSE (2.7 m) would be obtained by improving regional model cross sections towards more local estimates.

The behavior of water level anomaly was different from the other variables, since all evaluated model configurations showed a similar performance for this variable. The global modelling approach performed worse than the regional and local ones only when analyzing cross section geometry. Local geometry led to significantly smaller water level anomaly average RMSE than the regional one, although the values were relatively similar (0.8 and 0.7 m).

Flood extent boxplots indicate that the 1 km reach would lead to better average F values (51 % x 37 % and 26 %), while both SRTM 30 m (37 %) and SDS 30 m (34 %) DEM's would outperform SRTM 500 m (24 %). The global based cross section geometry obtained the best performance (68 %) in comparison to regional (27 %) and local (40 %) estimates. Although this result may be somehow surprising, it may be explained by the relatively smaller global bankfull depths if compared to local ones (Figure 10.3), what led to much more flooding and a better F metric. However, as observed in Figure 10.6, the global model tends to exaggerate discharge attenuation

with too much flooding basin-wide. Global model flood extent extended to the whole floodplain domain (i.e. behaving as a laterally constrained floodplain), and water depth maps (not presented here for brevity) showed that floodplain depths were indeed higher in the global model than HEC-RAS estimates. This indicates that the optimum flooding estimation would be attained by adopting an intermediate bankfull depth value (i.e., between local and global estimates). In such laterally constrained floodplains, flood extent may not be a suitable metric to be evaluated in such cases (HUNTER et al., 2007).

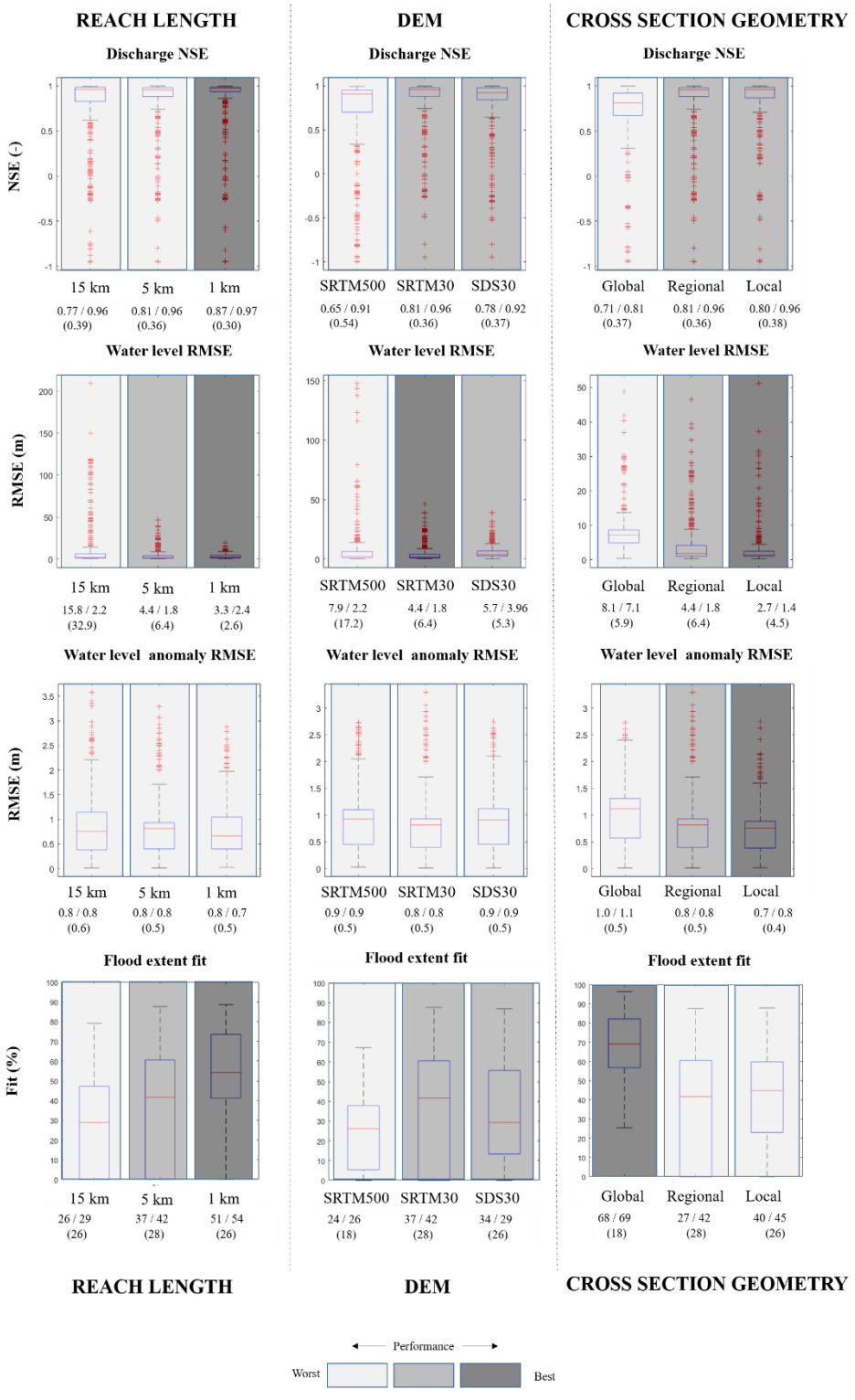

Figure 10.10. Effects of different factors on discharge NSE, water level (absolute and anomaly values) RMSE and flood extent *F* metrics. Boxplots relate to model performance in relation to HEC-RAS for the 620 cross sections (for discharge and water level analysis) and the unit-catchments within Itajaí and Rio do Sul regions (for flood extent analysis; see Figure 10.1b) due to alterations in the regional MGB model version of (a) reach length (15 km, 5 km, 1 km), (b) DEM (SRTM 500 m, SRTM 30 m, SDS 30 m) and (c) cross section geometry (global, regional and local geometries). Bottom numbers indicate average/median and standard deviation (in parenthesis) values for

each series. Shaded boxes represent a performance ranking based on paired Student-T test ($P < 0.05$). Light grey indicate the poorest, middle grey the intermediate, and dark grey the best performance among the three configurations.

10.4 Discussion

10.4.1 On the definition of locally relevant estimates in the context of regional/global hydrodynamic models

Regional to global hydrodynamic models are now a reality and have been proven to yield better estimates than non-hydrodynamic ones for variables as discharge, water surface elevation and flood extent in many locations (SIQUEIRA et al., 2018; YAMAZAKI; DE ALMEIDA; BATES, 2013; ZHAO et al., 2017). Although global models should be used for the purposes they were designed for (DE MOEL et al., 2015; WARD et al., 2018), it is a major and open question whether their estimates could be deemed as locally relevant, or to which scale could they be trusted.

The goal of attaining "locally relevant estimates everywhere" with global models have been recently discussed in the literature (BIERKENS, 2015; BIERKENS et al., 2015; DÖLL et al., 2016; PAU et al., 2016; WADA; DE GRAAF; VAN BEEK, 2016). However, a precise definition of what a locally relevant variable is and how it could be used as a measure of model performance is not yet available. The variable of interest itself depends on the model application, e.g. in flood related studies, water depths are more relevant for evaluating damage to buildings, while velocity are interesting for bridges and time and duration of flooding for agricultural crops (DE MOEL et al., 2015). Three main requirements for attaining locally relevant estimates in the context of river hydrodynamic models are then proposed (Table 10.2): the errors of a (regional to global) model should be equal or smaller (i) than the accuracy requirement for a particular application and location; (ii) than typical local, reach scale models' errors; and (iii) than observation uncertainties. Even more, if there is no information available for a particular location (e.g., absence of in situ data or local models), a global model will naturally be locally relevant, although it may present large yet possibly unknown errors.

The first is more subjective and depends on the local landscape (e.g., channel slope, floodplain geomorphology and river water level amplitude) and social factors (e.g., floodplain occupation and local water agencies/stakeholders/community perception of the river system; Pappenberger et al. (2007)), and thus it is not straightforward to define a general threshold of locally relevance. For flood forecasting, very short-term forecasts (e.g., within hours) may require high accuracy estimates (at the centimeter scale), while longer leading times (e.g., a few days) may accept errors at the meter scale, since each forecast will have a different role in the disaster management. If deterministic thresholds are adopted (e.g., warning, alert, flood level;

Todini, 2018), these may be used to define the required accuracy. In flood damage estimation (e.g., for flood insurance companies or flood risk estimation by governmental agencies), sensitivity of damage to different water levels in level-damage relationships could be used to define thresholds above which errors are not acceptable. The expected accuracy should also take into consideration that higher uncertainties may exist to define exposure and vulnerability than hazard itself (APEL et al., 2009; JONGMAN et al., 2012; SCHRÖTER et al., 2014). In the case of river structures such as reservoirs and levees, acceptable estimation errors tend to be small (i.e. few centimeters). In the United States, for example, levees are only allowed to be constructed if a local water level increase smaller than 30.5 cm (1 feet) is estimated for a 100-year flood (HEINE; PINTER, 2012). In turn, for studies related to water quality and biogeochemical cycles (carbon, nitrogen, phosphorus), it is understood that important retention occurs in very small water bodies as lakes, reservoirs and wetlands (BOUWMAN et al., 2013), so that this small scale features should be well represented in hydrodynamic models. The same occurs when analyzing sediments with relevant small scale processes such as sediment trapping, river bank erosion and bed load transport (BIERKENS et al., 2015). For water quality and sediments, small bias (< 10%) and a satisfactory dynamics (e.g., by adopting correlation coefficient values>0.8) of discharge, velocity and residence time should be pursued. For climatic and environmental impacts studies, the models should attain errors smaller than the magnitude of changes (e.g., smaller than the estimated increase in discharge under climate change). For studies focusing on comprehension of hydrologic and hydrodynamic processes (Fleischmann et al., 2018; Paiva et al., 2013), models should have errors smaller than the physical signals (e.g., smaller than water level amplitude along a floodplain if analyzing this variable).

The second requirement is related to the capacity of locally developed hydrodynamic models (i.e., state-of-the-art models as 1D or 2D HEC-RAS set up with detailed cross sections) in representing local features – this would be the maximum attainable performance for global models. Studies in the literature suggest that reach scale models obtain water level errors (RMSE) typically between 0.1 and 0.4 m (ADAMS; CHEN; DYMOND, 2018; ALTENAU et al., 2017; APEL et al., 2009; BERMÚDEZ et al., 2017; FEWTRELL et al., 2011; MATGEN et al., 2007; RUDORFF; MELACK; BATES, 2014), what may differ if the assessed RMSE metric refers to at-a-station water level series, water depth/level maps or longitudinal level profiles. For flood extent, the F fit metric has typical values above 65 % (ALTENAU et al., 2017; HORRITT; BATES, 2002; TAYEFI et al., 2007), depending on the floodplain geomorphology (HUNTER et al., 2007). The assessment of simulated discharge performance depends on the goal of the study (minimum, mean, maximum flows), but using the commonly adopted Nash-Sutcliffe metric one could argue that a 0.9 value could be a locally relevant threshold (Bermúdez et al., 2017; Moriasi et al., (2015) suggest a very good NSE above 0.8).

Lastly, global/regional model errors should be at the same magnitude of observation uncertainties, since it is not possible to reduce model errors for values below observation errors (i.e., models should be accepted within a range of observation uncertainty; McMillan et al., (2018); Schumann et al., (2008)). It is typically accepted that water level observation errors are much smaller than discharge ones, typically less than a few centimeters (DI BALDASSARRE; MONTANARI, 2009; TODINI, 2018). In turn, discharge observation errors depend on the employed method. Velocity-area methods may have 8-20 % errors in relation to the discharge value (PELLETIER, 1988), or errors below 5 % with ADCP measurements (HERSCHY, 2014). High uncertainty (estimated at 6.2 % - 42.8 % by Di Baldassarre and Montanari (2009)) occurs when using rating curves to estimate discharge from observed water level, especially when high flow extrapolation is performed (DI BALDASSARRE; MONTANARI, 2009; DOMENEGHETTI; CASTELLARIN; BRATH, 2012; DOTTORI; MARTINA; TODINI, 2009). In turn, flood extent mapping is subjected to errors associated with image-processing and classification methods, the physical principle itself (e.g., optical, passive and active microwave sensors) and the image spatial/temporal resolution (SCHUMANN et al., 2009), and the necessity of including the uncertainty of binary flood maps in model calibration/validation (e.g., through a fuzzy membership approach for image classification; Pappenberger et al., (2006)) has been discussed in the literature (HORRITT, 2006; PAPPENBERGER et al., 2006, 2007; SCHUMANN et al., 2008, 2009). Classification accuracies (usually defined as the percentage of total area with omission errors) rarely exceed 90 % for Synthetic Aperture Radar (SAR) datasets (SCHUMANN; MOLLER, 2015). Hess et al. (2003) reported, for a classification of JERS SAR images in the Amazon basin, accuracies higher than 90 % for open water but between 56 % and 87 % for vegetated flooded areas, and Clement et al. (2018) presented a SAR classification technique validated for floods in Yorkshire (UK) with an accuracy higher than 71.5 %.

From the above discussion, it is rather complicate to define a threshold for locally relevant estimates, being an open and interesting discussion in the scientific community. However, it is proposed here that water level RMSE values above 0.4 m, discharge NSE above 0.9, and *F* values above 65 % may be suitable thresholds to evaluate global/regional models, especially for flood studies.

Table 10.2. Summary of the proposed requirements to define whether a river hydrodynamic model provides locally relevant estimates.

Variable/process of interest	Locally relevance requirements
1) Accuracy requirements for particular applications	
a) Flood forecasting	Satisfactory discharge (e.g., NSE>0.9) and water level (e.g., RMSE < 10 cm) for very short lead times
b) Flood risk analyses	High accuracy (>90%) in flood mapping and low

	RMSE for water level (< tens of cm)
c) Effects of hydraulic structures	Low RMSE for water level (< tens of cm)
d) Sediments, water quality and biogeochemical cycles	Small bias (< tens of %) and satisfactory dynamic (high correlation coefficient, e.g., r>0.8) for discharge, velocity and residence time
e) Climatic and environmental impact studies	Error smaller than magnitude of changes
f) Hydrodynamic processes studies	Error smaller than physical signal
2) Typical reach scale HD models errors	
a) Discharge	NSE > 0.9 (hydrographs)[1]
b) Water level	RMSE < 0.4 m (water level profile, water level time series, water depth maps)[2]
c) Flood extent	F > 65% (binary flood maps)[3]
3) Observation uncertainties	
a) Discharge	Error up to ~40% for extrapolation with rating curves[4]; less than 5% with ADCP measurements[5]
b) Water level	Error < 5 cm[6]
c) Flood extent	Accuracy > 55% for vegetated flooded area but higher than 90% for open water; it depends on image processing and classification methods, physical principle, spatial/temporal resolution[7]

[1]Bermúdez et al., 2017; Moriasi et al., 2015.

[2]Adams et al., 2018; Altenau et al., 2017; Apel et al., 2009; Bermúdez et al., 2017; Fewtrell et al., 2011; Matgen et al., 2007; Rudorff et al., 2014.

[3] Altenau et al., 2017; Horritt and Bates, 2002; Tayefi et al., 2007.

[4]Di Baldassarre and Montanari, 2009; Schumann et al., 2009,Domeneghetti et al., 2012; Dottori et al., 2009

[5]Herschy, 2014

[6]Di Baldassarre and Montanari, 2009; Todini, 2018

[7]Hess et al,. 2003; Schumann et al., 2009; Schumann and Moller, 2015; Clement et al., 2018.

10.4.2 How locally relevant are the regional to global hydrodynamic model estimates?

Assuming the HEC-RAS model as a reference benchmark, it was compared to the global, regional and local MGB versions in order to understand to which degree can these models' estimates be trusted. Since calibrated rainfall-runoff parameters were adopted, and not global or regional runoff fields which are typically not calibrated and present important biases (Siqueira et al., 2018), results point to the maximum potentiality of the current hydrodynamic models.

The global MGB model has limitations in accurately estimating discharge and water levels (absolute values and anomalies), due to the coarse DEM (SRTM 500 m), the adopted reach length (15 km) and the cross section with relatively small bankfull depth values from the global database. These factors had different effects on each variable (water level anomaly was mainly improved with better cross sections). Locally relevant estimates (NSE > 0.9, RMSE < 0.4 m and F > 65%) could only be attained with the global approach for water level anomalies in certain sections along the basin, while this was not the case for discharge, absolute water level and flood extent. On the other hand, its performance was relatively satisfactory for discharges and water level anomalies from a global model perspective (i.e. for global assessment of water fluxes), with NSE>0.6 for most cross sections along Itajaí-Açu mainstem. Peak discharge differences between local and global models and HEC-RAS ranged from 2 % to 12 % in Rio do Sul and 3 % to 20 % in Blumenau location, what may be deemed satisfactory if compared to 5 % - 40 % uncertainties in observed discharges and rating curves (DI BALDASSARRE; MONTANARI, 2009; DOMENEGHETTI; CASTELLARIN; BRATH, 2012; DOTTORI; MARTINA; TODINI, 2009; PELLETIER, 1988).

Moving towards regional modeling approaches (i.e., higher resolution DEM, regionally derived cross section parameters and finer resolution computation units and reach lengths), results outperformed the global model for most analyzed variables, although only discharge could be deemed as locally relevant basin-wide with the regional model (NSE>0.9). In turn, the local MGB model satisfactorily represented the water longitudinal profile (or water slope) in the analyzed Itajaí-Açu and Trombudo rivers, which is an interesting signature of river hydrodynamics (GARAMBOIS et al., 2017), but it also could not lead to estimates with local relevance (RMSE of 2.1 m, smaller than the proposed threshold of 0.4 m). None of the MGB model versions yielded locally relevant estimates of flood extent. Improving reach lengths to 1 km led to the best F values of 51 % on average (despite the global cross section scenario, which led to exaggerated water depths and flooding but a satisfactory yet meaningless F), that may indicate the necessity of better representing local hydrodynamic features. Moving towards 2D modeling may also be relevant (ALTENAU et al., 2017). Comparisons between global hazard models' estimates with locally developed hazard maps reported F values between 45 % and 65 % for European rivers (ALFIERI et al., 2013), 59 % – 65% for Canadian rivers (SMITH; SAMPSON; BATES, 2015), 50 % - 55 % for United States nationwide FEMA flood hazard maps (WING et al., 2017) and 51 % - 90% for selected, high-quality United States USGS flood hazard maps (WING et al., 2017).

A reach length of 15 km yields poor results of water level profile in the Itajaí-Açu basin. Global hydrodynamic models use reach lengths even higher than this value (Yamazaki et al., 2013; Siqueira et al., 2018). While large lengths could increase numerical instabilities or numerical diffusion, their decrease would lead to much more computational units, what may be soon feasible under increasing computation power.

An interesting conclusion of this study is that the DEM source (SDS: 0.39 m vertical accuracy; and SRTM: 6.2 m at 90 m resolution, Rodríguez et al., (2006)) was less important than DEM spatial resolution (30 m and 500 m) and reach length (especially for larger reach lengths as 15 km). Speckhann et al., (2018) obtained similar conclusions for the SDS HAND based map in some cities of the Itajaí-Açu basin. This may be explained by the 1D nature of the simulations performed in this study, which integrate for each unit-catchment the DEM based floodplain topography. In turn, 2D simulations tend to be more sensitive to DEM quality and to local scale features (SMITH et al., 2018).

An important hydrodynamic factor that differentiates the local HEC-RAS model from the MGB versions is the representation of hydraulic controls such as rapids, waterfalls or channel constraints in the former, what may play an important role even in large rivers hydrodynamics (FRASSON et al., 2017; GARAMBOIS et al., 2017; O'LOUGHLIN et al., 2013). In the Itajaí-Açu basin, for example, important controls occur downstream of Rio do Sul city and along most of the basin, generating backwater effects and controlling upstream hydrodynamic processes. In regional modeling approaches, such local features (i.e. at scales smaller than a 1 km reach) are not fully represented. In this context, further research could be developed to infer the optimum reach length for regional models that best represents local features, similar to the hydraulic visibility concept proposed by Garambois et al. (2017), which aimed to assess the potential of satellite altimetry tracks to describe local hydraulic features (e.g., changes in water level slopes). It could also build upon the guidelines by Samuels (1990) and Castellarin et al., (2009) on the optimal location and spacing of cross sections, or on the suggestion by Grimaldi et al. (2018) for estimating river width values from remote sensing imagery near particular geomorphologic features.

The local MGB modelling approach involved inserting the surveyed cross sections through their bankfull width, effective bankfull depth (i.e., wetted area divided by bankfull width) and bank elevation values. The approximation of rectangular cross sections was adopted, which is a common assumption in large scale hydrodynamic models (Neal et al., 2012; Paiva et al., 2013; Schumann et al., 2016; Trigg et al., 2009), and this seemed to be satisfactory to estimate water levels. Indeed, many Itajaí-Açu sections tend to be relatively rectangular, and recent studies have showed the capacity of rectangular channels to simulate flooding processes (FEWTRELL et al., 2011; GRIMALDI et al., 2018; TRIGG et al., 2009). One further possibility would be to use the cross section hydraulic radius within the model (Neal et al., 2012), or by using an effective channel shape parameter (GRIMALDI et al., 2018; NEAL et al., 2015). For locally relevant estimates, a correct cross section shape plays a major role on flood

wave propagation and definition of the outflow hydrograph shape in general (COLLISCHONN et al., 2017; MEJIA; REED, 2011). In the case of regional and global models, the global database by Andreadis et al. (2013) provided a satisfactory bankfull width estimate, but an underestimated depth which lowered the global model performance, while the regional based one proved reasonable for both variables. Also, bank elevation estimation from average SRTM pixels above river pixels implies that bankfull depth becomes an effective parameter, since the estimated elevation represents the water level at the moment of SRTM shuttle passage. This explains why an intermediate bankfull depth between global and local estimates led to an optimum flood extent.

Assuming the 1D HEC-RAS simulations as a proxy of locally relevant hydrodynamic variables is reasonable given the widespread use of this software in practical, reach-scale engineering studies. The large number of surveyed cross sections (620) used in the Itajaí-Açu basin and the high density in some relevant urban centers (e.g. Rio do Sul and Itajaí cities) points to a higher confidence in the HEC-RAS estimates. In the case of Itajaí-Açu basin, flow tends to be 1D with storage zone floodplains along the channel mainstem for most basin but the downstream Itajaí city region. In the urban areas of the lower Itajaí-Açu, floods occur rather in a 2D flow pattern and current modeling developments point towards efficient 2D numerical simulations, with new software's like HEC-RAS 2D and LISFLOOD-FP (BATES; DE ROO, 2000; NEAL; SCHUMANN; BATES, 2012), although this is not still the reality in practical hydrologic engineering especially in developing countries. On the other hand, studies diverge on the comparison between 1D and 2D hydrodynamic models, and 1D models have been proven to perform satisfactorily if detailed topography is available (COOK; MERWADE, 2009; HORRITT; BATES, 2002). Hodges (2013) suggests that a complementary strategy between 1D, 2D and 3D approaches should be pursued. Furthermore, model structure differences between MGB and HEC-RAS did not seem very relevant, i.e. active (HEC-RAS; floodplain Manning's n set as 0.1) and inactive floodplains (MGB), and full Saint-Venant (HEC-RAS) and inertial equations (MGB; based on Bates et al., (2010)). Floodplain attenuation with MGB local version was very similar to HEC-RAS when discharges were compared, and indeed past studies showed small hydrodynamic model sensitivity to floodplain friction in 2D models (HORRITT; BATES, 2002). Differences between the two numerical solutions were evaluated by Fan et al., (2014) in a variety of channel geometries and were also considered small.

10.4.3 Perspectives on the improvement of regional/global hydrodynamic models

This study outcomes can be used to suggest directions for the improvement of regional and continental models. In hydrodynamic modeling (i.e., open channel and

floodplain flows), the physics is relatively well known (HODGES, 2013), but the use of regional to continental models for local scale estimates is still hampered by many difficulties as highlighted in this study, e.g., imperfect cross sections and coarse resolutions. On the other hand, to a certain spatial scale, all models will be rejected (SCHUMANN et al., 2008), and there must be taken into account the tradeoff between resolution and accuracy in hyper-resolution models (BIERKENS et al., 2015; DOTTORI; DI BALDASSARRE; TODINI, 2013), and the epistemic uncertainty that arises when moving towards local scales.

Cross section parameterization. From this study's results, the largest gain towards locally relevant water levels would be obtained by using better cross sections parameters, with more correct estimates of bankfull width and depth and bank elevation values at the basin scale. An interesting perspective in this context relates to low-cost remote sensing datasets (BATES et al., 2014; SCHUMANN et al., 2009; YAN et al., 2015) and its assimilation in hydrodynamic models to estimate cross section geometry and water levels (Durand et al., 2008; Paiva et al., 2013; Tourian et al., 2017; Yoon et al., 2012), as well as for model calibration and validation (Fleischmann et al., 2018; Paiva et al., 2013; Siqueira et al., 2018). Future missions such as SWOT (BIANCAMARIA; LETTENMAIER; PAVELSKY, 2016) and ICE-SAT 2 (ABDALATI et al., 2010) promise to bring more valuable altimetry information to models. Satellite imagery processing and classification of water masks seem to be the natural way forward to estimate basin scale river widths (PAVELSKY; SMITH, 2008; PEKEL et al., 2016; YAMAZAKI et al., 2014a). Alternatively, new robust methods for estimating regional geomorphic relationships are welcome. In this case, one should be careful when selecting in situ cross sections to derive these relations. For example, in many ungauged basins there is availability of local cross sections only for the locations of water level gauges, which tend to be located in incised valleys and may not be representative of the whole reach (MEYER et al., 2018). Trigg et al., (2009) and Domeneghetti (2016) present HEC-RAS based comparisons and suggestions of regional-like estimates of channel cross section with better bathymetry datasets.

Computational power. Improving simulation time (e.g., for floor forecasting) and computational storage capacity (for instance, to allow the simulated reach lengths to be decreased) is also a major concern to foster regional to continental hydrodynamic models. Today it is extremely tough to use high resolution products as the 1 m SDS DEM for a whole basin due to insufficient computational power, and the community should move toward new methods that can deal with too much topographic data (GOMES et al., 2015; HODGES, 2013). On the other hand, the presented HEC-RAS model application at large basin scale with more than 600 in situ cross sections is uncommon in literature. With recent computational power, there a few examples of HEC-RAS applications at large scales (in contrast to typical reach scale ones) with complex drainage network which are encouraging for improved flood estimation. These include HEC-RAS applications in the Ohio river basin for flood forecasting with over 3100 cross sections and a large number of lateral structures and storage areas (ADAMS;

CHEN; DYMOND, 2018), and simulation of the Brazilian Pantanal and the Ganges-Brahmaputra-Meghna Delta in Bangladesh with 340 (BRAVO et al., 2012; PAZ et al., 2010) and 226 locally surveyed cross sections (SIDDIQUE-E-AKBOR et al., 2011), respectively. Recent advances now enable the control of HEC-RAS inputs, runs and output post-processing with automated routines in MATLAB (LEON; GOODELL, 2016) and other programming languages, avoiding the time consuming process to deal with hundreds of cross sections in HEC-RAS (PAZ et al., 2010).

Digital Elevation Models. Although in this study the 1D model outputs proved the SRTM DEM to be satisfactory in comparison to SDS DEM, higher quality DEM's are required for local scale flood mapping, and recent advances are encouraging (e.g., Yamazaki et al., 2017). In turn, while flood defenses are not common in the Itajaí-Açu basin, it is recognized that the incorporation of flood defenses is a major challenge for global models to provide local estimates (DE MOEL et al., 2015), and there is a demand for improving global datasets of such structures. Regarding model structure, moving towards 2D simulation at continental to global scales is very promising, especially for flood hazard estimation, while coupling hydrologic and hydrodynamic processes seems to be relevant in region with intense feedbacks between them (e.g., wetland evapotranspiration and regional climate feedbacks in large wetlands, Bierkens, 2015; semi-arid basins, Fleischmann et al., 2018).

Necessity of cross-scale comparisons. Cross-scale assessments are required, together with comparisons between global models and local inundations maps (ALFIERI et al., 2013; SAMPSON et al., 2015; WING et al., 2017). While in hydrologic modeling such comparisons and discussions are common (ARCHFIELD et al., 2015; BLÖSCHL; SIVAPALAN, 1995; HATTERMANN et al., 2017; KUMAR; SAMANIEGO; ATTINGER, 2013; SAMANIEGO et al., 2017), this is not the case among river hydrodynamic models (HODGES, 2013), certainly because continental hydrodynamic models are still in their infancy (WARD et al., 2018). The importance of comparing global flood models were highlighted by the Global Flood Partnership (TRIGG et al., 2016), and, recently, Hoch and Trigg (2018) proposed a general framework to consistently evaluate global flood models, considering different model validation and benchmarking strategies. In a near future, global models could adopt the regional approaches presented in this study, largely improving its estimates toward locally relevant ones. Methods to upscale local estimates of river hydrodynamic parameters (e.g., cross section and roughness) to coarse scale models in order to achieve coherent fluxes at all scales are also welcome (e.g., Samaniego et al., (2017)). A recent comparison between six global flood models by Trigg et al., (2016) and Bernhofen et al., (2018) showed major mismatches between them in estimating flood extent in Africa. Discrepancies occurred mainly due to different model structures, while spatial resolution was not a major driver. More cross-scale evaluations could improve our understanding of the factors driving the differences among these models. For example, by comparing global and local models' results at the unit-catchment/cross section (local) scale, with this study it was possible to understand in which parts of the basin

there was higher confidence in the local level estimates, which is important since certain locations in the floodplain (e.g., an industrial park) will be more relevant for a particular evaluation (PAPPENBERGER et al., 2007). In terms of modeling strategy, Siqueira et al., (2018) compared a bottom-up approach (i.e. applying a model initially developed for basin scales to a whole continent domain) with a top-down one (i.e. evaluating continental scale estimates from global models), and discussed the complementary strategies that could be used towards more satisfactory estimates, e.g., by using regional expert knowledge from the bottom-up approach into the top-down one. In this study, a first-of-its-kind comparison was performed between local (detailed HEC-RAS or local based MGB hydrodynamic model) and regional/continental models (global and regional based MGB models) to investigate the limits of each model.

10.5 Conclusion

This study presented a cross-scale comparison of continental, regional and local hydrodynamic modeling approaches based on the MGB large scale hydrologic-hydrodynamic model. A detailed HEC-RAS model with 620 in situ cross sections and covering over 900 km of river reaches in the Itajaí-Açu river basin in Southern Brazil was firstly set up. Then, it was used as a reference to evaluate how much those model configurations can represent HEC-RAS estimates (discharge, water levels and flood extent). Three main requirements were proposed to define whether a hydrodynamic model yields locally relevant estimates, which may be used for future regional/global model evaluations: the model errors should be equal or smaller (i) than the accuracy requirement for a particular application and location, (ii) than typical local, reach scale models' errors, and (iii) than observation uncertainties. Then, main conclusions of this study are:

- Global river hydrodynamic models have important limitations in attaining locally relevant estimates, but by moving toward more regional methods (e.g., regionally based cross sections) they can provide satisfactory water level amplitude and discharge at local scales;
- Investing in locally based methods of cross section estimation (e.g., with satellite altimetry assimilation) is interesting to improve global hydrodynamic models, and seems to be more interesting than improving DEM quality (especially for 1D models);
- Moving towards local approaches, by refining reach lengths and DEM and by using locally surveyed cross sections, could improve water level estimates (basin-wide average RMSE of 2.1 m in comparison to 4.4 m with regional approach and 26.1 m with the global one);
- Long reach lengths (e.g., 15 km) may be unsuitable to represent discharges and water levels in basins like the Itajaí-Açu river basin (15,000 km²), especially for steep reaches, and adopting 1 km and 5 km lengths are preferable;

- For estimating flood extent, the local model yielded better estimates for the Rio do Sul city location (average F = 52 %), while for Itajaí city global, regional and local models led to similar results (F between 36 % and 41 %). The overall low F values suggest a difficulty of continental and regional models to infer flood extent at local scales;
- The assessment of global/regional models at cross section/unit-catchment scale, as performed in this study, provides an interesting picture of the model capacity to represent local hydrodynamic features as backwater effects, and evaluation of longitudinal water level profiles may assist this analysis.

Finally, cross-scale comparisons are fundamental to understand how far can current state-of-the-art river hydrodynamic models go and to which direction should we move to in future developments. We hope this study provides new insights on the ways forward for regional to global models.

11 Regional scale hydrodynamic modeling of the river-floodplain-reservoir continuum

This chapter is presented as a research article, which was published in Journal of Hydrology:

- Fleischmann, A.S., Brêda, J.P.F., Passaia, O.A., Wongchuig, S.C., Fan, F.M., Paiva, R.C.D., Marques, G.F., Collischonn, W., 2021. Regional scale hydrodynamic modeling of the river-floodplain-reservoir continuum. Journal of Hydrology 596, 126114. https://doi.org/10.1016/j.jhydrol.2021.126114

11. Modelagem hidrodinâmica do continuum rio-reservatório-planície de inundação em escala regional

Planícies de inundação e reservatórios interagem ao longo da rede de drenagem de uma bacia hidrográfica, definindo um sistema homem-água acoplado com múltiplas interações. Recentes desenvolvimentos de modelagem têm focado na melhoria da representação de tais processos em escalas regional a continental. No entanto, a maioria dos modelos hidrológicos de grande escala adotam esquemas simplificados de reservatórios (esquemas concentrados), onde uma rotina off-line é forçada com afluências estimadas pelo modelo hidrológico, com uma consideração limitada da complementaridade entre planícies de inundação e reservatórios na atenuação de cheias em escala regional. Este estudo apresenta uma nova abordagem que acopla modelos hidrológico e hidrodinâmico do sistema rio-reservatório-planície de inundação, melhorando significativamente a representação da dinâmica e operação de reservatórios ao longo do continuum rio-reservatório-planície de inundação em grandes escalas e múltiplas cascatas de barragens. O modelo é aplicado à bacia do rio Paraná, com uma simulação explícita de 31 grandes barragens. Três tipos de representação da batimetria de reservatórios são comparados, de métodos concentrados a distribuídos, em combinação com três tipos de esquemas de operação de reservatórios e diversos tipos de dados de entrada, além de dois cenários de parametrização (global e regional). Os esquemas de operação foram mais relevantes que a representação da batimetria dos reservatórios para estimar vazões e níveis a jusante de barragens. Enquanto o esquema de operação de reservatório baseados em dados (data-driven), utilizando regressões lineares entre observações de níveis e defluências de barragens, geraram as melhores estimativas tanto de volume ativo quanto de vazões, a operação mais genérica estimou vazões e atenuação de picos de forma razoável, embora não tão satisfatório para volume ativo. A parametrização global da operação de reservatórios resultou em uma pior performance se comparada à versão regional, mas modelou de forma satisfatória as vazões e a atenuação de picos. Em relação à representação da batimetria de reservatórios, uma comparação em escala de bacia dos esquemas concentrado e distribuídos indicaram a inabilidade do primeiro de representar efeitos de remanso. Isto foi corroborado também através da validação do perfil longitudinal dos níveis d'água do reservatório de Itaipu com dados de altimetria espacial da missão ICESat. Por fim, o modelo desenvolvido foi utilizado para mostrar a complementaridade entre planícies de inundação e reservatórios na atenuação de cheias em escala regional. Modelos de grande escala deveriam ir além das estratégias tradicionais de acoplamento off-line, e incluir esquemas de operação de reservatórios que sejam baseados em dados (data-driven), em combinação com uma representação distribuída da batimetria dos reservatórios dentro de esquemas hidráulicos de rio-planície de inundação. Esta estratégia vai melhorar a estimativa de vazões, níveis d'água e armazenamento de água em escala de bacia, e portanto a capacidade dos modelos em representar o continuum rio-reservatório-planície de inundação em escala regional.

Este capítulo é apresentado na forma de um artigo científico, publicado no periódico Journal of Hydrology:

- *Fleischmann, A.S., Brêda, J.P.F., Passaia, O.A., Wongchuig, S.C., Fan, F.M., Paiva, R.C.D., Marques, G.F., Collischonn, W., 2021. Regional scale hydrodynamic modeling of the river-floodplain-reservoir continuum. Journal of Hydrology 596, 126114. https://doi.org/10.1016/j.jhydrol.2021.126114*

Abstract

River floodplains and reservoirs interact throughout a basin drainage network, defining a coupled human-water system with multiple feedbacks. Recent modeling developments have aimed to improve the representation of such processes at regional to continental scales. However, most large-scale hydrological models adopt simplified lumped reservoir schemes, where an offline routine is run with inflows estimated by the model, with limited consideration of the complementarity between floodplains and reservoirs on attenuating floods at regional scale. This paper presents a novel approach that fully couples river-floodplain-reservoir hydrodynamic and hydrological models, significantly improving the representation of reservoir dynamics and operation in the river-floodplain-reservoir continuum at large scale and across multiple dam cascades. The model is applied to the Paraná River Basin with explicit simulation of 31 large dams and river hydraulic variables at basin scale. Three types of reservoir bathymetry representation are compared, from lumped to distributed methods, combined with three reservoir operation schemes and varying degrees of input data requirement within two parameterization scenarios (global and regional setups). The operation schemes were more relevant than the reservoir bathymetry representation to estimate downstream flows and water levels. While the data-driven operation scheme, based on linear regressions between observed water levels and dam outflows, provided the best estimates of both active storage and discharges, the more generic operation reasonably estimated discharges and peak attenuation, albeit not as accurately for active storage. The global parameterization of reservoir operation resulted in poorer performance compared to the regional-based one, but it satisfactorily modeled discharge and peak attenuation. Regarding the reservoir bathymetry representation, a basin scale comparison of the lumped and distributed schemes indicated the inability of the former to represent backwater effects. This was further corroborated by validating the longitudinal water level profile of Itaipu dam with ICESat satellite altimetry data. Finally, the model was used to show the complementarity between floodplains and reservoirs on attenuating floods at regional scale. Large scale models should move beyond offline coupling strategies, and include regional-based, data-driven reservoir operation schemes together with a distributed representation of reservoir bathymetry into river-floodplain hydraulic schemes. This will largely improve the estimation of river discharges, water levels and flood storage, and thus the model ability to represent the regional scale river-floodplain-reservoir continuum.

11.1 Introduction

Reservoirs are important infrastructure for energy production, flood control, flow regulation and water supply, among other uses (Lehner et al., 2011). Their construction and operation have also led to major socio-environmental concerns (GRILL et al., 2019;

NILSSON, 2005; POFF et al., 2010; RICHTER; THOMAS, 2007), and efforts to improve storage allocation (ALMEIDA et al., 2019; HO et al., 2017; SCHMITT et al., 2019). Reservoirs, however, operate in basins with a continuum in the river system connecting it to rivers and floodplains, through which human societies and ecosystems interact with dynamic two-way feedbacks (DI BALDASSARRE et al., 2013; PANDE; SIVAPALAN, 2017; VIGLIONE et al., 2014). At regional to continental scales, this river-floodplain-reservoir continuum is associated to a complex relationship among surface water processes. For example, in the La Plata River Basin in South America, dozens of large reservoirs have been built since the 1950's interacting with complex wetland systems as the Pantanal, Esteros del Iberá and Paraná floodplains (MINOTTI, 2018). In the basin, human society has settled around floodplains for centuries, leading to a fully coupled human-water system (DOYLE; BARROS, 2011; LEE et al., 2018). As the use and development of the floodplain by society evolve, there is an increasing need to better understand the hydrodynamic interactions in this river-floodplain-reservoir continuum, so we can better design and operate water systems to cope with human and ecosystem demands considering hydrological uncertainty, processes and current and future environmental changes.

Regional to continental scale hydrological-hydrodynamic models provide a unique opportunity to address these needs. While recent advances in large scale modeling have improved our capability to simulate river floods at both 1D and 2D dimensions (Bates et al., 2018; Fleischmann et al., 2020; Neal et al., 2012; Paiva et al., 2013; Schumann et al., 2013; Trigg et al., 2016; Yamazaki et al., 2011), most studies on reservoir simulation have focused on representing dam storage and operation (i.e., a water management model) within simpler hydrological models, with less physically based flow routing methods (DROPPERS et al., 2020; HANASAKI et al., 2018; YASSIN et al., 2019). In the studies by Mateo et al. (2014) and Pokhrel et al. (2018), for instance, a hydrodynamic model was run (offline) with observed or simulated dam outflows at the grid cell related to the dam, in order to estimate alterations in downstream flooding. Difficulties for detailed reservoir simulation included the unknown bathymetry and specific dam operation at very large scales, and are also a challenge.

Only recently the hydrodynamics of dam cascades were explicitly included into regional hydrodynamic models (Shin et al., 2019; Fleischmann et al., 2019a), aiming at representing the river-floodplain-reservoir system with a fully-coupled approach that allowed a distributed representation of variables as discharges, water levels and flood extent and storage in human-altered systems. As the representation of these processes improves, a better and integrated assessment of basin water resources and floods becomes possible. Examples include the understanding of the relative role of floodplains and reservoirs on flood attenuation (Fleischmann et al., 2019a), more detailed simulation of evaporation (SHIN; POKHREL; MIGUEZ-MACHO, 2019), and understanding of the reservoir influence on local climate (DEGU et al., 2011; HOSSAIN et al., 2012). The representation of the reservoir dynamics itself and

associated backwater effects and flooding in upstream areas, and simulation of carbon cycle and phytoplankton dynamics (e.g., lake emissions and degassing or downstream emissions; Bierkens et al. (2015)), can also benefit from such modeling systems. Ultimately, these tools will provide an important basis towards a fully coupled and distributed human-water modeling system within hyperresolution Earth system models (Nazemi & Wheater, 2015; Pokhrel et al., 2016; Wood et al., 2011), adopting detailed grids and daily temporal resolution (Gutenson et al., 2020; Zajac et al., 2017).

Regarding the representation of dam operation in regional to global models, there have been major improvements since pioneering studies by Hanasaki et al. (2006) and Haddeland et al. (2006), which have been used and adapted for many studies (Adam et al., 2007; van Beek et al., 2011; Biemans et al., 2011; Pokhrel et al., 2012; Shin et al., 2019; Wisser et al., 2010). Since these first generic algorithms, data-driven reservoir operation schemes are now feasible, while optimization methods have also been developed, involving storage, outflow and inflow observations (SOLANDER et al., 2016; WU; CHEN, 2012; YASSIN et al., 2019), and downstream water or energy demands (HADDELAND; SKAUGEN; LETTENMAIER, 2006). All these developments highlight the ongoing necessity to better estimate actual reservoir operation in order to achieve hyperresolution models that are locally relevant. Cross-scale comparisons among different approaches, from simpler, globally-based, to more complex, regionally-derived setups, can yield meaningful insights on the ways forward, especially using regionally set up models (Fleischmann et al., 2019c; Nazemi & Wheater, 2015; Trigg et al., 2016).

The need for a fully-coupled approach was explicitly highlighted by some authors (Fleischmann et al., 2019a; Shin et al., 2019). However, the benefits of representing the reservoir dynamics fully coupled within the river-floodplain-reservoir continuum processes with a distributed approach, over the traditional lumped and offline representation, remains a knowledge gap in the field for large scale models. The extent to which simple, level-pool reservoir simulations (i.e., lumped) may lead to similar results as distributed (i.e., dynamic), more complex ones, is not yet understood. Finally, a correct reservoir operation also needs to be incorporated to improve the understanding of the human feedback in the river-floodplain-reservoir continuum.

This study brings a novel contribution to these gaps with an improved representation of the river-floodplain-reservoir interactions within hydrologic-hydrodynamic models, followed by a broad analysis of the continuum of hydraulic variables basin-wide considering the reservoir operation effects. The contributions of this study address three main research questions: (i) what are the differences between simulating lumped and distributed reservoir bathymetry in coarse-scale, online coupled hydrologic-hydrodynamic models, in terms of different variables as water levels, discharge, flood extent and storage, and evapotranspiration? (ii) how do generic and more data-driven reservoir operation schemes differ in terms of hydrological variables estimation in regional scale models? And (iii) what is the relative role of floodplains and reservoirs on flood attenuation in large-scale anthropized systems, considering

basin-wide hydrological processes? To answer these questions, new modeling approaches to improve reservoir representation and operation are proposed and tested in a ~950,000 km² watershed (Upper Paraná River Basin, Brazil). Different simulation scenarios are performed to assess the dynamics of reservoirs in terms of complexity of bathymetry representation (lumped to distributed) and reservoir operation (from generic to data-driven approaches, and from globally to regionally derived parameterizations).

11.2 Methods

11.2.1 Study area: The Upper Paraná River Basin

The Upper Paraná River Basin (Figure 11.1) was selected as a study area given (i) its large number of dam cascades (in parallel and in series); (ii) the existence of large floodplains both upstream and downstream of dam cascades; and (iii) the availability of observed daily time series of dam inflows, outflows and storage from the Brazilian National Water Agency (ANA). Those are desirable characteristics to address in large scale modeling of river-floodplain-reservoir systems.

The Paraná River is formed by the confluence of Grande and Paranaíba rivers in Brazil, with major tributaries being the Tietê, Paranapanema, Ivaí and Iguaçu rivers, all in its left margin. The Upper Paraná River Basin has a drainage area of ~950,000 km² and it is among those with the largest hydropower installed capacity in the world (and almost 50% of the installed hydropower capacity of Brazil), including the Itaipu dam (ID 18 in Figure 11.1) which is one of the largest dams in the world (Itaipu, 2018). Large cities as São Paulo and Brasília (Brazil Federal Capital) are located within the basin, which holds a population of nearly 70 million people. The wet period usually occurs from November/January to May/June (Agostinho et al., 2000), with average annual rainfall of about 1400 mm (BOULANGER et al., 2005). There are contrasting hydroclimatic regions throughout the basin, with the northern (southern) regions presenting a seasonal (non-seasonal) precipitation regime.

The basin has 86 large dams (> 30 MW) in operation, with an installed capacity of 48,083 MW (ANEEL, 2020) (Figure 11.1). There are also 500 (58) small (large) proposed, planned or under construction dams, related to 5,643 (3,909) MW of installed capacity, respectively (ANEEL, 2020). Sixty-two large dams are currently connected to the Brazilian National Interconnected System (SIN), with 32 run-of-river and 30 flow regulation dams (ONS, 2020), which are coordinately operated with other power sources (e.g., thermal and wind) to generate and distribute energy to the whole system minimizing costs (Marques & Tilmant, 2013). Most dams are also operated with multiple uses, such as flood control, water supply and navigation. Overall, there is a

large hydrological alteration at the basin scale due to reservoir operation (SANTOS, 2015). The extensive floodplains throughout the basin, as the 230 km reach in the Paraná mainstem between Porto Primavera and Itaipu dams, harbor important ecosystem services (Agostinho et al., 2001, 2008; Baumgartner et al., 2018).

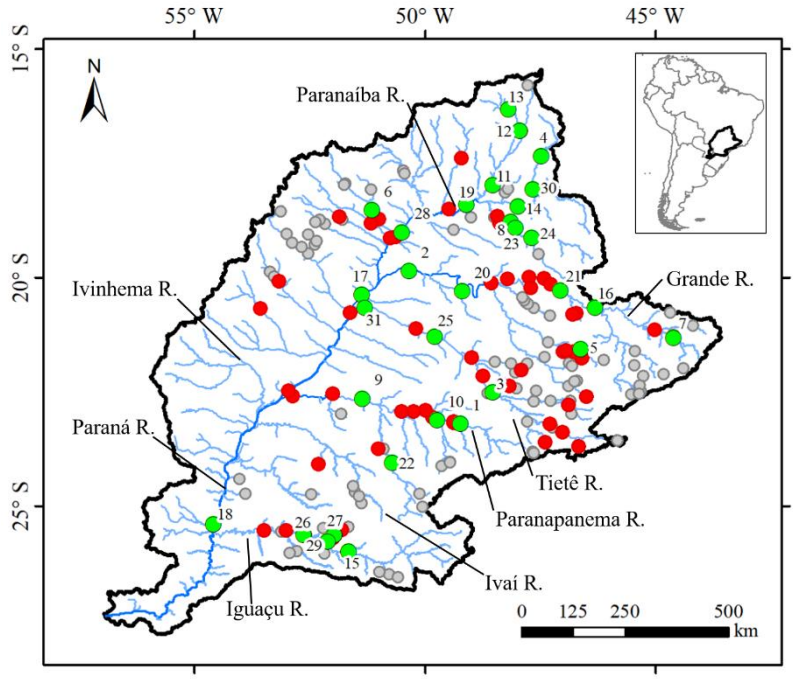

Figure 11.1. The Upper Paraná River Basin within South America, and the 31 simulated (green circles) and other non-simulated Brazilian dams (red: large dams – installed capacity > 30 MW; grey: small dams – capacity between 3 and 30 MW). The total number of large dams is 86 (green and red dots). Rivers of interest are labeled.

11.2.2 Hydrological and hydrodynamic representation of the river-floodplain-reservoir continuum

The MGB model (“Modelo de Grandes Bacias” in Portuguese, an acronym meaning “Model of Large Basins”) (COLLISCHONN et al., 2007; PONTES et al., 2017) is used to implement and test the proposed representation of the river-floodplain-reservoir continuum and reservoir operation. It is a semi-distributed, hydrological-hydrodynamic model developed to simulate large-scale basins. This model is chosen given its proven track record of simulation in several other river basins at different scales, from regional to continental domains (SIQUEIRA et al., 2018). First, the original MGB modeling approach is presented, followed by the proposed improved

representation of the reservoirs and their hydraulic and hydrodynamic relationships with the continuum.

In MGB's representation, the basin is divided into unit-catchments of equal river lengths, and within each the model simulates vertical hydrological processes as evapotranspiration, soil water infiltration and runoff generation (from surface, subsurface and groundwater reservoirs) (Figure 11.2). Local runoff is added as a lateral boundary condition to the drainage network, and a hydrodynamic routing is performed to simulate river, floodplains and reservoirs' surface water dynamics. Soil and vegetation model parameters are defined for each Hydrologic Response Units (HRU's) within a given sub-basin, and the HRU's are derived from a combination of soil and vegetation maps. Evapotranspiration is computed with the Penman-Monteith equation for soil/vegetated areas, and Penman equation for flooded areas (i.e., assumed as open water). A dynamic two-way feedback between the hydrologic and hydrodynamic modules is also considered, by which floodplain water can infiltrate into the unsaturated soil, and evapotranspiration/open water evaporation and runoff generation are dynamically computed considering the surface flooded fraction at each time step. More details on the hydrological model are presented in Supplementary Material S2 and in Collischonn et al. (2007), Pontes et al. (2017) and Siqueira et al. (2018). Recent MGB applications in the Paraná basin with the simpler, Muskingum-Cunge flood routing scheme were performed in Fleischmann et al., (2019b) and Quedi & Fan, (2020).

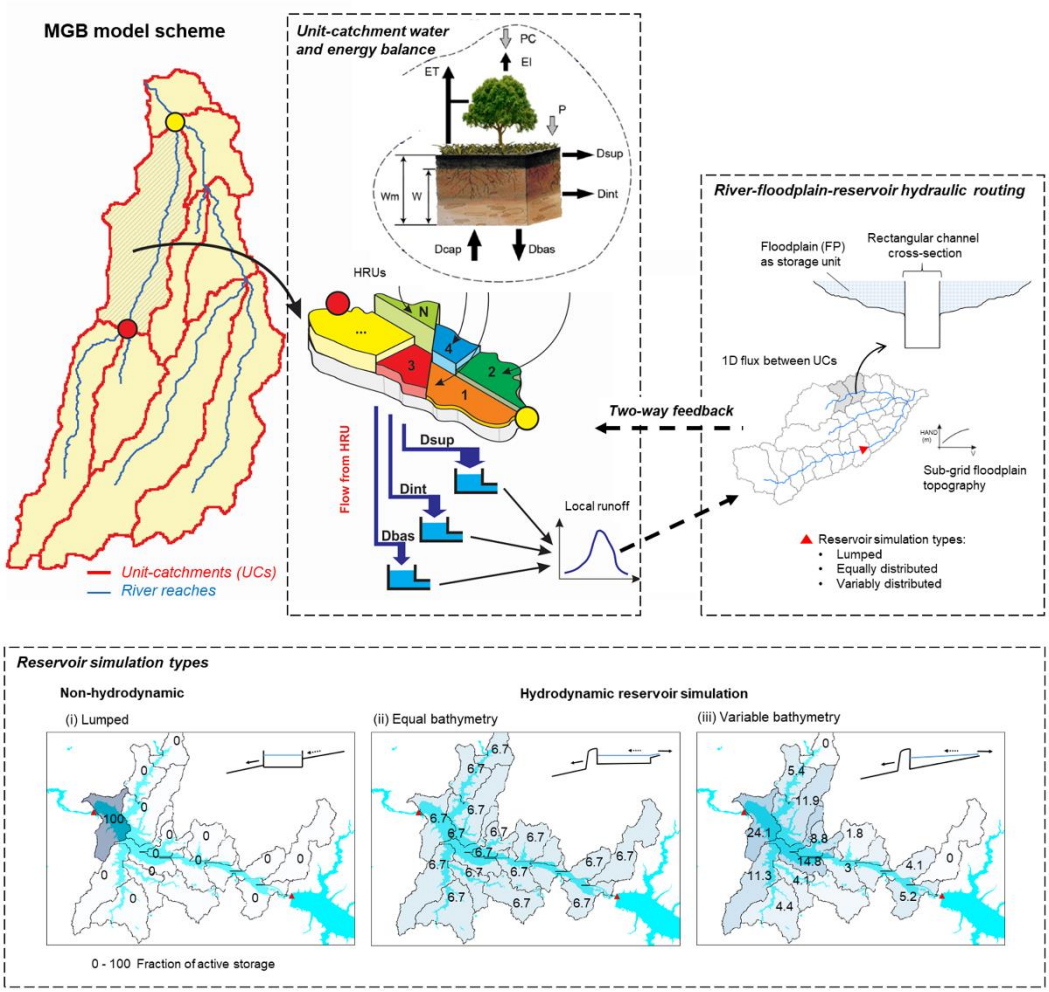

Figure 11.2. Overview of the MGB model structure: unit-catchment water and energy balance (middle panel), river-floodplain-reservoir hydraulic routing (upper right), and types of reservoir simulation (bottom panel).

11.2.3 MGB model river-floodplain hydrodynamic routing

The local inertia explicit method proposed by Bates et al. (2010) is adopted within MGB to simulate 1D flow propagation along the drainage network. This method is a simplification of Saint-Venant equations, neglecting the convective acceleration term from the momentum equation, which has been proven satisfactory to represent flood wave transport along rivers at both 1D and 2D dimensions (Getirana et al., 2017; Neal et al., 2012; Siqueira et al., 2018; Yamazaki et al., 2013). Within MGB, floodplains are represented as storage units, i.e., they are ineffective areas without active flow, river-floodplain water exchange is instantaneous, and water surface elevation is assumed the same along the river-floodplain system within a given unit-catchment

(Paiva et al., 2011). Channel cross sections are assumed rectangular, as typically adopted in large scale hydraulic modeling (Paiva et al., 2013; Trigg et al., 2009).

The flux between two adjacent unit-catchments is computed with the discretized momentum Equation 1:

$$Q_{out,i}^{t+\Delta t} = \frac{Q_i^t - gB_i\Delta t h_i S_i}{1+\frac{g\Delta t|Q_i^t|n^2}{B_i(h_i)^{7/3}}}$$

Equation 1

Where $Q_{out,i}^{t+\Delta t}$ is the discharge at unit-catchment i at time $t+\Delta t$, n is the Manning's coefficient, h_i the flow depth between unit-catchments i and $i+1$, S_i the water surface level slope, Δt the model time step, B_i the flow width, and g the gravitational acceleration.

The continuity equation can be approximated for each unit-catchment river reach as:

$$\frac{V_i^{t+\Delta t} - V_i^t}{\Delta t} = \sum Q_{in,i}^{t+\Delta t} - Q_{out,i}^{t+\Delta t} + Q_{local} + P_i - E_i$$

Equation 2

Where V is the stored volume in unit-catchment i, $\sum Q_{in,i}^{t+\Delta t}$ the sum of inflows from upstream unit-catchments, Q_{local} the locally generated runoff, P the precipitation over flooded areas (i.e. river reach surface area plus flooded floodplain or reservoir area), and E the flooded area open water evaporation computed with Penman equation.

Once the unit-catchment volume is updated with (2), water level in the unit-catchment is estimated from its level-volume relationship (hypsometric curve). For stages below bank elevation, this is derived from the channel cross section. For stages above bank elevation, it represents the floodplain topography, and it is obtained with a GIS pre-processing step that computes flooded areas associated to increments in Height Above Nearest Drainage values (HAND; Rennó et al. (2008)) extracted from the SRTM Digital Elevation Model (DEM) (Siqueira et al., 2018).

Effective hydraulic parameters that are required for each river reach are channel bed elevation, cross section bankfull width and depth, and Manning roughness coefficient. Bed elevation is derived for each unit-catchment from the average DEM river network pixels (Siqueira et al., 2018) subtracted by bankfull depth. The hydrodynamic routing time step is determined by the Courant-Friedrichs-Levy condition with an additional multiplier parameter for ensuring model numerical stability (BATES; HORRITT; FEWTRELL, 2010; YAMAZAKI et al., 2011).

11.2.4 Reservoir routing

Two main aspects differ the proposed improved reservoir representation from the original MGB river-floodplain routing scheme. First, at the unit-catchment corresponding to the dam location, the momentum equation (1) is replaced by the dam outflow equation (i.e., it is set as an internal boundary condition), which is based on simple spillway or outlet works equations, or on more complex reservoir operation derived from actual dam operational data.

Second, the reservoir storage (and bathymetry) is represented in MGB by adjusting the level-volume relationship in the unit-catchments located within the reservoir lake, originally extracted from a DEM. If the dam did not exist during the DEM acquisition date, the storage is already represented in the level-volume relationships, and thus no correction is necessary. In such cases, it is only required to define the dam outflow equation. On the other hand, if the reservoir already existed, the DEM will likely miss the storage representation (depicting a flat lake area instead). This demands additional bathymetry information (e.g., reservoir level-storage relationships) to correct the model. These two main aspects were added to the MGB framework by Fleischmann et al. (2019a). Open water evaporation and direct precipitation on lake are considered in the same way as for floodplain areas.

In the improved reservoir representation proposed in this paper, this scheme is further developed by comparing different types of reservoir bathymetry representation (Section 11.2.5) and operation (Section 11.2.6), which are detailed in the next sections.

11.2.5 Reservoir storage representation

To improve reservoir storage representation, three different types of reservoir storage/bathymetry representation are compared: (i) a lumped representation of the reservoir storage, by which all storage is concentrated in one only unit-catchment (associated to the dam location), and a distributed method in which the storage is (ii) equally and (iii) variably split among all unit-catchments that compound the reservoir lake, thus allowing the representation of reservoir dynamics. Figure 11.2 (bottom panel) presents the schemes for the three simulation methods.

The lumped method (i) (“Lum”) consists of concentrating the reservoir stage-volume curve (in this study, provided by the Brazilian National Electric System Operator - ONS) on the unit-catchment holding the dam location. This method is analogous to a level-pool routing method, used in simpler reservoir routing schemes and mainly assuming a horizontal water surface along the reservoir. This approaches a dynamic method (ii and iii) if reservoir length is short, depth is large, inflow hydrograph volume is large, and inflow hydrograph time of rise is long (FREAD, 1992). Unit-

catchments along the reservoir lake are considered as a river with rectangular cross section, and the downstream boundary condition at the dam location is considered as a simplified uniform flow (a local average slope was adopted in this case).

The equal bathymetry method (ii) ("Eq") consists of equally distributing the volume through the unit-catchments that composes the reservoir. For each level, the reservoir water surface area is equally distributed to the unit-catchments on the reservoir domain through the stage-area relationship. Thus, all the unit-catchments that compose a reservoir have the same storage capacity.

The variable bathymetry method (iii) ("Var") explicitly simulates the reservoir dynamics to improve accuracy in the distribution of reservoir volume across the unit-catchments associated to the reservoir lake. Since the DEM measures the surface water level, there is no information on it about the reservoir bathymetry. Thus, the proposed method estimates the stage-area curve below the reservoir water level (RWL) and combines it with the stage-area curve above the RWL to construct the reservoir actual stage-volume curve, which can be later checked against existing data (in this study, provided by the Brazilian National Electric System Operator - ONS). This method has four steps:

1) Estimation of the stage-area curve above the RWL in a given unit-catchment. This process is automatically obtained using the DEM information within a unit-catchment, by counting the number of cells lower than a specific elevation.

2) Estimation of the "original" river bank elevation in every unit-catchment within the reservoir lake. The "original" riverbanks (i.e., in pristine conditions) were inundated by the dam. Thus, the bank elevation of all unit-catchments that compose the reservoir were defined through a linear interpolation between the bank elevation just downstream of the dam, and the one immediately upstream of the reservoir lake (Equation 3).

$$Z_i = Z_{down} + \left(Z_{up} - Z_{down}\right) \times \left(\Delta X_{down,i} / \Delta X_{down,up}\right) \qquad \text{Equation 3}$$

Where Z represents the bank elevation and ΔX the distance between the river sections. The indices $i, down$ and up represent the sections of the i-th unit-catchment within the reservoir, and the sections immediately downstream to the dam and upstream to the reservoir lake, respectively.

3) Estimation of the stage-area curve for the levels below RWL: it is assumed that the water surface area below the RWL linearly increases with level, and that the water surface area at the river bank elevation is zero. Thus, the stage-area curve below RWL is a line going from an area equal to zero at the river bank elevation (Z_i) to the first point in the stage-area curve above RWL.

4) Matching the estimated reservoir stage-volume curve with the actual one: the reservoir stage-volume is a table relating reservoir volume (V_O) with level (Z). It can be

directly compared to the reservoir stage-area curve built with the combination of all the unit-catchments within the reservoir (hereafter Res), which is a table relating area (A_{Res}) to level (Z). In every position j on the stage-area table, a level increment ($Z^j - Z^{j-1}$) is multiplied by its related reservoir surface water area ($(A_{Res}^j + A_{Res}^{j-1})/2$), resulting in an incremental volume (ΔV_{Res}^j). Then, the incremental volume observed on the stage-volume curve related to the level Z^j ($\Delta V_O^j = V_O^j - V_O^{j-1}$) is divided by the calculated incremental volume calculated from the stage-area curve (ΔV_{Res}^j), generating a volume ratio ($VR^j = \Delta V_O^j \,/\, \Delta V_{Res}^j$). The stage-area curve of each unit-catchment (i) within the reservoir is recalculated independently to keep the same incremental volume as the actual stage-volume curve:

$$(a_{Res}^{*\,i,j} + a_{Res}^{i,j-1}) = VR^j \times (a_{Res}^{i,j} + a_{Res}^{i,j-1}) \qquad \text{Equation 4}$$

$$a_{Res}^{*\,i,j} = VR^j \times (a_{Res}^{i,j} + a_{Res}^{i,j-1}) - a_{Res}^{i,j-1} \qquad \text{Equation 5}$$

Where $a_{Res}^{i,j}$ is the water surface area of the unit-catchment i at the stage-area table position j related to the level Z^j. The superscript * indicates the recalculated a values. Equations 4 and 5 indicate an adjustment on the water surface area in level Z^j in order to preserve the incremental volume indicated by the actual stage-volume curve.

This process is repeated through all levels (Z^1 to Z^n) of the stage-volume curve, modifying the stage-area curve of each unit-catchment within the reservoir.

11.2.6 Reservoir operation

The dam release is set as an internal boundary condition of the hydrodynamic model (MGB), by replacing Equation 1 by a dam outflow equation. Three types of operation schemes are compared here, considering two different approaches each: one based on regionally available data, and another with global-based parameterization. The three operation types are representative of different approaches that have been implemented in state-of-the-art modeling systems, from generic to data-driven ones, described as follows.

Reservoir operation schemes H06 and H06Glob

This is a generic, inflow-based operation based on the equation proposed by Hanasaki et al. (2006) and adapted by Shin et al. (2019). This operation considers that the dam outflow is a simple function of the inflow modulated by the dam regulation capacity and the storage at the beginning of each hydrological year. Here, it is used at a

daily basis and for hydropower plants, so that it does not take into account downstream water demands for irrigation or other uses. Dam outflow is defined by Equation 6:

$$Q(i,t) = R_i K_{i,y} I_m + (1 - R_i) I_{t-1}$$
Equation 6

$$R_i = \min(1, \alpha c_i)$$
Equation 7

$$K_{i,y} = S_{first,y} / \alpha C_i$$
Equation 8

Where $Q(i,t)$ is the ith dam outflow at the time step t, R_i a regulation capacity constant that can be calibrated with observations or estimated with Equation 7 (SHIN; POKHREL; MIGUEZ-MACHO, 2019), I_m and I_{t-1} the annual average and dam inflow, respectively, and $K_{i,y}$ the storage fraction at the beginning of the hydrological year (Equation 8). The hydrological year of each dam is defined as the month where the naturalized flow becomes lower than the average (i.e., the beginning of the drawdown season) (Hanasaki et al., 2006).

The term c_i is the ratio between the reservoir maximum storage C_i and the annual average dam inflow ratio ($c_i = C_i / I_m$), $S_{first,y}$ is the storage at the beginning of each hydrological year y, and αC_i is the target storage, where α is a constant set to 0.85 following Hanasaki et al. (2006).

Scenario H06 estimates R from a calibration procedure based on regionally available observations, while scenario H06Glob (global) adopts equation (6) for estimating R.

Reservoir operation schemes 3PT and 3PTGlob (Three-point rule curve)

This is a target storage-and-release-based rule (Yassin et al. (2019), consisting of a three-point rule built upon simple dam characteristic parameters, as minimum and maximum operational levels, and maximum discharges (Figure 11.3a). Similar approaches were adopted by Zajac et al. (2017) and Yassin et al. (2019). This operation emulates a reservoir rule curve that is constant throughout the year with outflow as a linear function of water level, guided by three points. The regional approach (scenario 3PT) adopts the following points based on actual dam information (i.e. observations): minimum operational level (for which outflow is zero), average operational level (for which outflow is obtained from the average observed outflow), and maximum design level (associated to the dam design discharge). Supplementary Material S1 presents the adopted parameters for all dams. Scenario 3PTGlob (global approach) follows Zajac et

al. (2017), and adopts the percentiles 0.1, 0.3 and 0.97 for the minimum (conservative), normal, and maximum (flood) storages, which are associated to the 5th, 30th, and 97th percentiles of naturalized daily discharge, respectively.

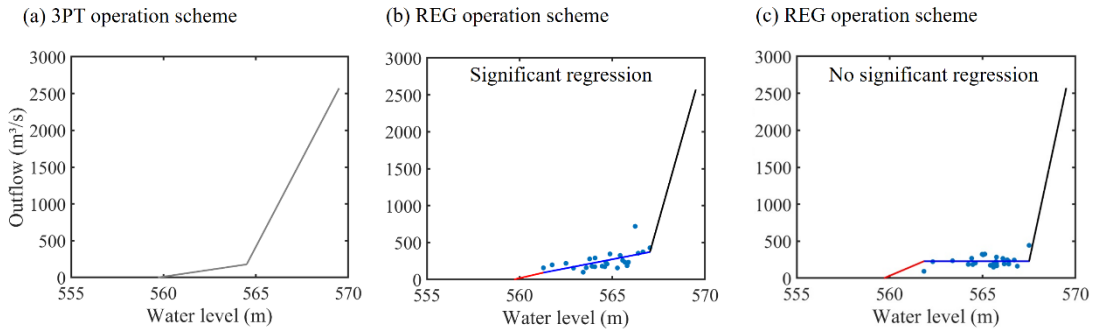

Figure 11.3. Reservoir operation exemplified for the Jurumirim Dam (ID 1 in Figure 11.1), for the (a) operation scheme '3PT', considering only three pre-defined points related to dam characteristics (water level and design discharges), (b) 'REG' scheme, with significant regression between observed monthly mean water level and dam outflow obtained for the month of December, and (c) 'REG' scheme, without significant regression for the month of September. The blue dots represent observations, and the lower extrapolation of the reservoir operation for ranges out of observations is depicted in red, while the upper extrapolation is shown in black. See description of the operation schemes in the text (Section 11.2.6).

Reservoir operation schemes REG and REGGlob (Regression-based rule)

This is also a target storage-and-release-based rule based on a data-intensive approach. Linear regressions are computed between observations of monthly average water levels and dam outflows, so that it emulates a rule curve for each month of the year following the actual operation (OLIVEIRA; LOUCKS, 1997). A similar operation was investigated by Solander et al. (2016). For each month, positive relationships are adopted as those with Pearson correlation higher than 0.4, which is considered satisfactory based on a visual inspection (Figure 11.3b). For non-positive relationships (Figure 11.3c), the monthly average discharge was used for all simulated days for a given month. For water levels out of the observed range for a given month, dam characteristics related to minimum operational level (for which outflow is zero), and maximum design level (dam design discharge) were adopted, and linearly interpolated with the observed ranges.

The global approach (scenario REGGlob) adopts long term outflow average instead of monthly regressions, making the operation similar to the standard operating policy (SOP) (DRAPER; LUND, 2004), considering the long term streamflow as the demand.

11.2.7 Model application in the Upper Paraná River Basin

The model was applied to the Upper Paraná River Basin with daily time step for the period 1st Jan 1979 to 31st Dec 2015 (35 years + 1 spin-up year). It was run with in situ daily precipitation from 2030 gauges from the following institutions: Brazilian National Water Agency (ANA), Water Resources Agency of *Argentina* (BDHI) (http://bdhi.hidricosargentina.gov.ar/) and National Meteorological and Hydrological Service of Paraguay (DMH) (https://www.meteorologia.gov.py/). Details on precipitation data interpolation to model units are provided in Supplementary Material S2. Long term climate averages from 195 stations of the Brazilian National Institute of Meteorology (INMET, available at <http://www.inmet.gov.br/>) were used to dynamically compute evapotranspiration with the Penman-Monteith Equation within the model.

Drainage network and unit-catchments (total of 9625 units with 10 km long river reaches) were derived from the 90 m Hydrosheds SRTM DEM (Lehner et al., 2008) with the IPH-HydroTools GIS toolkit (Siqueira, et al., 2016a). Hydrologic Response Units (HRU's) were used to define homogeneous regions for the rainfall-runoff parameters, and were derived from the South America HRU map developed by Fan et al. (2015). Model parameters related to soil, vegetation and river hydraulics (bankfull width and depth from geomorphic relationships, and Manning's roughness coefficient) are further discussed in Supplementary Material S2.

The model was calibrated for the period 1990-2010 and validated for 1980-1990 with 143 in situ discharge gauges from ANA considering the pristine scenario (i.e., without reservoirs). Naturalized flows from ONS were considered for gauges downstream of dams. Supplementary Material S2 presents details on the model adjustment, including performance metrics and simulated hydrographs. Overall, the model satisfactorily represented natural discharges basin-wide, with 78% and 79% of the gauges with NSE and NSElog > 0.6, respectively, and 79% for the validation period, and 42% of the gauges with the absolute value of bias < 10%.

The 30 regulation dams within SIN were considered, in addition to Itaipu dam (a run-of-river dam but very relevant in terms of size and energy production) (Figure 11.1). For simplicity, all other run-of-river reservoirs were not considered in the simulations, since our focus was on dams with regulation capacity. To properly address

basin-wide flow regulation, the dams were only considered after their year of inauguration, so that the model simulated the dam first filling. The effects of reservoirs were not used for model calibration, but only considered for the scenarios presented in the following Section 11.3.

11.3 Experimental design

A total of 12 simulation scenarios were run, considering the different reservoir bathymetry representation and reservoir operation schemes (Table 11.1). The performance of a given reservoir simulation was first assessed in terms of discharge and active storage for all dams. Observed time series of active storage and dam outflows were obtained from ANA (https://www.ana.gov.br/sar/). The hydrodynamics was assessed in terms of the water surface elevation longitudinal profile at Itaipu dam, by comparing simulations with satellite altimetry estimates from the ICESat mission (SCHUTZ et al., 2005). ICESat carries a LiDAR sensor and has a maximum inter-track distance of 30 km and a repeat cycle of 91 days. ICESat vertical datum was converted to EGM96 in order to be consistent with the SRTM datum reference. A basin scale assessment was also made by computing, for each river reach, the root mean squared deviation (RMSD) between simulated water levels under scenarios Lum, Eq and Var (Table 11.1).

Model performance for discharge was assessed with Nash-Sutcliffe (NSE) and Log Nash-Sutcliffe (NSElog, i.e., NSE considering the logarithm of discharges), normalized root mean squared error (NRMSE) of peak discharges, and relative errors in high (Q10, i.e., discharge that is exceeded 10% of the time) and low flows (Q90, i.e., discharge that is exceeded 90% of the time). For reservoir active storage, NRMSE and Pearson correlation metrics were adopted. Finally, the average peak attenuation for each dam was assessed by first computing the discharge reduction between dam inflow and outflow for each of the dam's maximum annual events, followed by estimation of the average of the annual values. The simulated peak attenuation was compared to the observed one with the NRMSE metric.

In addition, the role of the online coupling between hydrology and hydrodynamic processes was tested by performing tests with and without coupling in Section 11.4.1. The simulation without coupling was performed by considering that evapotranspiration only occurs from the non-flooded soil/vegetation system, i.e., reservoir open water evaporation is not considered into the evapotranspiration computation.

Since there is high uncertainty on the estimation of the active flow width (B in Equation 1) along the reservoir when it is simulated in a distributed way (i.e., reservoir storage types Eq and Var; Section 11.2.5), hydrographs are presented in Section 11.4.1

considering two types of computation: (i) adopting the original channel width estimated from geomorphic relationships, and (ii) considering the active width for unit-catchments within reservoirs as the unit-catchment flooded area divided by its length (10 km), i.e., considering that there is active flow along the whole reservoir cross section area.

Finally, the developed regional scale hydrodynamic model was used to investigate the relative role of floodplains and reservoirs on flood attenuation. This was carried out following the approach by Fleischmann et al. (2019a), where the model was run with three river/floodplain scenarios: (i) pristine flow scenario (naturalized flow; with floodplains but without reservoirs); (ii) without both floodplains and reservoirs, where cross sections were assumed always rectangular and thus disregarding floodplain topography; and (iii) with both floodplains and reservoirs. The role of reservoirs on flood attenuation was estimated by computing the peak attenuation between scenarios (i) and (iii) for the maximum flood event of each simulation year. The role of floodplains was similarly computed, but considering the difference between scenarios (ii) and (i). Table 1 summarizes the model runs.

Table 11.1. Reservoir simulation scenarios, considering operation schemes and types of storage representation.

Reservoir operation*	**Storage representation****	**Scenario name**	**Operation details**
H06 (Hanasaki *et al*. based operation)	Lumped (Lum)	H06Lum	R parameter calibrated
	Eq	H06Eq	
	Var	H06Var	
H06Glob (H06 operation with global parameterization)	Var	H06GlobVar	R estimated as min $(1, \alpha c_i)$ (Equation 7)
3PT (three-point rule curve)	Lum	3PTLum	Minimum, normal and maximum levels and outflows derived from dam characteristics
	Equal bathymetry (Eq)	3PTEq	
	Variable	3PTVar	

	bathymetry (Var)		
3PTGlob (3PT operation with global parameterization)	Var	3PTGlobVar	Minimum, normal and maximum levels and normal and maximum outflows estimated as simple percentiles as proposed by Zajac et al. (2017)
REG (regression-based operation)	Lum	REGLum	Monthly linear regressions between level and outflows; months with low correlation use monthly average outflow instead
	Eq	REGEq	
	Var	REGVar	
REGGlob (REG operation with global parameterization)	Var	REGGlobVar	Annual average outflow used for all months

11.4 Results

11.4.1 Effects of reservoir storage representation

This section presents the results and differences in the reservoir dynamics according to the storage representation approaches (Lum, Eq, Var). While all schemes yielded similar estimates of dam outflows, as exemplified for a few dams in Figure 11.4a, some key differences were identified. In some cases, the lumped method led to a discharge attenuation in relation to the other two methods (smaller and delayed peaks). This is due to the typical approach adopted on large-scale hydrological modeling in the lumped (offline) simulation, i.e., using as inflows the simulated discharges at the dam location, instead of computing the inflows as the modeled flows at the river reaches close to the most upstream reservoir lake area. This approach causes the flood wave to be routed along the reservoir as it was a river reach, adding artificial routing along the drainage network. Hence, for lumped model applications, it is best to select all tributaries that drain into the reservoir (along with direct lake inputs) and consider it as the dam inflow. This effect was clearer for Itaipu dam, which is located in the lower part of the basin, integrating the effects of all upstream dams and having a long reservoir.

Our results show that simpler, lumped reservoir models can simulate downstream discharge similarly to dynamic and distributed ones (Figure 11.4a).

However, the lumped method fails to represent backwater effects when compared to the distributed methods (Equal and Variable bathymetry) (Figure 11.5a). High deviation among Lum and Var scenarios (RMSD > 10 m for some reservoirs) occurs for most reaches upstream from dams.

As a validation experiment, ICESat satellite altimetry data were used to assess the simulated profile of water surface elevation along Itaipu reservoir under the three different storage schemes (Figure 11.5b). The lumped method is unable to simulate it properly, and the slope in the upstream part of the lake was better represented with the Var method. An intermediate behavior was obtained with the Eq method. Although this method considers the reservoir to behave as a large box with horizontal water level, the lake is assumed as connected to the rest of the drainage network, and thus the method is capable to represent backwater.

On the other hand, the actual level in the lake area closer to the dam is more dependent on the dam operation, and its simplification led to higher errors in the estimated Itaipu reservoir storage. For instance, the low water level in Oct/2003 (lake level closest to the dam at 216.6 m; Figure 11.5b) is related to the low simulated active storage (around 14 km³; see Figure 11.6d in next section), while actual values were around 219.3 m for level and 18.1 km³ for storage. Itaipu is also a large dam (~170 km long), and its lake is composed of many unit-catchments (which are 10 km long).

The hydrographs presented in Figure 11.4a also compare different ways of representing flow width in the distributed reservoir simulation (bold lines), as well as scenarios with and without reservoir open-water evaporation (i.e., not considering an online hydrologic-hydrodynamic coupling; dashed lines). Downstream discharges had mostly similar values, indicating a low sensitivity to both flow width conceptualization and the online coupling scheme.

Regarding evapotranspiration estimates, differences among Lum, Eq and Var scenarios would arise if reservoir flooded areas were largely divergent, but this difference was relatively small in comparison to other model uncertainties. Our estimations of reservoir evaporation rates are in agreement with other studies in the Paraná Basin (BUENO; MELLO; ALVES, 2016). Looking at the basin scale, we estimated an increase of annual ET rates by 15 mm/year due to existence of reservoirs. The net reservoir evaporation (i.e., reservoir evaporation minus the evapotranspiration that would occur without the lake, which is equal to the difference between blue and red lines in Figure 11.4b) for the assessed lakes varied between 21±12 mm/month (mean±SD) for Itaipu and 70±41mm/month for Itumbiara (located in the north of the basin; ID 19 in Figure 11.1). This loss can be relevant during dry periods, and thus must be accounted for in large scale models. For instance, loss in energy production due to reservoir evaporation in the Brazilian southeast region was estimated as 2% (over 900 MW; Zambon et al., 2018), and it is also an important measure to assess regional scale reservoirs' water footprint (SEMERTZIDIS; SPATARU; BLEISCHWITZ, 2019). At Itumbiara dam, the modeled evapotranspiration was highly constrained by soil moisture

during austral winter, what explains the large net evaporation losses. This difference led to a higher peak simulated under the scenario without open water evaporation (Figure 11.4a). When looking at finer scales, evapotranspiration rates will drastically differ. Since the lumped (offline) method is not able to represent the dynamic conversion between dry and flooded soil/vegetation, the representation of local scale coupled processes between surface and atmosphere will perform poorly, as well as the local scale runoff estimation.

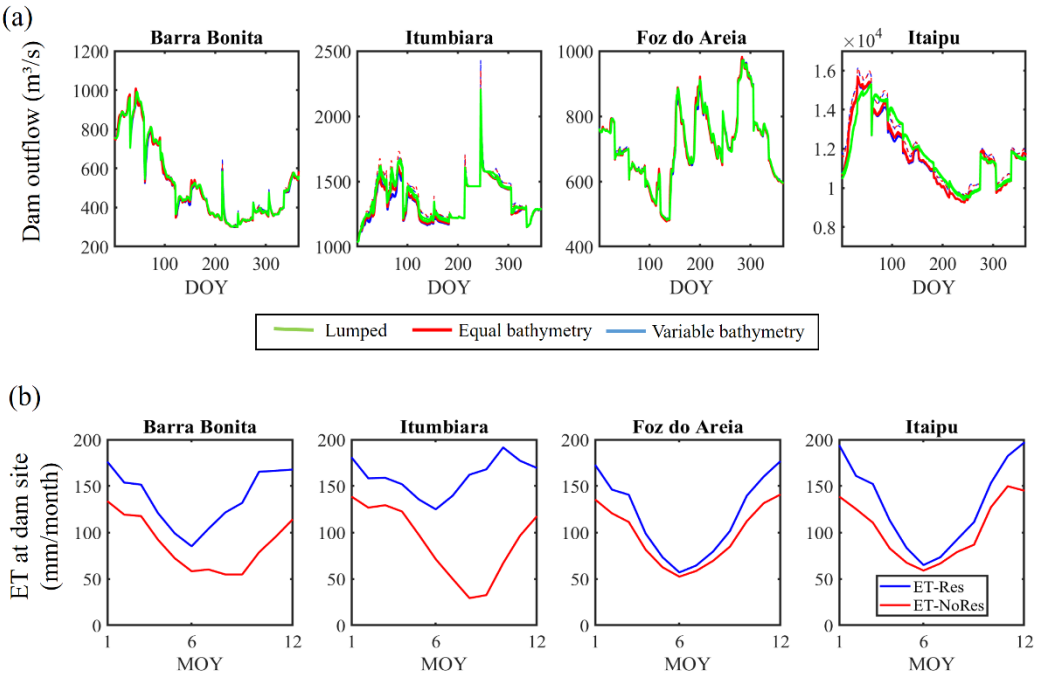

Figure 11.4. (a) Daily climatology of simulated dam outflows for the three types of storage representation (Lumped, Equal bathymetry, Variable bathymetry) and for Barra Bonita (ID 3 in Figure 11.1), Itumbiara (ID 19), Foz do Areia (ID 15) and Itaipu (ID 18) dams. Results adopt the operation R. Bold colors refer to default scenarios with two different flow width values (which converge to very similar values), while dashed lines with light colors are scenarios not computing reservoir open water evaporation. (b) Monthly climatology of open water evaporation (ET-Res; Penman equation) and evapotranspiration without reservoir effects (ET-NoRes; i.e., Penman-Monteith equation not considering reservoir surface area) at the location of the dam sites. The operation scheme REG is adopted for all plotted results.

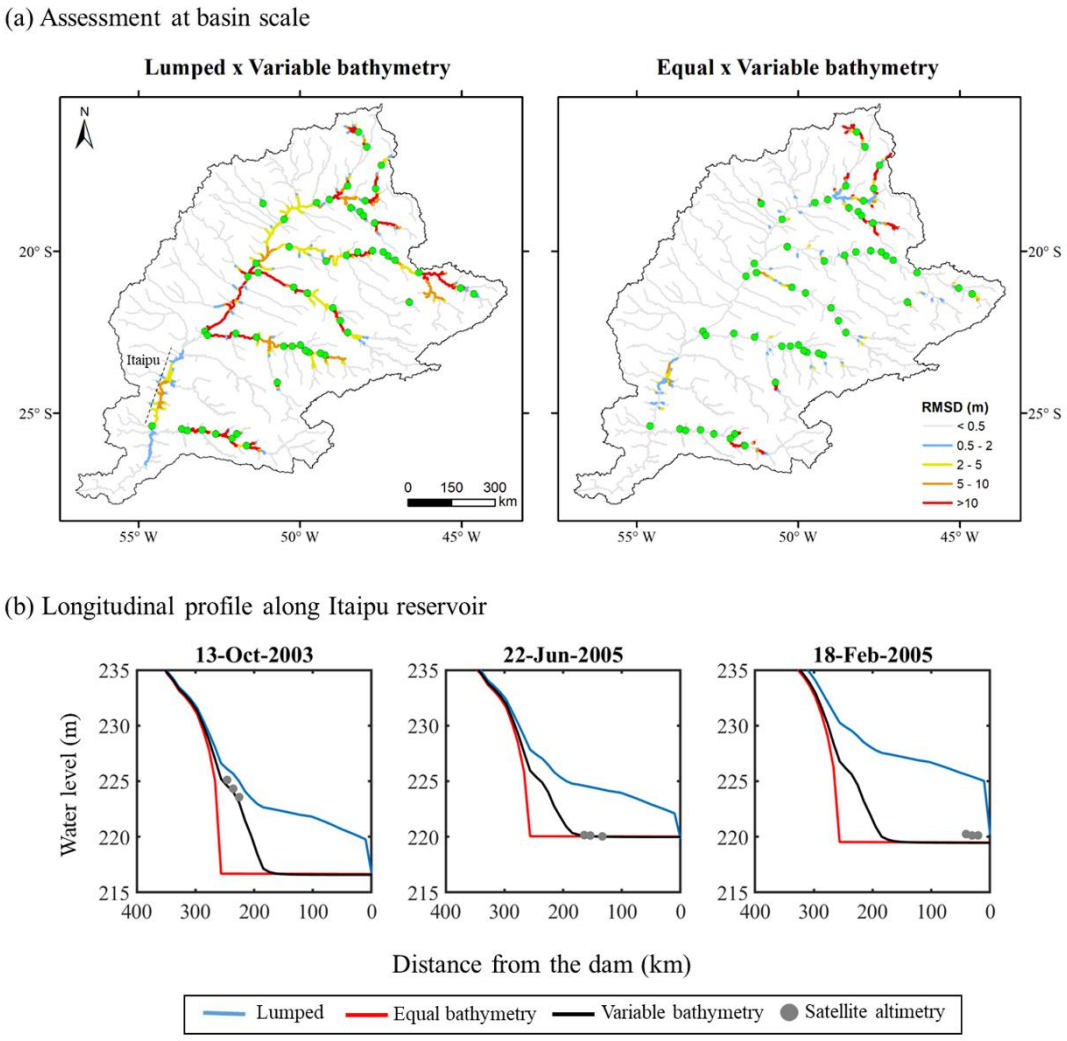

Figure 11.5. (a) Spatial assessment of RMSD regarding simulated water level, for scenarios lumped x variable bathymetry (left column) and equal x variable bathymetry (right column). Higher RMSD values indicate higher discrepancy between storage representation types to estimate backwater effects. Green circles refer to the simulated dams. (b) Validation of the simulated longitudinal water level profile along Itaipu reservoir with ICESat altimetry data for three different dates. The Itaipu reservoir lake area is highlighted in the panel a. The operation scheme REG is adopted for all plotted results.

11.4.2 Effects of reservoir operation

This section compares the different reservoir operation (H06, 3PT, REG, in order of increasing data requirement) and storage/bathymetry representation schemes (Lum, Eq, Var), addressed in terms of dam outflow and reservoir hydrodynamics. The differences among the simulated operation schemes are larger than among the reservoir

bathymetry types for discharge and active storage estimation (Figure 11.6 and Figure 11.7).

Results for the same four dams analyzed in the previous section show that the REG operation scheme led to far better outflow estimation for Itumbiara and Itaipu dams. In these cases, operations H06 and 3PT also outperformed the natural flows scenario (i.e., without reservoir effects). The overall model performance in representing basin-wide hydrologic regime alteration (as depicted by Itaipu dam) shows that the best performance was obtained for REG (NSE 0.69), followed by H06 (0.47) and 3PT (0.19), and that all of them outperformed the scenario without dams (-0.26). For Itumbiara, the better performance of REG for outflow compared to the other scenarios can be seen in the better depicted seasonality, also reflected on the storage simulation. For Foz do Areia dam, located in a river with low precipitation seasonality, all model versions led to similar estimates as the natural flow scenario, i.e., the inclusion of reservoirs did not lead to improvements. The simulation performance for active storage (NRMSE) was similarly satisfactory for the four dams and all scenarios, except for Itaipu under operation REG, which outperformed the others by significant margins (9% for REG, against 23% and 27% for H06 and 3PT, respectively).

A similar behavior was observed when looking at the ensemble of 31 dams (Figure 11.7 and Figure 11.8), which was supported by a basin-wide assessment for the whole drainage network (Supplementary Material S3). The highest differences were obtained for NSE, where REG had the best performance, followed by H06 and 3PT, and for active storage r, for which REG was followed by 3PT and H06. Indeed, a more satisfactory performance was expected for REG given its more data-intensive nature. The three-point rules (3PTLum, 3PTEq, 3PTVar and 3PTGlobVar) had the lowest performance for discharge in terms of NSE, but this was not the case for high (Q10) and low flows (Q90) and peak discharges. Interestingly, for low flows, all operation types were outperformed by the natural flow scenario, showing that the tested operations led to excessive discharge attenuation (i.e., overestimated base flows) during dry periods.

The operation scheme REG, which relies on observed data, provided the best discharge estimates with a median NSE of 0.3 and a maximum of 0.75 for the 31 reservoirs. Although the basin-wide hydrological alteration was relatively well captured, e.g., at Itaipu dam location (Figure 11.6), the non-data intensive schemes (H06 and 3PT) need further improvements if aiming at locally relevant estimates of dam operation.

The analysis of regional (H06, 3PT, REG) versus global-based parameterizations (H06Glob, 3PTGlob, REGGlob) showed that the global ones had a relatively poorer performance in relation to their regional counterparts. For instance, the regression with monthly values (REGGlob), considering long term averages as outflow, presented the poorest performance for peak NRMSE and high and low flows, while 3PTGlobVar scenario presented the poorest representation of active storage. However, for certain purposes these global approaches could already provide valuable discharge estimates,

e.g., for providing a general understanding of regional scale hydrological alteration. For example, median NSE values were 0.1 (0.1) for scenario H06 (H06Glob), and 0.3 (0.1) for REG (REGGlob), showing the just slightly better performance of the regional parameterization. The global setups were also more accurate than naturalized flows for all metrics except for low flows.

There was an overall satisfactory model performance to estimate peak attenuation, with Pearson correlation between 0.72 and 0.91, and NRMSE between 10% and 22% (Figure 11.8). The different types of storage representation led to very similar NRMSE values between simulation and observation, and the same occurred for the reservoir operation, although H06 was slightly better than 3PT, which in turn was marginally better than REG. This is interesting given the low degree of data requirement in the H06 scheme. The global-based parameterization led to less accurate results for scenarios H06Glob and REGGlob, but not for 3PTGlob, in relation to their counterparts H06, REG and 3PT. Among all assessed metrics in Figure 11.7, the only one for which a noticeable difference was obtained regarding storage representation was the correlation of peak attenuation, for which the variably distributed storage (Var) yielded better values than the other ones.

The capability of the dams' regulation capacity (total active storage divided by long term average discharge; red to blue colors in Figure 11.8) to predict peak attenuation was also investigated. A positive trend between regulation capacity and peak attenuation was clearer for REG (i.e., lower attenuation values with red color and higher ones with blue). The lack of a clear relation resulted from the behavior of the three dams with largest regulation capacity (Serra do Facão, Nova Ponte and Emborcação dams; ID's 30, 24 and 14 in Figure 11.1, respectively), which were associated to a relatively small peak attenuation (around 10%).

Finally, the dry years of 2000-2001 provide a stress test for our modeling system. During this period, a major drought affected the Brazilian hydropower system, which is associated to delays in generation investment leading to a large energy crisis in the country (JARDINI et al., 2002). In Jan/2000, Itaipu and Barra Bonita (ID 3 in Figure 1) dams reached their lowest levels (observations available since 1993). The same occurred for Itumbiara in Nov/2001. Among the four analyzed reservoirs in Figure 11.6, only Foz do Areia, located in the Brazilian southern region, did not have an extreme year during this period. The REG scenario was able to satisfactorily simulate some of dams' drawdowns, but there was no clear pattern among the representation of this extreme year: this scheme estimated a too high drawdown for Itaipu and a too low drawdown for Itumbiara dam, but yielded satisfactory estimates for Foz do Areia and Barra Bonita dams.

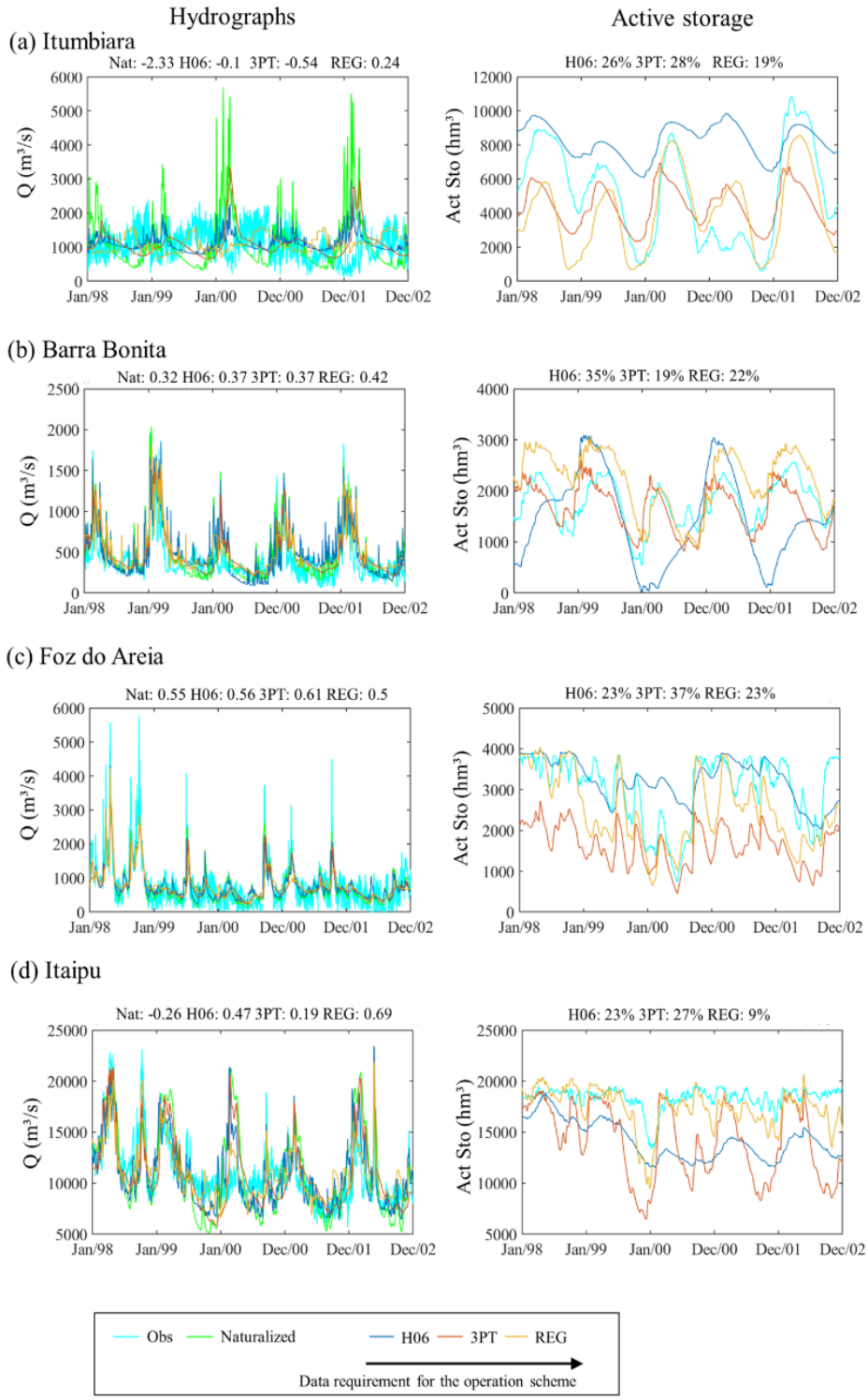

Figure 11.6. Simulated dam outflow (Q) and active storage (Act Sto) for the different operation types (H06, 3PT, REG), with the variably distributed reservoir simulation method, for four dams (Itumbiara, ID 19 in Figure 11.1; Barra Bonita, 3; Foz do Areia, 15; and Itaipu, 18). NSE and NRMSE performance metrics for each scenario are presented for discharges (left column) and storage (right column), respectively. Pristine simulated flows (i.e., without dams; "Nat") are also presented. The unit "hm³" stands for cubic hectometers (i.e., 106 m³).

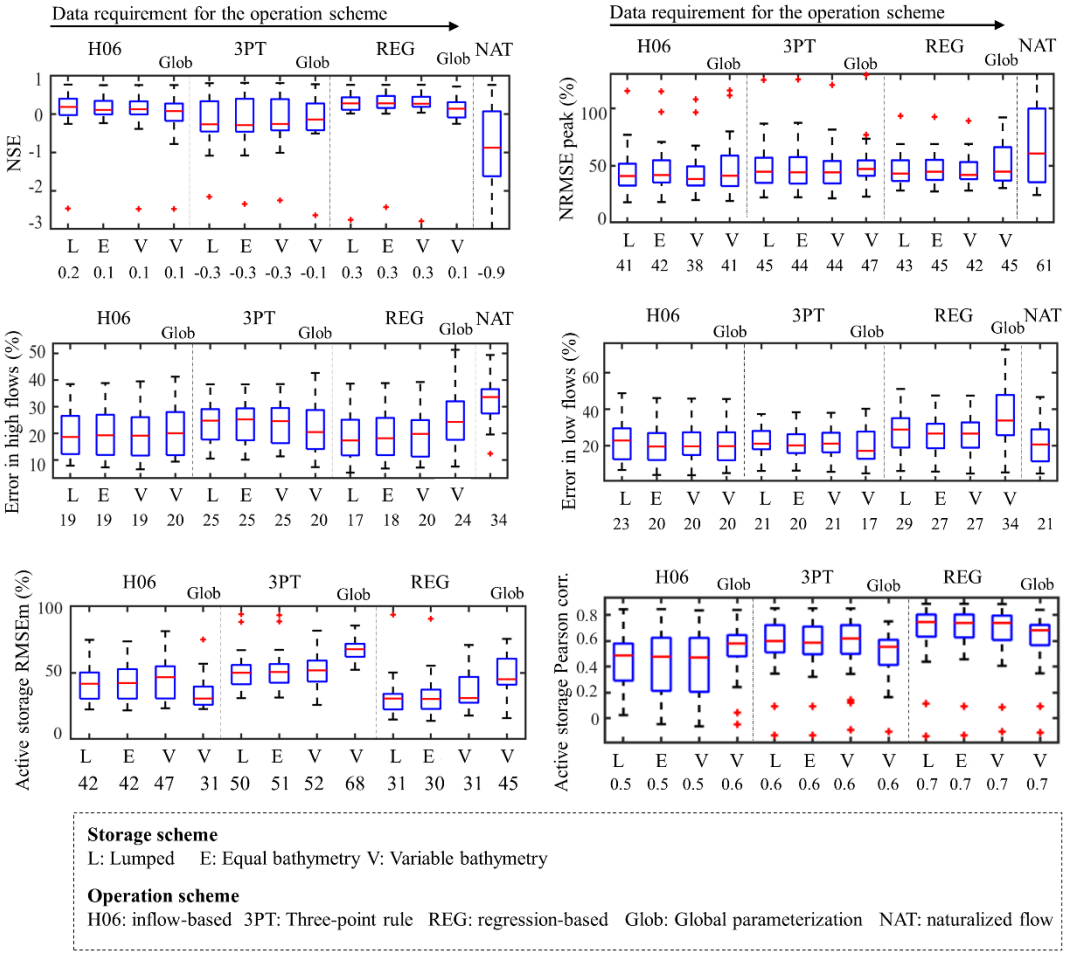

Figure 11.7. Model performance for discharge (NSE; NRMSE of peak discharges; and errors in high and low flows) and active storage (NRMSE and r) for the 12 scenarios of operation types and reservoir simulation methods, as well as for the naturalized (pristine) flow scenario (Nat; for discharge analysis only). Results are presented as boxplots containing values of the 31 simulated dams, and the metric median values are presented below the scenario names. From left to right, the operation schemes are ordered in terms of increasing data requirement.

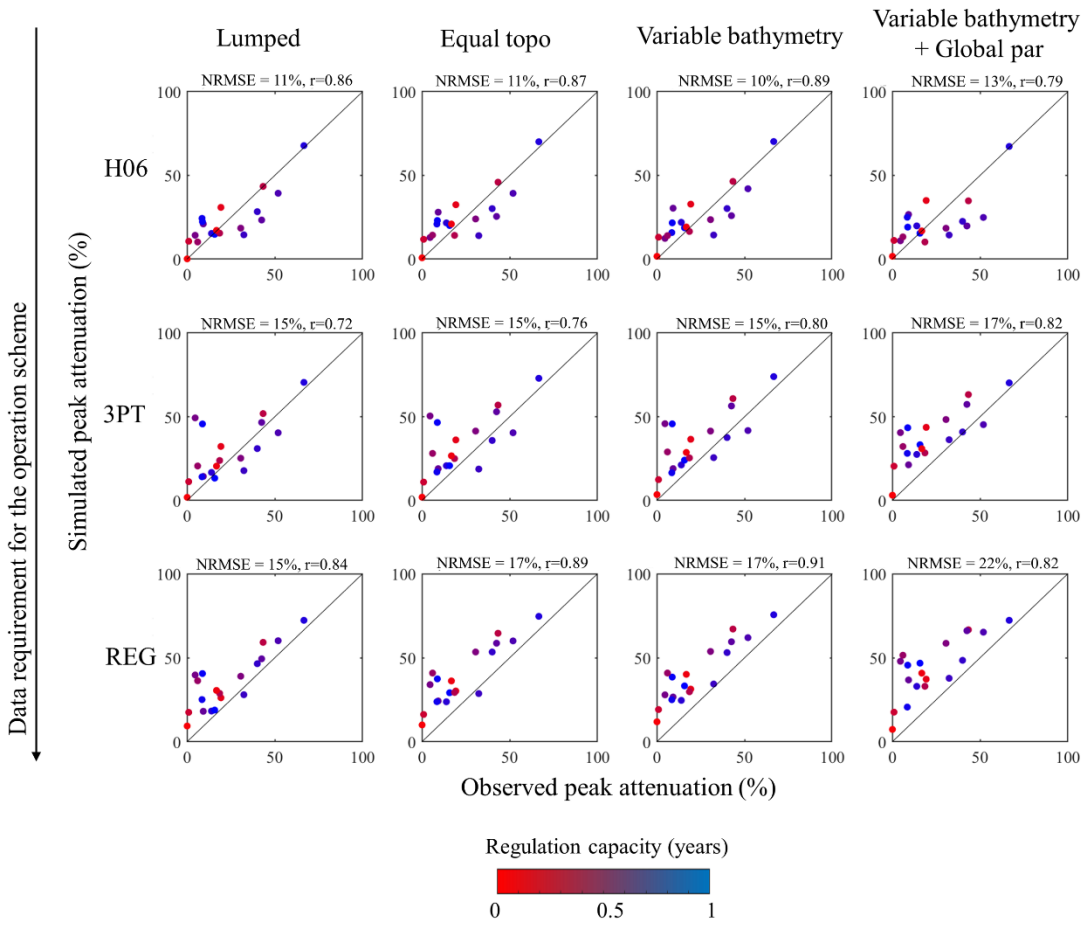

Figure 11.8. Comparison between observed and simulated peak attenuation for each of the 12 scenarios. Each row refer to a reservoir operation scheme (H06, 3PT, REG, with and without global parameterization – Global par), and each column to a storage representation scheme (Lumped, Equal bathymetry, Variable bathymetry). Each point refers to a simulated dam, and colors refer to the dam regulation capacity (total active storage divided by long term average discharge, in years).

11.4.3 The relative role of floodplains and reservoirs on flood attenuation

River-floodplain-reservoir hydrodynamic models have been used to understand the effects of reservoirs on downstream flooding (Fleischmann et al., 2019a; Mateo et al., 2014; Pokhrel et al., 2018; Shin et al., 2019, 2020). Here we follow the methodology proposed by Fleischmann et al. (2019a) and use the developed MGB model structure, with distributed representation of reservoir bathymetry and a fully coupled river-floodplain-reservoir scheme, to investigate the relative role of natural floodplains and reservoirs on flood attenuation along the Upper Paraná Basin. Generally, natural floodplains and reservoirs have a complementary role on flood attenuation in the basin. While floodplains are more important along tributaries' headwaters (e.g., Iguaçu,

Paranapanema, Grande and Ivinhema rivers) and in the lower reaches of the Paraná mainstem, reservoir effects are more relevant along medium to lower reaches of tributaries (Figure 11.9). Part of the reservoirs' storage is currently allocated for flood control during the wet season (Oct-Apr), following the coordinated operation of the Paraná dam cascades (ONS, 2019).

Located along the Paraná mainstem, the 230 km floodplain between Porto Primavera and Itaipu dams is known as the last natural large wetland in the Upper Paraná Basin (see Figure 11.1 for location), with important ecosystem processes relying on it (Agostinho et al., 2001). The flood storage along this area leads to major discharge attenuation that is propagated downstream, and it is fundamental for flood control in benefit of both Itaipu dam and riverine cities. If the reservoirs did not exist, the reaches flooded by the reservoir lakes would provide additional storage along the floodplain.

The comparison between scenarios with and without floodplains shows that the magnitudes of maximum flows are likely to be largely overestimated if basin-wide floodplain storage is not considered (Figure 11.9b). For instance, for the Iguaçu River at Fluviópolis, ignoring this effect would lead a 10-yr flood to be estimated as 6,000 m^3/s (green dots in Figure 11.9b) instead of 3,000 m^3/s (blue and red dots). The effect of upstream floodplains propagate downstream (Figure 11.9a), although they affect the lower reaches of only a few tributaries (e.g., Iguaçu river, with attenuation > 20% for all reaches along the river mainstem). Simulated and observed hydrographs at Água Vermelha and Itaipu dams also stress the role of floodplains and reservoirs on discharge alteration, for both high and low flows. The large effect of floodplains relates to the difference between green and black lines in Figure 11.9b. Furthermore, the major role of reservoirs on flood attenuation along main rivers makes their representation fundamental to correctly estimate flood frequencies in the downstream reaches.

Finally, performing an online, fully coupled simulation of the river-floodplain-reservoir continuum allows a continuous representation at the regional scale of the spatial-temporal variation of hydraulic variables as water levels. It is exemplified for the Iguaçu river mainstem, a major southern tributary of the Paraná (Figure 11.10). Longitudinal (maximum and minimum) water surface elevation profiles, as well as maximum flooded areas, highlight the connected hydrological-hydraulic processes that occur basin-wide. Along the Iguaçu, major floodplains occur in the upper reaches, from the most upstream parts close to Curitiba city (detail iii in b), to União da Vitória and Fluviópolis cities (see 11.10b and detail ii in 11.10b). A geologic control creates valleys with rapids between floodplains, setting up hydraulic controls and increasing upstream floodplain storage. União da Vitória is also affected by backwater effects from Foz do Areia dam, located a few kilometers downstream. In this study we only simulated regulation dams, while run-of-river ones were not considered and thus are not represented in the simulated water surface elevation continuum. Downstream of the cascade, the Iguaçu has again an incised valley with small floodplains, and the river width is controlled by the hydraulic control of the large Iguaçu Falls (detail i in 11.10b).

This example reinforces the model capability to represent the coupled human-water system at regional scale.

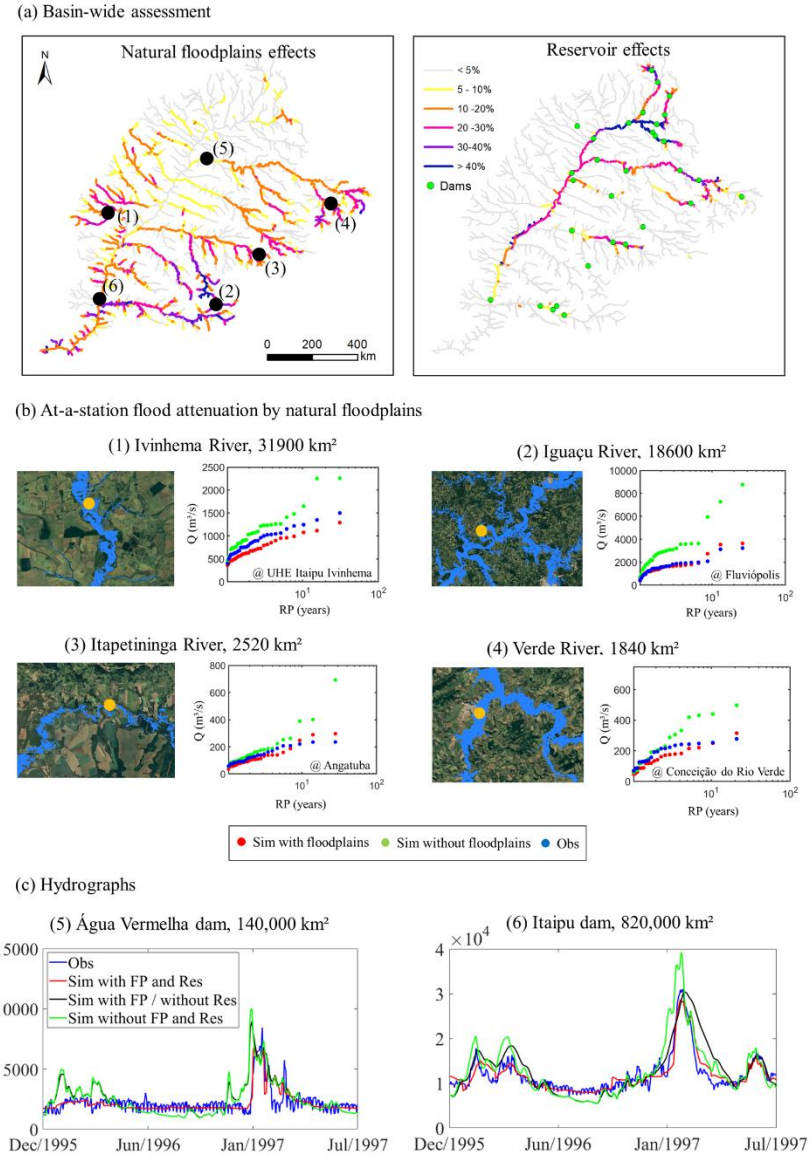

Figure 11.9. (a) Relative role of floodplains and reservoirs on flood attenuation, in terms of average attenuation of maximum annual events. The H06Var reservoir simulation scenario is adopted because of smallest peak attenuation NRMSE. (b) At-a-station assessment of flood attenuation by floodplains at four locations in upstream tributaries (location in figure a), in terms of simulations with and without floodplains, and observed (Obs) maximum annual discharges (flood frequency analysis). Maximum simulated flood extents are presented as blue areas in the left figures, together with Google Earth imagery and the location of the gauges (yellow). (c) Simulated and observed hydrographs at Água Vermelha and Itaipu dams (location in figure a) for different scenarios of floodplains (FP) and reservoirs (Res). The REGVar simulation scenario is used here because it led to the highest discharge NSE.

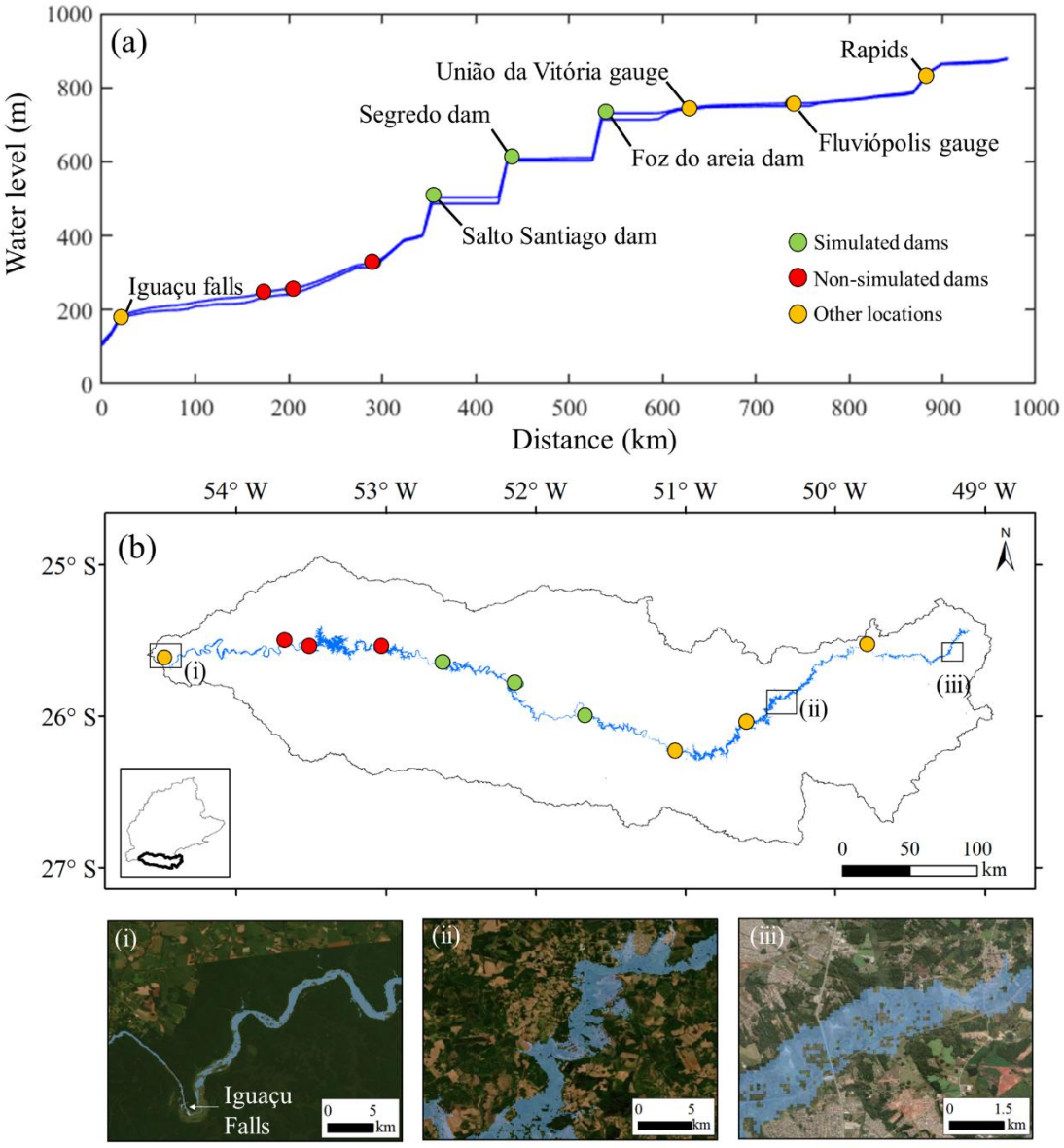

Figure 11.10. (a) Longitudinal profiles of maximum and minimum simulated surface water elevation (blue lines) along the Iguaçu river mainstem for the scenario REGVar. Distance is measured from the confluence between Iguaçu and Paraná rivers. The three regulation dams simulated along the Iguaçu mainstem are presented in the profile (green circles), as well as the run-of-river dams not simulated (red) and some locations of interest (yellow). (b) Maximum simulated flood extent for the same reaches from figure a. Details (i), (ii) and (iii) show particular areas together with Google Earth Imagery.

11.5 Discussion

11.5.1 Improving the representation of reservoir operation in large scale models

This study compared generic reservoir operation schemes (H06 scenario, based on Hanasaki et al. (2006)) to data-driven ones (scenarios 3PT, related to the three-point rule curve, and REG, associated to linear regressions between monthly water levels and dam outflows). As expected, the data-driven approach led to more accurate discharge and storage estimates. For example, while the operation H06 outperformed 3PT in the hydrology metrics, approaching REG, it provided the worst results in terms of tracking observed storage (Figure 11.7). In this case, accumulated flow errors lead to poor storage estimates (TURNER; DOERING; VOISIN, 2020). H06 has few parameters and it is apparently too simple for a complex interconnected system. In turn, the REG scheme is similar to the one by Solander et al. (2016) in the way that it fits a relation between storage and outflow. It is also related to Yassin et al. (2019), since it estimates the actual operational levels from observed data at a monthly basis, adopting dam characteristics for levels out of the observed ranges, thus emulating the actual reservoir rule curve. The satisfactory performance of this rule is also associated to relatively low bias in MGB estimates (see Supplementary Material S1), since inflow bias can largely affect reservoir simulation schemes (TURNER; DOERING; VOISIN, 2020).

The global-based parameterization (i.e., the one that does not require regionally/locally available detailed data) led to a slightly poorer performance in comparison to the regional-based one for discharge, and it was generally more accurate than naturalized flows, providing a reasonable approach to represent hydrological alteration at regional scales.

Finally, the results from the adopted operations should be analyzed by considering the context in which the real system is operated. In Brazil, the actual operation of all major dams is defined considering the large-scale interconnected hydrothermal power system (SIN), based on operational decisions reallocating storage inter-temporally throughout the system to minimize spills and energy production costs. The SIN is divided into regional interconnected subsystems (South, South-east, Central-west, Northeast and North) with significantly diverse hydrological characteristics. As the operation of a given hydropower plant affects others units downstream, a system wide operation strategy prevails over individual ones. First, an energy generation solution is determined for the whole system, which is later disaggregated to individual power units. Given the high contribution of hydropower in the mix (over 65%) and stochasticity of inflows, operating costs depend on present and future decisions. ONS defines the dispatch schedule for all generating units connected in the SIN (hydropower, thermal, wind and nuclear) on a monthly basis based on a merit order (from lower to higher cost), and considering current reservoir storage and flow forecasts. Hence, when a group of reservoirs is low in storage in a given region, hydropower plants from

another region can be dispatched and the energy transferred, avoiding the use of local thermal plants. The coordinated operation ranges from long term (four years) to dispatch scheduling (every half hour).

The improvement of regional scale models may involve hedging operations (reducing releases to minimize the probability of more severe cutbacks in the future ; You & Cai (2008)) and coordinated operations (Marques & Tilmant, 2013; Marques et al., 2006; Rougé et al., 2019), which are typically not considered. In this study, the REG scheme was designed to represent an average behavior (rule curve) of the coordinated system, which trades off its capability to depict anomalous years (especially dry ones). Approaches focusing on a single reservoir may disregard basin-scale flood or drought control that exists within a coordinated operation (ROUGÉ et al., 2019). Furthermore, to improve estimates, a detailed operation would require the representation of actual hydraulic structures (spillways, outlet works, etc.) (Fleischmann et al., 2019a) which is not always available to dams worldwide. As our purpose is to perform regional scale simulations, simplified operations were chosen for better model applicability. Potential future improvements should expand the REG operation to multiple regressions including other relevant explanatory variables beyond observed levels (e.g., Solander et al. (2016)). These relevant variables should be chosen based on homogeneous behavior in specific regions (i.e. not all regions would have the same explanatory variables with the same coefficients). On the other hand, the proposed methodology could be easily expanded to continental scale domains (e.g., Siqueira et al. (2018)), provided information on dam characteristics as stage-area curves and observed time series of storage and outflows is available. Finally, the proposed operation approaches do not take into account water withdrawals and consumptive demands associated (e.g. irrigation), as those are small in the context of the studied Paraná basin, and their effect is localized, so that we focused on hydropower generation dams instead. In future work, distributed modeling systems should explicitly simulate reservoir dynamics, as more information becomes available. In Brazil, recent national scale mapping of irrigation schemes (ANA, 2017) could be coupled to the MGB framework, combined with recent developments in large scale modeling of reservoir operation under timely varying water demands (BIEMANS et al., 2011; HADDELAND et al., 2014; HANASAKI; KANAE; OKI, 2006; VOISIN et al., 2017).

11.5.2 On the importance of representing the river-floodplain-reservoir continuum in large scale models

The presented model of the river-floodplain-reservoir continuum at regional scale provides a continuous depiction of the spatial-temporal variation of hydraulic variables as water surface elevation and flood extent and storage. The consideration of a distributed reservoir bathymetry was shown to be fundamental to estimate backwater effects, as revealed by a basin-scale comparison between lumped and distributed

schemes (equal and variable bathymetry), and an ICESat-based validation of the Itaipu reservoir longitudinal water level profile. Backwater effects are required for many applications, e.g., to perform real-time monitoring of the impact of a given reservoir on an upstream city (see the Iguaçu River case study in Section 11.4.3), or to correctly estimate the dam inflow along lateral tributaries.

A correct representation of hydrodynamics at the basin scale was also shown to be fundamental for flood frequency analysis, considering both reservoirs and floodplains' effects (Fleischmann et al., 2019a; Tanaka et al., 2017; Wang et al., 2017; Zajac et al., 2017; Zhao et al., 2020). Project flood discharges are usually estimated with simplified methods as unit hydrographs that do not consider river floodplain attenuation. An interesting and open research question relates to how far upstream can these floodplain storage effects go, what has major implications for water resources management. Floodplains alter the celerity of flood waves at the whole basin scale, and are a major driver of hydrograph shape across scales (Collischonn et al., 2017; Fleischmann et al., 2016). Besides, here we have assessed the role of flood attenuation in riverine wetlands, while at the very upstream reaches, upland rain-fed wetlands may also change towards flood generating areas, requiring further studies (ACREMAN; HOLDEN, 2013).

Natural floodplains provide valuable ecosystem services in terms of flood attenuation and resilience, and its quantification requires new tools (Ameli & Creed, 2019; Wu et al., 2020). Building new dams (especially if designed for purposes different than flood control), as well as new developments in floodplain areas (e.g., levees), may remove the large floodplain storage effects that protect downstream reaches against floods. This was shown for many rivers, as the Mississippi with hundreds of kilometers of levees deactivating the river natural flood storage (HEY; PHILIPPI, 1995) and the Danube river (SCHOBER; HAUER; HABERSACK, 2014). Furthermore, a benefit-cost analysis of acquiring floodplain lands to avoid flood damage was performed for the whole USA recently (JOHNSON et al., 2020), and suggested that the cumulative flood damages exceeds the costs of land acquisition for a 2070 scenario. The synergic effects of reservoirs and floodplains on flood attenuation have been increasingly addressed in the literature with large scale models (SHIN et al., 2020), and are in accordance with our results. The analysis and modeling improvements provided here indicate that the synergy between floodable areas and the operation of dam cascades at the whole basin scale is relevant and requires further understanding, which is beyond simpler large scale models relying solely on hydrodynamic simulations along downstream floodable areas. In the case of the Paraná basin, inserting the proposed methodology into a proper flood risk management framework will require real-time flood monitoring and forecasting.

11.5.3 Perspectives on simulating the river-floodplain-reservoir continuum at large scales

The development of coupled river-floodplain-reservoir modeling systems is associated to the hyper-resolution global modeling agenda, aiming for example to improve medium-range flood forecasts (ZAJAC et al., 2017) that are locally relevant (BIERKENS et al., 2015; FLEISCHMANN; PAIVA; COLLISCHONN, 2019; RAJIB et al., 2020; WOOD et al., 2011) within land surface, earth system or global hydrological models, and explicitly representing reservoir dynamics within detailed grids (Shin et al., 2019; Wada et al., 2016; Zajac et al., 2017). From continental to global scales, these models are powerful tools to assist national and world agencies on the coordinated planning of reservoir expansion, as well as understanding the effects of current and future dams on water and biogeochemical cycles (Bierkens et al., 2015; Wada et al., 2016), and their interaction with climate change, contributing to improve global water security (ADAM et al., 2007; ARIAS et al., 2020; DANG; CHOWDHURY; GALELLI, 2019; EHSANI et al., 2017; POFF et al., 2016; WILLIAMSON et al., 2009). On the other hand, from local to regional scales, they can be used for actual dam operation, real-time monitoring and forecasting systems, and estimation of locally relevant discharges at high spatial-temporal resolution.

The necessity of spatially and temporally continuous fields of state variables as river discharges and levels has prompted the combination of remote sensing datasets and hydraulic models (BRÊDA et al., 2019; GLEASON; DURAND, 2020). ICESat altimetry data provide valuable information for lakes (Gao, 2015; O'Loughlin et al., 2016) and are very promising for validating large scale reservoir modeling systems, while new missions as ICESat-2 (threefold increase in sampling density) and SWOT will increase our capability to remotely monitor reservoirs and estimate reservoir parameters and even reservoir operation (Bonnema & Hossain, 2017, 2019; Busker et al., 2019; Getirana et al., 2018; Van Den Hoek et al., 2019; Yao et al., 2019; Yoon et al., 2016; Yoon & Beighley, 2015). New global datasets of reservoir characteristics are also promising, including new methodologies to estimate reservoir area-depth-volume relationships based on remote-sensing datasets (CRÉTAUX et al., 2016; FASSONI-ANDRADE; DE PAIVA; FLEISCHMANN, 2020; GAO; BIRKETT; LETTENMAIER, 2012; LEHNER et al., 2011; LI et al., 2020b; LIEBE; VAN DE GIESEN; ANDREINI, 2005; MULLIGAN; VAN SOESBERGEN; SÁENZ, 2020; YIGZAW et al., 2018, 2019). These advances contributed to the development of reservoir representation in global hydrological models (Döll et al., 2009; Sutanudjaja et al., 2018; Voisin et al., 2013; Wada et al., 2016; Yassin et al., 2019; Zhou et al., 2017), including the data-driven operations schemes as presented here and in other recent studies (TURNER; DOERING; VOISIN, 2020), and are shaping the new generation of large scale water resources models.

Regarding large scale model improvement, we have adopted a 10 km river reach discretization for the Paraná basin, in accordance with current practices adopted in regional to global hydrological models (i.e., 5-10 km; Shin et al., 2019; Wada et al., 2016; Zajac et al., 2017). However, higher resolution (i.e., 1 km or smaller) are required to better represent relatively small dams. Our results indicate the need for better representation of reservoir bathymetry distribution in order to correctly address local scale hydraulic processes as backwater effects, corroborating recent studies (ADAM et al., 2007; SHIN; POKHREL; MIGUEZ-MACHO, 2019).

Finally, we have also discussed the role of fully coupling hydrological-hydrodynamic processes in a two-way scheme. The MGB model considers a dynamic surface water cover, and the associated changes in evapotranspiration/runoff generation, e.g., by alternating the soil/vegetation Penman-Monteith equation with the open water Penam evaporation scheme. Considering reservoir evaporation was also implemented by other modeling systems (ADAM et al., 2007; MAMEDE et al., 2018; ZHAO et al., 2016). This consideration is particularly important during dry periods, and even more important for reservoirs in semi-arid regions (BONNEMA et al., 2016; CELESTE; BILLIB, 2010; DÖLL; FIEDLER; ZHANG, 2009; MAMEDE et al., 2018). Besides a dynamic flood fraction cover, other reservoir processes at local scale should also be included, as reservoir sedimentation (ZHAO et al., 2016) and ground seepage.

11.6 Conclusions

In this study we presented the successful development and a thorough analysis of a regional scale model capable to simulate the daily river-floodplain-reservoir continuum that exists along large basins. A case study was performed in the ~950,000 km² Upper Paraná River Basin in South America, considering 30 regulation reservoirs and the Itaipu run-of-river dam, which is the largest in world in terms of energy production. Twelve simulation scenarios considering different reservoir bathymetry representation and reservoir operation schemes were performed, and assessed in terms of water levels, discharges, flood extent and reservoir storage. A methodology to assess the relative role of floodplains and reservoirs on basin-wide flood attenuation was presented, providing a powerful way to understand regional scale floods and the value of preserving natural floodplains' services. We conclude that:

- A distributed representation of reservoir bathymetry in large scale hydrological models is required for accurate predictions of backwater effects, upstream surface water elevation and flooding;
- The longitudinal water level profile of the large Itaipu dam was satisfactorily validated with ICESat altimetry data, which showed remote sensing data to be very promising, especially considering future satellite missions as SWOT;

- Both lumped and distributed representations of reservoir bathymetry in large scale hydrological-hydrodynamic models provide similar predictions of downstream river discharges and water levels;
- A data-driven operation scheme based on historical data of reservoir storage and outflows adds significant value to the accuracy of reservoir storage predictions, if compared to more generic algorithms;
- Although the data-driven approach outperforms more generic schemes (namely, the Hanasaki et al. (2006) - based method (H06)) in terms of discharge estimation, the simpler generic schemes provide reasonable estimates, and thus can be useful to estimate regional scale hydrological regime alteration;
- Global-based parameterizations of operation schemes lead to only slightly poorer performance in comparison to more regionally-based ones, providing reasonable estimates of regional scale hydrological regime alteration;
- However, to properly simulate the river-floodplain-reservoir continuum at regional scale, satisfactory simulation of water levels and reservoir storages are required, and thus large-scale models should include data-driven reservoir operation approaches based on regional parameterization, and distributed reservoir bathymetry (if possible, with a variable bathymetry scheme);
- In the Paraná River Basin, the floodplains are mainly located in upper parts of some tributaries and in the river mainstem, while reservoir effects are more important for flood attenuation along medium and lower reaches of tributaries. In this case, floodplains and reservoirs provide complementary flood attenuation at regional scale;
- The existence of river floodplains across the whole basin can lead to major flood attenuation at the regional scale, and not only in downstream lowland reaches, as usually assumed in large scale models;
- Major overestimation of flood design discharges can occur if the model does not consider upstream floodplain and reservoir storage effects, especially in the context of flood frequency analysis.

Finally, our results stress the importance of simulating the river-floodplain-reservoir continuum at large scales. Increasing computational capacity with intense cloud computing, and new remote sensing-based datasets and techniques, are quickly pushing the development of large to global scale models, and thus improving to a great extent our understanding and prediction capability regarding reservoir-floodplain interactions. The integration of large scale hydrodynamic models with newly available remote sensing data will provide great research opportunities in the near future.

12 Thesis conclusion and perspectives

The hydrology of South American wetlands and floods is assessed from multiple perspectives in this thesis. Firstly, by considering different wetland types, such as interfluvial wetlands and river floodplains, with their multiple subtypes, as floodable savannas, forested floodplains, open water areas, and urbanized floodplains. Secondly, by addressing different spatial scales, from continental to local. Remote sensing and flood models are now capable to estimate inundation dynamics and many other hydrological variables of interest at continental scale, and have revolutionized our understanding of the hydrological functioning of these systems. Thirdly, through a comparative hydrology approach, where similarities and dissimilarities among regions (i.e., multiple wetland complexes) and methodologies (i.e., different inundation datasets) provide interesting ways to understand floods across the continent.

In this thesis, it was shown how 2D hydrologic-hydrodynamic models are preferable over 1D ones to simulate hydrodynamic processes and variables such as surface water levels in complex, interfluvial wetlands, while river floodplains can be relatively satisfactorily simulated with both model types (Chapter 4). The case study in the Negro River basin in the Amazon evidenced the large discrepancies that exist among satellite- and model-based estimates of inundation extent over the Amazon. This prompted the intercomparison study presented in Chapter 5, whereby 29 inundation datasets were compared for different wetlands types across the Amazon basin. Results showed that a large agreement occurs over central Amazon River floodplains, and especially for the lower Amazon reaches with large open water areas, and that disagreements are higher over interfluvial areas such as the Llanos de Moxos and Roraima savannas. Especially over the Amazon mainstem and the northern Amazon basin, precipitation changes over the last four decades have largely increased the inundation extent over the Amazon river floodplains (Chapter 6), drastically affecting its biodiversity and the human societies that live along them.

The understanding of multiple wetlands with a comparative hydrology approach was then upscaled from the Amazon basin to the large South American wetlands in Part II. Wetlands associated with river floodplains (e.g., Magdalena, Pantanal, central Amazon, Paraná) have a slower flood propagation associated to river routing and feature a higher annual water level amplitude, while the interfluvial ones (e.g., Llanos de Orinoco, Llanos de Moxos, Bananal) are more dependent on local runoff and have a smaller delay between precipitation and flood peak as well as water level amplitude (Chapter 7). While most wetlands have a regular annual flood pulse, the Pampas in Argentina stand out as having a very erratic pattern with flood-rich years followed by drought-rich ones. Regarding evapotranspiration (Chapter 8), it was shown that major differences between wetlands and uplands occur in temperate climates (water-limited environments), while in equatorial ones the difference is smaller. In central Amazon, the high forest cover in upstream reaches compensates the higher flood fraction but lower forest cover in the downstream ones, maintaining high evapotranspiration year round.

Flood propagation along river floodplains is showed to be a major control of evapotranspiration dynamics in wetlands associated with a river flood pulse, especially for the Pantanal where the flood wave takes months to propagate across the system. These findings highlight the unique hydrological functioning of South America wetlands, and set forward the importance of performing comparative hydrology studies for wetlands worldwide.

Along river floodplains, millions of people live and are frequently affected by above-average floods, as the great 2021 flood in central Amazon (Chapter 6). The flood hazard topic was further assessed in this thesis for the great 1983 floods that devastated large portions of South America (Chapter 9). A continental scale hydrologic-hydrodynamic model (SIQUEIRA et al., 2018) was employed and showed the particular spatial-temporal dynamics of the 1983 floods, which were associated with an extreme El Niño event. The timing of the events had a southward direction throughout that year, with some of the largest ever recorded river discharges in northern areas such as the upper Araguaia and Tocantins rivers occurring in February 1983, and in July in southern regions as the Uruguay River. Yet the capability of such continental models to estimate peak discharges for an extreme event such as 1983 was shown to be satisfactory, it is still not clear whether they can provide locally relevant estimates of hydrodynamic variables (river discharges and water levels, and inundation extent). This topic was assessed for the Itajaí-Açu River basin, one of the most relevant flood-prone areas in the continent (Chapter 10). While it is still challenging to provide locally relevant estimates, based on the proposed criteria, some recommendations were provided, such as the need for better estimating at-a-station river cross sections. Furthermore, humans alter the river-floodplain systems through building of infrastructure such as dams. If we aim to correctly simulate the river-floodplain-reservoir continuum that exists along large drainage networks, which is fundamental to understand large-scale inundation patterns, the reservoir effects must be represented within large-scale models in a dynamic, fully distributed way (Chapter 11). This was shown for a modeling case study for the Paraná River basin, the most relevant one in South America in terms of total reservoir storage, whereby it was shown that floodplains and reservoirs have complementary roles in attenuating floods basin-wide.

The satellite era and advances in computational capabilities provide great opportunities for moving forward a continental wetland research agenda. While models and remote sensing data are not free of uncertainties, they are powerful tools to quantify the hydrology of wetlands and inundation processes. Future missions such as SWOT and NISAR will provide valuable information for monitoring water levels and inundation dynamics in near future. The understanding of water level variation in wetlands can also largely benefit from new large-scale methodologies based on InSAR, as well as from the processing of Sentinel-3 altimetry data. New methodologies to infer river channel and floodplain bathymetry (FASSONI-ANDRADE et al., 2020) are also necessary, and continental to local-scale hydrodynamic models will largely benefit from

the integration of these new remote sensing-based estimates through data assimilation, and model calibration and validation.

This thesis advances a continental wetland research agenda, in the context of continental hydrological researches that have been internationally developed in the last decade. The thesis outcomes move forward our comprehension of hydrological processes over wetlands and inundation in general, through understanding of differences among wetland types and inundation mapping methodologies, as well as dynamics of past hydroclimatic events and continental-scale flood hazard mapping. Wetlands provide important ecosystem services as climate (e.g., through surface-atmosphere interactions) and flood regulation (e.g., by floodplains that were shown to be widespread in basins such as the Paraná, and which largely affect basin-wide flood attenuation), and their functioning is dependent on a proper maintenance of the system lateral, longitudinal and vertical connectivity. Understanding wetlands as human-water systems, and advancing the remote sensing and modeling capabilities to map inundation and wetland dynamics is fundamental to assist continental-scale wetland inventories, which have been recently developed for some South American countries. Such efforts will also improve our understanding of continental-scale flood hazard, considering the vulnerability of ecosystems and human populations that live especially close to river floodplains. South American wetlands face current environmental changes and human pressures that must be better understood in order to manage them in a sustainable way, and to ensure the well-functioning of these fascinating areas that cover a large portion of the once called fluvial continent.

I would also like to stress that any scientific advance must have a dedicated science communication component, in order to facilitate its comprehension by any potential stakeholder, as well as by the general public. This is fundamental in periods of major science denial such as the one we are facing now. If science communication efforts are paramount, so do open science initiatives (e.g., standardization of wetland data and development of open data repositories), and there is a great need for the widespread investment by the scientific community in WebGIS and hydroinformatics systems that make any developed data easily accessible. For instance, two WebGIS platforms were developed in this thesis (http://etbrasil.org/wetlands and https://amazon-inundation.herokuapp.com/) to allow an easy visualization and data acquisition of wetland and inundation datasets.

By recognizing that we have multiple wetlandscapes, but one continent, long-term researches related to the hydrology of wetlands and floods at large scales must envision a seamless, cross-scale understanding of wetland processes. This involves mapping water storage in a seamless way (YU et al., 2021), i.e., mapping in a continuous way all surface water bodies that occur across landscapes, such as rivers, natural and artificial lakes, floodplains and interfluvial wetlands, as well as subsurface water storages. South American wetlands are connected through multiple pathways, from upstream-downstream links across drainage networks to climate teleconnections and national management policies and political decisions. Hydroclimate processes do not respect

river basin limits, and extreme flood events have the potential to affect human societies much further than the directly affected river floodplains. In the Anthropocene era, the tight relations between natural wetland ecosystems and human-water systems are continuously changing. At multiple scales, the South American floods reveal the fascinating world of a seamlessly connected nature.

In the introduction Section 1.1, I provide a list of research questions that have guided this thesis. Then, I finish the thesis by answering these questions, based on the thesis' findings:

- **How different are South American wetlands in terms of hydrological behaviors and hydrology-related ecosystem services?**

Many large South American wetland systems were studied in this thesis, covering the whole continent and multiple hydrological functioning, vegetation and climate types. In terms of hydrology, the main differences between wetlands were investigated in terms of the interfluvial and river floodplain classes, which are simple yet meaningful categories to understand the hydrology of wetlands. It was shown in Chapter 7 that the interfluvial ones have a smaller annual water level amplitude in comparison to river floodplains, which in turn are more connected to the main river systems and thus more sensitive to changes in their hydrological regime. Across the continent, the interfluvial areas are often associated with floodable savannas (sometimes referred to as "hyperseasonal savannas"), where the wetland tends to dry out during the dry season and gets largely flooded during the wet season (e.g., Bananal Island, Llanos de Moxos and Llanos de Orinoco). The time lag between precipitation and inundation is also smaller over interfluvial areas (two or less months), reflecting the longer downstream flood propagation that occurs over river-floodplain systems (e.g., along Paraná, Amazon and Paraguay rivers). Regarding ecosystem services, they were addressed in most chapters of this thesis in a general way, but were studied in more details in Chapter 8, in the context of climate regulation through changes in the surface energy balance (see discussion in the next research question), and in Chapter 11, in the context of flood attenuation. In the latter, it was shown how river floodplains are present across multiple parts of river basins, and provide an important flood regulation service basin-wide. A specific study case for the Paraná River basin showed the complementarity of floodplains and artificial dams in providing this service.

- **How do wetlands interact with regional/continental climate, e.g., through evapotranspiration fluxes?**

This was mainly addressed in Chapter 8, where a new cloud computation-based algorithm was used to investigate evapotranspiration (the main link between surface and atmosphere in the hydrological cycle) patterns and drivers across 12 large South American wetlandscapes. Major ET differences were found between wetlands and uplands in temperate climates (water-limited environments), while in equatorial ones the difference is smaller. In central Amazon, the high forest cover in upstream reaches compensates the higher flood fraction but lower forest cover in the downstream ones, maintaining high evapotranspiration year round. Flood propagation along river floodplains is shown to be a major control of ET dynamics in wetlands associated with a river flood pulse, especially for the Pantanal where the flood wave takes months to propagate across the system.

- **How do wetlands respond to, and interact with, current and future environmental alterations (e.g., climate change, dam building, land use and cover changes)?**

South American wetlands are still pristine in many areas, yet human pressure and climate change have been posing several threats to their well-functioning. In Chapter 7, the current and future environmental alterations were discussed. Different wetland types face environmental changes through different ways. While interfluvial wetlands are mainly subject to local climate and land cover changes, river floodplains also depend on discharge, sediment and nutrient alteration from the upstream basin, that can occur through upstream reservoir regulation, for instance. Today, major human pressure through land use change (typically agricultural use) occurs in many of the wetlands assessed here, mainly in the Pampas, Chaco, Llanos del Orinoco, Esteros del Iberá, Magdalena and lower Amazon wetlands. Large wetland systems currently affected by dams are the Magdalena and upper Paraná river. While a few dams exist today in the upper Paraguay basin surrounding the Pantanal wetlands, dozens of small ones are proposed and threaten the wetland system, especially with hydropeaking operation (i.e., sub-daily flow regime alteration) and alteration in sediment and nutrients. In the Amazon basin, multiple dams have been built in the last decade and affect downstream floodplains through hydropeaking operation, while new large storage reservoirs are planned for the Andean Amazonian portions and threaten especially the Llanos de Moxos and the upper Amazon river floodplains. Finally, the effect of climate change on the wetlands' hydrologic regime is better understood if differentiating interfluvial areas and river floodplains types of wetlands. While the former are more affected by local rainfall and temperature changes, which in turn affect local river tributaries, floodplains may also be affected by changes in upstream areas, sometimes thousands of kilometers upstream. Overall, climate change projections have suggested a decrease in water availability for wetlands worldwide by the middle of century.

- **How do remote sensing datasets, from global to local scales, depict inundation dynamics over multiple wetlands? Do they agree on inundation extent, and how to improve their performance?**

Multiple inundation datasets were used and compared in this thesis, especially for the Amazon region (Part I). In particular, Chapter 5 presented an intercomparison of 29 products for the Amazon wetlands, mostly based on remote sensing. Major agreements were found, in terms of inundation spatial distribution, along the central Amazon river floodplains, especially for the open water areas in the lower reaches. In turn, important disagreements persist for interfluvial areas such as the Negro, Roraima and Llanos de Moxos savannas, as well as for the Pacaya-Samiria region, for which further developments are needed by the international remote sensing and modeling communities. The comparison of remote sensing products with hydrological models, which was also performed in Chapter 4, showed that each dataset and method has its own advantages and disadvantages, so that the optimal solution is certainly pursuing an optimized fusion of all the datasets (e.g., data assimilation techniques). Furthermore, large discrepancies persist for mapping inundation at local scales (e.g., < 30 m), especially when assessing the temporal dynamics of inundation (e.g., flood frequency).

- **How do continental models represent wetlands and local hydrodynamic processes, and how to improve their performance?**

The increase in computational capacity, as well as the availability of remote sensing datasets to understand the environment at large scales, has allowed the development in the last years of multiple hydrologic-hydrodynamic models. In this thesis, large-scale models were applied at different dimensions (1D and 2D) and scales (local, regional and continental) to simulate flood dynamics. Results showed that 2D models are preferrable to simulate the hydrological dynamics of interfluvial wetlands (in a case study for the Negro River basin in the Amazon), while both 1D and 2D models are satisfactory to estimate variables such as river water levels, discharge and flood extent for river floodplains. Regarding the scale of analysis, continental-scale models were shown, for a case study in the Itajaí-Açu River basin, to be able to provide locally relevant estimates of discharges and water level anomalies, while flood extent and absolute water level estimates were less accurate. Model scenarios showed that the model improvement would be mainly achieved by including more detailed river cross sections within the model, which could be obtained through new remote sensing techniques. The satisfactory ability of the MGB South America hydrological model to understand extreme river discharges was assessed for the 1983 floods that affected a large portion of the continent. Finally, regarding model structure, the existence of human alterations in river basins, such as dams, must be included in the models to be able to accurately represent the basin's hydrological processes. This was shown for the Paraná River basin, for which the operation of 31 dams were simulated together with the flood dynamics along river floodplains at the basin scale. Thus, this allowed the explicit

simulation of the river-floodplain-reservoir continuum in terms of hydrological variables.

- **How humans are affected by, and affect, the normal and anomalous flood events along wetlands, especially along river floodplains?**

Humans alter the river basin landscape and have a two-way interaction with hydrology, in a way that the ultimate hydrological behavior of a given river depends on the socio-hydrological interactions. One example of human alteration is the building of dams. In Chapter 11, the complementarity of natural wetlands (in this case, river floodplains) and dams on attenuating floods was assessed, defining what was called the river-floodplain-reservoir continuum. Furthermore, the use of hydrologic-hydrodynamic models is very relevant for understanding large-scale flood patterns affecting societies that live along river floodplains. This was shown, in Chapter 9, for the great 1983 floods that affected a large portion of the continent, through the usage of the MGB South America model. This study allowed a broad understanding of the spatio-temporal dynamics of the 1983 events, which timing had a southward direction throughout that year, with some of the largest ever recorded river discharges in northern areas such as the upper Araguaia and Tocantins rivers occurring in February 1983, and in July in southern regions as the Uruguay River. Finally, Chapter 6 presented the analysis of inundation trends over the Amazon River basin, considering multiple remote sensing and modeling datasets. Results showed that riparian human communities along river floodplains have been facing an intensifying flood risk, with many record-break floods in the last decade, and an increase of around 20% of the maximum inundation extent in the region during the last four decades. Across the continent, riparian communities face an increasing need of adapting to such changing environments.

12. Conclusões e perspectivas gerais

Nesta tese, a hidrologia das áreas úmidas e inundações da América do Sul é avaliada a partir de múltiplas perspectivas. Primeiramente, considerando diferentes tipos de áreas úmidas, como áreas interfluviais e planícies de inundação, com os seus múltiplos subtipos, como savanas e florestas inundáveis, áreas de água aberta e planícies de inundação urbanizadas. Em segundo lugar, considerando diferentes escalas espaciais, do continental ao local. Produtos de sensoriamento remoto e modelos matemáticos de inundação são capazes de estimar a dinâmica de inundação e muitas outras variáveis hidrológicas de interesse em escala continental, e têm revolucionado nossa compreensão do funcionamento hidrológico desses sistemas. Em terceiro lugar, adotando uma abordagem de hidrologia comparativa, onde semelhanças e diferenças entre regiões (ou seja, diversos complexos de áreas úmidas) e metodologias (ou seja, diferentes produtos de inundação) fornecem formas interessantes de compreender as inundações em todo o continente.

Foi mostrado como modelos hidrológico-hidrodinâmicos 2D são preferíveis em relação a modelos 1D para simular processos hidrodinâmicos e variáveis como níveis d'água em complexas áreas úmidas, enquanto as planícies de inundação dos rios podem ser simuladas de forma relativamente satisfatória com ambos os modelos (Capítulo 4). O estudo de caso na bacia do rio Negro, na Amazônia, evidenciou as grandes discrepâncias existentes entre as estimativas de extensão da inundação na Amazônia baseadas em satélites e modelos. Isso levou ao estudo apresentado no Capítulo 5, em que 29 produtos de inundação foram comparados para diferentes tipos de áreas úmidas na bacia amazônica. Os resultados mostraram que ocorre uma grande concordância para as planícies de inundação da Amazônia central, e especialmente para o baixo rio Amazonas, com grandes extensões de água aberta, e que as divergências são maiores sobre áreas interfluviais, como as savanas de Llanos de Moxos e Roraima. Especialmente sobre as partes norte e central da bacia amazônica, o aumento da precipitação nas últimas quatro décadas aumentou em grande parte a extensão da inundação sobre as várzeas do rio Amazonas (Capítulo 6), afetando drasticamente a sua biodiversidade e as sociedades humanas que ali vivem.

A compreensão de múltiplas áreas úmidas através de uma abordagem de hidrologia comparativa foi ampliada da bacia amazônica para as grandes áreas úmidas da América do Sul na Parte II. As áreas úmidas associadas às planícies de inundação dos rios (por exemplo, Magdalena, Pantanal, Amazónia central, Paraná) têm uma propagação de cheias mais lenta ao longo dos rios, e apresentam uma maior amplitude anual do nível d'água, enquanto as áreas interfluviais (por exemplo, Llanos de Orinoco, Llanos de Moxos, Bananal) são mais dependentes do escoamento superficial local e têm um menor atraso entre a precipitação e o pico de cheia, bem como uma menor amplitude do nível d'água (Capítulo 7). Enquanto a maioria das áreas úmidas tem um pulso de inundação anual regular, os Pampas na Argentina destacam-se como tendo um padrão

muito errático com anos ricos em cheias seguido por períodos com sequências de secas. Em relação à evapotranspiração (Capítulo 8), mostrou-se que grandes diferenças entre áreas úmidas e áreas de terra firme ocorrem em climas temperados (ambientes limitados por água), enquanto em equatoriais a diferença é menor. Na Amazônia central, a alta cobertura florestal a montante compensa a maior fração de inundação e menor cobertura florestal que ocorre nas regiões de jusante, mantendo altas taxas de evapotranspiração durante todo o ano. Mostrou-se que a propagação de cheias ao longo das planícies de inundação é um importante controle da dinâmica de evapotranspiração em áreas úmidas associadas a pulsos de inundação fluviais, especialmente no Pantanal, onde a onda de cheia leva meses para se transladar através do sistema. Estes resultados destacam o funcionamento hidrológico único das áreas úmidas da América do Sul e realçam a importância da realização de estudos hidrológicos comparativos para áreas úmidas de todo o mundo.

Ao longo das planícies de inundação, milhões de pessoas vivem e são frequentemente afetadas por inundações extremas, como a grande enchente de 2021 na Amazônia central (Capítulo 6). O tema de perigo de inundação foi avaliado nesta tese para as grandes inundações de 1983, que devastaram grandes porções da América do Sul (Capítulo 9). Empregou-se um modelo hidrológico-hidrodinâmico de escala continental (SIQUEIRA et al., 2018) para avaliar a dinâmica espaço-temporal das inundações de 1983, que foram associadas a um evento extremo de El Niño. O *timing* dos eventos teve uma direção de norte a sul ao longo do ano, com algumas das maiores vazões de rios já registradas em áreas do norte, como os rios Araguaia e Tocantins, ocorrendo em fevereiro de 1983, e em julho, em regiões do sul como o rio Uruguai. No entanto, enquanto a capacidade de tais modelos continentais para estimar as vazões de pico para um evento extremo como 1983 mostrou-se satisfatória, ainda não é claro se eles podem fornecer estimativas localmente relevantes de variáveis hidrodinâmicas (descargas de rios e níveis d'água, e extensão da inundação). Este tópico foi avaliado para a bacia do rio Itajaí-Açu, uma das áreas mais propensas a inundações do continente (Capítulo 10). Embora ainda seja um desafio fornecer estimativas localmente relevantes, com base nos critérios propostos, algumas recomendações foram fornecidas, como a necessidade de uma melhor estimativa de seções transversais das calhas fluviais. Além disso, os seres humanos alteram os sistemas rio-área úmida através da construção de infraestruturas como barragens. Se pretendemos modelar corretamente o *continuum* rio-reservatório-áreas úmidas que existe ao longo de grandes redes de drenagem, o que é fundamental para entender padrões de inundação em grande escala, os efeitos dos reservatórios devem ser representados de forma dinâmica e totalmente distribuída (Capítulo 11). Isso foi investigado em um estudo de caso de modelagem para a bacia do rio Paraná, a mais relevante na América do Sul em termos de armazenamento total de reservatórios, em que foi mostrado que as planícies de inundação e os reservatórios têm papéis complementares em atenuar cheias em toda a bacia.

A era dos satélites e os avanços nas capacidades computacionais oferecem grandes oportunidades para avançar a agenda de pesquisa de áreas úmidas em escala continental.

Embora os modelos e os dados de sensoriamento remoto não sejam livres de incertezas, eles são ferramentas poderosas para quantificar a hidrologia de áreas úmidas e processos de inundação. Missões futuras como SWOT e NISAR fornecerão informações valiosas para monitorar os níveis d'água e a dinâmica de inundação em um futuro próximo. A compreensão da variação do nível d'água nas áreas úmidas também pode se beneficiar largamente de novas metodologias de grande escala baseadas em técnicas InSAR, bem como do processamento de dados de altimetria da missão Sentinel-3. São igualmente necessárias novas metodologias para inferir a batimetria dos canais fluviais e das planícies aluviais (FASSONI-ANDRADE et al., 2020). Os modelos hidrodinâmicos de escala continental a local serão beneficiados em grande medida pela integração destas novas estimativas oriundas do sensoriemanto remoto através da assimilação de dados e métodos de calibração e validação de modelos.

Esta tese promove uma agenda de pesquisa de áreas úmidas em escala continental, no contexto de pesquisas hidrológicas continentais a globais que têm sido desenvolvidas internacionalmente na última década. Os resultados da tese avançam a compreensão dos processos hidrológicos sobre áreas úmidas e inundação em geral, através da compreensão de diferenças entre tipos de áreas úmidas e metodologias de mapeamento de inundação, bem como dinâmicas de eventos hidroclimáticos passados e mapeamento de perigo de inundação em escala continental. As áreas úmidas fornecem serviços ecossistêmicos importantes como a regulação de clima (por exemplo, através de interações superfície-atmosfera) e inundações (por exemplo, por planícies de inundação que se mostraram generalizadas em bacias como o Paraná, e que amplamente afetam a atenuação de cheias em toda a bacia), e o seu funcionamento depende de uma manutenção adequada da conectividade lateral, longitudinal e vertical destes sistemas. Entender as áreas úmidas como sistemas sociedade-água, e melhorar as técnicas de sensoriamento remoto e modelagem para mapear a inundação e processos hidrológicos de áreas úmidas, é fundamental para auxiliar o desenvolvimento de inventários em escala continental, como os que têm sido elaborados nos últimos anos para alguns países da América do Sul. Esses esforços também irão melhorar a nossa compreensão do risco de inundação em escala continental, considerando a vulnerabilidade dos ecossistemas e das populações humanas que vivem especialmente perto de planícies de inundação. Hoje, as áreas úmidas da América do Sul enfrentam mudanças ambientais e pressões humanas que devem ser melhor compreendidas, a fim de gerenciá-las de forma sustentável e garantir o bom funcionamento dessas fascinantes áreas que cobrem uma grande porção do continente sul-americano.

Gostaria também de salientar que qualquer pesquisa científica deve ter uma componente de divulgação científica, a fim de facilitar a sua compreensão por qualquer potencial parte interessada (gestores públicos, etc.), bem como pelo público em geral. Isso é fundamental em períodos de grande negação da ciência, como o que estamos enfrentando agora. Se os esforços de divulgação científica são primordiais, o mesmo acontece com as iniciativas de ciência aberta (por exemplo, através de padronização de dados de áreas úmidas e desenvolvimento de repositórios de dados abertos), e há uma

grande necessidade de a comunidade científica investir em sistemas de WebGIS e hidroinformática, fazendo todos os dados desenvolvidos facilmente acessíveis. Por exemplo, duas plataformas WebGIS foram desenvolvidas nesta tese (http://etbrasil.org/wetlands e https://amazon-inundation.herokuapp.com/) a fim de permitir uma fácil visualização e aquisição de dados relacionados a áreas úmidas e inundação.

Ao reconhecer que temos múltiplas paisagens de áreas úmidas, mas um único continente, as pesquisas a longo prazo relacionadas com a hidrologia de áreas úmidas e inundações devem objetivar uma compreensão holística e em grande escala dos processos hidrológicos. Isso envolve mapear o armazenamento de água de forma contínua (YU et al., 2021), ou seja, mapear sem descontinuidades todos os corpos de água superficiais que ocorrem na paisagem, como rios, lagos naturais e artificiais, planícies de inundação e áreas úmidas interfluviais, bem como os armazenamentos subterrâneos de água. As áreas úmidas da América do Sul estão conectadas de várias formas, através de redes de drenagem, teleconexões climáticas e mesmo políticas nacionais de gestão. Os processos hidroclimáticos não respeitam os limites das bacias hidrográficas, e as inundações extremas têm o potencial de afetar sociedades humanas muito distantes das planícies de inundação diretamente afetadas. Na era do Antropoceno, as relações estreitas entre ecossistemas de áreas úmidas e sistemas sociedade-água estão em constante mudança. Em múltiplas escalas, as inundações sul-americanas revelam o fascinante mundo de uma natureza profundamente conectada.

Na Seção 1.1 de introdução, apresentei uma lista de questões de pesquisa que nortearam esta tese. Assim, termino esta tese respondendo a estas perguntas, com base nos resultados obtidos:

- **Quão diferentes são as áreas úmidas (AU's) da América do Sul em termos de comportamentos hidrológicos e serviços ecossistêmicos relacionados a hidrologia?**

Grandes sistemas de AU's da América do Sul foram estudados nesta tese, cobrindo todo o continente e vários tipos de funcionamento hidrológico, vegetação e clima. Em termos de hidrologia, as principais diferenças entre as AU's foram investigadas em termos das classes de planícies de inundação e áreas interfluviais, que são categorias simplificadas de AU's, mas significativas para compreender a hidrologia destas áreas. Foi mostrado no Capítulo 7 que as áreas interfluviais têm uma menor amplitude de nível de água anual em comparação com as planícies de inundação dos rios, que por sua vez estão mais conectados aos principais sistemas fluviais e, portanto, a mudanças em seu regime hidrológico. Em todo o continente, as áreas interfluviais são frequentemente associadas a savanas inundáveis (às vezes referidas como "savanas hipersazonais"), onde toda a área úmida seca durante a estação seca e fica em grande

parte inundada durante a estação chuvosa (por exemplo, Ilha do Bananal, Llanos de Moxos e Llanos de Orinoco). A defasagem de tempo entre a precipitação e a inundação também é menor em áreas interfluviais (dois ou menos meses), refletindo a lenta propagação de cheias que ocorre ao longo do sistema rio-planície (por exemplo, ao longo dos rios Paraná, Amazônia e Paraguai). Em relação aos serviços ecossistêmicos, estes foram abordados na maioria dos capítulos desta tese de forma geral, mas foram estudados mais detalhadamente no Capítulo 8, no contexto da regulação climática por meio de mudanças no balanço energético superficial (ver discussão na próxima questão), e no capítulo 11, no contexto da atenuação de cheias. Neste último, foi mostrado como as planícies de inundação dos rios estão presentes em várias partes das bacias hidrográficas, e fornecem um importante serviço de regulação de cheias em toda a bacia. Um caso de estudo específico para a bacia do rio Paraná mostrou a complementaridade destas AU's e de barragens artificiais na prestação desse serviço.

- **Como AU's interagem com o clima regional/continental, e.g., através de fluxos de evapotranspiração?**

Este tópico foi abordado principalmente no Capítulo 8, onde um novo algoritmo baseado em computação de nuvens foi usado para investigar padrões e fatores determinantes da evapotranspiração (ET; a principal conexão entre superfície e atmosfera no ciclo hidrológico) em 12 grandes AU's da América do Sul. Grandes diferenças de ET foram encontradas entre AU's e terra firme em climas temperados (ambientes limitados por água), enquanto que em equatoriais a diferença é menor. A propagação de cheias ao longo das planícies de inundação dos rios mostra-se um grande controle da dinâmica dos ET em AU's associadas a um pulso de inundação fluvial, especialmente para o Pantanal onde a onda de cheia leva meses para se propagar ao longo do sistema.

- **Como as AU's respondem e interagem com as atuais e futuras mudanças ambientais (e.g., mudanças climáticas, construção de barragens, mudanças de uso da terra)?**

As AU's da América do Sul continuam intocadas em muitas áreas, mas as pressões antrópicas e as mudanças climáticas têm ameaçado o seu bom funcionamento. No capítulo 7, foram discutidas as alterações ambientais atuais e futuras. Cada tipo de AU responde a alterações ambientais de uma forma diferente. Embora as AU's interfluviais estejam sujeitas principalmente a alterações do clima e da cobertura do solo locais, as planícies aluviais dos rios também dependem da vazão, dos sedimentos e da alteração de nutrientes da bacia a montante, que podem ocorrer através da regularização por reservatórios a montante, por exemplo. Hoje, grande pressão por mudança do uso da terra (uso tipicamente agrícola) ocorre em muitas das AU's avaliadas nesta tese, principalmente nos Pampas, Chaco, Llanos del Orinoco, Esteros del Iberá, Magdalena e planícies aluviais inferiores do Amazonas. Algumas AU's estão próximas de áreas

alteradas pelo ser humano, como a Ilha Bananal, no ecótono Amazônia-Cerrado. Grandes sistemas de AU's atualmente afetados por barragens são o Magdalena e o alto rio Paraná. Embora existam hoje poucas barragens na bacia do Alto Paraguai em torno das AU's do Pantanal, dezenas de pequenas estão propostas e ameaçam o sistema de AU's, especialmente com operação de "hydropeaking" e alteração em sedimentos e nutrientes. Na bacia amazônica, várias barragens foram construídas na última década e afetam planícies de inundação a jusante por meio de operação de "hydropeaking", enquanto novos grandes reservatórios de armazenamento são planejadas para as porções andinas da Amazônia e ameaçam especialmente os Llanos de Moxos e as planícies de inundação do alto rio Amazonas. Por último, o efeito das mudanças climáticas no regime hidrológico das AU's é mais bem compreendido se se diferenciarem as áreas interfluviais das planícies aluviais dos rios. Enquanto as primeiras são mais afetadas pelas chuvas e mudanças de temperatura locais, que por sua vez afetam os pequenos rios locais, as planícies de inundação também podem ser afetadas por mudanças em áreas a montante, às vezes milhares de quilômetros a montante. Em geral, as projeções de mudanças climáticas sugerem uma diminuição na disponibilidade de água para AU's ao redor do planeta para a metade do século.

- **Como produtos de sensoriamento remoto, de escalas global a local, descrevem a dinâmica de inundação em múltiplas AU's? Eles concordam em extensão de áreas inundadas? Como melhorar a sua performance?**

Múltiplos conjuntos de dados de inundação foram utilizados e comparados nesta tese, especialmente para a região amazônica (Parte I). Em particular, o Capítulo 5 apresentou uma intercomparação de 29 produtos para as AU's da Amazônia, a maioria baseada em sensoriamento remoto. Uma boa concordância foi encontrada, em termos de distribuição espacial de inundação, ao longo das planícies de inundação do rio Amazonas, especialmente para as áreas de águas abertas no baixo Amazonas. Por sua vez, importantes divergências persistem em áreas interfluviais como as savanas do rio Negro, Roraima e Llanos de Moxos, bem como para a região de Pacaya-Samiria, para a qual novos desenvolvimentos são necessários pelas comunidades internacionais de sensoriamento remoto e modelagem. A comparação de produtos de sensoriamento remoto com modelos hidrológicos, que também foi realizada no Capítulo 4, mostrou que cada conjunto de dados e método tem suas próprias vantagens e desvantagens, de modo que a solução ideal certamente está relacionada à fusão otimizada de todos os conjuntos de dados (por exemplo, técnicas de assimilação de dados). Além disso, persistem grandes discrepâncias para mapear a inundação em escalas locais (por exemplo, com 30 m de resolução espacial), especialmente ao avaliar a dinâmica temporal da inundação (por exemplo, frequência de inundação).

- **Como modelos matemáticos continentais (modelos baseados em processos) representam AU's e processos hidrodinâmicos locais, e como melhorar a sua performance?**

O aumento da capacidade computacional, bem como a disponibilidade de conjuntos de dados de sensoriamento remoto para compreender o meio ambiente em grandes escalas, permitiu o desenvolvimento nos últimos anos de múltiplos modelos hidrológico-hidrodinâmicos. Nesta tese, modelos de grande escala foram aplicados em diferentes dimensões (1D e 2D) e escalas (local, regional e continental) para simular a dinâmica de cheias. Os resultados mostraram que os modelos 2D são preferíveis para simular a dinâmica hidrológica de AU's interfluviais (em um estudo de caso para a bacia do rio Negro na Amazônia), enquanto os modelos 1D e 2D são satisfatórios para estimar variáveis como níveis d'água do rio, vazão e extensão de áreas inundadas nas planícies fluviais. Em relação à escala de análise, realizou-se um estudo de caso na bacia do Rio Itajaí-Açu (sul do Brasil), onde uma grande quantidade de dados de campo estavam disponíveis, buscando-se avaliar a capacidade de modelos continentais de fornecer estimativas de variáveis hidrodinâmicas que sejam localmente relevantes. Concluiu-se que estes modelos são capazes de estimar satisfatoriamente as vazões de rios e anomalias do nível d'água, enquanto as estimativas da extensão de áreas inundadas e do nível absoluto da água foram menos acuradas. Os cenários simulados mostraram que a melhoria do modelo seria alcançada principalmente através da inclusão de seções transversais mais detalhadas na modelagem, que poderiam ser obtidas através de novas técnicas de sensoriamento remoto. A capacidade do modelo hidrológico MGB, em sua versão aplicada à América do Sul, para entender as vazões extremas de rios foi avaliada para as cheias de 1983 que afetaram uma grande porção do continente. Finalmente, em relação à estrutura do modelo, mostrou-se que a existência de alterações humanas em bacias hidrográficas, como barragens, deve ser incluída nos modelos para poder representar com acurácia os processos hidrológicos da bacia. Isso foi demonstrado para a bacia do Rio Paraná, para a qual a operação de 31 barragens foi simulada juntamente com a dinâmica de cheias ao longo das planícies hidrográficas na escala da bacia. Assim, isso permitiu a simulação explícita do *continuum* rio-planície-reservatório em termos de variáveis hidrológicas e hidrodinâmicas.

- **Como seres humanos afetam e são afetados por eventos normais e anômalos de inundações em AU's, especialmente em planícies de inundação?**

Os seres humanos alteram a paisagem da bacia hidrográfica e têm uma interação bidirecional com a hidrologia, de uma forma que o comportamento hidrológico final de um determinado rio depende das interações socio-hidrológicas. Um exemplo de alteração humana é a construção de barragens. No capítulo 11, avaliou-se a complementaridade das AU's naturais (neste caso, planícies de inundação de rios) e barragens na atenuação de cheias, definindo o que foi chamado de *continuum* rio-planície-reservatório. Além disso, o uso de modelos hidrológico-hidrodinâmicos é

muito relevante para a compreensão de padrões de inundação em larga escala. Isso foi mostrado, no capítulo 9, para as grandes cheias de 1983 que afetaram uma grande porção do continente, através do uso do modelo MGB América do Sul. Este estudo permitiu uma ampla compreensão da dinâmica espaço-temporal dos eventos de 1983. Mostrou-se que múltiplos eventos extremos ocorreram ao longo do ano, com algumas das maiores vazões já registradas em áreas do norte, como os rios Araguaia e Tocantins, ocorrendo em fevereiro de 1983, e em julho, em regiões do sul, como o rio Uruguai. Finalmente, o capítulo 6 apresentou a análise das tendências de inundação na bacia do rio Amazonas, considerando múltiplos conjuntos de dados de sensoriamento remoto e modelagem. Os resultados mostraram que as comunidades humanas ribeirinhas ao longo das planícies aluviais têm enfrentado um risco de inundação crescente, com muitas inundações recordes na última década, e um aumento de cerca de 20% da extensão máxima de inundação na região ao longo das últimas quatro décadas. Em todo o continente, as comunidades ribeirinhas enfrentam uma necessidade crescente de se adaptar a tais ambientes em mudança.

References

ABDALATI, W. et al. The ICESat-2 laser altimetry mission. **Proceedings of the IEEE**, 2010.

ABRIL, G. et al. Amazon River carbon dioxide outgassing fuelled by wetlands. **Nature**, v. 505, n. 7483, p. 395–398, 15 jan. 2014.

ACREMAN, M.; HOLDEN, J. How wetlands affect floods. **Wetlands**, v. 33, n. 5, p. 773–786, 2013.

ADAM, J. C. et al. Simulation of reservoir influences on annual and seasonal streamflow changes for the Lena, Yenisei, and Ob' rivers. **Journal of Geophysical Research**, v. 112, n. D24, p. D24114, 28 dez. 2007.

ADAMS, T. E.; CHEN, S.; DYMOND, R. Results from Operational Hydrologic Forecasts Using the NOAA/NWS OHRFC Ohio River Community HEC-RAS Model. **Journal of Hydrologic Engineering**, v. 23, n. 7, p. 04018028, 2018.

AGOSTINHO, A. et al. **Biodiversity in the High Parana River Floodplain**, 2000.

AGOSTINHO, A.; GOMES, L. C.; ZALEWSKI, M. The importance of floodplains for the dynamics of fish communities of the upper river Paraná. **International Journal of Ecohydrology & Hydrobiology**, v. 1, n. 1–2, p. 209–217, 2001.

AGOSTINHO, A.; PELICICE, F.; GOMES, L. Dams and the fish fauna of the Neotropical region: impacts and management related to diversity and fisheries. **Brazilian Journal of Biology**, v. 68, n. 4 suppl, p. 1119–1132, nov. 2008.

AIRES, F. et al. A Global Dynamic Long-Term Inundation Extent Dataset at High Spatial Resolution Derived through Downscaling of Satellite Observations. **Journal of Hydrometeorology**, v. 18, n. 5, p. 1305–1325, maio 2017.

AIRES, F. et al. Comparison of visible and multi-satellite global inundation datasets at high-spatial resolution. **Remote Sensing of Environment**, v. 216, n. July 2017, p. 427–441, out. 2018.

AIRES, F.; PAPA, F.; PRIGENT, C. A Long-Term, High-Resolution Wetland Dataset over the Amazon Basin, Downscaled from a Multiwavelength Retrieval Using SAR Data. **Journal of Hydrometeorology**, v. 14, n. 2, p. 594–607, abr. 2013.

AL BITAR, A. et al. The global SMOS Level 3 daily soil moisture and brightness temperature maps. **Earth System Science Data**, v. 9, n. 1, p. 293–315, 6 jun. 2017.

AL ZAYED, I. S. et al. Satellite-based evapotranspiration over Gezira Irrigation Scheme, Sudan: A comparative study. **Agricultural Water Management**, v. 177, p. 66–76, 2016.

ALBERNAZ, A. L. et al. Tree species compositional change and conservation implications in the white-water flooded forests of the Brazilian Amazon. **Journal of Biogeography**, v. 39, n. 5, p. 869–883, 2012.

ALFIERI, L. et al. Advances in pan-European flood hazard mapping. **Hydrological**

Processes, 2013.

ALFIERI, L. et al. Advances in pan-European flood hazard mapping. **Hydrological Processes**, v. 28, n. 13, p. 4067–4077, 2014.

ALFIERI, L. et al. Modelling the socio-economic impact of river floods in Europe. **Natural Hazards and Earth System Sciences**, v. 16, n. 6, p. 1401–1411, 16 jun. 2016.

ALFIERI, L. et al. A global network for operational flood risk reduction. **Environmental Science and Policy**, v. 84, n. March, p. 149–158, 2018a.

ALFIERI, L. et al. Multi-Model Projections of River Flood Risk in Europe under Global Warming. **Climate**, v. 6, n. 1, p. 6, 24 jan. 2018b.

ALFIERI, L. et al. A global streamflow reanalysis for 1980-2018. **Journal of Hydrology X**, p. 100049, dez. 2019.

ALHO, P.; AALTONEN, J. Comparing a 1D hydraulic model with a 2D hydraulic model for the simulation of extreme glacial outburst floods. **Hydrological Processes**, v. 22, n. 10, p. 1537–1547, 15 maio 2008.

ALLEN, G. H.; PAVELSKY, T. M. Global extent of rivers and streams. **Science**, v. 361, n. 6402, p. 585–588, 10 ago. 2018.

ALLEN, R. et al. Satellite-based ET estimation in agriculture using SEBAL and METRIC. **Hydrological Processes**, v. 25, p. 4011–4027, 2011.

ALLEN, R. G. et al. Automated Calibration of the METRIC-Landsat Evapotranspiration Process. **JAWRA Journal of the American Water Resources Association**, v. 49, n. 3, p. 563–576, jun. 2013.

ALLEN, R.; TASUMI, M.; TREZZA, R. Satellite-Based Energy Balance for Mapping Evapotranspiration With Internalized Calibration (METRIC) – Model. **Journal of Irrigation and Drainage Engineering**, v. 133, 2007.

ALMEIDA, R. M. et al. Extreme floods increase CO2 outgassing from a large Amazonian river. **Limnology and Oceanography**, v. 62, n. 3, p. 989–999, 2017.

ALMEIDA, R. M. et al. Reducing greenhouse gas emissions of Amazon hydropower with strategic dam planning. **Nature Communications**, v. 10, n. 1, p. 4281, 19 dez. 2019.

ALMEIDA, R. M. et al. Hydropeaking Operations of Two Run-of-River Mega-Dams Alter Downstream Hydrology of the Largest Amazon Tributary. **Frontiers in Environmental Science**, v. 8, n. July, p. 1–11, 2020.

ALMEIDA, R. M. et al. Climate change may impair electricity generation and economic viability of future Amazon hydropower. **Global Environmental Change**, v. 71, n. January, p. 102383, nov. 2021.

ALMUDI, T. **Water up to our necks : learning and responses to hydroclimatic variability in Brazilian Amazon floodplain communities by**. [s.l: s.n.].

ALSDORF, D. et al. Spatial and temporal complexity of the Amazon flood measured from space. **Geophysical Research Letters**, v. 34, n. 8, 2007.

ALSDORF, D. E. Water Storage of the Central Amazon Floodplain Measured with GIS and Remote Sensing Imagery. **Main**, v. 93, n. 1, p. 55–66, 2003.

ALTENAU, E. H. et al. The effects of spatial resolution and dimensionality on modeling regional-scale hydraulics in a multichannel river. **Water Resources Research**, v. 53, n. 2, p. 1683–1701, fev. 2017.

ALVARENGA, G. C. et al. Spatial patterns of medium and large size mammal assemblages in várzea and terra firme forests, Central Amazonia, Brazil. **PLoS ONE**, v. 13, n. 5, p. 1–19, 2018.

AMELI, A. A.; CREED, I. F. Does Wetland Location Matter When Managing Wetlands for Watershed-Scale Flood and Drought Resilience? **JAWRA Journal of the American Water Resources Association**, v. 55, n. 3, p. 529–542, 12 jun. 2019.

ANA. **Atlas Irrigação: Uso da Água na Agricultura Irrigada**. Brasília: [s.n.]. Disponível em: <https://arquivos.ana.gov.br/imprensa/publicacoes/AtlasIrrigacao-UsodaAguanaAgriculturaIrrigada.pdf>.

ANDELMAN, M. et al. **Agua, soja y humedales: Aportes hacia un manejo responsable**. [s.l: s.n.]. Disponível em: <https://lac.wetlands.org/publicacion/agua-soja-y-humedales/>.

ANDERSON, E. P. et al. Fragmentation of Andes-to-Amazon connectivity by hydropower dams. **Science Advances**, v. 4, n. 1, 2018.

ANDERSON, M. C. et al. A Multiscale Remote Sensing Model for Disaggregating Regional Fluxes to Micrometeorological Scales. **Journal of Hydrometeorology**, v. 5, n. 2, p. 343–363, 2004.

ANDERSSON, J. C. M. et al. Process refinements improve a hydrological model concept applied to the Niger River basin. **Hydrological Processes**, v. 31, n. 25, p. 4540–4554, 2017.

ANDRADE, M. M. N. DE et al. Flood Risk Mapping in the Amazon. In: **Flood Risk Management**. [s.l.] InTech, 2017. p. 13.

ANDREADIS, K. M. et al. Can Atmospheric Reanalysis Data Sets Be Used to Reproduce Flooding Over Large Scales? **Geophysical Research Letters**, v. 44, n. 20, p. 10,369-10,377, 2017a.

ANDREADIS, K. M. et al. Can Atmospheric Reanalysis Data Sets Be Used to Reproduce Flooding Over Large Scales? **Geophysical Research Letters**, 2017b.

ANDREADIS, K. M.; SCHUMANN, G. J. P.; PAVELSKY, T. A simple global river bankfull width and depth database. **Water Resources Research**, v. 49, n. 10, p. 7164–7168, 2013.

ANEEL. **Sistema de Informações Geográficas do Setor Elétrico - SIGEL**. Disponível em: <https://sigel.aneel.gov.br/portal/home/>.

ANGARITA, H. et al. Basin-scale impacts of hydropower development on the Mompós Depression wetlands, Colombia. **Hydrology and Earth System Sciences**, v. 22, n. 5, p. 2839–2865, 8 maio 2018.

ANTHONY, E. J. et al. Sustainable management, conservation, and restoration of the amazon river delta and amazon-influenced guianas coast: A review. **Water (Switzerland)**, v. 13, n. 10, p. 1–23, 2021.

APEL, H. et al. Flood risk analyses - How detailed do we need to be? **Natural Hazards**, v. 49, n. 1, p. 79–98, 2009.

ARANTES, C. C. et al. Environmental influences on the distribution of arapaima in Amazon floodplains. **Environmental Biology of Fishes**, v. 96, n. 10–11, p. 1257–1267, 2013.

ARANTES, C. C. et al. Relationships between forest cover and fish diversity in the Amazon River floodplain. **Journal of Applied Ecology**, v. 55, n. 1, p. 386–395, 2018.

ARAÚJO, A. C. et al. Comparative measurements of carbon dioxide fluxes from two nearby towers in a central Amazonian rainforest: The Manaus LBA site. **Journal of Geophysical Research: Atmospheres**, v. 107, n. D20, p. LBA 58-1-LBA 58-20, out. 2002.

ARAUJO, A. G. DE J. et al. Relationships between variability in precipitation, river levels, and beef cattle production in the Brazilian Pantanal. **Wetlands Ecology and Management**, v. 26, n. 5, p. 829–848, 8 out. 2018.

ARCHFIELD, S. A. et al. Accelerating advances in continental domain hydrologic modeling. **Water Resources Research**, v. 51, n. 12, p. 10078–10091, dez. 2015.

ARHEIMER, B.; LINDSTRÖM, G. Climate impact on floods: changes in high flows in Sweden in the past and the future (1911–2100). **Hydrology and Earth System Sciences**, v. 19, n. 2, p. 771–784, 4 fev. 2015.

ARIAS, M. E. et al. Impacts of climate change and deforestation on hydropower planning in the Brazilian Amazon. **Nature Sustainability**, 16 mar. 2020.

ARMIJOS, E. et al. Rainfall control on Amazon sediment flux: synthesis from 20 years of monitoring. **Environmental Research Communications**, v. 2, n. 5, p. 051008, 2020.

ARNESEN, A. S. et al. Monitoring flood extent in the lower Amazon River floodplain using ALOS/PALSAR ScanSAR images. **Remote Sensing of Environment**, v. 130, p. 51–61, mar. 2013.

AROCA, R.; PORCEL, R.; RUIZ-LOZANO, J. M. Regulation of root water uptake under abiotic stress conditions. **Journal of Experimental Botany**, v. 63, n. 1, p. 43–57, 1 jan. 2012.

ARTEAGA, K.; TUTASI, P.; JIMÉNEZ, R. Climatic variability related to El Niño in Ecuador − a historical background. **Advances in Geosciences**, v. 6, p. 237–241, 22 fev. 2006.

ASCE. **The ASCE Standardized Reference Evapotranspiration Equation**. [s.l: s.n.].

ASNER, G. P. Cloud cover in Landsat observations of the Brazilian Amazon. **International Journal of Remote Sensing**, v. 22, n. 18, p. 3855–3862, 2001.

BALIAN, E. V. et al. The Freshwater Animal Diversity Assessment: An overview of the results. **Hydrobiologia**, v. 595, n. 1, p. 627–637, 2008.

BARICHIVICH, J. et al. Recent intensification of Amazon flooding extremes driven by strengthened Walker circulation. **Science Advances**, v. 4, n. 9, 2018.

BARREDO, J. I.; SAURÍ, D.; LLASAT, M. C. Assessing trends in insured losses from floods in Spain 1971–2008. **Natural Hazards and Earth System Sciences**, v. 12, n. 5, p. 1723–1729, 25 maio 2012.

BARRETO, M. A. Comportamiento del sistema urbano y la renta del suelo durante la crisis: Inundaciones en el gran resistencia durante 1982-1983. **Cuaderno de la Catedra de Sociología Urbana, Universidad Nacional del Nordest**, v. 1, p. 7–47, 1993.

BARROS, D.; ALBERNAZ, A. Possible impacts of climate change on wetlands and its biota in the Brazilian Amazon. **Brazilian Journal of Biology**, v. 74, n. 4, p. 810–820, nov. 2014.

BARROS, V. et al. The Major Discharge Events in the Paraguay River: Magnitudes, Source Regions, and Climate Forcings. **Journal of Hydrometeorology**, v. 5, n. 6, p. 1161–1170, dez. 2004.

BARTIKO, D. et al. Spatial and seasonal patterns of flood change across Brazil. **Hydrological Sciences Journal**, v. 64, n. 9, p. 1071–1079, 4 jul. 2019.

BASTIAANSSEN, W. G. . SEBAL-based sensible and latent heat fluxes in the irrigated Gediz Basin, Turkey. **Journal of Hydrology**, v. 229, n. 1–2, p. 87–100, mar. 2000.

BASTIAANSSEN, W. G. M. et al. A remote sensing surface energy balance algorithm for land (SEBAL). 1. Formulation. **Journal of Hydrology**, v. 212–213, p. 198–212, dez. 1998a.

BASTIAANSSEN, W. G. M. G. M. et al. A remote sensing surface energy balance algorithm for land (SEBAL): 1. Formulation. **Journal of Hydrology**, 1998b.

BATALHA, M. A. et al. Hyperseasonal cerrado, a new brazilian vegetation form. **Brazilian Journal of Biology**, v. 65, n. 4, p. 735–738, nov. 2005.

BATES, P. D. et al. Observing Global Surface Water Flood Dynamics. **Surveys in Geophysics**, v. 35, n. 3, p. 839–852, 2014.

BATES, P. D. et al. **Progress Toward Hyperresolution Models of Global Flood Hazard**. [s.l.] Elsevier Inc., 2018a.

BATES, P. D. et al. Progress Toward Hyperresolution Models of Global Flood Hazard. In: **Risk Modeling for Hazards and Disasters**. [s.l.] Elsevier, 2018b. p. 211–232.

BATES, P. D.; DE ROO, A. P. J. A simple raster-based model for flood inundation simulation. **Journal of Hydrology**, 2000.

BATES, P. D.; HORRITT, M. S.; FEWTRELL, T. J. A simple inertial formulation of the shallow water equations for efficient two-dimensional flood inundation modelling. **Journal of Hydrology**, 2010.

BAUER, P.; GUMBRICHT, T.; KINZELBACH, W. A regional coupled surface

water/groundwater model of the Okavango Delta, Botswana. **Water Resources Research**, 2006.

BAUMGARTNER, M. T. et al. Fish functional diversity responses following flood pulses in the upper Paraná River floodplain. **Ecology of Freshwater Fish**, v. 27, n. 4, p. 910–919, out. 2018.

BAYER, A. M. et al. The 1997-1998 El Niño as an unforgettable phenomenon in northern Peru : a qualitative study. **Disasters**, v. 38, n. 2, p. 351–374, 2014.

BECK, H. E. et al. MSWEP: 3-hourly 0.25° global gridded precipitation (1979-2015) by merging gauge, satellite, and reanalysis data. **Hydrology and Earth System Sciences**, 2017.

BEIGHLEY, R. E. et al. Simulating hydrologic and hydraulic processes throughout the Amazon River Basin. **Hydrological Processes**, v. 23, n. 8, p. 1221–1235, 15 abr. 2009.

BEJARANO, M. D.; JANSSON, R.; NILSSON, C. The effects of hydropeaking on riverine plants: a review. **Biological Reviews**, v. 93, n. 1, p. 658–673, fev. 2018.

BELGER, L.; FORSBERG, B. R.; MELACK, J. M. Carbon dioxide and methane emissions from interfluvial wetlands in the upper Negro River basin , Brazil. p. 171–183, 2011.

BELLO, O. D. et al. **Análisis retrospectivo de las inundaciones: lecciones y recomendaciones**. [s.l: s.n.]. Disponível em: <https://www.cepal.org/sites/default/files/pages/files/lcarts2018_1-final.pdf>.

BENZAQUEN, L. et al. **Regiones de Humedales de la Argentina.** Ministerio ed. [s.l: s.n.].

BERGHUIJS, W. R. et al. Dominant flood generating mechanisms across the United States. **Geophysical Research Letters**, v. 43, n. 9, p. 4382–4390, 2016.

BERGHUIJS, W. R. et al. Recent changes in extreme floods across multiple continents. **Environmental Research Letters**, v. 12, n. 11, p. 114035, 1 nov. 2017.

BERGIER, I. et al. Amazon rainforest modulation of water security in the Pantanal wetland. **Science of the Total Environment**, v. 619–620, p. 1116–1125, 2018.

BERMÚDEZ, M. et al. Quantifying local rainfall dynamics and uncertain boundary conditions into a nested regional-local flood modeling system. **Water Resources Research**, v. 53, n. 4, p. 2770–2785, 2017.

BERNHOFEN, M. V et al. A first collective validation of global fluvial flood models for major floods in Nigeria and Mozambique. **Environmental Research Letters**, v. 13, n. 10, p. 104007, 1 out. 2018.

BERRI, G. J.; GHIETTO, M. A.; GARCÍA, N. O. The Influence of ENSO in the Flows of the Upper Paraná River of South America over the Past 100 Years. **Journal of Hydrometeorology**, v. 3, n. 1, p. 57–65, fev. 2002.

BEVEN, K. **Rainfall-Runoff Modelling: The Primer: Second Edition**. [s.l: s.n.].

BIANCAMARIA, S. et al. Large-scale coupled hydrologic and hydraulic modelling of

the Ob river in Siberia. **Journal of Hydrology**, v. 379, n. 1–2, p. 136–150, 2009.

BIANCAMARIA, S.; LETTENMAIER, D. P.; PAVELSKY, T. M. **The SWOT Mission and Its Capabilities for Land HydrologySurveys in Geophysics**, 2016.

BIEMANS, H. et al. Impact of reservoirs on river discharge and irrigation water supply during the 20th century. **Water Resources Research**, v. 47, n. 3, p. 1–15, 2011.

BIERKENS, M. F. P. et al. Hyper-resolution global hydrological modelling: What is next?: "Everywhere and locally relevant" M. F. P. Bierkens et al. Invited Commentary. **Hydrological Processes**, v. 29, n. 2, p. 310–320, 2015.

BIERKENS, M. F. P. Global hydrology 2015: State, trends, and directions. **Water Resources Research**, v. 51, n. February, p. 600–612, 2015.

BIGGS, T. et al. Remote Sensing of Actual Evapotranspiration from Cropland: Chapter 3. In: THENKABAIL, P. S. (Ed.). . **Remote sensing handbook, Vol. III: Remote sensing of water resources, disasters, and urban studies**. [s.l.] CRC Press, 2015.

BIUDES, M. S. et al. Patterns of energy exchange for tropical ecosystems across a climate gradient in Mato Grosso, Brazil. **Agricultural and Forest Meteorology**, v. 202, p. 112–124, 2015.

BLATRIX, R. et al. The unique functioning of a pre-Columbian Amazonian floodplain fishery. **Scientific Reports**, v. 8, n. 1, 2018.

BLÖSCHL, G. et al. The June 2013 flood in the Upper Danube Basin, and comparisons with the 2002, 1954 and 1899 floods. **Hydrology and Earth System Sciences**, v. 17, n. 12, p. 5197–5212, 20 dez. 2013.

BLÖSCHL, G. et al. Increasing river floods: fiction or reality? **Wiley Interdisciplinary Reviews: Water**, p. 329–344, 2015.

BLÖSCHL, G. et al. Changing climate shifts timing of European floods. **Science**, 2017.

BLÖSCHL, G. et al. **Changing climate both increases and decreases European river floodsNature**, 2019.

BLÖSCHL, G.; SIVAPALAN, M. Scale issues in hydrological modelling: A review. **Hydrological Processes**, 1995.

BÓ, R.; QUINTANA, R. 5a. Subregión Ríos, esteros, bañados y lagunas del río Paraná. In: MINISTERIO DE AMBIENTE Y DESARROLLO SUSTENTABLE, FUNDACIÓN HUMEDALES/WETLANDS INTERNATIONAL, U. N. DE S. M. Y U. DE B. A. (Ed.). . **Regiones de humedales de Argentina**. [s.l: s.n.]. p. 113–133.

BODMER, R. et al. Major shifts in Amazon wildlife populations from recent intensification of floods and drought. **Conservation Biology**, v. 32, n. 2, p. 333–344, 2018.

BOISIER, J. P. et al. Projected strengthening of Amazonian dry season by constrained climate model simulations. **Nature Climate Change**, v. 5, n. 7, p. 656–660, 2015.

BONNEMA, M. et al. Understanding satellite-based monthly-to-seasonal reservoir outflow estimation as a function of hydrologic controls. **Water Resources Research**, v.

52, n. 5, p. 4095–4115, maio 2016.

BONNEMA, M.; HOSSAIN, F. Inferring reservoir operating patterns across the Mekong Basin using only space observations. **Water Resources Research**, v. 53, n. 5, p. 3791–3810, maio 2017.

BONNEMA, M.; HOSSAIN, F. Assessing the Potential of the Surface Water and Ocean Topography Mission for Reservoir Monitoring in the Mekong River Basin. **Water Resources Research**, v. 55, n. 1, p. 444–461, 19 jan. 2019.

BONNET, M. P. et al. Floodplain hydrology in an Amazon floodplain lake (Lago Grande de Curuaí). **Journal of Hydrology**, v. 349, n. 1–2, p. 18–30, jan. 2008.

BONNET, M. P. et al. Amazonian floodplain water balance based on modelling and analyses of hydrologic and electrical conductivity data. **Hydrological Processes**, v. 31, n. 9, p. 1702–1718, 2017.

BONTEMPS, S. et al. **Consistent global land cover maps for climate modelling communities: current achievements of the ESA's land cover CCI**. Proceedings of the ESA Living Planet Symposium. **Anais**...Edinburgh: 2013

BORMA, L. S. et al. Atmosphere and hydrological controls of the evapotranspiration over a floodplain forest in the Bananal Island region, Amazonia. **Journal of Geophysical Research: Biogeosciences**, v. 114, n. 1, p. 1–12, 2009.

BOULANGER, J. P. et al. Observed precipitation in the Paraná-Plata hydrological basin: Long-term trends, extreme conditions and ENSO teleconnections. **Climate Dynamics**, v. 24, n. 4, p. 393–413, 2005.

BOURGOIN, L. M. et al. Temporal dynamics of water and sediment exchanges between the Curuaí floodplain and the Amazon River, Brazil. **Journal of Hydrology**, v. 335, n. 1–2, p. 140–156, 2007.

BOURREL, L.; PHILLIPS, L.; MOREAU, S. The dynamics of floods in the Bolivian Amazon Basin. **Hydrological Processes**, v. 23, n. 22, p. 3161–3167, 2009.

BOUSQUET, P. et al. Contribution of anthropogenic and natural sources to atmospheric methane variability. **Nature**, v. 443, n. 7110, p. 439–443, 2006.

BOUWMAN, A. F. et al. Exploring changes in river nitrogen export to the world's oceans. **Global Biogeochemical Cycles**, v. 19, n. 1, p. 1–14, 2005.

BOUWMAN, A. F. et al. Nutrient dynamics, transfer and retention along the aquatic continuum from land to ocean: Towards integration of ecological and biogeochemical models. **Biogeosciences**, v. 10, n. 1, p. 1–23, 2013.

BRAKENRIDGE, G. R. **Global Active Archive of Large Flood Events, Dartmouth Flood Observatory**. Disponível em: <http://floodobservatory.colorado.edu/Archives/index.html>.

BRAVO, J. M. et al. Coupled Hydrologic-Hydraulic Modeling of the Upper Paraguay River Basin. **Journal of Hydrologic Engineering**, v. 17, n. 5, p. 635–646, 2012.

BRÁZDIL, R.; KOTYZA, O.; DOBROVOLNÝ, P. July 1432 and August 2002—two

millennial floods in Bohemia? **Hydrological Sciences Journal**, v. 51, n. 5, p. 848–863, 19 out. 2006.

BRÁZDIL, R.; KUNDZEWICZ, Z. W. Historical hydrology—Editorial. **Hydrological Sciences Journal**, v. 51, n. 5, p. 733–738, 19 out. 2006.

BRÁZDIL, R.; KUNDZEWICZ, Z. W.; BENITO, G. Historical hydrology for studying flood risk in Europe. **Hydrological Sciences Journal**, v. 51, n. 5, p. 739–764, 2006.

BRÊDA, J. P. L. F. et al. Assimilation of Satellite Altimetry Data for Effective River Bathymetry. **Water Resources Research**, 2019.

BRÊDA, J. P. L. F. et al. Climate change impacts on South American water balance from a continental-scale hydrological model driven by CMIP5 projections. **Climatic Change**, 30 jan. 2020.

BRINSON, M. M. A hydrogeomorphic classification for wetlands. **DTIC Document**, 1993.

BRINSON, M. M.; MALVÁREZ, A. I. Temperate freshwater wetlands: types, status, and threats. **Environmental Conservation**, v. 29, n. 2, p. 115–133, 21 jun. 2002.

BROWN, A. et al. **Bañado La Estrella: dinámica fluvial de un espacio compartido**. Ediciones ed. Buenos Aires: [s.n.].

BRUIN, H. A. . DE. **From penman to makkink**. [s.l: s.n.]. v. 39

BUENO, E. DE O.; MELLO, C. R. DE; ALVES, G. J. Evaporation from Camargos hydropower plant reservoir: water footprint characterization. **RBRH**, v. 21, n. 3, p. 570–575, set. 2016.

BUSKER, T. et al. A global lake and reservoir volume analysis using a surface water dataset and satellite altimetry. **Hydrology and Earth System Sciences**, 2019.

CABALZAR, A. **Ciclos anuais no Rio Tiquié–pesquisas colaborativas e manejo Ambiental no Noroeste amazônico**. 1. ed. São Paulo: ISA/FOIRN, 2016.

CAI, W. et al. Increasing frequency of extreme El Niño events due to greenhouse warming. **Nature Climate Change**, v. 4, n. 2, p. 111–116, 19 fev. 2014.

CAMILLONI, I. A.; BARROS, V. R. Extreme discharge events in the Paraná River and their climate forcing. **Journal of Hydrology**, v. 278, n. 1–4, p. 94–106, 2003.

CAMILLONI, I.; BARROS, V. The Paraná River Response to El Niño 1982–83 and 1997–98 Events. **Journal of Hydrometeorology**, v. 1, n. 5, p. 412–430, out. 2000.

CANISIUS, F. et al. SAR backscatter and InSAR coherence for monitoring wetland extent, flood pulse and vegetation: A study of the Amazon lowland. **Remote Sensing**, v. 11, n. 6, p. 1–18, 2019.

CAO, N. et al. Estimation of water level changes of large-scale Amazon wetlands using ALOS2 ScanSAR differential interferometry. **Remote Sensing**, v. 10, n. 6, 2018.

CAPUTO, M. G. et al. La inundación en el Gran Resistencia (Provincia del Chaco, Argentina) 1982-1983. In: **Desastres naturales y sociedad en América Latina**. Santa

Cruz de la Sierra: [s.n.]. p. 129–156.

CARABAJAL, C. C.; BOY, J.-P. Lake and reservoir volume variations in South America from radar altimetry, ICESat laser altimetry, and GRACE time-variable gravity. **Advances in Space Research**, v. v, abr. 2020.

CASTELLARIN, A. et al. Optimal Cross-Sectional Spacing in Preissmann Scheme 1D Hydrodynamic Models. **Journal of Hydraulic Engineering**, v. 135, n. 2, p. 96–105, 2009.

CASTELLO, L. Lateral migration of Arapaima gigas in floodplains of the Amazon. **Ecology of Freshwater Fish**, v. 17, n. 1, p. 38–46, 2008.

CASTELLO, L. et al. The vulnerability of Amazon freshwater ecosystems. **Conservation Letters**, v. 6, n. 4, p. 217–229, 2013.

CASTELLO, L. et al. Fishery yields vary with land cover on the Amazon River floodplain. **Fish and Fisheries**, v. 19, n. 3, p. 431–440, 2018.

CASTELLO, L.; ISAAC, V. J.; THAPA, R. Flood pulse effects on multispecies fishery yields in the Lower Amazon Subject Category : Subject Areas : 2015.

CASULLI, V.; STELLING, G. S. Semi-implicit subgrid modelling of three-dimensional free-surface flows. **International Journal for Numerical Methods in Fluids**, v. 67, n. 4, p. 441–449, 10 out. 2011.

CAVIEDES, C. N. Emergency and institutional crisis in Peru during El Nino 1982–1983. **Disasters**, 1985.

CELESTE, A. B.; BILLIB, M. The Role of Spill and Evaporation in Reservoir Optimization Models. **Water Resources Management**, v. 24, n. 4, p. 617–628, 10 mar. 2010.

CEPED/UFSC. **1983/1984 – Enchentes no Vale de Itajaí em Santa Catarina**. Disponível em: <http://www.ceped.ufsc.br/19831984-enchentes-no-vale-de-itajai-em-santa-catarina>. Acesso em: 24 set. 2018.

CHA, S. C.; MOON, J. H.; SONG, Y. T. A Recent Shift Toward an El Niño-Like Ocean State in the Tropical Pacific and the Resumption of Ocean Warming. **Geophysical Research Letters**, v. 45, n. 21, p. 11,885-11,894, 2018.

CHACÓN-MONTALVÁN, E. A. et al. Rainfall variability and adverse birth outcomes in Amazonia. **Nature Sustainability**, n. March, 2021.

CHAGAS, V. B. P. et al. CAMELS-BR: Hydrometeorological time series and landscape attributes for 897 catchments in Brazil. **Earth System Science Data**, v. 12, n. 3, p. 2075–2096, 2020.

CHAGAS, V. B. P.; CHAFFE, P. L. B. The Role of Land Cover in the Propagation of Rainfall Into Streamflow Trends. **Water Resources Research**, v. 54, n. 9, p. 5986–6004, set. 2018.

CHAPMAN, B. et al. Mapping Regional Inundation with Spaceborne L-Band SAR. p. 5440–5470, 2015.

CHATTERJEE, C.; FÖRSTER, S.; BRONSTERT, A. Comparison of hydrodynamic models of different complexities to model floods with emergency storage areas. **Hydrological Processes**, v. 22, n. 24, p. 4695–4709, 30 nov. 2008.

CHEN, J. L.; WILSON, C. R.; TAPLEY, B. D. The 2009 exceptional Amazon flood and interannual terrestrial water storage change observed by GRACE. **Water Resources Research**, v. 46, n. 12, dez. 2010.

CHEN, S. et al. Variance based sensitivity analysis of 1D and 2D hydraulic models: An experimental urban flood case. **Environmental Modelling and Software**, v. 109, n. August, p. 167–181, 2018.

CHOW, V. TE. **Open-Channel hydraulics**. [s.l: s.n.].

CLEMENT, M. A.; KILSBY, C. G.; MOORE, P. Multi-temporal synthetic aperture radar flood mapping using change detection. **Journal of Flood Risk Management**, v. 11, n. 2, p. 152–168, 2018.

COE, M. T.; COSTA, M. H.; HOWARD, E. A. Simulating the surface waters of the Amazon River basin: impacts of new river geomorphic and flow parameterizations. **Hydrological Processes**, v. 22, n. 14, p. 2542–2553, 1 jul. 2008.

COELHO, C. D. et al. Modelling surface water dynamics in an Amazonian sub-basin: impacts of hydraulic geometry refinement. **Hydrological Sciences Journal**, v. 66, n. 6, p. 1004–1014, 2021.

COLES, V. J. et al. The pathways and properties of the Amazon river plume in the tropical North Atlantic Ocean. **Journal of Geophysical Research: Oceans**, v. 118, n. 12, p. 6894–6913, 2013.

COLLISCHONN, W. et al. The MGB-IPH model for large-scale rainfall-runoff modelling. **Hydrological Sciences Journal**, 2007.

COLLISCHONN, W. et al. Hydraulic Causes for Basin Hydrograph Skewness. **Water Resources Research**, v. 53, n. 12, p. 10603–10618, 2017.

COLLISCHONN, W.; TUCCI, C. E. M.; CLARKE, R. T. Further evidence of changes in the hydrological regime of the River Paraguay: part of a wider phenomenon of climate change? **Journal of Hydrology**, v. 245, n. 1–4, p. 218–238, maio 2001.

COOK, A.; MERWADE, V. Effect of topographic data, geometric configuration and modeling approach on flood inundation mapping. **Journal of Hydrology**, v. 377, n. 1–2, p. 131–142, 2009.

COOMES, O. T. et al. Floodplain fisheries as natural insurance for the rural poor in tropical forest environments: Evidence from Amazonia. **Fisheries Management and Ecology**, v. 17, n. 6, p. 513–521, 2010.

COOMES, O. T. et al. Amazon river flow regime and flood recessional agriculture: Flood stage reversals and risk of annual crop loss. **Journal of Hydrology**, v. 539, p. 214–222, 2016.

CORDEIRO, C. L. DE O.; ROSSETTI, D. DE F. Mapping vegetation in a late Quaternary landform of the Amazonian wetlands using object-based image analysis and

decision tree classification. **International Journal of Remote Sensing**, v. 36, n. 13, p. 3397–3422, 2015.

COSTA, M. H.; BOTTA, A.; CARDILLE, J. A. Effects of large-scale changes in land cover on the discharge of the Tocantins River, Southeastern Amazonia. **Journal of Hydrology**, v. 283, n. 1–4, p. 206–217, dez. 2003.

COSTANZA, R. et al. The value of the world's ecosystem services and natural capital. **Nature**, v. 387, n. 6630, p. 253–260, 1998.

CRED. **EM-DAT website**. Disponível em: <https://www.emdat.be/>.

CRÉTAUX, J. F. et al. Lake Volume Monitoring from Space. **Surveys in Geophysics**, v. 37, n. 2, p. 269–305, 2016.

CZUBA, J. A. et al. Dynamics of Surface-Water Connectivity in a Low-Gradient Meandering River Floodplain. **Water Resources Research**, 2019.

DA MOTTA PACA, V. H. et al. Variability of trends in precipitation across the Amazon river basin determined from the CHIRPS precipitation product and from station records. **Water (Switzerland)**, v. 12, n. 5, 2020.

DA PAZ, A. R. et al. The influence of vertical water balance on modelling Pantanal (Brazil) spatio-temporal inundation dynamics. **Hydrological Processes**, v. 28, n. 10, p. 3539–3553, 2014.

DA ROCHA, H. R. et al. Patterns of water and heat flux across a biome gradient from tropical forest to savanna in Brazil. **Journal of Geophysical Research: Biogeosciences**, v. 114, n. G1, mar. 2009.

DA SILVA, J. S. et al. Radar altimetry aids managing gauge networks. **Water Resources Management**, 2014.

DALMAGRO, H. J. et al. Physiological responses to extreme hydrological events in the Pantanal wetland: heterogeneity of a plant community containing super-dominant species. **Journal of Vegetation Science**, v. 27, n. 3, p. 568–577, maio 2016a.

DALMAGRO, H. J. et al. Photosynthetic response of a wetland- and an upland-adapted tree species to seasonal variations in hydrology in the Brazilian Cerrado and Pantanal. **Acta Physiologiae Plantarum**, v. 38, n. 5, p. 107, 8 maio 2016b.

DALMAGRO, H. J. et al. Radiative forcing of methane fluxes offsets net carbon dioxide uptake for a tropical flooded forest. **Global Change Biology**, v. 25, n. 6, p. 1967–1981, 11 jun. 2019.

DANG, T. D.; CHOWDHURY, A. K.; GALELLI, S. On the representation of water reservoir storage and operations in large-scale hydrological models: implications on model parameterization and climate change impact assessments. **Hydrology and Earth System Sciences Discussions**, p. 1–34, 2019.

DARGAHI, B.; SETEGN, S. G. Combined 3D hydrodynamic and watershed modelling of Lake Tana, Ethiopia. **Journal of Hydrology**, v. 398, n. 1–2, p. 44–64, fev. 2011.

DARRAH, S. E. et al. Improvements to the Wetland Extent Trends (WET) index as a

tool for monitoring natural and human-made wetlands. **Ecological Indicators**, v. 99, n. December 2018, p. 294–298, 2019.

DAVID, C. H. et al. Enhanced fixed-size parallel speedup with the Muskingum method using a trans-boundary approach and a large subbasins approximation. **Water Resources Research**, v. 51, n. 9, p. 7547–7571, set. 2015.

DAVID, C. H. et al. Analytical Propagation of Runoff Uncertainty into Discharge Uncertainty through a Large River Network. **Geophysical Research Letters**, p. 2019GL083342, 29 maio 2019.

DAVIDSON, E. A. et al. The Amazon basin in transition. **Nature**, v. 481, n. 7381, p. 321–328, 2012.

DAVIDSON, N. C. Global extent and distribution of wetlands : trends and issues. p. 620–627, 2018.

DE CASTRO, F.; LOPES, G. R.; BRONDIZIO, E. S. The Brazilian Amazon in times of COVID-19: From crisis to transformation? **Ambiente e Sociedade**, v. 23, p. 1–13, 2020.

DE MOEL, H. et al. Flood risk assessments at different spatial scales. **Mitigation and Adaptation Strategies for Global Change**, v. 20, n. 6, p. 865–890, 2015.

DE PAIVA, R. C. D. et al. Advances and challenges in the water sciences in brazil: A community synthesis of the xxiii brazilian water resources symposium. **Revista Brasileira de Recursos Hidricos**, v. 25, p. 1–28, 2020.

DE RESENDE, A. F. et al. Fire damage in seasonally flooded and upland forests of the Central Amazon. **Biotropica**, v. 46, n. 6, p. 643–646, 2014.

DE TARSO ZUQUIM ANTAS, P. Migration and other movements among the lower Paraná River valley wetlands, Argentina, and the south Brazil/Pantanal wetlands. **Bird Conservation International**, v. 4, n. 2–3, p. 181–190, 1994.

DECHARME, B. et al. A new river flooding scheme for global climate applications: Off-line evaluation over South America. **Journal of Geophysical Research**, v. 113, n. D11, p. D11110, 6 jun. 2008.

DECHARME, B. et al. Global off-line evaluation of the ISBA-TRIP flood model. **Climate Dynamics**, 2012.

DEGU, A. M. et al. The influence of large dams on surrounding climate and precipitation patterns. **Geophysical Research Letters**, v. 38, n. 4, p. n/a-n/a, fev. 2011.

DENEVAN, W. M. A Bluff Model of Riverine Settlement in Prehistoric Amazonia. **Annals of the Association of American Geographers**, v. 86, n. 4, p. 654–681, dez. 1996.

DEPETRIS, P. J. et al. ENSO-controlled flooding in the Paraná River (1904-1991). **Naturwissenschaften**, v. 83, n. 3, p. 127–129, mar. 1996.

DEPETRIS, P. J.; KEMPE, S. The impact of the el Niño 1982 event on the paraná River, its discharge and carbon transport. **Global and Planetary Change**, v. 3, n. 3, p.

239–244, dez. 1990.

DI BALDASSARRE, G. et al. Towards understanding the dynamic behaviour of floodplains as human-water systems. **Hydrology and Earth System Sciences**, v. 17, n. 8, p. 3235–3244, 2013.

DI BALDASSARRE, G. et al. Hess Opinions: An interdisciplinary research agenda to explore the unintended consequences of structural flood protection. **Hydrology and Earth System Sciences**, v. 22, n. 11, p. 5629–5637, 30 out. 2018.

DI BALDASSARRE, G.; LAIO, F.; MONTANARI, A. Effect of observation errors on the uncertainty of design floods. **Physics and Chemistry of the Earth**, v. 42–44, p. 85–90, 2012.

DI BALDASSARRE, G.; MONTANARI, A. Uncertainty in river discharge observations: A quantitative analysis. **Hydrology and Earth System Sciences**, v. 13, n. 6, p. 913–921, 2009.

DIMITRIADIS, P. et al. Comparative evaluation of 1D and quasi-2D hydraulic models based on benchmark and real-world applications for uncertainty assessment in flood mapping. **Journal of Hydrology**, v. 534, p. 478–492, 2016.

DÖLL, P. et al. Modelling Freshwater Resources at the Global Scale: Challenges and Prospects. **Surveys in Geophysics**, v. 37, n. 2, p. 195–221, 2016.

DÖLL, P.; FIEDLER, K.; ZHANG, J. Global-scale analysis of river flow alterations due to water withdrawals and reservoirs. **Hydrology and Earth System Sciences**, v. 13, n. 12, p. 2413–2432, 22 dez. 2009.

DOLMAN, D. I. et al. Re-thinking socio-economic impact assessments of disasters: The 2015 flood in Rio Branco, Brazilian Amazon. **International Journal of Disaster Risk Reduction**, v. 31, n. November 2017, p. 212–219, 2018.

DOMENEGHETTI, A. On the use of SRTM and altimetry data for flood modeling in data-sparse regions. **Water Resources Research**, v. 52, n. 4, p. 2901–2918, 2016.

DOMENEGHETTI, A.; CASTELLARIN, A.; BRATH, A. Assessing rating-curve uncertainty and its effects on hydraulic model calibration. **Hydrology and Earth System Sciences**, v. 16, n. 4, p. 1191–1202, 2012.

DOTTORI, F. et al. Development and evaluation of a framework for global flood hazard mapping. **Advances in Water Resources**, v. 94, p. 87–102, 2016.

DOTTORI, F.; DI BALDASSARRE, G.; TODINI, E. Detailed data is welcome, but with a pinch of salt: Accuracy, precision, and uncertainty in flood inundation modeling. **Water Resources Research**, v. 49, n. 9, p. 6079–6085, set. 2013.

DOTTORI, F.; MARTINA, M. L. V.; TODINI, E. A dynamic rating curve approach to indirect discharge measurement. **Hydrology and Earth System Sciences**, v. 13, n. 6, p. 847–863, 2009.

DOTTORI, F.; TODINI, E. Testing a simple 2D hydraulic model in an urban flood experiment. **Hydrological Processes**, v. 27, n. 9, p. 1301–1320, 30 abr. 2013.

DOYLE, M. E.; BARROS, V. R. Attribution of the river flow growth in the Plata Basin. **International Journal of Climatology**, v. 31, n. 15, p. 2234–2248, 2011.

DRAPER, A. J.; LUND, J. R. Optimal Hedging and Carryover Storage Value. **Journal of Water Resources Planning and Management**, v. 130, n. 1, p. 83–87, jan. 2004.

DRAPER, F. C. et al. The distribution and amount of carbon in the largest peatland complex in Amazonia. **Environmental Research Letters**, v. 9, n. 12, 2014.

DROPPERS, B. et al. Simulating human impacts on global water resources using VIC-5. **Geoscientific Model Development**, v. 13, n. 10, p. 5029–5052, 2020.

DUFFIE, J. A.; BECKMAN, W. A. **Solar Engineering of Thermal Processes: Fourth Edition**. [s.l: s.n.].

DUPONCHELLE, F. et al. Conservation of migratory fishes in the Amazon basin. **Aquatic Conservation: Marine and Freshwater Ecosystems**, n. December 2020, p. aqc.3550, 19 mar. 2021.

DURÁN-QUESADA, A. M.; REBOITA, M.; GIMENO, L. Precipitation in tropical America and the associated sources of moisture: a short review. **Hydrological Sciences Journal**, v. 57, n. 4, p. 612–624, 2012.

DURAND, M. et al. Estimation of bathymetric depth and slope from data assimilation of swath altimetry into a hydrodynamic model. **Geophysical Research Letters**, 2008.

EHSANI, N. et al. Reservoir operations under climate change: Storage capacity options to mitigate risk. **Journal of Hydrology**, v. 555, p. 435–446, dez. 2017.

ENDO, W.; PERES, C. A.; HAUGAASEN, T. Flood pulse dynamics affects exploitation of both aquatic and terrestrial prey by Amazonian floodplain settlements. **Biological Conservation**, v. 201, p. 129–136, 2016.

ENTEKHABI, D. et al. The soil moisture active passive (SMAP) mission. **Proceedings of the IEEE**, 2010.

ERWIN, K. L. Wetlands and global climate change: The role of wetland restoration in a changing world. **Wetlands Ecology and Management**, v. 17, n. 1, p. 71–84, 2009.

ESPINOZA, J. C. et al. Climate variability and extreme drought in the upper Solimões River (western Amazon Basin): Understanding the exceptional 2010 drought. **Geophysical Research Letters**, 2011.

ESPINOZA, J. C. et al. The extreme 2014 flood in south-western Amazon basin: The role of tropical-subtropical South Atlantic SST gradient. **Environmental Research Letters**, 2014.

ESPINOZA, J. C. et al. Contrasting North–South changes in Amazon wet-day and dry-day frequency and related atmospheric features (1981–2017). **Climate Dynamics**, v. 52, n. 9–10, p. 5413–5430, 2019a.

ESPINOZA, J. C. et al. Regional hydro-climatic changes in the Southern Amazon Basin (Upper Madeira Basin) during the 1982–2017 period. **Journal of Hydrology: Regional Studies**, v. 26, n. November, p. 100637, dez. 2019b.

ESPINOZA VILLAR, J. C. et al. Spatio-temporal rainfall variability in the Amazon basin countries (Brazil, Peru, Bolivia, Colombia, and Ecuador). **International Journal of Climatology**, v. 29, n. 11, p. 1574–1594, set. 2009a.

ESPINOZA VILLAR, J. C. et al. Contrasting regional discharge evolutions in the Amazon basin (1974–2004). **Journal of Hydrology**, v. 375, n. 3–4, p. 297–311, set. 2009b.

ESRI. **World Imagery**. Disponível em: <https://www.arcgis.com/home/item.html?id=10df2279f9684e4a9f6a7f08febac2a9>. Acesso em: 3 out. 2020.

EVANS, T. L. et al. Remote Sensing of Environment Large-scale habitat mapping of the Brazilian Pantanal wetland : A syn- thetic aperture radar approach. **Remote Sensing of Environment**, 2014.

FALTER, D. et al. Spatially coherent flood risk assessment based on long-term continuous simulation with a coupled model chain. **Journal of Hydrology**, v. 524, n. February, p. 182–193, maio 2015.

FALTER, D. et al. Continuous, large-scale simulation model for flood risk assessments: Proof-of-concept. **Journal of Flood Risk Management**, v. 9, n. 1, p. 3–21, 2016.

FAN, F. et al. Avaliação de um método de propagação de cheias em rios com aproximação inercial das equações de Saint-Venant. **Revista Brasileira de Recursos Hídricos**, 2014.

FAN, F. et al. **Um mapa de unidades de resposta hidrológica para a América do Sul.** Anais do XXI Simpósio Brasileiro de Recursos Hídricos. **Anais**...Brasília: ABRH, 2015

FAN, F. M. et al. On the discretization of river networks for large scale hydrologic-hydrodynamic models. **RBRH**, v. 26, 2021.

FAN, Y. et al. Hydrologic regulation of plant rooting depth. **Proceedings of the National Academy of Sciences of the United States of America**, v. 114, n. 40, p. 10572–10577, 2017.

FAN, Y.; MIGUEZ-MACHO, G. A simple hydrologic framework for simulating wetlands in climate and earth system models. **Climate Dynamics**, 2011.

FANTIN-CRUZ, I. et al. Further Development of Small Hydropower Facilities Will Significantly Reduce Sediment Transport to the Pantanal Wetland of Brazil. **Frontiers in Environmental Science**, v. 8, n. November, 2020.

FARAH, H. O.; BASTIAANSSEN, W. G. M. Impact of spatial variations of land surface parameters on regional evaporation: a case study with remote sensing data. **Hydrological Processes**, v. 15, n. 9, p. 1585–1607, 30 jun. 2001.

FARR, T. et al. The shuttle radar topography mission. **Reviews of Geophysics**, 2007.

FASSONI-ANDRADE, A. C. et al. High-resolution mapping of floodplain topography from space: A case study in the Amazon. **Remote Sensing of Environment**, v. 251, n. April, p. 112065, 2020.

FASSONI-ANDRADE, A. C. et al. Comprehensive bathymetry and intertidal topography of the Amazon estuary. **Earth System Science Data**, v. 13, n. 5, p. 2275–2291, 2021.

FASSONI-ANDRADE, A. C.; DE PAIVA, R. C. D.; FLEISCHMANN, A. S. Lake Topography and Active Storage From Satellite Observations of Flood Frequency. **Water Resources Research**, 2020.

FASSONI-ANDRADE, A. C.; PAIVA, R. C. D. DE. Mapping spatial-temporal sediment dynamics of river-floodplains in the Amazon. **Remote Sensing of Environment**, 2019.

FASSONI-ANDRADE, A. C.; FLEISCHMANN, A. S.; PAPA, F. Amazon hydrology from space: scientific advances and future challenges. **ESSOAr**, 2021.

FENG, D. et al. Future climate impacts on the hydrology of headwater streams in the Amazon River Basin: Implications for migratory goliath catfishes. **Hydrological Processes**, n. October, p. hyp.13952, 5 nov. 2020.

FERRATI, R.; CANZIANI, G. A. An analysis of water level dynamics in Esteros del Ibera wetland. v. 186, p. 17–27, 2005.

FERREIRA-FERREIRA, J. et al. Combining ALOS/PALSAR derived vegetation structure and inundation patterns to characterize major vegetation types in the Mamirauá Sustainable Development Reserve, Central Amazon floodplain, Brazil. **Wetlands Ecology and Management**, v. 23, n. 1, p. 41–59, 11 fev. 2015.

FEWTRELL, T. J. et al. Geometric and structural river channel complexity and the prediction of urban inundation. **Hydrological Processes**, v. 25, n. 20, p. 3173–3186, 2011.

FIGUEIREDO, J. S. M. C. D. et al. Hydropeaking by Small Hydropower Facilities Affects Flow Regimes on Tributaries to the Pantanal Wetland of Brazil. **Frontiers in Environmental Science**, v. 9, n. March, 2021.

FIGUEROA, M. et al. On the relationship between reversal of the river stage (repiquetes), rainfall and low-level wind regimes over the western Amazon basin. **Journal of Hydrology: Regional Studies**, v. 32, n. November, p. 100752, 2020.

FILIZOLA, N. et al. 24 . Estudos alertam para desastre ambiental associado à construção da barragem de Bem Querer no Rio Branco , Roraima. n. September, 2020.

FISHER, J. B. et al. The land-atmosphere water flux in the tropics. **Global Change Biology**, v. 15, n. 11, p. 2694–2714, 2009.

FISHER, J. B. et al. The future of evapotranspiration: Global requirements for ecosystem functioning, carbon and climate feedbacks, agricultural management, and water resources. **Water Resources Research**, v. 53, n. 4, p. 2618–2626, abr. 2017.

FLEISCHMANN, A. et al. Modelling hydrologic and hydrodynamic processes in basins with large semi-arid wetlands. **Journal of Hydrology**, v. 561, n. August 2017, p. 943–959, jun. 2018.

FLEISCHMANN, A. et al. Precipitation as a proxy for climate variables: application for

hydrological modelling. **Hydrological Sciences Journal**, v. 64, n. 3, p. 361–379, 17 fev. 2019a.

FLEISCHMANN, A. et al. Modeling the role of reservoirs versus floodplains on large-scale river hydrodynamics. **Natural Hazards**, v. 99, n. 2, p. 1075–1104, 24 nov. 2019b.

FLEISCHMANN, A.; PAIVA, R.; COLLISCHONN, W. Can regional to continental river hydrodynamic models be locally relevant? A cross-scale comparison. **Journal of Hydrology X**, v. 3, p. 100027, abr. 2019.

FLEISCHMANN, A. S. et al. On river-floodplain interaction and hydrograph skewness. **Water Resources Research**, v. 52, n. 10, p. 7615–7630, out. 2016.

FLEISCHMANN, A. S. et al. The great 1983 floods in South American large rivers: a continental hydrological modelling approach. **Hydrological Sciences Journal**, p. 1–16, 8 abr. 2020a.

FLEISCHMANN, A. S. et al. Trade-Offs Between 1-D and 2-D Regional River Hydrodynamic Models. **Water Resources Research**, v. 56, n. 8, 19 ago. 2020b.

FLEISCHMANN, A. S. et al. River Flood Modeling and Remote Sensing Across Scales: Lessons from Brazil. In: SCHUMANN, G. J. P. (Ed.). . **Earth Observation for Flood Applications**. [s.l.] Elsevier, 2021. p. 61–103.

FLIPO, N. et al. Continental hydrosystem modelling: The concept of nested stream–aquifer interfaces. **Hydrology and Earth System Sciences**, v. 18, n. 8, p. 3121–3149, 2014.

FLORES, B. M. et al. Floodplains as an Achilles' heel of Amazonian forest resilience. **Proceedings of the National Academy of Sciences**, v. 114, n. 17, p. 4442–4446, 2017.

FLORES, B. M.; HOLMGREN, M. White-Sand Savannas Expand at the Core of the Amazon After Forest Wildfires. **Ecosystems**, 3 mar. 2021.

FLÓREZ, C. et al. Identificación espacial de los sistemas de humedales continentales de Colombia. **Biota Colombiana**, v. 16, n. 3, p. 44–62, 15 jul. 2016.

FLUET-CHOUINARD, E. et al. Development of a global inundation map at high spatial resolution from topographic downscaling of coarse-scale remote sensing data. **Remote Sensing of Environment**, v. 158, p. 348–361, 2015.

FOLLUM, M. L. et al. AutoRAPID: A Model for Prompt Streamflow Estimation and Flood Inundation Mapping over Regional to Continental Extents. **Journal of the American Water Resources Association**, v. 53, n. 2, p. 280–299, 2017.

FONSECA, L. D. M. et al. Phenology and Seasonal Ecosystem Productivity in an Amazonian Floodplain Forest. **Remote Sensing**, v. 11, n. 13, p. 1530, 28 jun. 2019.

FORSBERG, B. R. et al. The potential impact of new Andean dams on Amazon fluvial ecosystems. **PLOS ONE**, v. 12, n. 8, p. e0182254, 23 ago. 2017.

FRANK, B. Uma história das enchentes e seus ensinamentos. In: EDIFURB (Ed.). . **Enchentes na Bacia do Itajaí: 20 anos de experiências**. 1st. ed. Blumenau: [s.n.]. p. 15–62.

FRAPPART, F. et al. Floodplain water storage in the Negro River basin estimated from microwave remote sensing of inundation area and water levels. **Remote Sensing of Environment**, v. 99, n. 4, p. 387–399, dez. 2005.

FRAPPART, F. et al. Interannual variations of river water storage from a multiple satellite approach: A case study for the Rio Negro River basin. **Journal of Geophysical Research**, v. 113, n. D21, p. D21104, 5 nov. 2008.

FRAPPART, F. et al. Surface freshwater storage and dynamics in the Amazon basin during the 2005 exceptional drought. **Environmental Research Letters**, v. 7, n. 4, 2012.

FRAPPART, F. et al. Surface Freshwater Storage Variations in the Orinoco Floodplains Using Multi-Satellite Observations. **Remote Sensing**, v. 7, n. 1, p. 89–110, 24 dez. 2014.

FRAPPART, F. et al. The spatio-temporal variability of groundwater storage in the Amazon River Basin. **Advances in Water Resources**, v. 124, n. December 2018, p. 41–52, fev. 2019.

FRASSON, R. P. DE M. et al. Automated River Reach Definition Strategies: Applications for the Surface Water and Ocean Topography Mission. **Water Resources Research**, v. 53, n. 10, p. 8164–8186, out. 2017.

FRASSON, R. P. DE M. et al. Global Relationships Between River Width, Slope, Catchment Area, Meander Wavelength, Sinuosity, and Discharge. **Geophysical Research Letters**, v. 46, n. 6, p. 3252–3262, 28 mar. 2019.

FREAD, D. Flow routing. In: MAIDMENT, D. R. (Ed.). . **Handbook of Hydrology**. [s.l: s.n.].

FRIEDMAN, A. R. et al. Increased Amazon Basin wet-season precipitation and river discharge since the early 1990s driven by tropical Pacific variability. **Environmental Research Letters**, v. 16, n. 3, 2021.

FUNATSU, B. M. et al. Assessing precipitation extremes (1981–2018) and deep convective activity (2002–2018) in the Amazon region with CHIRPS and AMSU data. **Climate Dynamics**, 2021.

FUNK, C. et al. The climate hazards infrared precipitation with stations - A new environmental record for monitoring extremes. **Scientific Data**, v. 2, p. 1–21, 2015.

GALLANT, A. L. The challenges of remote monitoring of wetlands. **Remote Sensing**, v. 7, n. 8, p. 10938–10950, 2015.

GAO, B. C. NDWI - A normalized difference water index for remote sensing of vegetation liquid water from space. **Remote Sensing of Environment**, 1996.

GAO, H. Satellite remote sensing of large lakes and reservoirs: from elevation and area to storage. **Wiley Interdisciplinary Reviews: Water**, v. 2, n. 2, p. 147–157, mar. 2015.

GAO, H.; BIRKETT, C.; LETTENMAIER, D. P. Global monitoring of large reservoir storage from satellite remote sensing. **Water Resources Research**, v. 48, n. 9, p. 1–12, 2012.

GARAMBOIS, P. A. et al. Hydraulic visibility: Using satellite altimetry to parameterize a hydraulic model of an ungauged reach of a braided river. **Hydrological Processes**, v. 31, n. 4, p. 756–767, 2017.

GARAMBOIS, P.; MONNIER, J. Inference of effective river properties from remotely sensed observations of water surface. **Advances in Water Resources**, v. 79, p. 103–120, maio 2015.

GARCIA, A. M. et al. Comparison of 1982-1983 and 1997-1998 El Niño effects on the shallow-water fish assemblage of the Patos Lagoon estuary (Brazil). **Estuaries**, v. 27, n. 6, p. 905–914, 2004.

GARCÍA, N. O.; VARGAS, W. M. The temporal climatic variability in the "Rio de la Plata" Basin displayed by the river discharges. **Climatic Change**, 1998.

GARRISON, J. D.; ADLER, G. P. Estimation of precipitable water over the United States for application to the division of solar radiation into its direct and diffuse components. **Solar Energy**, v. 44, n. 4, p. 225–241, 1990.

GETIRANA, A. et al. Assessment of different precipitation datasets and their impacts on the water balance of the Negro River basin. **Journal of Hydrology**, v. 404, n. 3–4, p. 304–322, 2011.

GETIRANA, A. et al. The Hydrological Modeling and Analysis Platform (HyMAP): Evaluation in the Amazon Basin. **Journal of Hydrometeorology**, v. 13, n. 6, p. 1641–1665, 2012.

GETIRANA, A. et al. Trade-off between cost and accuracy in large-scale surface water dynamic modeling. **Water Resources Research**, v. 53, n. 6, p. 4942–4955, jun. 2017a.

GETIRANA, A. et al. Rivers and Floodplains as Key Components of Global Terrestrial Water Storage Variability. **Geophysical Research Letters**, v. 44, n. 20, p. 10,359-10,368, 28 out. 2017b.

GETIRANA, A.; JUNG, H. C.; TSENG, K. H. Deriving three dimensional reservoir bathymetry from multi-satellite datasets. **Remote Sensing of Environment**, v. 217, n. August, p. 366–374, 2018.

GIMENO, L. et al. Major Mechanisms of Atmospheric Moisture Transport and Their Role in Extreme Precipitation Events. **Annual Review of Environment and Resources**, v. 41, n. 1, p. 117–141, 2016.

GLEASON, C. J.; DURAND, M. T. Remote Sensing of River Discharge : A Review and a Framing for the Discipline. v. 2, p. 1–28, 2020.

GLOOR, M. et al. Intensification of the Amazon hydrological cycle over the last two decades. **Geophysical Research Letters**, v. 40, n. 9, p. 1729–1733, 2013.

GLOOR, M. et al. Recent Amazon climate as background for possible ongoing Special Section : **Global Biogeochemical Cycles**, v. 29, n. 9, p. 1384–1399, 2015.

GLYNN, P. W. El Nino-Southern Oscillation 1982-1983: Nearshore Population, Community, and Ecosystem Responses. **Annual Review of Ecology and Systematics**, v. 19, n. 1, p. 309–346, nov. 1988.

GOMES, T. L. et al. Efficiently computing the drainage network on massive terrains using external memory flooding process. **GeoInformatica**, 2015.

GONÇALVES, H.; MERCANTE, M.; SANTOS, E. Hydrological cycle. **Brazilian Journal of Biology**, v. 71, n. 1 suppl 1, p. 241–253, abr. 2011.

GOULDEN, M. L. et al. Diel and seasonal patterns of tropical forest CO2 exchange. **Ecological Applications**, v. 14, n. 4 SUPPL., p. 42–54, 2004.

GOULDING, M. et al. Ecosystem-based management of Amazon fisheries and wetlands. **Fish and Fisheries**, v. 20, n. 1, p. 138–158, jan. 2019.

GRILL, G. et al. Mapping the world's free-flowing rivers. **Nature**, v. 569, n. 7755, p. 215–221, 2019.

GRIMALDI, S. et al. Effective Representation of River Geometry in Hydraulic Flood Forecast Models. **Water Resources Research**, v. 54, n. 2, p. 1031–1057, 2018.

GRIMALDI, S. et al. Challenges, opportunities and pitfalls for global coupled hydrologic-hydraulic modeling of floods. **Water Resources Research**, p. 2018WR024289, 3 jun. 2019.

GRÜNDEMANN, G. J.; WERNER, M.; VELDKAMP, T. I. E. The potential of global reanalysis datasets in identifying flood events in Southern Africa. **Hydrology and Earth System Sciences**, v. 22, n. 9, p. 4667–4683, 6 set. 2018.

GUDMUNDSSON, L. et al. Observed Trends in Global Indicators of Mean and Extreme Streamflow. **Geophysical Research Letters**, v. 46, n. 2, p. 756–766, 28 jan. 2019.

GUILHEN, J. et al. Denitrification and associated nitrous oxide and carbon dioxide emissions from the Amazonian wetlands. **Biogeosciences**, v. 17, n. 16, p. 4297–4311, 28 ago. 2020.

GUIMARÃES, F.; BUENO, G. As campinas e campinaranas amazônicas. **Caderno de Geografia**, v. 26, n. 45, p. 113–133, 2016.

GUIMARÃES, R. **A Enchente de 1941**. Porto Alegre: Editora Libretos, 2009.

GUMBRICHT, T. et al. An expert system model for mapping tropical wetlands and peatlands reveals South America as the largest contributor. **Global Change Biology**, v. 23, n. 9, p. 3581–3599, 2017.

HAASE, R. Litterfall and nutrient return in seasonally flooded and non-flooded forest of the Pantanal, Mato Grosso, Brazil. **Forest Ecology and Management**, v. 117, n. 1–3, p. 129–147, 1999.

HADDELAND, I. et al. Global water resources affected by human interventions and climate change. **Proceedings of the National Academy of Sciences of the United States of America**, v. 111, n. 9, p. 3251–3256, 2014.

HADDELAND, I.; SKAUGEN, T.; LETTENMAIER, D. P. Anthropogenic impacts on continental surface water fluxes. **Geophysical Research Letters**, v. 33, n. 8, p. 2–5, 2006.

HÄFLIGER, V. et al. Evaluation of Regional-Scale River Depth Simulations Using Various Routing Schemes within a Hydrometeorological Modeling Framework for the Preparation of the SWOT Mission. **Journal of Hydrometeorology**, v. 16, n. 4, p. 1821–1842, ago. 2015.

HAGHTALAB, N. et al. Evaluating spatial patterns in precipitation trends across the Amazon basin driven by land cover and global scale forcings. **Theoretical and Applied Climatology**, v. 140, n. 1–2, p. 411–427, 17 abr. 2020.

HALL, J.; BLÖSCHL, G. Spatial patterns and characteristics of flood seasonality in Europe. **Hydrology and Earth System Sciences**, v. 22, n. 7, p. 3883–3901, 19 jul. 2018.

HAMILTON, S. K. et al. Remote sensing of floodplain geomorphology as a surrogate for biodiversity in a tropical river system (Madre de Dios, Peru). **Geomorphology**, v. 89, n. 1- 2 SPEC. ISS., p. 23–38, 2007.

HAMILTON, S. K.; SIPPEL, S. J.; MELACK, J. M. Comparison of inundation patterns among major South American floodplains. v. 107, n. July 2001, p. 1–14, 2002.

HAMILTON, S. K.; SIPPEL, S. J.; MELACK, J. M. Seasonal inundation patterns in two large savanna floodplains of South America: the Llanos de Moxos(Bolivia) and the Llanos del Orinoco(Venezuela and Colombia). **Hydrological Processes**, v. 18, n. 11, p. 2103–2116, 15 ago. 2004.

HANASAKI, N. et al. A global hydrological simulation to specify the sources of water used by humans. **Hydrology and Earth System Sciences**, v. 22, n. 1, p. 789–817, 29 jan. 2018.

HANASAKI, N.; KANAE, S.; OKI, T. A reservoir operation scheme for global river routing models. **Journal of Hydrology**, v. 327, n. 1–2, p. 22–41, jul. 2006.

HANSEN, M. C. et al. High-Resolution Global Maps of 21st-Century Forest Cover Change. **Science**, v. 342, n. 6160, p. 850–853, 15 nov. 2013.

HATTERMANN, F. F. et al. Cross-scale intercomparison of climate change impacts simulated by regional and global hydrological models in eleven large river basins. **Climatic Change**, 2017.

HAUGAASEN, T.; PERES, C. A. Tree Phenology in Adjacent Amazonian Flooded and Unflooded Forests. **Biotropica**, v. 37, n. 4, p. 620–630, dez. 2005.

HEDERRA, R. Environmental sanitation and water supply during floods in Ecuador (1982-1983). **Disasters: international journal of disasters studies and practice**, v. 11, n. 4, p. 297–309, 1987.

HEERSPINK, B. P. et al. Trends in streamflow, evapotranspiration, and groundwater storage across the Amazon Basin linked to changing precipitation and land cover. **Journal of Hydrology: Regional Studies**, v. 32, n. March, p. 100755, 2020.

HEILPERN, S. A. et al. Declining diversity of wild-caught species puts dietary nutrient supplies at risk. **Science Advances**, v. 7, n. 22, p. 1–9, 2021.

HEINE, R. A.; PINTER, N. Levee effects upon flood levels: An empirical assessment.

Hydrological Processes, v. 26, n. 21, p. 3225–3240, 2012.

HEROLD, M. et al. **Land Cover CCI, Product User Guide Version 2.0**. Disponível em: <https://maps.elie.ucl.ac.be/CCI/viewer/%0Adownload/ESACCI-LC-Ph2-PUGv2_2.0.pdf %0A>.

HERRAIZ, A. D.; GRAÇA, P. M. L. DE A.; FEARNSIDE, P. M. Amazonian flood impacts on managed Brazilnut stands along Brazil's Madeira River: A sustainable forest management system threatened by climate change. **Forest Ecology and Management**, v. 406, n. September, p. 46–52, 2017.

HERRERA, A. Responses to flooding of plant water relations and leaf gas exchange in tropical tolerant trees of a black-water wetland. **Frontiers in Plant Science**, v. 4, n. MAY, 2013.

HERSCHY, R. W. **Streamflow measurement**. London: CRC Press, 2014.

HESS, L. et al. Use of MODIS enhanced vegetation index to detect seasonal patterns of leaf phenology in central Amazon várzea forest. **International Geoscience and Remote Sensing Symposium (IGARSS)**, v. 4, p. 1007–1010, 2009.

HESS, L. L. et al. Dual-season mapping of wetland inundation and vegetation for the central Amazon basin. **Remote Sensing of Environment**, v. 87, n. 4, p. 404–428, 2003.

HESS, L. L. et al. Wetlands of the Lowland Amazon Basin: Extent, Vegetative Cover, and Dual-season Inundated Area as Mapped with JERS-1 Synthetic Aperture Radar. **Wetlands**, v. 35, n. 4, p. 745–756, 20 ago. 2015.

HEY, D. L.; PHILIPPI, N. S. Flood Reduction through Wetland Restoration: The Upper Mississippi River Basin as a Case History. **Restoration Ecology**, v. 3, n. 1, p. 4–17, 9 mar. 1995.

HINO, M.; NANCE, E. Five ways to ensure flood-risk research helps the most vulnerable. 2020.

HIRABAYASHI, Y. et al. Global flood risk under climate change. **Nature Climate Change**, 2013.

HO, M. et al. The future role of dams in the United States of America. **Water Resources Research**, v. 53, n. 2, p. 982–998, fev. 2017.

HOCH, J. M. et al. Assessing the impact of hydrodynamics on large-scale flood wave propagation: A case study for the Amazon Basin. **Hydrology and Earth System Sciences**, v. 21, n. 1, p. 117–132, 2017a.

HOCH, J. M. et al. GLOFRIM v1.0-A globally applicable computational framework for integrated hydrological-hydrodynamic modelling. **Geoscientific Model Development**, v. 10, n. 10, p. 3913–3929, 2017b.

HOCH, J.; TRIGG, M. A. Advancing global flood hazard simulations by improving comparability, benchmarking, and integration of global flood models. **Environmental Research Letters**, 26 nov. 2018.

HODGES, B. R. Challenges in continental river dynamics. **Environmental Modelling**

and Software, v. 50, p. 16–20, 2013.

HORRITT, M. S. A methodology for the validation of uncertain flood inundation models. **Journal of Hydrology**, v. 326, n. 1–4, p. 153–165, 2006.

HORRITT, M. S.; BATES, P. D. Evaluation of 1D and 2D numerical models for predicting river flood inundation. **Journal of Hydrology**, v. 268, n. 1–4, p. 87–99, 2002.

HOSSAIN, F. et al. Climate Feedback–Based Provisions for Dam Design, Operations, and Water Management in the 21st Century. **Journal of Hydrologic Engineering**, v. 17, n. 8, p. 837–850, ago. 2012.

HOUSPANOSSIAN, J. et al. Long-lasting floods buffer the thermal regime of the Pampas. **Theoretical and Applied Climatology**, v. 131, n. 1–2, p. 111–120, 2018.

HU, S.; NIU, Z.; CHEN, Y. Global Wetland Datasets: a Review. **Wetlands**, v. 37, n. 5, p. 807–817, 2017.

HUFFMAN, G. et al. The TRMM Multisatellite Precipitation Analysis (TMPA): Quasi-Global, Multiyear, Combined-Sensor Precipitation Estimates at Fine Scales. **Journal of Hydrometeorology**, 2007.

HUMPHREY, V.; GUDMUNDSSON, L. GRACE-REC: a reconstruction of climate-driven water storage changes over the last century. **Earth System Science Data Discussions**, 2019.

HUNTER, N. M. et al. Simple spatially-distributed models for predicting flood inundation: A review. **Geomorphology**, v. 90, n. 3–4, p. 208–225, 2007.

HURD, L. E. et al. Amazon floodplain fish communities: Habitat connectivity and conservation in a rapidly deteriorating environment. **Biological Conservation**, v. 195, p. 118–127, 2016.

IBGE. **O novo modelo de ondulação geoidal do Brasil - MAPGEO2015**. Disponível em: <ftp://geoftp.ibge.gov.br/modelos_digitais_de_superficie/modelo_de_ondulacao_geoidal/cartograma/rel_mapgeo2015.pdf>. Acesso em: 24 set. 2018.

IGARAPÉ. **Artigo estratégico 29: Migrantes invisíveis: a crise de deslocamento forçado no Brasil.** Disponível em: <https://igarape.org.br/wp-content/uploads/2018/03/Migrantes-invisíveis.pdf>.

IKEUCHI, H. et al. Modeling complex flow dynamics of fluvial floods exacerbated by sea level rise in the Ganges-Brahmaputra-Meghna Delta. **Environmental Research Letters**, 2015.

ISLA, F. I.; TOLDO JUNIOR, E. E. ENSO impacts on Atlantic watersheds of South America. **Quaternary and Environmental Geosciences**, v. 4, n. 1–2, 31 dez. 2013.

ITAIPU. RELATÓRIO ANUAL ITAIPU BINACIONAL. 2016.

IVORY, S. J. et al. Vegetation, rainfall, and pulsing hydrology in the Pantanal, the world's largest tropical wetland. **Environmental Research Letters**, v. 14, n. 12, 2019.

JAIN, S.; LALL, U. Floods in a changing climate: Does the past represent the future? **Water Resources Research**, v. 37, n. 12, p. 3193–3205, dez. 2001.

JARAMILLO, F. et al. Assessment of hydrologic connectivity in an ungauged wetland with InSAR observations. **Environmental Research Letters**, v. 13, n. 2, p. 024003, 1 fev. 2018.

JARDIM, C. M. et al. The influence of seasonal river flooding in food consumption of riverine dwellers in the central Amazon region: an isotopic approach. **Archaeological and Anthropological Sciences**, v. 12, n. 9, 2020.

JARDINI, J. A. et al. Brazilian Energy Crisis. **IEEE Power Engineering Review**, v. 22, n. 4, p. 21–24, abr. 2002.

JENSEN, K. et al. Assessing L-Band GNSS-Reflectometry and Imaging Radar for Detecting Sub-Canopy Inundation Dynamics in a Tropical Wetlands Complex. **Remote Sensing**, v. 10, n. 9, p. 1431, 7 set. 2018.

JENSEN, K.; MCDONALD, K. Surface Water Microwave Product Series Version 3: A Near-Real Time and 25-Year Historical Global Inundated Area Fraction Time Series From Active and Passive Microwave Remote Sensing. **IEEE Geoscience and Remote Sensing Letters**, v. 16, n. 9, p. 1402–1406, 2019.

JI, X. et al. Seasonal and Interannual Patterns and Controls of Hydrological Fluxes in an Amazon Floodplain Lake With a Surface-Subsurface Process Model. **Water Resources Research**, v. 55, n. 4, p. 3056–3075, 15 abr. 2019.

JOHNSON, K. A. et al. A benefit–cost analysis of floodplain land acquisition for US flood damage reduction. **Nature Sustainability**, v. 3, n. 1, p. 56–62, 9 jan. 2020.

JONGMAN, B. et al. Comparative flood damage model assessment: Towards a European approach. **Natural Hazards and Earth System Science**, v. 12, n. 12, p. 3733–3752, 2012.

JONGMAN, B. et al. Increasing stress on disaster-risk finance due to large floods. **Nature Climate Change**, v. 4, n. 4, p. 264–268, 2 abr. 2014.

JOYCE, R. J. et al. CMORPH: A Method that Produces Global Precipitation Estimates from Passive Microwave and Infrared Data at High Spatial and Temporal Resolution. **Journal of Hydrometeorology**, 2004.

JUNG, H. C. et al. Characterization of complex fluvial systems using remote sensing of spatial and temporal water level variations in the Amazon, Congo, and Brahmaputra rivers. **Earth Surface Processes and Landforms**, v. 35, n. 3, p. 294–304, 2010.

JUNG, Y.; MERWADE, V. Estimation of uncertainty propagation in flood inundation mapping using a 1-D hydraulic model. **Hydrological Processes**, v. 29, n. 4, p. 624–640, 2015.

JUNK, W. J. et al. A general review of tropical South American floodplains *. v. 2, n. 4, p. 231–238, 1993.

JUNK, W. J. et al. A classification of major naturally-occurring amazonian lowland wetlands. **Wetlands**, v. 31, n. 4, p. 623–640, 2011.

JUNK, W. J. et al. Current state of knowledge regarding the world's wetlands and their future under global climate change: A synthesis. **Aquatic Sciences**, v. 75, n. 1, p. 151–167, 2013.

JUNK, W. J. Current state of knowledge regarding South America wetlands and their future under global climate change. **Aquatic Sciences**, v. 75, n. 1, p. 113–131, 2013.

JUNK, W. J. et al. Brazilian wetlands: their definition, delineation, and classification for research, sustainable management, and protection. **Aquatic Conservation: Marine and Freshwater Ecosystems**, v. 24, n. 1, p. 5–22, fev. 2014.

JUNK, W. J. et al. Macrohabitat studies in large Brazilian floodplains to support sustainable development in the face of climate change. **Ecohydrology & Hydrobiology**, v. 18, n. 4, p. 334–344, dez. 2018.

JUNK, W. J.; BAYLEY, P. B.; SPARKS, R. E. The flood pulse concept in river-floodplain-systems. **Canadian Journal of Fisheries and Aquatic Sciences**, 1989.

KANDUS, P. et al. Identificación y Delimitación de Regiones de Humedales de Argentina. In: **Regiones de humedales de Argentina**. Buenos Aires: Ministerio de Ambiente y Desarrollo Sustentable, Fundación Humedales/Wetlands International, Universidad Nacional de San Martín y Universidad de Buenos Aires, 2017. p. 31–48.

KANDUS, P. et al. Remote sensing of wetlands in South America : status and challenges Remote sensing of wetlands in South America : status and. **International Journal of Remote Sensing**, v. 39, n. 4, p. 993–1016, 2018.

KANDUS, P.; MINOTTI, P.; MALVÁREZ, A. I. Distribution of wetlands in Argentina estimated from soil charts. p. 403–409, 2008.

KAUFFELDT, A. et al. Technical review of large-scale hydrological models for implementation in operational flood forecasting schemes on continental level. **Environmental Modelling and Software**, v. 75, p. 68–76, 2016.

KENDALL, M. G.; GIBBONS, J. D. **Rank correlation methods**. London: Griffin, 1975.

KERR, Y. H. et al. Soil moisture retrieval from space: The Soil Moisture and Ocean Salinity (SMOS) mission. **IEEE Transactions on Geoscience and Remote Sensing**, 2001.

KHALIL, A. F. et al. El Niño-Southern Oscillation-based index insurance for floods: Statistical risk analyses and application to Peru. **Water Resources Research**, v. 43, n. 10, p. 1–14, out. 2007.

KHANAL, S. et al. The impact of meteorological and hydrological memory on compound peak flows in the Rhine river basin. **Atmosphere**, v. 10, n. 4, 2019.

KIM, D. et al. Mapping spatio-temporal water level variations over the central Congo River using PALSAR ScanSAR and Envisat altimetry data. **International Journal of Remote Sensing**, v. 38, n. 23, p. 7021–7040, 2 dez. 2017.

KIPTALA, J. K. et al. Mapping evapotranspiration trends using MODIS and SEBAL model in a data scarce and heterogeneous landscape in Eastern Africa. **Water**

Resources Research, v. 49, n. 12, p. 8495–8510, 2013.

KIRCHNER, J. W. Getting the right answers for the right reasons: Linking measurements, analyses, and models to advance the science of hydrology. **Water Resources Research**, 2006.

KOKS, E. et al. The macroeconomic impacts of future river flooding in Europe. **Environmental Research Letters**, p. 0–15, 17 jul. 2019.

KOMORI, D. et al. Characteristics of the 2011 Chao Phraya River flood in Central Thailand. **Hydrological Research Letters**, v. 6, n. 0, p. 41–46, 2012.

KREPPER, C. M.; GARCÍA, N. O.; JONES, P. D. Low-frequency response of the upper Paraná basin. **International Journal of Climatology**, v. 28, n. 3, p. 351–360, 15 mar. 2008.

KRUEGER, T. et al. The role of expert opinion in environmental modelling. **Environmental Modelling and Software**, v. 36, p. 4–18, 2012.

KUMAR, R.; SAMANIEGO, L.; ATTINGER, S. Implications of distributed hydrologic model parameterization on water fluxes at multiple scales and locations. **Water Resources Research**, 2013.

KUNDZEWICZ, Z. W. et al. Flood risk and climate change: global and regional perspectives. **Hydrological Sciences Journal**, v. 59, n. 1, p. 1–28, 2 jan. 2014.

KUNDZEWICZ, Z. W.; PIŃSKWAR, I.; BRAKENRIDGE, G. R. Large floods in Europe, 1985–2009. **Hydrological Sciences Journal**, v. 58, n. 1, p. 1–7, jan. 2013.

KUNDZEWICZ, Z. W.; SZAMALEK, K.; KOWALCZAK, P. The Great Flood of 1997 in Poland. **Hydrological Sciences Journal**, v. 44, n. 6, p. 855–870, 25 dez. 1999.

KUPPEL, S. et al. What does it take to flood the Pampas?: Lessons from a decade of strong hydrological fluctuations. **Water Resources Research**, v. 51, n. 4, p. 2937–2950, abr. 2015.

L. GUTENSON, J. et al. Comparison of generalized non-data-driven lake and reservoir routing models for global-scale hydrologic forecasting of reservoir outflow at diurnal time steps. **Hydrology and Earth System Sciences**, v. 24, n. 5, p. 2711–2729, 2020.

LÄHTEENOJA, O. et al. The large Amazonian peatland carbon sink in the subsiding Pastaza-Marañón foreland basin, Peru. **Global Change Biology**, v. 18, n. 1, p. 164–178, 2012.

LAI, X. et al. Large-scale hydrodynamic modeling of the middle Yangtze River Basin with complex river-lake interactions. **Journal of Hydrology**, v. 492, p. 228–243, 2013.

LAIPELT, L. et al. Assessment of an Automated Calibration of the SEBAL Algorithm to Estimate Dry-Season Surface-Energy Partitioning in a Forest–Savanna Transition in Brazil. **Remote Sensing**, v. 12, n. 7, p. 1108, 31 mar. 2020.

LAIPELT, L. et al. Long-term monitoring of evapotranspiration using the SEBAL algorithm and Google Earth Engine cloud computing. **ISPRS Journal of Photogrammetry and Remote Sensing**, v. 178, n. April, p. 81–96, ago. 2021.

LANDERER, F. W. et al. Extending the Global Mass Change Data Record: GRACE Follow-On Instrument and Science Data Performance. **Geophysical Research Letters**, v. 47, n. 12, p. 1–10, 2020.

LANG, M. et al. Extrapolation of rating curves by hydraulic modelling, with application to flood frequency analysis. **Hydrological Sciences Journal**, v. 55, n. 6, p. 883–898, 2010.

LANGERWISCH, F. et al. Potential effects of climate change on inundation patterns in the Amazon Basin. **Hydrology and Earth System Sciences**, v. 17, n. 6, p. 2247–2262, 2013.

LANGILL, J. C.; ABIZAID, C. What is a bad flood? Local perspectives of extreme floods in the Peruvian Amazon. **Ambio**, v. 49, n. 8, p. 1423–1436, 2020.

LATRUBESSE, E. M. Amazon lakes. In: **Encyclopedia of Earth Sciences Series**. [s.l: s.n.].

LATRUBESSE, E. M. et al. Damming the rivers of the Amazon basin. **Nature**, v. 546, n. 7658, p. 363–369, 2017a.

LATRUBESSE, E. M. et al. Damming the rivers of the Amazon basin. **Nature**, v. 546, n. 7658, p. 363–369, 2017b.

LATRUBESSE, E. M.; BREA, D. Floods in Argentina. **Developments in Earth Surface Processes**, v. 13, n. C, p. 333–349, 2009.

LATRUBESSE, E. M.; FRANZINELLI, E. The late Quaternary evolution of the Negro River , Amazon , Brazil : Implications for island and floodplain formation in large anabranching tropical systems. v. 70, p. 372–397, 2005.

LATRUBESSE, E. M.; STEVAUX, J. C. The Anavilhanas and Mariuá Archipelagos: Fluvial Wonders from the Negro River, Amazon Basin. In: VIEIRA, B. C.; SALGADO, A. A. R.; SANTOS, L. J. C. (Eds.). . **Choice Reviews Online**. World Geomorphological Landscapes. Dordrecht: Springer Netherlands, 2015. v. 53p. 157–169.

LAWFORD, R. **The GEOSS Water Strategy: From Observations to Decisions**. [s.l: s.n.].

LEE, E. et al. Land cover change explains the increasing discharge of the Paraná River. **Regional Environmental Change**, v. 18, n. 6, p. 1871–1881, 2018.

LEHNER, B. et al. High-resolution mapping of the world's reservoirs and dams for sustainable river-flow management. **Frontiers in Ecology and the Environment**, v. 9, n. 9, p. 494–502, 2011.

LEHNER, B.; DÖLL, P. Development and validation of a global database of lakes, reservoirs and wetlands. **Journal of Hydrology**, v. 296, n. 1–4, p. 1–22, 2004.

LEHNER, B.; GRILL, G. Global river hydrography and network routing: Baseline data and new approaches to study the world's large river systems. **Hydrological Processes**, 2013.

LEHNER, B.; VERDIN, K.; JARVIS, A. New global hydrography derived from spaceborne elevation data. **Eos**, 2008.

LEON, A. S.; GOODELL, C. Controlling HEC-RAS using MATLAB. **Environmental Modelling and Software**, 2016.

LEOPOLD, L. B.; MADDOCK, T. J. **The Hydraulic Geometry of Stream Channels and Some Physiographic ImplicationsGeological Survey Professional Paper 252**. [s.l: s.n.].

LESACK, L. F. W.; MELACK, J. M. Flooding Hydrology and Mixture Dynamics of Lake Water Derived from Multiple Sources in an Amazon Floodplain Lake. **Water Resources Research**, v. 31, n. 2, p. 329–345, 1995.

LI, D. et al. Examining water area changes accompanying dam construction in the Madeira River in the Brazilian Amazon. **Water (Switzerland)**, v. 12, n. 7, 2020a.

LI, Y. et al. Hydrodynamic and Hydrological Modeling of the Poyang Lake Catchment System in China. **Journal of Hydrologic Engineering**, v. 19, n. 3, p. 607–616, mar. 2014.

LI, Y. et al. A high-resolution bathymetry dataset for global reservoirs using multi-source satellite imagery and altimetry. **Remote Sensing of Environment**, v. 244, n. July 2019, p. 111831, 2020b.

LIBONATI, R. et al. Rescue Brazil's burning Pantanal wetlands. **Nature**, v. 588, n. 7837, p. 217–219, 2020.

LIEBE, J.; VAN DE GIESEN, N.; ANDREINI, M. Estimation of small reservoir storage capacities in a semi-arid environment. **Physics and Chemistry of the Earth**, 2005.

LIN, P. et al. Global reconstruction of naturalized river flows at 2.94 million reaches. **Water Resources Research**, p. 2019WR025287, 24 jul. 2019.

LIST, G.; COOMES, O. T. Natural hazards and risk in rice cultivation along the upper Amazon River. **Natural Hazards**, v. 87, n. 1, p. 165–184, 2017.

LIU, M.; HU, D. Response of Wetland Evapotranspiration to Land Use/Cover Change and Climate Change in Liaohe River Delta, China. **Water**, v. 11, n. 5, p. 955, 7 maio 2019.

LIU, Y. et al. Advancing data assimilation in operational hydrologic forecasting: Progresses, challenges, and emerging opportunities. **Hydrology and Earth System Sciences**, 2012.

LIU, Z.; MERWADE, V. Accounting for model structure, parameter and input forcing uncertainty in flood inundation modeling using Bayesian model averaging. **Journal of Hydrology**, v. 565, n. February, p. 138–149, 2018.

LOBÓN-CERVIÁ, J. et al. The importance of forest cover for fish richness and abundance on the Amazon floodplain. **Hydrobiologia**, v. 750, n. 1, p. 245–255, 2015.

LOPES, V. A. R. et al. A first integrated modelling of a river-lagoon large-scale

hydrological system for forecasting purposes. **Journal of Hydrology**, v. 565, n. August, p. 177–196, 2018.

LUO, X. et al. Modeling surface water dynamics in the Amazon Basin using MOSART-Inundation v1.0: impacts of geomorphological parameters and river flow representation. **Geoscientific Model Development**, v. 10, n. 3, p. 1233–1259, 23 mar. 2017.

MACDONALD, N.; SANGSTER, H. High-magnitude flooding across Britain since AD 1750. **Hydrology and Earth System Sciences**, v. 21, n. 3, p. 1631–1650, 20 mar. 2017.

MACKAY, D. S. et al. Environmental drivers of evapotranspiration in a shrub wetland and an upland forest in northern Wisconsin. **Water Resources Research**, v. 43, n. 3, p. 1–14, 2007.

MALTBY, E.; ACREMAN, M. C. Ecosystem services of wetlands : pathfinder for a new paradigm Ecosystem services of wetlands : pathfinder for a new paradigm. v. 6667, n. December, p. 37–41, 2015.

MALTCHIK, L. et al. Legislation for wetland conservation in Brazil: Are existing terms and definitions sufficient? **Environmental Conservation**, v. 45, n. 03, p. 301–305, 11 set. 2018.

MAMEDE, G. L. et al. Modeling the Effect of Multiple Reservoirs on Water and Sediment Dynamics in a Semiarid Catchment in Brazil. **Journal of Hydrologic Engineering**, v. 23, n. 12, p. 05018020, dez. 2018.

MANSUR, A. V. et al. An assessment of urban vulnerability in the Amazon Delta and Estuary: a multi-criterion index of flood exposure, socio-economic conditions and infrastructure. **Sustainability Science**, v. 11, n. 4, p. 625–643, 2016.

MARCHETTI, Z. Y. et al. Vegetation and its relationship with geomorphologic units in the Parana River floodplain, Argentina. **Journal of South American Earth Sciences**, v. 46, p. 122–136, 2013.

MARENGO, J. A.; ESPINOZA, J. C. Extreme seasonal droughts and floods in Amazonia: causes, trends and impacts. **International Journal of Climatology**, v. 36, n. 3, p. 1033–1050, mar. 2016.

MARENGO, J. A.; TOMASELLA, J.; UVO, C. R. Trends in streamflow and rainfall in tropical South America: Amazonia, eastern Brazil, and northwestern Peru. **Journal of Geophysical Research: Atmospheres**, v. 103, n. D2, p. 1775–1783, 27 jan. 1998.

MARQUES, G. F.; TILMANT, A. The economic value of coordination in large-scale multireservoir systems: The Parana River case. **Water Resources Research**, v. 49, n. 11, p. 7546–7557, nov. 2013.

MARQUES, T. C.; CICOGNA, M. A.; SOARES, S. **Benefits of coordination in the operation of hydroelectric power systems: Brazilian case**. 2006 IEEE Power Engineering Society General Meeting. **Anais**...IEEE, 2006Disponível em: <http://ieeexplore.ieee.org/document/1709574/>

MARU, Y. T. et al. A linked vulnerability and resilience framework for adaptation pathways in remote disadvantaged communities. **Global Environmental Change**, v. 28, p. 337–350, 2014.

MASSON, S.; DELECLUSE, P. Influence of the Amazon River runoff on the tropical atlantic. **Physics and Chemistry of the Earth, Part B: Hydrology, Oceans and Atmosphere**, v. 26, n. 2, p. 137–142, jan. 2001.

MATEO, C. M. et al. Assessing the impacts of reservoir operation to floodplain inundation by combining hydrological, reservoir management, and hydrodynamic models. **Water Resources Research**, v. 50, n. 9, p. 7245–7266, 2014.

MATEO, C. M. R. et al. Impacts of spatial resolution and representation of flow connectivity on large-scale simulation of floods. **Hydrology and Earth System Sciences**, v. 21, n. 10, p. 5143–5163, 12 out. 2017a.

MATEO, R. C. et al. Impacts of spatial resolution and representation of flow connectivity on large-scale simulation of floods. **Hydrology and Earth System Sciences**, v. 21, n. 10, p. 5143–5163, 2017b.

MATGEN, P. et al. Integration of SAR-derived river inundation areas, high-precision topographic data and a river flow model toward near real-time flood management. **International Journal of Applied Earth Observation and Geoinformation**, v. 9, n. 3, p. 247–263, 2007.

MAZZOLENI, M. et al. Floodplains in the Anthropocene: A Global Analysis of the Interplay Between Human Population, Built Environment, and Flood Severity. **Water Resources Research**, v. 57, n. 2, 2021.

MCMILLAN, H. K.; WESTERBERG, I. K.; KRUEGER, T. Hydrological data uncertainty and its implications. n. April, p. 1–14, 2018.

MEA. **ECOSYSTEMS AND HUMAN WELL-BEING: WETLANDS AND WATER Synthesis**. World Reso ed. Washington, DC.: [s.n.].

MEADE, R. H. et al. Backwater Effects in the Amazon River of Basin. **Environmental Geology and Water Sciences**, v. 18, n. 2, p. 105–114, 1991.

MEJIA, A. I.; REED, S. M. Evaluating the effects of parameterized cross section shapes and simplified routing with a coupled distributed hydrologic and hydraulic model. **Journal of Hydrology**, v. 409, n. 1–2, p. 512–524, 2011.

MELACK, J. M. et al. Regionalization of methane emissions in the Amazon Basin with microwave remote sensing. **Global Change Biology**, v. 10, n. 5, p. 530–544, 2004.

MELACK, J. M. Aquatic Ecosystems. In: **Ecological Studies**. [s.l: s.n.]. v. 227p. 119–148.

MELACK, J. M.; COE, M. T. Amazon floodplain hydrology and implications for aquatic conservation. **Aquatic Conservation: Marine and Freshwater Ecosystems**, n. July 2020, p. 1029–1040, 2021.

MELACK, J. M.; FORSBERG, B. R. Biogeochemistry of Amazon Floodplain. In: MCCLAIN, M. E.; VICTORIA, R.; RICHEY, J. E. (Eds.). . **The Biogeochemistry of the Amazon Basin**. New York, USA: Oxford University Press, 2001.

MELACK, J. M.; HESS, L. L. Remote Sensing of the Distribution and Extent of Wetlands in the Amazon Basin. In: **Amazonian Floodplain Forests**. [s.l: s.n.]. p. 43–

59.

MELTON, J. R. et al. Present state of global wetland extent and wetland methane modelling : conclusions from a model inter-comparison project. p. 753–788, 2013.

MERZ, B.; NGUYEN, V. D.; VOROGUSHYN, S. Temporal clustering of floods in Germany: Do flood-rich and flood-poor periods exist? **Journal of Hydrology**, v. 541, p. 824–838, out. 2016.

MERZ, R.; BLÖSCHL, G. A process typology of regional floods. **Water Resources Research**, v. 39, n. 12, p. 1–20, 2003.

MEYER, A. et al. Empirical assessment of flood wave celerity-discharge relationships at local and reach scales. **Hydrological Sciences Journal**, 2018.

MEYER OLIVEIRA, A.; FLEISCHMANN, A.; PAIVA, R. On the contribution of remote sensing-based calibration to model multiple hydrological variables. **Journal of Hydrology**, 2020.

MIGUEZ-MACHO, G.; FAN, Y. The role of groundwater in the Amazon water cycle: 1. Influence on seasonal streamflow, flooding and wetlands. **Journal of Geophysical Research Atmospheres**, v. 117, n. 15, p. 1–30, 2012.

MINOTTI, P. G. The Paraná-Paraguay Fluvial Corridor (Argentina). In: **The Wetland Book**. Dordrecht: Springer Netherlands, 2018. v. 2p. 785–796.

MITSCH, W. J.; GOSSELINK, J. **Wetlands 4th Edition**. John Wiley ed. Hoboken, NJ: [s.n.].

MOHAMED, Y. A. et al. Wetland versus open water evaporation : An analysis and literature review Energy balance. **Physics and Chemistry of the Earth**, v. 47–48, p. 114–121, 2012.

MOHAMED, Y. A.; BASTIAANSSEN, W. G. M.; SAVENIJE, H. H. G. Spatial variability of evaporation and moisture storage in the swamps of the upper Nile studied by remote sensing techniques. **Journal of Hydrology**, v. 289, n. 1–4, p. 145–164, abr. 2004.

MOLINA-CARPIO, J. et al. Hydroclimatology of the Upper Madeira River basin: spatio-temporal variability and trends. **Hydrological Sciences Journal**, v. 62, n. 6, p. 911–927, 2017.

MONTAZEM, A. et al. Wavelet-based river segmentation using hydraulic control-preserving water surface elevation profile properties. **Geophysical Research Letters**, p. 2019GL082986, 28 maio 2019.

MONTERO, J. C.; LATRUBESSE, E. M. The igapó of the Negro River in central Amazonia: Linking late-successional inundation forest with fluvial geomorphology. **Journal of South American Earth Sciences**, v. 46, p. 137–149, out. 2013.

MONTROULL, N. B. et al. Assessment of climate change on the future water levels of the Iberá wetlands, Argentina, during the twenty-first century. **International Journal of River Basin Management**, v. 11, n. 4, p. 401–410, dez. 2013.

MOOMAW, W. R. et al. Wetlands In a Changing Climate: Science, Policy and Management. **Wetlands**, v. 38, n. 2, p. 183–205, 2018.

MOREIRA, A. A. et al. Assessment of terrestrial water balance using remote sensing data in South America. **Journal of Hydrology**, v. 575, p. 131–147, ago. 2019.

MORIASI, D. N. et al. Hydrologic and Water Quality Models: Performance Measures and Evaluation Criteria. **Transactions of the ASABE**, v. 58, n. 6, p. 1763–1785, 2015.

MU, Q. et al. Development of a global evapotranspiration algorithm based on MODIS and global meteorology data. **Remote Sensing of Environment**, 2007.

MULLIGAN, M.; VAN SOESBERGEN, A.; SÁENZ, L. GOODD, a global dataset of more than 38,000 georeferenced dams. **Scientific Data**, 2020.

MUNAR, A. M. et al. Coupling large-scale hydrological and hydrodynamic modeling: Toward a better comprehension of watershed-shallow lake processes. **Journal of Hydrology**, v. 564, n. March, p. 424–441, set. 2018.

NAGHETTINI, M. Statistical Hypothesis Testing. In: **Fundamentals of Statistical Hydrology**. [s.l: s.n.]. p. 251–309.

NARDI, F. et al. GFPLAIN250m, a global high-resolution dataset of Earth's floodplains. **Scientific Data**, v. 6, p. 180309, 15 jan. 2019.

NARDI, F.; VIVONI, E. R.; GRIMALDI, S. Investigating a floodplain scaling relation using a hydrogeomorphic delineation method. **Water Resources Research**, v. 42, n. 9, p. 1–15, 2006.

NAZEMI, A.; WHEATER, H. S. On inclusion of water resource management in Earth system models - Part 2: Representation of water supply and allocation and opportunities for improved modeling. **Hydrology and Earth System Sciences**, v. 19, n. 1, p. 63–90, 7 jan. 2015.

NEAL, J. et al. A data assimilation approach to discharge estimation from space. **Hydrological Processes**, v. 23, n. 25, p. 3641–3649, 15 dez. 2009.

NEAL, J. C. et al. Efficient incorporation of channel cross-section geometry uncertainty into regional and global scale flood inundation models. **Journal of Hydrology**, v. 529, p. 169–183, 2015.

NEAL, J.; SCHUMANN, G.; BATES, P. A subgrid channel model for simulating river hydraulics and floodplain inundation over large and data sparse areas. **Water Resources Research**, v. 48, n. 11, p. 1–16, 2012.

NEIFF, J. J. **Humedales de la Argentina: sinopsis, problemas y perspectivas futurasProyectos CONICET PIP N°4242, 4244, 0815**. Corrientes, Argentina: [s.n.].

NEIFF, J. J.; IRIONDO, M. H.; CARIGNAN, R. Large Tropical South American Wetlands: An Overview. In: LINK, G. L.; NAIMAN, R. J. (Eds.). . **The Ecology & Management of Aquatic-Terrestrial Ecotones**. [s.l: s.n.]. p. 155–165.

NEW, M. et al. A high-resolution data set of surface climate over global land areas. **Climate Research**, v. 21, p. 1–25, 2002.

NILSSON, C. Fragmentation and Flow Regulation of the World's Large River Systems. **Science**, v. 308, n. 5720, p. 405–408, 15 abr. 2005.

NOBRE, G. G. et al. The role of climate variability in extreme floods in Europe. **Environmental Research Letters**, v. 12, n. 8, p. 084012, 1 ago. 2017.

NUNES DA CUNHA, C.; JUNK, W. J. Year-to-year changes in water level drive the invasion of Vochysia divergens in Pantanal grasslands. **Applied Vegetation Science**, v. 7, n. 1, p. 103–110, 2004.

O'LOUGHLIN, F. et al. Hydraulic characterization of the middle reach of the Congo River. **Water Resources Research**, v. 49, n. 8, p. 5059–5070, 2013.

O'LOUGHLIN, F. E. et al. ICESat-derived inland water surface spot heights. **Water Resources Research**, v. 52, n. 4, p. 3276–3284, 2016a.

O'LOUGHLIN, F. E. et al. A multi-sensor approach towards a global vegetation corrected SRTM DEM product. **Remote Sensing of Environment**, v. 182, p. 49–59, set. 2016b.

O'LOUGHLIN, F. E. et al. A LISFLOOD-FP hydraulic model of the middle reach of the Congo. **Journal of Hydrology**, v. 580, n. May 2019, p. 124203, jan. 2020.

OFDA. **Disaster case report: Paraguay-floods 1982**. Washington, DC.: [s.n.].

OLIVEIRA, M. D. DE et al. Further Development of Small Hydropower Facilities May Alter Nutrient Transport to the Pantanal Wetland of Brazil. **Frontiers in Environmental Science**, v. 8, n. December 2020, 2020.

OLIVEIRA, R.; LOUCKS, D. P. Operating rules for multireservoir systems. **Water Resources Research**, v. 33, n. 4, p. 839–852, abr. 1997.

ONS. **Manual de procedimentos da operação 10.2.1**. Rio de Janeiro: [s.n.]. Disponível em: <http://extranet.ons.org.br/operacao/mpo.nsf/principalweb?openframeset>.

ONS. **Diagrama Esquemático das Usinas Hidroelétricas do SIN**. Disponível em: <http://www.ons.org.br/>.

OVANDO, A. et al. Extreme flood events in the Bolivian Amazon wetlands. **Journal of Hydrology: Regional Studies**, v. 5, p. 293–308, mar. 2016.

OVANDO, A. et al. Multi-temporal flood mapping and satellite altimetry used to evaluate the flood dynamics of the Bolivian Amazon wetlands. **International Journal of Applied Earth Observation and Geoinformation**, v. 69, n. August 2017, p. 27–40, 2018.

OVIEDO, A. F. P. et al. Implementing climate variability at the community level in the Amazon floodplain. **Environmental Science and Policy**, v. 63, p. 151–160, 2016.

PACA, V. H. DA M. et al. The spatial variability of actual evapotranspiration across the Amazon River Basin based on remote sensing products validated with flux towers. **Ecological Processes**, v. 8, n. 1, p. 6, 2019.

PAIVA, R. C. D. DE. Modelagem hidrológica e hidrodinâmica de grandes bacias.

Estudo de caso: bacia do rio Solimões. **Dissertação (Mestrado)**, p. 182, 2009.

PAIVA, R. et al. Large-scale hydrologic and hydrodynamic modeling of the Amazon River basin. **Water Resources Research**, v. 49, n. 3, p. 1226–1243, 2013a.

PAIVA, R. et al. Assimilating in situ and radar altimetry data into a large-scale hydrologic-hydrodynamic model for streamflow forecast in the Amazon. **Hydrology and Earth System Sciences**, v. 17, n. 7, p. 2929–2946, 2013b.

PAIVA, R. C. D. et al. Reduced precipitation over large water bodies in the Brazilian Amazon shown from TRMM data. **Geophysical Research Letters**, v. 38, n. 4, p. n/a-n/a, fev. 2011.

PAIVA, R. C. D. et al. **SAMEWATER : Uma agenda de pesquisa integrada da hidrologia da América do Sul**. SBRH 2017. **Anais**...Florianópolis, Brazil.: ABRH, 2017

PAIVA, R. C. D.; COLLISCHONN, W.; TUCCI, C. E. M. Large scale hydrologic and hydrodynamic modeling using limited data and a GIS based approach. **Journal of Hydrology**, v. 406, n. 3–4, p. 170–181, set. 2011.

PAL, S.; LEE, T. R.; CLARK, N. E. The 2019 Mississippi and Missouri River Flooding and Its Impact on Atmospheric Boundary Layer Dynamics. **Geophysical Research Letters**, v. 47, n. 6, p. 1–10, 28 mar. 2020.

PANDE, S.; SIVAPALAN, M. Progress in socio-hydrology: a meta-analysis of challenges and opportunities. **Wiley Interdisciplinary Reviews: Water**, v. 4, n. 4, p. e1193, jul. 2017.

PANGALA, S. R. et al. Large emissions from floodplain trees close the Amazon methane budget. **Nature**, v. 552, n. 7684, p. 230–234, 2017.

PAPA, F. et al. Variations of surface water extent and water storage in large river basins : A comparison of different global data sources. v. 35, p. 1–5, 2008a.

PAPA, F. et al. Variations of surface water extent and water storage in large river basins: A comparison of different global data sources. **Geophysical Research Letters**, v. 35, n. 11, p. L11401, 4 jun. 2008b.

PAPA, F. et al. Interannual variability of surface water extent at the global scale, 1993–2004. **Journal of Geophysical Research**, v. 115, n. D12, p. D12111, 19 jun. 2010.

PAPA, F. et al. Surface freshwater storage and variability in the Amazon basin from multi-satellite observations , 1993 – 2007. v. 118, p. 1993–2007, 2013.

PAPPENBERGER, F. et al. Uncertainty in the calibration of effective roughness parameters in HEC-RAS using inundation and downstream level observations. **Journal of Hydrology**, v. 302, n. 1–4, p. 46–69, 2005.

PAPPENBERGER, F. et al. Influence of uncertain boundary conditions and model structure on flood inundation predictions. **Advances in Water Resources**, v. 29, n. 10, p. 1430–1449, 2006.

PAPPENBERGER, F. et al. Grasping the unavoidable subjectivity in calibration of

flood inundation models: A vulnerability weighted approach. **Journal of Hydrology**, v. 333, n. 2–4, p. 275–287, 2007.

PAPPENBERGER, F. et al. Deriving global flood hazard maps of fluvial floods through a physical model cascade. **Hydrology and Earth System Sciences**, v. 16, n. 11, p. 4143–4156, 2012.

PARIS, A. et al. Stage-discharge rating curves based on satellite altimetry and modeled discharge in the Amazon basin. **Water Resources Research**, 2016.

PARK, E. Characterizing channel-floodplain connectivity using satellite altimetry: Mechanism, hydrogeomorphic control, and sediment budget. **Remote Sensing of Environment**, v. 243, n. November 2019, p. 111783, jun. 2020.

PARK, E.; LATRUBESSE, E. M. The hydro-geomorphologic complexity of the lower Amazon River floodplain and hydrological connectivity assessed by remote sensing and field control. **Remote Sensing of Environment**, v. 198, p. 321–332, 2017a.

PARK, E.; LATRUBESSE, E. M. The hydro-geomorphologic complexity of the lower Amazon River floodplain and hydrological connectivity assessed by remote sensing and field control. **Remote Sensing of Environment**, v. 198, n. September, p. 321–332, 2017b.

PARK, E.; LATRUBESSE, E. M. A geomorphological assessment of wash-load sediment fluxes and floodplain sediment sinks along the lower Amazon River. **Geology**, v. 47, n. 5, p. 403–406, 2019.

PARKER, R. J. et al. Evaluating year-to-year anomalies in tropical wetland methane emissions using satellite CH4 observations. **Remote Sensing of Environment**, v. 211, n. April, p. 261–275, 2018.

PAROLIN, P. Submerged in darkness: adaptations to prolonged submergence by woody species of the Amazonian floodplains. **Annals of Botany**, v. 103, n. 2, p. 359–376, jan. 2009.

PAROLIN, P.; WALDHOFF, D.; PIEDADE, M. T. F. Gas Exchange and Photosynthesis. In: JUNK, W. J. et al. (Eds.). . **Amazonian Floodplain Forests. Ecological Studies**. Dordrecht: Springer, 2010. p. 203–222.

PARRENS, M. et al. Mapping Dynamic Water Fraction under the Tropical Rain Forests of the Amazonian Basin from SMOS Brightness Temperatures. **Water**, v. 9, n. 5, p. 350, 17 maio 2017.

PARRENS, M. et al. High resolution mapping of inundation area in the Amazon basin from a combination of L-band passive microwave, optical and radar datasets. **International Journal of Applied Earth Observation and Geoinformation**, v. 81, n. April, p. 58–71, set. 2019.

PASCALE, S. et al. Analysis of rainfall seasonality from observations and climate models. **Climate Dynamics**, v. 44, n. 11–12, p. 3281–3301, 14 jun. 2015.

PASQUINI, A. I.; DEPETRIS, P. J. ENSO-triggered exceptional flooding in the Paraná River: Where is the excess water coming from? **Journal of Hydrology**, v. 383, n. 3–4, p. 186–193, 2010.

PASSAIA, O. A. et al. Impact of large reservoirs on simulated discharges of Brazilian rivers. **RBRH**, v. 25, 2020.

PATIÑO, J. E. Análisis espacial cuantitativo de la transformación de humedales continentales en Colombia. **Biota Colombiana**, v. 17, n. 1, p. 21, 2016.

PAU, G. S. H. et al. Accurate and efficient prediction of fine-resolution hydrologic and carbon dynamic simulations from coarse-resolution models. **Water Resources Research**, 2016.

PAVELSKY, T.; DURAND, M. **Developing new algorithms for estimating river discharge from space**. Eos. **Anais**...2012

PAVELSKY, T.; SMITH, L. C. RivWidth: A software tool for the calculation of river widths from remotely sensed imagery. **IEEE Geoscience and Remote Sensing Letters**, v. 5, n. 1, p. 70–73, 2008.

PAZ, A. R. et al. Large-Scale Hydrodynamic Modeling of a Complex River Network and Floodplains. **Journal of Hydrologic Engineering**, v. 15, n. 2, p. 152–165, 2010.

PAZ, A. R.; COLLISCHONN, W. River reach length and slope estimates for large-scale hydrological models based on a relatively high-resolution digital elevation model. **Journal of Hydrology**, v. 343, n. 3–4, p. 127–139, set. 2007.

PAZ, A. R.; COLLISCHONN, W.; LOPES DA SILVEIRA, A. L. Improvements in large-scale drainage networks derived from digital elevation models. **Water Resources Research**, v. 42, n. 8, p. 1–7, ago. 2006.

PAZ, A. R. DA. **Simulação hidrológica de rios com grandes planícies de inundação**. [s.l.] UFRGS, 2010.

PAZ, A. R. DA et al. Large-scale modelling of channel flow and floodplain inundation dynamics and its application to the Pantanal (Brazil). **Hydrological Processes**, v. 25, n. 9, p. 1498–1516, 2011.

PEKEL, J. et al. High-resolution mapping of global surface water and its long-term changes. **Nature**, v. 540, n. 7633, p. 418–422, 7 dez. 2016.

PELLET, V. et al. Coherent Satellite Monitoring of the Water Cycle Over the Amazon. Part 1: Methodology and Initial Evaluation. **Water Resources Research**, v. 57, n. 5, p. 1–21, 2021.

PELLETIER, P. M. Uncertainties in the single determination of river discharge: a literature review. **Canadian Journal of Civil Engineering**, v. 15, n. 5, p. 834–850, 1988.

PENATTI, N. C. et al. Satellite-based hydrological dynamics of the world's largest continuous wetland. **Remote Sensing of Environment**, v. 170, p. 1–13, dez. 2015.

PENNING-ROWSELL, E. C. Flood-Hazard Response in Argentina. **Geographical Review**, v. 86, n. 1, p. 72, jan. 1996.

PETTITT, A. N. A Non-Parametric Approach to the Change-Point Problem. **Applied Statistics**, v. 28, n. 2, 1979.

PHAM-DUC, B. et al. Comparisons of global terrestrial surface water datasets over 15 years. **Journal of Hydrometeorology**, v. 18, n. 4, p. 993–1007, 2017.

PIANOSI, F. et al. Sensitivity analysis of environmental models: A systematic review with practical workflow. **Environmental Modelling and Software**, v. 79, p. 214–232, 2016.

PICKENS, A. H. et al. Mapping and sampling to characterize global inland water dynamics from 1999 to 2018 with full Landsat time-series. **Remote Sensing of Environment**, v. 243, n. December 2019, p. 111792, jun. 2020.

PIDWIRNY, M. **Remote Sensing**. Disponível em: <https://editors.eol.org/eoearth/wiki/Remote_sensing>. Acesso em: 17 mar. 2019.

PINEL, S. et al. Flooding dynamics within an Amazonian floodplain: water circulation patterns and inundation duration. **Water Resources Research**, p. 2019WR026081, 22 dez. 2019.

PINHO, P. F.; MARENGO, J. A.; SMITH, M. S. Complex socio-ecological dynamics driven by extreme events in the Amazon. **Regional Environmental Change**, v. 15, n. 4, p. 643–655, 2015.

PIOLA, A. R. et al. The influence of the Plata River discharge on the western South Atlantic shelf. **Geophysical Research Letters**, v. 32, n. 1, p. 1–4, 2005.

POFF, N. L. et al. The ecological limits of hydrologic alteration (ELOHA): A new framework for developing regional environmental flow standards. **Freshwater Biology**, v. 55, n. 1, p. 147–170, 2010.

POFF, N. L. et al. Sustainable water management under future uncertainty with eco-engineering decision scaling. **Nature Climate Change**, v. 6, n. 1, p. 25–34, 14 jan. 2016.

POKHREL, Y. et al. Incorporating Anthropogenic Water Regulation Modules into a Land Surface Model. **Journal of Hydrometeorology**, v. 13, n. 1, p. 255–269, fev. 2012.

POKHREL, Y. et al. Potential Disruption of Flood Dynamics in the Lower Mekong River Basin Due to Upstream Flow Regulation. **Scientific Reports**, v. 8, n. 1, p. 17767, 2018.

POKHREL, Y. N. et al. Recent progresses in incorporating human land-water management into global land surface models toward their integration into Earth system models. **Wiley Interdisciplinary Reviews: Water**, v. 3, n. 4, p. 548–574, jul. 2016.

PONTES, P. R. M. et al. MGB-IPH model for hydrological and hydraulic simulation of large floodplain river systems coupled with open source GIS. **Environmental Modelling and Software**, v. 94, p. 1–20, 2017.

POSSE, G. et al. Carbon and water vapor balance in a subtropical pine plantation. **iForest - Biogeosciences and Forestry**, v. 9, n. 5, p. 736–742, 13 out. 2016.

PRIETO, M. D. R. ENSO signals in South America: rains and floods in the Paraná River region during colonial times. **Climatic Change**, v. 83, n. 1–2, p. 39–54, 24 abr.

2007.

PRIGENT, C. et al. Global inundation dynamics inferred from multiple satellite observations, 1993-2000. **Journal of Geophysical Research Atmospheres**, v. 112, n. 12, p. 1993–2000, 2007.

PRIGENT, C. et al. Impact of the inundation occurrence on the deep convection at continental scale from satellite observations and modeling experiments. **Journal of Geophysical Research: Atmospheres**, v. 116, n. D24, p. n/a-n/a, 27 dez. 2011.

PRIGENT, C.; JIMENEZ, C.; BOUSQUET, P. Satellite-Derived Global Surface Water Extent and Dynamics Over the Last 25 Years (GIEMS-2). **Journal of Geophysical Research: Atmospheres**, v. 125, n. 3, p. 1–18, 16 fev. 2020.

QUINONES, M. J. et al. Detection and characterizacion of Colombian wetlands using Alos Palsar and MODIS imagery. **ISPRS - International Archives of the Photogrammetry, Remote Sensing and Spatial Information Sciences**, v. XL-7/W3, n. May, p. 375–382, 2015.

RAJIB, A. et al. Towards a large-scale locally relevant flood inundation modeling framework using SWAT and LISFLOOD-FP. **Journal of Hydrology**, v. 581, n. October 2019, p. 124406, fev. 2020.

RAMALHO, E. E. et al. Walking on water: the unexpected evolution of arboreal lifestyle in a large top predator in the Amazon flooded forests. **Ecology**, v. 0, n. 0, p. 1–4, 25 fev. 2021.

RAMSAR CONVENTION SECRETARIAT. Wise use of wetlands: Concepts and approaches for the wise use of wetlands. **Ramsar handbooks for the wise use of wetlands**, 2010.

RÄSÄNEN, T. A.; KUMMU, M. Spatiotemporal influences of ENSO on precipitation and flood pulse in the Mekong River Basin. **Journal of Hydrology**, v. 476, p. 154–168, 2013.

RAST, M.; JOHANNESSEN, J.; MAUSER, W. Review of Understanding of Earth's Hydrological Cycle: Observations, Theory and Modelling. **Surveys in Geophysics**, v. 35, n. 3, p. 491–513, 2014.

READ, W. E.; ROBINSON, M. C. Lower Mississippi Valley Floods of 1982 and 1983. **Journal of Water Resources Planning and Management**, v. 111, n. 4, p. 434–453, set. 1985.

REIS, V. et al. A Global Assessment of Inland Wetland Conservation Status. v. 67, n. 6, p. 523–533, 2018.

REIS, V. et al. Conservation planning for river-wetland mosaics: A flexible spatial approach to integrate floodplain and upstream catchment connectivity. **Biological Conservation**, v. 236, n. May, p. 356–365, 2019a.

REIS, V. et al. Characterizing seasonal dynamics of Amazonian wetlands for conservation and decision making. **Aquatic Conservation: Marine and Freshwater Ecosystems**, n. October 2018, p. 1–10, 2019b.

RENNÓ, C. D. et al. HAND, a new terrain descriptor using SRTM-DEM: Mapping terra-firme rainforest environments in Amazonia. **Remote Sensing of Environment**, 2008.

RENÓ, V. F. et al. Assessment of deforestation in the Lower Amazon floodplain using historical Landsat MSS/TM imagery. **Remote Sensing of Environment**, v. 115, n. 12, p. 3446–3456, 2011.

RENÓ, V.; NOVO, E. Forest depletion gradient along the Amazon floodplain. **Ecological Indicators**, v. 98, n. September, p. 409–419, 2019.

RESENDE, A. F. DE et al. Massive tree mortality from flood pulse disturbances in Amazonian floodplain forests: The collateral effects of hydropower production. **Science of the Total Environment**, v. 659, p. 587–598, 2019.

RESTREPO A, J. D.; KETTNER, A. J.; ROBERT BRAKENRIDGE, G. Monitoring water discharge and floodplain connectivity for the northern Andes utilizing satellite data: A tool for river planning and science-based decision-making. **Journal of Hydrology**, v. 586, n. March, p. 124887, 2020.

RETSÖ, D. Documentary evidence of historical floods and extreme rainfall events in Sweden 1400-1800. **Hydrology and Earth System Sciences**, v. 19, n. 3, p. 1307–1323, 9 mar. 2015.

REVEL et al. A Physically Based Empirical Localization Method for Assimilating Synthetic SWOT Observations of a Continental-Scale River: A Case Study in the Congo Basin. **Water**, v. 11, n. 4, p. 829, 19 abr. 2019.

RICAURTE, L. F. et al. Wetland habitat diversity in the Amazonian Piedmont of Colombia. **Wetlands**, v. 32, n. 6, p. 1189–1202, 2012.

RICAURTE, L. F. et al. Future impacts of drivers of change on wetland ecosystem services in Colombia. **Global Environmental Change**, v. 44, n. July 2016, p. 158–169, maio 2017.

RICAURTE, L. F. et al. A Classification System for Colombian Wetlands: an Essential Step Forward in Open Environmental Policy-Making. **Wetlands**, v. 39, n. 5, p. 971–990, 25 out. 2019.

RICHEY, J. E. et al. Outgassing from Amazonian rivers and wetlands as a large tropical source of atmospheric CO2. **Nature**, v. 416, n. 6881, p. 617–620, abr. 2002.

RICHTER, B. D.; THOMAS, G. A. Restoring environmental flows by modifying dam operations. **Ecology and Society**, 2007.

ROCA, R. et al. The Megha-Tropiques mission: a review after three years in orbit. **Frontiers in Earth Science**, 2015.

RODELL, M. et al. The Global Land Data Assimilation System. **Bulletin of the American Meteorological Society**, 2004.

RODELL, M. et al. Emerging trends in global freshwater availability. **Nature**, v. 557, n. 7707, p. 651–659, 16 maio 2018.

RODRIGUEZ-ALVAREZ, N. et al. Classifying Inundation in a Tropical Wetlands Complex with GNSS-R. **Remote Sensing**, v. 11, n. 9, p. 1053, 4 maio 2019.

RODRIGUEZ, D. A.; TOMASELLA, J.; LINHARES, C. Is the forest conversion to pasture affecting the hydrological response of Amazonian catchments? Signals in the Ji-Paraná Basin. **Hydrological Processes**, v. 24, n. 10, p. 1254–1269, 2010.

RODRÍGUEZ, E.; MORRIS, C. S.; BELZ, J. E. A Global Assessment of the SRTM Performance. **Photogrammetric Engineering & Remote Sensing**, 2006.

ROGGER, M. et al. Land use change impacts on floods at the catchment scale: Challenges and opportunities for future research. **Water Resources Research**, v. 53, n. 7, p. 5209–5219, 2017.

ROSENQVIST, Å. et al. The use of spaceborne radar data to model inundation patterns and trace gas emissions in the central Amazon floodplain. **International Journal of Remote Sensing**, v. 23, n. 7, p. 1303–1328, 2002.

ROSENQVIST, J. et al. Mapping of Maximum and Minimum Inundation Extents in the Amazon Basin 2014–2017 with ALOS-2 PALSAR-2 ScanSAR Time-Series Data. **Remote Sensing**, v. 12, n. 8, p. 1326, 22 abr. 2020.

ROSENTRETER, J. A. et al. Half of global methane emissions come from highly variable aquatic ecosystem sources. **Nature Geoscience**, v. 14, n. 4, p. 225–230, 5 abr. 2021.

ROSINGER, A. Y. Household water insecurity after a historic flood: Diarrhea and dehydration in the Bolivian Amazon. **Social Science and Medicine**, v. 197, n. May 2017, p. 192–202, 2018.

ROSSETTI, D. F. et al. Late Quaternary sedimentary dynamics in Western Amazonia: Implications for the origin of open vegetation/forest contrasts. **Geomorphology**, v. 177–178, p. 74–92, dez. 2012.

ROSSETTI, D. F. et al. Late Holocene tectonic influence on hydrology and vegetation patterns in a northern Amazonian megafan. **Catena**, v. 158, n. June, p. 121–130, 2017a.

ROSSETTI, D. F. et al. The imprint of Late Holocene tectonic reactivation on a megafan landscape in the northern Amazonian wetlands. **Geomorphology**, v. 295, n. February, p. 406–418, 2017b.

ROUGÉ, C. et al. Coordination and Control: Limits in Standard Representations of Multi-Reservoir Operations in Hydrological Modeling. **Hydrology and Earth System Sciences Discussions**, n. November, p. 1–37, 2019.

RUDORFF, C. M.; DUNNE, T.; MELACK, J. M. Recent increase of river-floodplain suspended sediment exchange in a reach of the lower Amazon River. **Earth Surface Processes and Landforms**, v. 43, n. 1, p. 322–332, jan. 2018.

RUDORFF, C. M.; MELACK, J. M.; BATES, P. D. Flooding dynamics on the lower Amazon floodplain: 1. Hydraulic controls on water elevation, inundation extent, and river-floodplain discharge. **Water Resources Research**, v. 50, n. 1, p. 619–634, 2014.

RUIZ AGUDELO, C. A. et al. Land use planning in the amazon basin: Challenges from

resilience thinking. **Ecology and Society**, v. 25, n. 1, 2020.

SAHARIA, M. et al. Characterization of floods in the United States. **Journal of Hydrology**, v. 548, p. 524–535, maio 2017.

SALESKA, S. R. et al. Carbon in Amazon Forests: Unexpected Seasonal Fluxes and Disturbance-Induced Losses. **Science**, v. 302, n. 5650, p. 1554–1557, 2003.

SALIS, S. M. et al. Root behavior of savanna species in Brazil's Pantanal wetland. **Global Ecology and Conservation**, v. 2, p. 378–384, dez. 2014.

SAMANIEGO, L. et al. Toward seamless hydrologic predictions across spatial scales. **Hydrology and Earth System Sciences**, v. 21, n. 9, p. 4323–4346, 2017.

SAMPSON, C. C. et al. A high-resolution global flood hazard model. **Water Resources Research**, v. 51, n. 9, p. 7358–7381, set. 2015.

SAMUELS, P. G. **Cross-section location in 1-D models**. Proceedings of international conference on river flood hydraulics. **Anais**...Chichester: John Wiley, 1990

SAN JOSÉ, J. . et al. A comparative analysis of the flooding and fire effects on the energy exchange in a wetland community (Morichal) of the Orinoco Llanos. **Journal of Hydrology**, v. 242, n. 3–4, p. 228–254, fev. 2001.

SANCHES, L. et al. Seasonal Patterns of Evapotranspiration for a Vochysia divergens Forest in the Brazilian Pantanal. **Wetlands**, v. 31, n. 6, p. 1215–1225, 7 dez. 2011.

SÁNCHEZ-CARRILLO, S. et al. Evapotranspiration in semi-arid wetlands: Relationships between inundation and the macrophyte-cover:open-water ratio. **Advances in Water Resources**, v. 27, n. 6, p. 643–655, 2004.

SANDERS, B. F.; SCHUBERT, J. E.; GALLEGOS, H. A. Integral formulation of shallow-water equations with anisotropic porosity for urban flood modeling. **Journal of Hydrology**, v. 362, n. 1–2, p. 19–38, nov. 2008.

SANTOS, C. P. Efeitos da cascata de reservatórios sobre a variabilidade natural de vazões : o caso do rio Paraná em Porto Primavera. v. 20, p. 698–707, 2015.

SANTOS DA SILVA, J. et al. Water levels in the Amazon basin derived from the ERS 2 and ENVISAT radar altimetry missions. **Remote Sensing of Environment**, v. 114, n. 10, p. 2160–2181, 2010.

SANTOS, J. O. S.; NELSON, B. W.; GIOVANNINI, C. A. Corpos de areia sob leitos abandonados de grandes rios. **Ciência Hoje**, v. 16, n. 93, p. 22–25, 1993.

SANTOS, L. B. L. et al. An RS-GIS-Based ComprehensiveImpact Assessment of Floods—A Case Study in Madeira River, Western Brazilian Amazon. **IEEE Geoscience and Remote Sensing Letters**, v. 14, n. 9, p. 1614–1617, set. 2017.

SANTOS, M. J. et al. Seasonal Flooding Causes Intensification of the River Breeze in the Central Amazon. **Journal of Geophysical Research: Atmospheres**, v. 124, n. 10, p. 5178–5197, 27 maio 2019.

SAUNOIS, M. et al. The Global Methane Budget 2000–2017. **Earth System Science Data**, v. 12, n. 3, p. 1561–1623, 15 jul. 2020.

SAVAGE, JAMES; PIANOSI, FRANCESCA; BATES, PAUL; FREER, JIM; WAGENER, T. Quantifying the importance of spatial resolution and other factors through global sensitivity analysis of a flood inundation model. **Water Resources Research**, v. 52, n. 11, p. 9146–9163, 2016.

SAVAGE, J. T. S. et al. When does spatial resolution become spurious in probabilistic flood inundation predictions? **Hydrological Processes**, v. 30, n. 13, p. 2014–2032, 30 jun. 2016.

SCHAEFER, H. et al. A 21st-century shift from fossil-fuel to biogenic methane emissions indicated by 13CH4. **Science**, v. 352, n. 6281, p. 80–84, 1 abr. 2016.

SCHELLEKENS, J. et al. A global water resources ensemble of hydrological models: The eartH2Observe Tier-1 dataset. **Earth System Science Data**, 2017.

SCHIETTI, J. et al. Vertical distance from drainage drives floristic composition changes in an Amazonian rainforest. **Plant Ecology and Diversity**, v. 7, n. 1–2, p. 241–253, 2014.

SCHMITT QUEDI, E.; MAINARDI FAN, F. Sub seasonal streamflow forecast assessment at large-scale basins. **Journal of Hydrology**, 2020.

SCHMITT, R. J. P. et al. Planning dam portfolios for low sediment trapping shows limits for sustainable hydropower in the Mekong. **Science Advances**, v. 5, n. 10, p. eaaw2175, 23 out. 2019.

SCHMOCKER-FACKEL, P.; NAEF, F. More frequent flooding? Changes in flood frequency in Switzerland since 1850. **Journal of Hydrology**, v. 381, n. 1–2, p. 1–8, fev. 2010.

SCHOBER, B.; HAUER, C.; HABERSACK, H. A novel assessment of the role of Danube floodplains in flood hazard reduction (FEM method). **Natural Hazards**, v. 75, n. 1, p. 33–50, 2014.

SCHÖNGART, J. et al. Phenology and stem-growth periodicity of tree species in Amazonian floodplain forests. **Journal of Tropical Ecology**, v. 18, n. 4, p. 581–597, 12 jul. 2002.

SCHÖNGART, J. et al. The shadow of the Balbina dam: A synthesis of over 35 years of downstream impacts on floodplain forests in Central Amazonia. **Aquatic Conservation: Marine and Freshwater Ecosystems**, v. 31, n. 5, p. 1117–1135, 15 maio 2021.

SCHÖNGART, J.; JUNK, W. J. Forecasting the flood-pulse in Central Amazonia by ENSO-indices. **Journal of Hydrology**, v. 335, n. 1–2, p. 124–132, 2007.

SCHOR, T.; AZENHA, G. S. Ribeirinho Food Regimes, Socioeconomic Inclusion and Unsustainable Development of the Amazonian Floodplain. **EchoGéo**, n. 41, p. 0–14, 2017.

SCHOR, T.; AZENHA, G. S.; BARTOLI, E. Contemporary urbanization in the Brazilian Amazon: food markets, multisited households and ribeirinho livelihoods. **Confins**, v. 35, n. 37, p. 0–22, 24 set. 2018.

SCHRAPFFER, A. et al. Benefits of representing floodplains in a Land Surface Model: Pantanal simulated with ORCHIDEE CMIP6 version. **Climate Dynamics**, n. 0123456789, 13 jun. 2020.

SCHROEDER, R. et al. Development and Evaluation of a Multi-Year Fractional Surface Water Data Set Derived from Active / Passive Microwave Remote Sensing Data. p. 16688–16732, 2015.

SCHRÖTER, K. et al. How useful are complex flood damage models? **Water Resources Research**, v. 50, n. 4, p. 3378–3395, abr. 2014.

SCHRÖTER, K. et al. What made the June 2013 flood in Germany an exceptional event? A hydro-meteorological evaluation. **Hydrology and Earth System Sciences**, v. 19, n. 1, p. 309–327, 16 jan. 2015.

SCHUMANN, G. et al. Evaluating uncertain flood inundation predictions with uncertain remotely sensed water stages. **International Journal of River Basin Management**, v. 6, n. 3, p. 187–199, 2008.

SCHUMANN, G. et al. Progress in integration of remote sensing derived flood extent and stage data and hydraulic models. **Reviews of Geophysics**, v. 47, n. 2008, p. 1–20, 2009.

SCHUMANN, G. J. P. et al. Rethinking flood hazard at the global scale. **Geophysical Research Letters**, v. 43, n. 19, p. 10,249-10,256, 2016a.

SCHUMANN, G. J. P. et al. Unlocking the full potential of Earth observation during the 2015 Texas flood disaster. **Water Resources Research**, v. 52, n. 5, p. 3288–3293, 2016b.

SCHUMANN, G. J. P. et al. Assisting flood disaster response with earth observation data and products: A critical assessment. **Remote Sensing**, v. 10, n. 8, p. 1–19, 2018.

SCHUMANN, G. J. P.; MOLLER, D. K. Microwave remote sensing of flood inundation. **Physics and Chemistry of the Earth**, v. 83–84, p. 84–95, 2015.

SCHUMANN, J.-P. et al. A first large scale flood inundation forecasting model. **Water Resour. Res**, v. 49, p. 6248–6257, 2013.

SCHUTZ, B. E. et al. **Overview of the ICESat missionGeophysical Research Letters**, 2005.

SCOTT, A. D. A.; JONES, T. Classification and Inventory of Wetlands : A Global Overview Reviewed work (s): Classification and inventory of wetlands : A global overview. **Vegetatio**, v. 118, n. 1, p. 3–16, 2012.

SDS (DEVELOPMENT, S. OF S. FOR THE E. AND S. **Levantamento Aerofotogramétrico do Estado de Santa Catarina**. Florianópolis, Brazil.: [s.n.]. Disponível em: <http://sigsc.sds.sc.gov.br/download/index.jsp>.

SEMERTZIDIS, T.; SPATARU, C.; BLEISCHWITZ, R. The Nexus: Estimation of Water Consumption for Hydropower in Brazil. **Journal of Sustainable Development of Energy, Water and Environment Systems**, v. 7, n. 1, p. 122–138, mar. 2019.

SEYLER, F. et al. Inundation risk in large tropical basins and potential survey from radar altimetry: Example in the Amazon Basin. **Marine Geodesy**, 2009a.

SEYLER, F. et al. Watershed delineation for the Amazon sub-basin system using GTOPO30 DEM and a drainage network extracted from JERS SAR images. **Hydrological Processes**, v. 23, n. 22, p. 3173–3185, 30 out. 2009b.

SHARMA, A.; WASKO, C.; LETTENMAIER, D. P. If Precipitation Extremes Are Increasing, Why Aren't Floods? **Water Resources Research**, v. 54, n. 11, p. 8545–8551, 16 nov. 2018.

SHEFFIELD, J. et al. Satellite Remote Sensing for Water Resources Management: Potential for Supporting Sustainable Development in Data-Poor Regions. **Water Resources Research**, v. 54, n. 12, p. 9724–9758, dez. 2018.

SHERMAN, M. et al. Food system vulnerability amidst the extreme 2010–2011 flooding in the Peruvian Amazon: a case study from the Ucayali region. **Food Security**, v. 8, n. 3, p. 551–570, 2016.

SHIN, S. et al. High Resolution Modeling of River-Floodplain-Reservoir Inundation Dynamics in the Mekong River Basin. **Water Resources Research**, v. 56, n. 5, 29 maio 2020.

SHIN, S.; POKHREL, Y.; MIGUEZ-MACHO, G. High-Resolution Modeling of Reservoir Release and Storage Dynamics at the Continental Scale. **Water Resources Research**, v. 55, n. 1, p. 787–810, 30 jan. 2019.

SHUTTLEWORTH, W. J. **Terrestrial Hydrometeorology**. 1º Ed ed. [s.l: s.n.].

SIDDIQUE-E-AKBOR, A. H. M. et al. Inter-comparison study of water level estimates derived from hydrodynamic-hydrologic model and satellite altimetry for a complex deltaic environment. **Remote Sensing of Environment**, v. 115, n. 6, p. 1522–1531, 2011.

SILVA, A. T.; NAGHETTINI, M.; PORTELA, M. M. On some aspects of peaks-over-threshold modeling of floods under nonstationarity using climate covariates. **Stochastic Environmental Research and Risk Assessment**, v. 30, n. 1, p. 207–224, 2016.

SILVA, M. V. et al. Relationships between pacific and atlantic ocean sea surface temperatures and water levels from satellite altimetry data in the Amazon rivers. **RBRH**, v. 23, 19 jul. 2018.

SILVA, T. S. F.; MELACK, J. M.; NOVO, E. M. L. M. Responses of aquatic macrophyte cover and productivity to flooding variability on the Amazon floodplain. **Global Change Biology**, v. 19, n. 11, p. n/a-n/a, set. 2013.

SIMONIT, S.; CATTANEO, F.; PERRINGS, C. Modelling the hydrological externalities of agriculture in wetlands: The case of rice in Esteros del Iberà, Argentina. **Ecological Modelling**, v. 186, n. 1 SPEC. ISS., p. 123–141, 2005.

SIPPEL, S. J. et al. Passive microwave observations of inundation area and the area/stage relation in the amazon river floodplain. **International Journal of Remote Sensing**, v. 19, n. 16, p. 3055–3074, 1998.

SIQUEIRA, V. et al. IPH-Hydro Tools: uma ferramenta open source para determinação de informações topológicas em bacias hidrográficas integrada a um ambiente SIG. **Revista Brasileira de Recursos Hídricos**, v. 21, n. 1, p. 274–287, 2016.

SIQUEIRA, V. et al. Continental Hydrological modeling in South America: Recent Advances and Perspectives. In: SILVA, R. C. V.; TUCCI, C. E. M.; SCOTT, C. A. (Eds.). . **Water and Climate - Modeling in large basins 5**. 1. ed. Porto Alegre: ABRHidro, 2020.

SIQUEIRA, V. A. et al. IPH-Hydro Tools: a GIS coupled tool for watershed topology acquisition in an open-source environment. **Revista Brasileira de Recursos Hídricos**, v. 21, n. 1, p. 274–287, 2016.

SIQUEIRA, V. A. et al. Toward continental hydrologic–hydrodynamic modeling in South America. **Hydrology and Earth System Sciences**, v. 22, n. 9, p. 4815–4842, 18 set. 2018.

SIVAPALAN, M. From engineering hydrology to Earth system science: milestones in the transformation of hydrologic science. **Hydrology and Earth System Sciences**, v. 22, n. 3, p. 1665–1693, 7 mar. 2018.

SMITH, A. M. et al. Modeling and Mapping of Global Flood Hazard Layers. In: **Global Flood Hazard: Applications in Modeling, Mapping, and Forecasting**. [s.l: s.n.]. p. 133–155.

SMITH, A.; SAMPSON, C.; BATES, P. Regional flood frequency analysis at the global scale. **Water Resour.Res.**, v. 51, p. 539–553, 2015.

SMITH, E. A. et al. International global precipitation measurement (GPM) program and mission: An overview. In: **Advances in Global Change Research**. [s.l: s.n.].

SOLANDER, K. C. et al. Simulating human water regulation: The development of an optimal complexity, climate-adaptive reservoir management model for an LSM. **Journal of Hydrometeorology**, v. 17, n. 3, p. 725–744, 2016.

SORRIBAS, M. V. et al. Projections of climate change effects on discharge and inundation in the Amazon basin. p. 555–570, 2016.

SORRIBAS, M. V. et al. Hydrological Tracking Model for Amazon Surface Waters. **Water Resources Research**, v. 56, n. 9, 2020.

SOUZA, C. M. et al. Long-term annual surface water change in the Brazilian Amazon Biome: Potential links with deforestation, infrastructure development and climate change. **Water (Switzerland)**, v. 11, n. 3, p. 566, 19 mar. 2019.

SPECKHANN, G. A. et al. Flood hazard mapping in Southern Brazil: a combination of flow frequency analysis and the HAND model. **Hydrological Sciences Journal**, v. 63, n. 1, p. 87–100, 2018.

STEFFEN, P. C.; GOMES, J. Clustering of historical floods observed on Iguaçu River, in União da Vitória, Paraná. **RBRH**, v. 23, n. 0, 27 ago. 2018.

SUN, Z. et al. Evapotranspiration estimation based on the SEBAL model in the Nansi Lake Wetland of China. **Mathematical and Computer Modelling**, v. 54, n. 3–4, p.

1086–1092, ago. 2011.

SUTANUDJAJA, E. H. et al. PCR-GLOBWB 2: a 5arcmin global hydrological and water resources model. **Geoscientific Model Development**, v. 11, n. 6, p. 2429–2453, 20 jun. 2018.

SUTCLIFFE, J. V.; PARKS, Y. P. Comparative water balances of selected African wetlands. **Hydrological Sciences Journal**, 1989.

SZLAFSZTEIN, C. F. Development projects for small rural communities in the Brazilian Amazon region as potential strategies and practices of climate change adaptation. **Mitigation and Adaptation Strategies for Global Change**, v. 19, n. 2, p. 143–160, 2014.

SZLAFSZTEIN, C. F. Management of natural disasters in the Brazilian Amazon region. **Natural Hazards**, v. 76, n. 3, p. 1745–1757, 2015.

SZPILMAN, A. et al. **Vertedouro de Itaipu: operação e desempenho após 10 anos de funcionamento**. Anais do XX Seminário Nacional de Grandes Barragens. **Anais**...Curitiba: Comitê Brasileiro de Barragens, 1992Disponível em: <http://www.cbdb.org.br/>

TANAKA, T. et al. Impact assessment of upstream flooding on extreme flood frequency analysis by incorporating a flood-inundation model for flood risk assessment. **Journal of Hydrology**, v. 554, p. 370–382, 2017.

TANAKA, T. et al. An Integrated Hydrological-Hydraulic Model for Simulating Surface Water Flows of a Shallow Lake Surrounded by Large Floodplains. **Water**, v. 10, n. 9, p. 1213, 7 set. 2018.

TANG, T.; LI, W.; SUN, G. Impact of two different types of El Niño events on runoff over the conterminous United States. **Hydrology and Earth System Sciences**, v. 20, n. 1, p. 27–37, 15 jan. 2016.

TAPLEY, B. D. et al. GRACE measurements of mass variability in the Earth system. **Science**, 2004a.

TAPLEY, B. D. et al. The gravity recovery and climate experiment: Mission overview and early results. **Geophysical Research Letters**, v. 31, n. 9, p. 1–4, 2004b.

TARRAS-WAHLBERG, N. H.; CAUDWELL, S. W. B.; LANE, S. N. El Niño events, rainfall patterns and floods in the Puyango River Basin, southern Ecuador. **Brazilian Journal of Meteorology**, v. 21, n. 2, p. 201–210, 2006.

TASUMI, M.; ALLEN, R. G.; TREZZA, R. At-Surface Reflectance and Albedo from Satellite for Operational Calculation of Land Surface Energy Balance. **Journal of Hydrologic Engineering**, v. 13, n. 2, p. 51–63, fev. 2008.

TAYEFI, V. et al. A comparison of one- and two-dimensional approaches to modelling flood inundation over complex upland floodplains. **Hydrological Processes**, 2007.

TAYLOR, C. M. Feedbacks on convection from an African wetland. **Geophysical Research Letters**, v. 37, n. 5, 2010.

TAYLOR, C. M.; PRIGENT, C.; DADSON, S. J. Mesoscale rainfall patterns observed around wetlands in sub-Saharan Africa. **Quarterly Journal of the Royal Meteorological Society**, v. 144, n. 716, p. 2118–2132, out. 2018.

TEIXEIRA, A. et al. Use of MODIS Images to Quantify the Radiation and Energy Balances in the Brazilian Pantanal. **Remote Sensing**, v. 7, n. 11, p. 14597–14619, 4 nov. 2015.

THIEKEN, A. H.; APEL, H.; MERZ, B. Assessing the probability of large-scale flood loss events: a case study for the river Rhine, Germany. **Journal of Flood Risk Management**, v. 8, n. 3, p. 247–262, set. 2015.

THORSLUND, J. et al. Wetlands as large-scale nature-based solutions: Status and challenges for research, engineering and management. **Ecological Engineering**, v. 108, p. 489–497, 2017.

TODINI, E. **A keynote to understand the predictive uncertainty in flood forecasting**. Disponível em: <https://www.preventionweb.net/news/view/59445>. Acesso em: 25 set. 2018.

TOMASELLA, J. et al. The droughts of 1997 and 2005 in Amazonia: Floodplain hydrology and its potential ecological and human impacts. **Climatic Change**, v. 116, n. 3–4, p. 723–746, 2013.

TOOTCHI, A.; JOST, A. Multi-source global wetland maps combining surface water imagery and groundwater constraints. n. August, 2018.

TOURIAN, M. J. et al. Estimating river depth from SWOT-type observables obtained by satellite altimetry and imagery. **Water (Switzerland)**, v. 9, n. 10, 2017.

TOWNER, J. et al. Assessing the performance of global hydrological models for capturing peak river flows in the Amazon basin. **Hydrology and Earth System Sciences**, 2019.

TRIGG, M. A. et al. Amazon flood wave hydraulics. **Journal of Hydrology**, v. 374, n. 1–2, p. 92–105, jul. 2009.

TRIGG, M. A. et al. Floodplain channel morphology and networks of the middle Amazon River. **Water Resources Research**, v. 48, n. 10, p. 1–17, out. 2012.

TRIGG, M. A. et al. Surface water connectivity dynamics of a large scale extreme flood. **Journal of Hydrology**, v. 505, p. 138–149, 2013.

TRIGG, M. A. et al. The credibility challenge for global fluvial flood risk analysis. **Environmental Research Letters**, v. 11, n. 9, p. 094014, 1 set. 2016.

TSHIMANGA, R. M.; HUGHES, D. A. Basin-scale performance of a semidistributed rainfall-runoff model for hydrological predictions and water resources assessment of large rivers: The Congo River. **Water Resources Research**, v. 50, n. 2, p. 1174–1188, 2014.

TUCCI, C. E. M. et al. Brasil. In: TUCCI, C. E. M.; BERTONI, J. C. (Eds.). . **Inundaçoes e drenagem urbana nos paises da America do Sul**. 1st. ed. Porto Alegre: ABRH, 2003. p. 275–324.

TUCCI, C. E. M.; BERTONI, J. C. **Inundações urbanas na América do Sul**. Porto Alegre: [s.n.].

TUCCI, C. E. M.; CLARKE, R. T. Environmental issues in the la Plata Basin. **International Journal of Water Resources Development**, 1998.

TUOZZOLO, S. et al. The impact of reach averaging Manning's equation for an in-situ dataset of water surface elevation, width, and slope. **Journal of Hydrology**, jul. 2019.

TURNER, S. W. D.; DOERING, K.; VOISIN, N. Data-Driven Reservoir Simulation in a Large-Scale Hydrological and Water Resource Model. **Water Resources Research**, v. 56, n. 10, 2020.

UNEP-WCMC; IUCN. **Protected Planet: The World Database on Protected Areas (WDPA) and World Database on Other Effective Area-based Conservation Measures (WD-OECM)**. Disponível em: <www.protectedplanet.net>. Acesso em: 26 jul. 2021.

USACE. **HEC-RAS River Analysis System Hydraulic Reference Manual**. [s.l: s.n.].

USACE, U. S. A. C. OF E. **HEC-RAS River Analysis System: Hydraulic Reference Manual, Version 4.1,**. Davis, CA.: [s.n.].

VALENTE, C. R.; LATRUBESSE, E. M.; FERREIRA, L. G. Relationships among vegetation, geomorphology and hydrology in the Bananal Island tropical wetlands, Araguaia River basin, Central Brazil. **Journal of South American Earth Sciences**, v. 46, p. 150–160, 2013.

VAN BEEK, L. P. H.; WADA, Y.; BIERKENS, M. F. P. Global monthly water stress: 1. Water balance and water availability. **Water Resources Research**, v. 47, n. 7, jul. 2011.

VAN DEN HOEK, J. et al. Monitoring Reservoir Drought Dynamics with Landsat and Radar/Lidar Altimetry Time Series in Persistently Cloudy Eastern Brazil. **Remote Sensing**, v. 11, n. 7, p. 827, 6 abr. 2019.

VAN DIJK, A. I. J. M. et al. Global 5 km resolution estimates of secondary evaporation including irrigation through satellite data assimilation. **Hydrology and Earth System Sciences**, v. 22, n. 9, p. 4959–4980, 27 set. 2018.

VEIJALAINEN, N. et al. National scale assessment of climate change impacts on flooding in Finland. **Journal of Hydrology**, v. 391, n. 3–4, p. 333–350, 2010.

VIGLIONE, A. et al. Insights from socio-hydrology modelling on dealing with flood risk – Roles of collective memory, risk-taking attitude and trust. **Journal of Hydrology**, v. 518, n. PA, p. 71–82, out. 2014.

VISHWAKARMA, B. D. et al. Re-assessing global water storage trends from GRACE time series. **Environmental Research Letters**, v. 16, n. 3, p. 034005, 2021.

VOISIN, N. et al. On an improved sub-regional water resources management representation for integration into earth system models. **Hydrology and Earth System Sciences**, v. 17, n. 9, p. 3605–3622, 30 set. 2013.

VOISIN, N. et al. Effects of spatially distributed sectoral water management on the redistribution of water resources in an integrated water model. **Water Resources Research**, v. 53, n. 5, p. 4253–4270, maio 2017.

VON LANY, P. H. et al. Integrated flood risk management in the Río de La Plata Basin within Argentina. In: PARKER, D. J. (Ed.). . **Floods**. 1. ed. London: Routledge, 2000. p. 31.

VON RANDOW, R. DE C. S. et al. Evapotranspiration and gross primary productivity of secondary vegetation in Amazonia inferred by eddy covariance. **Agricultural and Forest Meteorology**, v. 294, n. September 2019, p. 108141, 2020.

VOROGUSHYN, S. et al. Evolutionary leap in large-scale flood risk assessment needed. **Wiley Interdisciplinary Reviews: Water**, v. 5, n. 2, p. e1266, mar. 2018.

VÖRÖSMARTY, C. J. et al. Extreme rainfall, vulnerability and risk: a continental-scale assessment for South America. **Philosophical Transactions of the Royal Society A: Mathematical, Physical and Engineering Sciences**, v. 371, n. 2002, p. 20120408, 13 nov. 2013.

WADA, Y.; DE GRAAF, I. E. M.; VAN BEEK, L. P. H. High-resolution modeling of human and climate impacts on global water resources. **Journal of Advances in Modeling Earth Systems**, v. 8, n. 2, p. 735–763, jun. 2016.

WANG, G. et al. Continued increase of extreme El Ninõ frequency long after 1.5 C warming stabilization. **Nature Climate Change**, v. 7, n. 8, p. 568–572, 2017a.

WANG, W. et al. Nonlinear Filtering Effects of Reservoirs on Flood Frequency Curves at the Regional Scale. **Water Resources Research**, v. 53, n. 10, p. 8277–8292, out. 2017b.

WANG, X. Y. et al. The strengthening of Amazonian precipitation during the wet season driven by tropical sea surface temperature forcing. **Environmental Research Letters**, v. 13, n. 9, 2018.

WARD, N. D. et al. Where Carbon Goes When Water Flows: Carbon Cycling across the Aquatic Continuum. **Frontiers in Marine Science**, v. 4, n. January, p. 1–27, 2017.

WARD, P. J. et al. Annual flood sensitivities to El Niño–Southern Oscillation at the global scale. **Hydrology and Earth System Sciences**, v. 18, n. 1, p. 47–66, 6 jan. 2014.

WARD, P. J. et al. Usefulness and limitations of global flood risk models. **Nature Climate Change**, v. 5, n. 8, p. 712–715, 24 ago. 2015.

WARD, P. J. et al. The Need for Mapping, Modeling, and Predicting Flood Hazard and Risk at the Global Scale. In: **Global Flood Hazard: Applications in Modeling, Mapping, and Forecasting**. [s.l: s.n.]. p. 1–15.

WATERS, R. et al. **SEBAL, Surface Energy Balance Algorithms for Land. Advance Training and Users Manual. Idaho: a NASA EOSDIS/Synergy grant from the Raytheon Company University of Idaho.** [s.l: s.n.]. Disponível em: <http://www.posmet.ufv.br/wp-content/uploads/2016/09/MET-479-Waters-et-al-SEBAL.pdf>.

WAYLEN, P. R.; CAVIEDES, C. N. El Niño and annual floods on the north Peruvian littoral. **Journal of Hydrology**, v. 89, n. 1–2, p. 141–156, dez. 1986.

WCS; CIESIN. **Last of the Wild Project, Version 2, 2005 (LWP-2): Global Human Footprint Dataset (Geographic)**. Disponível em: <https://doi.org/10.7927/H4M61H5F>. Acesso em: 19 jul. 2021.

WETLANDSINTERNATIONAL. **Programa Corredor Azul**. [s.l: s.n.]. Disponível em: <https://lac.wetlands.org/caso/programa-corredor-azul-conectando-gente-naturaleza-economias-lo-largo-del-sistema-humedales-parana-paraguay/>.

WETTER, O. The potential of historical hydrology in Switzerland. **Hydrology and Earth System Sciences**, v. 21, n. 11, p. 5781–5803, 2017.

WHALEN, S. C. Biogeochemistry of Methane Exchange between Natural Wetlands and the Atmosphere. **Environmental Engineering Science**, 2005.

WILLIAMSON, C. E. et al. Lakes and reservoirs as sentinels, integrators, and regulators of climate change. **Limnology and Oceanography**, v. 54, n. 6part2, p. 2273–2282, nov. 2009.

WILSON, C. et al. Large and increasing methane emissions from Eastern Amazonia derived from satellite data, 2010–2018. **Atmospheric Chemistry and Physics Discussions**, n. November, p. 1–38, 2020.

WILSON, M. D. et al. Modeling large-scale inundation of Amazonian seasonally flooded wetlands. **Geophysical Research Letters**, v. 34, n. 15, p. 4–9, 2007.

WING, O. E. J. et al. Validation of a 30 m resolution flood hazard model of the conterminous United States. **Water Resources Research**, v. 53, n. 9, p. 7968–7986, 2017.

WINSEMIUS, H. C. et al. A framework for global river flood risk assessments. **Hydrology and Earth System Sciences**, v. 17, n. 5, p. 1871–1892, 2013.

WINSEMIUS, H. C. et al. Global drivers of future river flood risk. **Nature Climate Change**, v. 6, n. 4, p. 381–385, 2016.

WISSER, D. et al. Reconstructing 20th century global hydrography: a contribution to the Global Terrestrial Network- Hydrology (GTN-H). **Hydrology and Earth System Sciences**, v. 14, n. 1, p. 1–24, 6 jan. 2010.

WITTMANN, F., SCHÖNGART, J., BRITO, J. M., OLIVEIRA-WITTMANN, A., PAROLIN, P., PIEDADE, M. T. F., & GUILLAUMET, J. L. **Manual of tree species from Central Amazonian white-water floodplains: Taxonomy, Ecology and Use**. Manaus: INPA, UEA, IDSM, 2010.

WITTMANN, F. et al. Implementation of the Ramsar Convention on South American wetlands: an update. **Research and Reports in Biodiversity Studies**, n. November, p. 47, 2015.

WITTMANN, F.; HOUSEHOLDER, E. Why Rivers Make the Difference: A Review on the Phytogeography of Forested Floodplains in the Amazon Basin. In: **Forest structure, function and dynamics in Western Amazonia**. [s.l: s.n.].

WMO. **Manual for Depth-area-duration Analysis of Storm Precipitation: This Publication is a Part of the Contribution of WMO to the International Hydrological Decade**. [s.l: s.n.].

WOLFARTH-COUTO, B.; FILIZOLA, N.; DURIEUX, L. Seasonal pattern of malaria cases and the relationship with hydrologic variability in the Amazonas State, Brazil. **Revista Brasileira de Epidemiologia**, v. 23, n. 016, p. 1–13, 2020.

WONGCHUIG CORREA, S. et al. Multi-decadal Hydrological Retrospective: Case study of Amazon floods and droughts. **Journal of Hydrology**, 2017.

WONGCHUIG, S. C. et al. Hydrological reanalysis across the 20th century: A case study of the Amazon Basin. **Journal of Hydrology**, v. 570, p. 755–773, mar. 2019.

WOOD, E. F. et al. Hyperresolution global land surface modeling: meeting a grand challenge for monitoring Earth's terrestrial water. **Water Resources Research**, v. 47, n. 5, p. 1–10, maio 2011.

WOODWARD, C. et al. The hydrological legacy of deforestation on global wetlands. **Science**, v. 346, n. 6211, p. 844–847, 14 nov. 2014.

WOODWARD, R. T.; WUI, Y.-S. The economic value of wetland services: a meta-analysis. **Ecological Economics**, v. 37, n. 2, p. 257–270, maio 2001.

WU, C.-L.; SHUKLA, S.; SHRESTHA, N. K. Evapotranspiration from drained wetlands with different hydrologic regimes: Drivers, modeling, and storage functions. **Journal of Hydrology**, v. 538, p. 416–428, jul. 2016.

WU, J. et al. The Reliability of Global Remote Sensing Evapotranspiration Products over Amazon. **Remote Sensing**, v. 12, n. 14, p. 2211, 10 jul. 2020a.

WU, Y. et al. On how wetlands can provide flood resilience in a large river basin: A case study in Nenjiang River Basin, China. **Journal of Hydrology**, p. 125012, abr. 2020b.

WU, Y.; CHEN, J. An Operation-Based Scheme for a Multiyear and Multipurpose Reservoir to Enhance Macroscale Hydrologic Models. **Journal of Hydrometeorology**, v. 13, n. 1, p. 270–283, fev. 2012.

WWF. **Living planet report 2016: Risk and resilience in a new era**. [s.l: s.n.].

XAVIER, A. C.; KING, C. W.; SCANLON, B. R. Daily gridded meteorological variables in Brazil (1980–2013). **International Journal of Climatology**, 2016.

XAVIER, A. C.; KING, C. W.; SCANLON, B. R. **An update of Xavier, King and Scanlon (2016) daily precipitation gridded data set for the Brazil**. Anais do XVIII Simposio Brasileiro de Sensoriamento Remoto. **Anais**...Santos: INPE, 2017

XI, Y. et al. Future impacts of climate change on inland Ramsar wetlands. **Nature Climate Change**, 2 nov. 2020.

YAMAZAKI, D. et al. A physically based description of floodplain inundation dynamics in a global river routing model. **Water Resources Research**, v. 47, n. 4, p. 1–21, 2011.

YAMAZAKI, D. et al. Analysis of the water level dynamics simulated by a global river model: A case study in the Amazon River. **Water Resources Research**, v. 48, n. 9, p. 1–15, 2012.

YAMAZAKI, D. et al. Development of the Global Width Database for Large Rivers. **Water Resources Research**, v. 50, n. 4, p. 3467–3480, abr. 2014a.

YAMAZAKI, D. et al. Regional flood dynamics in a bifurcating mega delta simulated in a global river model. **Geophysical Research Letters**, v. 41, n. 9, p. 3127–3135, 16 maio 2014b.

YAMAZAKI, D. et al. A high-accuracy map of global terrain elevations. **Geophysical Research Letters**, 2017.

YAMAZAKI, D.; DE ALMEIDA, G. A. M.; BATES, P. D. Improving computational efficiency in global river models by implementing the local inertial flow equation and a vector-based river network map. **Water Resources Research**, v. 49, n. 11, p. 7221–7235, nov. 2013.

YAMAZAKI, D.; TRIGG, M. A.; IKESHIMA, D. Development of a global ~90m water body map using multi-temporal Landsat images. **Remote Sensing of Environment**, 2015.

YAN, K. et al. A review of low-cost space-borne data for flood modelling: topography, flood extent and water level. **Hydrological Processes**, v. 29, n. 15, p. 3368–3387, 2015.

YANG, Y.; SHANG, S.; JIANG, L. Remote sensing temporal and spatial patterns of evapotranspiration and the responses to water management in a large irrigation district of North China. **Agricultural and Forest Meteorology**, v. 164, p. 112–122, 2012.

YAO, F. et al. Constructing long-term high-frequency time series of global lake and reservoir areas using Landsat imagery. **Remote Sensing of Environment**, v. 232, p. 111210, out. 2019.

YASSIN, F. et al. Representation and improved parameterization of reservoir operation in hydrological and land-surface models. **Hydrology and Earth System Sciences**, v. 23, n. 9, p. 3735–3764, 2019.

YIGZAW, W. et al. A New Global Storage-Area-Depth Dataset for Modeling Reservoirs in Land Surface and Earth System Models. **Water Resources Research**, 11 out. 2018.

YIGZAW, W. et al. A Multilayer Reservoir Thermal Stratification Module for Earth System Models. **Journal of Advances in Modeling Earth Systems**, v. 11, n. 10, p. 3265–3283, 2019.

YILMAZ, M. T. et al. Comparison of prognostic and diagnostic surface flux modeling approaches over the Nile River basin. **Water Resources Research**, v. 50, n. 1, p. 386–408, jan. 2014.

YOON, J. H.; ZENG, N. An Atlantic influence on Amazon rainfall. **Climate Dynamics**, v. 34, n. 2, p. 249–264, 2010.

YOON, Y. et al. Estimating river bathymetry from data assimilation of synthetic SWOT

measurements. **Journal of Hydrology**, 2012.

YOON, Y. et al. Improved error estimates of a discharge algorithm for remotely sensed river measurements: Test cases on Sacramento and Garonne Rivers. **Water Resources Research**, 2016a.

YOON, Y. et al. Estimating Flood Discharges in Reservoir-Regulated River Basins by Integrating Synthetic SWOT Satellite Observations and Hydrologic Modeling. **Journal of Hydrologic Engineering**, v. 21, n. 4, p. 05015030, 2016b.

YOON, Y.; BEIGHLEY, E. Simulating streamflow on regulated rivers using characteristic reservoir storage patterns derived from synthetic remote sensing data. **Hydrological Processes**, v. 29, n. 8, p. 2014–2026, 2015.

YOU, J.-Y.; CAI, X. Hedging rule for reservoir operations: 1. A theoretical analysis. **Water Resources Research**, v. 44, n. 1, p. 1–9, jan. 2008.

YU, W. et al. Storing water: A new integrated approach for resilient development About GWP. 2021.

YUAN, T. et al. Absolute water storages in the Congo River floodplains from integration of InSAR and satellite radar altimetry. **Remote Sensing of Environment**, v. 201, n. March, p. 57–72, 2017.

YUAN, W. et al. Increased atmospheric vapor pressure deficit reduces global vegetation growth. **Science Advances**, v. 5, n. 8, p. 1–13, 2019.

ZAJAC, Z. et al. The impact of lake and reservoir parameterization on global streamflow simulation. **Journal of Hydrology**, v. 548, p. 552–568, 2017.

ZAMBON, R.; BARROS, M. T. L.; YEH, W. W. G. **Evaporation Losses in the Brazilian Hydropower System**. World Environmental and Water Resources Congress. **Anais**...2018Disponível em: <https://earthexplorer.usgs.gov/>

ZARFL, C. et al. A global boom in hydropower dam construction. **Aquatic Sciences**, 2014.

ZEMP, D. C. et al. Self-amplified Amazon forest loss due to vegetation-atmosphere feedbacks. **Nature Communications**, v. 8, p. 1–10, 2017.

ZHANG, L. et al. Stream flow simulation and verification in ungauged zones by coupling hydrological and hydrodynamic models: a case study of the Poyang Lake ungauged zone. **Hydrology and Earth System Sciences**, v. 21, n. 11, p. 5847–5861, 24 nov. 2017a.

ZHANG, Q. et al. More frequent flooding? Changes in flood frequency in Pearl River. **Hydrology and Earth System Sciences**, v. 22, p. 2637–2653, 2018.

ZHANG, Z. et al. Emerging role of wetland methane emissions in driving 21st century climate change. **Proceedings of the National Academy of Sciences of the United States of America**, v. 114, n. 36, p. 9647–9652, 2017b.

ZHANG, Z. et al. Development and evaluation of the global Wetland Area and Dynamics for Methane Modeling dataset (WAD2M). **Earth System Science Data**, v. in

review, n. December, p. 1–50, 2020.

ZHAO, F. et al. The critical role of the routing scheme in simulating peak river discharge in global hydrological models. **Environmental Research Letters**, v. 12, n. 7, p. 075003, 1 jul. 2017.

ZHAO, G. et al. Advances in Water Resources Integrating a reservoir regulation scheme into a spatially distributed hydrological model R. **Elsevier**, v. 98, p. 16–31, 2016.

ZHAO, G.; BATES, P.; NEAL, J. The Impact of Dams on Design Floods in the Conterminous US. **Water Resources Research**, v. 56, n. 3, p. 1–15, mar. 2020.

ZHOU, H. et al. Characterizing drought and flood events over the Yangtze River Basin using the HUST-Grace2016 solution and ancillary data. **Remote Sensing**, v. 9, n. 11, 2017.

ZHOU, X.; PRIGENT, C.; YAMAZAKI, D. Toward improved comparisons between land-surface-water-area estimates from a global river model and satellite observations. **Water Resources Research**, v. 57, n. 5, p. e2020WR029256, 2021.

ZUBIETA, R. et al. Impacts of satellite-based precipitation datasets on rainfall-runoff modeling of the Western Amazon basin of Peru and Ecuador. **Journal of Hydrology**, v. 528, p. 599–612, 2015.

ZUBIETA, R. et al. Hydrological modeling of the Peruvian-Ecuadorian Amazon Basin using GPM-IMERG satellite-based precipitation dataset. **Hydrology and Earth System Sciences**, v. 21, n. 7, p. 3543–3555, 2017.

ZUBIETA, R. et al. Assessing precipitation concentration in the Amazon basin from different satellite-based data sets. **International Journal of Climatology**, v. 39, n. 7, p. 3171–3187, 2019.

ZULKAFLI, Z. et al. Projected increases in the annual flood pulse of the Western Amazon. **Environmental Research Letters**, v. 11, n. 1, 2016.

13 Appendix

13.1 Appendix 1: South American RAMSAR sites

Table 13.1 lists the current South American RAMSAR sites (inland wetlands only). Source: https://www.ramsar.org/.

Table 13.1. South American RAMSAR sites (inland wetlands only).

RAMSAR site number	Site Name	Country	Area (ha)	Latitude	Longitude
1023	Abras de Mantequilla	Ecuador	22500	-1.47	-79.75
2337	Amazon Estuary and its Mangroves	Brazil	3850253	-1.15	-46.80
2296	Anavilhanas National Park	Brazil	350470	-2.47	-60.82
885	Bahía de Samborombón	Argentina	243965	-36.25	-57.25
1020	Baixada Maranhense Environmental Protection Area	Brazil	1775036	-3.00	-44.95
290	Bañados del Este y Franja Costera	Uruguay	407408	-33.80	-53.83
1087	Bañados del Izozog y el río Parapetí	Bolivia (Plurinational State of)	615882	-18.45	-61.82
1176	Bañados del Río Dulce y Laguna de Mar Chiquita	Argentina	996000	-30.38	-62.77
1317	Bofedales y Laguna de Salinas	Peru	17657	-16.37	-71.13
2190	Cabo Orange National Park	Brazil	657328	3.65	-51.19
222	Carlos Anwandter Sanctuary	Chile	4877	-39.68	-73.18
2332	Complejo de Humedales Cuyabeno Lagartococha Yasuní	Ecuador	773668	-0.56	-75.77
2217	Complejo de Humedales de la Estrella Fluvial Inírida (EFI)	Colombia	250159	3.82	-67.86
1174	Complejo de humedales del Abanico del río Pastaza	Peru	3827329	-4.00	-75.42
2336	Complejo de humedales	Colombia	45464	-3.78	-70.54

	Lagos de Tarapoto				
1781	Complejo de Humedales Laguna del Otún	Colombia	6579	4.75	-75.42
1625	Complejo de Humedales Ñucanchi Turupamba	Ecuador	12290	-0.27	-78.15
877	Complejo Lacustre Laguna del Negro Francisco y Laguna Santa Rosa	Chile	62460	-27.45	-69.22
1780	Complejo LLanganati	Ecuador	30355	-1.10	-78.35
1030	Cuenca de Tajzara	Bolivia (Plurinational State of)	5500	-21.78	-65.10
2255	Delta del Paraná	Argentina	243126	-32.27	-60.72
1387	Delta del Río Baudó	Colombia	8888	4.88	-77.37
1089	El Pantanal Boliviano	Bolivia (Plurinational State of)	3189888	-18.00	-58.50
2310	Environmental Protection Area of Cananéia-Iguape-Peruíbe	Brazil	202307	-24.68	-47.60
731	Estero Milagro	Paraguay	25000	-23.57	-57.37
1433	Esteros de Farrapos e Islas del Río Uruguay	Uruguay	17496	-32.88	-58.08
1886	Glaciar Vinciguerra y Turberas Asociadas	Argentina	2760	-54.75	-68.33
2297	Guaporé Biological Reserve	Brazil	600000	-12.52	-62.79
2317	Guaratuba	Brazil	38329	-25.86	-48.70
878	Humedal el Yali	Chile	520	-33.83	-71.63
1785	Humedal Laguna Melincué	Argentina	92000	-33.72	-61.50
1627	Humedal Lucre - Huacarpay	Peru	1979	-13.62	-71.73
1366	Humedales Chaco	Argentina	508000	-27.33	-58.83
624	Ilha do Bananal	Brazil	562312	-10.52	-50.20
2316	Ilha Grande National Park	Brazil	76033	-23.68	-54.00
1112	Jaaukanigás	Argentina	492000	-28.75	-59.25
1028	La Segua	Ecuador	1836	-0.70	-80.20
1991	La Tembladera	Ecuador	1471	-3.50	-80.00
881	Lago Titicaca	Peru	460000	-15.83	-69.50
959	Lago Titicaca	Bolivia (Plurinational State of)	800000	-16.17	-68.87

728	Lago Ypoá	Paraguay	100000	-26.50	-57.55
1181	Lagos Poopó y Uru Uru	Bolivia (Plurinational State of)	967607	-18.77	-67.12
556	Laguna Blanca	Argentina	11250	-39.03	-70.35
1330	Laguna Chaco Lodge	Paraguay	2500	-22.28	-59.30
1175	Laguna Concepción	Bolivia (Plurinational State of)	31124	-17.52	-61.35
1143	Laguna de Cube	Ecuador	113	0.40	-79.65
1047	Laguna de la Cocha	Colombia	39000	1.05	-77.20
759	Laguna de Llancanelo	Argentina	65000	-35.75	-69.13
555	Laguna de los Pozuelos	Argentina	16224	-22.33	-65.98
2236	Laguna de Rocha	Uruguay	10933	-34.63	-54.28
858	Laguna de Tacarigua	Venezuela (Bolivarian Republic of)	9200	10.20	-65.93
1318	Laguna del Indio - Dique de los Españoles	Peru	502	-15.77	-71.05
1390	Laguna Teniente Rojas Silva	Paraguay	8470	-22.63	-59.05
1865	Lagunas altoandinas y puneñas de Catamarca	Argentina	1228175	-26.87	-67.93
1012	Lagunas de Guanacache, Desaguadero y del Bebedero	Argentina	962370	-33.00	-67.60
1040	Lagunas de Vilama	Argentina	157000	-22.60	-66.92
1691	Lagunas Las Arreviatadas	Peru	1250	-5.23	-79.27
1162	Lagunas y Esteros del Iberá	Argentina	24550	-28.52	-57.15
489	Los Lípez	Bolivia (Plurinational State of)	1427717	-22.17	-67.40
2306	Lund Warming	Brazil	23865	-19.50	-43.99
623	Mamirauá	Brazil	1124000	-2.30	-66.03
502	Manglares Churute	Ecuador	35042	-2.47	-79.70
1088	Palmar de las Islas y las Salinas de San José	Bolivia (Plurinational State of)	856754	-19.25	-61.00
1969	Palmar Yatay	Argentina	21450	-31.87	-58.32
602	Pantanal Matogrossense	Brazil	135000	-17.65	-57.42
1909	Parque Andino Juncal	Chile	13796	-32.92	-70.05

1203	Parque Nacional Cajas	Ecuador	29477	-2.83	-79.23
1626	Parque Provincial El Tromen	Argentina	30000	-37.08	-70.10
640	Reentrancias Maranhenses	Brazil	2680911	-1.68	-45.07
956	Reserva Biológica Limoncocha	Ecuador	4613	-0.42	-76.58
754	Reserva Costa Atlantica de Tierra del Fuego	Argentina	28600	-53.33	-68.50
1459	Reserva Ecológica Costanera Sur	Argentina	353	-34.62	-58.35
1292	Reserva Ecológica de Manglares Cayapas-Mataje	Ecuador	44847	1.27	-79.00
2085	Reserva Ecológica El Ángel	Ecuador	17003	0.73	-77.95
882	Reserva Nacional de Junín	Peru	53000	-11.00	-76.13
546	Reserva Nacional Pacaya-Samiria	Peru	2080000	-5.25	-74.67
1750	Reserva Natural Otamendi	Argentina	3000	-34.23	-58.88
2330	Reserva Natural Villavicencio	Argentina	62244	-32.59	-69.02
1864	Reserva Particular del Patrimonio Natural (RPPN) “Fazenda Rio Negro"	Brazil	7000	-19.54	-56.22
1270	Reserva Particular do Patrimonio Natural SESC Pantanal	Brazil	87871	-16.65	-56.25
1238	Reserva Provincial Laguna Brava	Argentina	405000	-28.40	-69.08
2092	Río Blanco	Bolivia (Plurinational State of)	2404916	-13.63	-63.39
1900	Rio Doce State Park	Brazil	35973	-19.68	-42.55
2362	Rio Juruá	Brazil	2136489	-5.16	-67.22
2093	Río Matos	Bolivia (Plurinational State of)	1729788	-14.82	-66.20
2335	Rio Negro	Brazil	12001614	-1.73	-64.09
729	Río Negro	Paraguay	370000	-19.87	-58.57
557	Rio Pilcomayo	Argentina	51889	-25.50	-58.50
2094	Río Yata	Bolivia (Plurinatio	2813229	-12.31	-66.10

		nal State of)			
1870	Salar de aguas Calientes IV	Chile	15529	-24.98	-68.63
1871	Salar de Pujsa	Chile	17397	-23.18	-67.53
873	Salar de Surire	Chile	15858	-18.85	-69.00
875	Salar de Tara	Chile	96439	-22.93	-67.25
874	Salar del Huasco	Chile	6000	-20.30	-68.83
951	Sistema Delta Estuarino del Río Magdalena, Ciénaga Grande de Santa Marta	Colombia	400000	10.75	-74.48
876	Sistema Hidrológico de Soncor del Salar de Atacama	Chile	67133	-23.30	-68.17
1782	Sistema Lacustre de Chingaza	Colombia	4058	4.50	-73.75
2086	Sistema Lacustre Lagunas del Compadre	Ecuador	28115	-4.21	-79.10
2087	Sistema Lacustre Yacuri	Ecuador	27762	-4.64	-79.35
2363	Taiamã Ecological Station	Brazil	11555	-16.86	-57.51
2298	Taim Ecological Station	Brazil	10939	-32.74	-52.60
730	Tifunque	Paraguay	280000	-24.25	-59.50
2295	Viruá National Park	Brazil	216427	1.29	-61.15
503	Zona Marina Parque Nacional Machalilla	Ecuador	14430	-1.00	-80.75

13.2 Appendix 2: Supplementary material of chapters

In this Appendix, the Supplementary materials of each chapter are presented.

13.2.1 Supplementary Material of Chapter 4

This Supplementary Material provides details on the model calibration and parameters. Figure S1a shows the hydrologic response units (HRU's) that the basin was divided into for model calibration, and Figure S1b the basin topography with MERIT DEM. Figure S1c shows the main floodable areas in the basin (with Hess product; Hess et al., 2015) and the drainage network by Seyler et al. (2009) which were combined to define the 2D model wetland cells without channels (Figure S1d). The orange cells are these cells, i.e., the cells within the water mask but without the drainage network.

Table S1 presents the calibrated rainfall-runoff parameters adopted for each sub-basin for both 1D and 2D model versions. Each parameter value is applied to a hydrologic response unit (HRU) within a sub-basin. The Negro River Basin was divided into two sub-basins: the Branco river and the Negro sub-basin (which contains all basin but the drainage area of Branco river). Please refer to Collischonn et al., (2007) for a thorough description of the model parameters.

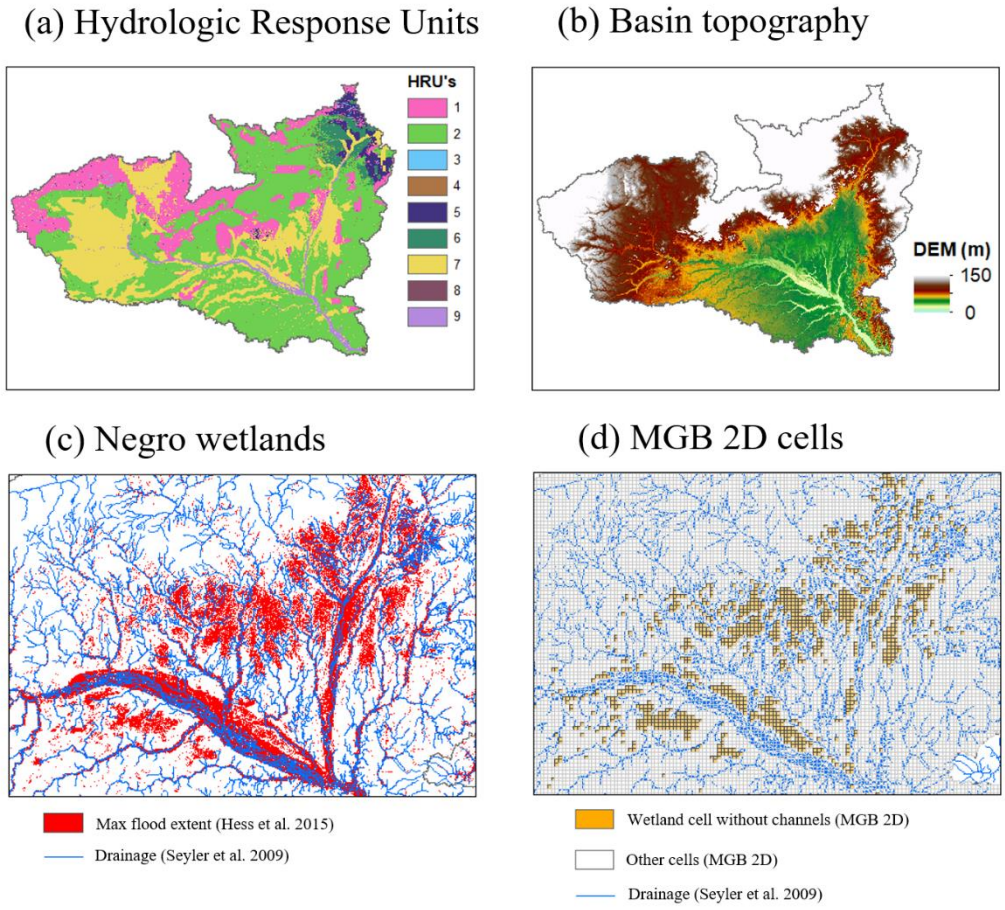

Figure S1. (a) Hydrologic Response Units (Fan et al., 2015) at the basin scale: forest with shallow soils (SS) (1), forest with deep soils (DS) (2), agriculture+SS (3), agriculture+DS (4), grasslands/savannas+SS (5), grasslands/savannas+DS (6), wetlands (7), urban areas (8) and open water (9). (b) Basin topography with MERIT DEM (YAMAZAKI et al., 2017). (c) Negro wetlands with Hess water mask product for the central Negro River Basin. (d) MGB 2D cells, highlighting the cells considered as wetland cells without channels (orange), which were defined as those within the water mask but without the drainage network presented in Figure S1c.

Table S1. Rainfall-runoff parameters adopted in both 1D and 2D MGB model applications. HRU's numbers refer to Figure S1a.

Negro River sub-basin	Parameters			
HRU	Wm (mm)	b (-)	Kbas (mm/d)	Kint (mm/d)
1-ForShal	70	1.5	3	10
2-ForDeep	70	1.5	3	10

3-AgriShal	70	1.5	3	10
4-AgriDeep	70	1.5	3	10
5-GrShal	70	1.5	3	10
6-GrDeep	70	1.5	3	10
7-Wetland	50	1.5	3	10
8-Urb	50	1.5	3	10
CS (-)	10			
CI (-)	30			
CB (hours)	200			
Branco River sub-basin				
1-ForShal	600	0.5	1	5
2-ForDeep	650	0.5	1	5
3-AgriShal	600	0.5	1	5
4-AgriDeep	650	0.5	1	5
5-GrShal	600	0.5	1	5
6-GrDeep	650	0.5	1	5
7-Wetland	80	0.5	1	5
8-Urb	80	0.5	1	5
CS (-)	10			
CI (-)	50			
CB (h)	500			

13.2.2 Supplementary Material of Chapter 5

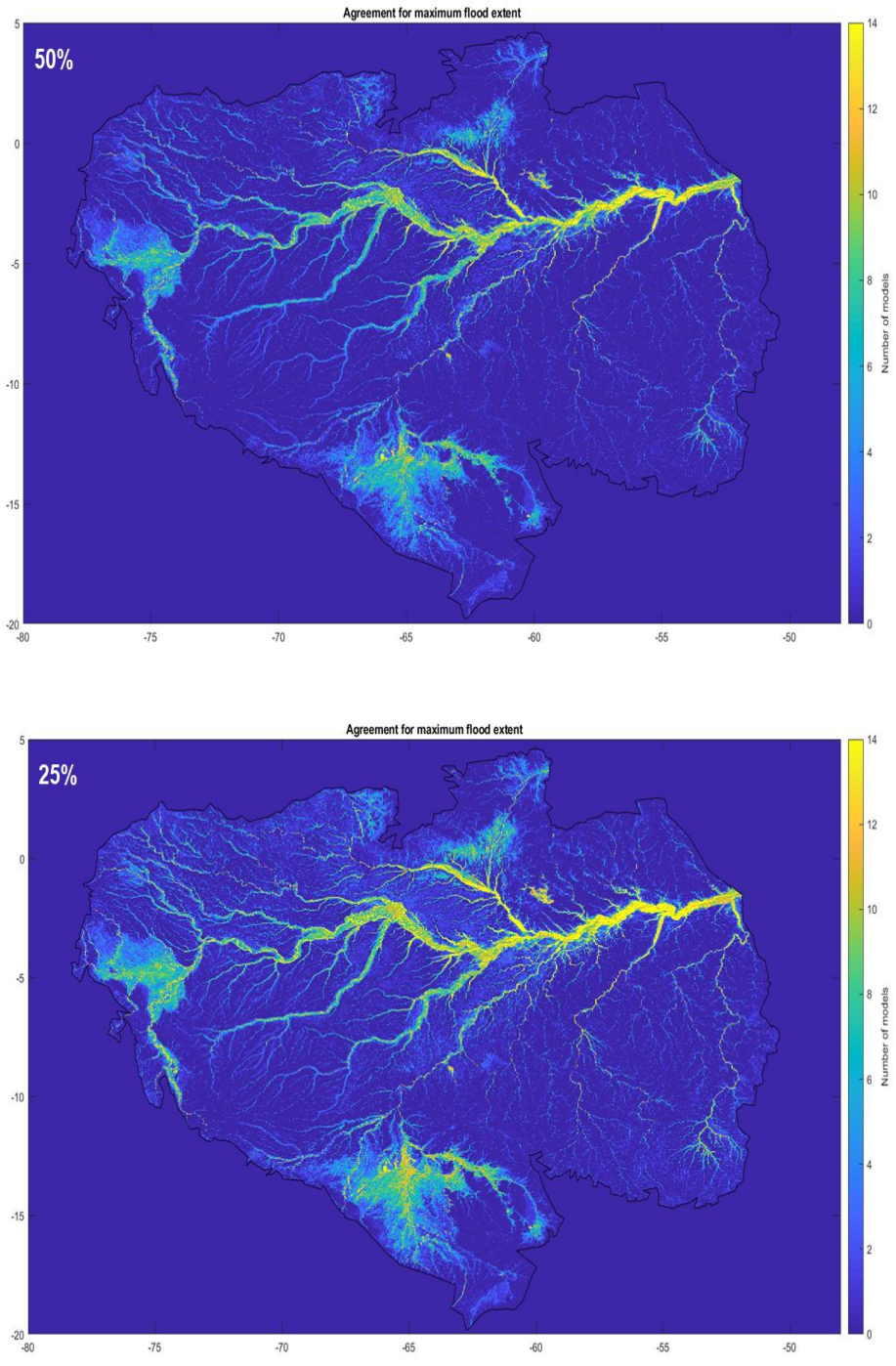

Fig S1. Sensitivity of the fraction used to define a flooded 1km pixel (25% and 50%).

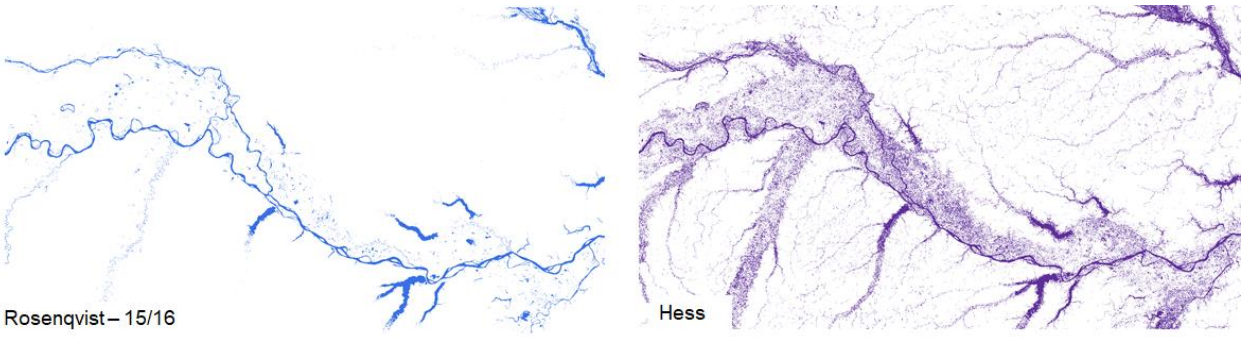

Fig S2. Minimum inundation extent, as estimated by Rosenqvist and Hess products for the Middle Amazon river between Jutaí-Amazon and Purus-Amazon river confluences.

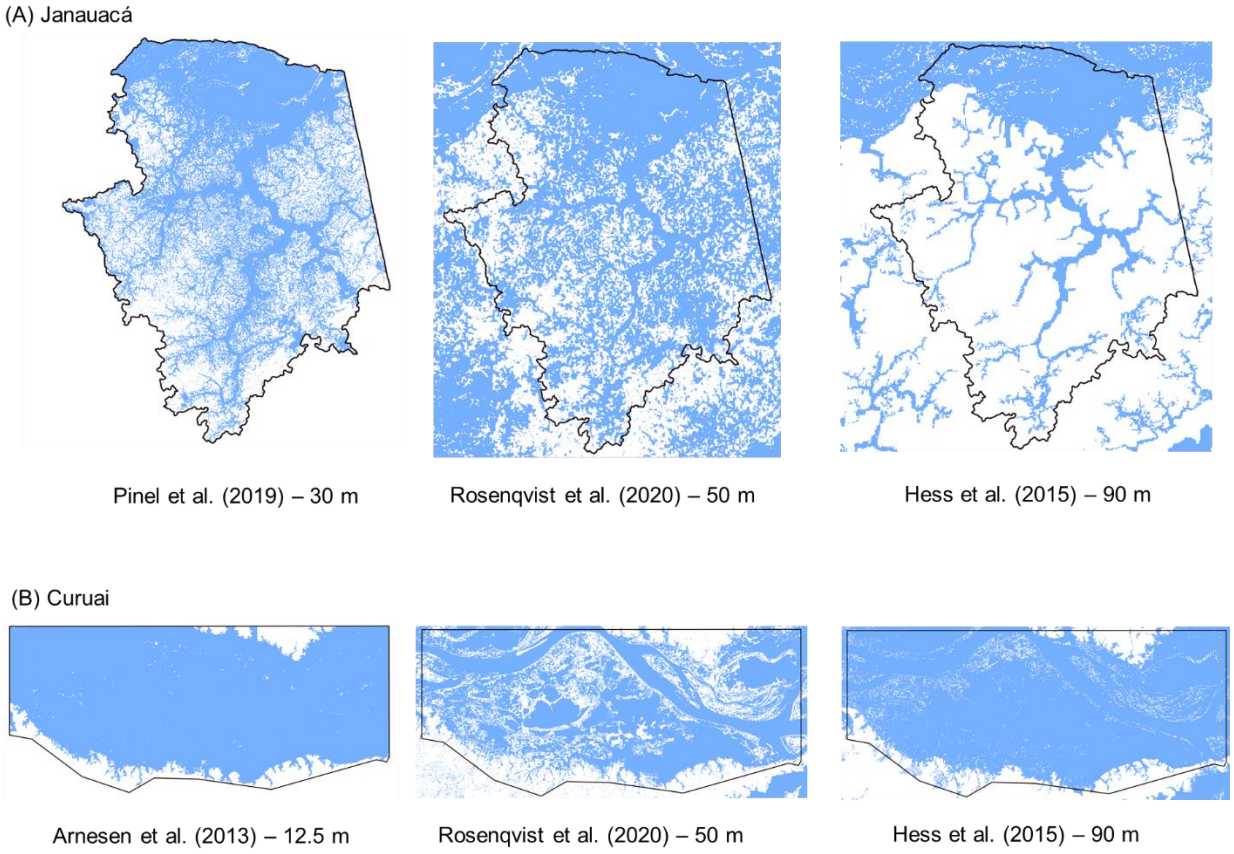

Figure S3. Comparison between the long-term maximum inundation for local references (Pinel and Arnesen' products), Rosenqvist and Hess datasets for the (a) Janauacá and (b) Curuai areas. The polygons refer to the area used to extract the values presented in Tables 4 and 5. The spatial resolution of each product is noted.

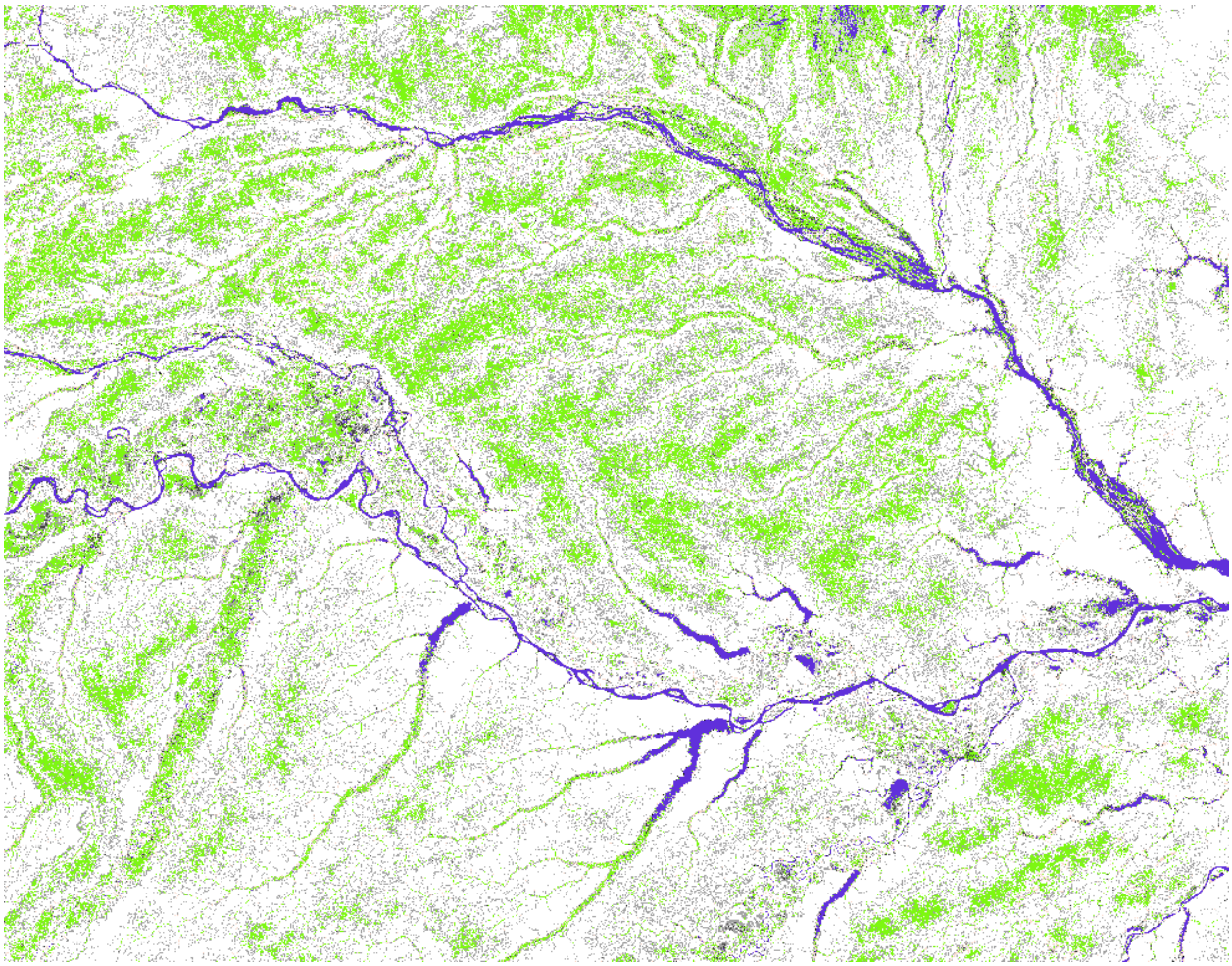

Figure S4. Estimation of wetlands by Gumbricht et al. (2017) across central Amazon. Green pixels relate to the product's "swamps (incl. bogs)" category, which is defined as "Wet all year around, but not necessarily inundated."

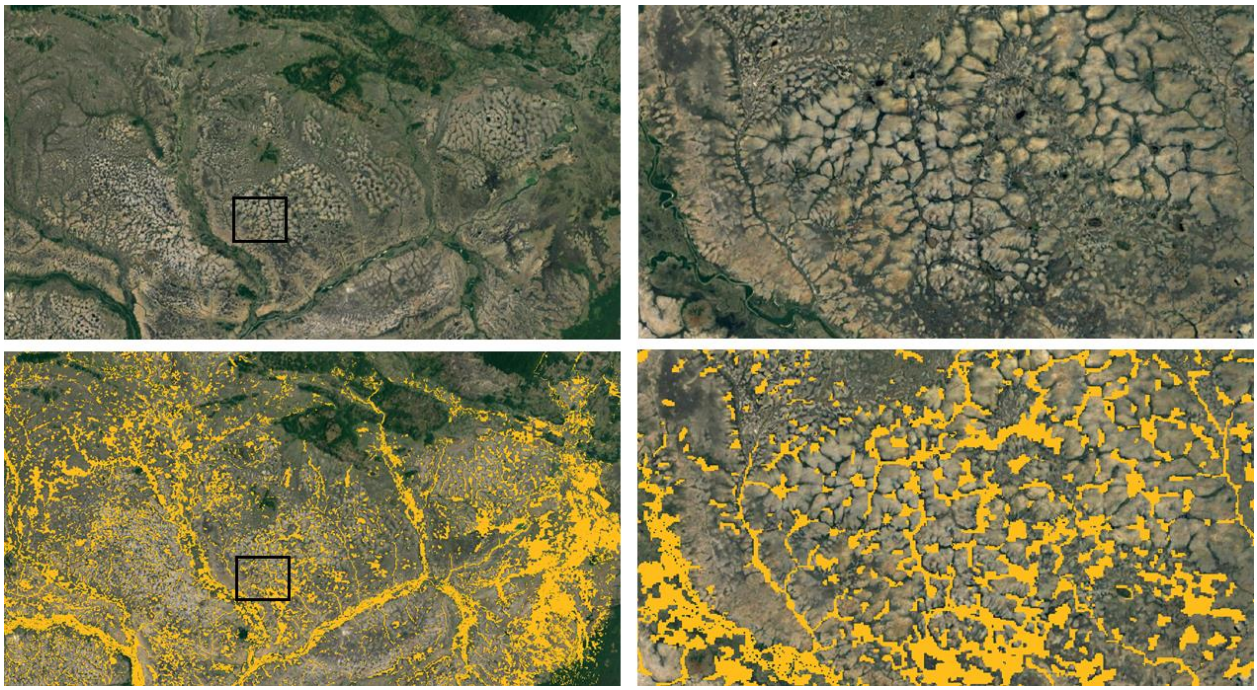

Fig S5. Roraima wetlands. Above: Google Earth imagery. Below: Hess SAR classification of floodable areas (at large scale in the left, and detailed scale in the right).

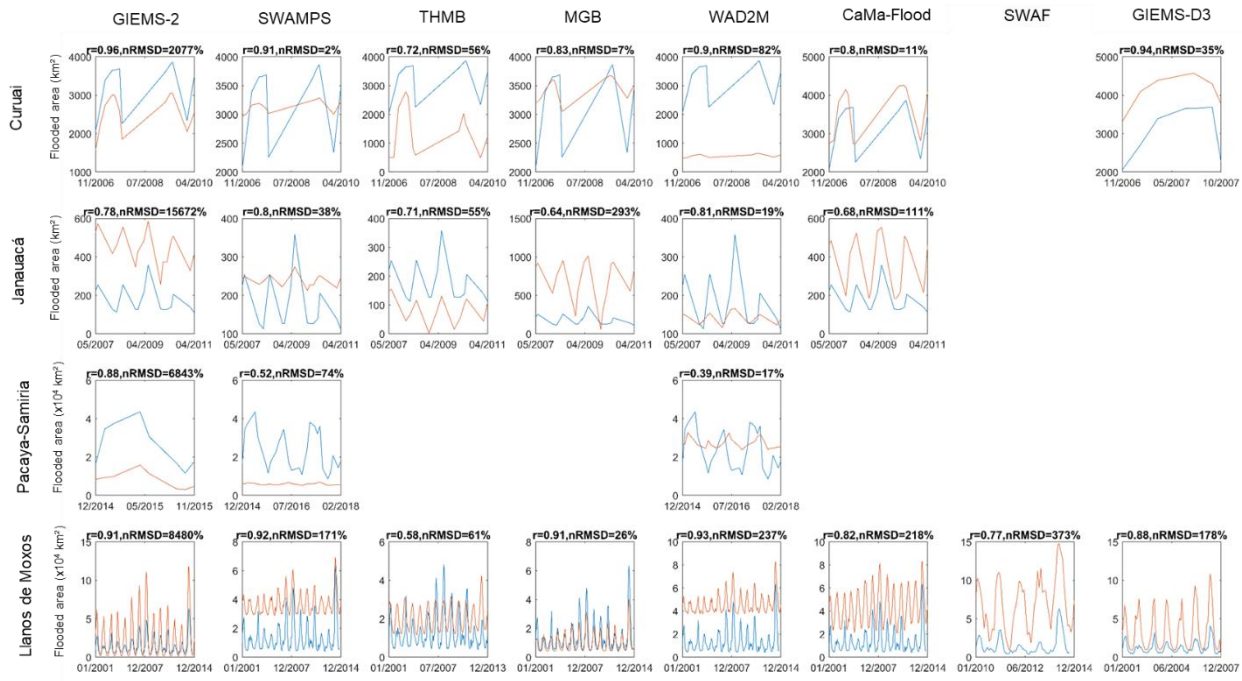

Fig S6. Inundation time series for the four wetlands with available datasets, and for the eight basin-scale dynamic products (GIEMS-2, SWAMPS, THMB, MGB, WAD2M, CaMa-Flood, SWAF-HR and GIEMS-D3). The subplots that are empty refer to areas where the basin-scale product's timespan did not overlap with the local product one.

13.2.3 Supplementary material of Chapter 6

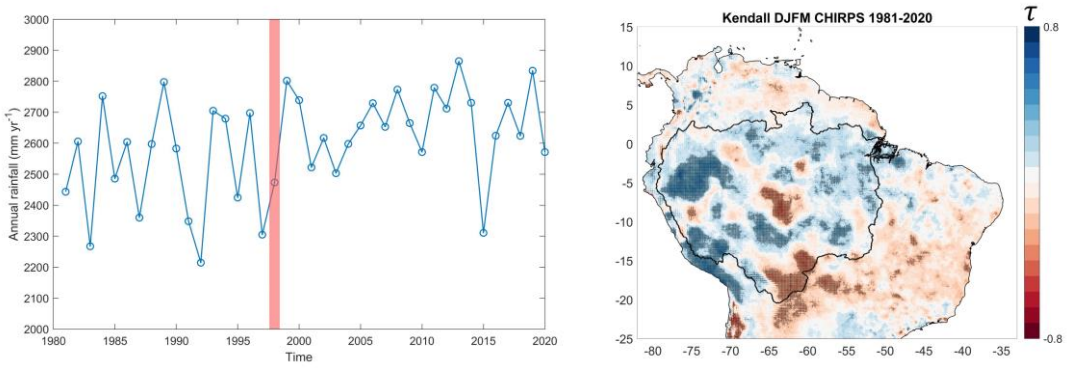

Fig S1. Annual total precipitation in the northern Amazon (>5°S) for the period 1981-2020. Precipitation trends during DJFM

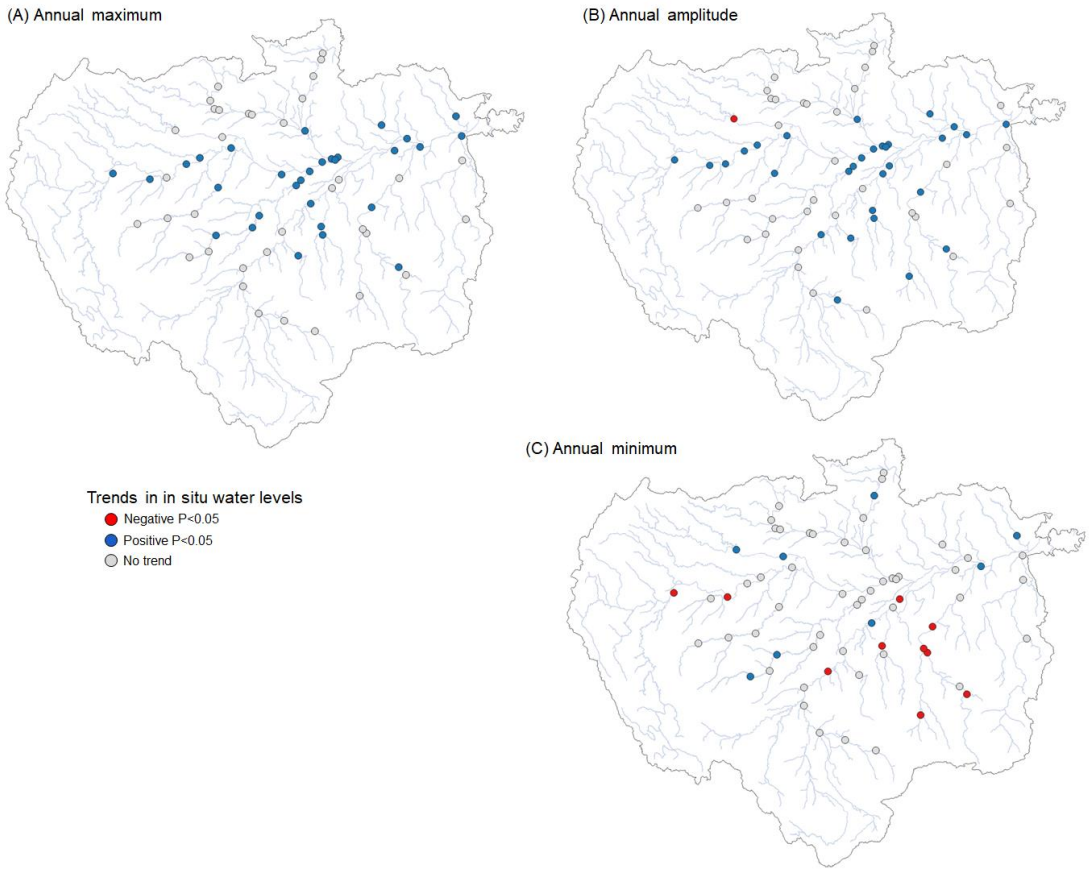

Fig S2. Trends in in situ water level gauges across the Amazon basin.

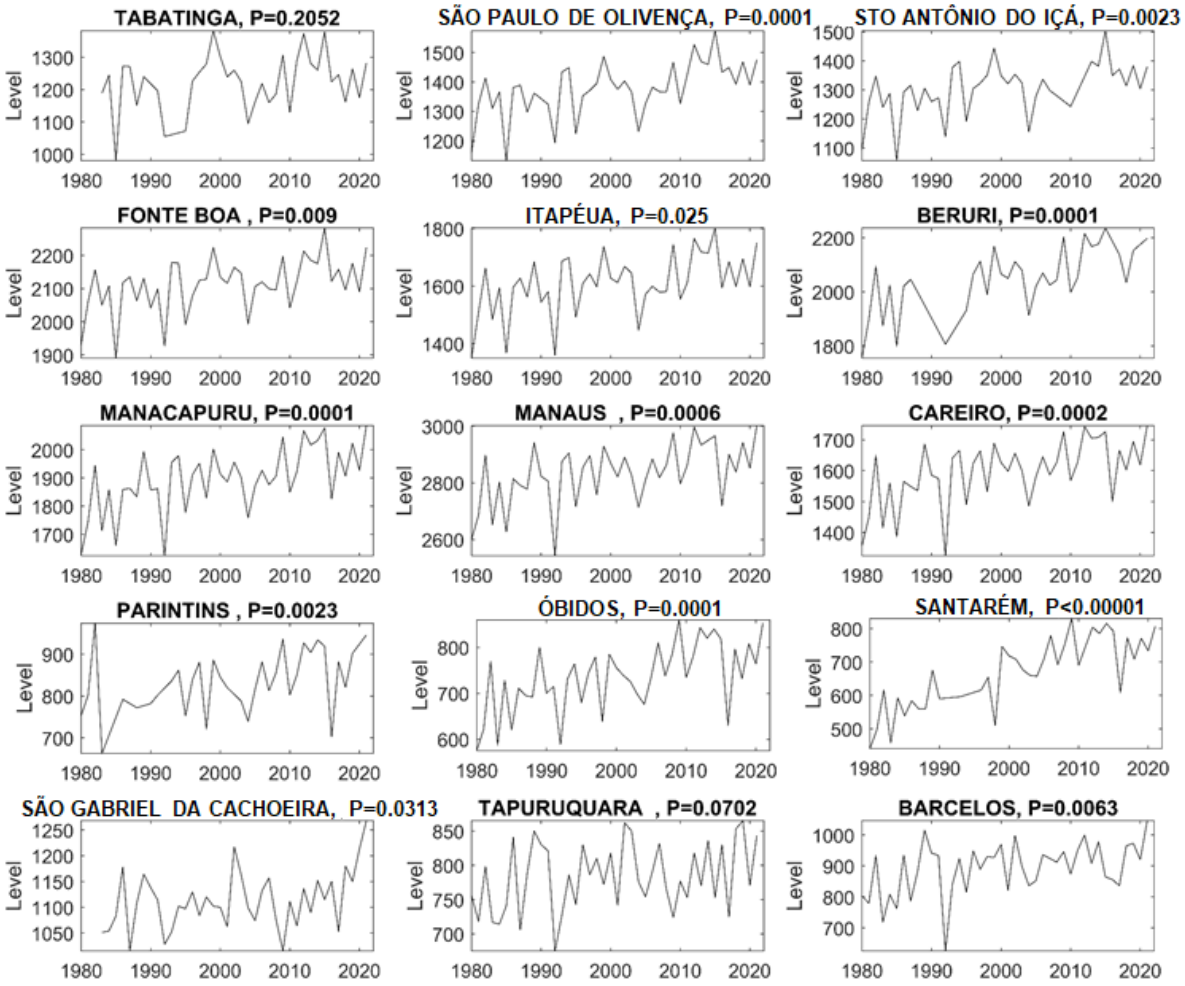

Fig S3. Time series of annual maximum water levels for the 12 gauges along the Amazon mainstem (the first 12 plots) and for three gauges along the Negro river (São Gabriel da Cachoeira, Tapuruquara and Barcelos).

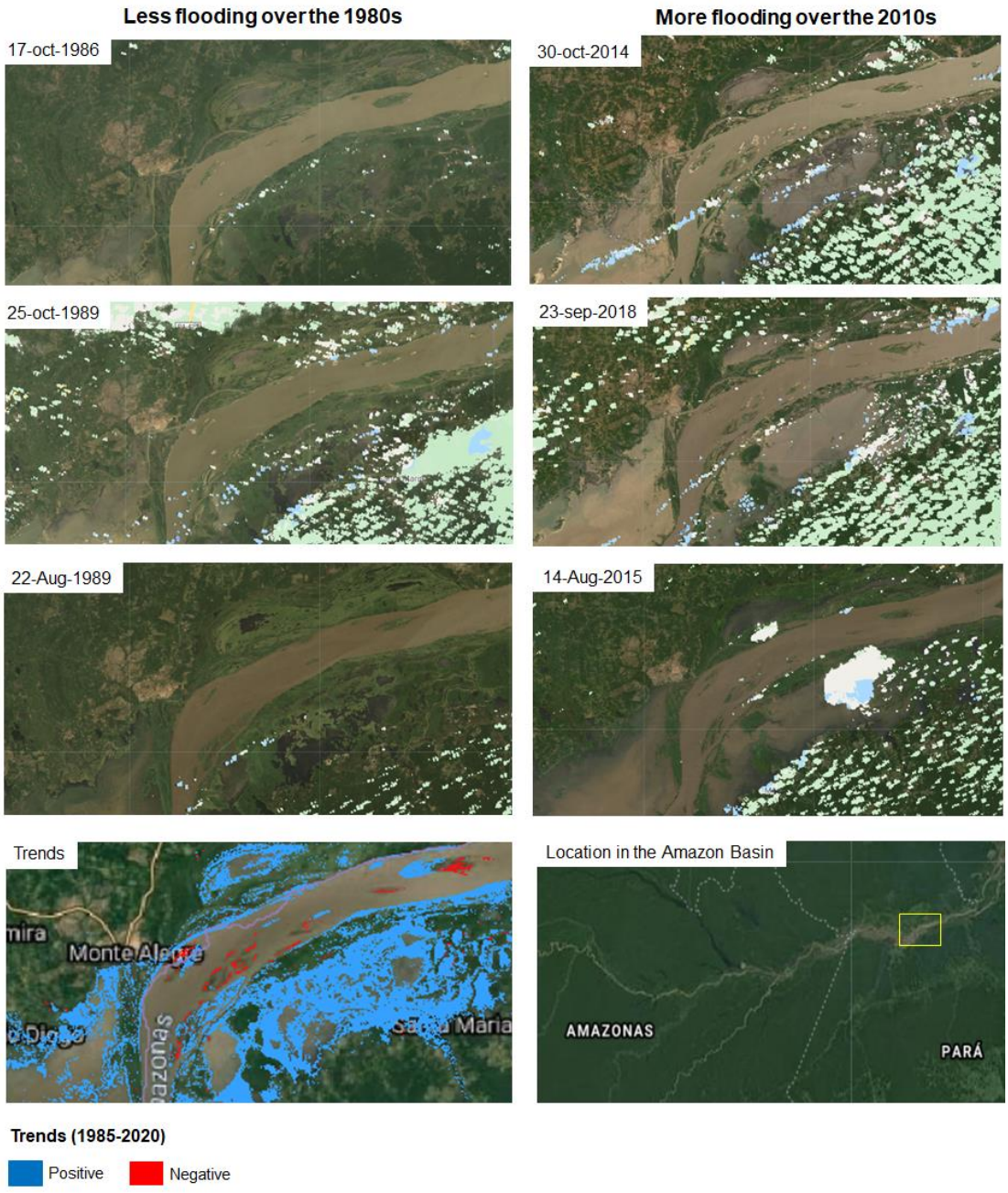

Fig S4. Google Earth imagery depicting inundation extent over the 1980s (left column) and 2010s (right column) decades. The bottom line shows the spatial trends and the location of the assessed Amazon floodplain area close to the Monte Alegre city.

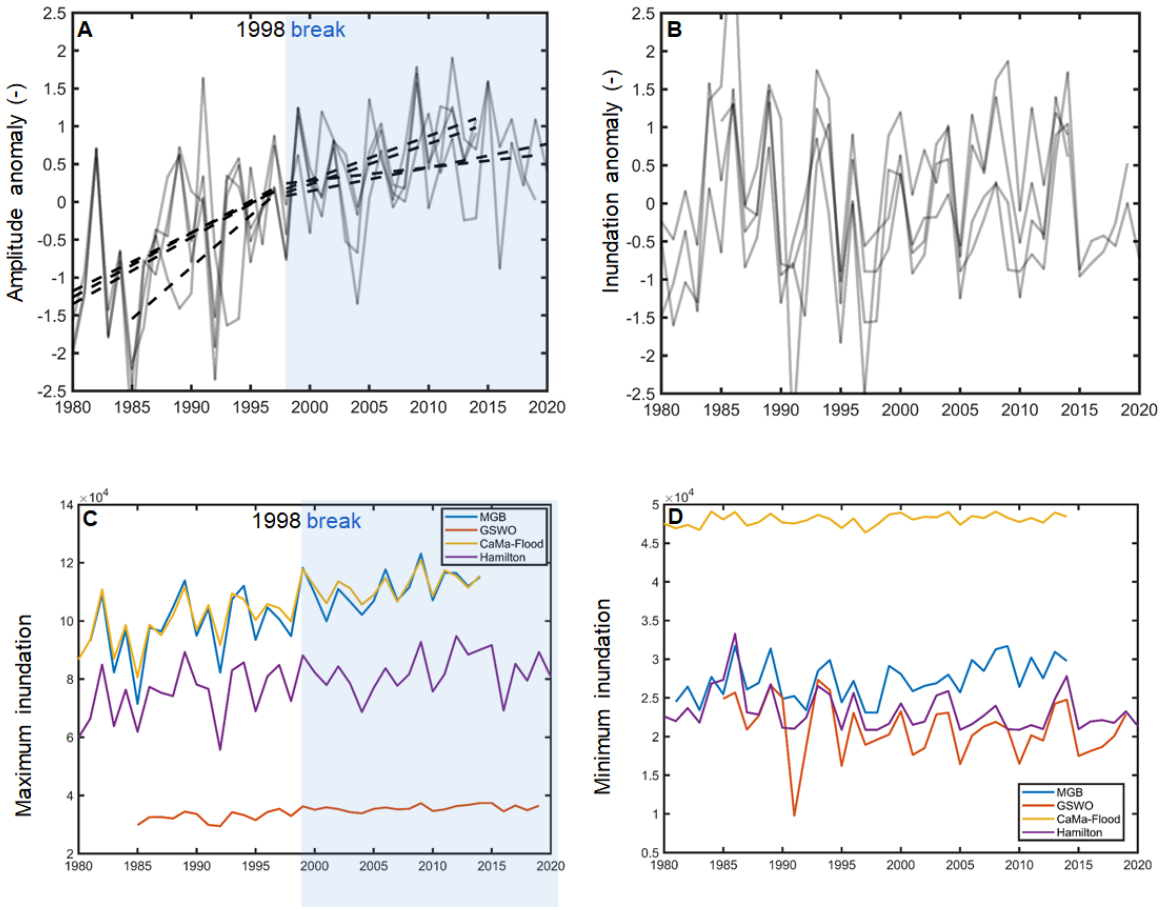

Fig S5. Series of anomalies of (A) amplitude and (B) minimum annual inundation extent, and absolute (C) maximum and (D) minimum inundation along the Amazon mainstem floodplains. In figures (A) and (B), each line relates to one of the four inundation datasets (MGB, GSWO, CaMa-Flood and Hamilton).

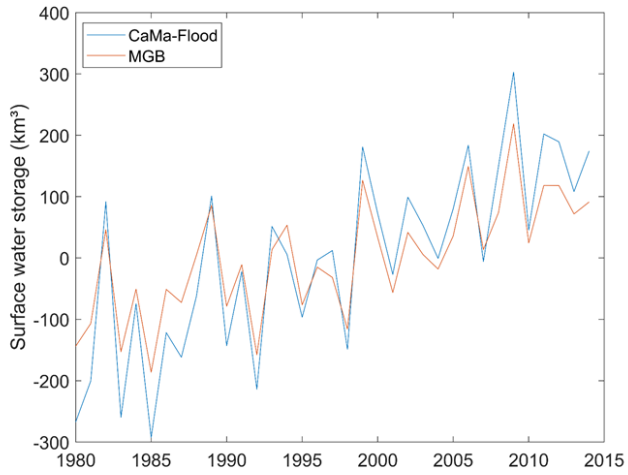

Fig S6. Annual maximum flood storage with CaMa-Flood and MGB models for the Amazon mainstem floodplains. Anomalies are computed by subtracting from each value the long-term average of the annual maximum values.

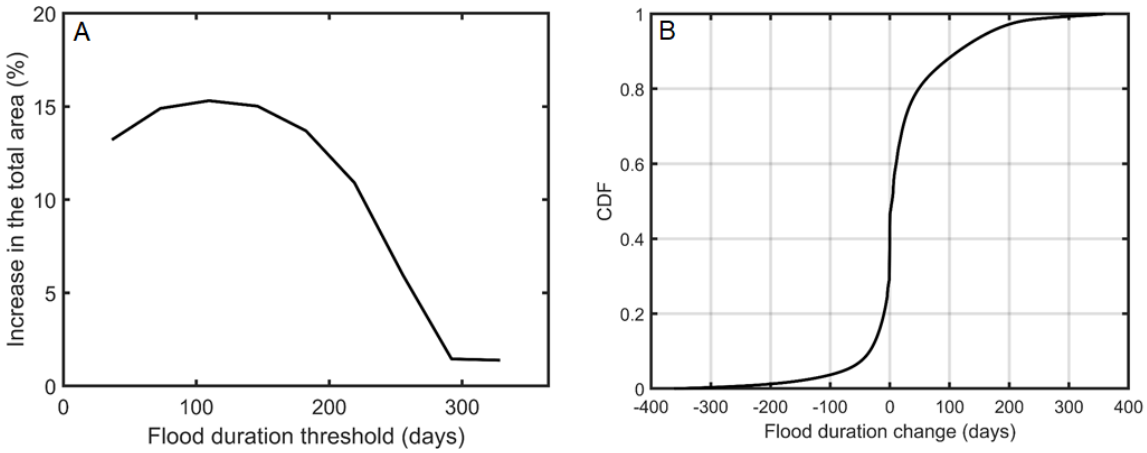

Fig S7. (A) Increase of the total floodplain area that is flooded for more than a given duration, e.g., there was an increase of 13.7% in the total area subjected to flood duration longer than 180 days. (B) Cumulative distribution function of the flood duration change between 2009-2020 and 1985-1996 decades for the Amazon floodplain area between Manaus and Monte Alegre cities.

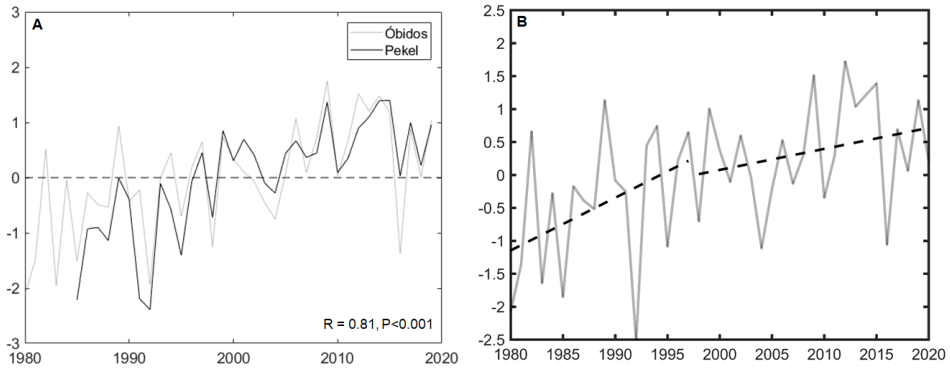

Fig S8. (A) Validation of GSWO annual maximum inundation with in situ annual maximum water levels at Óbidos, with a significant correlation with R=0.81 (P<0.001). (B) Annual time series of maximum inundation extent over the Amazon mainstem based on the methodology by Hamilton et al. (2002).

13.2.4 Supplementary material of Chapter 7

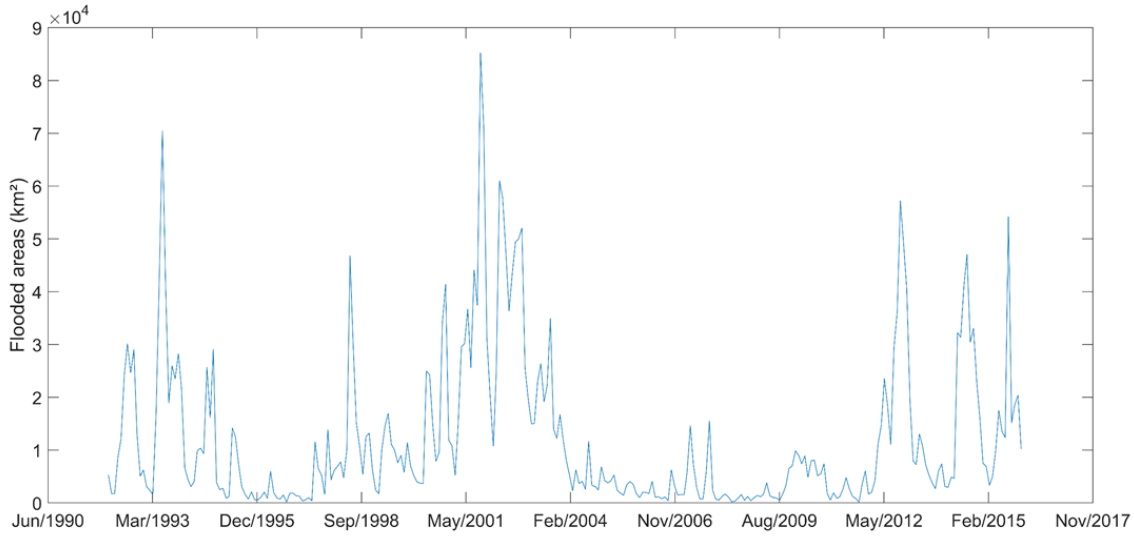

Figure S1. Inundation time series over the Pampas region with the GIEMS-2 dataset.

13.2.5 Supplementary material of Chapter 8

Site	Latitude	Longitude	Data availability	Land cover	Method	R^2	RMSE ($mm.day^{-1}$)
BDP(BIUDES et al., 2015)	-16.497°	-56.411°	Jun/2011-Ago/2015	Woodland Savanna	Bowen ratio	0.76	1.00
CAM(BIUDES et al., 2015)	-16.555°	-56.286°	Jan/2007-Jan/2009	Riparian Forest	Bowen ratio	0.05	1.20
FMI(BIUDES et al., 2015)	-15.731°	-56.071°	Abr/2009-Mai/2013	Savanna mixed grassland-woodland	Bowen ratio	0.07	1.14
K34(ARAÚJO et al., 2002)	-2.609°	-60.209°	Jan/2000-Set/2006	Evergreen Broadleaf Forest	Eddy covariance	0.73	1.08
K67(SALESKA et al., 2003)	-2.856°	-54.958°	Jun/2002-Jan/2006	Evergreen Broadleaf Forest	Eddy covariance	0.02	0.40
K83(GOULDEN et al., 2004)	-3.017°	-54.970°	Jun/2000-Mar/2004	Evergreen Broadleaf Forest	Eddy covariance	0.53	0.67
NPW(DALMAGRO et al., 2019)	-16.497°	-56.411°	Jan/2013-Sep-2016	Woodland Savanna	Eddy covariance	0.25	1.06
TNR	-12.831°	-69.283°	Jan/2017-May/2019	Mixed Forest	Eddy covariance	0.47	0.74
VIR(POSSE et al., 2016)	-28.239°	-56.188°	Dec/2009-May/2012	Evergreen Needleleaf Forest	Eddy covariance	0.67	1.16
BAN(BORMA et al., 2009)	-9.824°	-50.161°	Out/2003-Dez/2006	Woodland Savanna	Eddy covariance	0.04	0.85

Table S1. Summary of the 10 micrometeorological sites used for model validation. Provided data are location, period of data availability, land cover type, method type, and performance metrics for the SEBAL model application (R^2 and RMSE). The main reference for each tower is cited together with the site name.

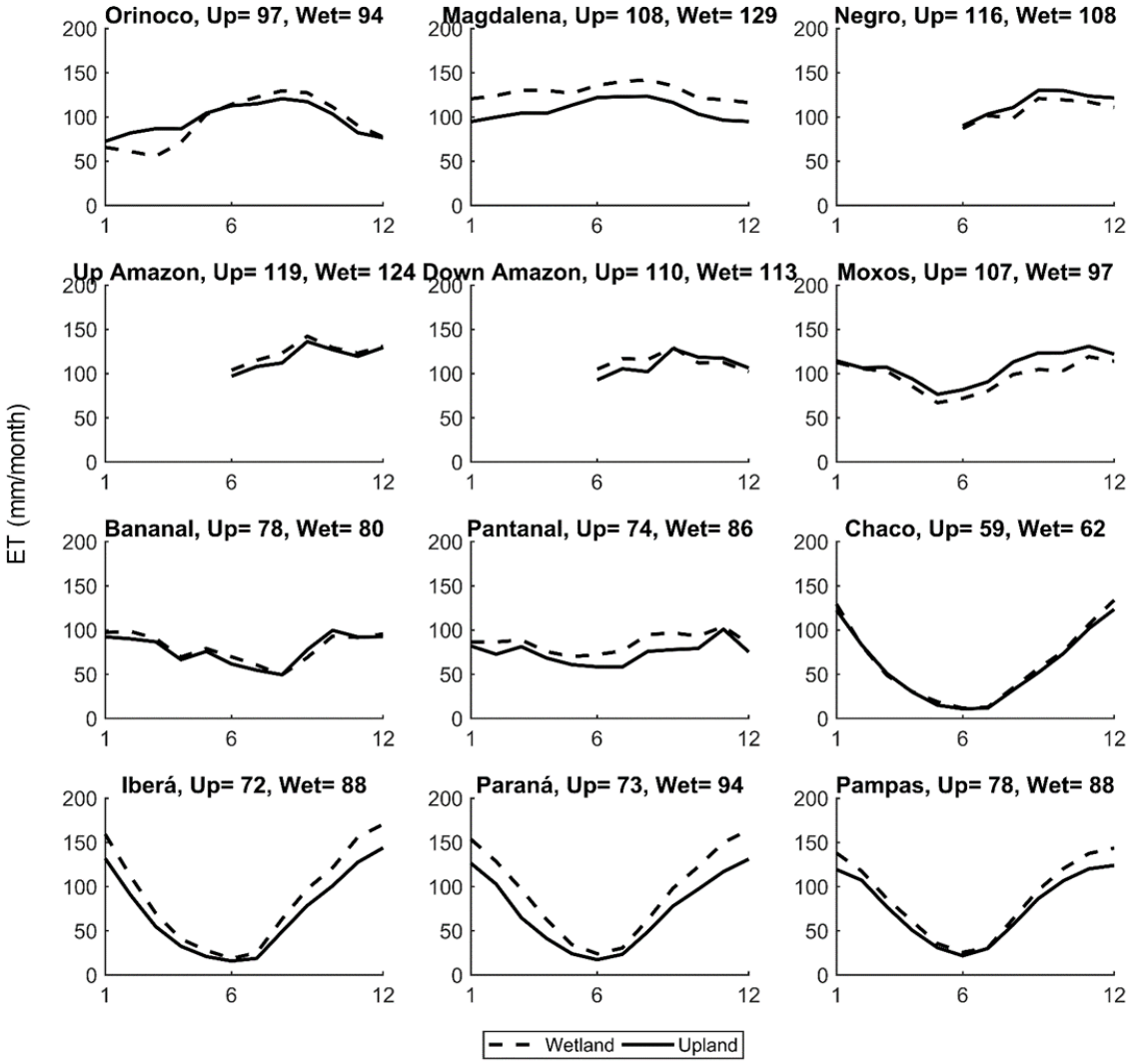

Figure S1. Climatology of average evapotranspiration in the wetland and adjacent upland regions. The value in each figure's title relates to the long term average ET for upland (Up) and wetland (Wet). Please note that ET data for Negro, Up and Down Amazon are not computed for the months from January to May because of persistent cloud cover which hampers the use of MODIS optical data.

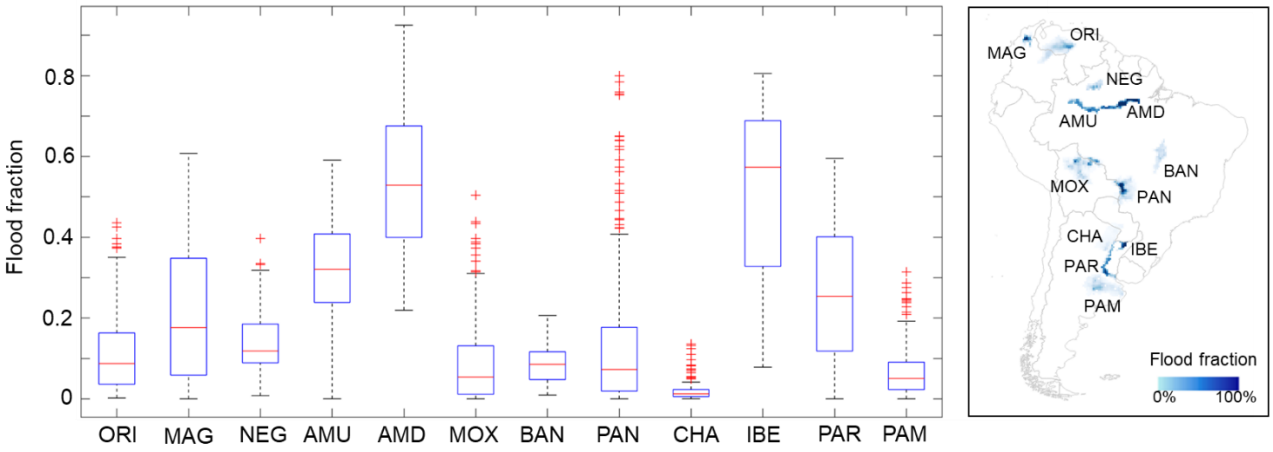

Figure S2. Long term flood fraction for South American wetlands. Each boxplot refers to long term (2000-2015) flood fraction values for all 25 km GIEMS-2 pixels within each wetland area. Red crosses are outlier values.

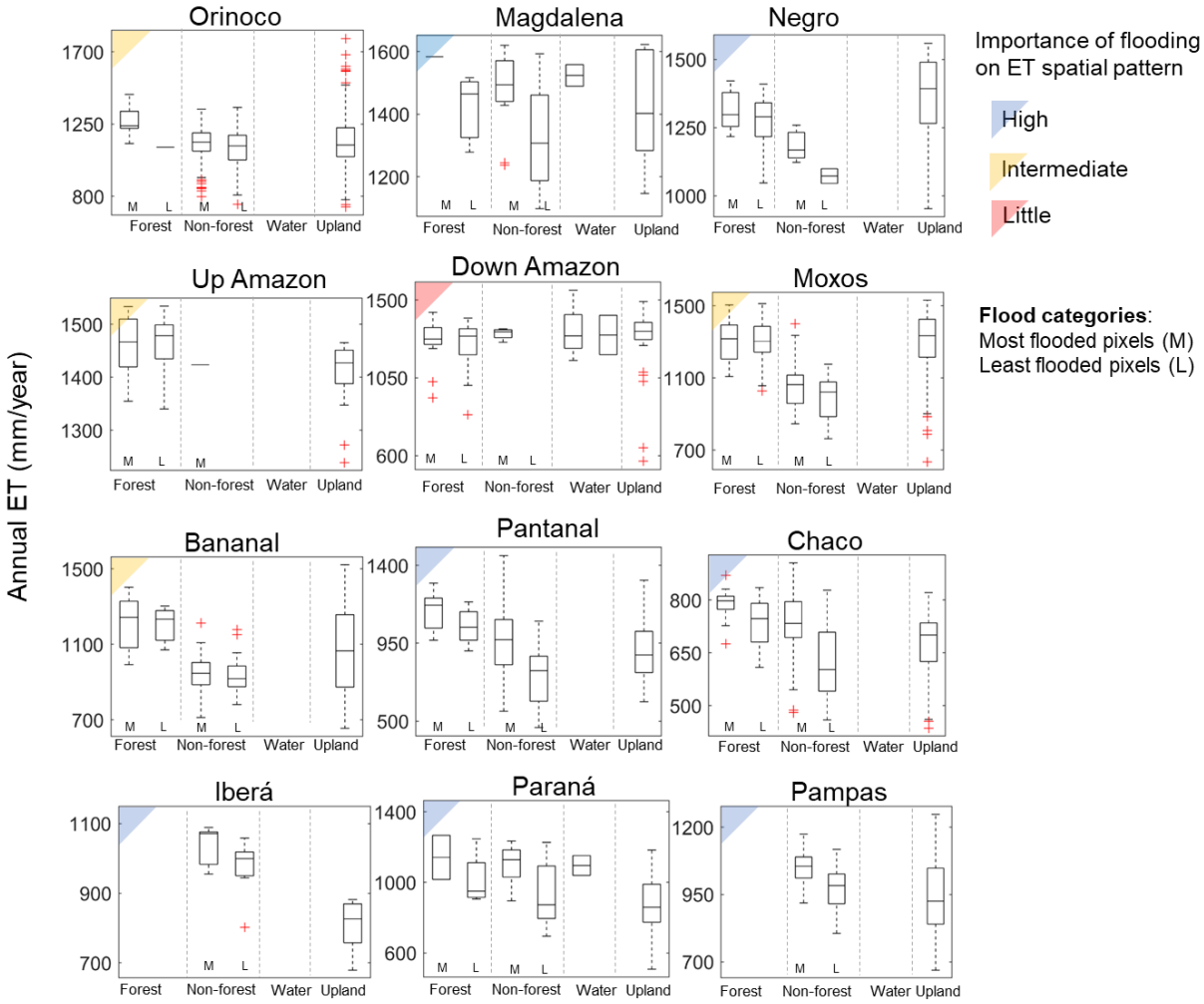

Figure S3. Spatial assessment of annual evapotranspiration across South American wetlands. Each boxplot refers to all annual ET (long term average; 2000-2015) pixels within a given land cover (wetland forest, wetland non-forest, open water, upland) and a flood category (most flooded pixels (M) and least flooded pixels (L), based on 50%-50% quantiles) for each wetland area. High importance of flooding on ET spatial pattern: wetlands where the most flooded pixels have higher ET (median values) than the least flooded pixels. Intermediate: the most flooded non-forest pixels have higher ET than the least flooded ones, but lower ET than forest or upland; or the most flooded forest pixels have higher ET than uplands. Little: no major difference among wetland and upland ET.

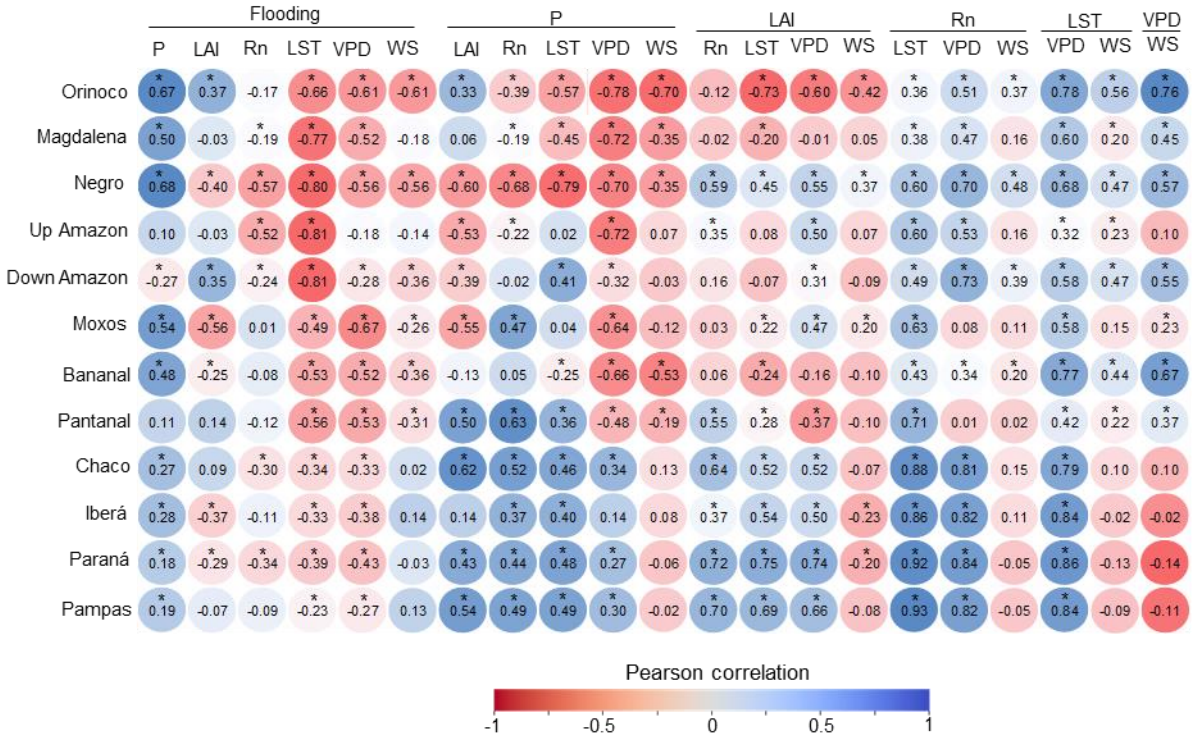

Figure S4. Correlation among environmental drivers for the South American wetlands. Pearson correlation values are presented for the correlation among the following drivers for each wetland: flood fraction (FF), precipitation (P), leaf area index (LAI), net radiation (Rn), land surface temperature (LST), vapor pressure deficit (VPD) and wind speed (WS). *Significant correlations with P<0.01.

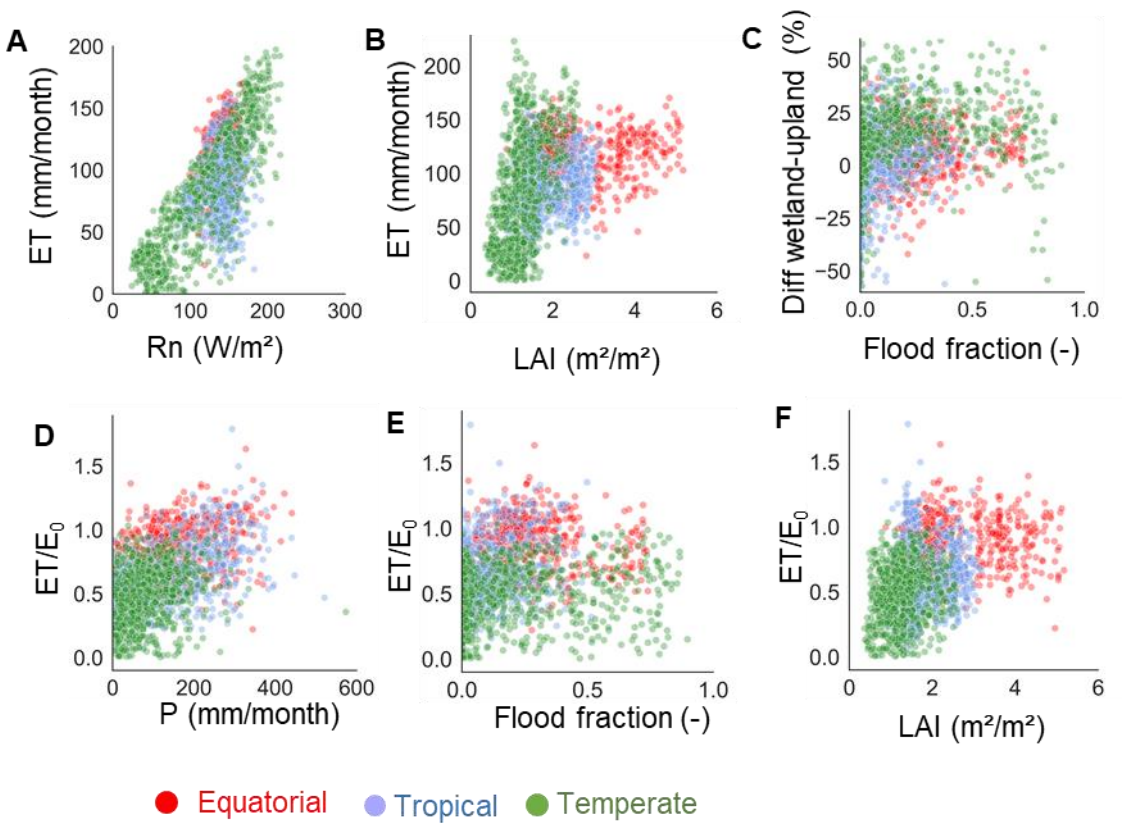

Figure S5. Correlation between evapotranspiration (ET), ET to evaporative demand ratio (ET/E_0), and environmental variables for South American wetlands. The assessed environmental variables are net radiation (Rn), leaf area index (LAI), flood fraction and precipitation (P).

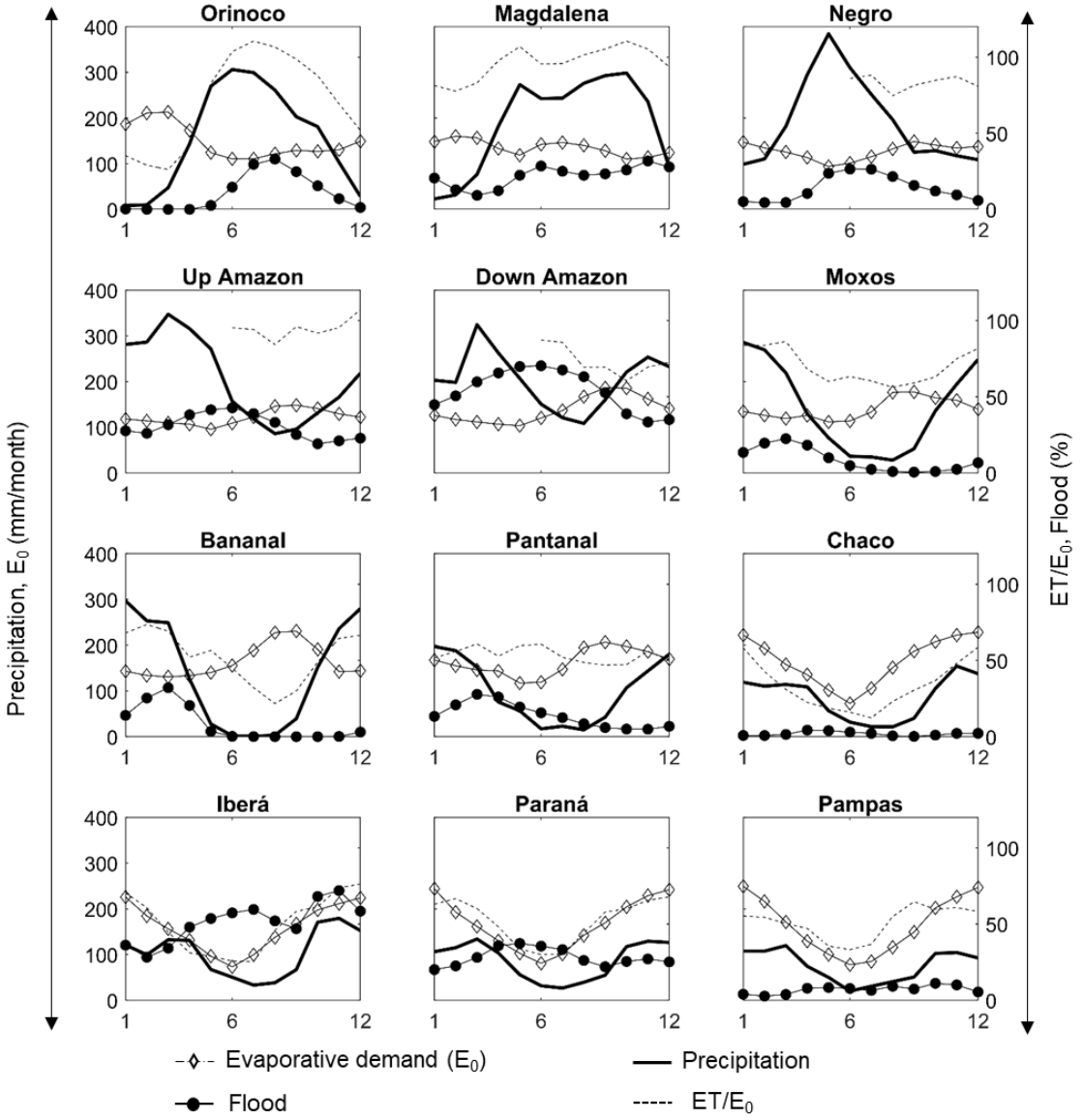

Figure S6. Climatology of evaporative demand, flood fraction, precipitation, and evapotranspiration to evaporative demand (ET/E_0) ratio for the 12 wetlands. Please note that ET data for Negro, Up and Down Amazon are not computed for the months from January to May because of persistent cloud cover which hampers the use of MODIS optical data.

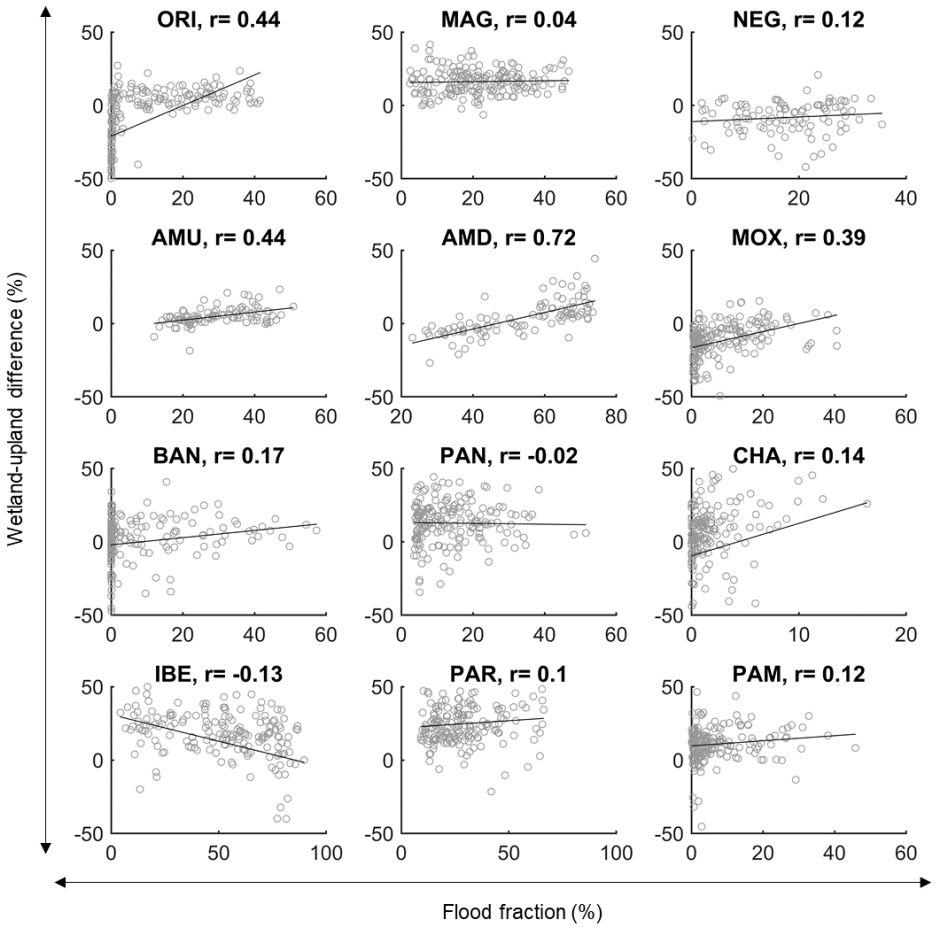

Figure S7. Scatterplot between wetland-upland ET difference and flood fraction for each wetland. The Pearson correlation value is presented for each wetland.

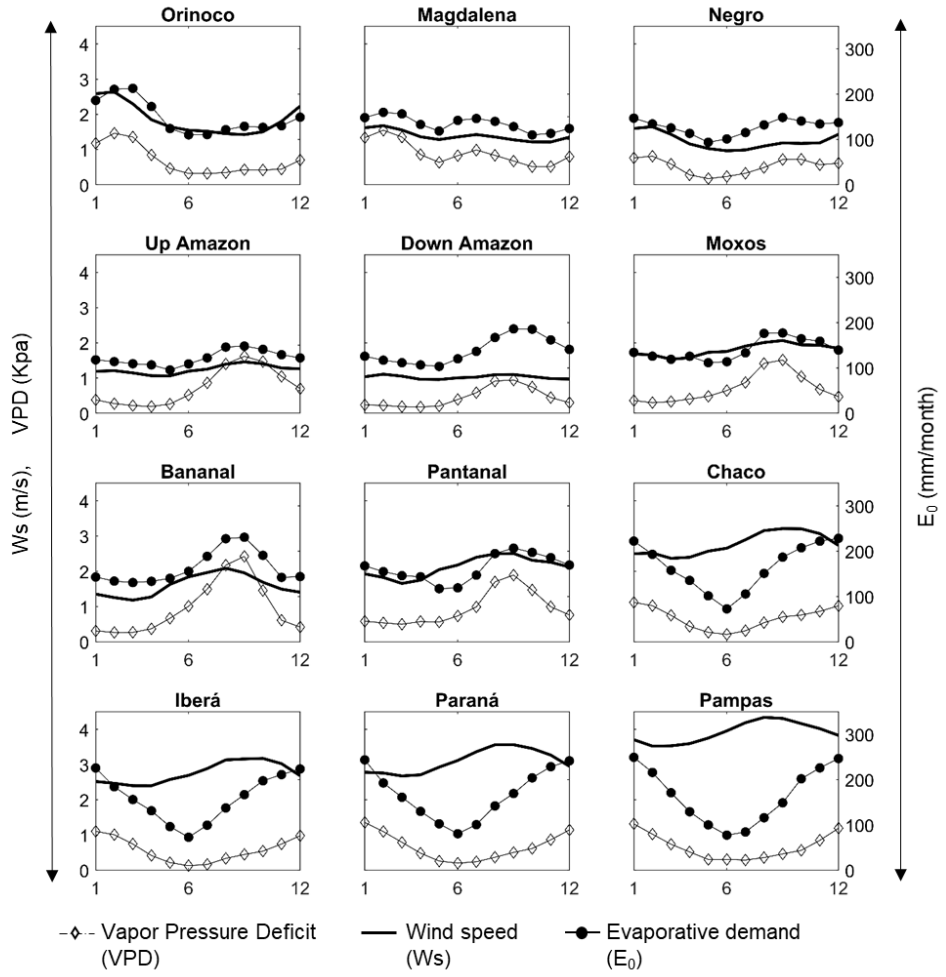

Figure S8. Climatology of wind speed (Ws), vapor pressure deficit (VPD), and evaporative demand (E_0) for the 12 wetlands. E_0 generally follows the VPD pattern, and Ws to a lesser extent.

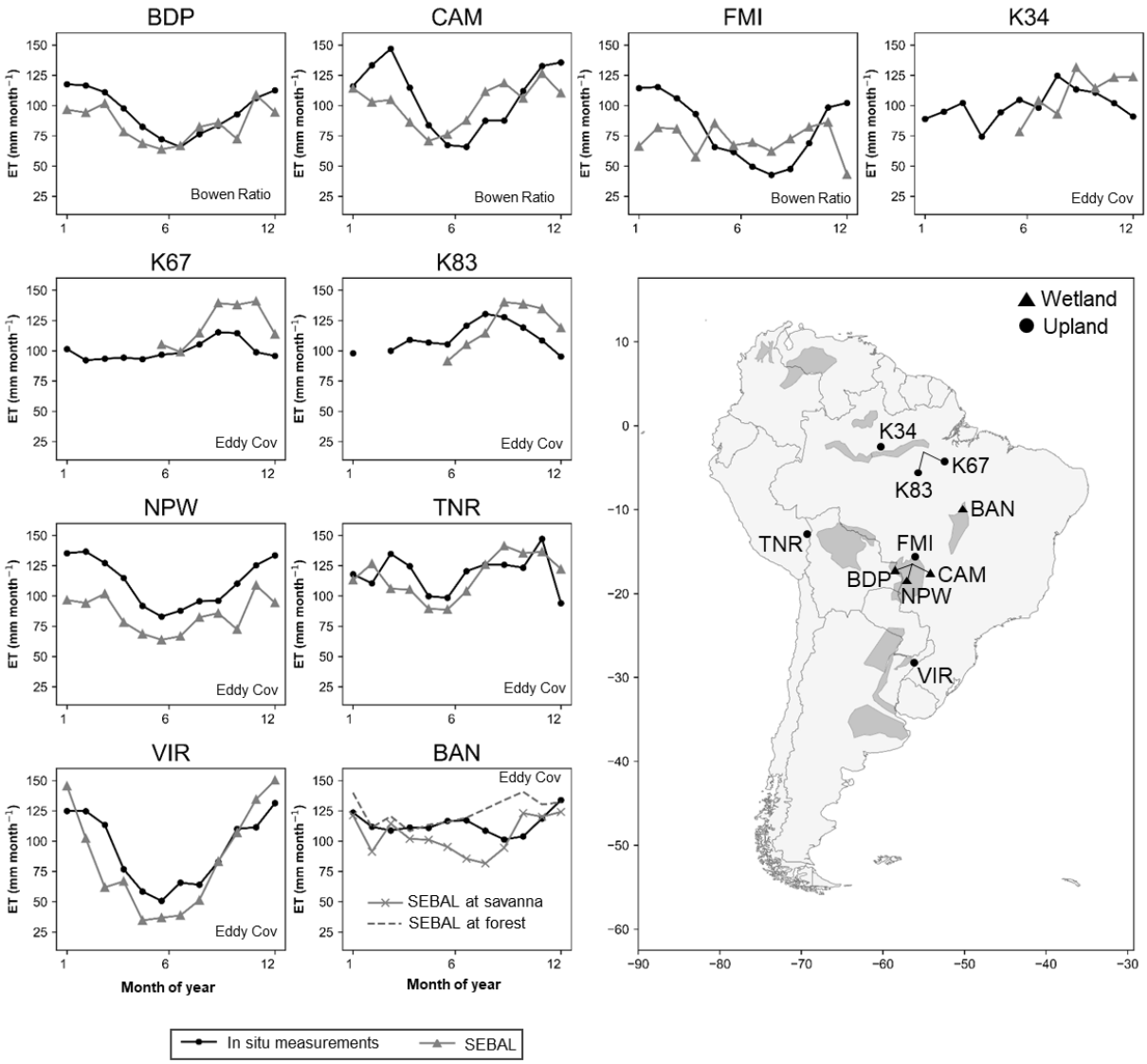

Figure S9. Validation of the SEBAL-based evapotranspiration (ET) climatology with in situ data from 10 in situ micrometeorological towers (three using the Bowen ratio and seven the eddy covariance method) located across South America. Because of lack of available MODIS data for many months in the tropical/equatorial regions, the SEBAL climatology is based on the whole time series (2000-2015), while the in situ data have different periods of availability (Table S1). For the in situ measurements, monthly data were obtained by averaging all daily values in months with at least 75% of data available. In the map, towers located within wetlands are marked with a triangle, and those within uplands with a circle. For the BAN tower, SEBAL results are presented for two adjacent pixels (1 km far from each other), one located in a predominantly savanna and another in a mainly forest area, to show the differences in ET depicted by the model in this heterogeneous area. In this case, the tower likely receives contribution from both savanna and forest areas.

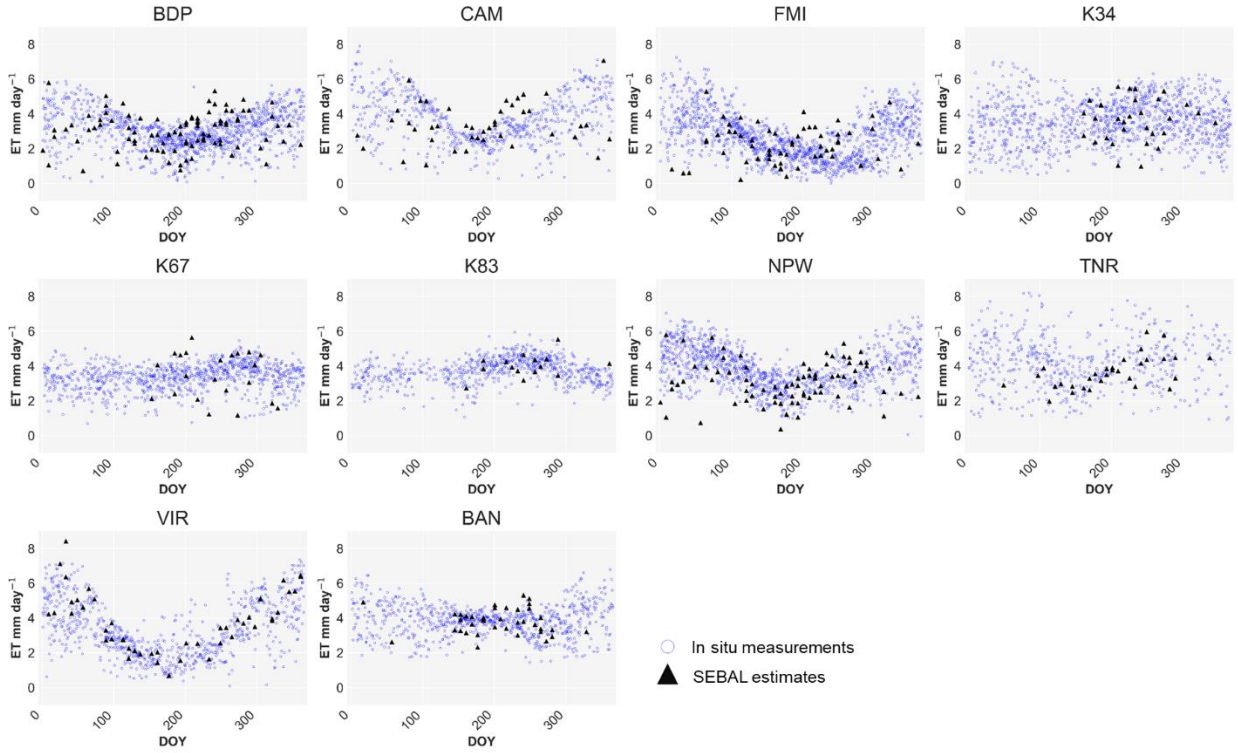

Figure S10. Validation of SEBAL-based monthly evapotranspiration (ET) with in situ data. All daily in situ measurements for the 10 flux towers presented in Figure S9 are plotted for each day of the year, and compared to the SEBAL-based 8-day estimates for the same period of data availability.

Detailed description of the SEBAL algorithm

The SEBAL algorithm (BASTIAANSSEN et al., 1998a) estimates the instantaneous evapotranspiration (or latent heat) rate as the residual of the surface energy balance (Equation 1), using remote sensing and meteorological data (wind speed, specific humidity, surface air temperature and incoming shortwave radiation).

$$LE = R_n - G - H \quad (1)$$

Where LE is the latent heat flux ($W\ m^{-2}$), R_n the net radiation ($W\ m^{-2}$), G the soil heat flux ($W\ m^{-2}$), and H the sensible heat flux ($W\ m^{-2}$).

The main model premise is that the near-surface vertical air temperature difference is linearly related to the surface temperature (BASTIAANSSEN et al., 1998b), and that there are two extreme pixels that characterize the landscape, namely the hot and cold pixels. At the hot pixel, the latent heat is assumed as zero so that all available energy

($R_n - G$) becomes sensible heat. Conversely, at the cold pixel all available energy becomes latent heat.

Our methodology adapts the SEBAL application by Laipelt et al. (LAIPELT et al., 2020) (originally using Landsat data) for MODIS imagery, and applied it within Google Earth Engine cloud computing environment (see SEBAL steps, as well as main input and output data in Figure S11). The instantaneous evapotranspiration rate estimated with Equation 1 is converted into 8-day evapotranspiration rate, which is the temporal resolution of the adopted MODIS products. This conversion is performed by assuming a constant evaporative fraction during the 8-day period. Finally, the 8-day values are averaged to yield monthly evapotranspiration.

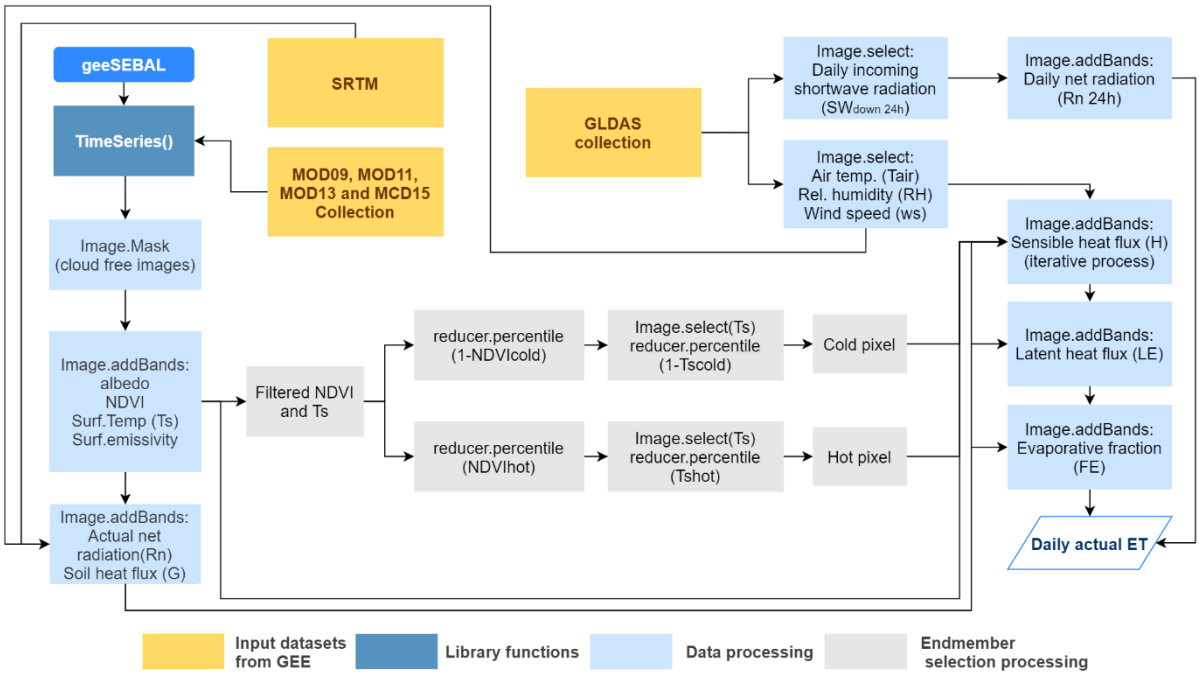

Figure S11. Flow chart of SEBAL steps, and input and output data from the Google Earth Engine cloud computing environment.

Net radiation

Net radiation is calculated as:

$$Rn = (1 - \alpha)Rs_{down} + Rl_{down} - Rl_{up} - (1 - \varepsilon_0)\, Rl_{down} \quad (2)$$

where α is the broad-band surface albedo, Rs_{down} the incoming short-wave radiation ($W\ m^{-2}$), Rl_{down} the incoming long-wave radiation ($W\ m^{-2}$), and Rl_{up} the outgoing long-wave radiation ($W\ m^{-2}$).

Rs_{down}, Rl_{down} and Rl_{up} were estimated following Allen et al. (ALLEN; TASUMI; TREZZA, 2007):

$$Rs_{down} = G_{sc} \cos(\theta_{rel})\, \tau_{sw}\, d^2 \quad (3)$$

$$Rl_{down} = 0.85(-\ln \tau_{sw})^{0.09}\, \sigma\, {T_s}^4 \quad (4)$$

$$Rl_{up} = \varepsilon_0\, \sigma\, {T_s}^4 \quad (5)$$

where G_{sc} is the solar constant ($1367\ W\ m^{-2}$), θ_{rel} the solar incidence angle, τ_{sw} the broad-band atmospheric transmissivity, d^2 the square of the eccentricity factor, σ the Stefan-Boltzmann constant ($5.67 * 10^{-9}\ W\ m^{-2} K^{-4}$), T_s the surface temperature (K) and ε_0 the broad-band surface emissivity.

$$\varepsilon_0 = 0.95 + (0.01 LAI) \quad (6)$$

The broad-band surface albedo (α) is calculated following Tasumi et al. (TASUMI; ALLEN; TREZZA, 2008):

$$\alpha = \sum(\omega_\lambda * \rho_\lambda) \quad (7)$$

where ω_λ is a weighting coefficient and ρ_λ the surface reflectance.

To calculate τ_{sw}, we used the equation suggested by ASCE-EWRI (ASCE, 2005):

$$\tau_{sw} = 0.35 + 0.627 \exp\left[\frac{-0.00146P}{K_t \cos\theta_{hor}} - 0.075\left(\frac{W}{\cos\theta_{hor}}\right)^{0.4}\right] \quad (8)$$

where P is the atmosphere pressure (kPa), W the water in the atmosphere (mm), θ_{hor} the solar zenith angle over a horizontal surface, and K_t the unitless turbidity coefficient where $K_t = 1$ for clean air.

Atmospheric pressure is estimated as:

$$P = 101.3\left(\frac{293-0.0065z}{293}\right)^{5.26} \quad (9)$$

where z is the elevation above sea level (m) obtained from the SRTM mission.

Water in the atmosphere is estimated according to Garrison & Adler (GARRISON; ADLER, 1990):

$$W = 0.14\, e_a P + 2.1 \quad (10)$$

where e_a is the actual vapor pressure (kPa) estimated as (SHUTTLEWORTH, 2012):

$$q = 0.622\frac{e_a}{P} \quad (11)$$

$\cos\theta_{hor}$ and d^2 equations are based on Duffie & Beckman (DUFFIE; BECKMAN, 2013):

$$\cos\theta_{hor} = \sin(\delta)\sin(\varphi) + \cos(\delta)\cos(\varphi)\cos(\omega) \quad (12)$$

$$d^2 = 1 + 0.033\cos((DOY\ 2\pi)/365) \quad (13)$$

where $\theta_{hor}$is the solar zenith angle over a horizontal surface, and δ the declination of the Earth,

δ = latitude of the pixel, ω = hour angle and DOY = day of year.

Soil heat flux

Soil heat flux (G) is computed with the following equation, calibrated with remote sensing data and ground measurements at the flux towers:

$$G = R_n(T_s - 273.15)(0.015\alpha)(1 - 0.8\,(NDVI)^{1/3}) \quad (14)$$

where T_s is the surface temperature (K).

Sensible heat flux

The following equation is used to estimate the sensible heat flux (H) (ALLEN et al., 2011):

$$H = \rho_{air} Cp \frac{dT}{r_{ah}} \quad (15)$$

where ρ_{air} is the air density ($kg.m^{-3}$), Cp the specific heat of air at constant pressure ($J.kg^{-1}K^{-1}$) and r_{ah} the aerodynamic resistance (s m^{-1}) between two near-surface heights, $z1$ and $z2$, where $z1$ = 0.1 and $z2$ = 2 m above the zero-plane displacement height. dT is the temperature gradient and represents a linear function of T_s, as proposed by Bastiaanssen et al. (BASTIAANSSEN et al., 1998b):

$$dT = aT_s + b \quad (16)$$

where a and b are empirically determined coefficients.

Since both H and r_{ah} are unknown, SEBAL uses an iterative process. For the first iterative process, r_{ah} is estimated assuming neutral stability (ALLEN; TASUMI; TREZZA, 2007):

$$r_{ah} = \frac{\ln(z2/z1)}{u_* k} \quad (17)$$

where z_1 and z_2 are the heights above the zero-plane displacement of the vegetation where dT are defined, u_* the friction velocity (m s^{-1}) and k the von Karman's constant (0.41).

To estimate u_* in the first iterative process, the following equation is used:

$$u_* = \frac{k\, u_{200}}{\ln(200/z_{om})} \quad (18)$$

where u_{200} is the wind speed (m s^{-1}) at 200m and z_{om} the momentum roughness length (m).

u_{200} is estimated as:

$$u_{200} = u_{*,ws}\, \frac{\ln\left(\frac{height}{z_{om}}\right)}{k} \quad (19)$$

where $u_{*,ws}$ is the friction velocity, and $height$ is assumed as 100 m (WATERS et al., 2002).

$u_{*,ws}$ is estimated as:

$$u_{*,ws} = \frac{k\, u_x}{\ln\left(\frac{z_{ws}}{z_{om}}\right)} \quad (20)$$

where z_{ws} is the height of the GLDAS information and u_x the wind speed (m s^{-1}).

z_{om} is assumed as:

$$z_{om} = 0.12(h) \quad (21)$$

where h is the vegetation height (m), assumed as $h = 3$ m.

In the iterative process, dT_{hot} is the gradient temperature at the hot pixel and is calculated with the following equation:

$$dT_{hot} = \frac{H_{hot}\, r_{ah\ hot}}{\rho_{hot}\, Cp} \quad (22)$$

where H_{hot}, $r_{ah\ hot}$ and ρ_{hot} are the sensible heat, aerodynamic resistance and air density at the hot pixel, respectively.

For H_{hot} and ρ_{hot} the following equations are used:

$$\rho_{hot} = -0.0046\, T_{s\ hot} + 2.5538 \quad (23)$$

$$H_{hot} = R_{n\ hot} - G_{hot} \quad (24)$$

where $T_{s\ hot}$, $R_{n\ hot}$ and G_{hot} are the land surface temperature, instantaneous net radiation and soil heat at the hot pixel, respectively.

To calculate the a and b coefficients of the linear relationship between T_s and dT, we consider dT_{cold} = 0 for the cold pixel (i.e., H_{hot}=0), which in combination with Equation 24 yields:

$$a = \frac{-dT_{hot}}{T_{s\ cold} - T_{s\ hot}} \quad (25)$$

$$b = dT_{hot} - a\, T_{s\ hot} \quad (26)$$

The next steps are the final part of the first iterative process. The Monin-Obukhov length (L) defines the stability conditions of the atmosphere in the iterative

process. This equation represents the height at which forces of buoyancy and mechanical mixing are equal (ALLEN; TASUMI; TREZZA, 2007):

$$L = -\frac{\rho_{air}\, Cp\, u*^3 T_s}{kgH} \quad (27)$$

where ρ_{air} is the air density (Kg m^{-3}), Cp the specific heat o fair at constant pressure (J Kg^{-1} K^{-1}), $u*$ the friction velocity (m s^{-1}), T_s the land surface temperature (K), k the von Karman's constant (0.41), g the gravitational acceleration (9.807 m s^{-2}) and H the sensible heat flux (W m^{-2}).

When L<0, the lower atmospheric boundary layer is unstable and when L>0, the boundary layer is stable. Momentum and heat transport ($\psi_m$and ψ_h) are computed using the following equations:

For L < 0:

$$\psi_{m\,(200\,m)} = 2\ln\left(\frac{1+x_{(200\,m)}}{2}\right) + \ln\left(\frac{1+x_{(200\,m)}^2}{2}\right) - 2\arctan\left(x_{(200\,m)}\right) + 0.5\pi \quad (28)$$

$$\psi_{h\,(2\,m)} = 2\ln\left(\frac{1+x_{(2\,m)}}{2}\right) \quad (29)$$

$$\psi_{h\,(0.1\,m)} = 2\ln\left(\frac{1+x_{(0.1\,m)}^2}{2}\right) \quad (30)$$

where:

$$x_{(200\,m)} = \left(1 - 16\frac{200}{L}\right)^{0.25} \quad (31)$$

$$x_{(2\,m)} = \left(1 - 16\frac{2}{L}\right)^{0.25} \quad (32)$$

$$x_{(0.1\,m)} = \left(1 - 16\frac{0.1}{L}\right)^{0.25} \quad (33)$$

For L>0:

$$\psi_{m\,(200\,m)} = -5\left(\frac{2}{L}\right) \quad (34)$$

$$\psi_{h\,(2\,m)=} -5\left(\frac{2}{L}\right) \quad (35)$$

$$\psi_{h\,(0.1\,m)=} -5\left(\frac{0.1}{L}\right) \quad (36)$$

In case of neutral conditions (L = 0), H=0, ψ_m=0 and ψ_h=0.

For the Equation 34, a value of 2 m is adopted instead of 200 m following the suggestion by Allen et al. (ALLEN; TASUMI; TREZZA, 2007), in order to avoid numerical instability.

Finally, r_{ah} and $u*$ are estimated again using the values obtained from $\psi_m$and ψ_h:

$$r_{ah} = -\frac{\ln(z_1/z_2)-\psi_{h(z_2)}+\psi_{h(z_1)}}{u*\,k} \quad (37)$$

$$u* = \frac{u_{200}\,k}{\ln(200/iz_{om})-\psi_{m\,(200\,m)}} \quad (38)$$

where iz_{om} is momentum roughness length for each pixel, which was based on the following equation, calibrated with remote sensing data and ground measurements at the flux towers:

$$iz_{om} = e^{((0.4\,(NDVI/\alpha)-2.4)} \quad (39)$$

The iterative process continues until the stability of stability conditions of the atmosphere is obtained and the absolute difference are lower than 0.1:

$$absolute\ difference = dT_{(n)} - dT_{(n-1)} + r_{ah\,(n)} - r_{ah\,(n-1)} \quad (40)$$

With the end of iterative process, we have a stable value of r_{ah}, and H is calculated using Equation 15.

Monthly evapotranspiration

The instantaneous latent heat is computed using the energy balance equation:

$$LE = R_n - G - H \quad (41)$$

The 8-day evapotranspiration (ET_{8-day}) is then computed with the following steps. Firstly, the evaporative fraction (Λ) is calculated:

$$\Lambda = \frac{LE}{R_n - G} \quad (42)$$

Then, the latent heat of vaporization (λ) (kJ kg^{-1}) is estimated as:

$$\lambda = 2.501 - 0.002361\,(T_s - 273.15) \quad (43)$$

The instantaneous evapotranspiration rate is computed as:

$$ET_{inst} = 0.0036\frac{LE}{\lambda} \quad (44)$$

ET_{8-day} is then calculated considering Λ constant during the 8-day period, while the 8-day net radiation ($R_{n,8-day}$) is estimated by averaging the daily net radiation ($R_{n\,24h}$) over eight days, which in turn is computed following de Bruin (BRUIN, 1987):

$$R_{n_{24h}} = (1-\alpha)Rs_{down\ 24h} - C_S(\frac{Rs_{down\ 24h}}{Ra_{24h}})$$

(45)

where $Rs_{down\ 24h}$ is the daily mean incoming shortwave radiation obtained from GLDAS 2.1 ($W\ m^{-2}$), C_S a constant set to 110, and Ra_{24h} the extraterrestrial radiation for a 24-hour period ($W\ m^{-2}$).

$$ET_{8-day} = 0.0864\ \Lambda \frac{R_{n,8-day}}{\lambda}$$

(46)

The monthly evapotranspiration is finally computed as the average of all 8-day values within a given month.

Validation of the SEBAL algorithm for evapotranspiration

The estimates from SEBAL algorithm are validated against 10 in situ flux towers for many years (Table S1; Figs. S9 and S10), which provide a massive amount of measured data considering data scarcity in South America. It includes four towers within the wetland areas and six in uplands close to the analyzed wetlands. Estimates from seven flux towers are based on the eddy covariance method, and three on the Bowen ratio method. Table S1 presents detailed information on the 10 towers.

Overall, the algorithm has a satisfactory performance for most flux towers, with Root Mean Square Error (RMSE) varying from 0.4 to 1.2 mm.day^{-1}, which is within the error range for most of the ET models used worldwide. The coefficient of determination (R^2) is found greater than 0.45 for five towers, and ET seasonality is generally well captured (Fig. S10). In the case of the Bananal wetland (BAN), the flux tower is located within a savanna-forest mosaic and this local landscape heterogeneity makes the ET estimate to be sensitive to the analyzed pixel (1 km resolution). Thus, if looking at two adjacent pixels the ET may become water-limited during the dry season (for savanna) or not (for forest). For the BAN tower, both ET pixels are shown in Fig. S9. Additionally, differences in the climatology, as seen in Fig. S9 may arise from the different period of analysis between the in situ (available period provided in Table S1) and SEBAL data (climatology for 2000-2015).

Finally, regarding the suitability of the adopted ET algorithm for estimating ET in wetlands, LST-based models as SEBAL have been argued as the most adapted ones, given the effects of surface water on LST (YILMAZ et al., 2014). This is especially true if compared to models based on vegetation indices and land cover maps, which have a poor representation of surface water(BIGGS et al., 2015). The applied SEBAL algorithm is the pioneer one and the most cited LST-based ET algorithm

(BASTIAANSSEN et al., 1998a), and the most used for wetlands so far, for both natural (AL ZAYED et al., 2016; FARAH; BASTIAANSSEN, 2001; KIPTALA et al., 2013; LAIPELT et al., 2020; LIU; HU, 2019; MOHAMED; BASTIAANSSEN; SAVENIJE, 2004; SUN et al., 2011) and artificial systems such as irrigated lands (AL ZAYED et al., 2016; BASTIAANSSEN, 2000; YANG; SHANG; JIANG, 2012). In addition, SEBAL also has a low sensitivity to input meteorological data, in comparison to other LST-based methods available at global scale (e.g., SSEBOp and METRIC) that are dependent on reference evapotranspiration estimates. This advantage makes SEBAL more suitable for poorly gauged areas as the South American wetlands. Given the overall satisfactory performance of SEBAL when compared to in situ data, and the suitability of its conceptualization, we conclude that SEBAL is today one of the most appropriate algorithms to be employed for the characterization of wetland ET dynamics.

13.2.6 Supplementary Material of Chapter 11

S1. Characteristics and simulation of reservoirs in the Upper Paraná River Basin

Table S1 presents characteristics of the 31 simulated dams: name, dam location (coordinates), regulation flag (1: regulation dam; 0: run-of-river dam), minimum and maximum operation levels, maximum exceptional level, simulated average discharge, design discharge, total (referring to total volume at maximum normal operation level) and active storage, and installed capacity. The dams in Table S1 are presented in the map of Figure 11.1.

Regarding the operation rule "R" (see Section 11.2.4), Table S2 presents the Pearson correlation coefficients obtained for each month for each dam, for the regressions between observed monthly average water levels and dam outflows. Months with correlation higher than 0.4 were considered as meaningful.

Regarding the operation rule "S" (see Section 11.2.4), based on (SHIN; POKHREL; MIGUEZ-MACHO, 2019), the parameter R was estimated with two values. Firstly, a generic estimation is derived from the proposal by (SHIN; POKHREL; MIGUEZ-MACHO, 2019) (i.e., $R_i = \min(1, \propto c_i)$, Equation 2). Secondly, it was calibrated based on observed daily dam outflows (minimizing RMSE of discharges). Then, Figure S1 presents (left column) a scatterplot between calibrated and estimated values for the parameter R, for each of the simulated dams. On the right, it shows the mean RMSE values obtained when considering calibrated and estimated R values.

Table S1

Main characteristics of the 31 simulated dams.

ID	Name	Lat	Lon	Reg. Flag	Min level (m)	Max level (m)	Max excep. level (m)	Average discharge (m³/s)	Design discharge (m³/s)	Total Storage (hm³)	Active Storage (hm³)	Installed capacity (MW)
1	Jurumirim	-23.211	-49.230	1	559.7	568	569.5	178	2572	7702	3165	101
2	Água Vermelha	-19.867	-50.346	1	373.3	383.3	383.4	1297	19848	11028	5169	1396
3	Barra Bonita	-22.519	-48.534	1	440.5	452.5	454	292	4530	3136	2566	141
4	Batalha	-17.348	-47.484	1	785	800	801	53	1648	1782	1352	52
5	Caconde	-21.577	-46.624	1	833	863	865.5	31	1778	555	540	80
6	Cacu	-18.532	-51.149	1	475	477	477.1	105	2953	232	35	65
7	Camargos	-21.326	-44.616	1	899	913	913.1	74	2242	792	672	45
8	Capim Branco 1	-18.790	-48.147	1	623.3	624	625.5	181	9354	241	13	240
9	Capivara	-22.658	-51.360	1	321	334	336	860	17248	10541	5725	627

10	Chavantes	-23.129	-49.731	1	465.23	474	475.5	278	3252	8795	3041	414
11	Corumba I	-17.989	-48.531	1	572	597	597.5	181	6800	1496	1025	375
12	Corumba III	-16.787	-47.941	1	768	772	772.1	61	1854	943	260	47
13	Corumba IV	-16.325	-48.188	1	837	842	843.3	50	1280	3727	810	127
14	Emborcação	-18.452	-47.986	1	615	661	661.3	195	8200	17725	13056	1192
15	Foz Do Areia	-26.010	-51.660	1	700	742	745	404	10030	5779	3805	2500
16	Furnas	-20.670	-46.317	1	751	769	770.3	566	13000	22950	17217	1312
17	Ilha Solteira	-20.382	-51.364	1	323	328	328.4	3075	37905	21059	5516	3444
18	Itaipu	-25.407	-54.589	0	197	220.3	223.1	8314	62200	29000	19000	14000
19	Itumbiara	-18.408	-49.098	1	496	521	522.2	713	16000	17027	12454	2280
20	Marimbondo	-20.305	-49.197	1	426	446.3	447.36	1131	21400	6150	5260	1488
21	Mascarenhas Moraes	-20.285	-47.064	1	653.12	666.12	666.92	625	10400	4040	2500	478
22	Mauá	-24.059	-50.712	1	626	635	636.5	162	7173	2137	664	363
23	Miranda	-18.912	-48.041	1	695	698	698.95	178	9000	1120	146	408
24	Nova Ponte	-19.133	-47.694	1	775.5	815	815.52	159	5800	12792	10380	510
25	Promissão	-21.296	-49.783	1	379.7	384	385.3	482	6680	7407	2127	264
26	Salto Santiago	-25.650	-52.620	1	481	506	509	598	27830	6775	4113	1420
27	Santa Clara	-25.650	-51.970	1	787.5	805	810.15	41	6550	431	262	118
28	Sao Simão	-19.018	-50.499	1	390.5	401	401.8	1226	24100	12540	5540	1710
29	Segredo	-25.790	-52.110	1	602	607	608	511	16200	2943	384	1260
30	Serra do Facão	-18.074	-47.665	1	732.5	756	756.98	75	2683	5199	3447	213
31	Três Irmãos	-20.669	-51.300	1	323	328	328.4	584	9500	13677	3448	808

Table S2

Correlation between monthly average water levels and dam outflows for each simulated dam.

ID	Name	Jan	Feb	Mar	Apr	May	Jun	Jul	Aug	Sep	Oct	Nov	Dec
1	Jurumirim	0.60	0.57	0.41	0.39	0.33	0.37	0.46	0.43	0.34	0.49	0.51	0.57
2	Água Vermelha	0.51	0.56	0.74	0.56	0.70	0.68	0.48	0.52	0.42	0.10	0.49	0.44
3	Barra Bonita	0.27	-0.03	0.04	0.20	0.22	0.30	0.16	0.24	0.14	0.42	0.35	0.22
4	Batalha	0.31	-0.66	-0.40	-0.34	-0.16	-0.02	0.40	0.42	0.72	0.45	0.19	0.79
5	Caconde	0.44	0.50	0.47	0.47	0.49	0.58	0.60	0.57	0.47	0.48	0.78	0.64
6	Cacu	0.71	0.76	0.45	0.89	0.58	0.62	0.54	0.55	0.55	0.38	0.72	0.89
7	Camargos	0.69	0.72	0.66	0.51	0.46	0.52	0.52	0.36	0.36	0.37	0.60	0.52
8	Capim Branco 1	-0.07	-0.56	0.16	0.10	-0.12	-0.03	-0.69	-0.60	0.19	0.17	0.24	0.32

9	Capivara	0.49	0.40	0.28	0.25	0.30	0.42	0.56	0.48	0.40	0.50	0.40	0.42
10	Chavantes	0.56	0.50	0.36	0.49	0.42	0.36	0.37	0.12	0.22	0.25	0.34	0.40
11	Corumba I	0.56	0.42	0.55	0.51	0.16	0.55	0.58	0.47	0.63	0.47	0.55	0.70
12	Corumba III	0.64	0.40	0.56	0.59	0.60	0.77	0.45	0.47	-0.10	0.06	0.17	0.44
13	Corumba IV	0.39	0.33	0.75	0.58	0.02	-0.65	-0.80	-0.29	0.46	0.68	-0.50	-0.03
14	Emborcação	0.36	0.49	0.67	0.66	0.56	0.55	0.74	0.71	0.69	0.24	0.35	0.32
15	Foz Do Areia	0.35	0.44	0.56	0.44	0.56	0.44	0.73	0.59	0.66	0.63	0.52	0.47
16	Furnas	0.56	0.57	0.61	0.52	0.65	0.58	0.64	0.58	0.42	0.18	0.45	0.46
17	Ilha Solteira	0.19	0.14	0.32	0.45	0.56	0.58	0.67	0.68	0.61	0.60	0.44	0.42
18	Itaipu	0.49	0.43	0.55	0.41	0.43	0.63	0.54	0.41	0.45	0.29	0.47	0.37
19	Itumbiara	0.37	0.41	0.57	0.58	0.60	0.61	0.37	0.39	0.34	0.20	0.37	0.22
20	Marimbondo	0.54	0.52	0.64	0.43	0.50	0.58	0.54	0.31	0.29	0.38	0.52	0.35
21	Mascarenhas Moraes	0.43	0.44	0.50	0.58	0.79	0.75	0.67	0.60	0.57	0.34	0.48	0.61
22	Mauá	0.71	0.97	0.79	0.96	0.93	-0.56	0.72	0.92	0.90	0.99	-0.96	0.85
23	Miranda	0.15	0.04	0.22	0.30	-0.30	0.13	0.24	0.29	0.34	-0.12	0.20	0.20
24	Nova Ponte	0.44	0.41	0.55	0.51	0.33	0.37	0.45	0.41	0.40	0.48	0.44	0.41
25	Promissão	0.73	0.46	0.58	0.30	0.21	0.33	0.55	0.51	0.54	0.68	0.63	0.43
26	Salto Santiago	0.47	0.50	0.58	0.48	0.67	0.57	0.69	0.57	0.62	0.61	0.62	0.56
27	Santa Clara	0.70	0.52	0.81	0.92	0.77	0.63	0.70	0.67	0.80	0.77	0.74	0.79
28	Sao Simão	0.39	0.39	0.51	0.52	0.61	0.69	0.74	0.61	0.39	0.11	0.42	0.46
29	Segredo	0.69	0.73	0.72	0.61	0.67	0.53	0.75	0.69	0.74	0.73	0.57	0.55
30	Serra Facão	0.88	0.80	0.89	0.92	0.75	0.55	0.50	0.30	0.60	0.72	0.54	0.65
31	Três Irmãos	0.22	0.26	0.46	0.40	0.51	0.57	0.52	0.42	0.50	0.26	0.15	0.38

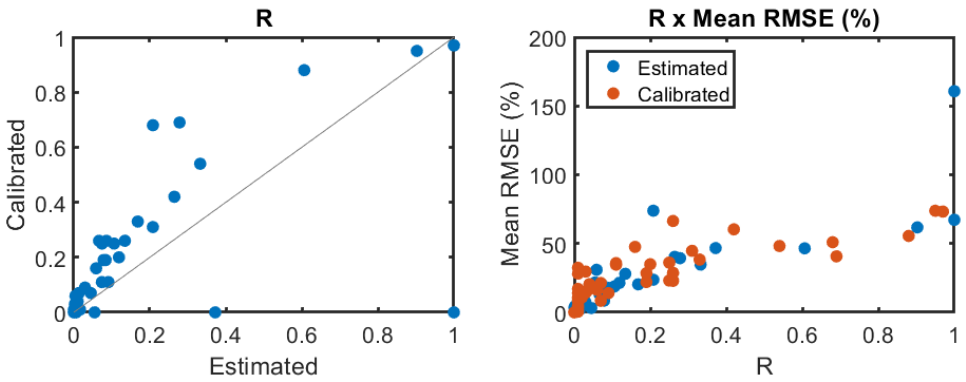

Figure S1. On the left scatterplot between calibrated and estimated values for the parameter R for each of the simulated dams from the operation rule "S" based on (Shin et al. 2019). On the right mean RMSE values between observed and simulated dam outflows when considering calibrated and estimated R values are presented.

S2. MGB model application in the Upper Paraná River Basin

Figures S2-S7 describe the MGB model application for the Upper Paraná River Basin.

The model was forced with in-situ precipitation data (Figure S2). Quality control was performed by discarding data considering the following criteria: i) rain stations with less than 75% of information in the historical series; ii) daily rainfall values above 200 mm in a continuous series (i.e. without failures) were considered as outliers; and iii) values above a certain threshold immediately after a day with missing data. The following methodology was adopted for the generation of daily rainfall for each unit-catchment: i) the in-situ daily rainfall data from 2030 stations were interpolated following the natural neighbor methodology for a rainfall grid with a spatial resolution of 0.25° (~25 kilometers at the Equator) usually adopted in global rainfall databases (e.g. satellites climate analysis etc.); and ii) therefore from this grid-shaped database the daily precipitation information was interpolated to the unit-catchment's centroids using the nearest neighbor's method.

Soil and vegetation parameters were calibrated based on Hydrological Response Units (HRU's) defined from soil and vegetation map classification (Figure S3b) and sub-basins (Figure S3a). The model was calibrated and validated against 143 in-situ daily discharge data considering the natural flow scenario (i.e. without reservoirs) (Figure S3b). Then for gauges downstream of dams we considered the pristine flows available by ONS. The basin was divided into unit-catchments (Figure S4a) and for which unit-catchment hydraulic parameter values of bankfull width and depth were defined (Figure S4b S4c and S4d). For large rivers bankfull width values were estimated from the global surface water mask from (Pekel et al. 2016). The surface water area within each unit-catchment was divided by the reach length (10 km) to yield the effective reach width. For smaller rivers for which there were no surface water data available width values

were estimated from specific geomorphic relationships estimated for major tributary's basins. They were derived by relating the unit-catchment drainage area and reach width for the unit-catchment that had surface water estimates (Figure S4d). Bankfull depth values were estimated from the (Andreadis et al. 2013) database. However given high bias in some of these estimates we adopted a multiplied of the depth value for each sub-basin which was manually calibrated to yield satisfactory flood attenuation during the discharge calibration step. The adopted effective bankfull width and depth values are presented in Figure S4b and S4c respectively. The basin downstream boundary condition was set as a constant water level (from SRTM) at Yaciretá dam the Manning coefficient was globally set to 0.03 and the time step alpha parameter for model stability adopted as $\propto$=0.3.

Model performance is presented in Figure S5 considering Nash-Sutcliffe of discharges (NSE) and logarithm of discharges (NSE-log) and bias metrics for the period of calibration (1990-2010) and validation (1980-1990). Selected simulated and observed hydrographs at sites representative of the basin hydrological behavior are presented in Figure S6 for the locations of Tibagi (Tibagi river) União da Vitória (Iguaçu River) Ivinhema (Ivinhema River) Furnas dam (Grande River) Itaipu dam (Paraná mainstem) and Itumbiara dam (Paranaíba river). Finally Figure S7 presents histograms of the performance metrics highlighting the overall satisfactory MGB model application in the Upper Paraná River Basin.

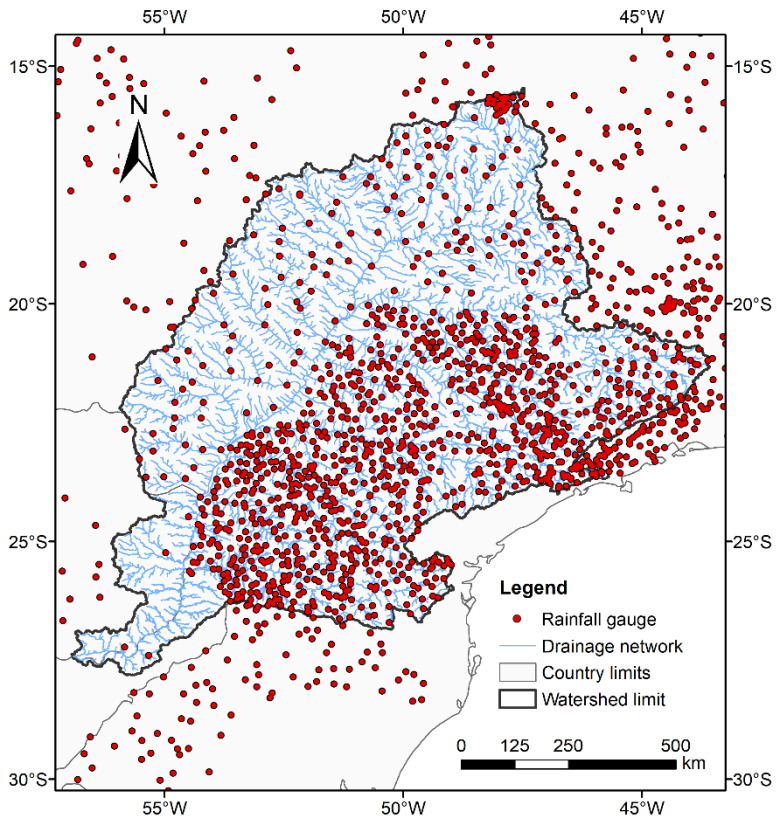

Figure S2. Spatial distribution of in-situ rainfall stations.

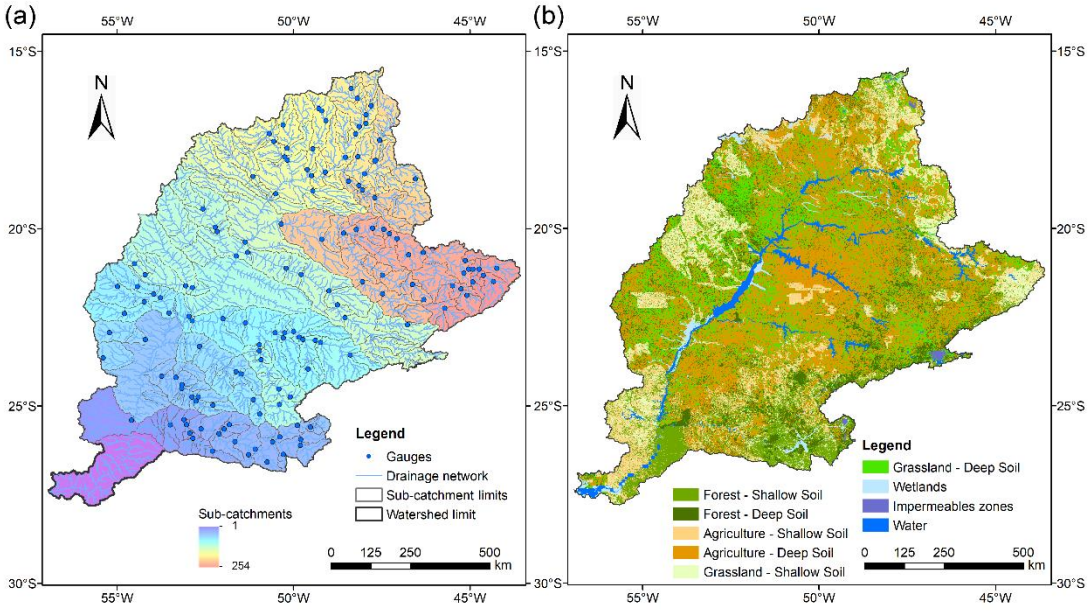

Figure S3. (a) Location of in-situ discharge gauges used for calibration and validation as well as sub-basins used for model calibration. (b) Map of HRU's used for defining model soil and vegetation parameters.

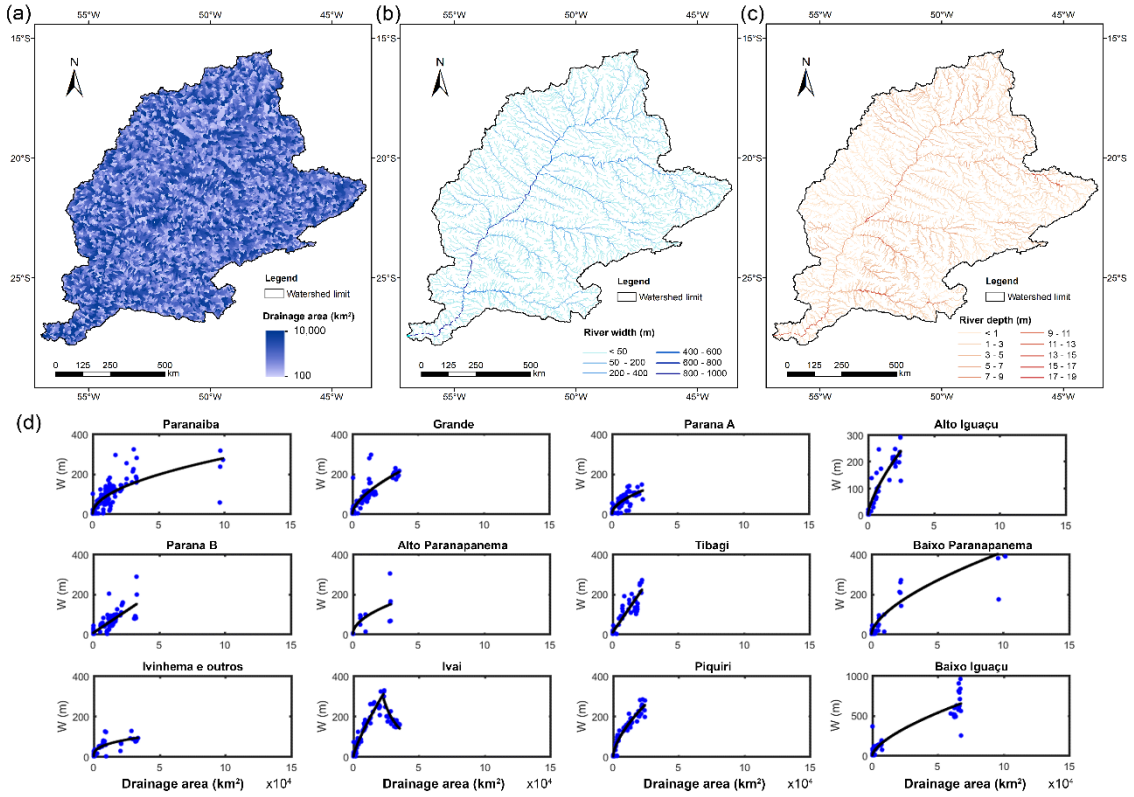

Figure S4. Maps of (a) unit-catchments (b) bankfull width and (c) bankfull depth. (d) Geomorphic relationships between bankfull width and drainage area obtained for each main tributary of the basin.

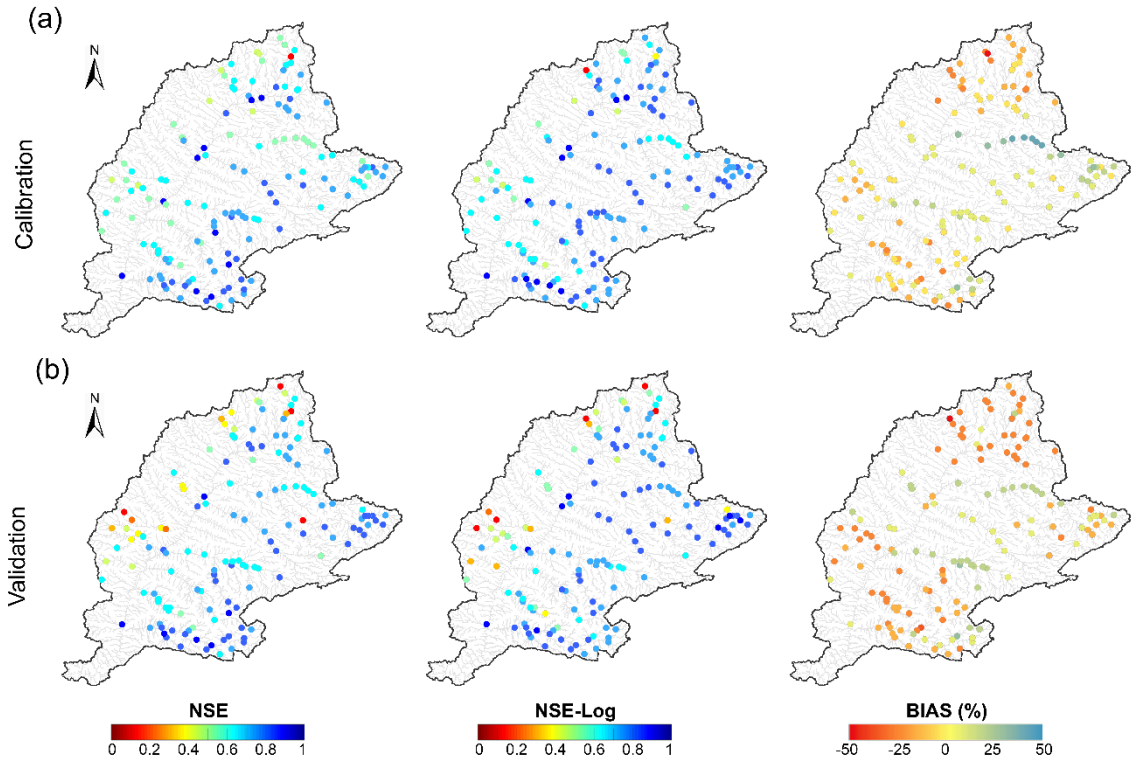

Figure S5. Performance of model calibration (1990-2010) and validation (1980-1990) for the in-situ discharge gauges for Nash-Sutcliffe of discharges (NSE) and logarithm of discharges (NSE-log) and bias metrics.

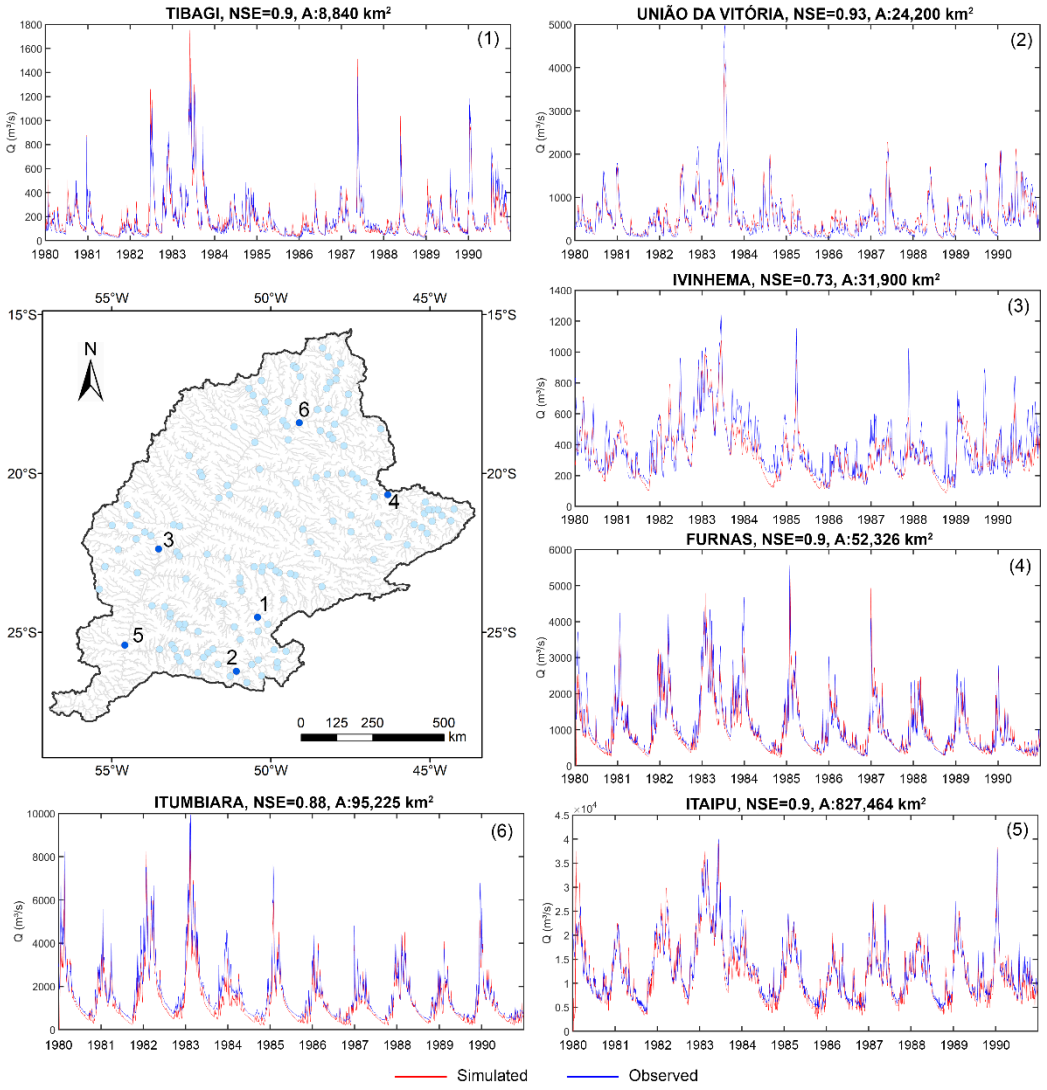

Figure S6. Simulated and observed hydrographs at Tibagi (Tibagi river) União da Vitória (Iguaçu River) Ivinhema (Ivinhema River) Furnas dam (Grande River) Itaipu dam (Paraná mainstem) and Itumbiara dam (Paranaíba river).

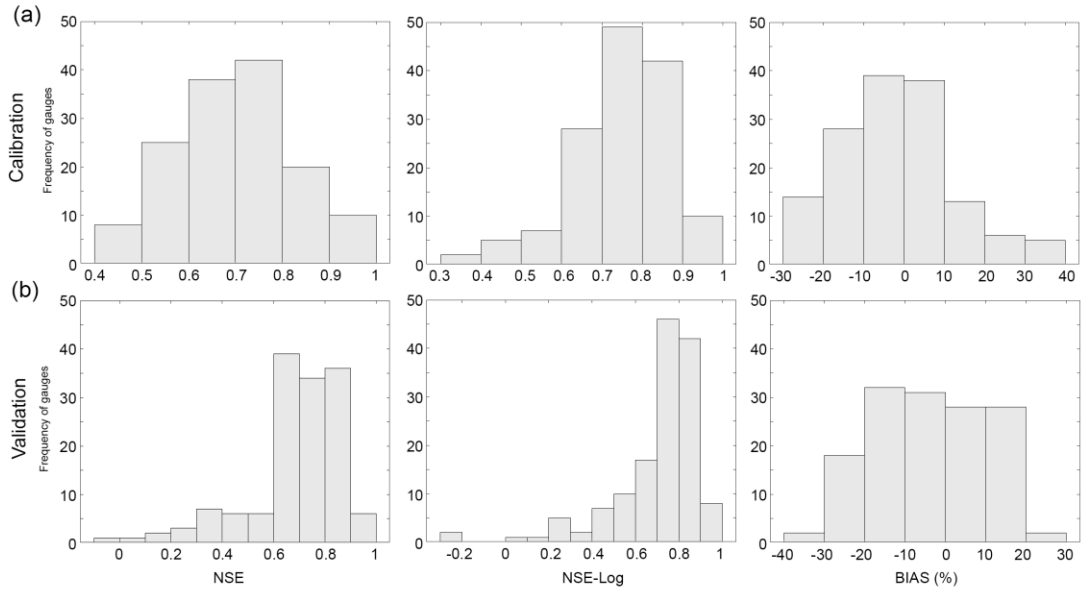

Figure S7. Histograms of model performance (NSE, NSE-log and Bias) for the calibration (1990-2010) and validation (1980-1990) periods for the 143 analyzed discharge gauges.

S3. Basin-wide spatial assessment of the simulation of reservoirs

A spatial assessment of the representation of reservoirs within the model was performed for the whole drainage network by comparing, for each river reach, the simulated discharges with operation rules with those estimated from a new model run forced with observed dam outflows. The latter was considered as a reference, since it only used MGB model estimates for lateral inflows between adjacent dams. This methodology follows the one proposed by Passaia et al. (2020) for Brazilian rivers.

When looking at the model performance across the whole drainage network, a similar pattern as **Erro! Fonte de referência não encontrada.**a arises (Figure S8). This analysis, however, stresses the capability of the model to estimate discharges along the lower parts of the Paraná mainstem and the Iguaçu river (NSE>0.6 with R rules). RV was just slightly better than RgV, especially for the Upper Paranaíba and Grande rivers, and both were better than SV and TV. This analysis also enables an easy, spatial understanding of how satisfactory each dam is being simulated: in the case of RV rule, Chavantes dam (ID 10) in the Paranapanema river should be improved (NSE<0), while when moving to a more global approach (RgV), Furnas (ID 16) in the Grande and several ones in the Upper Paranaíba river would require more attention.

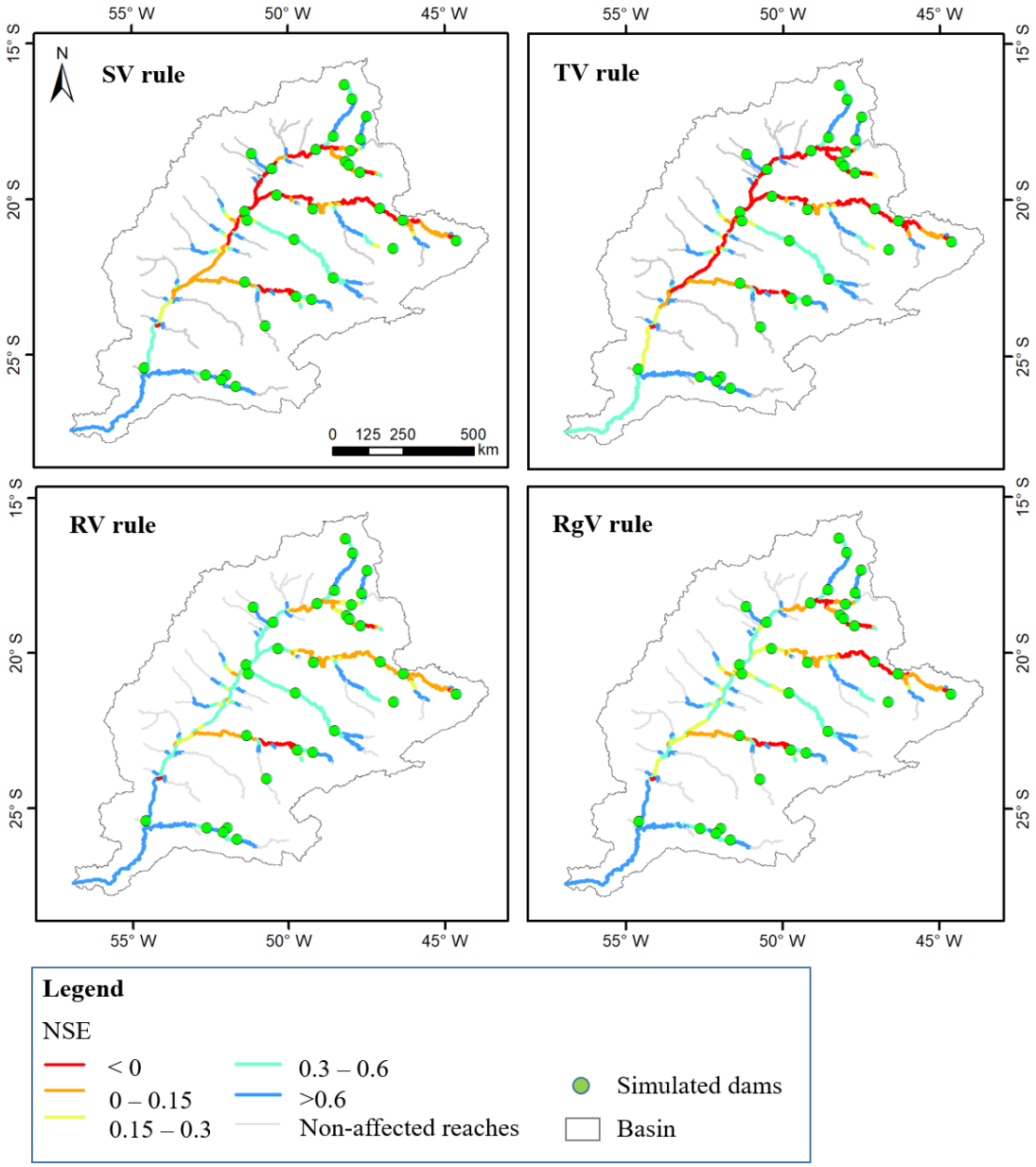

Figure S8. Basin-scale assessment of model performance for three operation rules with reservoir simulation type V (SV, TV, RV). The global approach RgV is also presented. For each river reach, model discharge estimates were compared to a run forced with observed dam outflows.